THREE-DIMENSIONAL SEDIMENT TRANSPORT MODEL

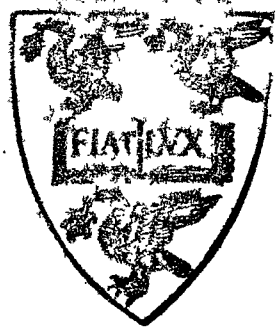

Thesis submitted in accordance with the requirements

of the University of Liverpool

for the degree of Doctor in Philosophy

by Hyoseob Kim

May 1993

to my wife Youngae

ACKNOWLEDGEMENT

I wish to thank my supervisor Professor B. A. O'Connor, Liverpool University, U.K. for his setting-up my thesis structure, introducing the vertical modelling area, improving my writing skill, advice on accurate presentation, extensive revision of the thesis, and arrangement of grants. I also wish to thank Dr. K.-D. Yum, and Dr. W. O. Song, Korea Ocean Research and Development Institute (KORDI), for providing me the opportunity to work at Liverpool University. I am grateful for financial assistance from the Department of Civil Engineering, Liverpool University, KORDI, the British Council in Seoul, and UNDP. I am indebted to Dr. J. Nicholson, Liverpool University, for providing me with technical information, and Mr. J. Harris, Liverpool University, for his help with my English in my draft thesis.

ABSTRACT

The thesis describes the development of a number of simplified numerical models for the simulation of sediment transport and medium-term bed level changes at coastal sites with structures, where flow processes are dominated by wave-induced currents. Emphasis is placed on the development of the simplest level of model which retains the dominating processes leading to bed level changes. The complete model system is found to be composed of wave-period-averaged, two-dimensional depth-mean wave and wave-induced current models combined with a three-dimensional suspended sediment model and an associated bed level change model.

Ebersole et al.'s(1986) elliptic evolution wave model is modified by ignoring the second derivative term of wave amplitude in the direction of main wave propagation. The modified model results gave close agreement with Ebersole et al.'s own model, and with experimental data. The numerical schemes are modified at land grid points for application to general seabed and coastal bathymetry. In the lee of coastal structures, it has been necessary to introduce a separate computational method based on Penney and Price's(1952) analytical diffraction method in order to reproduce the diffracting effect of the structures.

Yoo and O'Connor's(1986a) wave-induced current model was used to calculate wave-

induced currents but was modified to avoid the need for a complex lateral mixing sub-model. The unsteady momentum equations were simplified by ignoring the turbulent lateral mixing terms, but their effect was simulated by using a diffusion approach to spread the radiation stress terms over the surf zone. The spreading method was found to give good agreement with both Longuet-Higgins'(1970) velocity profile solutions and laboratory measurements on a plane beach.

The three-dimensional suspended sediment mass conservation equation and the seabed level change equation were adopted to reproduce seabed changes. The relevant equations were solved by finite difference numerical methods. The governing equation of suspended sediment was transformed into a boundary-fitted, and vertically stretched coordinate system. A new inter-wave-period (IWP) empirical formula for the reference level concentration was proposed and calibrated with laboratory and field data from Chukpyon Harbour, Korea; data being collected using a new four-trap device. Bed load was predicted by a new IWP formula, which was calibrated with Chukpyon data. The sediment model results were compared with analytical solutions and gave close agreement.

The bed shear stress, vertical diffusion coefficient profile, and horizontal velocity profiles in the sediment transport model were obtained from a new 2DV boundary layer model for wave and current flows. The boundary layer model included the effect of the nonlinear advection terms and the vertical velocity. This approach was able to simulate

different velocity profiles for following and opposing currents with waves. The 2DV boundary layer model results were compared with laboratory data and gave good agreement. For the simulation of siltation at Chukpyon, the 2DV model results were parameterized for a restricted range of general variables and stored in a tabular form in the computer; linear interpolation being used to obtain particular values.

The total wave, current, and sediment model system was applied to Chukpyon Harbour, Korea to reproduce bed level change over a five month period. The wave model results showed reasonable agreement with measurement. The wave-induced current model was found to give a similar order of velocity at field measurement points; velocities being measured with an RCM-5P current meter mounted on a bed frame. The sediment model was found to reproduce the measured suspended sediment concentration profiles quite well, although considerable scatter was found in the field results. Finally, the bed level change during a five month storm period was reasonably well reproduced by the total model system.

LIST OF CONTENTS

LIST OF TABLES

LIST OF FIGURES

LIST OF PLATES

LIST OF SYMBOLS

A	= near bed wave orbital excursion length amplitude; vertical coordinate transform coefficient
a	= wave amplitude; reference level
B	= spatial volume of interest
C	= Chezy coefficient; depth-mean concentration
C_i	= wave phase velocity vector
$C_1, C_2, \cdots$	= coefficients
c	= wave phase velocity; sediment concentration
c_a	= reference level concentration
c_a^∞	= equilibrium reference level concentration
c_g	= wave group velocity
c_0	= deep sea wave phase velocity
D	= deposition rate
D_x, D_y	= dispersion coefficients in the x, y directions
D_*	= non-dimensional particle diameter
d	= mean water depth
d_b	= depth at breakerline
d_{50}	= median diameter
d_{90}	= 90 % diameter

$\tilde{d}$ = instantaneous depth

d_r = depth under wave trough

E = wave energy density

$F_{b,i}$ = turbulent bed shear stress vector

$F_{b,x}$, $F_{b,y}$ = turbulent bed shear stress in the x, y directions

$F_{l,i}$ = turbulent lateral shear stress vector

f_a = a current-related friction factor

f_c = a current-related friction factor

f_c' = a current-related friction factor

f_w = wave friction factor

H = wave height

g = acceleration due to gravity

h = still water depth

H_b = breaking wave height

H_s = significant wave height

K_d = diffraction coefficient

K_i = wave number vector

k = wave number

k_a = apparent roughness

k_x, k_y = x, y components of wave number vector

k_s = Nikuradse roughness

L = wave length

L_{wc} = wave length relative to the fixed frame

l = mixing length

M_i = depth-integrated mass transport rate

N = a turbulent closure coefficient

n = c_g/c; normal direction; porosity of the seabed

P = pickup rate

P_c = current-related pressure gradient

$P_{c,f}$ = interpolated pressure gradient

$P_{c,1}$, $P_{c,2}$ = trial pressure gradients

P_i = pressure gradient vector

P_x, P_y = mean pressure gradient in the x, y directions

p = static pressure in the fluid

p_0 = hydrostatic pressure from mean water level

p_* = a non-dimensional constant

$\vec{Q}$ = vertically integrated function of horizontal velocity in the wave propagation direction

q_b = bed load

q_{bx}, q_{by} = x, y components of bed load

q_s = suspended load

q_t = total load

R_x, R_y = gradients of radiation stresses in the x, y directions

$R_{x,f}$, $R_{y,f}$ = spreaded gradients of radiation stresses in the x, y directions

S_{XX} = radiation stresses in the wave direction

S_{YY} = radiation stress in the wave normal direction

S_{ij} = radiation stress tensor

s = wave phase function

T = wave period

$\hat{T}_i$ = turbulent shear stress

T_* = non-dimensional shear stress parameter

t = time

U,V = depth-mean currents in the x,y directions

$U_i = \vec{U}$ = depth-mean current vector

U_x, U_y = depth-mean currents in the x,y directions

$\tilde{U}$ = instantaneous depth-mean current in the x direction

U_∞ = near bed wave orbital velocity amplitude

U_r = depth-mean return current

u,v,w = instantaneous velocities in the x,y,z directions

u_b = depth-mean velocity in the bed load layer

u_s,v_s,w_s = instantaneous sediment velocities in the x,y,z directions

u_* = shear velocity

$u_{*,c}$' = current-related effective shear velocity

V_* = Longuet-Higgins non-dimensional variable for velocity

V_b = V at breaker line

w' = transformed vertical velocity on (x',y',σ) coordinates

w'' = $w'd$

w_f = sediment particle fall velocity

w_f' = w_f/d

x,y,z = three components of Cartesian coordinate

x_b = x at breakerline

x_* = Longuet-Higgins non-dimensional variable for distance

z_a = $k_a/30$

z_b = seabed level

z_0 = k_s / 30

$z_{*,peak}$ = non-dimensional height for peak eddy viscosity

α = spreading coefficient

α_x, α_y = spreading coefficient for R_x, R_y

α_b = a breaking coefficient

α_{wc} = a wave current interaction coefficient

β = proportional constant between sediment diffusion coefficient and fluid eddy viscosity; bed slope angle

γ = breaking index; van Rijn's coefficient for apparent roughness

Δ = increment

Δ_r = ripple height

δ_{ij} = delta function

δ_s = sediment-related near-bed mixing layer thickness

δ_w = wave-related boundary layer thickness

$\epsilon_x, \epsilon_y, \epsilon_z$ = eddy viscosities in the x, y, z directions

$\epsilon_{sx}, \epsilon_{sy}, \epsilon_{sz}$ = sediment diffusion coefficients in the x, y, z directions

$\epsilon_{sz,w}$ = wave-related vertical sediment diffusion coefficient

$\epsilon_{sz,c}$ = current-related vertical sediment diffusion coefficient

$\epsilon_{z,*}$ = non-dimensional vertical diffusion coefficient

η = mean water level; a transformed vertical axis

θ_b = angle between bed contour and y axis

θ_{wc} = interaction angle between wave and current

$\theta = \theta_w$ = wave direction

θ_c = current direction

κ = von Karman constant (=0.4)

λ = ripple length

μ_c = efficiency factor for currents

μ_w = efficiency factor for waves

ν = water kinematic viscosity

ξ = instantaneous water level

π = 3.141592

ρ = water density

ρ_s = sediment density

σ = wave angular frequency; σ-transformed vertical coordinate

σ_0 = wave angular frequency on a moving frame

τ_{ij} = shear stress tensor

$\tau_{b,c}'$ = current-related effective bed shear stress

$\tau_{b,w}'$ = wave-related effective bed shear stress

$\tau_{b,wc}'$ = wave and current-related effective bed shear stress

τ_{cr} = critical shear stress

Φ_b = non-dimensional bed load transport rate

Φ = wave velocity potential (= Φ (x,y,t))

ϕ = wave velocity potential (= ϕ (x,y))

$\tilde{\phi}$ = wave velocity potential (= $\tilde{\phi}$ (x,y,z,t))

Ψ = Shields parameter; stream function

Ψ_c = current-related Shields parameter

Ψ_{cm} = modified current-related Shields parameter due to waves

Ψ_{cr} = critical Shields parameter

Ψ_r = modified Shields parameter due to ripples

Ψ = stream function

∇ = two-dimensional gradient operator

$\times$ = vector cross product

$\bar{}$ = turbulent, wave mean value

$\tilde{}$ = wave-related variation value

'	= turbulent variation value
ˆ	= current and wave components
$< >$	= wave-period-average value

Superscript

*	= temporary value

Subscript

α,β	= tensor indices (x,y,z)
b	= breaking
max	= maximum
m	= measured
c	= calculated
f	= final value
up	= upper layer
low	= lower layer
peak	= peak point
half	= peak/2 point
*	= non-dimensional value

CHAPTER 1. INTRODUCTION

1.1 Initiation of the Study

Many coasts have suffered erosion or accretion as a result of the development of new ports and harbours. Traditionally, such problems have been investigated by a combination of field and physical model studies supplemented by experience. In more recent times, numerical computer model studies have started to replace physical model studies. Such numerical modelling is potentially very cost effective.

Considerable progress has been made over the last decade in the computer modelling of coastal processes, see O'Connor(1991). Unfortunately, many of the newly-emerging models are too expensive to use for the study of medium or long-term($>$ 1 year) changes in coastal bathymetry. In addition, many recent models are very complex involving many interacting processes and are untested in field situations. A need exists, therefore, for the development of a series of relatively simple models which retain dominating processes but which can be used for medium to long-term simulation. The present work describes such a development and its application to study the seasonal variation of seabed bathymetry in the vicinity of Chukpyon Harbour, which is situated on the east coast of Korea, see Fig. 1.1, and Plate 1.1.

Initial work on the construction of a fishing harbour at Chukpyon began in 1905, but in 1963 increasing harbour siltation led to the construction of a western breakwater in an attempt to reduce the problem. Subsequently, the eastern breakwater was extended between 1968-1972 in a further attempt to limit harbour dredging, but with limited success, see Fig. 1.2. In 1986, a field study was initiated by the Pohang District Maritime and Port Authority in order to assist with both an understanding of the problem and the design of new works. Further fieldwork was undertaken in 1987, 1988, and 1989, by staff from the Korea Ocean Research and Development Institute(KORDI) in Korea. The present author, as a part-time member of KORDI's staff, has assisted in the planning and collection of data from the site for use in the present work.

Fieldwork at Chukpyon showed that tidal effects at the site were small with the amplitude of the major tidal components (M_2, S_2, O_1, K_1) being only 4.9 cm, 1.1 cm, 4.3 cm, and 4.2 cm, respectively, while wind and density-induced currents were also found to have a negligible influence on sediment movements. Wave periods were found to be in the range 4-10 seconds and to be associated with significant wave heights up to 3 m in size.

The fieldwork suggests that the sediment transport processes at Chukpyon are likely to be dominated by waves and nearshore wave-induced currents, produced by winds from only a limited number of directions. Consequently, it is possible to use a series of simplified models to study sediment movements at the site and to build up long-term bed level changes by combining together the seabed accretion/erosion patterns produced by

the dominated seasonal winds.

A key element in the development of accretion and erosion patterns along coastlines with fine to medium sandy sediments and coastal structures is the three-dimensional nature of sediment movements, particularly in suspension. The present work, therefore, adopts the combination of a two-dimensional horizontal wave height and direction model, an associated wave-induced current model and a three-dimensional sediment transport model to study the three-dimensional suspended sediment pattern. The associated seabed accretion/erosion pattern is then obtained by using a bed level change sub-model, which interfaces with the suspended sediment model.

The total model system thus involves the use of a wave propagation model to route the seasonal design wave (characterized by its significant height and peak period of the wave spectrum) inshore. The computed wave height field is then used to calculate wave radiation stresses in a wave-induced current model, assuming no interaction between the wave and current fields. The results from the wave and current models are then used to determine the movement of sediment in suspension and as bed load in the three-dimensional sediment transport model. Finally, seabed accretion/erosion zones are determined from a sediment continuity equation. The total model system is illustrated diagrammatically in Fig. 1.3.

For long term changes, the individual erosion/accretion patterns are combined together depending on the occurrence of the individual seasonal events.

1.2 Scope of the Study

In order to produce cost-effective, working engineering models, it is necessary to introduce a number of simplifications into the model system. These are listed below.

(i) It is assumed that all models use wave-period-average variables. Such a step is necessary to enable the choice of sensible model space and time steps and thus the coverage of a sufficiently large computational area so that model offshore boundaries are independent of nearshore effects, while model computation time and cost is kept to a minimum.

(ii) Wave boundary conditions are assumed to be provided at the open sea model boundary, either from a deep water wave hindcast model or preferably from measured field data. Wind growth effects are ignored, therefore, over the nearshore modelled area.

(iii) A design-wave approach is used for the wave model involving the significant wave height and peak period of the wave spectrum. Such an approach has been shown, O'Connor et al.(1992a), to give a good approximation of peak orbital velocities.

(iv) Linear wave theory is used to determine near-bed velocities. Such an approach has also been shown by recent EC MAST research (O'Connor personal communication) to describe peak velocities, even in the surf zone, although inter-wave distribution is distorted.

(v) Only turbulent wave and current flow is considered to be important to the transporting process. Wind-induced and tide-induced transport is neglected as suggested by field data at Chukpyon.

(vi) Individual seasonal storms are assumed to last long enough so that a steady-state transport pattern is established.

(vii) Eddy viscosity enhancement by wave and current motion is included but not by wave breaking in the surf zone; it being assumed that plunging breakers are not present due to the smallish bed slope (1/50).

(viii) On-offshore sediment transport and shoreline advance/retreat is neglected, since the shoreline movement is not the main interest of the present study; the main purpose being to look at siltation around the structures, which causes blockage of the harbour navigation channel.

1.3 Contents

Two wave and wave-induced current sub-models provide input data to the sediment transport model. Chapter 2, therefore, reviews existing wave and current flow models, while Chapter 3 reviews existing sediment transport models. Chapter 4 provides details of the proposed wave model, including modification to deal with deformation by structures as well as comparison with experimental data. Chapter 5 gives details of the wave-induced current model. Chapter 6 provides details of the three-dimensional suspended sediment transport model. Chapter 7 explains how coefficients are obtained for use in the suspended sediment model. Chapter 8 presents application of the series of models to the Chukpyon Harbour site, Korea. Finally, conclusions and suggestions for future work are given in Chapter 9.

CHAPTER 2. REVIEW OF WAVE AND WAVE-INDUCED CURRENT MODELS

2.1 Introduction

To determine sediment transport rates from a numerical model, it is necessary to have hydrodynamic information as input data. The accuracy of the hydrodynamic data cannot be under-estimated. The transport of sediment depends upon flow velocities raised to a high power (3-5). Consequently, small errors in the prediction of flow velocities, say 10 %, leads to much larger errors in transport rates, some 30-60 %. Given the accuracy of measuring flow velocities in the field, which is essential for the calibration of any hydrodynamic model, it is also important to minimize sediment transport errors by use of as much field information as possible. Fortunately, bed level changes are less sensitive to absolute values of the transport rates since they depend upon spatial gradients of the transport rate. Nevertheless, the use of a good hydrodynamic model helps to reduce possible sediment transport errors.

The objective of the present chapter is, therefore, to select an effective approach to providing accurate hydrodynamic information to enable the prediction of medium-term bed level changes in wave-dominated situations, such as that at Chukpyon Harbour, Korea. Such hydrodynamics involves two components. Firstly, the prediction of the

nearshore wave climate, including its modification by structures, and secondly, the prediction of the associated wave-induced currents. Consequently, the present chapter reviews approaches currently available for the prediction of both wave climate and wave-induced currents.

2.2 Review of Wave Propagation Models

2.2.1 Classification of Wave Propagation Models

Short-period waves are generated by wind, and propagate toward the coast. Usually the theories on the generation of waves have been developed separately from those on wave propagation and deformation in shallow water. The present review assumes that deep water (offshore) wave information is available and that existing wave theories are sufficient for present purposes. Thus the review concentrates on a discussion of wave propagation theories only.

Wave propagation modelling may be divided into two groups, horizontal (or plan) models and vertical (or laterally-uniform) models. The two-dimensional plan modelling assumes that wave boundary layer thickness is very small compared with the flow depth, and consequently the three-dimensional equation can bc depth-integrated using an appropriate wave theory. Such depth-average models are useful to track waves propagating inshore.

Vertical modelling, which involves longitudinal and vertical coordinates, has been used to examine wave deformation in one vertical section at wave breaking, or wave run-up on steep slopes for waves approaching normal to seabed contours or to structures. Since vertical modelling cannot be used for general plan areas, this approach is not included in the present study.

Wave propagation modelling has developed using linear mono-frequency waves, although real waves are always random in space and time domains. Horizontal wave model classification is not easy and can be done in several different ways. Waves used can be linear mono-frequency waves, or asymmetric mono-frequency waves, or long-crested random waves, or short-crested random waves. Different physical phenomena can also be included in the governing equations, such as: shoaling, refraction, diffraction, reflection, wave-current interaction, energy dissipation by sea bed friction, wave breaking or surface wind stress. Classification can also be made by the type of governing equation used. For example, it is possible to use a time-dependent hyperbolic equation, or a steady-state parabolic equation, or an elliptic equation. In addition, some models use a Lagrangean grid co-ordinate system, while others use a fixed Eulerian grid. Different numerical techniques have also been used. For example, finite difference methods, finite element methods, and boundary element methods. Equally, some models solve wave-period-average variables, while other models solve inter-wave-period variables.

Recently Yoo et al.(1988), Yoo et al.(1989), and O'Connor(1991) have presented summaries of plan wave propagation modelling, and argued that three main types exist, These are termed inter-wave-period(IWP), evolution, and wave-period-average(WPA). They have also argued that each type of model is adequate for different sizes of modelling area. The IWP model needs some 10 points per wavelength to provide an adequate description of the internal changes within the wave period, and is appropriate for small areas of some 1-10 km^2, while the evolution and WPA models are appropriate for large areas($> 10\ km^2$).

An examination of the technical literature shows that a wide range of wave models related to shoaling, bed and current refraction, diffraction, reflection, wave-current interaction, slope-related shoaling, bed friction, and wave breaking now exist. A selection of the more relevant ones is given below, and their merits and demerits are compared.

2.2.2 IWP Boussinesq Wave Equation Models

Boussinesq(1872) incorporated vertical accelerations in the depth-integrated horizontal motion equations. The assumptions used in the derivation of the Boussinesq equation are a uniform horizontal velocity distribution and a large wave length compared to the water depth, which are valid for long waves. Additional terms appear in the IWP Boussinesq equations that account for the excess horizontal momentum flux. These terms are higher

order differentials of the dependent variables, and equation solution determines the instantaneous currents and water surface elevations. Wave shoaling, diffraction, refraction, reflection, and current-interactions are automatically part of the solution due to the non-linear interaction terms. The basic Boussinesq equations for continuity and momentum conservation on a flat bottom in one-dimension can be written as:

$$\frac{\partial \tilde{d}}{\partial t}+\tilde{d}\frac{\partial \tilde{U}}{\partial x}+\tilde{U}\frac{\partial \tilde{d}}{\partial x}=0 \qquad (2.1)$$

$$\frac{\partial \tilde{U}}{\partial t}+\tilde{U}\frac{\partial \tilde{U}}{\partial x}+g\frac{\partial \tilde{d}}{\partial x}=\frac{1}{3}h^2\frac{\partial^3 \tilde{U}}{\partial x^2 \partial t} \qquad (2.2)$$

where $\tilde{d}$ is the instantaneous total water depth(ξ+h), see Fig. 2.1, h is the still water depth, ξ is the instantaneous water surface variation, t is the time, x is the longitudinal axis, $\tilde{U}$ is the depth-averaged instantaneous velocity, and g is the acceleration due to gravity.

Peregrine(1967) has derived a Boussinesq type equation for the propagation of arbitrary long waves over slowly-varying bathymetry. Peregrine's(1967) one-dimensional momentum equation is:

$$\frac{\partial \tilde{U}}{\partial t}+\tilde{U}\frac{\partial \tilde{U}}{\partial x}+g\frac{\partial \tilde{d}}{\partial x}=\frac{1}{2}h\frac{\partial}{\partial x}\left(\frac{\partial}{\partial x}\left(h\frac{\partial \tilde{U}}{\partial t}\right)\right)-\frac{1}{6}h^2\left(\frac{\partial}{\partial x}\left(\frac{\partial}{\partial x}\left(\frac{\partial \tilde{U}}{\partial t}\right)\right)\right) \qquad (2.3)$$

The equation (2.3) reduces to equation (2.2) for a horizontal bottom.

Abbott et al.(1978) have produced a class of Boussinesq equations for application over two-dimensional variable bathymetries, and Yoon and Lui(1986) produced a Boussinesq equation to account for the effect of current-interaction. Larsen and Darcy(1983), and Madsen and Warren(1984) used Boussinesq equations to describe combined refraction and diffraction of long waves around breakwaters adding extra-terms such as bed friction or porosity of breakwaters. Madsen and Sorensen(1992) have proposed a form of the Boussinesq equations for irregular wave propagation on a slowly varying bathymetry.

Although the Boussinesq equation models solve various wave deformation phenomena in an inter-wave-period mode, the approach still requires empirical wave breaking simulation which may play an important role in driving wave-induced current in the surf zone. Because the development of the model is based on weakly dispersive wave motion over the water depth(Massel,1989), its application is limited to shallow water (say, a water depth/wave length ratio less than 0.05). A satisfactory solution technique for the refined equations is yet to be developed for a wider range of applications. Furthermore, since any IWP model automatically involves large computer storage and long computation time, the Boussinesq approach is not desirable for long term simulation of siltation.

2.2.3 Elliptic, Parabolic, and Two-Equation Hyperbolic Mild-Slope Equation Models

2.2.3.1 Elliptic Mild-Slope equation Models

When the sea bed is sloped, not only diffraction but also refraction and shoaling occur. For such situations, a number of wave propagation models have been produced based on the "mild-slope equation". The mild-slope equation has been established as an adequate governing equation for describing combined refraction and diffraction from deep water to shallow water. It is a depth-averaged equation, and based on the requirement that wave energy is conserved and that the rate of change of depth and current within a typical wavelength is very small. The original mild-slope equation without the effect of current was derived by Berkhoff(1972,1976), and was named the "mild-slope equation" by Smith and Sprinks(1975).

A detailed derivation of the mild-slope equation is given by Berkhoff(1972). Berkhoff(1972) started from the conservation of wave energy which is the sum of the kinetic and potential energies, that is:

$$\frac{DE}{Dt}+\iiint_B \left(u\frac{\partial p}{\partial x}+v\frac{\partial p}{\partial y}+w\frac{\partial p}{\partial z}\right) dx\ dy\ dz=0 \qquad (2.4)$$

where E is the wave energy density, $D/Dt=\partial/\partial t+(u\partial/\partial x+v\partial/\partial y+w\partial/\partial z)$, B is a spatial volume of interest, and p is the static pressure in the fluid.

With the assumption of incompressibility of fluid, and a steady state, harmonic solution, the mild-slope equation of Berkhoff(1972), ignoring energy dissipation, can be derived in the form:

$$\frac{\partial}{\partial x}\left(cc_g\frac{\partial\phi}{\partial x}\right)+\frac{\partial}{\partial y}\left(cc_g\frac{\partial\phi}{\partial y}\right)+\sigma^2\frac{c_g}{c}\phi=0 \qquad (2.5)$$

where $\phi(x,y)$ is a complex velocity potential which is obtained from $\Phi(x,y,t)=\phi\cdot e^{-i\sigma t}$; i is $\sqrt{(-1)}$; Φ is obtained from the velocity potential $\tilde{\phi}(x,y,z,t) = F(z)\cdot\Phi$, $F = \cosh k(z+h)/\cosh kh$; x,y are the longitudinal and lateral spatial cartesian co-ordinates, respectively; c, c_g are the wave phase velocity and group velocity, respectively; σ is the angular wave frequency (defined to be $2\pi/T$); and T is the wave period.

Equation (2.5) is a two-dimensional second-order partial differential equation. Second-order partial differential equations are often classified as elliptic, parabolic, or hyperbolic equations. A general two-dimensional second-order partial differential equation has the form:

$$C_1\frac{\partial^2\phi}{\partial x^2}+C_2\frac{\partial^2\phi}{\partial x\partial y}+C_3\frac{\partial^2\phi}{\partial y^2}+C_4\frac{\partial\phi}{\partial x}+C_5\frac{\partial\phi}{\partial y}+C_6\phi+C_7=0 \qquad (2.6)$$

where x,y are arbitrary independent variables, ϕ is an arbitrary dependent variable, C_1,C_2,C_3,C_4,C_5,C_6, and C_7 are arbitrary coefficients. The equations are often said to be elliptic when $C_2^2-4C_1C_3<0$, parabolic when $C_2^2-4C_1C_3=0$, and hyperbolic when $C_2^2-4C_1C_3>0$. Each type of equation has different characteristic directions, and requires

different initial or boundary conditions for the solution.

Using the above classification, Berkhoff's(1972) mild-slope equation (2.5) is an elliptic equation, so that equation (2.5) can be solved as a boundary-value problem with appropriate boundary conditions along the entire boundary. Since transmission and reflection boundary conditions are easily implemented into the solution schemes, this approach is a popular one for modelling the response of harbours to short and long waves.

Later Lui(1983), and Kirby(1984) also produced modified forms of the equation for interacting wave/current situations. The inclusion of current effects on the wave field in the same type of elliptic wave equation is useful, but if the current speed and its spatial gradient are small so that they do not affect the wave propagation, the current-related terms may be neglected. Thus the selection of model type, that is, whether to use the mild-slope equation with of without modification for currents for a particular problem is dependent upon the order of magnitude of the current speed and its gradient in the computational domain.

Although the mild-slope equations solve for the spatial distribution of the potential function, the solution can consists of a rapid variation within a wave length due to the presence of reflected or crossing wave trains. Consequently, such models need to be used with small space increments in order to resolve the variation in the potential function.

To simulate a wave-induced current in the surf zone, wave-breaking is involved. Unfortunately, the location of wave-breaking is usually not known a priori. Thus, it becomes difficult to model wave transformation using the mild-slope equation directly.

The mild-slope method also becomes computationally unsuitable for large areas, as well as for short-wave problems because of its great expense. Firstly, grid size has to be small enough that there are at least some ten nodes within each wavelength. Secondly, the entire domain of interest must be discretized and solved simultaneously, either involving large matrix inversion or use of an iteration method.

Parabolic approximation models or two-equation hyperbolic equation models have been developed more recently to overcome some defects of the elliptic mild-slope equations.

2.2.3.2 Parabolic Approximation Models

Radder(1979), and Booij(1981) have derived simplified forms of the wave energy equation, which are generally referred to as the parabolic wave equations with some approximation, as an alternative method to solve the wave propagation problem. Radder(1979) split the velocity potential into two, one for forward-propagating waves, the other for backward-propagating waves with respect to the x axis which is the main wave propagation direction. The velocity potential for backward-propagating waves was

ignored. Radder's equation is as follows:

$$\frac{\partial \phi}{\partial x} = \left(ik - \frac{1}{2kcc_g} \frac{\partial (kcc_g)}{\partial x} + \frac{i}{2kcc_g} \frac{\partial}{\partial y} cc_g \frac{\partial}{\partial y} \right) \phi \qquad (2.7)$$

where k is the wave number (2π/L), and L is the wave length. Only one-directional second order derivative exists in equation (2.7) in contrast to the elliptic equation (2.5).

It has been reported that equation (2.7) is numerically efficient for the calculation of refraction and diffraction. Reflection has also been included in the parabolic approach through an iterative computational scheme. Kirby and Dalrymple(1986) have also proposed a modification of the parabolic equation to include the effect of currents.

However, there is a limit of wave propagation direction relative to the computation grid, since the wave angle inside the calculation domain should not exceed a narrow range relative to the x axis for an accurate solution.

The "external" diffraction, that is diffraction produced by structures can not be accurately solved by this approach. The grid size should still be a small fraction of the wave length as for the elliptic mild-slope equation (2.5) due to the nature of the composite velocity potential.

2.2.3.3 IWP Hyperbolic Two-Equation Wave Models

Another alternative way to solve the mild-slope equation has been developed by Copeland(1985). He developed a two-equation form of the mild-slope equation. This can be used from deep water to shallow water, using a similar technique to that of Ito and Tanimoto(1972), who developed two-equations for long waves. Copeland(1985) transformed the Berkhoff's(1972) equation to a pair of first order equations by including separation of the variables in the velocity potential function in time and space. Copeland(1985) suggested the following equations, which have been described as "Hyperbolic Two-equation type models", see Yoo et al.(1989):

$$\frac{\partial}{\partial t}(\vec{Q}) + cc_g \nabla \xi = 0 \qquad (2.8)$$

$$\frac{\partial \xi}{\partial t} + \frac{c}{c_g} \nabla \cdot (\vec{Q}) = 0 \qquad (2.9)$$

where $\vec{Q}$ is a vertically integrated function of horizontal velocity and is used as a dummy variable in the mutual integration of equations (2.8) and (2.9), and ∇ is the two-dimensional spatial gradient operator ($\partial/\partial x$, $\partial/\partial y$).

Watanabe and Maruyama(1986), and Yoo et al.(1989) have modified equations (2.8) and (2.9) to include the effect of a current.

Copeland(1985) showed that the pair of first-order hyperbolic equations are easier to solve than the second-order elliptic equation in some ways due to the simpler boundary conditions at inland boundary. The major advantage of the IWP hyperbolic type wave models is that they have no limitation on the wave angle, and consequently represent a distinct improvement over the parabolic models in the treatment of external diffraction.

However, simulation of partial wave reflection, wave transmission, or absorption at rigid or open boundaries in the hyperbolic two-equation models involves a complex calculation of wave angle which is not straightforward due to the existence of superimposed reflective waves.

The IWP hyperbolic two-equation models have similar drawbacks to the IWP Boussinesq equation models. They take a long computational time until the solution reaches final equilibrium. A minimum of about ten grid nodes per wave length are needed for simulation of IWP wave transformation. In addition, the hyperbolic two-equation models still rely on empirical methods for the calculation of wave breaking.

2.2.4 Evolution Wave Models

As previously stated, the mild-slope equation models reviewed in Section 2.2.3 require a minimum number of ten nodes per wave length for computational purposes. Evolution

models, so called by Yoo, O'Connor and McDowell(1989), have been developed to provide greater computational efficiencies over that of IWP mild-slope equation models.

For the development of the evolution model, the velocity potential for linear waves is expressed in a complex notation as:

$$\phi = a e^{is} \tag{2.10}$$

where a(x,y) is the wave amplitude, s(x,y) is the wave phase function ($=k_x x + k_y y$), k_x, k_y are the x, y components of wave number vector ($k=2\pi/L$), and L is the wavelength.

Berkhoff(1976) substituted equation (2.10) into equation (2.5), and obtained the following two equations from real and imaginary parts of the equation (2.5):

$$\frac{1}{a}\left(\frac{\partial^2 a}{\partial x^2}+\frac{\partial^2 a}{\partial y^2}+\frac{1}{CC_g}(\nabla a\cdot\nabla(CC_g)\right)+k^2-|\nabla s|^2=0 \tag{2.11}$$

$$\nabla\cdot(a^2 CC_g \nabla s)=0 \tag{2.12}$$

The above equation (2.11) is still an elliptic form with regard to wave amplitude (a). The dependent variables of the evolution model, thus become wave amplitude (a) and the gradient of wave phase function (∇s) instead of the velocity potential function of Berkhoff's(1972) elliptic mild-slope equation.

In the evolution model, each position has a single value of wave amplitude and gradient of wave phase function, and the superimposed waves at a point are given by a single

representative wave amplitude and phase function, so that a smoothed approximate wave field is solved by the model. Since the representative wave amplitude and the gradient of wave phase function are considered to vary more slowly in space than the original velocity potential function, much coarser grids can be used for the evolution model.

Ebersole et al.(1986) used the evolution elliptic wave equations (2.11) and (2.12) for a simple propagation problem without reflection. They used equation (2.11) for the solution of the gradient of wave phase function. In order to obtain the wave direction, they used the idea of irrotationality of wave phase function, which is mathematically expressed by the curl of the gradient of the phase function (s) being zero, that is:

$$\nabla \times (\nabla s) = 0 \qquad (2.13)$$

where $\times$ represents a vector cross product.

Decomposing the gradient of the wave phase function into two components using the wave direction θ, equations (2.12) and (2.13) can then be expressed as:

$$\frac{\partial}{\partial x}(a^2 c c_g |\nabla s| \cos\theta) + \frac{\partial}{\partial y}(a^2 c c_g |\nabla s| \sin\theta) = 0 \qquad (2.14)$$

$$\frac{\partial}{\partial x}(|\nabla s| \sin\theta) - \frac{\partial}{\partial y}(|\nabla s| \cos\theta) = 0 \qquad (2.15)$$

where θ is the counter-clockwise wave propagation direction relative to the negative x axis.

Ebersole et al.(1986) solved equations (2.11), (2.14) and (2.15) on a square grid of computation points using a simple forward marching finite difference technique. The model was tested against experimental results from a hydraulic model of wave propagation over a submerged shoal. The results were generally in good agreement with the laboratory data, see Ebersole et al.(1986). The evolution elliptic model is very efficient in computation time due to use of a direct solution procedure in one direction, and a grid size which is only dependent upon the rate of change of seabed contours.

Ebersole et al.(1986) used a non-centred finite difference scheme for second order derivatives along the x axis. However, no proof was given that such an approach using a non-centred scheme for the second derivative along the x axis increases the accuracy of the solution of the two-directional second-order partial differential elliptic equation. The evolution elliptic model has not been tested on any external diffraction phenomena around structures.

Not only have evolution elliptic models been developed, but also evolution parabolic models(Liu(1983), Kirby(1986)) have been developed from the parabolic models, see Section 2.2.3.2. The evolution parabolic models are known to be efficient in terms of computation time. They are also able to describe weakly reflected waves after minor modification. However, the use of the evolution parabolic model is limited if wide angle external diffraction occurs, as with the original parabolic model.

An evolution hyperbolic two-equation model has also been presented by Madsen and Larsen(1987) modifying hyperbolic two-equation models. Yoo et al.(1989) have proposed a modified evolution hyperbolic two-equation model to include the effect of a current. The evolution hyperbolic model can handle external diffraction as well as internal diffraction. However, when using the evolution hyperbolic model, the solution can only be obtained asymptotically involving an iterative procedure. The evolution hyperbolic model has a short history and few applications to engineering situations have been made as of yet.

2.2.5 Wave-Period-Average Models

2.2.5.1 Introduction

Another class of wave model has been developed using the kinematic conservation equation, which is different from the mild-slope equation. These models can be classified as "wave-period-average" models, see Yoo et al.(1989). Wave-period-average models include the traditional ray approach which uses a Lagrangian method, and a recent hyperbolic WPA model which uses a Eulerian grid system.

2.2.5.2 Ray-Tracking Approach

The traditional WPA type model is represented by the Ray-Tracking approach, whereby, a wave ray (and hence wave energy) is tracked forward from offshore to inshore (forward tracking) or from inshore to offshore (back-tracking). These models have traditionally been used with a design-wave approach, and ignore many processes such as diffraction, both by the seabed and by structures, seabed friction, and wave-current interaction. More recently, modifications have been suggested to include seabed friction and wave-current interaction by Barber(1981), for seabed diffraction by Yoo and O'Connor(1986b), and for random waves by Gilvert and Abernethy(1975), and for diffraction and reflection by structures by Southgate(1989).

While WPA ray models have advanced over the years, their major drawback is that wave information is determined along a set of non-uniformly-spaced *computation points.* Inclusion of wave-current interaction effects requires, some form of interpolation procedure, which can be inaccurate in areas of widely scattering rays. An Eulerian mesh of computation points is to be preferred, therefore, if wave-induced currents are to be calculated.

2.2.5.3 Hyperbolic WPA Refraction-Diffraction Model

Yoo and O'Connor(1986b,1988a,b), and Yoo et al.(1989) have developed a hyperbolic WPA refraction-diffraction model by modifying the existing kinematic conservation equation, which is normally used for the determination of wave ray tracks. Their model includes diffraction effects, and uses an Eulerian grid system.

The kinematic conservation equation and the energy conservation equation constitute a complete governing equation system for the hyperbolic WPA model. The equations are:

$$\frac{\partial K_i}{\partial t} + (U_j + nC_j)\frac{\partial K_i}{\partial x_j} + K_j\frac{\partial U_j}{\partial x_i} + \frac{\sigma_0(2n-1)}{2d}\frac{\partial d}{\partial x_i} + \frac{nC}{2ka}\left(\frac{1}{a}\frac{\partial a}{\partial x_i}\frac{\partial^2 a}{\partial x_j^2} - \frac{\partial^3 a}{\partial x_i \partial x_j^2}\right) = 0 \qquad (2.16)$$

$$\frac{\partial a}{\partial t} + \frac{1}{2a}\frac{\partial}{\partial x_i}(U_i + nC_i)a^2 + \frac{S_{ij}}{\rho g a}\frac{\partial U_j}{\partial x_i} = 0 \qquad (2.17)$$

where the tensor subscripts i,j are x, and y, d is the water depth, σ_0 is the angular frequency relative to the water mass (on a moving frame with the water mass), k is a separation factor given by $\sigma_0^2 = gk \tanh kd$, σ is the angular frequency relative to the sea bed (on a fixed frame, $\sigma = \sigma_0 - K_i U_i$), K_i is the wave number vector, U_i is the depth-mean horizontal velocity vector, C_i is the wave phase velocity vector, a is the wave amplitude, n is c_g/c, ρ is the water density, and S_{ij} is the radiation stress tensor which has the form:

$$S_{ij}=(n\frac{K_i}{k}\frac{K_j}{k}+(n-\frac{1}{2})\delta_{ij})\frac{1}{2}\rho g a^2 \qquad (2.18)$$

where δ_{ij} is the delta function (=1 for i=j, =0 for i≠j).

Since the wave energy equation (2.17) was obtained by wave-period averaging as well as depth-integrating the fundamental energy conservation equation, there is no computational restriction on the selection of the size of computational grid. The model can solve internal and external diffraction, and includes the effect of currents. However, since the governing equations are of hyperbolic type, solution requires iterative procedure which involves long computation time as with other hyperbolic type models.

2.3 Review of Wave-Induced Current Models

2.3.1 Classification of Wave-Induced Current Models

Once details of the wave number and wave amplitude are known, it is possible to determine the wave-induced current pattern in the study area. This can be done either in a coupled method (solving wave and wave-induced current coincidently) or in a decoupled method (solving wave and wave-induced current sequentially), using the same computational grid as for the wave model.

Comprehensive reviews on nearshore circulation modelling have been done by Basco(1982,1983), Basco and Coleman(1982), Yoo and O'Connor(1986a), Arcilla and Lemos(1990), and Battjes et al.(1990). Basco(1982,1983) and Basco and Coleman(1982) presented a state-of-the-art on surf zone currents, reviewing laboratory experiments, field measurements, and numerical modelling, and stressed that the Boussinesq type approach will improve in the future. Yoo and O'Connor(1986a) reviewed existing models, and argued that a depth-integrated, horizontal, two-dimensional, wave-induced flow model which is run with a hyperbolic WPA wave model (see Section 2.2.5.3) in a coupled way is one of the most comprehensive of existing wave-induced current models. Battjes et al.(1990) presented a state-of-the-art review on nearshore circulation phenomena, laboratory and numerical experiments, and highlighted the quasi-three-dimensional approach as the prospective research direction for the future.

Model approaches are generally described in the present review in dimensional order, starting from three-dimensional models for convenience and following the transformation of the governing equations.

Recently, with the increased power of computers, multi-layer three-dimensional models have been produced, which have also been suggested for use in nearshore areas, see Nizam(1992). Three-dimensional modelling implies that information is obtained in x, y, and z directions.

Horizontal modelling means that basic equations have been depth-averaged so that only variations in lateral (y) and longitudinal (x) co-ordinates are retained. Vertical modelling implies that lateral averaging or uniformity has been done or assumed so that only variations in vertical (z) and longitudinal (x) co-ordinates are retained.

Most of the existing models solve WPA variables. The Boussinesq type wave/current models are an exception, solving the depth-integrated IWP variation of water surface level and horizontal velocities. The WPA wave-induced current can be obtained by wave-period-averaging after IWP calculation by a Boussinesq wave model. However, the Boussinesq type model has been developed mainly for the study of wave transformation as of the present so that any application of direct calculation of wave-induced current using this approach has not been presented yet. This may be due to the difficulty of IWP treatment of wave breaking in the Boussinesq model. The Boussinesq model requires small mesh size and long computational time, which are major drawbacks for long term simulation of siltation, and is not considered further in the present review.

The existing WPA models may be grouped into three-dimensional models and depth-integrated two-dimensional horizontal models. Three-dimensional modelling work is a more recent development than the depth-integrated, two-dimensional modelling, and the basic equations solved are more general than those for depth-integrated two-dimensional horizontal equations. Vertical two-dimensional models are considered to be a subset of the three-dimensional models, and are briefly referred to Section 2.3.2.

Depth-integrated continuity and momentum equations are derived from three-dimensional equations, and are widely used for horizontal circulation modelling. Horizontal models can be divided into two groups, one solves primitive variable equations, see Section 2.3.3, and the other solves a stream function equation, see Section 2.3.4. One-dimensional horizontal models for longshore current parallel to a plane beach are a subset of depth-integrated two-dimensional horizontal models, and are briefly reviewed in Section 2.3.3.

2.3.2 Three-Dimensional WPA Models

All existing wave-induced current models are based on universal laws of conservation of mass, and momentum. Three-dimensional models solve the three-dimensional mass continuity and momentum equations.

The law of governing the conservation of matter is expressed as:

$$\frac{\partial \rho}{\partial t}+\frac{\partial \rho u}{\partial x}+\frac{\partial \rho v}{\partial y}+\frac{\partial \rho w}{\partial z}=0 \qquad (2.19)$$

where ρ is the water density, and u,v,w are the instantaneous fluid velocities in the x,y,z directions, respectively. If the fluid is assumed to be incompressible, which is usually accepted for free surface water flows, equation (2.19) is reduced to:

$$\frac{\partial u}{\partial x}+\frac{\partial v}{\partial y}+\frac{\partial w}{\partial z}=0 \qquad (2.20)$$

The Navier-Stokes equations are used for the basic equations for the momentum conservation. These are:

$$\frac{\partial u}{\partial t}+u\frac{\partial u}{\partial x}+v\frac{\partial u}{\partial y}+w\frac{\partial u}{\partial z}=-\frac{1}{\rho}\frac{\partial p}{\partial x}+\nu\nabla^2 u \qquad (2.21)$$

$$\frac{\partial v}{\partial t}+u\frac{\partial v}{\partial x}+v\frac{\partial v}{\partial y}+w\frac{\partial v}{\partial z}=-\frac{1}{\rho}\frac{\partial p}{\partial y}+\nu\nabla^2 v \qquad (2.22)$$

$$\frac{\partial w}{\partial t}+u\frac{\partial w}{\partial x}+v\frac{\partial w}{\partial y}+w\frac{\partial w}{\partial z}=-\frac{1}{\rho}\frac{\partial p}{\partial z}-g+\nu\nabla^2 w \qquad (2.23)$$

where ν is the kinematic viscosity, and ∇ is the three-dimensional gradient operator. Since the inter-wave-period simulation of instantaneous velocities is not feasible due to the large computational effort, existing three-dimensional models solve WPA equations. To obtain the WPA basic equations from the equations (2.20), (2.21), (2.22), and (2.23), a decomposition of variables can be applied for flow with oscillatory wave and turbulence, similar to the Reynolds' decomposition for turbulent flow without wave:

$$\begin{aligned} u&=\overline{u}+\tilde{u}+u' \;;\; v=\overline{v}+\tilde{v}+v' \\ w&=\overline{w}+\tilde{w}+w' \;:\; p=\overline{p}+\tilde{p}+p' \end{aligned} \qquad (2.24)$$

where bar($\bar{}$) is for the turbulent and wave mean values, tilde($\tilde{}$) is for the wave-related variation values, and dash(') is for the turbulent variation values.

Substituting equation (2.24) into equation (2.20), the three-dimensional WPA continuity equation is obtained as:

$$\frac{\partial \overline{u}}{\partial x}+\frac{\partial \overline{v}}{\partial y}+\frac{\partial \overline{w}}{\partial z}=0 \qquad (2.25)$$

Ignoring the laminar shear stresses, and substituting equation (2.24) into equations (2.21), (2.22), and (2.23), wave-period and turbulence-period-average momentum equations can also be derived, see Nizam(1992), as follows:

$$\frac{\partial \overline{u}}{\partial t}+\frac{\partial \overline{u}^2}{\partial x}+\frac{\partial \overline{u}\,\overline{v}}{\partial y}+\frac{\partial \overline{u}\,\overline{w}}{\partial z}=-\frac{1}{\rho}\frac{\partial \overline{p}}{\partial x}-\frac{\partial}{\partial x}\left(\langle \tilde{u}^2\rangle-\langle \tilde{w}^2\rangle\right)-\frac{\partial}{\partial y}\langle \tilde{u}\tilde{v}\rangle$$
$$-\frac{\partial}{\partial z}\langle \tilde{u}\tilde{w}\rangle-\frac{\partial}{\partial x}\left(\langle u'^2\rangle-\langle w'^2\rangle\right)-\frac{\partial}{\partial y}\langle u'v'\rangle-\frac{\partial}{\partial z}\langle u'w'\rangle \qquad (2.26)$$

$$\frac{\partial \overline{v}}{\partial t}+\frac{\partial \overline{u}\,\overline{v}}{\partial x}+\frac{\partial \overline{v}^2}{\partial y}+\frac{\partial \overline{v}\,\overline{w}}{\partial z}=-\frac{1}{\rho}\frac{\partial \overline{p}}{\partial y}-\frac{\partial}{\partial x}\langle \tilde{u}\tilde{v}\rangle-\frac{\partial}{\partial y}\left(\langle \tilde{v}^2\rangle-\langle \tilde{w}^2\rangle\right)$$
$$-\frac{\partial}{\partial z}\langle \tilde{v}\tilde{w}\rangle-\frac{\partial}{\partial x}\langle u'v'\rangle-\frac{\partial}{\partial y}\left(\langle v'^2\rangle-\langle w'^2\rangle\right)-\frac{\partial}{\partial z}\langle v'w'\rangle \qquad (2.27)$$

where $\langle\ \rangle$ means the wave-period average($=1/T\ \int_0^T dt$). The vertical momentum equation (2.23) is often simplified and results in the equation:

$$\overline{p}=p_0-\rho\langle \tilde{w}^2\rangle \qquad (2.28)$$

where p_0 is the hydrostatic pressure ($=\rho g(\eta-z)$).

The normal or shear stress terms appearing in equations (2.26) and (2.27) require closure schemes (that is, equations to relate the turbulence terms to the variables $\bar{u}$, $\bar{v}$) to complete the equations.

Examination of equation 2.26 and 2.27 shows that the effect of wave motion is to introduce extra "stress-type" terms. These have been called "Radiation Stress" terms by several authors.

Battjes et al.(1990) have presented a review on the three-dimensional modelling of nearshore circulation. They described full three-dimensional modelling, and quasi-three-dimensional modelling. The former solves the wave and turbulent-average equations in x,y,z directions, see Nizam(1992). The lattermost approach is simply an extension of the horizontal, two-dimensional circulation model, and seeks to establish approximately, both the depth-averaged flow and the vertical structure in the lower two or three layers. For three layers, top layer is often taken between the wave crest and the wave trough levels; the middle layer is taken between the wave trough and the upper boundary of the bed wave boundary layer; and the bottom layer is taken as the lower wave boundary layer, see de Vriend and Stive(1987), and Svendsen and Lorentz(1989).

It should be noted that the continuity and momentum equations (2.25), (2.26), and (2.27) are valid only below wave trough level, since the flow above this level is not continuous due to the temporary exposure of the computational grid points to the atmosphere. The radiation stress in the top layer has been treated as a sort of surface stress at mean water level or wave trough level, which is a drawback of the three-dimensional model. Although three-dimensional modelling is flexible and general, it has had little laboratory or field testing to assess its usefulness. Such three-dimensional flow models also require

considerable computation time and consequently, it is less suited to long term siltation calculations.

Recently two-dimensional vertical models have been applied to the simulation of undertow currents across a beach during storms. The two-dimensional vertical current model is a subset of the three-dimensional current model. However, vertical modelling is only appropriate in existing models (also called profile models) to laterally-uniform beaches and consequently is not considered further.

2.3.3 Depth-averaged Horizontal Models Solving Primitive Variables

Since the wave boundary layer thickness is rather small in comparison with the water depth, it is possible to decompose the instantaneous velocities and pressure. Then, by depth-averaging the basic turbulent-mean fluid flow momentum and mass continuity equations, a depth-integrated, wave-period-average, two-dimensional in plan, wave-induced current governing equations can be produced.

Two-dimensional horizontal modelling is useful for simulation of wave-induced circulation in relatively shallow sea areas, where the water is not stratified by density differences. Depth-integrated continuity and momentum equations have been used widely for describing shallow water turbulent flows for currents and/or waves.

So far, many researchers have presented two-dimensional horizontal numerical models of wave-induced current, but the main features of all such approaches are similar with regard to the type of governing equations finally used. To incorporate wave effects, depth-integrated wave-period-average continuity and momentum equations have been derived using the decomposition of variables shown in equation (2.24). Phillips(1977), Yoo and O'Connor(1986a), and Arcilla and Lemos(1990) have presented a similar procedure of depth-integration and wave-period-averaging of the basic three-dimensional continuity and momentum equations.

Yoo and O'Connor(1986a)'s typical derivation of depth-integrated and wave-period-average continuity and momentum equations are briefly described here. Applying the kinematic boundary condition (describing the movement of a water particle at the water surface), and Leibnitz's rule (related to differentiation of the integrated quantity) to the continuity equation (2.20), the horizontal depth-integrated continuity equation becomes:

$$\frac{\partial}{\partial t}(\rho d) + \frac{\partial}{\partial x_i}(\overline{M}_i + \tilde{M}_i) = 0 \qquad (2.29)$$

where d is the mean water depth, see Fig. 2.1, and $\overline{M}_i$, $\tilde{M}_i$ are the current-related and wave-related depth-integrated mass transport rates, respectively in tensor notation, which have the form:

$$\overline{M}_i = \left\langle \int_{-h}^{\xi} \rho \overline{u}_i dz \right\rangle \; ; \; \tilde{M}_i = \left\langle \int_{-h}^{\xi} \rho \tilde{u}_i dz \right\rangle \qquad (2.30)$$

where ξ is the instantaneous water surface level, and h is the still water depth.

Defining the depth-mean velocity U_i (U_x=U, U_y=V) as the summation of current and wave-induced flow so that the wave-induced mass flux is implicitly included in the variable U_i, we have

$$\frac{\partial \eta}{\partial t} + \frac{\partial}{\partial x_i}(dU_i) = 0 \qquad (2.31)$$

where η is the WPA mean water level.

In a similar manner to the continuity equation, the horizontal momentum equations are depth-integrated and wave-period-averaged. Depth-integration of the momentum equations and the use of an eddy viscosity closure for turbulent terms lead to:

$$\frac{\partial}{\partial t}\int_{-h}^{\xi} \rho \hat{u}_i dz + \frac{\partial}{\partial x_j}\int_{-h}^{\xi} (\rho \hat{u}_i \hat{u}_j + p\delta_{ij})\, dz - P_h \frac{\partial h}{\partial x_i} = \int_{-h}^{\xi} \frac{\partial}{\partial x_\beta} \rho \epsilon \frac{\partial \hat{u}_\alpha}{\partial x_\beta} dz \qquad (2.32)$$

where ϵ is the turbulent eddy viscosity coefficient, α,β are tensor indices x,y,z, hat(^) is for a sum of current and wave components($\bar{}$ + $\tilde{}$), and P_h is the pressure at the sea bed.

By defining the radiation stress, the turbulent shear stress, and the depth-mean pressure gradient as:

$$S_{ij}=<\int_{-h}^{\xi}(\rho\tilde{u}_i\tilde{u}_j+p\delta_{ij})\,dz>-\int_{-h}^{\eta}p_0\delta_{ij}dz \qquad (2.33)$$

$$\hat{T}_i=<\int_{-h}^{\xi}\frac{\partial}{\partial x_\beta}\rho\epsilon\frac{\partial\hat{u}_\alpha}{\partial x_\beta}dz> \qquad (2.34)$$

$$P_i=\frac{\partial}{\partial x_i}\int_{-h}^{\xi}p_0dz-<P_h\frac{\partial h}{\partial x_i}> \qquad (3.35)$$

and applying the decomposition of variables and the wave-period-averaging process, the horizontal momentum equation (2.32) is expressed in a compact form:

$$\frac{\partial\hat{M}_i}{\partial t}+\frac{\partial}{\partial x_j}(\hat{U}_i\hat{M}_j-\tilde{U}_i\tilde{M}_j+S_{ij})+P_i=\hat{T}_i \qquad (2.36)$$

Yoo and O'Connor(1986a) have presented a general form of the WPA radiation stress terms for linear waves on a sloping bed, equation (2.18). The simplest expressions for the WPA radiation stress terms for linear waves have been derived by Longuet-Higgins and Stewart(1960,1961,1962,1964), Longuet-Higgins(1970a,b).

According to Longuet-Higgins and Stewart(1960), the component S_{XX} of the radiation stress along a wave ray is explained as the time-average value of the total flux of horizontal momentum across a vertical plane minus the still water hydrostatic pressure force. They have taken the main X axis as the wave propagation direction first, and transformed the expressions for arbitrary wave direction later. Assuming $\eta=0$, the normal radiation stress S_{XX} (in direction X) is:

$$S_{XX}=<\int_{-d}^{\xi}(p+\rho u^2)\,dz>-\int_{-d}^{0}p_0 dz \qquad (2.37)$$

Similarly, the transverse stress component S_{YY} (in direction Y, normal to X) is:

$$S_{YY}=<\int_{-d}^{\xi}(p+\rho v^2)\,dz>-\int_{-d}^{0}p_0 dz \qquad (2.38)$$

Inserting small-amplitude linear wave theory for the particle orbital velocities (u,v), water elevation (ξ), and dispersion relation ($\sigma^2=gk\tanh kd$), and wave-period-averaging the two radiation stress terms leads to the results:

$$S_{xx}=S_{XX}\cos^2\theta+S_{YY}\sin^2\theta \qquad (2.39)$$

$$S_{xy}=S_{XX}\sin\theta\cos\theta-S_{YY}\cos\theta\sin\theta \qquad (2.40)$$

$$S_{yy}=S_{XX}\sin^2\theta+S_{YY}\cos^2\theta \qquad (2.41)$$

$$S_{XX}=E\left(\frac{2c_g}{c}-0.5\right),\quad S_{YY}=E\left(\frac{c_g}{c}-0.5\right) \qquad (2.42)$$

where E is the wave energy per unit area of sea surface ($\rho ga^2/2$), θ is the counter-clockwise wave direction from the negative x axis, S_{xx}, S_{xy}, S_{yy} are the radiation stress components in the cartesian co-ordinate system (x,y,z).

Equation (2.35) for the pressure term can be further approximated as:

$$P_i=\rho g d\frac{\partial\eta}{\partial x_i} \qquad (2.43)$$

If the advection terms are also approximated ignoring the terms of second order, which implies strong currents and weak waves, then the depth-integrated WPA momentum equations become:

$$\frac{\partial U}{\partial t}+U\frac{\partial U}{\partial x}+V\frac{\partial U}{\partial y}+\frac{g\partial \eta}{\partial x}+\frac{1}{\rho d}\left(\frac{\partial S_{xx}}{\partial x}+\frac{\partial S_{xy}}{\partial y}\right)-\frac{\hat{T}_x}{\rho d}=0 \qquad (2.44)$$

$$\frac{\partial V}{\partial t}+U\frac{\partial V}{\partial x}+V\frac{\partial V}{\partial y}+\frac{g\partial \eta}{\partial y}+\frac{1}{\rho d}\left(\frac{\partial S_{xy}}{\partial x}+\frac{\partial S_{yy}}{\partial y}\right)-\frac{\hat{T}_y}{\rho d}=0 \qquad (2.45)$$

where U,V are the depth-average velocities in the x, y co-ordinate directions, respectively.

Comparing the wave-period-average, depth-integrated continuity and momentum equations (2.44), and (2.45) with those without waves, we can see that the contribution of the wave motion to the current field is via the new *radiation stress terms* (S_{xx}, S_{xy}, S_{yy}), and interacted friction terms ($\hat{T}_x$, $\hat{T}_y$), which contain both bed friction and lateral mixing components. While the WPA wave-induced radiation stress terms can be obtained explicitly for periodic waves, the turbulent stress (friction) terms can not be calculated algebraically due to the random nature of the motion which occupies a wide range of frequencies. The basic unsteady momentum equations can only be solved if some closure schemes are provided for both lateral mixing and turbulent shear stresses at the sea bed and water surface.

The turbulent stress terms which appear in the last terms on the left-hand-side of equation (2.44) and (2.45) can be split into the bed shear stress term ($F_{b,i}$) and the lateral mixing term ($F_{l,i}$) as:

$$\hat{T}_i = F_{b,i} + F_{l,i} \qquad (2.46)$$

Several different models for the calculation of bed friction term ($F_{b,i}$) for wave and current flows have been developed using different assumptions and solution techniques. The level of sophistication of each model varies from a constant coefficient to one-dimensional (vertical) Reynolds stress closure models.

The lateral mixing term ($F_{l,i}$) has also been modelled by many different ways, from a simple eddy viscosity assumption to two-equation turbulence closure sub-models, see Longuet-Higgins(1970), Basco(1982), Yoo and O'Connor(1986a), and Wind and Vreugdenhill(1986). However, the use of the more sophisticated approaches adds considerably to the complexity and operational use of such models.

The late 1970's and 1980's has seen the development of various numerical models for general seabed geometry. Such numerical models are distinguished by the type of dependent variables (primitive or stream function) used; by the approximations adopted to simplify them; and by the particular formulation of bed friction, lateral mixing, wave breaking, and numerical techniques used. However, most existing WPA depth-integrated numerical models for wave-induced currents solve the primitive continuity and

momentum equations (2.31), (2.44) and (2.45). Some particular examples are given below.

Birkemeier and Dalrymple(1975) developed a model of wave-induced current which solves time-dependent primitive variables, for water level, and horizontal velocities. Their model included the effects of set-up and coastal flooding, but excluded nonlinear advection and lateral mixing terms.

Ebersole and Dalrymple(1980) presented a model similar to Birkemeier and Dalrymple(1975). Their model included the advection and lateral mixing terms, but excluded current interaction on waves.

Liang(1983) reported a finite-element model of wave-induced current. An interesting feature of the solution technique is that he neglected the time-dependent term and solved the resulting continuity and momentum equations to obtain equilibrium solution directly, while most existing models of wave-induced current solve the unsteady depth-integrated basic equations. The limitation of the model is that the numerical method used in the model requires more computation effort than explicit finite difference methods used by other researchers, and that the water level set-down or set-up due to the radiation stress cannot be calculated due to the use of the approximation of water level that the water level is the same as still water level.

Wind and Vreugdenhill(1986) developed an implicit finite difference wave-induced current model. They included advection and mixing terms, and compared the model result with a laboratory experiment on mono-frequency waves with general agreement. They used a two-equation turbulence closure sub-models for the calculation of the lateral mixing terms, which require a long computation time.

Yoo and O'Connor(1986a) developed one of the most comprehensive wave-induced current model including both coastal flooding (set-up) and wave-current interaction, which was coupled with an unsteady WPA wave model, see Section 2.2.5.2. The formulations of bed friction and lateral mixing are based on a mixing length and a two-equation turbulence model, respectively, so that the model requires a long computation time. However, their comprehensive model may be useful for comparison or verification of any other simplified wave-induced current models.

When seabed contours are assumed to be parallel along the y axis, and only a steady state situation is considered, then the momentum equations are reduced to a much simpler one-dimensional form, which is useful for describing on-offshore longshore current distribution on parallel beaches. This approach is a sub-set of general two-dimensional horizontal modelling. Early models produced in the 1960's and 1970's produced the first results for longshore current distribution on parallel beaches.

Ignoring the water surface wind shear stress, the momentum equation (2.45) is reduced to:

$$\frac{\partial S_{xy}}{\partial x} - F_{b,y} - F_{l,y} = 0 \qquad (2.47)$$

where $F_{b,y}$ is the WPA bed shear stress for wave and current flows in the y direction, and $F_{l,y}$ is the lateral mixing stress in the y direction. Bowen(1969) produced one of the first longshore current profiles using the momentum balance equation (2.47). Longuet-Higgins(1970) also developed a longshore current model, but used a different formulation of the three terms in equation (2.47) from Bowen(1969). Longuet-Higgins' solution is introduced later in Chapter 5. Other models have been presented by Thornton(1970), Jonsson et al.(1974), Kraus and Sasaki(1979) with minor differences in the formulations for the three terms involved. However, the application of the one-dimensional horizontal model is limited to the concept of parallel bathymetry, and is not adequate for general engineering problems.

2.3.4 Depth-averaged Horizontal Models Solving Stream Function

Another group of models have used a transformation of the momentum equation by changing the dependent variables of primitive velocities and mean water level for a stream function. Researchers, such as Bowen(1967, 1969), obtained an analytical solution of the stream function for simple beach cases, although considerable approximations were

needed. Noda(1972) was one of the first to model nearshore circulation for general two-dimensional geometries using the stream function approach. Noda's(1972) model results showed the presence of circulation cells (rip current), although the model was unstable with wave and current interaction.

Noda(1974) introduced a stream function ψ defined by:

$$\frac{\partial \psi}{\partial y} = -Ud \; ; \quad \frac{\partial \psi}{\partial x} = Vd \tag{2.48}$$

Ignoring water level set-up, Noda(1974) induced the following equation.

$$\begin{aligned} &\frac{\partial^2 \psi}{\partial x^2} + \frac{\partial^2 \psi}{\partial y^2} + \frac{1}{F}\frac{\partial F}{\partial y}\frac{\partial \psi}{\partial y} + \frac{1}{F}\frac{\partial F}{\partial x}\frac{\partial \psi}{\partial x} \\ &= \frac{g}{F}\left(\frac{\partial}{\partial y}\left(\frac{1}{d}\left(\frac{\partial S_{xx}}{\partial x} + \frac{\partial S_{xy}}{\partial y}\right)\right) - \frac{\partial}{\partial x}\left(\frac{1}{d}\left(\frac{\partial S_{yy}}{\partial y} + \frac{\partial S_{xy}}{\partial x}\right)\right)\right) \end{aligned} \tag{2.49}$$

where F is $2fH/d^2T$ sinh kd, f is a friction coefficient(=0.01), H is the wave height, d is the water depth.

Sasaki(1975), Liu and Mei(1975), and Dalrymple et al.(1977) have also used the stream function approach with particular bed shear stress formulations, and showed various applications. Advection terms and lateral mixing terms have not been included in their stream function approaches, probably due to the difficulty of numerical treatment of the nonlinear terms.

The steady state stream function equation was solved as a boundary value problem. Therefore, all boundary values should be properly specified a priori. It is rather simple to assign the boundary values for the stream function where the velocities are known a priori. However, it is not easy to give adequate boundary conditions where currents exist, which are part of the solution that is desired. It is also difficult for the stream function approach to include the modification of the mean water level due to the existence of waves and currents, since the water depths are kept unchanged while the stream function is solved.

2.4 Conclusions

2.4.1 Wave Models

For simulation of sediment transport and bathymetric change for medium or long term periods, the simplicity of each wave or current model is vital for the whole system. But, the models used should still reproduce important mechanisms, so that they should not be oversimplified.

The present short review of wave propagation models indicates that a wide range of models have been described to predict nearshore wave climate.

The IWP-type model, such as the Boussinesq model, appears to offer the best possibilities for including all nearshore transformation processes. However, the cost of using such approaches for medium-term siltation modelling is likely to be prohibitive for the foreseeable future.

While Elliptic, Parabolic, and Hyperbolic models which solve for the wave velocity potential directly require a large number of computational grid points, Evolution approaches allow the use of coarse grids. Evolution Parabolic or Elliptic approaches solve on regular grids but the assumptions made in some Parabolic models make them unsuitable for situations with widely scattering wave energy, since they have been derived under the assumption that wave motion is largely propagated in the direction of the main axis of the computational grid.

At present, engineering design makes extensive use of WPA Ray models, but these have difficulty when dealing with diffraction processes. It is also difficult to use the Ray approach to calculate wave-induced currents. The hyperbolic WPA wave model has flexibility for external diffraction and current interaction, but it requires an iteration procedure until the final steady state solution is obtained.

For present purposes, it is proposed to use the Evolution Elliptic approach of Ebersole et al.(1986), since it retains the essential processes of seabed shoaling, refraction and diffraction; it being assumed that reflection and wave-current interaction effects are

small. The model will be modified to include the external diffraction produced by structures.

2.4.2 Wave-Induced Current Models

The short review of wave-induced current models shows that both WPA two and three-dimensional models have been developed but that the three-dimensional approaches lack laboratory and field testing. They are also likely to be expensive to use for long-term simulations.

It is also considered that the stream function approach for the WPA depth-integrated horizontal two-dimensional modelling is less useful for general geometry than the primitive variable approach, since the stream function approach is more restricted by the approximations involved.

Thus, for present purposes, it is proposed to use the WPA depth-average primitive variable approach of Yoo and O'Connor(1986a) but to simplify it in the surf zone.

CHAPTER 3. REVIEW OF SEDIMENT TRANSPORT MODELS FOR WAVE AND CURRENT FLOWS

3.1 Introduction

Coastal sediment transport problems arise generally from the siltation of port and harbour navigation channels or pipeline trenches, from siltation within the relatively calm areas in harbours behind breakwaters, and in the re-alignment of coastlines produced by the construction of harbour breakwaters, land reclamations, coastal jetties or beach protection structures, such as groynes, revetments and offshore breakwaters. Such problems have generally been tackled by physical models, but more recently by computer models. For example, Irie and Nadaoka(1984) used a physical model to examine depth changes caused by wave and wave-induced currents around a breakwater, while Deigaard et al.(1986b) used a computer model to study siltation of a pipeline trench along the Danish coastline.

The majority of coastal situations involve sandy sediment and consequently, the present chapter is not concerned with cohesive sediment problems. Similarly, because many situations are dominated by wave-induced currents, it is proposed to ignore tidal modelling, and any influences of long-term unsteady sediment behaviour produced by variations in tidal conditions.

The chapter is concerned with providing a background to the choice of sediment model to be used to study medium term bed level changes at sites such as Chukpyon Harbour. Previous authors have produced extensive reviews of both scientific computer models, which have been used to reproduce detailed coastal processes on time-scales of a few seconds, to the more general engineering models which involve time-scales from several hours during a storm to many tens of years as coastlines slowly adjust to the impact of new structures. Typical reviews include those by McDowell and O'Connor(1977), O'Connor(1979), Sleath(1984), Horikawa(1986), O'Connor and Nicholson(1988b), Nielsen(1988), van Rijn(1990), and O'Connor(1991). For present purposes, only a short review is given with emphasis on the more recent three-dimensional approaches.

All particulate sediment numerical models require information of bed roughness. The bed roughness value may be one of the most important parameters to simulate sediment transport. Theoretical and experimental researches have been done by many workers including Nielsen(1981), Vonvisessomjai(1984), Hedegaard(1985), Raudkivi(1988), Sato(1988), Amos et al.(1988), Lee-Young and Sleath(1990), and O'Connor(1992). Van Rijn(1982) has also shown an analysis of experimental data to determine the relation of bed geometric shape and resultant conceptual bed roughness. More recently, Madsen et al.(1990) has modified the description of bed roughness to include the smoothing effect of random waves. Despite such advances, it is generally recognized that the techniques for prediction of bed roughness for wave and current flows is still at an early stage. Consequently, in the present study, it is assumed that the bed roughness is known for the

sediment transport model by direct field measurement of bed grain size and bed form size.

Considering a relatively shallow sea area, including the surf zone, sediment is found to move not only along the depth-mean longshore current direction but also in the wave propagation direction. The former is called longshore sediment transport or current direction sediment transport. The latter is called onshore-offshore sediment transport or cross-shore sediment transport. Considering wave transformations on a beach with parallel seabed contours, it is known that the wave direction becomes almost normal to the beach as the waves approach breaking while the wave-induced current flows parallel to the beach along the seabed contours.

The modelling of onshore-offshore sediment transport and longshore sediment transport has generally developed separately due to the different mechanism for each of them. Onshore-offshore sediment transport has been studied by Watanabe and Horikawa(1980), Nairn(1988), and O'Connor et al.(1992c) using a Box approach, and by Deigaard et al.(1986a) using a 1DV IWP approach.

Since the instantaneous behaviour of sediment transport is related to both the magnitude of the total (wave + steady current flow) current and wave phase, other researchers have proposed a combined onshore-offshore and longshore sediment transport model for general use, see Watanabe et al.(1986), and O'Connor and Nicholson(1989).

In the present study, onshore-offshore transport is neglected, since the main objective of the study is to simulate horizontal two-dimensional bed level change near harbour entrances, rather than shoreline changes.

In the absence of tides, engineering modelling has developed along two main lines dictated by time-scale. For short term predictions covering 5-10 hours - the so-called "worst storm" situation in the lifetime of a structure - either a "Continuum" approach or a "Box" approach has been used. For long term (100 years) predictions, one- and multi- (also called n-) line models have been developed in which the surf zone is described by a single or by n-lines of computational points spaced along the beach direction.

The Continuum approach uses a mesh of computation points but solves either depth-average two-dimensional or three-dimensional time-dependent suspended sediment equations coupled with a bed level change mass continuity equation. Such equations can operate through the wave-period (IWP) but more usually operate in a WPA mode.

The Box approach distributes a "mesh" of computation points over the coastal area and then uses the sediment transport rates at the mesh intersections to calculate the bed level changes using a two-dimensional-horizontal, depth-averaged, sediment mass conservation equation. The sediment transport rates are either calculated from WPA empirical formulae or from IWP one-dimensional vertical over the depth (1DV) time-dependent suspended sediment equations.

For the present siltation modelling study, only WPA type models are considered to be adequate for medium or long term morphological change due to their small total computational time. WPA modelling of sediment transport is conceptually divided into 3 groups as Continuum models, Box models, and shoreline change models. Continuum models are further divided into three-dimensional models and depth-integrated two-dimensional horizontal models.

3.2 Three-Dimensional Continuum Models

3.2.1 Introduction

Sediment transport is usually described by suspended load and bed load or total load. The movement of suspended sediment can be described by a diffusion-advection mathematical equation. When sediment transport is separately described by suspended sediment transport and bed load transport, bed level change can be obtained from the information of suspended sediment concentration and bed load transport. Final bed level changes are calculated from the difference in vertical erosion rate and deposition rate, and the effects of spatial gradients on the bed load transport rate. Entrainment is usually calculated from empirical equations using local flow and sediment characteristics, while deposition is calculated from a numerical solution of the suspended sediment equation. Bed load transport is usually estimated by an empirical formula.

Solving the three-dimensional equation of the movement of suspended sediment concentration is the most general method to incorporate the non-uniformity of the suspended sediment concentration accurately. Three-dimensional modelling also includes the minimum number of assumptions and can consider non-uniformity or unsteadiness, although it involves more computational effort as a compensation for the generality. Model accuracy to predict the suspended sediment transport is dependent on the mixing coefficients, bed reference level concentration, and velocity distribution.

Typical models involving currents have been described by a number of authors. For example, Nicholson(1978,1983), who reviewed 3D sediment transport modelling for current flows up to 1983, and presented 3D sediment transport models for particulate and cohesive sediments using a regular grid system; Sheng(1983), who presented a 3D cohesive sediment transport model which is linked to a 3D hydrodynamic flow model using a sigma coordinate transformation; Nicholson and O'Connor(1986), who described a 3D cohesive sediment transport model and its application to a field situation; O'Connor and Nicholson(1988a), who described a 3D particulate sediment transport model and its application to a laboratory experiment situation.

Typical models involving both waves and currents have been described by van Rijn(1985), who described a 2DV particulate sediment transport model; van Rijn and Meijer(1988, 1991), who described a 3D particulate sediment model using a finite element method; Van Rijn(1989), and van Rijn and Kroon(1992) described a 1DV

sediment transport model which has relevant theories for their 3D model. A description of the essential features of such models is given below.

3.2.2 Basic Equation of Suspended Sediment Concentration

Sediment mass is conserved in a finite fixed volume of fluid moving by advection, and can be described by the equation, see Fischer et al.(1979):

$$\frac{\partial}{\partial t}(\rho c)+\frac{\partial}{\partial x}(\rho c u_s)+\frac{\partial}{\partial y}(\rho c v_s)+\frac{\partial}{\partial z}(\rho c w_s)=0 \qquad (3.1)$$

where u_s, v_s, w_s are the instantaneous sediment velocities in the x,y,z directions, respectively; c is the instantaneous sediment concentration in volume of sediment per unit volume of solution; and ρ is the sediment/water mixture density in mass per unit volume of mixture.

It is next assumed that only very small changes in mixture density occur and that all quantities can be written in terms of turbulent ('), turbulent mean ($\bar{}$), and wave-phase-point mean ($\tilde{}$) values, that is:

$$c=\bar{c}+\tilde{c}+c' \;;\; u_s=\bar{u}_s+\tilde{u}_s+u_s' \qquad (3.2a)$$

$$v_s=\bar{v}_s+\tilde{v}_s+v_s' \;;\; w_s=\bar{w}_s+\tilde{w}_s+w_s' \qquad (3.2b)$$

Substitution of equation (3.2) into equation (3.1) and wave-period averaging (denoted by

bracket < >) produces the result:

$$\begin{aligned}&\frac{\partial \overline{c}}{\partial t}+\frac{\partial}{\partial x}(\overline{u}_s\overline{c})+\frac{\partial}{\partial y}(\overline{v}_s\overline{c})+\frac{\partial}{\partial z}(\overline{w}_s\overline{c})\\&=-\frac{\partial}{\partial x}\langle u_s'c'\rangle-\frac{\partial}{\partial y}\langle v_s'c'\rangle-\frac{\partial}{\partial z}\langle w_s'c'\rangle\\&\quad-\frac{\partial}{\partial x}\langle \tilde{u}_s\tilde{c}\rangle-\frac{\partial}{\partial y}\langle \tilde{v}_s\tilde{c}\rangle-\frac{\partial}{\partial z}\langle \tilde{w}_s\tilde{c}\rangle\end{aligned} \qquad (3.3)$$

Use is now made of Fick's law to relate the turbulent sediment fluxes to turbulent diffusion coefficients (ϵ_x, ϵ_y, ϵ_z), that is:

$$-\langle u_s'c'\rangle=\epsilon_x\frac{\partial \overline{c}}{\partial x}\ ;\ -\langle v_s'c'\rangle=\epsilon_y\frac{\partial \overline{c}}{\partial y}\ ;\ -\langle w_s'c'\rangle=\epsilon_z\frac{\partial \overline{c}}{\partial z} \qquad (3.4)$$

While the sediment velocities are related to hydrodynamic fluid velocities by the equation:

$$\overline{u}_s=\overline{u}\ ;\ \overline{v}_s=\overline{v}\ ;\ \overline{w}_s=\overline{w}-w_f \qquad (3.5)$$

where $\overline{u}$, $\overline{v}$, $\overline{w}$ are the wave-period-average fluid velocities, and w_f is the particle fall velocity, and the z axis is assumed to be positive in an upward vertical direction. Equation (3.3) can now be reduced to the equation:

$$\begin{aligned}&\frac{\partial \overline{c}}{\partial t}+\frac{\partial}{\partial x}(\overline{uc})+\frac{\partial}{\partial y}(\overline{vc})+\frac{\partial}{\partial z}((\overline{w}-w_f)\overline{c})\\&=\frac{\partial}{\partial x}(\epsilon_x\frac{\partial \overline{c}}{\partial x})+\frac{\partial}{\partial y}(\epsilon_y\frac{\partial \overline{c}}{\partial y})+\frac{\partial}{\partial z}(\epsilon_z\frac{\partial \overline{c}}{\partial z})\\&\quad-\frac{\partial}{\partial x}(\tilde{u}_s\tilde{c})-\frac{\partial}{\partial y}(\tilde{v}_s\tilde{c})-\frac{\partial}{\partial z}(\tilde{w}_s\tilde{c})\end{aligned} \qquad (3.6)$$

In many past studies, the wave correlation terms (the last three terms of equation (3.6)) have been neglected. However, Van Rijn(1989) and O'Connor(1991) have suggested that

these terms are not zero but that their effect can be included into the diffusion terms. The diffusion terms are thus renamed to ϵ_{sx}, ϵ_{sy}, and ϵ_{sz}, respectively.

Finally, making use of the fluid continuity equation (2.25), that is:

$$\frac{\partial \overline{u}}{\partial x}+\frac{\partial \overline{v}}{\partial y}+\frac{\partial \overline{w}}{\partial z}=0 \qquad (2.25)$$

the basic three-dimensional WPA equation for suspended sediment is given below after dropping the overbars for convenience:

$$\frac{\partial c}{\partial t}+u\frac{\partial c}{\partial x}+v\frac{\partial c}{\partial y}+(w-w_f)\frac{\partial c}{\partial z} -\frac{\partial}{\partial x}(\epsilon_{sx}\frac{\partial c}{\partial x})-\frac{\partial}{\partial y}(\epsilon_{sy}\frac{\partial c}{\partial y})-\frac{\partial}{\partial z}(\epsilon_{sz}\frac{\partial c}{\partial z})=0 \qquad (3.7)$$

3.2.3 Basic Equation of Seabed Level Change

While the suspended sediment concentration above a reference level near to the sea-bed is solved by equation (3.7), the change in bed level is obtained from the sediment mass conservation equation:

$$(1-n)\frac{\partial z_b}{\partial t}+\frac{\partial q_{bx}}{\partial x}+\frac{\partial q_{by}}{\partial y}-(D-P)=0 \qquad (3.8a)$$

$$D=w_f c_a \;;\; P=(\epsilon_{sz}\frac{\partial c}{\partial z})_{bed}=w_f c_a^{\infty} \qquad (3.8b)$$

where z_b is the mean bed level above a horizontal datum; D, P are the amounts of

sediment deposition and erosion at the bed, respectively in net volume per unit area per unit time; c_a, c_a^{∞} are the near-bed suspended sediment concentrations at time t and at $t=\infty$ (infinity), respectively; $(\epsilon_{sz}\,\partial c/\partial z)_{bed}$ is the entrainment of sediment at the nearbed level (a), usually taken as half the bed form height(Δ_r) for a rippled bed, see Fig. 3.1; n is the porosity of the seabed; q_{bx}, q_{by} are the x, y components of the bed load transport rate (q_b) which has units of net volume per unit area per unit time.

If the wave and current field lasts long enough to achieve a steady state situation ($\partial c/\partial t=0$), then the deposition minus erosion rate (D-P) becomes identical to the gradient of suspended sediment load as can be shown by depth-integration of equation (3.7), which leads to equation (3.9):

$$D-P=-\frac{\partial q_{sx}}{\partial x}-\frac{\partial q_{sy}}{\partial y} \qquad (3.9)$$

Substituting equation (3.9) into equation (3.8), the bed level change can be obtained from the spatial gradients (q_{tx}, q_{ty} of the total (bed+suspended) sediment load (q_t):

$$(1-n)\frac{\partial z_b}{\partial t}+\frac{\partial q_{tx}}{\partial x}+\frac{\partial q_{ty}}{\partial y}=0 \qquad (3.10a)$$

$$q_{tx}=q_{bx}+q_{sx}\ ;\ q_{sx}=\int_{z_b}^{\eta} uc\ dz \qquad (3.10b)$$

$$q_{ty}=q_{by}+q_{sy}\ ;\ q_{sy}=\int_{z_b}^{\eta} vc\ dz \qquad (3.10c)$$

where η is the mean water level, see Fig. 3.1.

Solution of the equation for bed level change (3.10) requires details of the location of the "near bed level", the bed load transport in waves and currents, and the suspended load transport in waves and currents, which is obtained from the solution of the equation of suspended sediment concentration (3.7), which, in turn, requires velocity distribution. Solution of the equation for suspended sediment concentration (3.7) requires details of the near-bed concentration (c_a^∞), the diffusion coefficients ϵ_{sx}, ϵ_{sy}, and ϵ_{sz}, and details of the three-dimensional flow field (u,v,w).

3.2.4 Reference Level Concentration (c_a^∞)

The two near-bed quantities, bed load (q_b) and reference level concentration (c_a^∞) are usually predicted by empirical formula, and they are closely related. Ideally, both formula for bed load and reference level concentration should be calibrated by direct measurements. However, once one quantity is calibrated by direct measurements, the other quantity can be predicted from the relation between the two quantities.

Various authors have proposed empirical equations for c_a^∞. Nielsen(1984) proposed a formula for waves:

$$c_a^\infty = 0.005\psi_r^3 \qquad (3.11)$$

where ψ_r is a grain-related Shields parameter modified to include the effect of ripples.

Fredsoe et al.(1985) related the instantaneous reference level suspended sediment concentration within a wave period with a Shields parameter for a flat bed.

Van Rijn(1989) is one of the few authors to address the case of waves and currents. He proposed an empirical formula for the reference level sediment concentration for wave and current flows over a rippled or flat bed, and represents the most recently published formula. Originally he developed the formula for reference level suspended sediment concentration for situations with only currents, and he compared it with measured data for currents. The formula was also calibrated by laboratory measurements for wave situations. The reference level for "near-bed" position was selected to be half a ripple height for rippled sediment beds, or the sediment boundary layer thickness for a flat bed. Van Rijn's equation has the form in net sediment volume per water volume (m^3/m^3):

$$c_a^{\infty}=0.015\frac{d_{50}}{a}\frac{T_*^{1.5}}{D_*^{0.3}} \tag{3.12}$$

where

$$T_*=\frac{\tau'_{b,wc}-\tau_{cr}}{\tau_{cr}}, \quad if\ \tau'_{b,wc}\geq\tau_{cr}$$
$$T_*=0, \quad if\ \tau'_{b,wc}<\tau_{cr} \tag{3.13}$$

$$\tau'_{b,wc}=\tau'_{b,w}+\tau'_{b,c} \tag{3.15}$$

$$\tau'_{b,w}=\frac{1}{4}\rho\mu_w f_w U_{\infty}^2 \tag{3.16}$$

$$D_*=d_{50}\left((s-1)g/\nu^2\right)^{\frac{1}{3}} \tag{3.14}$$

$$\tau'_{b,c}=\rho\alpha_{wc}\mu_c f_a U^2 \tag{3.17}$$

$$\tau_{cr}=(\rho_s-\rho)gd_{50}\psi_{cr} \tag{3.18}$$

$$\begin{aligned}\psi_{cr}&=0.24\ D_*^{-1}, && 1<D_*\le 4\\ &=0.14\ D_*^{-0.64}, && 4<D_*\le 10\\ &=0.04\ D_*^{-0.1}, && 10<D_*\le 20\\ &=0.013\ D_*^{0.29}, && 20<D_*\le 150\\ &=0.055, && D_*\ge 150\end{aligned} \tag{3.19}$$

$$\mu_c=\frac{f'_c}{f_c} \tag{3.20}$$

$$\mu_w=\frac{0.6}{D_*} \tag{3.21}$$

$$\alpha_{wc}=\frac{\ln^2(90\frac{\delta_w}{k_a})}{\ln^2(90\frac{\delta_w}{k_s})} \tag{3.22}$$

$$f'_c=0.24\ \log^{-2}(12d/3d_{90}) \tag{3.23}$$

$$f_c=0.24\ \log^{-2}(12d/k_s) \tag{3.24}$$

$$f_a=0.24\ \log^{-2}(12d/k_a) \tag{3.25}$$

$$\delta_s=3k_s \tag{3.26}$$

$$\begin{aligned}k_s&=3\ \Delta_r, && \textit{for a rippled bed}\\ k_s&=\delta_w, && \textit{for a flat bed}\end{aligned} \tag{3.27}$$

$$\delta_w = 0.072\, A (A/k_s)^{-0.25} \tag{3.28}$$

$$A = \frac{H}{2 \sinh(\frac{2\pi d}{L})} \tag{3.29}$$

$$U_\infty = \frac{\pi H}{T \sinh(\frac{2\pi d}{L})} \tag{3.30}$$

where a is the reference level from the mean bed level, d_{50} is the median diameter of bed material, T_* is the dimensionless shear stress parameter, D_* is the dimensionless particle diameter, $s = (\rho_s-\rho)/\rho$, ρ_s is the sediment density, ρ is the water density, ν is the water kinematic viscosity, $\tau_{b,wc}$' is the wave and current-related effective (grain-drag) bed-shear stress (N/m^2), $\tau_{b,w}$' is the wave-related effective (grain-drag) bed-shear stress (N/m^2), $\tau_{b,c}$' is the current-related effective (grain-drag) bed-shear stress, τ_{cr} is the critical bed-shear stress according to Shields (N/m^2), U is the depth-mean current velocity, U_∞ is the near-bed wave maximum orbital velocity given by linear wave theory, μ_w is an efficiency factor for waves, μ_c is an efficiency factor for currents, k_s is the bed roughness, k_a is the apparent roughness, see Fig. 3.2, f_c, f_c', f_a are current-related friction factors, f_w is a wave-related friction factor, α_{wc} is the wave-current interaction coefficient, δ_w is the wave-related boundary layer thickness, δ_s is the sediment-related near-bed mixing layer thickness, A is the wave orbital excursion length amplitude near the bed, U_∞ is the wave orbital velocity amplitude near the bed, H is the wave height, d is the water depth, L is the wave length, and T is the wave period.

For a rippled bed, the selection of the reference level height is an important problem, considering the rapid variation of wave-period-average suspended sediment concentration near the bed. Van Rijn(1989) selected half a ripple height from the mean bed level as the reference level. He also treated a flat bed differently from a rippled bed by using the concept of the near-bed mixing layer thickness, equation (3.26).

Van Rijn(1989) calibrated equation (3.12) with a set of laboratory data involving waves. The factor μ_w was needed to fit the calculated reference concentration values to the measured reference concentration data, and resulted in the functional dependence (equation 3.21) on effective bed grain size (D_*).

At first sight Van Rijn's expression for c_a^∞ appears to be a combination of the non-dimensional groups a/d_{50}, T_* and D_*. However, if the critical shear stress term is ignored in the numerator of the expression for T_*, and putting the weak relation of c_a^∞ with $D_*^{-0.3}$ and the proportional relation between a and d_{50} (implied by existing bed roughness models) into the scaling parameter C_1, the equation reduces to the form:

$$c_a = C_1 |\psi'|^{1.5} \qquad (3.31)$$

where ψ' is an effective (grain-drag) Shields parameter for wave and current ($=\tau_{b,wc}'/(\rho_s-\rho)gd_{50}$). The functional relationship of the reference level concentration in equation (3.31) is a simple function of the Shields paramcter, as the Nielsen(1984)'s equation (3.11). However, the power of 1.5 in equation (3.31) is smaller than Nielsen's(1984) value of 3.

Van Rijn(1989) obtained the representative bed-shear stress for waves and current by adding the two separate shear stresses for waves and current, with somewhat arbitrary reduction parameters, μ_w, and μ_c. It is hardly expected that the correlation between the efficiency factor for waves (μ_w) with the particle size parameter (D_*) can be explained by a physical mechanism. Therefore, it is suggested that if variation of instantaneous shear stress can be properly accounted for without involving any reduction factor, the relationship between the WPA reference level concentration and the Shields parameter could be improved.

For present purposes, a new formula for specifying the WPA reference level suspended sediment concentration is proposed. The formula for the suspended sediment concentration in terms of net volume of sediment per unit volume (m^3/m^3) has the form:

$$c_a^{\infty} = C_2 < |\vec{\Psi}_{wc}|^{1.5} > \qquad (3.32)$$

where C_2 is a scale factor, $\vec{\Psi}_{wc}$ is the instantaneous vector Shields parameter based on the total shear stress, defined as:

$$\vec{\Psi}_{wc}(t) = \frac{\vec{\tau}_{b,wc}(t)}{(s-1)\rho g d_{50}} \qquad (3.33)$$

$$\vec{\tau}_{b,wc}(t) = \vec{\tau}_{b,cm} + \vec{\tau}_{b,w}(t) \qquad (3.36)$$

$$\vec{\tau}_{b,cm} = \frac{f_{cm}}{f_c}\vec{\tau}_{b,c} \; ; \; \vec{\tau}_{b,c} = \rho f_c \vec{U}|\vec{U}| \qquad (3.34)$$

$$\vec{\tau}_{b,w}=\rho\frac{f_w}{2}\vec{U}_\infty|\vec{U}_\infty|\cos(\sigma t) \qquad (3.35)$$

where $\vec{\tau}_{b,wc}$ is the wave and current-related total bed shear stress; $\vec{\tau}_{b,cm}$ is the current-related total bed shear stress which includes the effect of waves; $\vec{\tau}_{b,w}$ is the instantaneous wave-related vector shear stress, see Fig. (3.3); σ is the wave angular frequency (2π/T); $\vec{U}$ is the depth-mean current velocity vector; $\vec{U}_\infty$ is the near-bed maximum wave orbital velocity vector; f_w is the wave friction coefficient (no currents); f_c is the current friction factor (no waves, $=\kappa^2/(\ln(d/z_0)-1)^2$; κ is the von Karman constant, $z_0 = k_s/30$; and f_{cm} is a current friction factor modified by waves. The bracket $< >$ indicates a wave-period-average, that is $1/T\cdot\int_0^T()dt$.

The wave friction coefficient f_w is obtained from a 1DV wave boundary layer model, see Chapter 7, as:

$$f_w=0.000684\ \exp\left(7.80\left(\frac{A}{z_0}\right)^{-0.106}\right) \qquad (3.37)$$

The current friction factor modified by waves (f_{cm}) is introduced in Chapter 7 in detail. For a flat bed, van Rijn's(1989) bed roughness (k_s) may be used. The power of 1.5 is suggested as that of van Rijn(1989)'s equation (3.12) for the wave-period-average reference concentration.

The above equation (3.32) ignores the minimum or critical Shields parameter which is needed for incipient motion of bed sediment. However, the error by ignoring the

minimum Shields value may not be significant in strong current or wave situations. Considering waves in the field, especially random wave and current situations, which occur in real fields, the maximum bed shear stress within a wave period is usually much larger than the WPA bed shear stress so that the critical Shields value becomes less important. Davies(1991) also excluded the effect of critical Shields parameter from the calculated Shields parameter for the IWP simulation of suspended sediment concentration in his 1DV suspended sediment model so as to always obtain a non-zero positive reference level concentration.

Equation (3.32) implies that the instantaneous suspended sediment concentration is directly related to the instantaneous near-bed shear stress and that the wave-period-average value is obtained by a direct time average. Equation (3.32) is also different from van Rijn(1989)'s formula (3.12), since it uses a vector-summed shear stress rather than a scalar addition of wave and current shear stresses; the wave-period-average value then being obtained by a direct time integration. Clearly, it may be possible to parameterize this approach, but it is not attempted in the present work. Instead, direct integration is done at each grid point by using 16 time-steps per wave-period.

It should be noted that the Shields parameter for combined waves and currents in equation (3.32) is for total shear stress. Ideally, the skin-friction component of the shear stress should be used since this quantity is directly responsible for moving grains. In the present work, it is assumed that the skin-friction component is related to the total shear

stress and the self-adjusted bed roughness. Such simplification is considered justified for present purposes.

In order to complete equation (3.32) for an engineering usage, the scale factor C_2 needs to be calibrated. The calibration of the factor is shown in Chapter 6 using limited data sets from laboratories and a field (Chukpyon, Korea).

3.2.5 Bed Load (q_b)

Sediment transport by rolling bed-grain or a saltation process has usually been called bed load. Since the movement of sediment and water mixture within a thin bed load layer is very complex, the bed load transport has been predicted by empirical formulae. Typical empirical bed load formulae for current flows have been proposed by Einstein(1950), Brown(1950), and van Rijn(1984). Empirical bed load formulae for wave and current flows have also been proposed by Bijker(1967), Grant and Madsen(1976), and van Rijn(1989).

Brown(1950) suggested an empirical bed load formula for current flows as follows:

$$\phi_b = 40\psi^3 \qquad (3.38)$$

where ϕ_b is the non-dimensional bed load transport, ψ is the Shields parameter, which have the form:

$$\phi_b = \frac{q_b}{w_f d_{50}} \tag{3.39}$$

$$\psi = \frac{\tau_b}{\rho (s-1) g d_{50}} \tag{3.40}$$

Grant and Madsen(1976) proposed a modified scale factor in equation (3.38) for wave-period-mean bed load transport.

Einstein(1950) proposed a relationship between the bed load and the reference level sediment concentration for current flows on a flat bed. He assumed that the concentration is constant inside the bed load layer and that the bed load can be obtained by multiplying the reference level concentration (c_a^{∞}), the bed load layer thickness (a), and the depth-mean velocity in the layer (u_b), which is:

$$q_b = c_a^{\infty} \cdot a \cdot u_b \tag{3.41}$$

He further assumed that the thickness for the bed load on a flat bed is $2d_{50}$, and approximated the mean horizontal velocity inside the bed load layer to be 11.6 u_*, where u_* is the shear velocity.

Bijker(1971) also proposed a relationship between the bed load and the reference level sediment concentration for wave and current flows on a rippled bed. He assumed the thickness of the bed load as half the ripple height ($\Delta_r/2$), and the mean velocity inside the bed load layer as 6.34 u_*, where u_* is the total bed friction velocity.

Van Rijn's (1989) bed load formula (3.41) is the most recently published formula for wave and current flows. Van Rijn(1989) proposed an empirical bed load formula for wave and current flows, which is a simple extension of his bed load formula for current flow alone. Thus:

$$q_b = 0.25 \cdot u'_{*,c} d_{50} \frac{T_*^{1.5}}{D_*^{0.3}} \qquad (3.42)$$

where $u_{*,c}' = (\tau_{b,c}'/\rho)^{0.5}$, d_{50} is the median diameter of the bed material. Van Rijn(1989) has not specifically mentioned about the usage of his formula (3.43) for the surf zone. Van Rijn does not report if the formula has been calibrated against measured bed load data for wave and current flows. Comparing van Rijn's(1989) equation (3.12) for the reference level suspended sediment concentration and equation (3.42) for the bed load, the depth-mean velocity inside the bed load layer results in 16.7 $u_{*,c}'$, which is somewhat greater than Einstein's value. However, since Einstein used u_* rather than u_*', it is possible that van Rijn's value is reasonably close to Einstein's value. The coefficient for the bed load formula (3.42) was from the bed load formula for current-only flows, and not from direct calibration with measurements of bed load for wave and current flows, while the scale factor for the empirical equation (3.12) for reference level concentration was calibrated from laboratory measurements for wave only flows.

Similarly to van Rijn's(1989) equation (3.12) for the reference level concentration, equation (3.42) uses the scalar sum of the bed shear stresses for waves and currents with efficiency coefficients. Such an approach is reasonable for co-linear motion but less so

for angled wave and current flows. Therefore, it is proposed that a direct integration of the instantaneous bed shear stress for combined wave and current be used and may improve the accuracy of the prediction of bed load transport in a similar way to the formula for the reference level concentration.

When a non-dimensional expression for the bed load transport is to be used, and the depth-mean velocity inside the bed load layer is assumed to be proportional to the bed friction velocity as in Einstein's(1950) or Bijker's(1971) equations, equation (3.41) has the form:

$$\phi_b = C_3 \frac{a((s-1)g)^{0.5}}{w_f d_{50}^{0.5}} \psi_{cm}^{0.5} C_a^{\infty} \qquad (3.43)$$

where ϕ_b is the dimensionless bed load ($=q_b/w_f d_{50}$), C_3 is a proportional constant of the bed layer velocity to the friction velocity, ψ_{cm} is the current-related Shields parameter modified by waves ($=u_{*,c}^2/(s-1)gd_{50}$). If it is assumed that the variation of $a((s-1)g)^{0.5}/w_f d_{50}^{0.5}$ is small (for example, a is proportional to d_{50} according to existing bed roughness theories, w_f is proportional to $d_{50}^{0.5}$ according to experimental results for a coarse particle), equation (3.43) can be expressed in a similar form to Brown's(1950) equation (3.38), but with a power of 2 rather than 3.

For present purposes, a formula for the bed load for wave and current flows is proposed to obtain compatibility with equation (3.32) for the reference level suspended sediment concentration, which is expressed in a non-dimensional form as follows:

$$|\vec{\Phi}_b| = C_4 \vec{\Psi}_{cm}^{0.5} < |\vec{\Psi}_{wc}|^{1.5} > \qquad (3.44)$$

where $\vec{\Phi}_b = \vec{q}_b / w_f d_{50}$, the unit of bed load (q_b) is net volume per unit width per unit time; and $\vec{\Psi}_{cm}$ is the Shields parameter for the modified current-related shear stress due to waves.

The functional relationship of the bed load equation (3.44) is also similar to Brown's formula, which relates the dimensionless sediment transport rate to the Shields parameter, although Brown's formula was originally developed for steady current flow. However, the power of 1.5 is proposed for equation (3.44) for the compatibility with equation (3.32) for the reference level concentration, while Brown's formula uses a power of 3. The former current-related Shields parameter represents the transport capability, while the latter wave and current-related Shields parameter represents the agitation capability.

The equation has a scaling coefficient C_4. Up to the present, there are not many bed load data available for wave and current situations. The calibration of the bed load equation (3.44) for waves and currents is done later in the theses (Chapter 6) using a limited number of field data sets from Chukpyon Harbour, Korea.

3.2.6 Diffusion Coefficients (ϵ_{sx}, ϵ_{sy}, ϵ_{sz})

Selection of the appropriate diffusion coefficient values to use for three-dimensional

models is not an easy task since there is no relevant theory to produce analytical expressions because of the complexity of real flows. Most modellers assume that sediment mixing coefficients are proportional to fluid eddy viscosity coefficients with the coefficient of proportionality being almost unity or slightly less. The diffusion coefficients for waves have been described differently from those for currents by several researchers.

In steady uniform open channel flows, it is possible to derive an analytical expression for the vertical eddy viscosity coefficient, see McDowell and O'Connor(1977). The common parabolic distribution of the diffusion coefficient over the depth for current flows ($\epsilon_{sz,c}$) has the form:

$$\epsilon_{sz,c}=\kappa\beta u_{*,c} z\left(1-\frac{z}{d}\right) \qquad (3.45)$$

where β is the proportional constant between the sediment diffusion coefficient and the fluid eddy viscosity; and $u_{*,c}$ is the current-related total friction velocity. Van Rijn(1984) has proposed a modification of equation (3.45) for the upper half of the water depth, based on the analysis of measurements, as follows:

$$\epsilon_{sz,c}=0.25\kappa\beta u_{*,c} d, \quad for\ z\geq 0.5d \qquad (3.46)$$

Many modellers then use the depth-average value of this vertical diffusion coefficient for lateral and longitudinal directions with appropriate scale factors, see O'Connor and Nicholson(1988). Due to lack of accurate experimental measurements, some researchers

have used a constant horizontal diffusion coefficient through the depth. Van Rijn and Meijer(1988) used 0.1 to 1.0 m^2/s. Kalinske and Pien(1943) argued from their experiments in steady currents that the lateral diffusion coefficient for sediment mass is slightly greater than its vertical counterpart. Considering the general turbulence characteristics, there should be a close relationship between vertical and horizontal diffusion coefficients.

For waves, many researchers have tried to produce empirical equations. For example, Homma and Horikawa(1962), Bijker(1967), Lungren(1972), Swart(1976), Nielsen(1979), and Kosyan(1985) have proposed empirical theories to describe the vertical diffusion coefficient for suspended sediment. Some workers have derived the vertical coefficient from the solution of a 1DV bed boundary layer model. For example, typical 1DV models include van Kesteren and Bakker(1984), Deigaard et al.(1986a), Fredsoe et al.(1985), Justesen et al.(1986), and Davies(1990). In some of these cases, the researchers have assumed flat bed conditions as might occur in sheet flow in the surf zone. However, recent work, see O'Connor et al.(1992a), has shown the importance of including mass transport effects in such models, otherwise incorrect results are obtained.

Van Rijn(1989) has examined many of the previous attempts to produce empirical expressions or 1DV model results for sediment diffusion coefficients, see Fig. 3.4. He concluded that each produces widely different results. Van Rijn(1989), therefore, analyzed various laboratory data sets and suggested his own set of empirical equations

based upon fitting the 1DV steady state(P=D) sediment equation to the laboratory data and thereby balancing ϵ_{sz} and its vertical distribution directly.

van Rijn(1989)'s empirical equations for diffusion coefficient related to wave flows ($\epsilon_{sz,w}$) are thus:

$$\epsilon_{sz,w}=\epsilon_{sz,w,bed}, \quad for\ z\le\delta_s \tag{3.47a}$$

$$\epsilon_{sz,w}=\epsilon_{sz,w,max}, \quad for\ z\ge 0.5d \tag{3.47b}$$

$$\epsilon_{sz,w}=\epsilon_{sz,w,bed}+(\epsilon_{sz,w,max}-\epsilon_{sz,w,bed})\left(\frac{z-\delta_s}{0.5d-\delta_s}\right), \quad for\ \delta_s<z<0.5d \tag{3.47c}$$

where

$$\epsilon_{sz,w,bed}=0.004D_*\alpha_{br}\delta_s U_\infty \tag{3.48}$$

$$\epsilon_{sz,w,max}=0.035\alpha_{br}\frac{dH}{T} \tag{3.49}$$

$$\alpha_{br}=3\left(\frac{H}{d}\right)-0.8, \quad for\ \frac{H}{d}\ge 0.6$$
$$\alpha_{br}=1, \quad for\ \frac{H}{d}<0.6 \tag{3.50}$$

where α_{br} is a breaking coefficient (>1 for plunging breakers, $=1$ for spilling breakers). For wave and current flows, van Rijn(1989) proposed the following equation:

$$\epsilon_{sz}=(\epsilon_{sz,w}^2+\epsilon_{sz,c}^2)^{0.5} \tag{3.51}$$

Since the above equations are purely based on the analysis of experimental data, the applicability of van Rijn's(1989) equation (3.47) may be limited to the range of variables covered by the measurement data.

3.2.7 Velocity Data Input

One final problem in dealing with three-dimensional models is that the solution of the suspended sediment equation (3.7) needs details of the three-dimensional flow field. In previous models, researchers have either used direct measurements of the horizontal flow field, see O'Connor and Nicholson(1988a), and then determined the vertical velocity from the local equation for fluid continuity (2.25), or have assumed a simple logarithmic velocity profile matched to a predicted depth-mean velocity, typical of steady, open-channel flow, see for example, Van Rijn and Meijer(1988). However, Lungren(1972), van Kesteren and Bakker(1984), O'Connor and Yoo(1988), and van Rijn(1989) have suggested that the simple logarithmic profile should be modified in wave/current flows to allow for the enhanced frictional dissipation in the bed boundary layer, which causes a distortion of the current velocity profile; near-bed velocity being reduced, see Fig. 3.2.

Van Rijn(1989) suggests splitting the mean-velocity profile into two straight lines as indicated by the following equation:

$$\vec{u}=\frac{\vec{U}\ln(\frac{30z}{k_a})}{-1+\ln(\frac{30z}{k_a})},\quad for\ z\geq 3\delta_w \tag{3.52a}$$

$$\vec{u}=\frac{\vec{u}_\delta\ln(\frac{30z}{k_s})}{\ln(\frac{90\delta_w}{k_s})},\quad for\ z<3\delta_w \tag{3.52b}$$

where

$$\vec{u}_\delta=\frac{\vec{U}\ln(\frac{90\delta_w}{k_a})}{-1+\ln(\frac{30d}{k_a})} \tag{3.53}$$

where $\vec{u}_\delta$ is the velocity vector at the upper edge of the wave boundary layer. Van Rijn(1989) used an empirical equation for the effective Nikuradse roughness height (k_a) related to the strength of the wave and currents fields

($U_\infty/|\vec{U}|$, $|\vec{U}|=\sqrt{U^2+V^2}$) as:

$$\begin{aligned} k_a&=k_s\exp(\frac{\gamma U_\infty}{|\vec{U}|}), && if\ k_a\leq 10\\ k_a&=10, && if\ k_a\geq 10 \end{aligned} \tag{3.54}$$

where γ is an empirical parameter. The parameter γ is 0.75, 0.75, 1.1 for wave-current interaction angles (θ_{wc}) of 0, $\pi/2$, π radians, respectively; the parameter for an intermediate angle being obtained by linear interpolation, see van Rijn(1989), or by the following equation, see van Rijn and Kroon(1992):

$$\gamma = 0.8 + \theta_{wc} - 0.3\theta_{wc}^2 \qquad (3.55)$$

where θ_{wc} is in radian. Van Rijn's(1989) and van Rijn and Kroon's(1992) engineering formulae for velocity profile (3.52) include an important effect. Their formulae include the effect of wave-current interaction up to angles of 180 °, and produce different velocity profiles for following and opposing currents, while Lungren's(1972), and van Kesteren and Bakker's(1984) 1DV boundary layer models treat the following currents and opposing currents identically. The different flow pattern for both flows has been pointed out by many experimentalists, but no prediction method had been proposed until Van Rijn(1989).

Once the horizontal velocities are obtained, the vertical velocity can be calculated from the two horizontal velocities using the water mass conservation equation (2.25) as:

$$w = \int_{z_0}^{z} \frac{\partial u}{\partial x} dz + \int_{z_0}^{z} \frac{\partial v}{\partial y} dz \qquad (3.56)$$

3.3 Depth-Average Two-Dimensional Horizontal Continuum Models

Some researchers have used a depth-integrated horizontal two-dimensional form of the three-dimensional sediment mass conservation equation (3.7) to simulate sediment transport. The governing equation has the form:

$$\frac{\partial C}{\partial t}+U\frac{\partial C}{\partial x}+V\frac{\partial C}{\partial y}=\frac{1}{d}\frac{\partial}{\partial x}\left(dD_x\frac{\partial C}{\partial x}\right)+\frac{1}{d}\frac{\partial}{\partial y}\left(dD_y\frac{\partial C}{\partial y}\right)+SS \qquad (3.57)$$

where C is the depth-mean suspended sediment concentration, D_x, D_y are the dispersion coefficients in the x, y axis, respectively, SS is the source or sink term due to the entrainment from the bed or deposition onto the bed. The dispersion coefficients represent the effect of shear dispersion and turbulent diffusion.

Traditionally this type of modelling has been widely used for studying the unsteady movement of mud, fine silts and sands, where it is assumed that the variation of concentration over the depth of the water column is not too large or can be calculated on the basis of local equilibrium conditions. Bed level changes are then determined in the same way as for the three-dimensional Continuum approach. Such modelling is traditionally used for tidal flows with wave effects introduced on a WPA basis. Typical model examples include Jin et al.(1992) for current flows, de Vriend(1987), Katopodi and Ribberink(1992) for wave and current flow, and O'Connor and Nicholson(1989), who calculated the siltation at a trench along the Danish coastline.

The problem with such modelling is the need to specify the vertical distribution of suspended sediment. The use of a vertical equilibrium profile is only an approximation and is usually based on current-dominant conditions, as assumed by Bijker(1967). The non-uniformity effects of structures and spatial non-uniformity of the flow and wave field are less easy to incorporate into this type of model.

3.4 Box Models

The simplest method to calculate bed level change for both longshore and onshore-offshore sediment transport is to use a ready-made sediment transport formulae or one-dimensional vertical (1DV) suspended sediment model at each model grid point, and then solve the bed level change equation. Such an approach assumes that the flow and sediment transport at every point is in equilibrium with local conditions. The assumption can be accepted for mildly-sloped sea bed with coarse sediment grains, since such material rapidly adjusts to local changes in flow and wave conditions, see O'Connor(1991).

The main requirement of such models is a predictor of bed and suspended sediment transport separately or combined (the total load approach) under local waves and currents.

Many sediment transport formula can be found in the literature and are either modifications of river or tidal formulae with modification for waves or are obtained by applying the river formulae to local conditions during a wave cycle and then averaging the result over a wave period.

Some widely used formulae for total load are Engelund and Hansen(1967), Ackers and White(1973) for current flows, and Grant and Madsen(1976) for wave and current flows. Bed and suspended load approaches are due to Bijker(1967), van Rijn(1989), and Raudkivi and Dette(1991).

A better approach is to use a 1DV suspended sediment model and to solve it as an IWP basis, see Ribberlink and Al-Salem(1990), Fredsoe et al.(1985), and O'Connor et al.(1992a). These include modelling of IWP suspended sediment modelling over a rippled or a flat bed, on a 1DV or 2DV dimensional domain. Some researchers included the effect of the enhanced eddy viscosity due to wave breaking. Typical 1DV wave boundary layer flow and suspended sediment models are briefly described below.

Nielsen(1986) modelled IWP suspended sediment for wave flow, and Ribberink and Al-Salem(1990) modelled IWP suspended sediment for wave and current flows over a rippled bed by a 1DV model. Justesen et al.(1986) and Ifuku and Kakinuma(1988) have included enhanced eddy viscosity by wave breaking in their IWP suspended sediment models. Davies(1990) has stressed the importance of IWP suspended sediment modelling, showing the quite big difference between WPA and IWP suspended sediment transport rate. Blondeaux and Vittori(1990), and Chapalain and Boczar-Karakiewicz(1992) modelled IWP suspended sediment over ripples using 1DV flow and sediment models.

Bakker(1974), Fredsoe at al.(1985), and Armanini and Ruol(1988) modelled IWP variation of the suspended sediment concentration over a flat bed. Sheet flow of water and sediment mixture over a flat bed has also been studied by Bakker et al.(1988).

More fundamental studies have been done by some researchers using detailed 2DV flow and suspended sediment models. The flow and the suspended sediment concentration has been modelled over a ripple length using a periodic condition for both side boundaries. The 2DV modelling approach on a non-sloped bed may be regarded as a point model in a broad meaning, since it assumes a horizontally uniform condition. Typical works on the 2DV flow or suspended sediment modelling are listed below.

Du Toit and Sleath(1981), Broker and Fredsoe(1983), Sato(1987) have done experiment on 2DV flows over ripples. Kennedy and Locher(1972) and Bosman(1982b) has measured the 2DV IWP variation of the suspended sediment concentration over ripples.

Sleath(1974a,1974b,1982,1984),Longuet-Higgins(1981),Macpherson(1984),Sato(1987), Horikawa and Ikeda(1990), Hansen et al.(1991) have done numerical modelling on 2DV flows over ripples, and Macpherson(1984) Sato(1987) and Hansen et al.(1991) have carried out 2DV flow and suspended sediment modelling.

Asaeda et al.(1989) have tried to separate bed sediment entrainment over a rippled bed into two sources, vortex entrainment and skin friction-induced entrainment on a ripple

surface for uniform current flows. O'Connor et al.(1992a) have also proposed to separate the sea-bed entrainment for wave and current flows into the vortex entrainment and the sea-bed surface entrainment, and to use two different levels for the two entrainments.

Measurements or modelling for random waves include Green and Vincent(1990), who have shown near-breakerline IWP field measurement of suspended sediment concentration in random waves; and O'Connor et al.(1992a), who have compared a set of field measurements of the near-bed velocity variation inside the wave boundary layer with a 1DV model result, which incorporates short-crested random wave and current flows.

Unfortunately, these detailed IWP, 1DV or 2DV micro-scale modelling approaches have not yet been well established or parameterized to be used for field sediment transport applications due to insufficient data to verify the various theories. The direct use of IWP modelling for a field problem is also prohibited by its long computation time.

Although the Box approach is simple to use, this type of modelling is based on an equilibrium state at each computational point, so that it cannot reflect the effect of non-uniform or unsteady sediment behaviour around structures nor the lateral dispersion that results from non-uniform flow fields. It has been pointed out that the inclusion of non-uniformity has a smoothing effect on the final bed level change, see Kadopodi and Ribberink(1992). Conversely, when non-uniformity is ignored, the bed level change may be exaggerated.

3.5 Simple Shoreline Change Models

These models calculate onshore-offshore movement of the coastline due to longitudinal differences in sediment transport rate. The longitudinal sediment transport rate is usually calculated from an empirical formula, such as the CERC formula(U.S. Corps of Engineers,1984) which relates the total integrated longshore transport rate across the surf zone to the wave energy at breaking and the angle of wave breaking, see also Horikawa(1986), and Gravens et al.(1991). Since the model involves simple empirical formulae and numerical techniques, it has been effectively used for long-term calculation of shoreline change. If the bulk longshore sediment transport rate is distributed across the surf zone, it is then possible to form a multi-line (n-line) model, see Perlin and Dean(1983), Horikawa(1986).

In most one-line applications, any onshore-offshore transport due to wave motion asymmetry, beach slope or undertow current is neglected. However, on-offshore sediment transport can be added to the model, using the concept of an equilibrium profile, so that more realistic shoreline change can be included in the model, see Cacoutas(1982). A simpler onshore-offshore approach is used in n-line models.

While such models provide a useful description of shore-line changes, they are less useful if structures are present since the effect of the structure can only be included by altering model boundary conditions. Unfortunately, structures also change the onshore-offshore

distribution of sediment and the shape of the equilibrium profile. Such effects cannot readily be included in such simple models.

3.6 Conclusions

Sediment transport around structures is highly non-uniform due to the rapidly varying wave and current field around them. Unfortunately while many modelling approaches now exist, the majority are unable to provide full details of the non-uniform flow and sediment transport processes. Depth-mean two-dimensional horizontal Continuum modelling provides a reasonable approximation but still requires details of the depth variation in sediment concentration. Three-dimensional Continuum modelling of suspended sediment transport is the most general and effective model approach to simulate particulate sediment distribution and transport around structures, but needs to be used in a WPA mode to reduce costs.

In the present work, it is proposed to use the three-dimensional Continuum approach to sediment modelling and to make use of many of van Rijn's(1989) equations to allow for wave-current interaction effects on current profiles as well as with seabed entrainment. While Van Rijn also proposes a methodology for vertical diffusion coefficients it is proposed to look at a 1DV bed boundary model as a means of improving the specification of the vertical diffusion coefficients as suggested by O'Connor et al.(1992a).

CHAPTER 4. WAVE PROPAGATION MODEL

4.1 Introduction

Ebersole et al.(1986) have developed an evolution elliptic wave propagation model based upon the solution of an elliptic wave equation. The model includes the processes of wave shoaling, refraction, diffraction, and breaking. Because the model solves the equilibrium form of the wave equation without the unsteady term, it provides a very efficient model. Ebersole et al.(1986)'s general approach is adopted for the present study, although some simplification is done to produce a more efficient result; the resulting equations being solved by finite difference methods.

Ebersole et al.(1986) applied the model to an open coast without structures. However, in the present application, it is proposed to use the model for a situation with structures and consequently some modification to Ebersole et al.'s approach is introduced.

The usefulness of the modified model is tested against laboratory tests of Berkhoff et al.(1982) for an elliptic-shaped shoal located on a sloping seabed as well as against Penney and Price's(1952) analytical results for conditions in the lee of a semi-infinite breakwater.

4.2 Governing Equations

The basic equations used by Ebersole et al.(1986) have already been given in Chapter 2. Thus equation (2.11) is needed for the gradient of wave phase function:

$$\frac{1}{a}\left(\frac{\partial^2 a}{\partial x^2}+\frac{\partial^2 a}{\partial y^2}+\frac{1}{cc_g}(\nabla a\cdot\nabla(cc_g)\right)+k^2-|\nabla s|^2=0 \qquad (2.11)$$

where a is the wave amplitude; x,y are longitudinal and lateral spatial cartesian co-ordinates; c, c_g are the wave phase velocity and group velocity, respectively; ∇ is the two-dimensional spatial gradient operator ($\partial/\partial x$, $\partial/\partial y$), k is the wave number; and s is the wave phase function, while equation (2.14) and (2.15) are needed for wave amplitude and wave direction, respectively, in the open sea away from structures:

$$\frac{\partial}{\partial x}(a^2 cc_g|\nabla s|\cos\theta)+\frac{\partial}{\partial y}(a^2 cc_g|\nabla s|\sin\theta)=0 \qquad (2.14)$$

$$\frac{\partial}{\partial x}(|\nabla s|\sin\theta)-\frac{\partial}{\partial y}(|\nabla s|\cos\theta)=0 \qquad (2.15)$$

where θ is the counter-clockwise wave direction relative to the negative x direction.

However, these equations can be further simplified for open sea situations to produce a somewhat simpler model than that of Ebersole et al.(1986). Several approximate parabolic wave equations have been proposed by many researchers including Radder(1979), Booij(1981), and Liu and Boissevain(1988). The parabolic approximations

are based on the assumption of small diffraction along the x axis(main wave propagation direction), see Section 2.2.3.2. Dalrymple and Kirby(1988) have examined the error produced by Radder's(1979) approximation of the elliptic mild slope equation, and have shown that it is insignificant within an angle of some $\pm$ 43 $^\circ$ of the main direction of wave propagation.

Liu and Boissevain(1988) proposed a simple approximation by transforming the elliptic mild slope equation into the Helmholtz equation and then simply neglecting the second derivative of the potential function with respect to x. Consequently, the second derivative of wave amplitude along the main wave propagation direction (x) in equation (2.4) is simply omitted in the present model. The assumption is similar to that used by Liu and Boissevain(1988) in their parabolic modelling. The new equation for wave phase function can then be written as:

$$|\nabla S|^2 = k^2 + \frac{1}{a}\left(\frac{\partial^2 a}{\partial y^2} + \frac{1}{CC_g}(\nabla a \cdot \nabla(CC_g)\right) \qquad (4.1)$$

while equations (2.14) and (2.15) are retained and solved for wave amplitude and wave direction.

In the surf zone a wave breaking criterion must be used. Various methods exist related to quantities such as bed slope, wave steepness, and Iribarren Number (bed slope over square root of wave steepness). For present purposes, a simple criterion is used, that is:

$$H_b = \gamma d \qquad (4.2)$$

where H_b is the breaking wave height and a γ value of 0.78 has been used as suggested for a solitary wave by McCowan(1894).

4.3 Boundary and Initial Conditions

When modelling a general area, the model is likely to have four boundaries. Firstly, an offshore boundary along which wave height and direction are assumed known. Secondly, two open boundaries are likely, one to the left of the direction of wave propagation, and the other to the right of it. Thirdly, a land boundary along which a breaking wave criterion is assumed.

If the offshore boundary is not in deep water, Snell's law is used to provide the wave amplitude and direction along the boundary from values in deep water; it being assumed that the water depth at the offshore boundary is deep enough so that diffraction effects are small.

At side boundaries, a parallel beach condition is applied, that is:

$$\frac{\partial a}{\partial y}=0 \;;\; \frac{\partial \theta}{\partial y}=0 \;;\; \frac{\partial |\nabla s|}{\partial y}=0 \qquad (4.3)$$

Since the solution near the side boundaries may not be very accurate, the side boundary should be selected sufficiently far from the main study area as possible.

When waves reach a land boundary, the waves are modified by breaking or absorbed or partially reflected. While the waves are modified by a type of breaking (spilling, plunging or surging) on a mild slope plane beach, they are modified by plunging or run-up on a steep slope structure or a rocky cliff. For present purpose, wave reflection is ignored under the assumption that the whole wave energy is dissipated at land boundaries. Thus a proper decaying condition is used for both plane beach and abrupt structure boundaries so that the waves disappear when they reach a land boundary. The plan shape of the land boundary is not always straight so that computation grid for the land boundary includes saw-tooth shaped grids, if a rectangular grid system is used. In order to deal with the irregular land boundary grids, some modification of finite difference schemes for the open sea area are required.

If there is a protected area in the study area, such as in the lee of a structure, the solution for the protected area is provided separately from the finite difference model calculation domain, since the present model cannot solve the external diffraction situation which involves wide angle deviation from the x axis. Details are given in Section 4.6.

The elliptic wave problem does not require an initial condition, since it solves the equilibrium state directly. However, the model has iterations at each calculation step, which increases the computation effort somewhat. Initial values are simply used in the model as a first guess, and do not affect the final solution. The number of iterations for wave height, wave angle, and wave phase function gradient can be reduced if the initial

values are accurately provided. Snell's law of refraction is generally used for the initial values. Details are given in Appendix A.

4.4 Numerical schemes

A convenient coordinate system is selected, which assigns the x axis as the opposite direction of main wave propagation, and the y axis as the longshore direction, see Fig. 4.1.

Any partial derivatives in the three governing equations (4.1), (2.14), and (2.15) are substituted by finite difference equations. A simple space-centred finite difference equation is used for the second order derivative along the x axis of the wave amplitude in equation (4.1). A simple second-order correct centred scheme is used for any first order derivative of any variable along the y axis, while a first-order upwind scheme is used along the x axis, since the direction of propagation is from offshore to inshore. Detailed schemes are given in Appendix B.

Unfortunately, the wave direction relative to the x axis is limited. Since the diffusion term of the governing equation (4.1) is discretized by a second order scheme, the computational domain of influence is confined within $\pm$ 45 $^\circ$ relative to the negative x direction from a reference grid point (when assuming $\Delta x = \Delta y$). Furthermore, Dalrymple

and Kirby(1988) have recommended that the wave direction should be within $\pm$ 43 ° relative to the negative x axis for an accurate solution (a wider range is allowed if a higher order accurate scheme is used).

No restriction exists for the selection of grid sizes, since the model solves the evolution equations, which are derived on the assumption of a smooth spatial variation of the model variables. Therefore, the user can choose a grid size dependent upon the desired accuracy, the resolution of the seabed, and computation costs.

4.5 Test on an Elliptic Shoal

The model was tested on Berkhoff et al.(1982)'s laboratory experimental data for wave transformation over a submerged shoal. Berkhoff et al.(1982) used monochromatic waves and determined wave heights at a number of points covering a submerged elliptic-shaped shoal and adjacent plane-sloped seabed.

The geometry used in the laboratory tests is shown in Fig. 4.2. The location of the outer boundary of the shoal is given by the equation:

$$(\frac{y''}{3})^2+(\frac{x''}{4})^2=1 \qquad (4.4)$$

where x" and y" are local coordinates in metric units, whose origin is located at the centre of the shoal and rotated 20 ° in the clockwise direction relative to the x and y axes.

Water depths are calculated from the following equations:

$$h=0.45\ m, \quad for\ y''\geq 5.84\ m \tag{4.5a}$$

$$h=0.45-0.02(5.84-y'')\ m, \quad outside\ the\ shoal \tag{4.5b}$$

$$h=0.45-0.02(5.84-y'')+0.3-0.5\left(1-\left(\frac{x''}{5}\right)^2-\left(\frac{y''}{3.75}\right)^2\right)^{0.5}\ m, \quad inside\ the\ shoal \tag{4.5c}$$

The model experiments were undertaken with an incident wave of period 1.0 second, a height of 10.6 mm, and a direction of 0 ° from the negative x direction.

A model boundary was set up with a length of 25 m in the x axis direction, and 20 m in the y axis direction. An x-directional grid size of 0.25 m and y-directional grid size of 0.20 m are used for the model simulation so that the longitudinal axis of elliptic shoal had about 50 grid points.

The calculated model wave height and wave direction distribution are shown in Fig. 4.3, where the length of arrows represents wave height, and the direction of the arrow

represents wave propagation direction. The general refraction and diffraction behind the shoal is seen from Fig. 4.3 to be well simulated, including the caustic zone and beyond. Calculated wave heights (in terms of amplification ratio = wave height at a point divided by offshore incident wave height) along several profiles are shown in Figs. 4.4a-h for Ebersole et al.'s(1986) model result, the modified model, and the measured data. In general, both model results show good agreement with the measured data. Ebersole et al.'s(1986) model, which includes the second order derivative of wave amplitude along the x axis produces almost the same results as the present model. This supports the assumption of the small magnitude of the second order derivative along the x axis. The maximum relative error of peak wave height calculated by the present model to the maximum wave height calculated by Ebersole et al.'s(1986) model is -7 % at profile 2 and less than 1 % at profile 3,4 and 5. These are negligible values from an engineering point of view. The maximum relative error of wave height calculated by the present model to the maximum wave height measured in the laboratory at profile 5 is 20 %. The error becomes bigger as waves approach the shoreline. Considering the simplification involved in the model, the results seem to be satisfactory.

A discrepancy between the data and the model results is seen around the small wave amplitude zones just next to the largest peaks, see Figs. 4.4c-4.4e. While the measurements show a shape change of wave amplitude next to the caustic peak, the model results show a smoother variation of the wave amplitude (minimum values of model results are much larger than those of measurements). The smoothing effect is

produced by the assumption involved in the derivation of the evolution wave equations that the wave amplitude and the wave phase function are represented by values of a single wave. Actually, after the waves pass over the submerged shoal, waves of a wide range of angle converge on the caustic zone, and low amplitude zones appear due to the phase difference of the waves. Although the present model contains local smoothing, the overall capability of the model is shown to be good.

The present results can be improved further, since Kirby(1983) has shown that the incorporation of a nonlinear wave theory (Stoke's second order wave) can simulate the experimental conditions better. His model results gave slightly better agreement after profile 3 of Fig. 4.2. However, any improvement is only likely to be marginal, and consequently, wave nonlinearity is not considered further in the present study.

4.6 Test on a Semi-Infinite Breakwater

When an artificial structure, such as a breakwater, exits, inside the computation domain with a lee protected area, restrictions are necessary when applying the present modified Ebersole et al.'s(1986) model. Firstly, boundary values behind the breakwater are not available (wave amplitude, wave direction). Secondly, the wave direction in the lee region exceeds the limit of the allowable range (within 45 ° on both sides of the negative x direction). Therefore, any protected area behind a structure is split from the main

computation domain; the solution in the protected area being obtained by another method, Penney and Price's(1952) analytical method. Penney and Price's (PP) solution is based on the assumption of constant water depth, so that the solution is less accurate if the protected area behind the structure has a sloping bed. In order to reduce the area in which the PP solution is used, the dividing line between the two solutions is selected as close to the structure as possible, i.e. 45 ° relative to the negative x direction from the tip of the breakwater, see Fig. 4.5.

Penney and Price's(1952) solution along the dividing line is also used as boundary values for the calculation in the open computation domain for the present numerical model.

Penney and Price's solution is based on constant water depth and full reflection at the rear wall of the structure. It can be obtained from a tabular form of the Fresnel integral, or by means of an approximation functions, see Abramowitz and Stegun(1965). Details are given in Appendix B.

The Penney and Price modified model was next tested for the case of a semi-infinite breakwater which lies parallel to the y axis with constant water depth for three incident wave angles, -45, 0, and 45 ° expressed in the model variable notation and corresponding to 45, 90 and 135 ° from the breakwater direction, respectively, see Figs. 4.6a-c. The calculated diffraction coefficient (the ratio of wave height to incident wave height) for each test is shown in Figs. 4.6a-c (the diffraction coefficient in the lee area

calculated by Penney and Price's method is not shown), while Penney and Price's(1952) analytical solutions are shown in Figs. 4.7a-c. Detailed comparisons along two sections at (-x/L=2, 8) are also shown in Figs. 4.8a-f.

Due to the relatively poor resolution just around the breakwater tip where the gradient of wave height is large, the solution near the breakwater tip is not expected to be so accurate. The diffraction coefficient along the straight line starting from the breakwater tip along the incident wave angle and inside the shadow zone shows slightly larger values than the analytical solution for all three incident wave angles. The solution outside the shadow zone is close to the analytical solution, but the oscillatory shape of the analytical solution is not reproduced by the model. The major reasons for this are again the singleness of wave phase function gradient smoothing effect shown in the elliptic shoal tests described in Section 4.5. The maximum relative error of computed wave height to incident wave height is 11, 12, and 14 % for 45, 90, and 135 °, respectively for -x/L=2 (where L is the wavelength), and 12, 13, and 18 % for 45, 90, and 135 °, respectively for -x/L=8. All are less than 20 %. These errors are considered to be acceptable for engineering use.

4.7 Conclusions

The Elliptic mild slope wave equation proposed by Berkhoff(1972) has been solved by a modification of Ebersole et al.'s(1986) evolution elliptic approach. The modification follows the idea of Liu and Boissevain(1988) in so far that the second order derivative term of wave amplitude along the x axis is ignored, since it is considered to be of small value. At present the model uses a simple constant wave height to water depth ratio to simulate wave breaking.

Ebersole et al.'s(1986) model can be applied only to a rectangular domain with a straight shoreline. For the present purpose, Ebersole et al.'s model was modified to treat non-straight-shaped land boundary, by omitting the second derivative of the wave amplitude along the y axis and using an upwind scheme for the first derivative of variables along y axis instead of the central scheme.

The model was tested against Berkhoff et al.'s(1982) laboratory data which involves shoaling, diffraction and refraction of waves over a submerged elliptic-shaped shoal, and for constant depth diffraction around a semi-infinite breakwater. The test on the elliptic shoal shows reasonable agreement with the measured data, and only minor differences between the present model and Ebersole et al.'s(1986) approach.

The model was also tested for the case of wave diffraction behind a semi-infinite breakwater with constant depth. The model was applied to a part of the sea area except the lee area of the breakwater. The boundary values along the dividing line were provided by Penney and Price's(1952) analytical solution. Penney and Price's(1952) analytical solution was also used for the lee area between the 45 ° line relative to the negative x axis and the structure. The wave height inside this shadow zone is so small, that it is expected that the analytical solution is acceptable if the depth variation in the zone is not large. The test for a semi-infinite breakwater shows good agreement with Penney and Price's(1952) analytical solution, although some wave-length scale oscillation is not produced.

Both applications for an elliptic shoal and a breakwater showed the smoothing nature of the evolution model. However, the model operates generally well for the two geometries, and is considered to be useful for engineering use. The model can be effectively used for most seabed geometry with structures. The scheme is able to give accurate answers ($<$ 20 % maximum error) solution within the range of $\pm$ 45 ° from the negative x direction.

CHAPTER 5. WAVE-INDUCED CURRENT MODEL

5.1 Introduction

Field and laboratory measurements of wave-induced currents on plane beaches always show smooth profiles in the cross-shore direction, see Sonu(1975). Such smooth profiles are produced in mathematical models by the use of a lateral (cross-shore) eddy viscosity term, although Basco(1982) has argued that the mechanism of lateral turbulent eddy viscosity is still very poorly understood. This is apparent in the technical literature, where turbulent length scales have been assumed to be related to many variables including water depth, wave particle excursion, surf zone width, plunging wave breaking shear stress, bore-bore interactions, and swash zone mixing length. Nielsen(1977) has argued that the lateral mixing that occurs in the surf zone is not a true turbulent eddy viscosity but is a combined transport-dispersion process, since much fluid is advected shoreward in the upper layer of a breaking wave between the wave crest and the wave trough. Horikawa(1978) suggests that from the point of view of a momentum balance, the common belief is that the bottom shear stresses only dictate the strength of the longshore current, while the lateral turbulent stresses only redistribute or smooth the velocity profile normal to the shore. Jonnson et al.(1974) also showed from their numerical model sensitivity test that the bottom roughness was more important than the

lateral eddy viscosity in determining longshore current magnitude. Many computer models also make use of linear wave theory in the surf zone, although the wave motion at breaking is non-linear. Errors are involved, therefore, if the radiation stress calculated by linear wave theory is used inside the surf zone.

From a modelling point of view, early work on nearshore circulation has involved numerical models without lateral mixing terms, see Birkemeier and Dalrymple(1975, 1976), and Ebersole and Dalrymple(1979, 1980). Bettes et al.(1978) showed that even a constant horizontal mixing coefficient could simulate wave-induced currents around structures reasonably well. Spatially-variable surf zone eddy viscosity coefficients have also been used in models by many authors using a range of formulations. Typical examples are given by Bowen(1969), Longuet-Higgins(1970), Madsen et al.(1978), Vreugdenhill(1980), Yoo(1986), and Yoo and O'Connor(1986a). Battjes(1983) has suggested that two-equation (k,e) turbulent closure methods are needed to get correct answers.

Considering the uncertainties of the physical processes and the weak base of the eddy viscosity concept for lateral mixing, the present work adopts a more engineering approach to the simulation of lateral mixing which results in a more efficient model for wave-induced currents. Thus in the present work the lateral mixing term is eliminated and replaced by an appropriate spatial spreading operator applied directly to the wave-produced radiation stresses. This has merits in saving computational time and in

enforcing numerical stability.

The present chapter describes the methods used to simulate the lateral mixing process in the surf zone, the finite difference solution of the relevant hydrodynamic equations, and the testing of the finite difference model against laboratory data of Nishimura et al.(1985) for the case of wave-driven currents around a nearshore breakwater.

5.2 Governing Equations

The water mass continuity equation (2.31) is used for the calculation of water surface elevation:

$$\frac{\partial \eta}{\partial t} + \frac{\partial}{\partial x}(dU) + \frac{\partial}{\partial y}(dV) = 0 \qquad (2.31)$$

where η is the WPA water level; t is time; x, y are the longitudinal and lateral cartesian co-ordinates, respectively; d is the mean water depth; and U, V are the depth-mean velocities in the x, y direction, respectively.

The depth-integrated WPA momentum equations (2.44) and (2.45) form the basic equations:

$$\frac{\partial U}{\partial t}+U\frac{\partial U}{\partial x}+V\frac{\partial U}{\partial y}+g\frac{\partial \eta}{\partial x}+\frac{R_x}{\rho d}-\frac{\hat{T}_x}{\rho d}=0 \qquad (2.44)$$

$$\frac{\partial V}{\partial t}+U\frac{\partial V}{\partial x}+V\frac{\partial V}{\partial y}+g\frac{\partial \eta}{\partial y}+\frac{R_y}{\rho d}-\frac{\hat{T}_y}{\rho d}=0 \qquad (2.45)$$

where g is the acceleration due to gravity, ρ is the water density, R_x, R_y are the driving force terms due to the gradient of the wave radiation stress in the x, y direction, respectively ($R_x=\partial S_{xx}/\partial x+\partial S_{xy}/\partial y$, $R_y=\partial S_{xy}/\partial x+\partial S_{yy}/\partial y$), and $\hat{T}_x$, $\hat{T}_y$ are the turbulent shear stresses in the x, y direction, respectively.

The turbulent shear stress terms ($\hat{T}_x$, $\hat{T}_y$) can be split into bed friction terms ($F_{b,x}$, $F_{b,y}$) and lateral mixing terms ($F_{l,x}$, $F_{l,y}$), respectively, as:

$$\hat{T}_i=F_{b,i}+F_{l,i} \qquad (2.46)$$

where i is the index for x,y. Equations (2.44) and (2.45) are then simplified by the elimination of the lateral mixing terms as follows:

$$\frac{\partial U}{\partial t}+U\frac{\partial U}{\partial x}+V\frac{\partial U}{\partial y}+g\frac{\partial \eta}{\partial x}+\frac{R_{x,f}}{\rho d}-\frac{F_{b,x}}{\rho d}=0 \qquad (5.1)$$

$$\frac{\partial V}{\partial t}+U\frac{\partial V}{\partial x}+V\frac{\partial V}{\partial y}+g\frac{\partial \eta}{\partial y}+\frac{R_{y,f}}{\rho d}-\frac{F_{b,y}}{\rho d}=0 \qquad (5.2)$$

where $R_{x,f}$, $R_{y,f}$ are the smoothed driving force terms in the x, y direction, respectively.

The bed frictional force terms ($F_{b,x}$, $F_{b,y}$) are calculated by a separate sub-model taking account of wave-current interaction in boundary layer, see Section 7.7. Radiation stress

terms (S_{xx}, S_{xy}, S_{yy}) are calculated by equations (2.39)-(2.42). A smoothing process applied to the driving force terms is proposed to compensate for the elimination of the lateral mixing terms, and an appropriate method is introduced in the following sections.

5.3 Representation of Lateral Mixing

In order to simplify the lateral mixing terms in the wave-induced current model, use is made of Longuet-Higgins' analytical approach to the calculation of longshore currents on an infinitely long plane beach in the y direction as shown in Fig. 5.1. Under such conditions, the longitudinal momentum equation (2.45) reduces to the simple form:

$$R_y - F_{b,y} - F_{l,y} = 0 \qquad (5.3)$$

where $R_y = \partial S_{xy}/\partial x$, since $\partial S_{yy}/\partial y = 0$ for a parallel beach. In the absence of lateral mixing ($F_{l,y}=0$), equation (5.3) shows that the driving force or the local longshore gradient of the radiation stress (R_y) balances the local dissipation of wave energy by bed friction ($F_{b,y}$).

$$R_y - F_{b,y} = 0 \qquad (5.4)$$

Longuet-Higgins(1970) derived an analytical expression for R_y which has the following form:

$$R_y=\frac{5}{16}\rho\gamma^2(gd)^{\frac{3}{2}}\left(\frac{\sin\theta}{c}\right)\frac{\partial d}{\partial x}$$
$$\propto\frac{5}{16}\rho g^{\frac{3}{2}}\gamma^2(\tan\beta)^{\frac{5}{2}}\left(\frac{\sin\theta}{c}\right)x^{\frac{3}{2}}, \qquad (5.5a)$$

for $x \leq x_b$ (inside the surf zone)

$$R_y=0, \quad for\ x>x_b\ (outside\ the\ surf\ zone) \qquad (5.5b)$$

where γ is the breaker ratio, θ is the wave direction at the calculation point relative to the negative x direction, β is the angle of the sea bed slope relative to the still water level, x is the distance from the shoreline in the offshore direction, c is the wave phase celerity, and the subscript b is for the breaking point, see Fig. 5.1.

Longuet-Higgins derived an equation for the calculation of the bed friction term $F_{b,y}$ in strong waves and weak currents given by the equations:

$$F_{b,y}=\frac{2}{\pi}f_{cm}\rho U_\infty V \qquad (5.6)$$

where f_{cm} is the friction coefficient for mean current modified by waves, and U_∞ is the absolute maximum wave orbital velocity at the top of the boundary layer. By using linear wave theory in shallow water for U_∞, equation (5.6) reduces to the form:

$$F_{b,y}=\frac{1}{\pi}\rho f_{cm}g^{\frac{1}{2}}\gamma(\tan\beta)^{\frac{1}{2}}x^{\frac{1}{2}}V \qquad (5.7)$$

By equating equation (5.5) to equation (5.7), Longuet-Higgins(1970) obtained an equation for the offshore distribution of the longshore current when the lateral mixing term is ignored, that is:

$$V=\frac{V_b}{x_b}x, \quad for \quad x\le x_b$$
$$V=0, \quad for \quad x>x_b \tag{5.8a}$$

where

$$V_b=\frac{5}{16}\frac{\gamma}{f_{cm}}(gd_b)\tan\beta\ (\frac{\sin\theta}{c})_b \tag{5.8b}$$

Longuet-Higgins(1970) then introduced a depth-dependent eddy viscosity formulation for the lateral mixing term, that is:

$$F_{1,y}=-\frac{\partial}{\partial x}(d\epsilon_x\frac{\partial V}{\partial x}) \tag{5.9}$$

where ϵ_x is the turbulent eddy viscosity. Longuet-Higgins(1970) assumed:

$$\epsilon_x=N\rho x(gd)^{\frac{1}{2}} \tag{5.10}$$

where N is a turbulent closure coefficient for the lateral mixing to be of the order $N\le 0.016$. Defining three constants as:

$$\begin{aligned} r&=\frac{5}{16}\rho g^{\frac{3}{2}}\gamma^2(\tan\beta)^{\frac{5}{2}}(\sin\frac{\theta}{c})_b \\ q&=\frac{1}{\pi}\rho f_{cm}\gamma(\tan\beta)^{\frac{1}{2}} \\ p&=N\rho g^{\frac{1}{2}}(\tan\beta)^{\frac{3}{2}} \end{aligned} \tag{5.11}$$

the lateral momentum equation (5.3) becomes:

$$rx^{\frac{3}{2}}-qx^{\frac{1}{2}}V+(px^{\frac{5}{2}}\frac{\partial^2 V}{\partial x^2}+\frac{5}{2}px^{\frac{3}{2}}\frac{\partial V}{\partial x})=0 \tag{5.12}$$

Longuet-Higgins(1970) next introduced the non-dimensional variables, x_* and V_* and a constant p_* defined as follows:

$$x_*=\frac{x}{x_b} \;;\; V_*=\frac{V}{V_b} \;;\; p_*=\frac{pV_b}{rx_b}=\frac{N\pi\tan\beta}{f_{cm}\gamma} \tag{5.13}$$

Equation (5.12) can then be expressed as follows:

$$x_*^{\frac{3}{2}}-x_*^{\frac{1}{2}}V_*+p_*x_*^{\frac{5}{2}}\frac{\partial^2 V_*}{\partial x_*^2}+\frac{5}{2}p_*x_*^{\frac{3}{2}}\frac{\partial V_*}{\partial x_*}=0 \tag{5.14}$$

Longuet-Higgins obtained the solution of equation (5.14) with two boundary conditions, $V_*=0$ at $x_*=0$, and the gradient of the velocity solution is continuous at $x_*=1$, as follows:

$$\begin{aligned} V_*&=Ax_*+B_1x_*^{p1} && 0<x_*\le 1\\ V_*&=B_2x_*^{p2} && x_*>1 \end{aligned} \tag{5.15}$$

where

$$\begin{aligned} A&=\frac{1}{(1-\frac{5}{2}p_*)}\\ p_1&=-\frac{3}{4}+\sqrt{\frac{9}{16}+\frac{1}{p_*}} \;;\; p_2=-\frac{3}{4}-\sqrt{\frac{9}{16}+\frac{1}{p_*}}\\ B_1&=\frac{p_2-1}{p_1-p_2}A \;;\; B_2=\frac{p_1-1}{p_1-p_2}A, \quad p_*\neq 0.4 \end{aligned} \tag{5.16}$$

For p_* is 0.4, Horikawa(1978) gave the solution:

$$\begin{aligned} V_*&=\frac{10}{49}x_*-\frac{5}{7}x_*\ln x_*, && 0<x_*\le 1\\ V_*&=\frac{10}{49}x_*^{-\frac{5}{2}}, && x_*>1 \end{aligned} \tag{5.17}$$

Longuet-Higgins(1970) suggested that constant p_* lies in the range 0.1-0.4 after comparing the solution with laboratory data. The peak non-dimensional velocities for $p_* = 0.1$ and $p_* = 0.4$ are 0.52 and 0.38, respectively, compared to the no lateral mixing solution, see Fig. 5.2. It is interesting to note that more than half of the velocity profiles that have been measured in the laboratory or the field, see Sonu(1975), are confined in the range which was suggested by Longuet-Higgins(1970), see Fig. 5.3.

It is clear from Fig. 5.2 that the effect of the lateral mixing term is to "diffuse" the triangular "non-lateral-mixing" velocity solution in the offshore direction. An alternative approach to this "diffusion" process is suggested, therefore, by applying a diffusion-type process (or smoothing approach) not to the velocity profile directly but to the radiation stress term, see Fig. 5.4.

In order to determine an appropriate smoothing operator, it is proposed to treat the spreading of the radiation stress term in the *offshore direction as a transient (time-*dependent) diffusion-problem. Thus taking the initial shape (for the non-dimensional time $t_*=0$) of the driving force term (the gradients of the radiation stress terms) as:

$$R_y(x_*,0) = C_1 x_*^{\frac{3}{2}}, \quad 0<x_*\leq 1 \qquad (5.18)$$
$$= 0, \quad x_*>1$$

where R_y is a function of x_* and t_* ($R_y=R_y(x_*,t_*)$), and $C_1=rx_*^{3/2}$. The coefficient C_1 is eliminated when the velocity profile is calculated ($V_*=R_{y,f}/C_1x_*^{1/2}$, where $R_{y,f}$ is the spread driving force at time $t_{*,f}$, $t_{*,f}$ is the time when the artificial diffusion stops). The

diffusion equation is now written in the form:

$$\frac{\partial R_y}{\partial t_*} = \epsilon_* \frac{\partial^2 R_y}{\partial x_*^2} \qquad (5.19)$$

where ϵ_* is a non-dimensional diffusion coefficient.

According to Longuet-Higgins(1970), the lateral turbulent eddy viscosity coefficient varies with x_* as the power 1.5, see equation (5.10). The present diffusion coefficient (ϵ_*) is not strictly the same as Longuet-Higgins' lateral mixing coefficient (ϵ_x), although the former has similarity with the latter. However, when comparing Longuet-Higgins' solution with laboratory data, his model is found to underestimate the velocity at large x_* values, see Fig. 5.3. Basco(1982) has also argued that random wave-induced longshore current models also enhance the velocity for large x_* values.

Considering the uncertainty of the problem and the convenience of modelling, the non-dimensional diffusion coefficient ϵ_* is assumed to have a quadratic variation with x_*, that is:

$$\epsilon_* = \epsilon_{*,1} \cdot x_*^2 \qquad (5.20)$$

where $\epsilon_{*,1}$ is the value of ϵ_* at the breaker line ($x_*=1$). The solution to equation (5.19) is obtained by a numerical method using a simple forward-time space-centred explicit finite-difference scheme. Thus:

$$\frac{R_{y,i}^{n+1}-R_{y,i}^{n}}{\Delta t_*}=\epsilon_*\frac{R_{y,i-1}^{n}-2R_{y,i}^{n}+R_{y,i+1}^{n}}{\Delta x_*^2} \qquad (5.21)$$

which can be rearranged to give the equation:

$$R_{y,i}^{n+1}=\alpha\,(R_{y,i-1}^{2}+R_{y,i+1}^{n})+(1-2\alpha)\,R_{y,i}^{n} \qquad (5.22)$$

where $\alpha=\epsilon_*\Delta t_*/\Delta x_*^2$. The coefficient α is a function of x_* as is ϵ_*, that is:

$$\alpha\,(x_*)=\alpha_1 x_*^2 \qquad (5.23)$$

where $\alpha_1=\epsilon_{*,1}\Delta t_*/\Delta x_*^2$.

In order to obtain a stable solution from the finite difference solution, it is necessary to keep the value of $\alpha \leq 0.50$. Given that the offshore limit of the simple plane beach surf-zone is located at $x_* \simeq 4$, where the longshore current velocity V = 0.1 % of the reference velocity V_b for Longuet-Higgins' $p_*=0.1$, a value of $\alpha_1 = 0.015625$ will ensure that $\alpha = 0.25$ at $x_* = 4$ and hence a stable solution.

The longshore velocity distribution at any time $t_* = n\Delta t_*$, where n is an integer with successive values $1,2,3,\cdots,n_f$ (where subscript f is for a final value that ensures good agreement with Longuet-Higgins' maximum velocity value). Once the value of R_y is known at each $n\Delta t$, the longshore velocity profile is obtained by equating R_y to $F_{b,y}(=C_1 x_*^{1/2} V_*)$. The calculation procedure is continued up to $t_{*,f} = n_f\Delta t_*$ (or $\epsilon_{*,1}t_{*,f} = \alpha_1\Delta x_*^2 n_{t,f}$) until the best fit is obtained between the peak velocities calculated from the

radiation stress diffusion approach and either the Longuet-Higgins analytical solution or the laboratory measurements used by Sonu(1975). A typical example of the velocity profile obtained at various times ($32 \cdot 2^{(ip-1)}\Delta t_*$, ip=1,2,3,$\cdots$) is shown in Fig. 5.5.

For $\alpha_1 = 0.015625$ and $\Delta x_* = 0.1$, the number of iterations, n_f were found to be between 670 and 2000, which correspond to $\epsilon_{*,1}t_{*,f}$ values of 0.11 and 0.32, respectively. The solution becomes less-sensitive when $\epsilon_{*,1}t_{*,f}$ becomes larger. This can be seen from the analytical solution of the diffusion equation for a delta function for which the initial condition corresponds to a mass M released at time $t_* = 0$ at a point $x_* = 0$, this is:

$$F(x_*, 0) = M\delta(0) \tag{5.24}$$

The analytical solution at time t_* is:

$$F(x_*, t_*) = \frac{M}{\sqrt{4\pi\epsilon_* t_*}} \exp\left(\frac{-x_*^2}{4\epsilon_* t_*}\right) \tag{5.25}$$

At $x_* = 0$, the solution is:

$$F(0, t_*) = \frac{M}{\sqrt{4\pi\epsilon_* t_*}} \tag{5.26}$$

Although the initial condition of the present longshore velocity problem is different from the delta function, both solutions are similar in so far that the peak velocity will reduce at a rate of $(\epsilon_{*,1}t_*)^{-1/2}$.

Fig. 5.6 shows the numerical model results for an α_1 value of 0.015625, and $\epsilon_{*,1}t_{*,f}$ of 0.1 and 0.3, with Longuet-Higgins analytical solutions for $p_* = 0.1$ and 0.4. It is clear

that a very good fit has been achieved with the velocity profile shape for both cases, although the present diffusion model with its diffusion coefficient related to x_*^2 seems to give higher offshore values and slightly lower inshore values.

However, comparison with Sonu's experimental data shows that the diffusion model provides a better fit in the offshore area, see Fig. 5.7. For present purposes, where the interest is in the offshore region as well as the inshore region, the present diffusion approach has been used for wave-induced current modelling. It can also readily be adjusted for a specific field situation, if adequate field data is available.

Since the above solution is for a specific combination of numerical parameters, a general method is needed for the case when the effect of using different degrees of spatial resolution in the diffusion solution is needed, although the use of 10 points per wavelength (of the surf zone width) is usually considered to be adequate for numerical calculations. The solutions for additional different Δx_* values of 0.05 (20 points) and 0.2 (5 points) were investigated, therefore, with the model, see Fig. 5.8. Using an α_1 value of 0.015625, the value of $\epsilon_{*,1}t_{*,f}$ was found to be between 0.10-0.30, and between 0.12-0.39, respectively, which are very similar to the previous values of 0.11 - 0.32 for $\Delta x_* = 0.1$. The differences are due to the non-normally distributed shape of the initial radiation stress function, the existence of a limit on the maximum value of coefficient α_1, and numerical computational errors. Nevertheless, the differences are still considered to be quite small for engineering purposes.

In order to use the diffusion approach in a computer model, it is simply necessary to calculate the radiation stress term (R_y) at each grid point, and then to use equation (5.22) with α given by equation (5.23) (α=0.015625) for n_f time steps. It is suggested that a value of between 670 and 2000 be used for n_f.

When the surf zone width is known before calculation and is constant in the computation domain, the coefficients of the diffusion approach can be directly assigned from the non-dimensional x_* values. However, the surf zone width varies spatially by wave shoaling, refraction, and diffraction on a general arbitrary geometry. If the surf zone width cannot accurately be estimated due to the complex geometry, or the width varies spatially in the computation domain, it is necessary to estimate the expected surf zone width in order to produce a non-dimensional x_* value and related coefficients. Thus to use the approach for general geometry, it is necessary to iterate the calculation using the appropriate surf zone width at the end of each iteration. Fortunately, there is no need to change the number of diffusion steps between iterations, as explained below.

There are two sets of parameters for a correctly non-dimensionalized situation (x_*=1 at the breaking point) and an incorrectly non-dimensionalized situation (an iteration) ($x_*=x_{*,a}$ at the breaking point). Then, to ensure the same total "diffusion" time $\epsilon_{*,1}t_{*,f}$ and $c_{*,a}t_{*,f,a}$ for the two situations, where subscript a is for the incorrect iteration case, we can express the diffusion time as:

$$\epsilon_{*,1} t_{*,f} = \alpha_1 \Delta x_*^2 n_f$$
$$\epsilon_{*,a} t_{*,f,a} = \alpha_a \Delta x_{*,a}^2 n_{f,a} \qquad (5.27)$$

where α_a is the coefficient for the incorrect spatial increment ($\Delta x_{*,a}$), and $\Delta x_{*,a}$ is the relative spatial increment for the incorrect surf zone width. The appropriate α_a and $\Delta x_{*,a}$ values to use, are then simply given by the expression:

$$\alpha_a = \alpha_1 x_{*,a}^{\ 2} \ ; \ \Delta x_{*,a} = \frac{\Delta x_*}{x_{*,a}} \qquad (5.28)$$

Multiplying these two items (α_c, $\Delta x_{*,a}$), it is seen that the iteration numbers n_f and $n_{f,a}$ for the two cases are identical, if both values of diffusion coefficient multiplied by time ($\epsilon_{*,1} t_{*,f}$ and $\epsilon_{*,a} t_{*,f,a}$) are to be identical. This shows that the coefficient α and the iteration number of the finite difference scheme n_f do not need adjustment between iterations. We can obtain the spreading coefficient and iteration number from the estimated surf zone width for the whole calculation domain. Furthermore, once the coefficients are provided for a model grid system, they can be used repeatedly for various conditions of wave height or direction.

To date all discussion has been confined to a one-dimensional plane beach situation. However, the natural beach is not always parallel or single-sloped as assumed in the Longuet-Higgins approach. It is often curved with a varying bed slope.

For general geometry, the non-dimensionalization of horizontal distance by the surf zone width is changed to a scaling of the local depth to the depth at the breaking point. The

spreading factor α is thus given as:

$$\alpha=\alpha_1\left(\frac{d}{d_b}\right)^2 \tag{5.30}$$

where d_b is the water depth at the breaking point. This is still valid for a plane beach, and may be used for complex geometry.

In order to extend the plane-beach approach to two-dimensional situations, it is proposed to make use of the two-dimensional diffusion equation:

$$\frac{\partial F}{\partial t_*}=\epsilon_*\left(\frac{\partial^2 F}{\partial x_*^2}+\frac{\partial^2 F}{\partial y_*^2}\right) \tag{5.31}$$

where F is now either R_x or R_y, $R_x = \partial S_{xx}/\partial x+\partial S_{xy}/\partial y$ in equation (2.44), $R_y = \partial S_{xy}/\partial x+\partial S_{yy}/\partial y$ in equation (2.45), and $y_* = y/x_b$. Equation (5.31) is identical with equation (5.3) for a plane beach since $\partial S_{yy}/\partial y = 0$, $\partial S_{xy}/\partial x=0$, and $\partial S_{xy}/\partial y=0$.

The finite difference form of equation (5.31) is thus:

$$\begin{aligned} R^{n+1}_{x,i,j}&=\alpha_x\left(R^n_{x,i,j+1}+R^n_{x,i,j-1}+R^n_{x,i+1,j}+R^n_{x,i-1,j}\right)\\ &\quad+(1-4\alpha_x)\,R^n_{x,i,j}\\ R^{n+1}_{y,i,j}&=\alpha_y\left(R^n_{y,i,j+1}+R^n_{y,i,j-1}+R^n_{y,i+1,j}+R^n_{y,i-1,j}\right)\\ &\quad+(1-4\alpha_y)\,R^n_{y,i,j} \end{aligned} \tag{5.32}$$

where superscript n is the value of the driving force at time level $n\Delta t_*$, and subscript (i,j) is for a space-staggered grid point (i,j), and α_x and α_y are the coefficient α's, defined to the points where R_x, R_y are defined, respectively. The driving force terms R_x and R_y are defined to the points of depth-mean velocities U and V, respectively, see Fig. 5.9. Once

the spread solutions of the driving forces ($R_{x,f}$ and $R_{y,f}$) are obtained from equation (5.37), they are then used in equations (5.1) and (5.2).

5.4 Initial and Boundary Conditions

The solution of the governing equations (2.31), (5.1), and (5.2) requires initial conditions. In the present approach, a simple "cold start" condition is used in the whole computation domain for the present wave-induced current flow model, which is:

$$\eta = U = V = 0 \qquad (5.33)$$

The solution of the governing equations also requires boundary conditions. Again three types of boundary need to be considered. Firstly, the offshore open sea boundary, secondly, lateral open sea boundaries, and thirdly, solid boundaries such as occur with coastal structures or natural beaches.

Normally, on the open sea boundary, the water surface elevation, or the horizontal velocity across the boundary, or both can be given.

For present purposes, it is proposed to use the conditions related to the water elevation. Thus, the water elevation is prescribed for each grid point adjacent to and inside the model boundary. Then the equation of continuity for a grid element can be re-arranged

to give the component of current across the boundary in terms of known quantities. On a y-directed open boundary, see Fig. 5.9, the continuity equation is re-arranged as:

$$\frac{\partial dU}{\partial x} = -\frac{\partial \eta}{\partial t} - \frac{\partial dV}{\partial y} \qquad (5.34)$$

Equation (5.34) can be discretized to form a finite difference equation, see Appendix C. On an x-directed open boundary, a similar re-arrangement can be done to obtain an explicit expression for the current across the open boundary.

Ignoring tidal water level variations, a fixed water elevation can be given throughout the calculation. For the present steady state wave-induced current flow modelling (the final solution is for a steady state), the water elevation approach can be used if the open sea boundary is far enough away from the area of interest not to have any significant set-up or set-down on the boundary.

A radiational boundary condition can also be applied on the open sea boundary which allows disturbances generated within the model to propagate outwards across the boundary as free progressive waves. However, the radiation condition requires both water elevation and the water flux which involves complex numerical treatment, see Proctor et al.(1992). For modelling tidal situations, the fast removal of the unwanted internal numerical oscillation is important, since the solution also has the time variation. However, for steady wave-induced current situations, numerical disturbances do not need to be removed quickly since the final solution can be selected after a sufficient model

computation time when the solution reaches equilibrium, and the numerical oscillation disappears. Therefore, for the present wave-induced current model, radiation conditions are not used, and the condition to assign the water elevation on the boundary is used instead.

Lateral open boundaries need more complex conditions compared to the offshore open sea boundary. The water elevation or velocity along the side boundary is not known beforehand. In most cases the side boundary is assumed to be a parallel beach so that the parallel condition can be used, which is:

$$\frac{\partial \eta}{\partial y} = \frac{\partial V}{\partial y} = 0 \qquad (5.35)$$

If the lateral boundary lies on an arbitrary bed geometry, it is necessary to have field data on velocities and elevations in order to adjust the model values to reproduce observed conditions. Because of the difficulties of the measurement of field data, it is essential that the lateral boundary line should be taken as far away as possible from the area of interest.

For land boundaries or those at structures, a simple no-flux condition normal to the boundary is used ($U_n=0$, where U_n is the normal velocity to the boundary). For the velocity parallel to the land boundary, there can be two conditions, a slip or non-zero velocity boundary condition ($U_p \neq 0$ or $\partial U_p/\partial n \simeq 0$, where U_p is the parallel velocity to the boundary), and non-slip or zero-velocity condition ($U_p=0$). Around a structure, the

former non-zero velocity condition is adequate, since the drag friction of the structure is usually negligible. Along a natural beach boundary, the velocity component parallel to the shoreline is reduced as the distance from the shoreline becomes smaller, and is zero at the shoreline. Thus a non-slip boundary condition is adequate for it. However, the non-zero velocity condition also gives a correct solution at the shoreline, since the velocity is still reduced near the shoreline by the reduction of the driving force and the relative increment of the bed frictional force as water depth is reduced, even if the slip boundary condition is used. Therefore, the non-zero velocity condition is used for both structure and beach boundaries.

For comparison with laboratory experiments, the offshore or lateral open boundaries are replaced by a land boundary, which should be set-up far from the area of interest. This technique can also be used for the wave-induced current computer models which do not involve long period tidal motion. In this case, the boundary should also be placed far from the area of interest.

5.5 Numerical Schemes

In order to determine the wave-induced currents from equations (2.31), (5.1), and (5.2) using the diffusion approach, a regular uniform grid system identical to that of the wave model is adopted, which can make use of the wave model results directly. The numerical

grid system is shown in Fig. 5.9. It is seen that the U and V velocity components are evaluated on either side of the grid while the surface elevations are evaluated at the centre of the grid to ensure proper centring of variables for the continuity equation.

The choice of numerical solution procedure is not a simple matter. Explicit finite difference schemes have some merits compared to implicit schemes, especially for regular horizontal grids. First of all, they generally require small computational time steps compared to implicit schemes which gives low truncation errors and avoids the inversion problem of a big matrix. Finite element techniques may be included in implicit schemes but produce more complicated computer programmes than finite difference approaches. Although some implicit schemes have unconditional stability, they can still exhibit oscillatory behaviour if large intervals are used. Implicit methods also smooth solutions which is not desirable for treatment of any discontinuities. Explicit schemes ensure that the characteristics of the flow are propagated locally, and that the solution is not oversmoothed by the numerical procedure.

Consequently, for present purposes, an explicit finite difference approach is adopted. In particular, the explicit numerical schemes of Flather and Heaps(1975) are used for the present governing equations. Details of the finite difference equations are given in Appendix C.

Since the governing momentum equations are nonlinear, a special stability condition is required. Flather and Heaps(1975) suggested that the Courant-Friedrichs-Lewy (CFL) criterion (Richtmyer and Morton, 1967) could be used as a guide for the stability condition, that is:

$$\Delta t \leq \frac{\Delta x}{\sqrt{2gd_{max}}} \; ; \; \Delta t \leq \frac{\Delta y}{\sqrt{2gd_{max}}} \qquad (5.33)$$

where Δx, Δy are the spatial increments in the x, y directions, respectively; Δt is the time increment; and d_{max} is the maximum depth in the computation domain.

However, as Flather and Heaps(1975) mentioned, the true stability condition is more restricted than the above criterion, and can only be found by trials for each specific modelling site and condition.

5.6 Application of the Model to a Laboratory Experiment

The present wave-induced current model is applied to a laboratory experiment on wave-induced current circulation behind a detached nearshore breakwater, see Nishimura et al.(1985). The bed slope of the model beach was 1/50. A detached breakwater was installed parallel to the shoreline at a depth of 0.06 m. The breakwater length was 2.7 m, corresponding to three wave lengths. The beach and breakwater were exposed perpendicularly to incident waves 20 mm in height and 1.2 seconds in period.

Under such conditions, waves are transformed by diffraction in the lee of the breakwater, and a pair of symmetric circulation cells are generated behind the breakwater. This will lead to the formation of a tombolo in the field. Unfortunately, Nishimura et al.(1985) have not presented the bed roughness of the laboratory experiment, but used a friction coefficient of 0.01 in their flow computation.

The wave propagation model (described in the previous Chapter) and the present wave-induced current model used a regular grid with 0.2 m spacing on both axes. A special boundary condition was assigned along the rear of the breakwater. Two solutions are superimposed behind the detached breakwater, each of which is obtained from Penney and Price's method. The wave height at a point on the breakwater rear was approximated using a weighting of the square of the two wave heights obtained from both sides of the breakwater, and the wave direction was also approximated using a weighting of the square of the two wave amplitudes from both sides.

The wave information was then modified by the diffusion spreading operator in order to be used as the input data for the wave-induced current flow model. The parameters of the diffusion spreading operator were chosen as $\alpha_1 = 0.015625$; $\Delta x_* = 0.1$; $n_f = 670$. The same friction coefficient (=0.01) as Nishimura et al.(1985) was used. The calculated wave height and current velocities are shown in Figs. 5.10, and 5.11, respectively. The calculated wave field seems reasonable, but it could not be compared with measurements, since Nishimura et al.(1985) did not report on wave measurements. The calculated wave-

induced flow field generally agrees with the measured flow field on the circulation size, the position of the centre of the circulation cells, and the velocity magnitude, see Fig. 5.12. However, the computer model results show weak secondary circulation in front of the detached breakwater, which may be due to basin scale oscillation which has not completely disappeared, although the model was run until the main flow pattern behind the breakwater reached equilibrium. Velocity profiles along three profiles (profiles 1,2,3 in Fig. 5.11) were compared with measurements, see Figs. 5.13a-c. The maximum magnitude and the variance of velocity along the profiles were reasonably reproduced, although the calculated rip current velocities were generally slightly smaller than the measured one, which showed some irregularity, see Fig. 5.12. Irregularity in velocity data can normally be expected, considering the difficulty of measuring velocity and controlling the whole circulation system in the laboratory. In view of the lack of further information about the laboratory tests, it was decided not to conduct any further fitting tests. In general, it appears that the accuracy of calculation is satisfactory.

5.7 Conclusions

Wave-induced currents can be calculated from appropriate depth-averaged fluid continuity and momentum equations, provided wave data in the calculation domain are available. The effect of waves is included in these basic equations via radiation stress terms, while lateral mixing in the surf zone is simulated by using effective eddy viscosity terms. By

examining Longuet-Higgins'(1970) one-dimensional solution of the basic equation for a plane-beach situation, a methodology is suggested to replace the effect of the lateral mixing terms. In essence, the lateral mixing terms are neglected, and their effect is simulated by smoothing out the radiation stress terms using a simple time-dependent diffusion equation; the finite difference equation for the diffusion equation being applied iteratively for a specified number of time steps. Comparison of the diffusion approach with Longuet-Higgins' analytical solution for longshore velocity distribution on a plane beach and with Sonu's(1975) experimental data showed good results, and enabled estimates to be made of a suitable diffusion time and model constants.

For general application, the one-dimensional diffusion approach is extended to a two-dimensional form and the model scale factors for non-dimensional distance related to the depth of breaking rather than the width of the surf zone, since the width is more difficult to determine in a general situation. Both approaches are identical for a plane beach.

The diffusion approach has a number of advantages. Since the governing equations do not include the lateral mixing terms, there is no need to include any effect in the numerical stability criteria for the finite difference scheme. It is known that the mixing coefficient for adequate reproduction of the longshore current profile is so large that it can seriously restrict the time increment for explicit schemes, see Yoo(1986). Also, since the smooth driving force (the gradient of the radiation stress) remains steady throughout the numerical calculation up to final equilibrium, computational time is saved.

The new wave-induced current model solves continuity and horizontal momentum equations without lateral mixing terms using an explicit numerical scheme in a similar manner to Flather and Heaps(1975). The model stability condition can be estimated by a CFL criterion, but is more restricted by the nonlinear advection terms. Model details are given in Appendix C.

The present wave-induced current model has been applied to Nishimura et al.'s(1985) laboratory situation involving the generation of wave-induced currents behind a nearshore breakwater. Quite good agreement was obtained with measured velocity data using reasonable values for model constants. The application suggests that the present model can be used for any general geometry, although more extensive laboratory testing is needed.

CHAPTER 6. THREE-DIMENSIONAL SEDIMENT TRANSPORT MODEL

6.1 Introduction

A wave-period-average, three-dimensional suspended load equation has been chosen for the present study to take account of the spatial non-uniformity of the sediment field near structures and the large vertical concentration gradients produced by sandy sediments. The sediment model is used in conjunction with a two-dimensional plan wave propagation model and a two-dimensional plan wave-induced current model; the same horizontal grid being used by the wave propagation model, the wave-induced flow model, and the present sediment transport model.

The movement of sediment in the coastal zone is described by a combination of suspended and bed load. The present chapter gives details of the governing equations for suspended sediment and bed level change, boundary conditions, coordinate transformation of the governing equation for suspended sediment, and the numerical schemes. The suspended sediment model is applied to simple situations, and the results are compared with analytical solutions in the present chapter.

6.2 Model Description

6.2.1 Governing Equation for Suspended Sediment Concentration

The governing equation for suspended sediment concentration has been given in Chapter 3, that is:

$$\frac{\partial c}{\partial t} + u\frac{\partial c}{\partial x} + v\frac{\partial c}{\partial y} + (w - w_f)\frac{\partial c}{\partial z} - \frac{\partial}{\partial x}\left(\epsilon_{sx}\frac{\partial c}{\partial x}\right) - \frac{\partial}{\partial y}\left(\epsilon_{sy}\frac{\partial c}{\partial y}\right) - \frac{\partial}{\partial z}\left(\epsilon_{sz}\frac{\partial c}{\partial z}\right) = 0 \qquad (3.7)$$

where c is the WPA sediment concentration; t is the time; u,v,w are the WPA velocities in the x,y,z direction, respectively; x,y,z are longitudinal, lateral, and vertical cartesian coordinates, respectively; w_f is the sediment settling velocity; and $\epsilon_{sx}, \epsilon_{sy}, \epsilon_{sz}$ are the WPA diffusion coefficients in the x,y,z directions, respectively.

If a three-dimensional model is to be used for general bathymetry (water depth varies), two grid systems can be used. One is a undistorted regular cubic grid in cartesian coordinates, and the other is a distorted cubic grid obtained by a boundary fitted coordinate. The former regular grid represents the sloped bed by steps so that it requires very many vertical grid numbers if there is a shallow area in the computational domain. The lattermost boundary fitted grid can express a sloped bed smoothly, although it involves a coordinate transformation of the governing equation and boundary conditions. In the present work, a sigma-transformation (one of the latter coordinate transformation methods) is adopted, since the modelling area includes a shallow surf zone.

The new vertical coordinate σ is defined as:

$$\sigma = \frac{z - z_b}{d} \tag{6.1}$$

where z_b is the mean bed level, and d is the mean water depth.

The new coordinates x' and y' are not orthogonal to the z coordinate so that the transformation of the derivatives in the (x,y,z) directions introduces additional terms in the new (x',y',σ) directions:

$$\frac{\partial \sigma}{\partial z} = \frac{1}{d} \tag{6.2}$$

$$\frac{\partial f}{\partial x} = \frac{\partial f}{\partial x'} + \frac{\partial f}{\partial \sigma}\frac{\partial \sigma}{\partial x} \tag{6.3}$$

$$\frac{\partial f}{\partial y} = \frac{\partial f}{\partial y'} + \frac{\partial f}{\partial \sigma}\frac{\partial \sigma}{\partial y} \tag{6.4}$$

$$\frac{\partial f}{\partial z} = \frac{\partial f}{\partial \sigma}\frac{\partial \sigma}{\partial z} \left(= \frac{1}{d}\frac{\partial f}{\partial \sigma}\right) \tag{6.5}$$

where f is an arbitrary dependent function.

Equation (3.7) is then transformed into:

$$\frac{\partial c}{\partial t}+u\frac{\partial c}{\partial x'}+v\frac{\partial c}{\partial y'}+(w'-w_f')\frac{\partial c}{\partial \sigma}$$
$$-\{\frac{\partial}{\partial x'}(\epsilon_{sx}\frac{\partial c}{\partial x'})+HOT_1\}-\{\frac{\partial}{\partial y'}(\epsilon_{sy}\frac{\partial c}{\partial y'})+HOT_2\} \qquad (6.6)$$
$$-\frac{1}{d}\frac{\partial}{\partial \sigma}(\frac{\epsilon_{sz}}{d}\frac{\partial c}{\partial \sigma})=0$$

where HOT_1, HOT_2 are higher order derivative terms, and w' is the vertical velocity defined in the new (x',y',σ) coordinate system which has the form:

$$w'=u\frac{\partial \sigma}{\partial x}+v\frac{\partial \sigma}{\partial y}+w\frac{\partial \sigma}{\partial z} \qquad (6.7)$$

and w_f' is w_f/d. The new governing equation (6.6) has additional terms, HOT_1 and HOT_2, which are from horizontal diffusion terms. If the sea bed slope is mild with typical maximum values of 1/20, see van Rijn and Meijer(1988), the extra terms (HOT_1 and HOT_2) arising from the curvature of the new horizontal axis, see Sheng(1983), can be ignored. For present purposes, the bed slope is assumed to be mild, and the higher order terms are ignored.

In order to obtain various numerical advantages, a splitting technique is applied to the governing equation, see O'Connor(1971). Equation (6.6) is split into the following three partial differential equations:

$$1st\ step:\ \frac{\partial c}{\partial t}+(w'-w_f')\frac{\partial c}{\partial \sigma}-\frac{1}{d}\frac{\partial}{\partial \sigma}(\frac{\epsilon_{sz}}{d}\frac{\partial c}{\partial \sigma})=0 \qquad (6.8)$$

$$2nd\ step:\ \frac{\partial c}{\partial t}+u\frac{\partial c}{\partial x'}+v\frac{\partial c}{\partial y'}=0 \qquad (6.9)$$

$$3rd\ step:\ \frac{\partial c}{\partial t}-\frac{\partial}{\partial x'}(\epsilon_{sx}\frac{\partial c}{\partial x'})-\frac{\partial}{\partial y'}(\epsilon_{sy}\frac{\partial c}{\partial y'})=0 \qquad (6.10)$$

In order to resolve the suspended sediment concentration near the bed where the concentration gradient is large, a further non-uniform transformation of the vertical coordinate σ needs to be introduced. Several types of transformation have been used by previous researchers. Although these transformations take somewhat different forms, the basic concepts are almost the same (using a fine grid near the seabed and a coarse grid near the water surface), see, for example, Davies et al.(1988), and Fredsoe et al.(1985).

In the present work, use is made of a power relation transformation, as indicated by the following equation:

$$\eta=\sigma^{-A}=(\frac{z-z_b}{d})^{-A} \qquad (6.11)$$

where η is the new vertical co-ordinate, and A is a scale parameter which controls the relative size of the bed grid to the surface grid.

Equation (6.11) has an infinite value at $z\text{-}z_b = 0$, but this does not cause any problem since this point is outside the computation domain, which starts at a level dictated by the effective roughness height (z_b+a) of the sediment boundary.

In order to use the transformation approach with the three-dimensional equation, it is also necessary to choose an appropriate value for the parameter A in the computation domain.

Fredsoe et al.(1985) have used the magnitude of the bed shear stress to select the parameter of conversion for their 1DV sediment diffusion equation. However, using the local shear stress at every plan grid point is unsuitable for an area model, since a spatially non-uniform value of A should be used, that is, the new vertical coordinate η becomes non-orthogonal to the x' and y' coordinates, and introduces extra terms.

In the present study, therefore, the parameter A has been selected to be a constant for the whole domain for convenience. This gives the same proportional vertical positions at all plan grid points, and thus the vertical velocity relative to the transformed model grid will be minimal provided unseparated flow exists, that is, the lines joining adjacent lateral grid points will have the character of streamlines. Therefore, only equation (6.8) is transformed into a new form, while equations (6.9) and (6.10) keep the same form. The derivative of a function in the z direction is changed to:

$$\frac{\partial f}{\partial z} = \frac{\partial f}{\partial \eta}\frac{\partial \eta}{\partial z} \qquad (6.12)$$

$$\frac{\partial \eta}{\partial z} = -\frac{A}{d}\eta^{\frac{1}{A}+1} \qquad (6.13)$$

Equation (6.8) is thus replaced by the transformed equation:

$$\frac{\partial c}{\partial t} = F\frac{\partial c}{\partial \eta} + G\frac{\partial^2 c}{\partial \eta^2} \qquad (6.14)$$

where

$$F(\eta) = (w''-w_f)\frac{A}{d}\eta^{\frac{1}{A}+1} + \frac{A^2}{d^2}\eta^{\frac{1}{A}+1}H(\eta)$$
$$G(\eta) = \frac{A^2}{d^2}\eta^{\frac{2}{A}+2}\epsilon_{sz} \qquad (6.15)$$
$$H(\eta) = \frac{\partial}{\partial\eta}(\eta^{\frac{1}{A}+1}\epsilon_{sz})$$

where w" is defined as w'd.

The effect of the vertical coordinate transformation by equation (6.11) on vertical concentration profiles can be demonstrated by use of Rouse's equilibrium ($t=\infty$) vertical sediment profile, which is represented by the equation:

$$\frac{c}{c_a} = \left(\frac{d/z-1}{d/a-1}\right)^{Z} \qquad (6.16)$$

where Z is the Rouse exponent ($=w_f/\beta\kappa u_*$), w_f is the sediment fall velocity, β is the ratio of sediment to fluid eddy viscosity, κ is Von Karman's constant, u_* is the flow shear velocity ($=(\tau_{b,c}/\rho)^{0.5}$), $\tau_{b,c}$ is the bed shear stress due to a uniform current, and ρ is the flow density.

By relating u_* to the depth-mean flow velocity (U), that is:

$$u_* = \frac{g^{0.5}}{C}U \qquad (6.17)$$

where C is Chezy's coefficient and g is the acceleration due to gravity (9.81 m/s^2), and using a typical coastal velocity of U = 1 m/s and friction values of $C/g^{0.5} = 15$, equation (6.16) indicates Z values of 0.12-1.08 for sediment grain sizes between 100 - 500 μm,

see Table 6.1.

Table 6.1 Variation of Z with d_{50}.

d_{50} (μm)	w_f (mm/s)	u_* (cm/s)	Z
100	7.8	6.67	0.12
250	35	6.67	0.53
500	72	6.67	1.08

d_{50}=median grain size; κ=0.40; β=1; U=1 m/s; $C/g^{0.5}$=15; Water Temperature=20°C

Fig. 6.2 shows the effect of the vertical transformation on equation 6.16 for a Z value of 1.0, and for A values of 0.1,0.5,1.0, respectively. The effect of the exponential transformation is clearly seen to linearize the high concentration gradients near the seabed.

6.2.2 Initial and Boundary Conditions

The time-dependent suspended sediment model needs initial and boundary conditions. The present model produces a steady state solution, since tidal variations are ignored. Thus, bed shear stress and bed reference level concentration, the three diffusion coefficients, and the three directional velocities (u,v,w) are all steady throughout the calculation. Since the initial condition does not affect the final steady state solution, the initial condition of suspended sediment concentration can be arbitrarily given. A simple zero or constant concentration or an estimated concentration profile may be used. In the

present work, a zero concentration condition was used.

The final solution can then be selected by a reasonable equilibrium criterion. For example, the condition that the absolute or relative concentration change between time steps at every grid point is within a particular range can be used for the criterion. In the present model, The condition that the change of concentration at each grid point is within 0.1 % of the maximum reference level concentration in the computational domain was used.

The model has four boundaries at the water surface, at the seabed, at the open sea, and at the land.

Firstly, at the water surface boundary, the no-sediment-flux condition is used, that is:

$$w_f C + \epsilon_{sz} \frac{\partial C}{\partial Z} = 0 \qquad (6.18)$$

Equation (6.18) is transformed into the form:

$$w_f C - \left(\frac{A}{d} \eta^{\frac{1}{A}+1} \right) \epsilon_{sz} \frac{\partial C}{\partial \eta} = 0 \qquad (6.19)$$

Secondly, at the seabed, two kinds of boundary conditions can be used. One is a specified bed boundary concentration:

$$C_a = C_a^{\infty} \qquad (6.20)$$

and the other is a specified vertical gradient of suspended sediment concentration:

$$\frac{\partial c_a}{\partial z} = -\frac{w_f}{\epsilon_{sz}} c_a^{\infty} \qquad (6.21)$$

Equation (6.21) is transformed into the form:

$$\frac{\partial c_a}{\partial \eta} = \left(\frac{d}{A}\eta^{-\frac{1}{A}-1}\right) \frac{w_f}{\epsilon_{sz}} c_a^{\infty} \qquad (6.22)$$

Van Rijn(1985) and van Rijn and Meijer(1991) have shown that both boundary conditions produce almost the same results for practical field applications, which may reflect the relatively long length scale in the horizontal direction compared to the vertical length scale, and the fact that the near bed sediment concentration is almost at its equilibrium value for mild slopes, especially for coarse materials. For present purposes, it has been decided to adopt the former condition of assigning a bed reference level concentration at the bed for field application, since it is easier to use in the model. However, it is also designed that the model still has an option to select any one bed boundary type for any specific calculation. For example, the model is compared to an analytical solution of Dobbins(1944) which is the case of a gradient bed boundary condition, see Section 6.4.

Thirdly, at the open sea boundaries, two possibilities exist. Firstly, for an incoming flow boundary, the suspended sediment concentration should be known. The suspended sediment concentration information can be provided from direct field measurement, or other estimation method. Secondly, for an outgoing open flow boundary, no condition

is needed, since information is provided by "upstream" model values.

Fourthly, at the land (solid) boundary, a no-sediment-flux condition is applied:

$$-\epsilon_{sn}\frac{\partial c}{\partial n}=0 \qquad (6.23)$$

where n is the normal direction to the land, ϵ_{sn} is the diffusion coefficient in the normal direction. For a horizontally rectangular grid system, equation (6.23) becomes:

$$-\epsilon_{sx}\frac{\partial c}{\partial x'}=0 \;;\; -\epsilon_{sy}\frac{\partial c}{\partial y'}=0 \qquad (6.24)$$

This boundary condition indicates that there is no diffusive sediment transport across a land boundary. A no-sediment-flux condition is not needed, since a no-water-flux condition is already applied in the flow model.

6.2.3 Basic Equation for Seabed Level Change

The governing equation for the bed level change has been given in Chapter 3, that is:

$$(1-n)\frac{\partial z_b}{\partial t}+\frac{\partial q_{tx}}{\partial x}+\frac{\partial q_{ty}}{\partial y}=0 \qquad (3.10a)$$

$$q_{tx}=q_{bx}+q_{sx} \;;\; q_{sx}=\int_{z_b}^{\eta} uc\, dz \qquad (3.10b)$$

where z_b is the seabed level above a horizontal datum; n is the porosity of the seabed;

$$q_{ty}=q_{by}+q_{sy} \;;\; q_{sy}=\int_{z_b}^{\eta} vc \; dz \qquad (3.10c)$$

q_{tx}, q_{ty} are the total (bed+suspended) sediment load in the x, y directions, respectively; q_{bx}, q_{by} are the bed load in the x, y directions, respectively; q_{sx}, q_{sy} are the suspended load in the x, y directions, respectively; and η is the mean water level, see Fig. 3.1.

The calculated suspended sediment concentration is multiplied by the steady velocity profile to produce the suspended load per unit flow width, while integration of the sediment flux over the water depth plus the bed load at each point gives the total sediment flux at each point. The bed level change is calculated from the gradient of the total load (equation (3.10)).

6.2.4 Reference Level Concentration

For present purposes, a new formula for specifying the WPA reference level suspended sediment concentration has been proposed in Chapter 3. The unit of suspended sediment concentration is in terms of net volume of sediment per unit volume (m^3/m^3), that is:

$$c_a=C_2<|\vec{\psi}_{wc}|^{1.5}> \qquad (3.32)$$

where c_a is the reference concentration at the reference level (z_b+a), a is half a ripple height for a rippled bed, C_2 is a scale factor, $\vec{\psi}_{wc}$ is the instantaneous vector Shields parameter based on the total shear stress, defined as:

$$\Psi_{wc}(t)=\frac{\vec{\tau}_{b,wc}(t)}{(s-1)\rho g d_{50}} \tag{3.33}$$

$$\vec{\tau}_{b,wc}(t)=\vec{\tau}_{b,cm}+\vec{\tau}_{b,w}(t) \tag{3.34}$$

$$\vec{\tau}_{b,cm}=\frac{f_{cm}}{f_c}\vec{\tau}_{b,c} \;;\; \tau_{b,c}=\rho f_c \vec{U}|\vec{U}| \tag{3.35}$$

$$\vec{\tau}_{b,w}=\rho\frac{f_w}{2}\vec{U}_\infty|\vec{U}_\infty|\cos(\sigma t) \tag{3.36}$$

where $\vec{\tau}_{b,cm}$ is the current-related total bed shear stress which includes the effect of waves; $\vec{\tau}_{b,w}$ is the instantaneous wave-related vector shear stress, see Fig. (3.4); σ is the wave angular frequency ($2\pi/T$); $\vec{U}$ is the depth-mean current velocity vector; $\vec{U}_\infty$ is the near-bed maximum wave orbital velocity vector; f_w is the wave friction coefficient; f_c is the current friction factor ($=\kappa^2/(\ln(d/z_0)-1)^2$; and f_{cm} is the current friction factor modified by the existence of waves. The bracket $<\ >$ indicates a wave period average, that is $1/T\cdot\int_0^T()dt$. The wave friction coefficient f_w is obtained from a 1DV wave boundary layer model, see Chapter 7, as:

$$f_w=0.000684\ \exp\left(7.80\left(\frac{A}{z_0}\right)^{-0.106}\right) \tag{3.37}$$

The modified current friction factor f_{cm} is introduced in Chapter 7 in detail.

The scaling factor C_2 in equation (3.32) is calibrated from a limited number of laboratory data, and from field measurement data at the Chukpyon Site, in Korea. At present, there is a lack of direct measurement data of near-bed reference level concentration over

rippled beds. Consequently, the scaling parameter (C_2) may need to be adjusted on any new site.

The available laboratory data obtained from the literature are those of Nieuwjaar and van der Kaaij(1987), Nap and van Kampen(1988), Bosman(1982), van Rijn(1987), and van der Valden(1986). A total of 36 data sets have been used for the calibration of the scaling factor C_2. However, in the use of Van der Valden's(1986) data, which were obtained from a water tunnel, it has been necessary to use an artificial wave height with a water depth of 1.0 m in order to produce a consistent data set. The wave height and depth were chosen so as to reproduce the same orbital near-bed velocity as measured in the flume when using linear wave theory.

Table 6.2 Laboratory reference concentrations and associated C_2 values.

d (m)	U (m/s)	H (m)	T (s)	θ_{wc} (°)	d_{50} (μm)	d_{90} (μm)	Δ_r (mm)	a (mm)	Te (°C)	$\rho_s C_{a,m}$ (kg/m^3)	$\langle \lvert \vec{\Psi}_{wc} \rvert^{1.5} \rangle$ (-)	$10^3 C_2$ (-)
.51	0.	.077	2.5	0.	200	280	15	7.5	21.	.08	0.0627	0.482
.50	0.	.101	2.5	0.	200	280	15	7.5	21.	.3	0.116	0.975
.50	0.	.122	2.4	0.	210	320	18	9	23.	.6	0.191	1.18
.50	0.	.153	2.4	0.	205	310	18	9	24.	1.6	0.326	1.85
2.1	0.	.5	5.1	0.	220	280	20	10	8.	3.	0.524	2.16
2.1	0.	.4	5.1	0.	220	280	20	10	8.	2.	0.315	2.40
2.1	0.	.3	5.1	0.	220	280	20	10	7.	.8	0.164	1.84
2.1	0.	.21	5.1	0.	220	280	20	10	7.	.2	0.0739	1.02
2.72	0.	.67	5.1	0.	215	270	20	10	5.	1.7	0.724	0.886
.4	0.	.27	2.2	0.	105	150	15	7.5	20.	20.	3.82	1.98
.6	0.	.234	2.	0.	105	150	15	7.5	20.	12.	1.48	3.06
.6	0.	.154	1.8	0.	105	150	15	7.5	20.	6.	0.561	4.04
.5	0.	.241	2.0	0.	105	150	15	7.5	20.	20.	2.13	3.55
.4	0.	.114	1.8	0.	105	150	15	7.5	20.	8.	0.571	5.28
.4	0.	.135	2.0	0.	105	150	15	7.5	20.	10.	0.824	4.58
.4	0.	.191	2.0	0.	105	150	15	7.5	20.	17.	1.78	3.61
.5	0.	.223	2.0	0.	105	150	15	7.5	20.	35.	1.79	7.39
.5	0.	.136	1.8	0.	105	150	15	7.5	20.	8.	0.588	5.14
.6	0.	.256	2.0	0.	105	150	15	7.5	20.	22.	1.81	4.59
.6	0.	.153	1.9	0.	105	150	15	7.5	20.	5.	0.569	3.31
.5	0.	.248	2.1	0.	105	150	15	7.5	20.	25.	2.28	4.14
.4	0.	.15	1.9	0.	105	150	15	7.5	20.	14.	1.04	5.07
1.	0.	.290	2.	0.	360	725	20	10	16.	3.	0.178	6.36
1.	0.	.387	2.	0.	360	725	28	14	16.	7.	0.440	6.00
1.	0.	.484	2.	0.	360	725	35	17.5	16.	11.	0.861	4.82

1.	0.	.209	4.	0.	360	725	50	25	16.	1.	0.214	1.77
1.	0.	.279	4.	0.	360	725	60	30	16.	1.5	0.465	1.22
1.	0.	.314	4.	0.	360	725	60	30	16.	2.6	0.601	1.63
1.	0.	.199	6.	0.	360	725	80	40	16.	.2	0.226	0.334
1.	0.	.290	2.	0.	220	240	15	7.5	16.	6.	0.295	7.67
1.	0.	.387	2.	0.	220	240	16	8	16.	10.	0.588	6.42
1.	0.	.484	2.	0.	220	240	23	11.5	16.	15.	1.28	4.41
1.	0.	.190	4.	0.	220	240	23	11.5	16.	1.3	0.193	2.54
1.	0.	.209	4.	0.	220	240	28	14	16.	1.5	0.279	2.03
1.	0.	.279	4.	0.	220	240	30	15	16.	4.5	0.558	3.04
1.	0.	.199	6.	0.	220	240	35	17.5	16.	1.1	0.242	1.72

U=depth mean velocity; H=wave height; T=wave period; θ_{wc}=wave and current interaction angle; Δ_r=ripple height; Te=water temperature; $c_{a,m}$=measured reference concentration.

The scaling factor C_2 is found to be 0.0033 (mean) $\pm$ 0.0020 (variance) from Table 6.2. The IWP calculation of the shear stress term ($\langle|\Psi_{wc}|^{1.5}\rangle$) for the first data set in Table 6.2 is given in Appendix D.

In order to obtain more information on near-bed suspended sediment concentrations for further calibration of the scale factor C_2 in equation (3.32), a new device has been developed and applied at Chukpyon field site by the author and his colleagues at KORDI.

A review of the technical literature reveals that a number of approaches have been used to measure the near-bed suspended sediment concentration. Typical types of device of HR Ltd (Wallingford, UK), Rosati et al.(1990), Kinderen(1982), Jansen(1981), and Salkield et al.(1981) are shown in Fig. 6.3a-e, respectively.

For example, HR Ltd. uses an intake nozzle mounted on a weighted triangular framework and connected to a small centrifugal pump on-board a ship or walking platform. The water-sediment sample is pumped through a filter which separates all

particles larger than the mesh size of the filter. The sample is simply analyzed in a laboratory. However, the intake nozzle has a limited angle of horizontal rotation, it being connected to a large vertical fin so as to ensure alignment with the flow, and was designed for sampling in tidal currents. The device is thus less useful in heavy wave action. It can also only sample down to some 10 cm above the seabed. The large supporting framework is also likely to produce considerable disturbance in wave-dominated regions.

The streamer-type trapping device for use in the nearshore was introduced by Katori(1982), and has been refined by Kraus et al.(1989) and Rosati et al.(1990). They simultaneously mounted several streamers (gauze bags) vertically on stainless steel racks. However, the method involves difficulty to analyze the trapped sediment amount if the contribution of short wave orbital velocity is significant.

Kinderen(1982) has presented an optical probe. The method is based on the principle of transmission and scattering of light. The measurement is sensitive to ambient light. Jansen(1981) has presented an acoustic probe. The method is based on the transmission and scattering of ultrasonic sounds by the suspended sand particles. Both optical and acoustic probes enable the continuous automatic measurement of sediment concentration even in short wave period mode. However, the devices require frequent calibration, and are large, expensive, fragile electronic equipments, which are readily damaged in field applications.

Salkield et al.(1981) have presented an impact probe based on the momentum -transfer principle. High density sediment particles tend to strike a transducer placed in the stream. The output is a count of frequency of impacts. The probe has small dimensions compared to the optical or acoustical probe. However, velocity information measured simultaneously with sediment concentration is needed for conversion of the output signal, which makes the measurement more complex.

Conclusively, the streamer-type device is easy to handle and cheap, while electronic equipment (optical, acoustic, impact probes) has common drawbacks of frequent calibration and fragility. If the streamer-type device is to be used for a surf-zone where waves are strong, the arrangement of the traps needs to be modified from that used by Rosati et al.(1990).

For present purposes, a new streamer-type device has been produced based on the use of gauze bags (made from polyester). The new measuring device consists of four near-bed traps, see Plate (6.1) and Fig. (6.4). The shape of trap is similar to Rosati et al.'s(1990) device. The four openings of the present device have four directions, while Rosati et al. used a vertical array of traps with all openings in the same direction of measurement of sediment transport for uni-directional current flows. The mouth opening of the traps is designed to be 100 mm long, and 50 mm high, similar to the ARNHEM bed load sampler. The mesh size of the basket was selected to be 40 μm, which is similar to the lower limit of gauze filter used in the pumping line of the HR Ltd. pumped-

sampler. Each gauze fits over the end of the steel frame and is held in place by tying a piece of string around the steel frame.

To measure the longshore sediment transport, one trap is considered to be insufficient for a coexisting wave-current field. The wave orbital velocity can add sediment to the traps although it does not actually contribute to longshore sediment transport. Thus, the new device has two traps with opposite directional openings, which coincide with the longshore direction, see Fig. (6.4). The difference in trapped sediment quantity between the two traps is regarded as the net longshore sediment transport quantity. In order to obtain the on-offshore directional sediment transport rate, two more traps are installed at right-angles to the longshore traps. However, the on-offshore sediment transport rate is not analyzed in the present study. The four traps are mounted on a support frame, which has four poles to adjust the height of the traps, so that the number of traps and the heights can be adjusted at each measuring point. The frame is designed to be very open and to be capable of mounting two traps in the vertical direction also, so that some idea of vertical suspended sediment profile can be obtained. However, actual measurements were undertaken using only one trap at each direction at the reference level.

The total device is held in place by the self-weight of the supporting frame. The weight of the total device is 15 kg. The new device is moored at each measurement point in a fixed orientation. Mooring the trap in an accurate direction which matches the flow is a problem, since two of the traps are intended for the longshore direction, while the other

two are for the onshore-offshore direction. If the water depth is small, the direction of orientation can be distinguished on the ship, helped by painting the two alongshore and two onshore-offshore traps in different colours. In order to distinguish the four traps after the device is collected from the field, the four traps need to have different colours. If the water depth is large, a skin diver should check the device direction. A small marker buoy is attached to the device for collection later. The mooring time was found to be between 8 - 24 hours, depending on the weather. It is important that the gauze traps should not be too full for accurate measurement. If the trapped sediment quantity is too small, the data is not used for analysis.

The analysis of the measured results is not straightforward since the wave orbital velocity is non-negligible. If a pumping device is used for the measurement of the reference concentration, and the direct measurement at the reference level is not available, the reference level concentration can be obtained by plotting the measured concentrations at several level on a semi-logarithmic scale and applying a straight line fit which is extrapolated to the required reference level. However, in the present measurement, the concentration was not directly measured. In order to convert the trapped sediment amount to the concentration value, the measured trapped sediment amount at the reference level is divided by the measurement time and the mean velocity at mid-height of the trap opening which is calculated from the 2DV wave current boundary layer model, see Chapter 7, as:

$$C_{a,m} = \frac{M_m}{\rho_s t_m u_a A_a} \qquad (6.25)$$

where M_m is the trapped sediment amount in weight (kg), ρ_s is the sediment density, t_m is the measurement duration time, u_a is the horizontal velocity at the centre of the trap opening, and A_a is the cross-sectional area of the trap opening. The measured reference concentrations are used for the calibration of the scale coefficient C_2 in Table 6.3.

Table 6.3 Chukpyon reference concentrations and associated C_2 values.

d (m)	U (m/s)	H (m)	T (s)	θ_{wc} (°)	d_{50} (μm)	d_{90} (μm)	Δ_r (mm)	a (mm)	Te (°C)	$\rho_s C_{a,m}$ (kg/m^3)	$\langle \lvert \Psi_{wc} \rvert^{1.5} \rangle$ (-)	$10^5 C_2$ (-)
3.1	.449	1.05	7	90	200	300	62	31	15	0.173	4.31	1.52
3.1	.239	.63	7	90	200	300	62	31	15	0.311	1.32	8.90
1.6	.234	.20	7	90	200	300	32	16	15	0.0126	0.169	2.80
2.1	.178	.26	7	90	200	300	42	21	15	0.0360	0.234	5.82
3.8	.387	.51	7	90	200	300	76	38	15	0.0475	0.866	2.07
3.5	.234	.73	7	90	200	300	70	35	15	0.0270	1.69	0.600
7.1	.948	.83	7	90	200	300	142	71	15	0.0390	3.47	0.424
2.1	.249	.92	7	90	200	300	42	21	15	0.276	3.82	2.73
5.1	*.737*	*1.20*	*7*	*90*	*200*	*300*	*102*	*51*	*15*	*0.182*	*5.17*	*1.33*
2.9	.426	.81	7	90	200	300	58	29	15	0.0833	2.55	1.23
5.0	.506	.70	7	90	200	300	100	50	15	0.0148	1.55	0.360

The IWP calculation of the shear stress term ($\langle \lvert \Psi_{wc} \rvert^{1.5} \rangle$) is given in Appendix E. The scaling coefficient C_2 is found to be $2.5 \times 10^{-5} \pm 2.5 \times 10^{-5}$ for Chukpyon field data. These values are much smaller than those for laboratory data. The reason for this difference may be on the different measurement methods between the laboratory and the Chukpyon site. Since the gauze bags of the present device have fine holes of size 40 μm, the bag and the steel frame act as resistance to the flow so that the flow velocity through the trap is reduced compared with the free flow. Unfortunately, it has not been possible to calibrate the sand trap in a laboratory flume, since no flume existed in KORDI during

the time the device was used at the Chukpyon site (A large wave/current flume was installed in 1991).

When the different scaling coefficients for the laboratory and field are used, the calculated concentrations agree well with the measured values, see Fig. 6.5. Analysis of the results indicate that 68 % of the predictions lie within a factor of 2 of actual values while 87 % lie within a factor of 3. It is also clear from Fig. 6.5 that the field data are more scattered than the laboratory data. The calculated concentrations for small bed shear stresses also give slightly larger concentrations than the measured ones.

Van Rijn's(1989) empirical equation is also applied to the same data sets for comparison with the present results. Van Rijn's results show that 72 % of the predictions lie within a factor of 2 of measured value, and 94 % within a factor of 3, see Fig. 6.6. These values are slightly bigger than those for the present results, but are very close to each other.

Given that most sediment transport theories have been judged as acceptable in engineering if they predict within a factor of two, it is proposed that both van Rijn's(1989) and the present prediction formula for the reference level concentration can be used, until more laboratory or field data for wave and current situations become available. In the present work, the present approach will be used for the field simulations of bed level change in Chapter 8.

6.2.5 Bed Load (q_b)

For present purposes, a formula for the bed load for wave and current flows has been proposed in Chapter 3, which is expressed in a non-dimensional form:

$$|\vec{\Phi}_b| = C_4 \Psi_{cm}^{0.5} < |\vec{\Psi}_{wc}|^{1.5} > \qquad (3.44)$$

where $\vec{\phi}_b = \vec{q}_b / w_f d_{50}$ (in net volume per unit width per unit time), Ψ_{cm} is the Shields parameter for the modified current-related shear stress due to waves, and C_4 is a scale coefficient.

No existing measurements of the bed load for wave and current situations were available from the literature. In order to obtain field data to calibrate the scaling coefficient C_4, eight direct measurements of bed load were undertaken at Chukpyon site, using a basket type device (ARNHEM) developed by Delft Hydraulics Laboratory. The method traditionally has been used in Holland for river situations, see van Rijn(1985), and Plate 6.2. ARNHEM consists of a stainless steel bag mounted on an open support framework and held in contact with the seabed by a steel spring. Measurement duration time was in a range of 8 to 24 hours, depending on the weather. After recovery of the instrument, the sediment is washed out of the bag, and then dried, and weighed. The bed load was then calculated from the equation:

$$q_b = \frac{M_b}{t_b b_b} \qquad (6.26)$$

where M_b is the trapped sediment amount, t_b is the measurement duration time, and b_b is the width of the opening mouth. The measured data is given in Table 6.4. However, some data for low amount of trapped sediment were discarded for analysis.

Table 6.4. Chukpyon bed load rate and associated C_4 values.

d (m)	U (m/s)	H (m)	T (s)	θ_{wc} (°)	d_{50} (μm)	d_{90} (μm)	Δ_r (mm)	a (mm)	Te (°C)	$10^7 \rho_s q_{b,m}$ (kg/ms)	$\langle \lvert \vec{\Psi}_{wc} \rvert^{1.5} \rangle$ -	$10C_4$ -
2.0	.314	0.415	7	90	200	300	40	20	18	0.122	0.718	0.0853
3.0	.222	0.287	7	90	200	300	60	30	18	0.0611	0.260	0.168
1.0	.231	0.320	7	90	200	300	20	10	20	0.420	0.542	0.485
3.1	.106	0.685	7	90	200	300	62	31	15	1.94	1.54	1.48
3.4	.166	0.750	7	90	200	300	68	34	15	1.94	1.80	0.807
1.0	.189	0.255	7	90	200	300	20	10	18	0.559	0.318	1.34
6.3	.318	0.684	7	90	200	300	126	63	15	0.0765	1.09	0.0341
7.0	.336	0.662	7	90	200	300	140	70	15	0.0814	0.975	0.0391

The coefficient C_4 is found to be 0.055 (mean) $\pm$ 0.055 (variance). The variance is quite large. The reason may be partially due to errors involved in measurement of input variables (velocity, wave height, ripple size), and partially due to the errors arising from the scouring near the device opening. Since the bed is usually rippled, then setting of the bed load sampler on a rippled bed may also cause error.

After multiplying the scaling coefficient, the calculated bed load values were compared to measured values in Fig. 6.7, which shows a large scatter. 50 % of the data are inside a factor of 3 lines, and 100 % of the data are inside a factor of 10 lines. Until more accurate measurements become available, the present mean scaling coefficient value of

0.055 is suggested for use in a field situation.

6.2.6 Diffusion Coefficients ($\epsilon_{sx}, \epsilon_{sy}, \epsilon_{sz}$)

The WPA diffusion coefficients should be provided to solve the governing equation (6.8) and (6.10) for suspended sediment concentration. The sediment diffusion coefficients are assumed to be the same as flow eddy viscosity coefficients ($\beta = 1$).

Ideally, the flow eddy viscosity should be obtained from direct measurement or from a full three-dimensional turbulent wave-current flow model. However, a detailed three-dimensional flow model requires long computation time, and thus is not desirable from an engineering point of view.

The WPA vertical eddy viscosity for wave current flow can be approximated from a 1DV or 2DV boundary layer model, assuming locally uniform flow conditions at each plan grid point.

The new method consists of using a 2DV bed boundary layer model to reproduce the inter-wave-period eddy viscosity profiles for a mono-wave at arbitrary-angles and steady currents. Operation of the model for a number of wave periods allows the formation of the wave-modified WPA eddy viscosity profile. By running this 2DV model for a number

of typical wave and current combinations for water depths and bed roughness similar to those at Chukpyon, it is possible to produce a series of results which can be schematized into a suitable tabular form for interpolation at each model grid point. Full details are given in Chapter 7.

The value of the horizontal diffusion coefficients ϵ_{sx}, and ϵ_{sy} cannot be calculated from theory. However, O'Connor and Nicholson(1988a) have shown that the exact value of these coefficients is less important in three-dimensional models since the spreading process is dominated by the three-dimensional nature of the flow field. Thus, for present purposes, the horizontal diffusion coefficients ϵ_{sx}, ϵ_{sy} are assigned to the same value as the vertical diffusion coefficient at each grid point.

6.2.7 Velocities

Wave-period-average flow velocities u, v, and w can be provided from field measurements, or from numerical models. Given that a depth-average type of flow model is to be used for the present work, it is necessary to generate local velocity values from depth-average values. In tidal conditions where vertical velocities are small compared with horizontal values, it is possible to distribute the depth-average value over the flow depth with a logarithmic function, see Van Rijn and Meijer(1988). Unfortunately this method is less useful when waves and currents are present due to enhanced eddy

viscosity in the wave boundary layer, which modifies the depth-distribution of horizontal velocity.

Some researchers have attempted to overcome the problem by using a logarithmic spreading function but with an enhanced bed roughness, see Van Rijn(1989). Such approaches allow for the reduction of wave-period-average velocity near the sea bed, using two separate log functions which involve various empirical parameters. This lattermost approach could have been used in the present work. However, a better method, which does not include such arbitrary assumptions, and provides full details of the velocity profile in the lower layers of the water column, where the largest sediment concentrations exist, is proposed in the present work.

The new method consists of using a 2DV bed boundary layer model to reproduce the inter-wave-period velocity profiles for a mono-wave at arbitrary-angled waves and steady currents. Operation of the model for a number of wave periods allows the formation of the wave-modified steady velocity profile as for the eddy viscosity. By running this 2DV model for a number of typical wave and current combinations for water depths and bed roughness similar to those at Chukpyon, it is possible to produce a series of results which can be schematized into a suitable tabular form for interpolation at each model grid point. Full details are also given in Chapter 7.

Once the horizontal velocity is known at four adjacent model grid points, it is possible to determine the vertical velocity from the water mass continuity equation (2.25), that is:

$$\frac{\partial u}{\partial x}+\frac{\partial v}{\partial y}+\frac{\partial w}{\partial z}=0 \qquad (2.25)$$

Making use of the definition of w', equation (6.7), equation (2.25) is transformed into:

$$\frac{\partial ud}{\partial x'}+\frac{\partial vd}{\partial y'}+\frac{\partial w'd}{\partial \sigma}=0 \qquad (6.27)$$

Transforming equation (6.26) into (x',y',η) coordinates:

$$\frac{\partial ud}{\partial x'}+\frac{\partial vd}{\partial y'}+(-A\eta^{\frac{1}{A}+1})\frac{\partial w'd}{\partial \eta}=0 \qquad (6.28)$$

Equation (6.28) is solved for w' by a simple finite difference method starting from the seabed where w'=0.

6.3 Numerical Schemes

Following the splitting of the governing equation, each split partial differential equation is transformed into a finite difference equation. The splitting approaches are known to have some merits from the computational point of view. One merit is the reduction of computation time compared to non-split implicit schemes, since solution matrices are smaller in size. A further merit is that the computer programme is much simpler

compared to unsplit schemes.

For present purposes the governing equation is split into three steps: a vertical diffusion and vertical advection step, a horizontal advection step, and a horizontal diffusion step.

The numerical grid system used by the suspended sediment model is shown in Fig. 6.1a-b. The suspended sediment concentration (c), seabed level (z_b), are defined at the centre of the horizontal grid, while velocities, and bed load fluxes are defined at the border of the square grid.

Solution of the vertical diffusion and vertical advection step is done by a second-order accurate Crank-Nicolson implicit finite-difference scheme, while the horizontal advection step is solved by the method of characteristics, which is also called the projection method, see Verboom(1975), and Nicholson(1983). Finally, the horizontal diffusion step is solved by a second order explicit finite-difference scheme. Further details of the numerical schemes for the split governing equations and boundary conditions at the water surface, bed, and side boundaries are given in Appendix G.

The governing equation (3.10) for the seabed level change has been solved using finite difference methods. A simple explicit finite difference equation for the partial differential equation (3.10) is used for the present work, see Appendix H.

Vertical velocities are calculated between horizontal velocities, and four-point-averaged for the solution of the vertical diffusion-settling equation. Details are given in Appendix I.

6.4 Commutability, Consistency, and Stability of the Numerical Schemes

The commutability of the splitting technique has been checked by Nicholson(1984). Nicholson mentioned that the splitting of the governing equation does not fulfil the commutability condition. However, he suggested that the error occurring from the non-commutability is likely to be small. In the present work, the governing equation is solved with the sequence: horizontal advection, horizontal diffusion, and vertical diffusion and settling with vertical advection.

Consistency, also called compatibility, of the finite difference equations for the first vertical diffusion and vertical advection step, and the third horizontal diffusion step is satisfied for the schemes adopted. The consistency of the present second order schemes for the governing equation (6.8) and (6.10) is examined and found to be satisfied, see Appendix J.

Each numerical method used to solve the individual steps of the splitting approach must also be checked for stability of computation. Stability for the implicit scheme for vertical

diffusion and vertical advection is known to be unconditionally satisfied, see Smith(1965). A stability condition is not required for the characteristic scheme for horizontal advection due to its geometrical interpolation aspect, although errors can arise from the interpolations needed in the approach, see Nicholson(1983). The explicit scheme for horizontal diffusion has a stability condition, see O'Connor and Nicholson(1988a) of the form:

$$\Delta t \leq \frac{\Delta x^2}{2\epsilon_{sx}} \; ; \; \Delta t \leq \frac{\Delta y^2}{2\epsilon_{sy}} \qquad (6.29)$$

where Δt is the time increment; Δx, Δy are the spatial increments in the x and y direction, respectively.

6.5 Accuracy of the Numerical Schemes for Suspended Sediment Concentration

Numerical solutions always involve numerical error. To appraise the reliability and accuracy of a numerical model for general use for complex geometry, it is usual to apply the general model to simple ideal situations which have analytical solutions. Unfortunately, analytical solutions exist for only quite restricted flow and sediment conditions. Thus, for unsteady diffusion and settling, Dobbins(1944) has given a solution for a vertically constant diffusion coefficient over the depth. Mei(1969) has solved the steady state two dimensional vertical non-uniform solution for the case of a constant diffusion coefficient, while Hjelmfelt and Lenau(1970) have produced a solution to the

same problem with a parabolic shape of diffusion coefficient over the flow depth.

The present numerical solution of the three-dimensional equation is compared with Dobbins'(1944) analytical time-varying solution and with Hjelmfelt and Lenau's(1970) steady state non-uniform solution.

Firstly, the model solution is compared with Dobbins' solution. The values of independent variables and the parameters used for the numerical calculation are the same as for Dobbin's analytical solution, see Table 6.5. The same time increment of 414.8148 as in Dobbins' solution was used for the numerical calculation (there is no limitation on the time increment). A number of vertical grid points of 20 was used for the numerical calculation.

Table 6.5 Values assigned to variables in Dobbins'(1944) analytical solution.

Variable	Value	Remarks
d (m)	17.07	56.00 ft
w_f (mm/s)	4.115	0.0135 ft/s
ϵ_{sz} (m^2/s)	0.04561	0.491 ft^2/s
$\rho_s c_a$ (kg/m^3)	1.0	
Δt (s)	414.8148	

Initial condition=zero concentration; Bed boundary condition: gradient condition used.

Fig. 6.8 and Table 6.6 show that the model is accurate near the bed, but less accurate near the water surface. The maximum error relative to the equilibrium bed concentration is 3 % at mid-depth and surface after 5000 seconds, which is quite satisfactory for engineering use.

Table 6.6 Comparison of numerical and analytical solutions (Dobbins, 1944).

nt	c/c_a bed A	c/c_a bed N	c/c_a mid-depth A	c/c_a mid-depth N	c/c_a surface A	c/c_a surface N
1	37.14	34.08	2.49	3.11	0.07	0.50
2	48.82	46.68	7.48	7.94	1.00	1.89
3	56.55	54.99	12.09	12.69	2.69	3.77
4	62.41	61.30	16.17	16.98	4.61	5.77
5	67.18	66.43	19.76	20.78	6.49	7.67
6	71.21	70.75	22.92	24.12	8.21	9.41
7	74.69	74.47	25.71	27.05	9.77	10.96
8	77.73	77.68	28.16	29.63	11.15	12.33
9	80.39	80.46	30.33	31.88	12.37	13.54
10	82.73	82.94	32.23	33.86	13.35	14.60
11	84.79	85.08	33.91	35.59	14.40	15.53
12	86.60	86.96	35.39	37.11	15.24	16.35

Values are %; nt=time step; A=analytical solution; N=numerical solution.

Secondly, the present model solution is compared with Hjelmfelt and Lenau's solution. When the unsteady equation is used for the steady solution, it is necessary to run it for a sufficiently large time so as to reach equilibrium. Thus the numerical model solution for the equilibrium state is chosen when the variation of solution with time at each grid point falls within a limit sufficiently small (0.1 % relative to the bed reference concentration per time step).

Hjelmfelt and Lenau(1970) proposed an analytical solution for a simplified situation which excludes horizontal diffusion. The same variable values were used for the

comparison of the numerical and analytical solutions, see Table 6.7. A number of vertical grid points of 20, $\Delta x=0.2$ m, $\Delta t=0.2$ s were used for the numerical calculation.

Table 6.7 Values assigned to variables in Hjelmfelf and Lenau's(1970) analytical solution.

Variable	Value	Remarks
d (m)	1.0	
U (m/s)	1.0	Uniform along Depth
w_f (cm/s)	2	
u_* (m/s)	0.1	
$\rho_s c_a$ (kg/m_3)	1.0	

u_*=seabed shear velocity; $\epsilon_{sz}=\kappa u_* z(1-z/d)$; Initial condition: zero concentration.

Fig. 6.9 and Table 6.8 show the model results compared with the analytical solution. The numerical solution is generally quite accurate compared to the analytical solution. The solution near the bed is clearly more accurate than at high levels due to the improved bed boundary condition. Maximum error relative to the bed concentration is found to be some 4 % at high level, and is again considered to be acceptable.

Table 6.8 Comparison of numerical and analytical solutions (Hjelmfelt and Lenau, 1970).

	c/c_a=0.05		c/c_a=0.1		c/c_a=0.2		c/c_a=0.5	
No.	A	N	A	N	A	N	A	N
0	0.050	0.050	0.050	0.050	0.050	0.050	0.050	0.063
1	0.199	0.213	0.164	0.173	0.129	0.133	0.083	0.084
2	0.269	0.279	0.214	0.219	0.160	0.163	0.093	0.093
3	0.324	0.332	0.252	0.257	0.183	0.185	0.099	0.100
4	0.371	0.378	0.286	0.290	0.203	0.205	0.105	0.105
5	0.410	0.415	0.316	0.319	0.219	0.221	0.109	0.109
6	0.451	0.457	0.341	0.344	0.235	0.236	0.112	0.113
7	0.483	0.487	0.366	0.369	0.248	0.249	0.115	0.116
8	0.517	0.522	0.389	0.391	0.260	0.261	0.118	0.118
9	0.548	0.552	0.408	0.410	0.273	0.274	0.121	0.121

10	0.573	0.576	0.429	0.431	0.283	0.284	0.123	0.123
11	0.599	0.603	0.449	0.451	0.293	0.294	0.125	0.126
12	0.627	0.630	0.467	0.468	0.303	0.304	0.127	0.127
13	0.650	0.652	0.482	0.484	0.313	0.314	0.129	0.129
14	0.671	0.672	0.498	0.500	0.322	0.323	0.131	0.131
15	0.690	0.689	0.516	0.517	0.331	0.331	0.132	0.132
16	0.710	0.707	0.532	0.532	0.339	0.339	0.134	0.134
17	0.731	0.726	0.546	0.546	0.346	0.346	0.135	0.135
18	0.749	0.741	0.560	0.559	0.353	0.353	0.136	0.137
19	0.766	0.755	0.572	0.570	0.362	0.362	0.138	0.138
20	0.781	0.768	0.584	0.581	0.370	0.369	0.139	0.139
21	0.794	0.778	0.598	0.593	0.377	0.376	0.141	0.141
22	0.806	0.788	0.611	0.604	0.384	0.383	0.142	0.142
23	0.817	0.797	0.624	0.615	0.391	0.389	0.143	0.143
24	0.827	0.805	0.635	0.625	0.397	0.395	0.144	0.144
25	0.836	0.812	0.646	0.634	0.403	0.400	0.146	0.145
26	0.843	0.818	0.656	0.642	0.408	0.405	0.147	0.146
27	0.849	0.824	0.665	0.649	0.414	0.410	0.148	0.147
28	0.854	0.829	0.674	0.656	0.420	0.414	0.149	0.148
29	0.859	0.834	0.682	0.663	0.426	0.419	0.149	0.149
30	0.863	0.838	0.690	0.669	0.432	0.424	0.150	0.150
31	0.867	0.842	0.697	0.674	0.438	0.429	0.151	0.150
32	0.871	0.845	0.705	0.679	0.443	0.434	0.152	0.151
33	0.874	0.848	0.712	0.684	0.448	0.438	0.153	0.152
34	0.877	0.851	0.719	0.689	0.453	0.442	0.154	0.153
35	0.880	0.853	0.726	0.693	0.458	0.445	0.154	0.153
36	0.882	0.855	0.732	0.697	0.462	0.449	0.155	0.154
37	0.884	0.858	0.738	0.701	0.466	0.452	0.156	0.154
38	0.886	0.860	0.743	0.704	0.470	0.455	0.156	0.155
39	0.888	0.861	0.748	0.708	0.474	0.458	0.157	0.155

Values are z/d; A=analytical solution; N=numerical solution.

6.6 Conclusions

Near structures the suspended sediment concentration distribution is not uniform. The present three-dimensional sediment transport model can simulate the non-uniform behaviour of sediment diffusion-advection.

The model requires bed reference level concentration, bed load transport, three diffusion coefficient components, and three velocity components. A modified Brown's empirical

formula for the reference level suspended sediment concentration, which is based on the analysis of laboratory and field data, was calibrated using laboratory and field data. The field data were obtained using a new four-directional near-bed sand trap. An empirical bed load transport formula was also calibrated from field measurements.

Model diffusion coefficients are obtained from a wave-current boundary layer model described in Chapter 7. Depth-mean horizontal velocities are obtained from a depth-averaged wave-induced flow model, and the horizontal velocity profiles over the depth are calculated using depth-average velocities and the wave-current boundary layer model results in Chapter 7. The vertical velocity is obtained from the WPA fluid continuity equation.

The three-dimensional governing equation is transformed using a sigma-transformation so that it is applicable for general geometry. The equation is split into three equations for numerical convenience. The vertical diffusion and advection equation (6.8) is further transformed to give a more accurate solution near the seabed.

The split equations are solved by appropriate numerical schemes. The vertical diffusion and advection terms are solved by an implicit scheme, the horizontal advection step is solved by a characteristic method, and the horizontal diffusion step is solved by a second order explicit scheme.

General model coding and accuracy are tested by numerical calculations for two analytical solutions, that is an unsteady one-dimensional vertical diffusion-settling problem (Dobbins, 1944), and a non-uniform two-dimensional vertical diffusion-settling problem (Hjelmfelt and Lenau, 1970). Both numerical solutions show small numerical errors (<5 % at the surface), which are considered satisfactory for engineering use.

CHAPTER 7. CHARACTERISTICS OF WAVE CURRENT BOUNDARY LAYER FLOWS

7.1 Introduction

The three-dimensional suspended sediment model needs information on wave-period-average bed shear stress for the calculation of the reference concentration, diffusion coefficients, and horizontal velocity profiles at each plan grid point in the model computational domain for wave and current situations.

In the past, such information has been provided by either empirical equations or by using one-dimensional models of wave/current processes at a plan grid point, so called 1DV point models.

Empirical methods are based on the analysis of a limited number of experimental data, and consequently, the variable values are in a very restricted range.

Existing 1DV models for wave and currents, for example, Deigaard et al.(1986a) for the surf zone or Davies(1990) for the offshore zone, usually neglected the effect of vertical wave-induced flow velocities. Such models have shown their capability to describe

various experimental features reasonably well, including the IWP variation of velocity, shear stress, and eddy viscosity in the boundary layer, and WPA enhanced eddy viscosity and modified velocity profile near the seabed due to wave-current interaction.

However, recent experiments by Bakker and van Doorn(1978), Kemp and Simons(1982,1983), Nieuwjaar and van der Kaaij(1987), and Nap and Kampen(1988) have revealed not only the existence of wave-induced mass transport but the fact that the depth-mean horizontal velocity of the steady current in a combined wave and steady current situation for the same wave conditions but with opposite current directions are much different from each other due to the effect of vertical wave-induced velocities. Such a difference caused by opposite current directions cannot be described by existing 1DV models.

In order to explain the wave-induced wave mass transport phenomena, another group of vertical wave boundary layer numerical models have been presented in the literature. These include the effect of wave-induced vertical orbital velocity. However, this approach has been confined to wave only situations up to the present time.

For present purposes, therefore, a new two-dimensional (longitudinal and vertical coordinates, x-z) numerical model has been developed and tested for various different situations, to take account of both co-existing wave and current situations at arbitrary intersection angles as well as the effect of wave-induced vertical orbital velocities. The

model uses a vertical two-dimensional periodic grid to include the effect of the vertical wave-induced orbital velocities, and also adopts a mixing-length turbulence closure.

The model is applied to situations with waves to study Eulerian mass transport, and to situations with waves; and in-line following, and opposing currents with waves; and currents with waves at arbitrary angles, to study the interaction effects on horizontal velocity profiles. The inter-wave-period variation of velocity, shear stress, and eddy viscosity over the flow depth is described by the model as are also wave-period-averaged properties such as increase in seabed roughness.

Model results are first compared with experimental data to show the relative accuracy of the new approach, and secondly, to determine its sensitivity to input variables. Finally, model results are obtained for a range of variables appropriate to the Chukpyon site and parameterized to enable the rapid calculation of the wave-period-average bed shear stress, the diffusion coefficients, and the wave-period-average horizontal steady-current velocity profiles within the three-dimensional model .

7.2 Review

7.2.1 Experiments and Empirical Methods

Experimental work on wave-only flows has been done by a number of workers including Bijker and Pieters(1974), Nadaoka et al.(1982), Hwung and Lin(1990), Kyriacou(1988), and Simons and Kyriacou(1990). The experiments have generally shown the existence of wave-induced mass transport in the bed boundary layer.

Laboratory experimental work for wave and current flow have been done by various researchers including van Doorn and Godefroy(1978), van Doorn(1981), Kemp and Simons(1982,1983), Tanaka et al.(1983), Savell(1986), Coffey and Nielsen(1986), Nieuwjaar and Kaaij(1987), Sleath(1987,1990), Nap and van Kampen(1988), Kyriacou(1988), Lee-Young and Sleath(1988). The experiments have shown the existence enhanced eddy viscosity inside the wave boundary layer, and the enhanced bed roughness near the bed due to the enhanced eddy viscosity.

Coffey and Nielsen(1986) proposed an engineering method based on a logarithmic velocity profile with an enhanced (apparent) bed roughness z_a. The ratio of z_a/z_b was obtained from experimental data and was related to the ratio of the wave shear velocity to the current shear velocity. However, their method requires an iterative computational procedure.

Van Rijn(1989) also proposed an engineering method for the modification of the steady current horizontal velocity profile for wave and current situations based on the analysis of Nap and van Kampen's(1988) experimental data, see Section 3.2.7. His analysis clearly showed that the apparent roughness for opposing currents is much larger than that for following currents. His formula retains the aspect that the following and opposing current to the waves produce two different velocity profiles. However, since his formula is driven from a limited number of experimental data, it is only valid for a limited range of conditions. For example, the ratio of apparent roughness to bed roughness can only have a maximum value of 10 according to his formula.

Both empirical models are based on the analysis of a limited number of experimental data within a narrow range of input variable values. Little information exists for waves and currents at arbitrary intersection angles, mainly because such experiments require special facilities. Therefore, in order to develop an engineering model for the general wave and current situations, it is necessary to develop a general turbulent flow computer model.

7.2.2 1DV Boundary Layer Models Ignoring Vertical Orbital Motion

Various theories have been used as the basis for 1DV models, which have then been used to study a wide range of problems, not only for waves, but also for co-linear waves and currents, and arbitrary angled waves and currents; it being assumed that the wave motion

is similar to water oscillations in a water tunnel.

A large number of different models have been developed with a range of closure options. Typical examples include Kajiura(1968), Lungren(1972), Bakker(1974), Bakker and van Doorn(1978), Jonsson(1978), Grant and Madsen(1979), Tanaka and Shuto(1981,1984), Sheng(1983), van Kesteren and Bakker(1984), Fredsoe(1984), Tanaka(1989), Myrhaug(1989), Myrhaug and Slaattelid(1990), Huynh-Thanh and Temperville(1990), Davies(1988,1990), Sleath(1991), Davies, A.M.(1991,1992), Davies, A.M. and Jones(1991), Justesen(1991), Soulsby et al.(1993),44 and O'Connor et al.(1992a). Basic features of the models are described below.

Bakker(1974), Bakker and van Doorn(1978), and van Kesteren and Bakker(1984) examined wave and current boundary layer flows by using a mixing-length closure. For this lattermost approximation, they stressed the importance of second harmonics in the wave motion. However, considering the inherent non-linearity of the relation between shear stress and velocity gradient, it is expected that higher harmonics than second are not negligible, see Trowbridge et al.(1986).

Davies(1988) has used a one-equation (k) turbulence closure for combined wave and current boundary layer flow simulation. Use of this model shows that when the depth-mean velocity is given, the pressure gradient is not the same as for current-only flow due to the enhanced bed shear stress. More recently, Davies(1991) has used a method to

obtain the given depth-mean velocity in his 1DV numerical model by adjusting the pressure gradient value at every wave period.

Justesen(1991) has compared the performance and the effectiveness of three turbulence closures (mixing length, k equation, k-e and k-l equations) for 1DV wave boundary layer modelling, and showed that k equation and k-e equation models give similar results.

Tanaka(1989) has modelled the non-linear wave boundary layer flow, using a mixing length theory.

O'Connor et al.(1992a) have modelled both long and short-crested directional random waves and steady currents with a 1DV numerical model and a mixing length closure, and shown reasonable comparison of near-bed flows with data from the North Sea.

While a great deal of useful modelling has been done, the influence of vertical wave-induced motion has generally been neglected so that the wave-induced mass transport cannot be simulated by 1DV model. The difference in the WPA velocity profiles for following and opposing currents to waves cannot be shown by the 1DV model, either.

7.2.3 Wave Boundary Layer Theories Including Wave-Induced Vertical Orbital Velocity

The mass transport current in wave motion is relatively small in size compared to the maximum wave orbital velocity. However, when the bed boundary layer thickness becomes comparable to the whole depth, possibly due to long period motion or large bed roughness, the mass transport rate can no longer be treated as negligible.

Given that sediment movement depends upon a high power (usually 3-5) of the water velocity, it follows that wave-period-average sediment transport is sensitive to the non-linearity of the wave motion. Previous work on residual wave-induced current flows (mass transport currents) has looked at the wave situation analytically or by using a pseudo-two-dimensional-vertical modelling technique for a laminar or turbulent wave boundary layer.

Considerable modelling of wave-induced mass transport flows has been done using a wide variety of approaches. Typical approaches are due to Longuet-Higgins(1953), Johns(1970,1975,1977), Sleath(1972,1973), Isaacson(1976,1978), Door(1977,1982), Thomas(1981,1990), Craik(1982), Jacobs(1984), Trowbridge and Madsen(1984a, 1984b), Trowbridge et al.(1986), Takhar and Thomas(1991), Iskandarani and Liu(1991a,b), and Soulsby et al.(1993). Relevant works are described below in more detail.

Longuet-Higgins(1953) proposed a solution for the depth-distribution of mass transport velocity for boundary layers in laminar progressive waves and standing waves (obtained by superposition of reflected waves). He derived his solution from the x-directional horizontal momentum equation which retains advection terms ($u\partial u/\partial x$, $w\partial u/\partial z$), but simply treated the first advection term as a part of the pressure gradient term. He obtained the vertical orbital velocity from the continuity equation (in the x-z domain) by numerical integration. He used a non-slip boundary condition and a zero shear stress or vertical zero-gradient of horizontal velocity at the top of the wave boundary layer. The main features of his solution are as follows:

1. A positive (in the wave direction) Eulerian mass transport velocity occurs just near the bed for a progressive wave.
2. A negative Eulerian mass transport velocity occurs just near the bed for a standing wave.

Johns(1970) extended the Longuet-Higgins work from laminar wave flow to turbulent wave flow. He used similar governing equations as Longuet-Higgins(1953), but adopted a time-invariant turbulent eddy viscosity assumption. His solution showed a similar trend to that for laminar flow with the same maximum mass transport velocity but with a much bigger boundary layer thickness than for laminar waves.

Johns(1977) adopted a turbulence energy equation (k) closure, so that the eddy viscosity varied during the wave period. Due to the complex time and spatial variation of the

turbulent energy, he used a finite difference method for the horizontal momentum equation, and "pseudo-spectral" technique to calculate the advection term which included the vertical velocity. He approximated the spatial gradient of the horizontal velocity ($\partial u/\partial x$) by a time gradient of the horizontal velocity ($1/c \cdot \partial u/\partial t$). Then at the end of each wave period, he applied a Fourier transformation, and integrated the spatial gradient value up to the calculation point to obtain the vertical velocity. However, he used a smoothing technique to suppress the development of instability, and chopped out higher harmonics than 3. His model result showed that the maximum mass transport over the depth closely matches with Longuet-Higgins' maximum mass transport velocity for a turbulent wave. However, Johns(1977) has not quantitatively described the error caused by the smoothing and chopping procedure.

Hedegaard(1985) has calculated Eulerian and Lagrangean wave mass transport using Fredsoe's 1DV wave boundary layer flow model, and graphically presented a functional relationship between three non-dimensional variable groups, the ratio of the horizontal WPA velocity at the top of the wave boundary layer (U) to the wave-induced orbital velocity amplitude (U_∞), the wave orbital excursion length amplitude (A) to the bed roughness divided by 30 (z_0), and the wave length (L) to the wave excursion length amplitude (A). She stressed the importance of including Lagrangean mass transport in the suspended sediment transport calculation.

Trowbridge et al.(1986) have used a 1DV finite difference model with two nonlinear advection terms. They used the conversion of the spatial (x) derivative to the time derivative of the horizontal velocity as did Johns(1977) to obtain the vertical velocity. Since the problem includes a highly implicit expression, including vertical integration of the time derivative of velocity, the x-derivative of the horizontal velocity and some other terms were approximated from a first order solution (1DV), which did not include the effect of the nonlinear terms with the vertical velocity. However, they did not quantitatively describe the error caused by the approximation.

Although existing models, which take account of the vertical velocity, can quite accurately predict the wave-induced mass transport phenomena, the previous studies have been confined to the situation involving only waves; the objective of the study being to understand experimental mass transport phenomena produced by waves in a flume or in deep water without currents. Thus previous work has largely remained isolated from any engineering usage, and is limited to situations involving only waves.

For large waves and weak onshore currents, such as occurs in shallow water near the wave breaker line, where the depth-mean velocity remains quite small, mass transport flow becomes relatively more important, and is significantly modified by wave current interaction. The effect of wave direction on the mean velocity profile is also significant, when the current is weak.

7.2.4 Conclusions

A review of the prediction methods for bed shear stress, eddy viscosity, and steady current velocity distribution has revealed that empirical methods, 1DV numerical models ignoring the vertical velocity effect, and 1DV numerical models including the vertical velocity effect have their own defects. For example, empirical methods can provide accurate solutions for only a narrow range of variable values, while 1DV models, which ignore the vertical velocity, cannot predict the wave-induced mass transport; the latter being important for wave-dominated situations.

1DV numerical models, including the vertical velocity effect, have been successfully applied for various wave situations. However, this approach has two major drawbacks. Firstly, a method to adjust the WPA pressure gradient for wave and current situations has been lacking, so that these techniques could not be applied for such flows. Secondly, the vertical velocity has been approximated either by Fourier analysis at the end of wave period or by using an other simplified model solution. Therefore, the 1DV numerical models of Johns(1977) or Trowbridge(1986), which retain the vertical velocity effect need to be further modified to have pressure gradient adjustment method for wave and current flows, and also a method to obtain a more accurate vertical velocity value and advection term($w\partial u/\partial z$).

For present purposes, therefore, a two-dimensional vertical (2DV) numerical model has been set-up to obtain a better solution to the combined wave and current problems for waves and currents at arbitrary angles, since it does not involve any undesirable approximation for the calculation of the vertical velocity, although it requires more computational time due to the larger number of points required compared with 1DV methods. The present model also uses Davies's(1991) modified scheme for adjusting the pressure gradient for wave-current flows for faster conversion of the solution.

7.3 2DV Boundary Layer Model

7.3.1 Introduction

A two-dimensional model is presented here to simulate the combined wave and current boundary layer flow for general arbitrary angles of wave and current intersection. The isometric view of modelling space is shown in Fig. 7.1, while the numerical grid system used in the model is shown in Fig. 7.2 and is seen to include a non-uniformly-spaced vertical grid so as to provide details of the near-bed velocities. For a convenient representation of the 2DV model results, a simplified one-dimensional vertical (1DV) model, which omits the vertical orbital velocity term, is also used in Section 7.6.

The model uses simplified forms of the two horizontal momentum equations. The vertical momentum equation is ignored, since the vertical orbital velocity magnitude is relatively small compared to horizontal velocity magnitudes. The vertical wave velocity is obtained from the local mass continuity equation.

The model adopts a mixing length closure to simulate turbulent effects. The mixing length hypothesis was developed originally for steady flow near a plane rough wall, but has been successfully applied to a very wide range of turbulent flow situations, including unsteady flows. It implies an equilibrium situation in which production and dissipation of turbulence is in equilibrium, which is not absolutely true in unsteady flows. However, experimental work by Sato(1987) and Taplin(1989) suggests that even in unsteady wave flows, the mixing length approach may be a reasonable assumption in so far that turbulent production and dissipation are approximately equal. Taplin(1989) has analyzed laboratory experimental data conducted on a flume at Manchester University, see O'Connor et al.(1993), on turbulence production rate and dissipation rate for 1.5 second waves at height 0.36 mm from the bed within the wave boundary layer, and showed that both rates follow very closely, see Fig. 7.3. Sato(1987) has shown similar results from an experiment over a rippled bed for a 4.0 second wave, see Fig. 7.4. Although the two data sets may be insufficient to prove that mixing length theory is accurate for all short wave motion, the experiments suggest that the effect of delay of turbulence energy between production and dissipation rate is small for both flume scale waves as well as field-scale waves.

It is also noted that Trowbridge et al.(1986) tested two different turbulence models, a mixing length hypothesis and a one-equation model for simulating boundary layer flows, and showed that the difference between the two models were negligible for velocity or shear stress fields. Thus the mixing length theory is adopted for the present study.

Four further approximations are used in the present model. Firstly, the mixing length is assumed to increase linearly with elevation near the seabed but to return to zero at mean water level. Secondly, the water depth is assumed to be shallow enough so that variation of the wave-induced horizontal velocity outside the wave boundary layer can be neglected. Thirdly, the effects of vertical shear stresses are assumed to be small in comparison with horizontal stresses. Fourthly, large-scale vertical momentum exchange is neglected so that pressure distributions outside the thin wave boundary layer are hydrostatic. Wave-induced vertical velocities are calculated by integration of the water mass conservation equation over a water depth.

7.3.2 Governing Equations

The model uses momentum equations (2.21), (2.22), and (2.23) derived from the Euler equations for turbulent flow.

The horizontal axis x and y can be chosen arbitrarily regardless of wave and current

direction. However, for present purposes, the x-axis is set in the wave propagation direction for convenience ($\theta_w=0$, $\theta_{wc}=\theta_c$). Then y-derivatives of velocities disappear, that is:

$$\frac{\partial u}{\partial y}=\frac{\partial v}{\partial y}=0 \qquad (7.1)$$

where u,v are the horizontal velocities in the x,y direction, respectively; and y is the lateral cartesian coordinate.

The simplified horizontal momentum equations in the boundary layer are thus given as:

$$\frac{\partial u}{\partial t}=-u\frac{\partial u}{\partial x}-w\frac{\partial u}{\partial z}-\frac{1}{\rho}\frac{\partial p}{\partial x}+\frac{1}{\rho}\frac{\partial \tau_{xz}}{\partial z} \qquad (7.2)$$

$$\frac{\partial v}{\partial t}=-u\frac{\partial v}{\partial y}-w\frac{\partial v}{\partial z}-\frac{1}{\rho}\frac{\partial p}{\partial y}+\frac{1}{\rho}\frac{\partial \tau_{yz}}{\partial z} \qquad (7.3)$$

where t is time; x,z are the longitudinal and vertical cartesian coordinates, respectively (the mean bed level is used for a datum level, that is, $z_b=0$); w is the vertical velocity; p is the pressure; ρ is the water density; and τ_{xz}, τ_{yz} are the turbulent shear stresses in the x, y directions, respectively.

The pressure gradients, $-(1/\rho \cdot \partial p/\partial x)$ and $(-1/\rho \cdot \partial p/\partial y)$ are assumed to be composed of contributions from the wave pressure field and the steady current pressure field. For nearly-horizontal steady flows, the current pressure field is assumed to be hydrostatic, while for a thin wave boundary layer, the wave pressure field is assumed constant over

the wave boundary layer thickness and to be related to the local acceleration. Thus,

$$-\frac{1}{\rho}\frac{\partial p}{\partial x}=P_x=\frac{\partial \tilde{U}}{\partial t}+P_{c,x} \tag{7.4}$$

$$-\frac{1}{\rho}\frac{\partial p}{\partial y}=P_{c,y} \tag{7.5}$$

where $P_{c,x}$, $P_{c,y}$ are the current related pressure gradients in the x, y directions, respectively (=-g$\partial\eta/\partial$x, -g$\partial\eta/\partial$y); η is the WPA water elevation above a horizontal datum; g is the acceleration due to gravity; $\tilde{U}$ is the wave-induced horizontal velocity component at the top of the wave boundary layer and is given by the equation:

$$\tilde{U}=U_{\infty}\cdot\cos(\sigma t-kx) \tag{7.6}$$

where σ is the wave angular frequency, and k is the wave number.

The equations generally used in the 1DV model are obtained by discarding the two advection terms on the right hand sides of equations (7.2) and (7.3). The result is then:

$$\frac{\partial u}{\partial t}=-\frac{1}{\rho}\frac{\partial p}{\partial x}+\frac{1}{\rho}\frac{\partial \tau_{xz}}{\partial z} \tag{7.7}$$

$$\frac{\partial v}{\partial t}=-\frac{1}{\rho}\frac{\partial p}{\partial y}+\frac{1}{\rho}\frac{\partial \tau_{yz}}{\partial z} \tag{7.8}$$

Equations (7.7) and (7.8) for 1DV models are used only for the presentation of the 2DV model results in the present work.

The shear stress terms are then replaced using the eddy viscosity concept with a mixing length hypothesis. Thus:

$$\tau_{xz}=\rho\epsilon_z\frac{\partial u}{\partial z} \;;\; \tau_{yz}=\rho\epsilon_z\frac{\partial v}{\partial z} \qquad (7.9)$$

$$\epsilon_z=l^2\sqrt{(\frac{\partial u}{\partial z})^2+(\frac{\partial v}{\partial z})^2} \qquad (7.10)$$

$$l=\kappa z\sqrt{1-\frac{z}{d}}, \quad for \quad z\geq z_0 \qquad (7.11)$$

where ϵ_z is the vertical eddy viscosity, l is the mixing length, d is the water depth, z_0 is the equivalent Nikuradse roughness of the seabed divided by 30, and κ is the von Karman constant (=0.4).

It should be noted that the mixing length expression, equation (7.11) represents the analytical form for a steady flow with a constant shear stress distribution over the flow depth and a logarithmic horizontal velocity profile. However, the mixing length theory has been developed for the near wall region ($l=\kappa z$), but is often used for the whole depth, see Bakker and van Doorn(1978). The form of equation (7.11) is thought to be more appropriate than Bakker and van Doorn(1978), since it gives the same mixing length values very close to the bed, but it also satisfies the requirement for a logarithmic profile of the steady current in the absence of waves.

The momentum equations are next transformed in the vertical direction using a power relationship:

$$\eta = \left(\frac{z}{d}\right)^{-A} \tag{7.12}$$

Such an approach produces a higher resolution of flow variables near the seabed. The vertical derivative of an arbitrary function has the form:

$$\frac{\partial f}{\partial z} = F\frac{\partial f}{\partial \eta} \quad ; \quad F = \frac{\partial \eta}{\partial z} = -\frac{A}{d}\eta^{\frac{1}{A}+1} \tag{7.13}$$

The equations are modified, therefore, to give the forms:

$$\frac{\partial u}{\partial t} = -u\frac{\partial u}{\partial x} - wF\frac{\partial u}{\partial \eta} + P_x + F\frac{\partial}{\partial \eta}\left(\epsilon_z F\frac{\partial u}{\partial \eta}\right) \tag{7.14}$$

$$\frac{\partial v}{\partial t} = -u\frac{\partial v}{\partial x} - wF\frac{\partial v}{\partial \eta} + P_{c,y} + F\frac{\partial}{\partial \eta}\left(\epsilon_z F\frac{\partial v}{\partial \eta}\right) \tag{7.15}$$

where

$$\epsilon_z = l^2 F\sqrt{\left(\frac{\partial u}{\partial \eta}\right)^2 + \left(\frac{\partial v}{\partial \eta}\right)^2} \tag{7.16}$$

$$l = \kappa d\eta^{-\frac{1}{A}}\sqrt{1-\eta^{-\frac{1}{A}}} \tag{7.17}$$

and A is a scale parameter which affects the distortion of the grid.

The effect of the transformation on a steady, uniform, open-channel, logarithmic velocity profile, that is:

$$\frac{u}{u_*} = \frac{1}{\kappa} \ln\left(\frac{z}{z_0}\right) \qquad (7.18)$$

is shown in Fig. 7.5 for three A values (0.1, 0.5, 1.0). It is clear that the truncation error is smallest when the transformed solution is linear. The model used a constant of 0.1 for the coefficient A.

The model vertical velocity is calculated from the local fluid mass conservation equation:

$$\frac{\partial u}{\partial x} + \frac{\partial v}{\partial y} + \frac{\partial w}{\partial z} = 0 \qquad (2.25)$$

which is simplified using the assumption of parallel conditions along the y direction. Thus:

$$\frac{\partial u}{\partial x} + \frac{\partial w}{\partial z} = 0 \qquad (7.19)$$

Equation (7.19) is transformed into:

$$\frac{\partial u}{\partial x} + F\frac{\partial w}{\partial \eta} = 0 \qquad (7.20)$$

7.3.3 Initial and Boundary Conditions

The momentum equations (7.15), (7.16) and the continuity equation (7.20) need to be solved subject to appropriate initial and boundary conditions.

The final equilibrium solution is not affected by the choice of the initial condition. However, accurate initial conditions can reduce the iteration number of wave periods required to reach the final state. A constant horizontal current velocity over the depth (U, V in the x, y direction, respectively) is given as the initial condition. A constant wave-induced horizontal orbital velocity over the depth ($\tilde{U}$) is also added to the current velocity.

Three boundary conditions are needed, at the mean water level, at the seabed, and at both x-directional sides of the computation domain.

The surface boundary condition is taken to be zero shear stress ($\tau_{xz}=\tau_{yz}=0$) which corresponds to a zero vertical gradient of horizontal velocity ($\partial u/\partial z=\partial v/\partial z=0$). Due to the coordinate transformation used in the model, which produces a relatively large grid size near the water surface, the zero gradient of velocity can give a somewhat different shape from an ideal logarithmic profile. However, since the interest of the present study is in the near-bed flow structure, the boundary condition of zero gradient of surface velocity is adopted in the present work.

The bed boundary condition is a simple non-slip horizontal velocity condition ($u=v=0$) at a level, z_0. This non-zero level ensures a positive finite mixing length, and excludes the singularity at $z=0$. The vertical velocity at the bed is also zero ($w=0$). The bed roughness is simply expressed as a constant times some representative physical height of

the bed shape (for example, $3d_{50}$ for a flat bed of sediment grains of size d_{50}, or $3\Delta_r$ for a rippled bed of ripple height Δ_r). The level of zero horizontal velocity for a steady current flow (z_0) is set, therefore, to one-thirtieth of the bed roughness.

The side boundary condition is given by a periodic condition governed by the wave length of the water motion.

$$u(L_{wc}, z, t) = u(0, z, t) \;\; ; \;\; v(L_{wc}, z, t) = v(0, z, t) \qquad (7.21)$$

where L_{wc} is the wave length relative to the fixed frame for a combined wave and current flow. Assuming that the wave is transforming from no-current region to a with-current region for a constant water depth, and that same number of waves passes at every point(Barber,1969), that is:

$$\frac{1}{T} = \frac{C}{L} = \frac{C+U}{L_{wc}} \qquad (7.22)$$

where T is the wave period, c is the wave celerity, L is the wave length, and U is the depth-mean horizontal current velocity vector in the x direction. The wave length can then be simply calculated by the equation:

$$L_{wc} = L + TU \qquad (7.23)$$

7.3.4 Numerical Schemes and Solution Procedure

The governing equations (7.15), (7.16) are transformed into appropriate finite difference equations using an implicit scheme. The continuity equation (7.20) is solved by numerical integration. Details are given in Appendix K.

Required input data are water depth, bed roughness, wave period, wave height or wave near-bed orbital velocity amplitude, depth-mean current velocity, and wave-current intersection angle. The surface pressure gradient is not given as an input variable in the present work, but is obtained through the model calculation.

When the wave-interacted depth-mean steady velocity is known from the start of a model simulation, as for example with experimental data, then the horizontal pressure gradient in the model is adjusted by a trial and error method to reach final equilibrium conditions.

When the required condition for equilibrium is reached, that is 0.1 % change of mean pressure gradient from that of a former wave period at every grid point, then the execution is stopped. In most cases the criterion is satisfied within about 30 wave periods.

7.4 Model Characteristics

7.4.1 Initial Model Tests

The number of time steps to be used in the model during a wave period is not limited by any stability criteria, since an implicit scheme is used in the numerical solution. However, if too large a time step is used, unwanted oscillations can occur, as reported by Roache(1982), although the oscillations may eventually be dampened out after a long execution time. For present purposes, the minimum number of time steps was set to 256 in a wave period, although a larger number was used for small z_0/d cases if the oscillatory behaviour did not vanish in about 10 wave periods.

The number of vertical grids also needs to be properly chosen. Ideally, the solution should be insensitive to the number of vertical grids. To see the effect of different vertical grid numbers, the 1DV model instead of the 2DV model was tested for three different values, namely, 16, 32 and 64, for exactly the same flow conditions, see Table 7.1.

Table 7.1 Values assigned to variables in the initial model tests.

Variable	Value	Remarks
d (m)	5.0	
z_0 (mm)	5	
H (m)	0.745	

T (s)	7.0	

U_∞=0.449 m/s; wave excursion length amplitude=0.5 m; L=45.63 m.

Figs 7.6-8 shows the relatively insensitive nature of the model solution to the number of grids for wave orbital velocity, shear stress, and eddy viscosity. It is clear from the figures that 16 intervals is sufficient to describe the variation of orbital velocity and shear stress but that a larger number is needed for the eddy viscosity in the upper layers of the flow. The variation of the shear stress amplitude and the maximum eddy viscosity at 4 cm from the bed for several vertical grid numbers are shown in Fig. 7.9, and Fig. 7.10, respectively. Taking the solution from a vertical grid number of 128 for an accurate one, to a grid number of 32 gives 6 % error in the shear stress, and 4 % in the eddy viscosity, which is quite small. For the majority of the flow depth, 32 intervals is sufficient. Consequently, for most subsequent tests, 32 intervals was used unless greater precision was required.

7.4.2 Asymptotic Behaviour of the Model Solution

For situations involving a steady depth-mean current, two situations are possible. One is to assume that the energy gradient (water surface slope) is the same for the current-alone case and for the combined wave and current case. If the value of the depth-mean velocity is unknown, it is necessary to operate the model until an equilibrium situation

is reached, and the effect of the enhanced eddy viscosity in the wave boundary layer has had a chance to influence the solution. Davies(1991) has shown that when a constant pressure gradient is applied to his 1DV wave and current boundary layer model, the near-bed flow structure approaches the equilibrium value earlier than the water surface flow.

The second possibility is to keep the water flux across the whole depth constant. If we consider the situation in which the water flux is controlled in a laboratory experiment by a particular valve setting in a water circulation system, it is clear that a numerical model needs a similar function to control water flux. In such a case, the surface pressure gradient is unknown beforehand, and so some trial and error system is needed whereby the surface gradient is gradually adjusted until a specified depth-mean velocity is obtained.

In the present study, the lattermost case is considered, assuming that the depth-mean velocity of the steady current is known or given. A proper method for adjustment of the pressure gradient is thus needed for model operation as described below.

Davies(1991) has also faced the same problem referred to above, and presented a method to obtain a depth-mean velocity after many wave periods of computation. He started the model from an incorrect depth-mean velocity condition, and then adjusted the mean pressure gradient every wave period. It is not clearly described in his paper how he

adjusted the pressure gradient, but it is anticipated that the pressure gradient is modified at the end of the wave period by a scale parameter related to the ratio of the target depth-mean velocity value and the depth-mean current value averaged for a wave period. His method allows the depth-mean velocity to change every wave period, and to approach the given depth-mean velocity asymptotically by applying an appropriate new pressure gradient at each end of wave period.

A new method to obtain the desired depth-mean current and the pressure gradient is proposed in the present work. Instead of running the model forward every wave periods, the present model is run forward twice for every wave period as trials and is then run as a final computation using an interpolation of solutions of the two trials. Firstly, an initial condition is given with the exact value of the desired depth-mean velocity. This can easily be done by assigning a constant velocity over the water depth. The flow condition at the beginning of the calculation wave period should be stored so that the two trials can start from exactly the same condition. The first trial is run for a wave period with a guessed value of the mean pressure gradient ($P_{c,1}$), where P_c is the pressure gradient in the current direction ($= (P_{c,x}^2+P_{c,y}^2)^{0.5}$), and a new WPA depth-mean velocity ($|\vec{U}|_1$) is obtained. Then, the second trial is run for the same wave period starting from the same starting condition as the first trial with another guess value of the mean pressure gradient ($P_{c,2}$), and another WPA depth-mean velocity ($|\vec{U}|_2$) is obtained. The appropriate pressure gradient for the wave period is then approximated from the results of the two trials:

$$P^*_{c,f} = \frac{P_{c,2} - P_{c,1}}{|\vec{U}|_2 - |\vec{U}|_1} \left(|\vec{U}| - |\vec{U}|_1 \right) + P_{c,1} \qquad (7.24)$$

where $P_{c,f}^*$ is the pressure gradient which is to be finally applied to the wave period, and $\vec{U}$ is the given depth-mean velocity. Superscript * is for a temporary value.

By starting at the beginning of the same wave period, and applying the pressure gradient $P_{c,f}^*$, desired depth-mean velocity can be obtained at the end of the wave period. This procedure is applied at every wave period.

The present interpolation method can only be used when the response of the depth-mean-velocity is linear to the applied pressure gradient for one wave period. Although the relationship between mean pressure gradient and the resultant depth-mean-velocity for current flow is nonlinear, for example, the relationship is a "squared" one for the steady current problem, the short period response of the depth-mean-velocity to the pressure gradient is very close to linear, since flow modification is largely confined to the near bed zone.

The almost linear response is shown for a situation of 5 m depth, z_0=5 mm, depth-mean-velocity of 0.336 m/s, and excursion length amplitude of 0.5 m. After 3 wave periods, three different pressure gradients are applied and show the linear response of Fig. 7.11.

However, if the calculated pressure gradient $P_{c,f}^{*}$ is applied at the end of each wave period, the model result show two wave-period oscillations. Although the oscillations eventually disappear, it takes very many wave periods to reach the final equilibrium. In order to reach thc final equilibrium state sooner, oscillations are suppressed by using a new pressure gradient obtained by averaging the temporary pressure gradient ($P_{c,f}^{*}$) with the pressure gradient value of the former wave period (P_c^{-1}):

$$P_{c,f}^{=} \frac{P_{c,f}^{*}+P_c^{-1}}{2} \qquad (7.25)$$

This averaging ensures that the oscillation amplitude is reduced by a half every wave period. Since it takes a certain number of wave periods to modify the internal full-depth flow structure, and this number is usually larger than 10, the error induced by halving the pressure gradient is less than $1/2^{10}$ or 0.1 % in ten wave periods, which is negligible.

In order to compare the efficiency of the present method to find the final pressure gradient with a given depth-mean velocity value for the present 2DV model (or 1DV model) with that of Davies(1991), the simplified 1DV model is applied to the same flow condition as Davies(1991). The variable values of the test run are shown in Table 7.2.

Table 7.2 Test condition for pressure gradient adjustment method.

Variable	Values	Remarks
d (m)	10.0	$>> \delta_w$
z_0 (mm)	5	Δ_r= 50 mm, λ= 500 mm

Variable	Values	Remarks
H (m)	2.33	
T (s)	10	
U (m/s)	0.5	
θ_{wc} (°)	0	
A (m)	1.59	
U_∞ (m/s)	1.00	
L (m)	92.4	>> depth

Δ_r=ripple height; λ=ripple length; δ_w=wave boundary layer thickness.

The variation of the pressure gradient with time is shown in Fig. 7.12. The final pressure gradient values from the two models show slightly different values, but this is because of the different turbulence closures, not the pressure gradient adjusting method. Since the present method keeps the depth-mean-velocity from the first wave period, it shows a faster adjustment of the pressure gradient. The present method shows the peak pressure gradient at the end of the first wave period, while Davies' method shows a peak value at the second wave period. The peak value of the present method is larger than that of Davies'. The pressure gradient approaches the final equilibrium value at 6 wave periods with 10 % error from the present method, compared to about 11 wave periods from Davies' method for the same 10 % error. The test results support the view that the present method is an efficient method to obtain a desired depth-mean velocity.

7.4.3. Model Sensitivity Tests

In order to have an insight into the mechanisms in the boundary layer through sensitivity testing, the non-dimensional forms of the governing equations needs to be analyzed. The non-dimensional variables are then changed to see the model sensitivity.

Non-dimensional variables are defined as follows:

$$\begin{aligned} t_* &= \frac{1}{T} t \\ z_* = \frac{1}{z_0} z \;\; ; \;\; x_* &= \frac{1}{A} x \\ u_* = \frac{T}{A} u \;\; ; \;\; w_* &= \frac{T}{z_0} w \end{aligned} \tag{7.26}$$

Using equation (7.26), other variables are non-dimensionalized as follows:

$$\begin{aligned} \epsilon_* &= \frac{T}{A z_0} \epsilon \;\; ; \;\; \left(\frac{\tau}{\rho}\right)_* = \frac{T^2}{A^2} \left(\frac{\tau}{\rho}\right) \\ P_{c,x,*} &= \frac{T^2 z_0}{A^2} P_{c,x,*} \;\; ; \;\; P_{c,y,*} = \frac{T^2 z_0}{A^2} P_{c,y,*} \end{aligned} \tag{7.27}$$

The governing equations (7.2) and (7.3) are transformed into:

$$\frac{\partial u_*}{\partial t_*} = -u_* \frac{\partial u_*}{\partial x_*} - w_* \frac{\partial u_*}{\partial z_*} + \frac{\partial \tilde{U}_*}{\partial t_*} + \frac{A}{z_0} P_{c,x,*} + \frac{A}{z_0} \left(\frac{\partial (\tau_{xz}/\rho)_*}{\partial z_*} \right) \tag{7.28}$$

$$\frac{\partial v_*}{\partial t_*} = -u_* \frac{\partial v_*}{\partial x_*} - w_* \frac{\partial v_*}{\partial z_*} + \frac{A}{z_0} P_{c,y,*} + \frac{A}{z_0} \left(\frac{\partial (\tau_{yz}/\rho)_*}{\partial z_*} \right) \tag{7.29}$$

with the non-dimensional mixing length:

$$l_* = \kappa z_* \sqrt{1 - \frac{z_*}{d_*}} \qquad (7.31)$$

where $d_* = d/z_0$.

The wave related pressure gradient is obtained from the non-dimensional wave horizontal orbital velocity at the top of the wave boundary layer ($\tilde{U}_*$), that is:

$$\tilde{U}_* = 2\pi \cos\left(2\pi t_* - 2\pi \frac{A}{L_{wc}} x_*\right) \qquad (7.32)$$

The periodic condition at both sides of the computation domain is transformed into:

$$\begin{aligned} u_*\left(\frac{L_{wc}}{A}, t_*\right) &= u_*(0, t_*) \\ v_*\left(\frac{L_{wc}}{A}, t_*\right) &= v_*(0, t_*) \end{aligned} \qquad (7.31)$$

Since the model assumes the mixing length to be a function of bed roughness and water depth, the non-dimensional governing equation shows that the solution is a function of (A/z_0, L_{wc}/A, $P_{c,*}$, θ_c, and d/z_0). When assuming the mixing length relation with depth is weak, then the solution is a function of (A/z_0, L_{wc}/A, $P_{c,*}$, and θ_c). When the mean pressure gradient is not involved (wave-only situation), the solution is a function of (A/z_0, L_{wc}/A). When the two advection terms, and related periodic condition are excluded (1DV model without advection terms), the solution is a function of (A/z_0) only.

A typical set of values for the above variables are next selected to test the sensitivity of the model results, see Table 7.3.

Table 7.3 Values assigned to variables in the model sensitivity tests.

Variable	Value	Remarks
d (m)	5.0	
z_0 (m)	0.005	
T (s)	7.0	
A (m)	0.5	U_∞=0.449 m/s
L (m)	45.6	
U (m/s)	0.336	
θ_c (°)	0	

H=0.745 m.

The variable values in Table 7.3 were selected by considering the field situation near natural beaches, especially near Chukpyon Harbour, Korea.

The non-dimensional pressure gradient term can also be replaced by other non-dimensional variable groups. For example, ($\tau_{b,c}/\tau_{b,w}$ where $\tau_{b,c}=$ $|\vec{\tau}_{b,c}|$, and $\tau_{b,w}=$ maximum of $|\vec{\tau}_{b,w}|$) has been widely used for presentation of wave and current boundary layer model results, see Bakker and van Doorn(1978), and Soulsby et al.(1993), since it explicitly represents the relative strength of the wave and current forces near the bed. In the present work, the non-dimensional variable group ($\tau_{b,c}/\tau_{b,w}$) is also adopted. The current-related bed shear stress ($\tau_{b,c}$) is calculated from the current

friction factor (f_c), that is:

$$\tau_{b,c}=\rho f_c U^2 \; ; \; f_c=\{\frac{0.4}{\ln(\frac{d}{z_0})-1}\}^2 \qquad (7.33)$$

while the wave related bed shear stress can be calculated from the wave friction factor (f_w) ($\tau_{b,w}=\rho f_w U_\infty^2/2$).

There exist empirical formulae for the wave friction factor. The simplified version (1DV without advection terms) of the present model results can also be used to produce an expression for the wave friction factor, for example:

$$f_w=C_1\exp(C_2(\frac{A}{z_0})^{C_3}) \qquad (7.34)$$

where the coefficients can be obtained by fitting the equation to model results. In fact, a Newton-Raphson method was subsequently used together with data from three model runs. Equation (7.34) was found to have the form:

$$f_w=0.000684\exp(7.80(\frac{A}{z_0})^{-0.106}) \qquad (3.37)$$

The wave friction factor calculated by the present model was also compared with the results of other authors and found to lie between Swart's(1976) formula and Myrhaug's(1991) two equation turbulence closure model results, see Fig. 7.13. For small A/z_0, the factor approaches Myrhaug's solution, and for large A/z_0, the factor is closer to Swart's expression. All three model results are in agreement with measurements which

show a quite widely scattered results. This fact may mean that the measurement of near bed shear stress and its analysis is still a difficult problem.

The variable values in Table 7.3 correspond to non-dimensional variable groups of $z_0/d=0.001$, $A/z_0=100$, $L_{wc}/A=91.3$, $\tau_{b,w}/\tau_{b,c}=0.0625$, and $\theta_c=0$.

While other non-dimensional variables are kept constant, each non-dimensional variable is changed to see the effect of only one term. Considering that the peak wave period at Chukpyon site is about 7 seconds, and that the wave length at a point does not vary, the variable (L/A) is not separately considered. The variation of wave orbital excursion length amplitude (A) is indirectly included in the variable A/z_0.

The sensitivity of the model solution (WPA pressure gradient response) to other variable values are discussed below. Firstly, the mean pressure gradient solution shows only minor variation with z_0/d, see Fig. 7.14. Existing theories have shown that the response of the final pressure gradient value to z_0/d is relatively sensitive for small $\tau_{b,w}/\tau_{b,c}$, see Davies and Li(1991). Even though the $\tau_{b,w}/\tau_{b,c}$ value of 0.0625 was quite small for the present test, the variation of pressure gradient with z_0/d was not significant. Secondly, the A/z_0 ratio was found to give a quite sensitive response to the solution for the pressure gradient, see Fig. 7.15. Equally, a very sensitive response was also found for $\tau_{b,c}/\tau_{b,w}$, see Fig. 7.16. The high sensitivity of the solution to the latter variable has also been described by other existing theories, see van Kesteren and Bakker(1984). Fourthly, the

model was run for every 22.5° intersection angle (θ_{wc}) from 0° to 180° for a given condition. The variation of horizontal velocity profiles for various wave and current intersection angle (θ_{wc}) are shown in Fig. 7.17. The solution of the mean pressure gradient for several wave and current intersection angles was also found to follow a sinusoidal shape of curve. An equation is proposed to express the variation of the solution along the wave and current angle by the summation of two cosine functions which involve three known values for 0°, 90°, 180° as:

$$f_{\theta_{wc}} = \frac{1}{2}\left(\frac{f_0 + f_{180}}{2} + f_{90}\right) - \frac{f_{180} - f_0}{2}\cos\theta_{wc} + \frac{1}{2}\left(\frac{f_0 + f_{180}}{2} - f_{90}\right)\cos 2\theta_{wc} \qquad (7.35)$$

where f is an arbitrary variable of the model solution, subscript 0, 90, 180 are for the wave and current intersection angle (θ_{wc}). The approximate curve calculated from equation (7.35) was found to represent the model solutions very accurately, see Fig. 7.18.

7.5 Comparison of the Model Results with Measurements

7.5.1 Wave-Only Flows

To examine the model accuracy for the wave-only flow case, the model was run for two experimental conditions of van Doorn and Godefroy's(1978) and O'Connor et al.(1993).

Firstly, van Doorn and Godefroy's(1978) experimental condition is given in Table 7.4.

Table 7.4 Values assigned to variables in van Doorn and Godefroy's(1978) experiment.

Run No.	RB
d (m)	0.3
z_0 (mm)	0.2
H (cm)	12.0
T (s)	2.0
U (cm/s)	-3.0
θ_{wc} (°)	180
U_∞ (cm/s)	30.8

The velocity over the wave trough was not measured due to the exposure of the flow measuring device. Although the experiment was done for purely wave motion, a net return flow was measured due to the enclosure of the water mass in the flume (net depth-mean water mass flux at a section in a flume should be zero). Nadaoka et al.(1982) have also measured the existence of such return flow on a sloping beach.

Dalrymple(1976) has derived an equation for the net mass transport in the top layer of water between the wave crest and the trough for an unbounded situation from linear wave theory, that is:

$$\tilde{M}=\frac{g}{8}\frac{H^2}{c} \qquad (7.36)$$

An approximate depth-mean return flow velocity (U_r) can then be obtained by dividing

Dalrymple's(1976) mass transport value ($\tilde{M}$) at the top layer by the height between the bed and the wave trough (d_r), that is:

$$U_r = -\frac{\tilde{M}}{d_r} \qquad (7.37)$$

The calculated depth-mean return flow velocity from equation (7.37) is -2.8 cm/s for van Doorn and Godefroy's(1978) condition (Table 7.4), which is similar to the value of -3 cm/s from the measurements.

Figs. 7.19, 7.20, and 7.21 show the calculated velocity, shear stress, and eddy viscosity profiles, respectively, and give good agreement with van Doorn's measured velocity data. The height where the WPA velocity profile bends agrees well with the measurements.

The near bed Eulerian mass transport shows qualitatively a good agreement with the measured values, but the order of magnitude of the WPA velocity inside the wave boundary layer is slightly smaller than that of the experimental data. The mixing length hypothesis is known to slightly overestimate the vertical eddy viscosity, see van Doorn(1981), which may be the reason for the present discrepancy between model results and the measurements of van Doorn and Godefroy(1978).

Secondly, the variable values for O'Connor et al.'s(1993) experiment conducted at Manchester University, U.K. is given in Table 7.5, see also Wong(1985).

Table 7.5 Values assigned to variables in O'Connor et al.'s(1993) experiment.

Run No.	53	Remarks
d (m)	0.3	
z_0 (mm)	0.03	k_s=1.04 mm
T (s)	1.53	
θ_{wc} (°)	0	
U_∞ (cm/s)	17.0	

k_s=bed roughness.

Fig. 7.22 shows the data and model simulation, and indicates that the agreement is reasonable. The height of overshooting is a little higher than the measurements, and this again may be due to the overestimation of eddy viscosity by the mixing length theory. The simulated oscillation amplitude near the bed is slightly smaller than the measured values. The measurement of the velocity inside the very thin wave boundary layer is quite a difficult problem, since the bed roughness has a two-dimensional or three-dimensional shape, and the measured velocity values at a level very near the mean bed level may be much different depending upon the exact horizontal position of the measurement device. The approximation adopted in the model (neglecting laminar molecular viscosity) is likely to produce some errors, especially near the bed, where the laminar viscosity becomes more important relative to the turbulent eddy viscosity. This error may also cause the discrepancy between the calculated and measured velocity profiles near the bed.

7.5.2 In-Line Current Flows with Waves

The present model was applied to two experimental conditions of Nieuwjaar and van der Kaaij(1987) and Nap and van Kampen(1988) for wave and in-line current flows.

Firstly, the model was applied to the Nieuwjaar and van der Kaaij's(1987) experimental conditions with waves and in-line currents. Nieuwjaar and van der Kaaij's(1987) experimental conditions are given in Table 7.6.

Table 7.6 Values assigned to variables in Nieuwjaar and van der Kaaij's(1987) experiment.

Run No.	T15,10	T15,-10	Remarks
d (cm)	50.3	0.49.8	
k_s (cm)	6.0	6.0	Δ_r=0.02 m
H (cm)	14.6	14.9	
T (s)	2.37	2.49	
U (cm/s)	10.7	13.2	
θ_{wc} (°)	0	180	
U_∞ (cm/s)	28.2	26.8	

Fig. 7.23 shows comparison of the model result and Nieuwjaar and van der Kaaij's experimental data for a following current, while Fig. 7.24 shows that for an opposing current. The calculated mean velocity profile for the following current agrees reasonably well with the measured data, although the calculated velocity profile deviate slightly from the measurements near the bed. The calculated mean velocity profile for the opposing

current gives a better agreement with the measured data than that for a following current.

Secondly, the model was applied to Nap and van Kampen's(1988) experimental conditions, which were used by van Rijn(1989) for the determination of an empirical parameter in van Rijn's engineering formula to predict the ratio of apparent roughness to physical roughness. Nap and van Kampen(1988) had target flow conditions which appear in the run titles (for example, T15,10 means 15 cm wave height and 10 cm/s depth mean velocity), but the measured flow conditions were slightly different from the target conditions, see Table 7.7. For application of the present model, 12 conditions were selected similar to Nap and van Kampen's target conditions, see also Table 7.7.

Table 7.7 Values assigned to variables in Nap and van Kampen's(1988) experiment.

Run No.	T15,10	T15, -10	T0, -10	T7.5,40	T7.5, -40	Present Tests
d (m)	0.5	0.5	0.5	0.5	0.5	0.5
k_s (cm)	2.3	2.3	2.3	4.0	4.0	4.0
H (cm)	14.7	14.9	0.0	7.7	7.23	7.5, 15.0
T (s)	2.6	2.3	-	2.3	2.4	2.4
U (cm/s)	9.2	12.1	12.1	36.4	38.8	10,20, 40
θ_{wc} (°)	0	180	-	0	180	0, 180
U_∞ (cm/s)	28.2	26.8	-	15.6	13.2	

The calculated ratio of the apparent roughness to physical roughness are shown in Fig. 7.25 with the measured values and van Rijn's lines to fit the measured data. Generally

the model results show fairly good agreement with measurements, considering the widely scattered experimental data. The model results also show a similar trend with van Rijn's(1989) approximation lines. However, there are two differences between van Rijn's fittings and the present model results. Firstly, the model results show that the relation between the logarithm of the ratio of the apparent roughness and physical roughness ($\log(k_a/k_s)$) and the ratio of current velocity to wave orbital velocity (U/U_∞) is nonlinear. For bigger U/U_∞ values, the increment of ($\log(k_a/k_s)$) is smaller according to the present model, in contrast to van Rijn's linear relation. Secondly, the relationship between the roughness enhancement and the current velocity and wave orbital velocity amplitude ratio from the present model is not a single function for the two other wave heights: van Rijn assumed a single relationship between them. This implies that the single relationship between the non-dimensional roughness ratio and other non-dimensional wave-current velocity-ratio seems not to be sufficient. The effects of other non-dimensional variable groups (wave length to wave orbital velocity amplitude (L_{wc}/A), or wave orbital velocity to bed roughness (A/z_0)) need to be considered. If the wave period is kept constant, the effect of the latter variable group (A/z_0) needs to be considered.

7.5.3 Wave and Current Flows with General Intersection Angle

The data for arbitrary wave-current interaction angle is still very rare. Van der Stel and Visser's(1985) experimental data for 90° angle of wave and current intersection was

available for comparison with the model results. Van Rijn(1989) obtained a value of 0.75 for the parameter (γ) in his empirical formula to estimate the enhanced bed roughness from van der Stel and Visser's(1985) experimental data. In order to compare the present model results with measurements for cases of 90° wave and current intersection angle, the model was applied to van der Stel and Visser's experimental condition, which is given in Table 7.8.

Table 7.8 Values assigned to variables in van der Stel and Visser's(1985) experiment.

Run No.	T441
d (m)	0.2
k_s (cm)	1.0
H (cm)	6.8
T (s)	2.0
V (cm/s)	10.5
θ_{wc} (°)	90
U_∞ (cm/s)	21.0

Calculated and measured velocity profiles for run T441 match very well, see Fig. 7.26, although there is a slight difference near the bed. It should be noted that the experiments were carried out on a natural gravel bed so that measured WPA horizontal velocity data very near the bed may be influenced by gravel-induced vortex motion.

7.6 Use of the Results for Engineering Use

7.6.1 Presentation of Model Results for Engineering Use

There are a few ways to make use of the present time-dependent point numerical model. Firstly, the present wave-current boundary layer model can be applied at each plan grid point of the sediment transport model to obtain necessary information for the sediment model. However, this method involves a very long computation time, which is not economic. Secondly, the model results could be fully parameterized over a very wide range of variables. The model results are then replaced by algebraic functions which can be used easily for engineering purposes. However, it is not an easy thing to find adequate mathematical functions for a multi-variable, highly nonlinear problem. If non-adequate functions are used for the parameterization, errors are induced through the curve fitting procedure. Thirdly, a piecewise interpolation method can be used based upon linear or nonlinear interpolation methods. This method is especially useful for the presentation of a highly nonlinear problem. However, solutions with small increments of dependent variables need to be stored in the form of Tables or Figures for engineering use.

For present purposes, the third method is adopted. Only a limited range of variables are considered, aiming for application to a specific site, Chukpyon Harbour, Korea. For general use of the model results for the sediment transport model, many runs were executed for selected conditions and stored in a tabular form.

Since the sensitivity test shows the non-sensitivity of the model results to the z_0/d variable, the variation of this quantity is not considered here. The wave data at Chukpyon showed that the typical wave period is about 7 seconds. Consequently, we confine the wave period to 7 seconds for convenience. Therefore, the variation of variable group (L_{wc}/A) can be ignored. However, the variation of (A/z_0) is taken into account. Only the minimum number of runs was selected. Namely, two values of A/z_0, 100 and 500; 7 values of $\tau_{b,c}/\tau_{b,w}$, 1, 0.5, 0.25, 0.125, 0.0625, 0.03125, and 0.015625.

The objective of the execution was to store model results in a form which could be used to obtain information on the WPA bed shear stresses modified by waves; on the WPA eddy viscosity profile; and on the WPA velocity profiles (u,v); which are needed for the sediment transport model.

Firstly, bed shear stress values calculated from the present 2DV boundary layer model were expressed by a non-dimensional value C_4, defined as:

$$C_4 = \frac{\tau_{b,cm}}{\tau_{b,c}} = \frac{f_{cm}}{f_c} \qquad (7.38)$$

The WPA bed shear stress from the present 2DV boundary layer model is expressed by the ratio of shear stress for wave-only flow to that for current-only flow. It is seen that bed shear stress is biased toward the wave propagation direction in Fig. 7.27, 28. For an opposing current, the mean bed shear stress is more enhanced than for following or perpendicular currents.

Secondly, model results for WPA eddy viscosity values need to be stored in a convenient form. Since the sediment model requires eddy viscosity values at every vertical grid point over the depth, the model results are needed over the flow depth.

A method to make use of the model results for the eddy viscosity is proposed in the present work. The eddy viscosity profile is approximated by functions, and the coefficients of the functions are stored, instead of storing the whole eddy viscosity information over the depth. The present method using functions can then provide a simple and effective procedure to obtain the eddy viscosity profile from the stored model results.

The eddy viscosity profiles calculated from the present 2DV model show a rather complex shape over the water depth, see Fig. 7.29. When waves are strong compared to current, the WPA eddy viscosity profile has two peaks over the depth, one near the bed and the other at mid-depth. When currents are strong, the WPA eddy viscosity profile has only one peak at mid-depth, since the magnitude of the current related eddy viscosity is bigger than that of the wave related eddy viscosity over the whole water depth. Therefore, it is convenient to split the eddy viscosity profile into two parts, a wave related part (lower zone) and a current related part (upper zone).

Both eddy viscosity profiles in the lower zone calculated from the 2DV model and the simplified 1DV model which ignores the advection terms have a similar shape, see Fig. 7.30. The eddy viscosity profile obtained from the present 2DV model is assumed to be proportional to that from the 1DV model in the lower zone. Therefore, the ratio of the 2DV eddy viscosity model results to the 1DV eddy viscosity model results in the lower zone are stored. This ratio expresses the relative enhancement of the wave-related eddy viscosity in the lower zone due to the presence of a current.

The WPA eddy viscosity profile from the 1DV model for a given (A/z_0) is assumed to have the form:

$$\epsilon_{z,*,low}=C_5 z_* \exp\left(C_6 z_*^{C_7}\right) \qquad (7.39)$$

The three coefficients in equation (7.39) for a given (A/z_0) can be obtained by the Newton-Raphson method with three known sets of (z_*, $\epsilon_{z,*}$ or $\partial\epsilon_{z,*}/\partial z_*$). In the present work, the peak eddy viscosity value ($\epsilon_{z,*,peak}$) and the zero vertical gradient ($\partial\epsilon_{z,*}/\partial z_*=0$) are given at the peak height ($z_{*,peak}$). The third piece of information is provided by the height, where the eddy viscosity is half the peak eddy viscosity value. Of course, there exists two heights, which have half the peak value. In the present work, the height above the peak height is chosen, as the fitting parameter.

The three coefficients in equation (7.39) for (A/z_0) of 100, 3000, and 100000 were obtained by the Newton-Raphson method, which are given in Table 7.9.

Table 7.9 Computed coefficients for eddy viscosity profiles.

A/z_0	C_5	C_6	C_7
100	0.2570	-0.009099	1.454
3000	0.1336	-0.0007857	1.261
100000	0.06560	-0.000003433	1.435

The approximated eddy viscosity profiles for the three A/z_0 values in Table 7.9 using equation (7.39) give close agreement with the model results over the depth, see Fig. 7.31a-c.

In order to obtain the coefficients of equation (7.39) for intermediate A/z_0 value, two possibilities exist. The first possibility is to obtain the peak height, the peak eddy viscosity value, and the height of half the peak eddy viscosity in an appropriate method. For example, the peak height, peak eddy viscosity value at the peak height, and the height for half the peak eddy viscosity ($z_{*,half}$) can be obtained from the following equations:

$$z_{*,peak}=7.14\cdot10^{-6}\exp\left(12.0\left(\frac{A}{z_0}\right)^{0.0460}\right) \qquad (7.40)$$

$$\epsilon_{z,*,peak}=0.00210\exp\left(3.56\left(\frac{A}{z_0}\right)^{0.0845}\right) \qquad (7.41)$$

$$z_{*,half}=2.33\,z_{*,peak} \qquad (7.42)$$

Equations (7.40), (7.41) are shown in Fig. 7.32, 7.33, respectively. However, the Newton-Raphson method should be used to obtain the three coefficients of equation

(7.39), although we have necessary three sets of information from three equations (7.40), (7.41), and (7.42).

A simpler method is to use interpolation for the three coefficients in Table 7.9 for a particular A/z_0 value. This method may be justified if the intervals of A/z_0 in the tabular form are small. In the present work, the latter method is used to avoid the iterative Newton-Raphson method.

It is assumed here that the peak eddy viscosity height does not change even when a current is superimposed, and the vertical profile of eddy viscosity is multiplied by a constant inside the whole wave boundary layer when a current is imposed. The ratio of the eddy viscosity from the present 2DV model to that from the 1DV model is defined as:

$$C_8 = \frac{\epsilon_{*,peak}\ (2DV)}{\epsilon_{*,peak}\ (1DV)} \qquad (7.43)$$

The model results (C_8) are shown in Figs. 7.34 and 7.35. An interesting feature of the near bed eddy viscosity for wave and current situations is that the enhancement of the eddy viscosity due to current is dominant for opposing currents for large A/z_0. This explains the results that the effect of the vertical wave orbital motion is more significant when the wave length (wave length changed by the current) is small, and the orbital excursion length amplitude is large.

The upper part of the vertical diffusion coefficient is approximated by a parabolic function over z, similar to that for steady current. But for the present purposes, the eddy viscosity is related to the calculated mean pressure gradient instead of bed shear stress, since the WPA shear stress profile varies rapidly near bed, see for example Fig. 7.20.

$$\epsilon_{z,up}=\kappa\sqrt{dP_c}\,z\left(1-\frac{z}{d}\right) \qquad (7.44)$$

The pressure gradient multiplied by water depth (dP_c) is non-dimensionalized by the current related shear stress ($\tau_{b,c}$) as:

$$C_9=\frac{dP_c}{\tau_{b,c}/\rho} \qquad (7.45)$$

Thus, C_9 represents the degree of enhancement of the pressure gradient relative to the current-related pressure gradient. The pressure gradient and the mid-depth eddy viscosity are more enhanced for opposing currents, and for large A/z_0, see Figs. 7.36 and 7.37.

Thirdly, the calculated WPA velocity profile is approximated by two straight lines, one for the near-bed layer (lower layer), the other for the upper layer, see Fig. 7.38. For an accurate expression of the velocity profile in the lower layer, the gradient of velocity at the bed ($z=z_0$) is obtained from the calculated velocity profile. Defining a coefficient as:

$$C_{10}=\frac{\left(\frac{\kappa u}{\ln(z/z_0)}\right)^2}{\tau_{b,c}/\rho} \qquad (7.46)$$

then, C_{10} expresses the relative degree of reduction of the velocity gradient. The calculated coefficients C_{10} from the model are shown in Figs. 7.39 and 7.40. The change

of the near bed velocity gradient variation shows the same trend as that of eddy viscosity or shear stress, but more severe for an opposing current, and for large A/z_0.

The velocity profile in the upper zone can be approximated by a logarithmic function using an apparent roughness. Defining a coefficient as:

$$C_{11}=\frac{z_a}{z_0} \tag{7.48}$$

The calculated coefficient C_{11} (ratio of apparent roughness to given roughness from the present 2DV model are plotted in Figs. 7.41 and 7.42. It should be noted that Nap and van Kampen's(1988) experimental data have shown that the enhancement of bed roughness for 180° is larger than for 0° or 90°. The present model also confirms this trend for both $A/z_0=100$ and 500 cases, but more clearly for the $A/z_0=500$ case.

7.6.2 Calculation Procedure of Seabed Shear Stress, Eddy Viscosity Profile, and Velocity Profiles

For present purposes, a simple linear interpolation is used for most variables. The only exception is for the wave current intersection angle, where the solution can be approximated by equation (7.35) which uses two cosine functions.

Given the values of the variables, for example, d, z_0, H, T, U, θ_{wc}, then A is calculated from linear wave theory (H/sinh(kd)), $\tau_{b,c}/\rho$ is calculated from $f_c |\vec{U}|^2$, f_c is from $(0.4/(\ln(d/z_0)-1))^2$, and $\tau_{b,w}/\rho$ is calculated from equation (7.37).

Firstly, the WPA bed shear stress is obtained by interpolation of coefficients C_4 for given A/z_0, and $\tau_{b,c}/\tau_{b,w}$ values, and by equation (7.35) using C_4 values for three wave-current intersection angles. C_4 values are interpolated for a known $\tau_{b,c}/\tau_{b,w}$ value. Next, they are interpolated for A/z_0 value. Finally, equation (7.35) is applied to obtain C_4 for a given wave current-intersection angle.

Secondly, the eddy viscosity in the lower zone is calculated in a similar manner to the bed shear stress. Coefficient C_8 is obtained by interpolation in a similar manner to the case for bed shear stress. Three coefficients C_5, C_6, and C_7 are also interpolated for A/z_0. The eddy viscosity profile in the lower zone can then be obtained from:

$$\epsilon_{z,*,low}=C_8 C_5 z_* \exp(C_6 z_*^{C_7}) \qquad (7.49)$$

$$\epsilon_{z,low}=\frac{z_0 A}{T}\epsilon_{z,*,low} \qquad (7.50)$$

The eddy viscosity profile in the upper zone can be obtained from coefficient $C_9 dP_c$ with equation (7.44), where dP_c is obtained from $C_9\tau_c$.

The eddy viscosity over the water depth is obtained from:

$$\epsilon_z = \max(\epsilon_{z,low}, \epsilon_{z,up}) \tag{7.51}$$

The velocity profile in the lower zone can be obtained from coefficient C_{10} with equation:

$$|\vec{u}_{low}| = \frac{1}{\kappa}\left(C_{10}\frac{|\vec{\tau}_{b,c}|}{\rho}\right)^{0.5} \ln\left(\frac{z}{z_0}\right) \tag{7.52}$$

The velocity profile in the upper zone can be obtained from coefficient C_{11} with equation:

$$|\vec{u}_{up}| = |\vec{U}|\frac{\ln(z/ez_a)}{\ln(d/ez_a)} \tag{7.53}$$

The velocity profile over the water depth is obtained from:

$$|\vec{u}| = \max(|\vec{u}_{low}|, |\vec{u}_{up}|) \tag{7.54}$$

7.7 Conclusions

The flow structures for wave and current flows in nature are different from those produced in a water tunnel due to the existence of vertical wave orbital velocity. In order to obtain precise wave-period-average information on bed shear stress, eddy viscosity, and horizontal velocity over the water depth, a 2DV numerical model has been used instead of existing empirical methods or 1DV models which ignore the wave-induced

vertical orbital velocity effect.

A 2DV Boundary layer model was set up to incorporate the vertical wave orbital velocity effect for co-existing wave-current flows. A simple mixing length hypothesis was used to take account of time and space varying eddy viscosity characteristics inside the wave boundary layer. The bed roughness was simply assumed to be a constant, proportional to geometric shape.

Model results were compared with several experimental data sets, and gave good agreement on overall aspects. In particular, the difference between the following and opposing current profiles were well reproduced by the present model. The model results show that the wave and current interaction can be simulated by the present general turbulent theory with no ad-hoc parameter or assumption.

Sensitivity testing of the model showed that the model results are sensitive to (A/z_0), and $(\tau_{b,c}/\tau_{b,w})$. The variation of the model results with θ_{wc} was accurately expressed by a cosine function.

In order to use the results from the 2DV model in the 3D sediment model, a method has been proposed to parameterize the eddy viscosity profiles in waves and combined wave and current flows as well as the horizontal steady current profile - as affected by waves - and the increase in WPA bed shear stress. Tests of the proposed parameterizing

approach showed good comparison with the full 2DV model results.

The bed shear stress obtained from the present model is used for the calculation of the reference level concentration, and the eddy viscosity and velocity profiles are used for the calculation of suspended sediment in the 3D diffusion-advection model.

CHAPTER 8. MODEL APPLICATION TO CHUKPYON HARBOUR, KOREA

8.1 Introduction

The present chapter brings together all the elements needed to operate the new three-dimensional sediment model and shows the results of applying them to a field situation at Chukpyon Harbour on the East Coast of Korea. Because of continual siltation at the harbour site following the construction of breakwaters in 1905, the area has been the subject of study by the Korea Ocean Research and Development Institute (KORDI). During the 1980's, KORDI staff undertook a number of field campaigns, KORDI(1987, 1988, 1989), to provide data on waves, currents, and sediment transport rates, all of which have helped with the calibration of the new model. Some of the model application results have already been reported by O'Connor et al.(1992b).

8.2 Site Characteristics

Chukpyon Harbour is situated on the east coast of Korea and is used by fishing vessels. The inner harbour size at present is about 400 m by 400 m. The mean water depth of the harbour is about 5 m. Two breakwaters have been constructed in stages since 1905. Since the

construction started, the bathymetry around the harbour has suffered significant change, see Fig. 1.2. The bed slope toward deep water is about 1/50 up to a water depth of 20 m. The bed material around the coast is composed of sand and rocks. The Chukpyon beach has a pocket shape with rock projections at either end, see Fig. 1.2. Inside the pocket, a sandy beach is developed. There is a small stream which supplies sand from inland during the stormy season. However, measurements by KORDI(1987) have revealed that the amount supplied from the stream is negligible. Outside the Chukpyon beach region, there are a few small rivers, which supply sand to the coast. However, the movement of sand beyond the northern and southern limit of the Chukpyon Harbour region is not thought to have a major influence upon conditions at Chukpyon because of the protruded shape of the rocky sections at both ends of the Chukpyon Harbour region limits.

The annual wave climate at the Chukpyon site (measured between 1 Jan. 1975 and 31 Dec. 1985, excluding 1 Jan. 1977 to 31 Dec. 1977) is given in Fig. 8.1 in terms of percentage of time for each wave condition. Fig. 8.1 reveals that NE waves are dominant during the winter season, while NE, E, or SE waves are equally distributed during the summer season at Chukpyon.

Measurements were undertaken on several items to understand the dominant mechanism of sediment transport, and to provide calibration or verification of the numerical models from 1987 to 1989, see KORDI(1987, 1988, 1989).

A wide range of items have been covered in the field work, although a limited amount of the data has been used directly in the present thesis.

Wind direction and speed, temperature, and humidity were measured by a Weather Station manufactured by Aanderaa, Norway. Tidal levels were measured by a WLR-5 current meter instrument manufactured by Aanderaa, Norway. Wind-induced flow field data were obtained by floating drogues, and tidal currents were measured with an RCM-5 manufactured by Aanderaa, Norway. Bed material was collected from more than 100 points over the whole study area using a grab sampler.

Directly used data sets are described in each relevant section below.

8.3 Application of the Wave Propagation Model

Waves were measured during every field work period, using waverider buoys. Some of the measured wave data sets are used for comparison with the present model results. Details of wave measurements are given in Table 8.1, and Fig. 8.2.

Table 8.1 Details of wave measurements at Chukpyon (after KORDI, 1987).

Station	X(EW)	Y(NS)	d (m)	Period	θ_w	H_w (m)
W	239,509	394,011	39.0	14 Aug 87 -14 Sep 87	ESE	
W3	237,050	394,802	5.5	16 Aug 87 11:05-13:11	ESE	0.748
W4	237,259	394,723	6.3	16 Aug 87 16:55-18:08	ENE	0.654
W5	237,185	394,514	8.2	9 Sep 87 12:35-14:35	ENE	0.421
W6	238,358	394,883	6.6	9 Sep 87 10:20-12:20	ENE	0.419
W8	237,274	394,244	12.0	10 Sep 87 11:30-13:30	ENE	0.457
W9	237,628	394,342	14.0	10 Sep 87 15:55-17:55	ENE	0.599
W11	237,477	394,052	13.0	10 Sep 87 13:40-15:45	ENE	0.566
W12	238,072	393,637	22.0	11 Sep 87 9:10-11:10	ENE	0.768
W13	237,524	393,804	9.0	11 Sep 87 11:20-13:20	ENE	0.740

d=depth relative to MSL; θ_w=wave direction; H_W=wave height at Station W.

The wave propagation model was applied to strong wave conditions of incident wave height of 5.5 m, and directions of ENE and ESE, and the results (wave height distribution) are shown in Figs. 8.3a, and b.

Unfortunately, the large significant wave heights at shallow water (water depth $<$ 15 m) were not obtained during the field measurements. Since large wave data could not directly be obtained, except for the deep water station (W), Yoo and O'Connor's(1986a) numerical model was applied to a case of deep water wave height of 5.5 m, and a direction of ESE for comparison with the present model results. Yoo and O'Connor's model result is shown in Fig. 8.3c. Both models showed very similar wave height values.

It is clear that the Eastern Breakwater provides significant protection to the harbour. ENE waves produce quite a small wave height distribution around Chukpyon Harbour due to strong refraction towards the Eastern breakwater. The present wave propagation model was also applied

to each wave condition in Table 8.1. The significant wave height at station W was assigned to the incident wave condition. The calculated ratios of the wave height at a shallow depth station (W1-W13) to the wave height at station W were compared to measured ratios, see Table 8.2.

Table 8.2 Comparison of calculated and measured wave heights.

Station	Measured Wave Height Ratio (H / H at W)	Calculated Wave Height Ratio (H / H at W)	Relative Error to Incident Wave (%)
W3	0.63	0.60	-0.5
W4	0.74	0.35	-7.1
W5	0.62	0.54	-1.5
W6	0.18	0.42	4.3
W8	0.77	0.71	-1.1
W9	0.80	0.76	-0.7
W11	0.86	0.80	-1.1
W12	0.94	0.96	0.3
W13	0.86	0.85	-0.2

In most cases, the calculated wave height ratios agree well with measured wave height ratios. However, the calculated wave height ratios at Stations W4 and W6 are quite different from the measured ones. These two points are near a strong diffraction area, so that the solution is sensitive to the exact position. In general, the present wave propagation model reproduced accurate wave height distribution in the whole computational domain.

8.4 Application of the Wave-Induced Current Model

8.4.1 Field Measurements of Wave-Induced Currents

Ideally the wave-induced current profile on a beach should be measured at several stations in a direction normal to the beach, especially for big waves. Unfortunately, budget and time-scheduling allowed only a minimum number of direct measurements to be undertaken to confirm the trend and magnitude of the wave-induced currents at Chukpyon beach and to calibrate the wave-induced current flow model.

An RCM-5P propeller type current meter was used for the measurement of wave-induced current flow, see Plate 8.1, and Fig. 8.4. The device is equipped with a reversible propeller which can measure instantaneous currents in both forward and backward wave directions. The sensor counts the number of rotation on both sides of zero flow. The device was fixed on a frame and moored on the seabed, so that the current probe did not move even for large wave or current actions. The RCM-5P was set to take measurements at a time interval of 10 minutes at Station L2. The current meter also has a second time setting which determines the integration time period over which the count of number of revolutions of the propeller is recorded. At Chukpyon, this second time setting was put to 10 minutes. The number of revolutions was simply converted to a current speed by a conversion curve which was calibrated by the manufacturer. Since the orbital velocity of the short period waves are included in the number of revolutions, the net

residual current can be obtained by subtracting one direction current readings from the other. For a pure wave case without a steady current, the residual current will result in an almost zero value.

The frame for the RCM-5P was carefully designed not to disturb the main flow, see Fig. 8.4 and Plate 8.1. The frame consisted of two cylindrical frames one inside the other. The inner frame (the upper part in Fig. 8.4) could be moved telescopically and fixed in position by nuts and bolts. The propeller was generally placed at 60 % of the water depth, since the 60 % of the water depth velocity gives a good representation of the depth-mean velocity for steady flows, see Chow(1959). The frame also had enough weight to resist quite severe external forces.

The measurement Station (L2) is shown in Fig. 8.5, and the details of its deployment are in Table 8.3.

Table 8.3 Details of wave-induced current measurement at Chukpyon.

Station	X(EW)	Y(NS)	Period	Δt(m)	d(m)	Remarks
L2	236,790	394,305	30 Jun 88-11 Jun 88	10	2.0	good quality

Δt=record interval; d=water depth.

The measured residual flow velocity with wind direction and strength, and significant wave height and peak wave period for Station L2 is shown in Fig. 8.6. During the observation period, the significant wave height had two peaks. The wave-induced current record at the bottom box in Fig. 8.4 also shows two peaks, one peak for southerly flow on the 3-4 July 1988 and the

acceleration due to gravity, d_b is the breaking water depth (=1.6/0.78), c is the wave phase velocity, θ_b is the breaking wave direction (=22.5 °), β is the bed slope angle (=1/50).

The velocity at depth 2 m for the wave-induced current model for a plane beach with "artificial diffusion" is found from Fig. 5.7 to be 0.2 to 0.3 of the reference velocity (V_b), i.e. 5.4 to 8.1 cm/s. Thus the measured maximum velocity of 8 cm/s agrees reasonably well with the model result. The southern wave-induced current flow at 16:00 hrs. on 6 July 1988 also gives a similar agreement with calculated values. For this case, the significant wave height was 1.0 m and the maximum measured velocity was 9 cm/s.

It seems that the wave-induced current model can reproduce the correct order of magnitude of the wave-induced current for a significant wave height of up to 1.6 m, although quite a lot of uncertainties can be involved in measuring wind or wave direction, and the wave-induced currents.

8.4.3 Comparison of the Computed Results (Present Model and Yoo and O'Connor, 1986a)

Direct measurement of wave-induced currents could not be performed due to the severe wave and wind forces during typhoon conditions. For bigger wave conditions, sediment transport is stronger, and has a large effect on bed levels.

other peak for northerly flow on the 6-7 July 1988. The significant wave heights for the measurement periods were between 0.3 m to 1.6 m. These are relatively small wave heights compared to the extreme wave conditions which may cause large sediment transport, including movement in relatively deep water. However, the measured wave-induced current data could be used for evaluating the present wave-induced current model.

8.4.2 Comparison of the Model Results with Measurements

The model results were compared to field measurements for small wave conditions under an assumption of plane beach bathymetry. To evaluate the measured wave-induced current data by a simple method, a 1DH parallel beach solution was used instead of the 2DH model results.

The artificial maximum velocity at the breakerline without lateral mixing term can be calculated for a plane beach from Longuet-Higgins'(1970) theory. For the peak wave height with a northerly direction for noon on 3 July 1988, the result is:

$$
\begin{aligned}
v_b &= \frac{5}{16}\frac{\gamma}{f_{cm}}(gd_b)\tan\beta\left(\frac{\sin\theta}{c}\right)_b \\
&= \frac{5}{16}\frac{0.78}{0.01}(9.8\cdot 2.05)\frac{1}{50}\left(\frac{\sin 22.5}{\sqrt{9.8\cdot 2.05}}\right) \\
&= 0.27\ (m/s)
\end{aligned}
\qquad (5.8b)
$$

where γ is the breaking constant (=0.78), f_{cm} is a current friction factor (=0.01), g is the

In order to confirm the model applicability for larger wave conditions, the model was next applied to Chukpyon Harbour for combinations of significant wave heights of 5.5 m, 4.5 m, and 3.5 m, and wave directions of ENE and ESE. The model bed roughness was assumed to be 6 % of the water depth over the whole computation domain, based on echo sounder records. Typical wave-induced current results for the two typhoon cases (H=5.5 m, ENE and ESE) are shown in Fig. 8.7a, b.

It can be seen from Figs. 8.7a,b that both wave directions produce strong nearshore currents which are capable of moving sediment into the harbour area. The wave-induced-flow is seen to be more strongly developed for the southern waves than for the northern waves. This is the effect of the distance needed for the development of a spatially uniform wave-induced current.

Figs. 8.7a,b also show that the longshore current in front of the beach in the southern direction from the West Breakwater is always directed to the north, contributing sediment towards the harbour entrance. Equally, the wave-induced current for both incident wave directions is seen to generate a South-West current in front of the Eastern Breakwater. It is expected that unless the incident wave direction is S or SSE, which is very rare or impossible considering the large scale geometry of the site, the wave-induced current in front of the Eastern Breakwater will mostly be directed towards the harbour entrance. This also contributes to siltation near the harbour entrance.

In order to check the accuracy of the present model approach, the model result for a wave height of 5.5 m and direction of ESE was compared with Yoo and O'Connor's(1986a) model result for the same field situation but with the harbour considered as a land area in order to avoid the use of very small grid spacings in the shallow harbour area. Yoo and O'Connor's comprehensive numerical wave-induced current model has been used for various laboratory and field situations, see Section 2.3.3. The calculated wave-induced current fields from the two models shows a very similar results, and the same order of maximum velocities on two profiles, see Fig. 8.9a-b. The minor differences in the current profiles may be due to the different wave model, the turbulent lateral mixing closure, and the bed friction closure. It is concluded that the present model is likely to give reasonable results for bigger wave conditions.

8.5 Application of the Sediment Transport Model

8.5.1 Comparison of Calculated and Measured Suspended Sediment Concentrations

Measurement of suspended sediment concentration was undertaken at several stations, using an HR Ltd. (U.K.) suspended sediment pump sampler, see Plate 8.2. Measurement stations are shown in Fig. 8.10, and the details of the measurements are given in Table 8.4.

Table 8.4 Details of suspended sediment concentration measurements at Chukpyon

Station	X(EW)	Y(NS)	Period	d (m)	θ_w	H (m)
R2	237,288	394,834	16 Aug 87 12:30-13:30	5.3	ESE	0.817
R4	237,053	393,899	17 Aug 87 10:00-13:30	2.0	ENE	0.745
R6	236,769	393,802	16 Aug 87 15:00-18:00	3.9	ENE	0.758

The wave conditions given in Table 8.4 were simulated by the wave propagation model, the wave-induced current model, and the sediment transport model. The same horizontal grid (92 x 68) was used for the sediment model. The spatial increments in the x, y directions (Δx, Δy) were both 30 m. The number of vertical grid points (nk) was 10, and the coordinate transformation coefficient A of 0.1 was used. The time increment Δt was set to 1.0 second. The scaling parameters for the reference level concentration (C_2), and for the bed load (C_4) were set to 2.5×10^{-5}, and 0.055, respectively.

The calculated suspended sediment concentration profiles over the depth at three stations are shown in Fig. 8.11a-c. The model results give reasonable agreement with the measured suspended sediment concentrations at the three stations. However, it is clear that the measurements show a wide scatter. The measurement heights were also quite high starting from 0.5 m from the bed. For future work, a greater number of measurement points over the depth, including levels closer to the bed, would be of more value.

8.5.2 Comparison of the Calculated and Measured Bed Level Change

The seabed bathymetry around Chukpyon Harbour was measured several times using an echo-sounder. The period between 10 June 1987 to 3 November 1987 was selected for simulation of bathymetric change, since bathymetric charts were available for the start and end of the period and the Harbour area was subjected to two grade B typhoons on the 10 July 1987 (Thelma) and 30 August 1987 (Dinah) with maximum significant wave heights of 5.4 m and 5.6 m, respectively. Fortunately, continuous wave recordings were made during the period. The wave data for the period between 10 June 1987 to 3 Nov. 1987 is summarized in Table 8.5.

Table 8.5 Distribution of the significant wave heights and the wave directions between 10 June 1987 and 3 Nov. 1987.

Wave Height (m)	Wave Direction			Total (hour)
	NE	E	SE	
1.0-2.0	12	520	12	544
2.0-3.0	72	57	2	131
3.0-4.0	46		2	48
4.0-5.0	18		2	20
5.0-6.0	8		1	9

Data below 1.0 m wave height were counted as for calm periods.

Ideally, the whole system can be sequentially applied for the full time-series of wave conditions (for example, the wave condition varies every three hours). The bed geometry should be continuously modified, too. However, the total time-series simulation of a field situation for

medium or long term simulations requires enormous computation time, which is not desirable from the engineering point of view. Some alternative ways have been proposed.

Firstly, a simulation technique can be used, see Vemulakonda et al.(1988). A synthetic time-series wave conditions can be generated. The artificial record is expected to represent the real wave statistics at the field. Since the number of wave conditions is still much smaller than that of the measured full time-series wave conditions, the computation time can be reduced.

Secondly, one representative wave can be used, which is the minimum number of wave condition. Therefore computation time is reduced. Chesher and Miles(1992) have described a methodology to select the representative wave height, period, and direction by a weighting method. However, if too small a number of wave conditions is used, the characteristics of the sediment transport pattern at a specific site may not be properly reproduced, especially for the cases when the effect of wave direction is significant.

Thirdly, the wave conditions at a field site can be grouped into a small number of wave conditions. The number should be chosen carefully, considering both the accuracy and the calculation efficiency. The grouped wave conditions represent the wave height, period, and direction. Each wave condition is applied on the same initial bed geometry. Then the total bathymetric change is obtained by summation of each bed level change for each wave condition with an appropriate time weighting. For present purposes, the lattermost grouping method is

adopted.

Analysis of the wave records suggested that the wave climate over the study period could be divided into six representative groups composed of two predominant directions (ENE and ESE) and three wave height bands with a peak period of 7 sec: the largest wave heights corresponding to the typhoon conditions. The wave data during the period were grouped into 6 groups. The minimum number of wave directions, ENE and ESE, were chosen to distinguish the directional effect of incident waves on wave-induced flow and resulting sediment transport. The ENE direction included NE waves and 50 % of E waves, while the ESE direction included SE waves and 50 % of E waves. Wave heights were grouped into three representative sizes, 5.5 m, 4.5 m, and 3.5 m. Smaller waves were simply included in the 3.5 m wave group with a simple weighting proportional to the square of the wave height (the time for 2.5 m wave height was reduced by $2.5^2/3.5^2$, and the time for 1.5 m wave height was reduced by $1.5^2/3.5^2$ and the two reduced times were added to the time for the 3.5 m wave height). The weighting power of two was selected from existing empirical integrated longshore transport formulae, see Kraus et al.(1982), and Ozasa and Brampton(1980). The times for the six wave condition are given in Table 8.6.

Table 8.6 Weighting times for the six wave conditions.

H (m)	Wave Direction ENE	ESE
3.5	147.2	67.5
4.5	18	2
5.5	8	1

Unit: hour

Measured and calculated depth changes are shown in Fig. 8.12, and 8.13, respectively. The general accretion or erosion pattern matches each other quite well. Comparison of the sediment model bed level changes with those from the bathymetric charts confirms the effect of the wave-induced currents. The measured average accretion height during the period around Chukpyon Harbour (in the square area surrounded by x grid numbers 40-68, y grid numbers 60-92, excluding inner harbour) was 0.4 m, while the calculated average accretion height in the area was 0.2 m. Fig. 8.12 and Fig. 8.13 clearly show accretion near the Western Breakwater and off the tip of the Eastern Breakwater, although coastline accretion is less well represented. The erosion zone off the harbour entrance is also well reproduced. Detailed bed level changes on EW and NS transects are also shown in Fig. 8.14a-b. Seeing two profiles around the two breakwaters, the magnitude of erosion or accretion is within an order of 2, which is considered to be a reasonable reproduction. Quite good qualitative agreement is obtained along the EW transect with less good agreement along the NS transect. A very good location is obtained for the major shoal area. Possibly a better comparison could be obtained by allowing a feedback loop in the model system whereby the changes in bed level are allowed to influence the wave and current flows, and thereby the sediment transport rates.

Fluorescent tracer tests were conducted to obtain qualitative information on sediment transport direction around Chukpyon. Sandy material at Chukpyon was covered with fluorescent paints, and was deposited at three points on 30 June 1988, see Fig. 8.15. 26 days after deposition, bed material was collected at over 300 points around the three original points. The number of fluorescent sand particles in a unit volume was counted, see Fig. 8.15. The wave climate during the period was similar to the typical wave climate in the season (Fig. 8.1). The test results revealed the sediment transport pattern toward the harbour entrance from both the Eastern Breakwater and south beach. This also supports the validity of the calculated wave-induced current pattern and the calculated bed level change pattern.

8.6 Conclusions

The relatively simple system of nearshore coastal models has been applied to study a particular siltation problem at Chukpyon in eastern Korea. The lack of nearshore tidal currents in the study area enables wave and current fields to be decoupled while the dominance of sediment movements by typhoon conditions has enabled the wave climate to be synthesized by a limited number of wave patterns. The new three-dimensional wave-period-average sediment model has been interfaced with both an inshore wave prediction model and a wave-induced current model and shown to be capable of giving quite a good representation of sediment load and seabed changes in the vicinity of the harbour.

Comparison of model results with rather limited field data confirms the accuracy of the wave and wave-induced current models, the new 3D sediment model concentrations and the presence of residual sediment movement towards the harbour entrance as well as the location of shoal zones near the west groyne and east breakwater. Overall sediment bed level change accuracy appears to be within a factor of two and is considered to be good enough for engineering use, provided sediment field data can be obtained to calibrate the model constants. Further work is needed to include bed level change feed back into the model system to see if this approach would increase model accuracy.

CHAPTER 9. CONCLUSIONS AND SUGGESTIONS FOR FUTURE WORK

9.1 Assessment of the Present Model System

A numerical model system for the simulation of suspended sediment transport and bed level changes around structures due to wave and wave-induced currents has been established. Compared with existing approaches, the new models are the simplest level of model for simulation of medium or long term siltation.

The new model system is composed of three sub-models: a 2D plan wave propagation model; a 2D plan wave-induced current model; and a 3D suspended sediment transport model and a 2D plan bed level change model.

Wave propagation model

Berkhoff's(1972) evolution elliptic mild-slope wave equation is solved by numerical schemes modified from those of Ebersole et al.(1986). The second order derivative term of wave amplitude (diffraction term) in the direction of wave propagation is ignored, and land boundaries are treated without diffraction terms. The model reproduces shoaling, refraction, diffraction and breaking processes, and was tested on a caustic wave propagating over a submerged elliptic

shoal, with good results. It was shown that the simplification of the governing equation does not significantly affect the accuracy of the solution. Diffraction around structures was also reproduced in the model. However, it was found necessary to use a special approach for condition in the lee of structures. The modified Ebersole et al. model has a limitation of a wave propagation angle of $\pm$ 45 ° from the x-axis (set in the opposite direction of main wave propagation) due to the one-directional sweep calculation procedure used. For conditions in the zone outside the 45° sector at structures, it is necessary to use a subsidiary solution when dealing with diffraction by structures. In the present model, Penney and Price's analytical solution is used to provide boundary conditions for the numerical model along a line taken 45° from the direction of wave propagation (negative x axis) at the tip of the structure. For angles greater than 45° in the shadow zone, the Penney and Price solution is used completely. If crossing wave trains occur in the shadow zone, an averaging approach is used to determine wave heights and directions. Generally, the wave model was found to be fast and cost-effective, and useful for general bathymetry. Tests against Penney and Price's analytical method for semi-infinite breakwaters showed good results and suggested that model coding error were absent.

Wave-induced current model

Wave-induced currents are simulated by a new current flow model, using information on wave directions and heights from the wave propagation model. The new model uses a similar approach to that of Flather and Heaps(1975) with the addition of wave-induced radiation stress terms. The

approach is further simplified by introducing a spreading of the gradients of radiation stress terms in the surf zone. The spreading approach is run separately from the unsteady momentum difference equations, and replaces lateral mixing terms. Application of the spreading concept to a plane beach situation shows similar longshore velocity profiles to those of Longuet-Higgins'(1970) solution. The model was applied to a laboratory experiment of circulation behind a detached breakwater. The model results showed good agreement with the measured velocity distribution. Model computer runs were again found to be fast due to the simplification of the lateral mixing terms.

Sediment transport model

With information on wave conditions and wave-induced currents, the suspended sediment concentration and the bed level change are calculated from a new three-dimensional suspended sediment transport model and an associated bed level change model. The non-uniformity of suspended sediment distribution around structures can be reflected by the three-dimensional suspended sediment model. The model adopts a splitting technique of processes for efficient calculation.

A new empirical formula for the reference level suspended sediment concentration was proposed, and calibrated with existing laboratory data, and Chukpyon field data. The formula reflects the variation of Shields parameter in a wave period, which has not been taken into account in

existing formula.

The Chukpyon data sets were obtained by a new four-trap device. The four openings on the device have four different orientations (down-contour, up-contour, onshore, offshore), so that the net sediment transport can be obtained by subtraction of one value from the other. The scaling coefficient for the reference level concentration was obtained from existing laboratory and field data. A new bed load formula was also proposed, and the scale parameter was obtained from field data. The field bed load data showed rather scattered plots, and the scaling coefficients in the new empirical formulae need to be further calibrated for each field site.

3D model results were compared with two analytical solutions for simple situations and gave accurate solutions.

The three-dimensional sediment transport model requires a knowledge of WPA bed shear stress, vertical diffusion coefficient profile, and horizontal velocity profiles at each plan grid point. These are supplied from a two-dimensional vertical (2DV) wave and current boundary layer model.

Existing empirical methods as well as existing 1DV wave and current boundary layer models, which do not include the vertical velocity term, together with 1DV wave boundary layer models, which do not include the current effect have some drawbacks. Therefore, a new boundary layer

model, which takes account of the effect of both wave (vertical) orbital velocities, and the steady current, has been developed. The model enables the wave-period-average velocity profiles for waves with a following current and for waves with an opposing current, which are different for strong wave situations, to be simulated. This phenomena has already been pointed out by experimentalists, such as Kemp and Simons(1982), Nieuwjaar and van der Kaaij(1987), and Nap and van Kampen(1988). The model can also be applied for situations involving arbitrary wave and current intersection angles. Model results were obtained for a limited general range of wave and current parameters at Chukpyon, and stored in the computer in a tabular form. Values at a particular plan grid point were then obtained by interpolation.

Chukpyon Application

The model system was applied to the real field situation at Chukpyon Harbour, Korea. Each sub-model was found to give reasonable agreement with measured data for wave height field (Waverider buoy), wave-induced currents (RCM-5P on a bed frame), suspended sediment concentration (HR pump sampler), and seabed level change (echo-sounder); the various field data being obtained between 1987 and 1989 at Chukpyon. The depth-change for a stormy period of 143 days was reasonably reproduced by the present model system. It is thought that the models can be used for other similar situations to simulate past bathymetric change, or to predict future medium or long term bed level change. However, field data must be used to set-up and calibrate the model for each site.

9.2 Future Work

The present work involves three separate models, wave, wave-induced current, and sediment transport models. These models contain various empirical parameters which have been calibrated from only a small number of data. Each model can, therefore, be improved by further calibration with more data sets, and with more accurate data sets.

Firstly, the recommended future research for the wave propagation model is listed below:

- Comparison of the present wave model with nonlinear wave, or random wave models on accuracy and efficiency

- Comparison of the present model with models which includes other terms, such as wave-current interaction

Future work for the wave-induced current model include:

- Comparison of the model with three-layer or three-dimensional modelling

- Comparison of the model with nonlinear wave, or random wave-induced current models

Future work for the sediment transport model include:

- Research on the near bed vortex movement behaviour (It is known to play an important role in the sediment transport, see O'Connor(1991), and O'Connor et al.(1992a). This effect becomes more dominant when waves are strong, bed roughness is large, and bed material is coarse.

- Linking IWP modelling with separation of entrainment into vortex and skin friction entrainments

- Making use of the results of 2DV flow or 2DV sediment model over a rippled bed

  Comparison of the present model with nonlinear or random wave sediment models

- Inclusion of on-offshore sediment transport, bed slope effect, sediment grading effect, and sheet flow transport for a flat bed zone

- Inclusion of an adequate bed roughness prediction model

- Inclusion of the enhancement of the eddy viscosity due to wave breaking

The wave-current boundary layer model supplies the important parameters for the sediment model. The sub-model may be refined as follows:

- Comparison of the present mixing-length hypothesis with higher order turbulence closure models

- Parameterization of the model result for a wider range of variable values for general use for other sites

- Further comparison of the model with other accurately obtained laboratory or field data

- Extension of the model for random wave and current situations, and tidal situations

While upgrading or refining the model system in the future, the simplification of the whole system will also need to be looked at for better engineering use for long term siltation predictions.

The four-trap device for measuring suspended sediment near the seabed needs further calibration in a flume. It may also be desirable to install a probe for measuring near bed velocity on the device.

APPENDIX A. FINITE DIFFERENCE EQUATIONS FOR THE WAVE PROPAGATION MODEL

The three governing equations (4.1), (2.14), and (2.15) are solved using finite-difference numerical methods applied to a regular grid of computation points of constant sized, rectangular cells, see Fig. 4.1. The governing equations are:

$$|\nabla s|^2 = k^2 + \frac{1}{a}\left(\frac{\partial^2 a}{\partial y^2} + \frac{1}{cc_g}(\nabla a \cdot \nabla(cc_g)\right) \qquad (4.1)$$

$$\frac{\partial}{\partial x}(a^2 cc_g |\nabla s| \cos\theta) + \frac{\partial}{\partial y}(a^2 cc_g |\nabla s| \sin\theta) = 0 \qquad (2.14)$$

$$\frac{\partial}{\partial x}(|\nabla s| \sin\theta) - \frac{\partial}{\partial y}(|\nabla s| \cos\theta) = 0 \qquad (2.15)$$

where ∇ is the two-dimensional spatial gradient operator ($\partial/\partial x$, $\partial/\partial y$); s is the wave phase function; k is the wave number; a is the wave amplitude; x,y are longitudinal and lateral spatial cartesian co-ordinates, respectively; c, c_g are the wave phase velocity and group velocity, respectively; and θ is the counter-clockwise wave direction relative to the negative x direction.

All variables which vary as a function of space are defined at the cell centre, see Fig. 4.1. When a dependent variable F and its derivatives are single-valued, finite, and continuous functions, it

can be expanded by Taylor's theorem. Then, the following central-difference, second order correct finitc diffcrence operators are used to approximate the partial derivatives of F at position (i,j):

$$\frac{\partial^2 F}{\partial y^2}=\frac{1}{(\Delta y)^2}(F_{i,j+1}-2F_{i,j}+F_{i,j-1})+O(\Delta y^2) \qquad (A.1)$$

$$\frac{\partial F}{\partial y}=\frac{1}{2\Delta y}(F_{i,j+1}-F_{i,j-1})+O(\Delta y^2) \qquad (A.2)$$

where $O(\Delta y^2)$ denotes terms containing second and higher powers of Δy; subscripts i,j are x,y grid point numbers, respectively; and superscript n is the time step number. The following upwind, first order correct finite difference operator is used to approximate the partial derivative of F at position (i,j):

$$\frac{\partial F}{\partial x}=\frac{1}{\Delta x}(F_{i+1,j}-F_{i,j})+O(\Delta x) \qquad (A.3)$$

where $O(\Delta x)$ denotes terms containing first and higher powers of Δx.

The magnitude of the gradient of wave phase function at any point (i,j) is then computed from the following finite difference equation, that is:

$$\begin{aligned}|\nabla s|^2_{i,j}&=k^2_{i,j}+\frac{a_{i,j+1}-2a_{i,j}+a_{i,j-1}}{(\Delta y)^2}\\ &+\frac{1}{cc_{g_{i,j}}}\times\left(\left(\frac{a_{i+1,j}-a_{i,j}}{\Delta x}\right)\left(\frac{cc_{g_{i+1,j}}-cc_{g_{i,j}}}{\Delta x}\right)\right.\\ &\left.+\left(\frac{a_{i,j+1}-a_{i,j-1}}{2\Delta y}\right)\left(\frac{cc_{g_{i,j+1}}-cc_{g_{i,j-1}}}{2\Delta y}\right)\right)\end{aligned} \qquad (A.4)$$

The equations (2.14), and (2.15) can both be expressed in the general form:

$$\frac{\partial F}{\partial x}+\frac{\partial G}{\partial y}=0 \qquad (A.5)$$

where F, G are $a^2cc_g|\nabla s|\cos\theta$, and $a^2cc_g|\nabla s|\sin\theta$, respectively, for equation (2.14); or F, G are $|\nabla s|\sin\theta$, $-|\nabla s|\cos\theta$, respectively, for equation (2.15). If partial derivatives in both x and y directions are estimated using central differences about the point (i+1/2,j), see Fig. A.1, then the following finite difference equation results:

$$\frac{\partial F}{\partial x}\Big|_{i+\frac{1}{2},j}+\frac{\partial G}{\partial y}\Big|_{i+\frac{1}{2},j}=0 \qquad (A.6)$$

$$\frac{\partial F}{\partial x}\Big|_{i+\frac{1}{2},j}=\frac{F_{i+1,j}-F_{i,j}}{\Delta x} \qquad (A.7)$$

$$\begin{aligned}\frac{\partial G}{\partial y}\Big|_{i+\frac{1}{2},j}&=W\frac{\partial G}{\partial y}\Big|_{i,j}+(1-W)\frac{\partial G}{\partial y}\Big|_{i+1,j}\\ &=W\left(\frac{G_{i,j+1}-G_{i,j-1}}{2\Delta y}\right)+(1-W)\left(\frac{G_{i+1,j+1}-G_{i+1,j-1}}{2\Delta y}\right)\end{aligned} \qquad (A.8)$$

where W is a weighting factor ($0\le W\le 1$) which designates the relative importance between the two calculation columns i, and i+1. If W = 0.5, the finite difference equation is spatially exactly centred at (i+1/2,j). The factor W is given 1.0 here as Ebersole et al.(1986). Substituting equations (A.7) and (A.8) into equation (A.6), equation (A.6) becomes:

$$\frac{F^*_{i+1,j}-F_{i,j}}{\Delta x}+W\left(\frac{G_{i,j+1}-G_{i,j-1}}{2\Delta y}\right)+(1-W)\left(\frac{G_{i+1,j+1}-G_{i+1,j-1}}{2\Delta y}\right)=0 \qquad (A.9)$$

where $F_{i+1,j}^*$ is an intermediate value for $F_{i+1,j}$, which is introduced in the following

approximation.

The additional approximation is made by the following weighted sum for function F:

$$F^{*}_{i+1,j}=\alpha F_{i+1,j+1}+(1-2\alpha)\,F_{i+1,j}+\alpha F_{i+1,j-1} \qquad (A.10)$$

The above "dissipative interface" is used to enhance the stability of the numerical scheme. The value of α is set to be 0.167 as Ebersole et al.(1986), see Abbott(1975). Then the equations (A.9) and (A.10) give:

$$\begin{aligned} F_{i,j}=&\alpha F_{i+1,j+1}+(1-2\alpha)\,F_{i+1,j}+\alpha F_{i+1,j-1} \\ &+\Delta x\Big(W\Big(\frac{G_{i,j+1}-F_{i,j-1}}{2\Delta y}\Big) \\ &+(1-W)\Big(\frac{G_{i+1,j+1}-G_{i+1,j-1}}{2\Delta y}\Big)\Big) \end{aligned} \qquad (A.11)$$

Substituting the following expressions for F and G,

$$F=|\nabla s|\sin\theta \;;\; G=-|\nabla s|\cos\theta \qquad (A.12)$$

the finite difference form of equation (2.15) becomes:

$$\begin{aligned} \sin\theta_{i,j}=&\frac{1}{|\nabla s|_{i,j}}\Big(\big(\alpha|\nabla s|_{i+1,j+1}\sin\theta_{i+1,j+1} \\ &+(1-2\alpha)\,|\nabla s|_{i+1,j}\sin\theta_{i+1,j} \\ &+\alpha|\nabla s|_{i+1,j-1}\sin\theta_{i+1,j-1}\big) \\ &-\frac{W\Delta x}{2\Delta y}\big(|\nabla s|_{i,j+1}\cos\theta_{i,j+1}-|\nabla s|_{i,j-1}\cos\theta_{i,j-1}\big) \\ &-\frac{(1-W)\,\Delta x}{2\Delta y}\big(|\nabla s|_{i+1,j+1}\cos\theta_{i+1,j+1}-|\nabla s|_{i+1,j-1}\cos\theta_{i+1,j-1}\big)\Big) \end{aligned} \qquad (A.13)$$

Using the substitutions as:

the finite difference form of equation (2.14) becomes:

$$F=a^2A \;;\; G=a^2B \tag{A.14a}$$

$$A=cc_g|\nabla s|\cos\theta \;;\; B=cc_g|\nabla s|\sin\theta \tag{A.14b}$$

$$\begin{aligned} a^2_{i,j}=&\frac{1}{A_{i,j}}\Big((\alpha a^2_{i+1,j+1}A_{i+1,j+1} \\ &+(1-2\alpha)\,a^2_{i+1,j}A_{i+1,j}+\alpha a^2_{i+1,j-1}A_{i+1,j-1}) \\ &+\frac{W\Delta x}{2\Delta y}(a^2_{i,j+1}B_{i,j+1}-a^2_{i,j-1}B_{i,j-1}) \\ &+\frac{(1-W)\,\Delta x}{2\Delta y}(a^2_{i+1,j+1}B_{i+1,j+1}-a^2_{i+1,j-1}B_{i+1,j-1})\Big) \end{aligned} \tag{A.15}$$

At the offshore open boundary, wave direction, wave height, and the gradient of wave phase function should be given. Given deep water wave conditions, Snell's law is used for the cases when bottom contours are parallel with the y-axis:

$$\frac{\sin\theta}{c}=\frac{\sin\theta_0}{c_0} \tag{A.16}$$

where c_0 is the wave phase celerity at deep water, θ_0 is the wave direction at deep water. If the bottom contours make a non-zero angle with the y-axis, the following equation can be used for better approximation of the wave solution, as in Ebersole et al.(1986):

$$\theta=\pi-\sin^{-1}\left(\frac{\sin(\theta_0-\theta_b)}{\frac{c_0}{c}}\right)+\theta_b \tag{A.17}$$

where θ_b is the angle between the bottom contours and the y axis.

The wave heights at the open boundary are then estimated as the product of the deep water wave height, a shoaling coefficient K_s, and a refraction coefficient K_r, thus:

$$H=H_0 K_s K_r \tag{A.18}$$

where

$$K_s=\{\frac{1}{(1+\frac{2kd}{\sinh(2kd)})\tanh(kd)}\}^{\frac{1}{2}} \tag{A.19}$$

$$K_r=(\frac{\cos\theta_0}{\cos_\theta})^{\frac{1}{2}} \tag{A.20}$$

The gradient of wave phase function at the open boundary is approximated as the wave number ($|\nabla s|=k$). Initial values inside the computation domain can be provided by the same way as for the open sea boundary, since the initial conditions are simply used as a first guess.

At the side open boundaries, the parallel condition is applies as:

$$|\nabla s|_{i,1}=|\nabla s|_{i,2} \; ; \; a_{i,1}=a_{i,2} \; ; \; \theta_{i,1}=\theta_{i,2} \tag{A.21}$$

$$|\nabla s|_{i,nj}=|\nabla s|_{i,nj-1} \; ; \; a_{i,nj}=a_{i,nj-1} \; ; \; \theta_{i,nj}=\theta_{i,nj-1} \tag{A.22}$$

At the land boundary, the decaying wave condition is used. If there is any land boundary grid point in the calculation column (i), the finite difference equations (A.4), (A.13), and (A.15) for the open sea cannot be used, since the equations involve values on the land. In the present study, the numerical schemes are modified for the calculation at the land boundary. Firstly, the diffraction term involving the second derivative of amplitude along the y direction is omitted.

Secondly, the lateral first order derivatives along the x axis are expressed by an upwind scheme.

For a grid point which has a land boundary in the positive y direction, see Fig. A.2, the finite difference equation (A.4) is reduced to:

$$|\nabla S|^2_{i,j}=k^2_{i,j}+\frac{1}{cc_{g_{i,j}}}\times\left(\left(\frac{a_{i+1,j}-a_{i,j}}{\Delta x}\right)\left(\frac{cc_{g_{i+1,j}}-cc_{g_{i,j}}}{\Delta x}\right)+\left(\frac{a_{i,j}-a_{i,j-1}}{\Delta y}\right)\left(\frac{cc_{g_{i,j}}-cc_{g_{i,j-1}}}{\Delta y}\right)\right) \tag{A.23}$$

Equation (A.13) is reduced to:

$$\begin{aligned}\sin\theta_{i,j}=\frac{1}{|\nabla S|_{i,j}}\Big(&(\alpha|\nabla S|_{i+1,j+1}\sin\theta_{i+1,j+1}\\&+(1-2\alpha)|\nabla S|_{i+1,j}\sin\theta_{i+1,j}\\&+\alpha|\nabla S|_{i+1,j-1}\sin\theta_{i+1,j-1})\\&-\frac{W\Delta x}{\Delta y}(|\nabla S|_{i,j}\cos\theta_{i,j}-|\nabla S|_{i,j-1}\cos\theta_{i,j-1})\\&-\frac{(1-W)\Delta x}{\Delta y}(|\nabla S|_{i+1,j}\cos\theta_{i+1,j}-|\nabla S|_{i+1,j-1}\cos\theta_{i+1,j-1})\Big)\end{aligned} \tag{A.24}$$

And equation (A.15) is reduced to:

$$\begin{aligned}a^2_{i,j}=\frac{1}{A_{i,j}}\Big(&(\alpha a^2_{i+1,j+1}A_{i+1,j+1}\\&+(1-2\alpha)a^2_{i+1,j}A_{i+1,j}+\alpha a^2_{i+1,j-1}A_{i+1,j-1})\\&+\frac{W\Delta x}{\Delta y}(a^2_{i,j}B_{i,j}-a^2_{i,j-1}B_{i,j-1})\\&+\frac{(1-W)\Delta x}{\Delta y}(a^2_{i+1,j}B_{i+1,j}-a^2_{i+1,j-1}B_{i+1,j-1})\Big)\end{aligned} \tag{A.25}$$

Similarly, for a grid point which has a land boundary in the negative y direction, see Fig. A.3, the finite difference equation (A.4) is reduced to:

$$|\nabla s|^2_{i,j}=k^2_{i,j}+\frac{1}{cc_{g_{i,j}}}\times\left(\left(\frac{a_{i+1,j}-a_{i,j}}{\Delta x}\right)\left(\frac{cc_{g_{i+1,j}}-cc_{g_{i,j}}}{\Delta x}\right)+\left(\frac{a_{i,j+1}-a_{i,j}}{\Delta y}\right)\left(\frac{cc_{g_{i,j+1}}-cc_{g_{i,j}}}{\Delta y}\right)\right) \tag{A.26}$$

Equation (A.13) is reduced to:

$$\begin{aligned}\sin\theta_{i,j}=&\frac{1}{|\nabla s|_{i,j}}\left(\left(\alpha|\nabla s|_{i+1,j+1}\sin\theta_{i+1,j+1}\right.\right.\\&+(1-2\alpha)|\nabla s|_{i+1,j}\sin\theta_{i+1,j}\\&\left.+\alpha|\nabla s|_{i+1,j-1}\sin\theta_{i+1,j-1}\right)\\&-\frac{W\Delta x}{\Delta y}\left(|\nabla s|_{i,j+1}\cos\theta_{i,j+1}-|\nabla s|_{i,j}\cos\theta_{i,j}\right)\\&\left.-\frac{(1-W)\Delta x}{\Delta y}\left(|\nabla s|_{i+1,j+1}\cos\theta_{i+1,j+1}-|\nabla s|_{i+1,j}\cos\theta_{i+1,j}\right)\right)\end{aligned} \tag{A.27}$$

And equation (A.15) is reduced to:

$$\begin{aligned}a^2_{i,j}=&\frac{1}{A_{i,j}}\left(\left(\alpha a^2_{i+1,j+1}A_{i+1,j+1}\right.\right.\\&+(1-2\alpha)a^2_{i+1,j}A_{i+1,j}+\alpha a^2_{i+1,j-1}A_{i+1,j-1}\\&+\frac{W\Delta x}{\Delta y}\left(a^2_{i,j+1}B_{i,j+1}-a^2_{i,j}B_{i,j}\right)\\&\left.+\frac{(1-W)\Delta x}{\Delta y}\left(a^2_{i+1,j+1}B_{i+1,j+1}-a^2_{i+1,j}B_{i+1,j}\right)\right)\end{aligned} \tag{A.28}$$

At the special boundary where the computation domain is divided between the present model and Penney and Price's method, the wave heights obtained from Penney and Price's method are simply assigned. Wave direction is approximated geometrically (straight from the breakwater tip), see Fig. A.4. The wave phase function gradient is also approximated by the wave number.

The offshore boundary values are given along the column (ni), and the solution of the computation domain is obtained column by column starting from the column (ni-1).

The solutions of equations (A.13) and (A.15) for the wave angle and the wave amplitude along the calculation column (i) are obtained iteratively because of the implicit finite difference formulation used (W=1.0). For the calculation, the initial guess values for the wave phase function gradient are used. Iteration for the calculation of the wave angle and the wave amplitude continues until the average change along a column in each variable from one iteration to the next is less than a particular limit. The convergence criteria of 1.4° for wave angles, 0.15 mm for wave heights are used for present purposes.

When the wave angle and the wave amplitude are obtained along the calculation column (i), the wave phase function gradient is solved by equation (A.4). Using the new wave phase function gradients, equations (A.13) and (A.15) are solved again. When equation (A.4) is solved using the new wave angles and wave amplitudes, the values are different from the former solution. This iteration continues until the change in new wave phase function gradient from one iteration to the next is less than a limit, say 0.5 percent of the newly computed value at each cell along the computation column (i). As the new wave phase function gradients are obtained, the values are averaged with the old values at each grid cell to remove cell-to-cell oscillations, see Sheng et al.(1978).

APPENDIX B. DIFFRACTION BY THE PENNEY AND PRICE(1952) METHOD

Penney and Price(1952) have presented a solution for the elliptic wave equation for a specific case of uniform depth around a semi-infinite breakwater at the ends of a breakwater, and also for the case of a gap in a breakwater. Penney and Price(1952) have used Sommerfeld's(1896) solution of diffraction of light to simulate water wave diffraction for constant water depth and a rigid breakwater, see also Wiegel(1964). The diffraction coefficients for a semi-infinite rigid impermeable breakwater with the incident waves approaching the breakwater at any angle can be calculated by Penney and Price's method.

Defining the incident wave angle θ_0 as a counter-clockwise angle relative to the breakwater direction; r as the distance of the calculation point from the breakwater tip; and θ as the counter-clockwise wave angle of the line from the breakwater tip to the calculation point, the area around the breakwater is divided into three regions, shadow region S, open region Q, and reflection region R, see Fig. B.1. Then the diffraction coefficient can be calculated for each region as follows.

In Region S, the diffraction coefficient (K_d) is obtained by:

$$K_d^2 = (D_1)^2 + (D_2)^2 \tag{B.1}$$

where

$$\begin{aligned} D_1 = & \cos(kr\cos(\theta-\theta_0))\cdot\left(\frac{1}{2}(1.0+C+S)\right) \\ & +\sin(kr\cos(\theta-\theta_0))\cdot\left(-\frac{1}{2}(S-C)\right) \\ & +\cos(kr\cos(\theta+\theta_0))\cdot\left(\frac{1}{2}(1.0+C'+S')\right) \\ & +\sin(kr\cos(\theta+\theta_0)\cdot\left(\frac{1}{2}(S'-C')\right) \end{aligned} \tag{B.2}$$

$$\begin{aligned} D_2 = & \cos(kr\cos(\theta-\theta_0))\cdot\left(-\frac{1}{2}(S-C)\right) \\ & +\sin(kr\cos(\theta-\theta_0))\cdot\left(\frac{1}{2}(1.0+C+S)\right) \\ & +\cos(kr\cos(\theta+\theta_0))\cdot\left(\frac{1}{2}(S'-C')\right) \\ & +\sin(kr\cos(\theta+\theta_0)\cdot\left(\frac{1}{2}(1.0+C'+S')\right) \end{aligned} \tag{B.3}$$

$$\begin{aligned} \sigma &= 2\sqrt{\frac{kr}{\pi}}\sin\frac{1}{2}(\theta-\theta_0) \\ \sigma' &= -2\sqrt{\frac{kr}{\pi}}\sin\frac{1}{2}(\theta-\theta_0) \end{aligned} \tag{B.4}$$

$$\begin{aligned} C &= \int_0^{\sigma}\cos\frac{1}{2}\pi u^2 du \\ S &= \int_0^{\sigma}\sin\frac{1}{2}\pi u^2 du \end{aligned} \tag{B.5}$$

$$C'=\int_0^{\sigma'}\cos\frac{1}{2}\pi u^2 du$$
$$S'=\int_0^{\sigma'}\sin\frac{1}{2}\pi u^2 du \qquad \text{(B.6)}$$

where k is the wave number. The values of Fresnel integral (C,S,C',S') are found from rational approximation functions, see Abramovitz and Stegun(1965). Using the functions is more convenient than using interpolation from tabular forms of solutions.

$$C(\sigma)\simeq\frac{1+0.926\sigma}{2+1.792\sigma+3.104\sigma^2} \qquad \text{(B.7)}$$

$$S(\sigma)\simeq\frac{1}{2+4.142\sigma+3.492\sigma^2+6.670\sigma^3} \qquad \text{(B.8)}$$

The solution for open region Q is obtained similarly,

$$\begin{aligned} D_1=&\cos(kr\cos(\theta-\theta_0))\\ &-\cos(kr\cos(\theta-\theta_0))\cdot(\frac{1}{2}(1.0+C+S))\\ &-\sin(kr\cos(\theta-\theta_0))\cdot(-\frac{1}{2}(S-C))\\ &+\cos(kr\cos(\theta+\theta_0))\cdot(\frac{1}{2}(1.0+C'+S'))\\ &+\sin(kr\cos(\theta+\theta_0)\cdot(\frac{1}{2}(S'-C')) \end{aligned} \qquad \text{(B.9)}$$

$$
\begin{aligned}
D_2 = & -\sin(kr\cos(\theta-\theta_0)) \\
& -\cos(kr\cos(\theta-\theta_0))\cdot(-\tfrac{1}{2}(S-C)) \\
& +\sin(kr\cos(\theta-\theta_0))\cdot(\tfrac{1}{2}(1.0+C+S)) \\
& +\cos(kr\cos(\theta+\theta_0))\cdot(\tfrac{1}{2}(S'-C')) \\
& -\sin(kr\cos(\theta+\theta_0)\cdot(\tfrac{1}{2}(1.0+C'+S'))
\end{aligned}
\qquad \text{(B.10)}
$$

The solution for reflection region (R) can be obtained similarly, but is not used here, since reflection is ignored in the present work.

APPENDIX C. FINITE DIFFERENCE EQUATIONS FOR THE WAVE-INDUCED CURRENT MODEL

The continuity and momentum equations constitute the governing equations for the wave-induced current model, see Chapter 5. The continuity equation has the form:

$$\frac{\partial \eta}{\partial t} + \frac{\partial}{\partial x}(dU) + \frac{\partial}{\partial y}(dV) = 0 \qquad (2.31)$$

where η is the WPA water level; t is time; x, y are the longitudinal and lateral cartesian co-ordinates, respectively; d is the mean water depth; and U, V are the depth-mean velocities in the x, y direction, respectively.

The depth-integrated WPA momentum equations are:

$$\frac{\partial U}{\partial t} + U\frac{\partial U}{\partial x} + V\frac{\partial U}{\partial y} + g\frac{\partial \eta}{\partial x} + \frac{R_{x,f}}{\rho d} - \frac{F_{b,x}}{\rho d} = 0 \qquad (5.1)$$

$$\frac{\partial V}{\partial t} + U\frac{\partial V}{\partial x} + V\frac{\partial V}{\partial y} + g\frac{\partial \eta}{\partial y} + \frac{R_{y,f}}{\rho d} - \frac{F_{b,y}}{\rho d} = 0 \qquad (5.2)$$

where $R_{x,f}$, $R_{y,f}$ are the modified driving force terms (derived from R_x, R_y) *in the* x, y *direction*, respectively; R_x, R_y are the driving force terms due to the gradient of the wave radiation stress in the x, y direction, respectively ($R_x = \partial S_{xx}/\partial x + \partial S_{xy}/\partial y$, $R_y = \partial S_{xy}/\partial x + \partial S_{yy}/\partial y$); g is the

acceleration due to gravity; ρ is the water density; and $F_{b,x}$, $F_{b,y}$ are the turbulent bed shear stresses in the x, y directions, respectively.

The radiation stress terms (S_{xx}, S_{xy}, S_{yy}) and the driving force terms (R_x, R_y) are calculated from equations (2.39)-(2.42), and the modified driving force terms ($R_{x,f}$, $R_{y,f}$) are obtained through the application of the spreading operators (explained in Section 5.4) to the driving force terms (R_x, R_y).

The bed frictional force terms ($F_{b,x}$, $F_{b,y}$) are calculated by the relationship between the depth-mean velocity and the shear stress:

$$F_{b,x}=f_{cm}U\sqrt{U^2+V^2}$$
$$F_{b,y}=f_{cm}V\sqrt{U^2+V^2} \qquad (C.1)$$

where f_{cm} is the friction coefficient modified by waves, and can be obtained from the separate sub-model taking account of wave-current interaction in the boundary layer, see Section 7.7.

The variable $\eta_{i,j}^{n}$ is defined at the centre of grid (i,j) at a time step n, where subscript i,j are the indices for the grid numbers in the x, y direction, respectively. Superscript n is the index for the time step number, see Fig. 5.8. The variables $U_{i,j}^{n}$, $R_{x,f,i,j}$ are defined at the grid border in the x direction, while $V_{i,j}^{n}$, $R_{y,f,i,j}$ are defined at the grid border in the negative y direction.

Equation (2.31) is then represented by the following finite difference equation using simple differences as:

$$\frac{\eta_{i,j}^{n+1}-\eta_{i,j}^{n}}{\Delta t}=-\frac{d_{i,j}^{n}U_{i,j}^{n}-D_{i-1,j}^{n}U_{i-1,j}^{n}}{\Delta x}-\frac{e_{i,j+1}^{n}V_{i,j+1}^{n}-e_{i,j}^{n}V_{i,j}^{n}}{\Delta y} \qquad (C.2)$$

where Δx, Δy are the spatial increments in the x, y direction, respectively; Δt is the time increment; d, e are the average depths defined by the following equations:

$$d_{i,j}=\frac{1}{2}(h_{i,j}+\eta_{i,j}+h_{i+1,j}+\eta_{i+1,j}) \qquad (C.3)$$

$$e_{i,j}=\frac{1}{2}(h_{i,j}+\eta_{i,j}+h_{i,j-1}+\eta_{i,j-1}) \qquad (C.4)$$

The two depth-averaged momentum equations are expressed in finite difference form following the approach of Flather and Heaps(1975). However, the present equations are distinguished from Flather and Heaps'(1975) equations for tidal current without waves by the radiation stress terms and the modified friction coefficient for wave and current flows.

Flather and Heaps(1975) proposed three numerical schemes with different treatments for the non-linear advection terms. The advection terms were ignored in their first scheme. For the second and third schemes, they used the angled-derivative approach of Roberts and Weiss(1966). In these cases, the advection terms are properly centred in space and time. The second scheme used

a two-step calculation procedure for the advection terms, while the third scheme used a one-step calculation process. In the present work, Flather and Heaps(1975)'s third scheme (one-step scheme) is adopted for the momentum equations due to the simple calculation procedure.

The angled-derivative scheme uses two finite difference equations for each of the momentum equations for time and space-centring. For time-centring, the newly-obtained velocity values at the (n+1) time step ($U_{i,j}^{n+1}$, $V_{i,j}^{n+1}$) are immediately used for the calculation of the velocity values at the next calculation grid point when the calculation grid point moves from one spatial point to the next. For space-centring, the calculation order of the two variables (U, V) is reversed every time step, and the calculation grid point order of each variable is reversed, too. For an odd time step, the calculation of U starts from the top row (nj) to the bottom row (1) (from the left grid (1) to the right grid (ni) in each row). And the calculation of V follows the same order. For even time steps, the calculation of V starts from the bottom row to the top (from the right grid to the left in each row), and the calculation of U is followed.

The x direction momentum equation (5.1) has the following finite difference form for odd time steps:

$$\begin{aligned}\frac{(U_{i,j}^{n+1}-U_{i,j}^{n})}{\Delta t} = & -\frac{1}{2\Delta x}\overline{U}_{i,j}^{n}(U_{i+1,j}^{n}-U_{i,j}^{n}+U_{i,j}^{n+1}-U_{i-1,j}^{n+1}) \\ & -\frac{1}{4\Delta y}((V_{i,j+1}^{n}+V_{i+1,j+1}^{n})(U_{i,j+1}^{n+1}-U_{i,j}^{n+1}) \\ & +(V_{i,j}^{n}+V_{i+1,j}^{n})(U_{i,j}^{n}-U_{i,j-1}^{n})) \\ & -\frac{f_{cm}U_{i,j}^{n+1}((U_{i,j}^{n})^{2}+(\tilde{V}_{i,j}^{n})^{2})^{0.5}}{D_{i,j}^{n}} \\ & -g\frac{\eta_{i+1,j}^{n+1}-\eta_{i,j}^{n+1}}{\Delta x}-\frac{R_{x,f,i,j}}{\rho D_{i,j}^{n}}\end{aligned} \qquad (C.5)$$

and for even time steps:

$$\begin{aligned}\frac{(U_{i,j}^{n+1}-U_{i,j}^{n})}{\Delta t} = & -\frac{1}{2\Delta x}\overline{U}_{i,j}^{n}(U_{i+1,j}^{n+1}-U_{i,j}^{n+1}+U_{i,j}^{n}-U_{i-1,j}^{n}) \\ & -\frac{1}{4\Delta y}((V_{i,j+1}^{n}+V_{i+1,j+1}^{n})(U_{i,j+1}^{n}-U_{i,j}^{n}) \\ & +(V_{i,j}^{n}+V_{i+1,j}^{n})(U_{i,j}^{n+1}-U_{i,j-1}^{n+1})) \\ & -\frac{f_{cm}U_{i,j}^{n+1}((U_{i,j}^{n})^{2}+(\tilde{V}_{i,j}^{n})^{2})^{0.5}}{D_{i,j}^{n}} \\ & -g\frac{\eta_{i+1,j}^{n+1}-\eta_{i,j}^{n+1}}{\Delta x}-\frac{R_{x,f,i,j}}{\rho D_{i,j}^{n}}\end{aligned} \qquad (C.6)$$

where

$$\begin{aligned}D_{i,j} &= \max(d_{i,j}, d_{\min}) \\ E_{i,j} &= \max(e_{i,j}, d_{\min}) \\ \tilde{U}_{i,j} &= \frac{1}{4}(U_{i-1,j}+U_{i,j}+U_{i-1,j-1}+U_{i,j-1}) \\ \tilde{V}_{i,j} &= \frac{1}{4}(V_{i,j+1}+V_{i+1,j+1}+V_{i,j}+V_{i+1,j}) \\ \overline{U}_{i,j} &= \frac{1}{4}(U_{i-1,j}+2U_{i,j}+U_{i+1,j}) \\ \overline{V}_{i,j} &= \frac{1}{4}(V_{i,j+1}+2V_{i,j}+V_{i,j-1})\end{aligned} \qquad (C.7)$$

where d_{min} is assigned as the minimum depth for the denominator in the frictional terms which

could otherwise contain a singularity at d=0 or e=0.

The y direction momentum equation (5.1) has the following finite difference form of equation for odd time step:

$$\begin{aligned}\frac{(V_{i,j}^{n+1}-V_{i,j}^{n})}{\Delta t} =& -\frac{1}{2\Delta y}\overline{V}_{i,j}^{n}(V_{i,j+1}^{n+1}-V_{i,j}^{n+1}+V_{i,j}^{n}-V_{i,j-1}^{n}) \\ & -\frac{1}{4\Delta x}((U_{i,j}^{n}+U_{i,j-1}^{n})(V_{i+1,j}^{n}-V_{i,j}^{n}) \\ & +(U_{i-1,j}^{n}+U_{i-1,j-1}^{n})(V_{i,j}^{n+1}-V_{i-1,j}^{n+1})) \\ & -\frac{f_{cm}V_{i,j}^{n+1}((\tilde{U}_{i,j}^{n})^{2}+(V_{i,j}^{n})^{2})^{0.5}}{E_{i,j}^{n}} \\ & -g\frac{\eta_{i,j}^{n+1}-\eta_{i,j+1}^{n+1}}{\Delta y}-\frac{R_{y,f,i,j}}{\rho E_{i,j}^{n}}\end{aligned} \qquad (C.8)$$

and for even time steps:

$$\begin{aligned}\frac{(V_{i,j}^{n+1}-V_{i,j}^{n})}{\Delta t} =& -\frac{1}{2\Delta y}\overline{V}_{i,j}^{n}(V_{i,j+1}^{n}-V_{i,j}^{n}+V_{i,j}^{n+1}-V_{i,j-1}^{n+1}) \\ & -\frac{1}{4\Delta x}((U_{i,j}^{n}+U_{i,j-1}^{n})(V_{i+1,j}^{n+1}-V_{i,j}^{n+1}) \\ & +(U_{i-1,j}^{n}+U_{i-1,j-1}^{n})(V_{i,j}^{n}-V_{i-1,j}^{n})) \\ & -\frac{f_{cm}V_{i,j}^{n+1}((\tilde{U}_{i,j}^{n})^{2}+(V_{i,j}^{n})^{2})^{0.5}}{E_{i,j}^{n}} \\ & -g\frac{\eta_{i,j}^{n+1}-\eta_{i,j+1}^{n+1}}{\Delta y}-\frac{R_{y,i,j}}{\rho E_{i,j}^{n}}\end{aligned} \qquad (C.9)$$

Boundary conditions

Three types of boundaries exist. Namely, an offshore open boundary, an open side boundary, and a land boundary.

Firstly, consider that the offshore open boundary faces in the x direction, see Fig. (C.1). Then, the velocity across the boundary is calculated from the finite difference form of the continuity equation (5.34) as:

$$\frac{d^n_{i,j}U^n_{i,j}-d^n_{i-1,j}U^n_{i-1,j}}{\Delta x}=-\frac{\eta^{n+1}_{i,j}-\eta^n_{i,j}}{\Delta t}-\frac{e^n_{i,j+1}V^n_{i,j+1}-e^n_{i,j}V^n_{i,j}}{\Delta y} \qquad (C.10)$$

The water elevation at the new time step should be provided in the above equation. If the set-up or set-down at the open sea boundary is negligible, zero elevation can be given at the open boundary grid points.

Secondly, at the side boundaries, a parallel boundary condition ($\partial\eta/\partial y=\partial V/\partial y=0$) (equation 5.35) is applied. The finite difference forms of the boundary condition for the side boundary facing in the y direction, see Fig. (C.2), are:

$$\begin{aligned} V^n_{i,j}&=V^n_{i,j-1}\\ \eta^n_{i,j}&=\eta^n_{i,j-1}\end{aligned} \qquad (C.11)$$

For the side boundary facing in the negative y direction, the finite difference forms are given as:

$$V^n_{i,j}=V^n_{i,j+1}$$
$$\eta^n_{i,j}=\eta^n_{i,j+1} \qquad \text{(C.12)}$$

Thirdly, at the land boundary, the simple condition of no-flux in the normal direction to the land boundary is used. Thus, any velocity U or V across the land boundary is zero, see Fig. (C.3). That is:

$$U_{i,j}=0, \quad \text{if } d_{i,j}<0 \text{ or } d_{i+1,j}<0$$
$$V_{i,j}=0, \quad \text{if } d_{i,j}<0 \text{ or } d_{i,j-1}<0 \qquad \text{(C.13)}$$

The various equations have been coded in FORTRAN 77, and calculated results were obtained using the SUN-4/690 machine at Liverpool University. The programme requires 80 KB storage for a typical 68 x 92 area with 6256 computation points. A typical run for Chukpyon Harbour requires 600 cpu seconds. Results from program were obtained in a datafile, which storage mean water elevation, x, y components of current vector at each grid point. Vector plots, see Fig. 8.7a, were obtained from the datafile using standard UNIRAS software.

APPENDIX D. EXAMPLE CALCULATION OF IWP SHIELDS PARAMETER:

TABLE 6.2

The WPA calculation of $|\Psi_{wc}|^{1.5}$ is done numerically by dividing the wave period into 16 equal time intervals. An example calculation for the first data set in Table 6.2 is given below.

No.	$\tau_{b,cm}$	$\tau_{b,w}$	$\lvert\vec{\tau}_{b,wc}\rvert/\rho$	$\lvert\Psi_{wc}\rvert$
1	0.0000	0.6990	0.6990	0.2159
2	0.0000	0.5350	0.5350	0.1653
3	0.0000	0.2895	0.2895	0.0894
4	0.0000	0.0000	0.0000	0.0000
5	0.0000	-0.2895	0.2895	0.0894
6	0.0000	-0.5350	0.5350	0.1653
7	0.0000	-0.6990	0.6990	0.2159
8	0.0000	-0.7566	0.7566	0.2337
9	0.0000	-0.6990	0.6990	0.2159
10	0.0000	-0.5350	0.5350	0.1653
11	0.0000	-0.2895	0.2895	0.0894
12	0.0000	0.0000	0.0000	0.0000
13	0.0000	0.2895	0.2895	0.0894
14	0.0000	0.5350	0.5350	0.1653
15	0.0000	0.6990	0.6990	0.2159
16	0.0000	0.7566	0.7566	0.2337

$|\Psi_{wc}|^{1.5} = 0.0627$

APPENDIX E. EXAMPLE CALCULATION OF IWP SHIELDS PARAMETER:

TABLE 6.3

The WPA calculation of $|\vec{\Psi}_{wc}|^{1.5}$ is done numerically by dividing the wave period into 16 equal time intervals. An example calculation for the first data set in Table 6.3 is given below.

No.	$\tau_{b,cm}$	$\tau_{b,w}$	$\lvert\vec{\tau}_{b,wc}\rvert/\rho$	$\lvert\vec{\Psi}_{wc}\rvert$
1	2.3553	11.1894	11.4346	3.5321
2	2.3553	8.5640	8.8820	2.7436
3	2.3553	4.6348	5.1989	1.6059
4	2.3553	0.0000	2.3553	0.7275
5	2.3553	-4.6348	5.1989	1.6059
6	2.3553	-8.5640	8.8820	2.7436
7	2.3553	-11.1894	11.4346	3.5321
8	2.3553	-12.1113	12.3382	3.8113
9	2.3553	-11.1894	11.4346	3.5321
10	2.3553	-8.5640	8.8820	2.7436
11	2.3553	-4.6348	5.1989	1.6059
12	2.3553	0.0000	2.3553	0.7275
13	2.3553	4.6348	5.1989	1.6059
14	2.3553	8.5640	8.8820	2.7436
15	2.3553	11.1894	11.4346	3.5321
16	2.3553	12.1113	12.3382	3.8113

$|\vec{\Psi}_{wc}|^{1.5}$ = 4.3121

APPENDIX F. EXAMPLE CALCULATION OF IWP SHIELDS PARAMETER:

TABLE 6.4

The WPA calculation of $|\Psi_{wc}|^{1.5}$ is done numerically by dividing the wave period into 16 equal time intervals. An example calculation for the first data set in Table 6.4 is given below.

No.	$\tau_{b,cm}$	$\tau_{b,w}$	$\lvert\vec{\tau}_{b,wc}\rvert/\rho$	$\lvert\Psi_{wc}\rvert$
1	0.9751	3.2516	3.3946	1.0486
2	0.9751	2.4887	2.6729	0.8256
3	0.9751	1.3468	1.6628	0.5136
4	0.9751	0.0000	0.9751	0.3012
5	0.9751	-1.3468	1.6628	0.5136
6	0.9751	-2.4887	2.6729	0.8256
7	0.9751	-3.2516	3.3946	1.0486
8	0.9751	-3.5195	3.6521	1.1281
9	0.9751	-3.2516	3.3946	1.0486
10	0.9751	-2.4887	2.6729	0.8256
11	0.9751	-1.3468	1.6628	0.5136
12	0.9751	0.0000	0.9751	0.3012
13	0.9751	1.3468	1.6628	0.5136
14	0.9751	2.4887	2.6729	0.8256
15	0.9751	3.2516	3.3946	1.0486
16	0.9751	3.5195	3.6521	1.1281

$|\Psi_{wc}|^{1.5} = 0.7184$

APPENDIX G. FINITE DIFFERENCE EQUATIONS FOR THE SEDIMENT TRANSPORT MODEL

The split governing equations (6.14), (6.9), and (6.10) are solved by finite difference methods. Thus each equation is solved sequentially using starting values obtained from the previous solution. The splitting technique, see Verboom(1975), has the advantage that advection and diffusion steps can be separated and an appropriate numerical method selected for each separate step.

Vertical diffusion and advection step is:

$$\frac{\partial c}{\partial t} = F\frac{\partial c}{\partial \eta} + G\frac{\partial^2 c}{\partial \eta^2} \qquad (6.14)$$

where c is the suspended sediment concentration, t is the time, η is the vertical coordinate ($=((z-z_b)/d))^{-A}$, z_b is the mean bed level, A is the transformation constant, and F and G are defined as:

$$\begin{aligned} F &= (w''-w_f)\frac{A}{d}\eta^{\frac{1}{A}+1} + \frac{A^2}{d^2}\eta^{\frac{1}{A}+1}H \\ G &= \frac{A^2}{d^2}\eta^{\frac{2}{A}+2}\epsilon_{sz} \\ H &= \frac{\partial}{\partial \eta}(\eta^{\frac{1}{A}+1}\epsilon_{sz}) \end{aligned} \qquad (6.15)$$

where w" is the distorted local vertical velocity (=dw') on the boundary-fitted coordinates, (w' has been defined in equation (6.7)), w_f is the sediment settling velocity, d is the water depth, and

ϵ_{sz} is the vertical sediment diffusion coefficient.

Horizontal advection step is:

$$\frac{\partial c}{\partial t}+u\frac{\partial c}{\partial x'}+v\frac{\partial c}{\partial y'}=0 \qquad (6.9)$$

and Horizontal diffusion step is:

$$\frac{\partial c}{\partial t}-\frac{\partial}{\partial x'}(\epsilon_{sx}\frac{\partial c}{\partial x'})-\frac{\partial}{\partial y'}(\epsilon_{sy}\frac{\partial c}{\partial y'})=0 \qquad (6.10)$$

G.1 First step: vertical diffusion and vertical advection

Firstly, equation (6.14) is transformed into a finite difference equation using an implicit scheme.

Three terms in equation (6.14) are discretized as follows:

$$\frac{\partial c}{\partial t}\Big|_{i,j,k}^{n+W}=\frac{1}{\Delta t}(c_{i,j,k}^{n+1}-c_{i,j,k}^{n}) \qquad (G.1)$$

$$F\frac{\partial c}{\partial \eta}\Big|_{i,j,k}^{n+W}=\frac{F}{2\Delta\eta}(W(c_{i,j,k+1}^{n+1}-c_{i,j,k1}^{n+1})+(1-W)(c_{i,j,k+1}^{n}-c_{i,j,k1}^{n})) \qquad (G.2)$$

$$G\frac{\partial^2 c}{\partial \eta^2}\Big|_{i,j,k}^{n+W}=\frac{G}{\Delta\eta^2}(W(c_{i,j,k+1}^{n+1}-2c_{i,j,k}^{n+1}+c_{i,j,k1}^{n+1}) + (1-W)(c_{i,j,k+1}^{n}-2c_{i,j,k}^{n}+c_{i,j,k1}^{n})) \qquad (6.3)$$

where each derivative term is located at a spatial grid point $i\Delta x'$, $j\Delta y'$, $k\Delta\eta$ (i,j,k are integer

values) at time level (n+W)Δt (n is an integer) in the four-directional space-time continuum. W is a weighting factor ($0.5 \leq W \leq 1$) which designates the relative importance of the old and new time step values; subscript i,j,k are the grid numbers in the x',y',η directions, respectively; and superscript n is the index for the time step number. Equation (6.14) is then expressed in the following general form for a general computational grid point:

$$\left(\frac{WF}{2\Delta\eta}-\frac{WG}{\Delta\eta^2}\right)c_{i,j,k-1}^{n+1}+\left(\frac{1}{\Delta t}+\frac{2WG}{\Delta\eta^2}\right)c_{i,j,k}^{n+1}+\left(-\frac{WF}{2\Delta\eta}-\frac{WG}{W\eta^2}\right)c_{i,j,k+1}^{n+1}$$
$$=\frac{1}{\Delta t}c_{i,j,k}^{n}+\frac{F}{2\Delta\eta}(1-W)\left(c_{i,j,k+1}^{n}-c_{i,j,k-1}^{n}\right)+\frac{G}{\Delta\eta^2}(1-W)\left(c_{i,j,k+1}^{n}-2c_{i,j,k}^{n}+c_{i,j,k-1}^{n}\right) \quad (G.3)$$

Defining L,D,U, and B as:

$$L_{i,j,k}=\left(\frac{WF}{2\Delta\eta}-\frac{WG}{\Delta\eta^2}\right)$$
$$D_{i,j,k}=\left(\frac{1}{\Delta t}+\frac{2WG}{\Delta\eta^2}\right)$$
$$U_{i,j,k}=\left(-\frac{WF}{2\Delta\eta}-\frac{WG}{\Delta\eta^2}\right)$$
$$B_{i,j,k}=\frac{1}{\Delta t}c_{i,j,k}^{n}+\frac{F}{2\Delta\eta}(1-W)\left(c_{i,j,k+1}^{n}-c_{i,j,k-1}^{n}\right)$$
$$\frac{G}{\Delta\eta^2}(1-W)\left(c_{i,j,k-1}^{n}-2c_{i,j,k}^{n}+c_{i,j,k-1}^{n}\right)$$

equation (G.4) is briefly written as follows.

$$L_{i,j,k}c_{i,j,k1}^{n+1}+D_{i,j,k}c_{i,j,k}^{n+1}+U_{i,j,k}c_{i,j,k+1}^{n+1}=B_{i,j,k}, \qquad for \;\; 2\leq k\leq nk1$$

At the water surface, the zero-flux condition, equation (6.19) is applied:

$$w_f c-\left(\frac{A}{d}\eta^{\frac{1}{A}+1}\right)\epsilon_{sz}\frac{\partial c}{\partial\eta}=0 \qquad (6.19)$$

which is written in finite difference form at time step (n+1) for the surface grid point (i,j,1) as:

$$w_f c_{i,j,1}^{n+1} - \frac{A}{d}\eta^{\frac{1}{A}+1}\epsilon_{sz}\frac{1}{\Delta\eta}\left(c_{i,j,2}^{n+1} c_{i,j,1}^{n+1}\right) = 0 \qquad (G.5)$$

Matrix elements are next defined as:

$$D_{i,j,1} = w_f + \frac{A}{d}\eta^{\frac{1}{A}+1}\epsilon_{sz}\frac{1}{\Delta\eta}$$

$$U_{i,j,1} = -\frac{A}{d}\eta^{\frac{1}{A}+1}\epsilon_{sz}\frac{1}{\Delta\eta}$$

At the sea bed, two kinds of boundary condition can be used, either suspended sediment concentration or the concentration gradient.

If the concentration condition is used, that is:

$$c_a = c_a^{\infty} \qquad (6.20)$$

at grid point i,j,nk and time level (n+1):

$$c_{i,j,nk}^{n+1} = c_a^{\infty} \qquad (G.6)$$

The general finite difference equation for general grid point (nk-1) is then modified as:

$$L_{i,j,nk-1} c_{i,j,nk-2}^{n+1} + D_{i,j,nk-1} c_{i,j,nk-1}^{n+1} = B_{i,j,nk-1}^{*}$$
$$B_{i,j,nk-1}^{*} = -U_{i,j,nk1} c_{i,j,nk}^{n+1} + B_{1,j,nk-1} \qquad (G.7)$$

where

$$B_{i,j,nk-1}=B^{*}_{i,j,nk-1}-U_{i,j,nk-1}c^{n+1}_{i,j,nk}$$

By application of the general finite difference equation to each grid point over the flow depth, including the surface and bed boundary points, a series of (nk-1) equations are obtained, which can be written in tridiagonal matrix form:

$D_{i,j,1}$	$U_{i,j,1}$						x $c_{i,j,1}$ =	$B_{i,j,1}$
$L_{i,j,2}$	$D_{i,j,2}$	$U_{i,j,2}$						$B_{i,j,2}$
	$L_{i,j,3}$	$D_{i,j,3}$	$U_{i,j,3}$					$B_{i,j,3}$
		.	.	.				.
			.	.	.			.
				.	.	.		.
					$L_{i,j,nk-1}$	$D_{i,j,nk-1}$		$B_{i,j,nk-1}$

If the gradient boundary condition is used, that is:

$$\frac{\partial c_a}{\partial \eta}=\frac{d}{A}\eta^{-\frac{1}{A}-1}\frac{w_f}{\epsilon_{sz}}c_a^{\infty} \qquad (6.22)$$

Equation (6.22) is transformed for point i,j,nk at time level (n+W) into:

$$\frac{C_{i,j,nk}^{n+1} - C_{i,j,nk-1}^{n+1}}{\Delta\eta} = \frac{d}{A}\eta^{-\frac{1}{A}-1}\frac{W_f}{\epsilon_{sz}}C_a^{\infty} \qquad (G.8)$$

The following relationship can thus be defined as:

$$\begin{aligned} L_{i,j,nk} &= \frac{1}{\Delta\eta} \\ D_{i,j,nk} &= -\frac{1}{\Delta\eta} \\ B_{i,j,nk} &= \frac{d}{A}\eta^{-\frac{1}{A}-1}\frac{W_f}{\epsilon_{sz}}C_a^{\infty} \end{aligned} \qquad (G.9)$$

The solution of the above finite difference equations over a time step, thus reduces to the solution of the following (nk) by (nk) tridiagonal matrix:

$D_{i,j,1}$	$U_{i,j,1}$						x $c_{i,j,1}$ =	$B_{i,j,1}$
$L_{i,j,2}$	$D_{i,j,2}$	$U_{i,j,2}$						$B_{i,j,2}$
	$L_{i,j,3}$	$D_{i,j,3}$	$U_{i,j,3}$					$B_{i,j,3}$
		.	.	.				.
			.	.	.			.
				.	.	.		.
					$L_{i,j,nk}$	$D_{i,j,nk}$		$B_{i,j,nk}$

G.2 Second step: Horizontal advection

The horizontal advection step is solved by a four-point interpolation characteristic method (first order characteristic method, see O'Connor(1971), and Nicholson(1983)). This approach enables an update of sediment concentration (cc) from known values (c). The straight projection line from the calculation point follows in the opposite direction of the flow. Then, the "projection point" P lies ($-u\Delta t$,$-v\Delta t$) in the x' and y' directions, respectively, from the calculation point, see Fig. G.1. The "projection square" is defined as a square which links four grid centres surrounding the projection point. The plan grid indices for the projection square are (ip,jp), (ip+1,jp), (ip+1,jp+1), and (ip,jp+1), and the ratio of the fraction of distance between the point (ip,jp) and P to the x', y' grid increments are termed r_x, r_y in the x,', y' direction, respectively, see Fig. G.1. Then the concentration at the grid centre is calculated from the following equations.

$$
\begin{aligned}
C_{upper} &= C_{ip,jp,k} + (C_{ip+1,jp,k} - C_{ip,jp,k}) \cdot r_x \\
C_{lower} &= C_{ip,jp+1,k} + (C_{ip+1,jp+1,k} - C_{ip,jp+1,k}) \cdot r_x \\
C_{left} &= C_{ip,jp,k} + (C_{ip,jp+1,k} - C_{ip,jp,k}) \cdot r_y \\
C_{right} &= C_{ip+1,jp,k} + C_{ip+1,jp+1,k} C_{ip+1,jp,k}) \cdot r_y \\
C_{up,low} &= C_{upper} + (C_{lower} C_{upper}) \cdot r_y \\
C_{l,r} &= C_{left} + (C_{right} - C_{left}) \cdot r_x \\
CC_{i,j,k} &= \frac{(C_{up,low} + C_{l,r})}{2}
\end{aligned}
\qquad \text{(G.10)}
$$

where cc is the sediment concentration after the second step, and the superscript (n+1) are omitted for all c and cc in equation (G.10) for convenience.

At the incoming flow open boundary, the projection point P lies outside the computation domain, see Fig. G.2. The sediment concentration value is given by interpolation of boundary values as defined by intersection of the projection vector with the boundary grid points.

G.3 Third step: Horizontal diffusion

Equation (6.10) is solved by an explicit scheme, and enables an update of concentration values (ccc) from known values (cc). The finite difference form for general grid point $i\Delta x$, $j\Delta y$, $k\Delta\eta$ using a forward difference for the time step and weighted forward and backward differences for the diffusion terms is:

$$\begin{aligned}
&\frac{ccc_{i,j,k}^{n+1}-ccc_{i,j,k}^{n}}{\Delta t} \\
&=\frac{1}{\Delta x'}\left(\epsilon_{sx,i+1/2,j,k}\frac{ccc_{i+1,j,k}^{n}-ccc_{i,j,k}^{n}}{\Delta x'}\right. \\
&\left.-\epsilon_{sx,i-1/2,j,k}\frac{ccc_{i,j,k}^{n}-ccc_{i-1,j,k}^{n}}{\Delta x'}\right) \\
&+\frac{1}{\Delta y'}\left(\epsilon_{sy,i,j+1/2}\frac{ccc_{i,j+1,k}^{n}-ccc_{i,j,k}^{n}}{\Delta y'}\right. \\
&\left.-\epsilon_{sy,i,j-1/2,k}\frac{ccc_{i,j,k}^{n}-ccc_{i,j-1,k}^{n}}{\Delta y'}\right)
\end{aligned} \qquad \text{(G.11)}$$

where $ccc_{i,j,k}^{n}$ is equivalent to $cc_{i,j,k}^{n+1}$.

If any grid next to the plan calculation point (i,j) is a land grid, the concentration value at the

adjacent land grid has the same concentration value as the calculation point ($\partial c/\partial n$, n is the normal direction to the land). For example, if grid (i-1,j) is a land grid ($c_{i-1,j,k}=c_{i,j,k}$), see Fig. G.3, then, equation (G.11) is reduced to:

$$\frac{ccc_{i,j,k}^{n+1}-ccc_{i,j,k}^{n}}{\Delta t} = \frac{1}{\Delta x'}\left(\epsilon_{sx}\frac{ccc_{i+1,j,k}^{n}-ccc_{i,j,k}^{n}}{\Delta x'}\right) + \frac{1}{\Delta y'}\left(\epsilon_{sy}\frac{ccc_{i,j+1,k}^{n}-ccc_{i,j,k}^{n}}{\Delta y'}-\epsilon_{sy}\frac{ccc_{i,j,k}^{n}-ccc_{i,j-1,k}^{n}}{\Delta y'}\right) \qquad (G.12)$$

For other directional land boundaries, similar modification of the finite difference equation is applied.

The finite difference equations have been coded in FORTRAN 77, and results were obtained using the SUN-4/690 machine at Liverpool University. The program requires 53 KB storage for a typical 68 x 92 x 10 area with 6256 plan computation points and 10 grid point at every plan point. A typical run for Chukpyon Harbour required 1200 cpu seconds. Results from the programme were obtained in a datafile, which storage suspended sediment concentration at each grid points, and bed level change at each plan grid point. Concentration profile plots, see Fig. 8.11, and bed level change contours, see Fig. 8.13, were obtained from the datafile using standard UNIRAS software.

APPENDIX H. FINITE DIFFERENCE EQUATION FOR THE BED LEVEL CHANGE

Bed level change is calculated from equation (3.10):

$$(1-n)\frac{\partial z_b}{\partial t}+\frac{\partial q_{tx}}{\partial x}+\frac{\partial q_{ty}}{\partial y}=0 \qquad (3.10)$$

where z_b is the mean bed level above a horizontal datum; and q_{tx}, q_{ty} are the total sediment loads along x, y axis, respectively. The sediment transports along x and y directions ($q_{tx,i,j}$, $q_{ty,i,j}$) are defined at each grid border as the water velocities, where i,j are the indices for the grid number in the x, y directions, see Fig. 6.1a. Equation (3.10) is then approximated by an explicit finite difference equation:

$$z_{b,i,j}^{n+1}=z_{b,i,j}^{n}+\frac{\Delta t}{1-n}\left(\frac{q_{tx,i,j}-q_{tx,i1,j}}{\Delta x}+\frac{q_{ty,i,j}-q_{ty,i,j-1}}{\Delta y}\right) \qquad (H.1)$$

where Δx, Δy are the grid sizes along x, y direction, respectively; Δt is the time increment; and subscript n is the time step number.

At the open boundary, bed level change is assumed to be zero ($z_{b,i,j}^{n+1}=z_{b,i,j}^{n}$).

At the side boundary, bed level change is also zero due to the parallel (lateral uniformity) condition, since the gradient of the sediment flux along the x axis is zero.

At the land boundary, the sediment flux across the land boundary is automatically zero due to the zero water flux. Therefore equation (A.1) is used without any modification.

The finite difference equation is solved in a subroutine in the 3D sediment transport model (Appendix G).

APPENDIX I. NUMERICAL CALCULATION OF VERTICAL VELOCITY

Equation (6.28) is used for calculation of the WPA vertical velocity field, that is:

$$\frac{\partial ud}{\partial x'}+\frac{\partial vd}{\partial y'}-A\eta^{\frac{1}{A}+1}\frac{\partial w'''}{\partial \eta}=0 \qquad (6.28)$$

The vertical velocity can be obtained by numerical integration in a water column (i,j), that is:

$$w''=\frac{1}{A}\eta^{-\frac{1}{A}-1}\int_{\eta}^{\eta_{bed}}\left(\frac{\partial ud}{\partial x'}+\frac{\partial vd}{\partial y'}\right)d\eta \qquad (I.1)$$

Starting from the bottom grid, w" is calculated as:

$$w''_{i,j,k}=w''_{i,j,k+1}-\frac{1}{A}\eta_k^{-\frac{1}{A}-1}\left(\frac{u_{i,j,k}\bar{d}_{i,j,k}-u_{i-1,j,k}\bar{d}_{i-1,j}}{\Delta x'}+\frac{v_{i,j,k}\hat{d}_{i,j}-v_{i,j-1,k}\hat{d}_{i,j-1}}{\Delta y'}\right)\Delta\eta \qquad (I.2)$$

for k=nk-1, nk-2, ···, 2. At the water surface (k=1), $w''_{i,j,1}=0$, $\bar{d}=(d_{i+1,j}+d_{i,j})/2$, and $\hat{d}_{i,j}=(d_{i,j+1}+d_{i,j})/2$.

The finite difference equation is solved in a subroutine in the 3D sediment transport model (Appendix G).

APPENDIX J. CONSISTENCY OF THE FINITE DIFFERENCE EQUATIONS FOR SUSPENDED SEDIMENT

The finite difference equations (G.4), (G.10), and (G.11) for the three split governing equations (6.14), (6.9),and (6.10) should be consistent to their original governing equations.

The consistency of the vertical diffusion and vertical advection equations is considered below. The governing equation for the vertical direction has the form:

$$\frac{\partial c}{\partial t} = F\frac{\partial c}{\partial \eta} + G\frac{\partial^2 c}{\partial \eta^2} \qquad (6.14)$$

Consider the time derivative first. Expanding an arbitrary function f to the time step (n+1) and (n) from m(n+W) by the Taylor theorem:

$$f^{n+1} = f^{n+W} + (1-W)\,\Delta t\frac{\partial f}{\partial t} + \frac{(1-W)^2\Delta t^2}{2!} + \cdots$$
$$f^{n} = f^{n+W} - W\Delta t\frac{\partial c}{\partial t} + \frac{W^2\Delta t^2}{2!} + \cdots \qquad (J.1)$$

Equating f to c, and subtracting the two equations in equation (J.2), we obtain:

$$\left(\frac{\partial c}{\partial t}\right)^{n+W} = \frac{c^{n+1}-c^{n}}{\Delta t} + (1-2W)\frac{\Delta t}{2!}\frac{\partial^2 c}{\partial t^2} + \cdots \cong \frac{c^{n+1}-c^{n}}{\Delta t} \qquad (J.2)$$

Equation (J.2) is first order accurate to Δt. If W=0.5 (Crank-Nicolson scheme), the accuracy imposes to second order.

Consider the righthand-side term of equation (6.14). Defining a function f as:

$$f = F\frac{\partial c}{\partial \eta} + G\frac{\partial^2 c}{\partial \eta^2} \qquad (J.3)$$

Then, the value f at time step (n+W} can be approximated by equation (J.2) as:

$$f^{n+W} = Wf^{n+1} + (1-W)f^{n} - W(1-W)\Delta t\frac{\partial^2 f}{\partial t} + \cdots \cong Wf^{n+1} + (1-W)f^{n} \qquad (J.4)$$

Equation (J.4) has first order accuracy as equation (J.2).

Consider the spatial (vertical) derivative on the righthand-side of equation (6.14). Time step index (n+W) and horizontal spatial indices (i,j) are omitted afterwards for convenience. c_{k+1}, c_{k-1} are expanded from c_k as:

$$c_{k+1} = c_k + \Delta\eta\frac{\partial c}{\partial \eta} + \frac{\Delta\eta^2}{2!}\frac{\partial^2 c}{\partial \eta^2} + \frac{\Delta\eta^3}{3!}\frac{\partial^3 c}{\partial \eta^3} + \cdots \qquad (J.5)$$

The derivative of c to η is obtained by:

$$c_{k-1} = c_k - \Delta\eta \frac{\partial c}{\partial \eta} + \frac{\Delta\eta^2}{2!} \frac{\partial^2 c}{\partial \eta^2} - \frac{\Delta\eta^3}{3!} \frac{\partial^3 c}{\partial \eta^3} + \cdots \qquad (J.6)$$

$$\frac{\partial c}{\partial \eta} = \frac{c_{k+1} - c_{k-1}}{2\Delta\eta} - \frac{\Delta\eta^2}{3!} \frac{\partial^3 c}{\partial \eta^3} + \cdots \qquad (J.7)$$

$$\frac{\partial^2 c}{\partial \eta^2} = \frac{c_{k-1} - c_k + c_{k+1}}{\Delta\eta^2} - \frac{2\Delta\eta^2}{4!} \frac{\partial^4 c}{\partial \eta^4} + \cdots \qquad (J.8)$$

Both equations (J.5) and (J.6) are second order accurate. Equations (J.4), (J.5) and (J.6) constitute the original partial differential equation (6.14) and the truncation error. As Δt and $\Delta\eta$ tend to zero so does the truncation error. Thus, the finite difference equation (G.4) is consistent with the original differential equation (6.14).

The application of the above procedure to the other two finite difference equations for the second and third steps shows that they are also consistent with their respective differential equations.

APPENDIX K. FINITE DIFFERENCE EQUATIONS FOR THE 2DV BOUNDARY LAYER MODEL

The two governing horizontal momentum equations have been given in Chapter 7, these are:

$$\frac{\partial u}{\partial t} = -u\frac{\partial u}{\partial x} - wF\frac{\partial u}{\partial \eta} + P_x + F\frac{\partial}{\partial \eta}\left(\epsilon_z F\frac{\partial u}{\partial \eta}\right) \qquad (7.14)$$

$$\frac{\partial v}{\partial t} = -u\frac{\partial v}{\partial x} - wF\frac{\partial v}{\partial \eta} + P_{c,y} + F\frac{\partial}{\partial \eta}\left(\epsilon_z F\frac{\partial v}{\partial \eta}\right) \qquad (7.15)$$

where x is the longitudinal cartesian coordinate, η is the vertical coordinated ($=(z/d)^{-A}$, A is a scale parameter which controls the relative grid size of the seabed grid and the water surface grid); d is the water depth; u, v, w are WPA velocities in the x, y, and z directions, respectively; P_x is the pressure gradient due to wave and current in the x direction ($= \partial\tilde{U}/\partial t + P_{c,x}$); $P_{c,x}$, $P_{c,y}$ are the steady pressure gradients in the x, y directions, respectively; $\tilde{U}$ is the wave horizontal orbital velocity at the top of the wave boundary layer; and ϵ_z and l are defined by:

$$\epsilon_z = l^2 F \sqrt{\left(\frac{\partial u}{\partial \eta}\right)^2 + \left(\frac{\partial v}{\partial \eta}\right)^2} \qquad (7.16)$$

$$l = \kappa d\eta^{-\frac{1}{A}} \sqrt{1-\eta^{-\frac{1}{A}}} \qquad (7.17)$$

Since the solution of equation (7.15) (7.16) involves three co-ordinates (t, x, η), the equations are solved in three-dimensions.

These equations are solved on a uniform rectangular transformed grid of dimensions Δx, $\Delta\eta$ as shown in Fig. 7.2. The horizontal and vertical grid sizes are calculated by:

$$\Delta\eta = \frac{\eta_{bed} - \eta_{surface}}{nk-1} \; ; \; \Delta x = L_{wc}/ni \qquad (K.1)$$

where ni, nk are grid numbers in the x, and η directions, respectively; and L_{wc} is the wave length relative to a fixed frame. Two horizontal velocities are defined at the same position on a square grid side, and vertical velocities are defined at another grid side, see Fig. 7.2.

The various terms in the equations (7.15) and (7.15) are thus discretized using an implicit, space-centred finite difference scheme as follows:

$$\frac{\partial u}{\partial t} = \frac{u_{i,k}^{n+1} - u_{i,k}^{n}}{\Delta t} \qquad (K.2)$$

$$
\begin{aligned}
&F\frac{\partial}{\partial\eta}\left(\epsilon_{zF}\frac{\partial u}{\partial\eta}\right)\\
&=WF_{i,k}\frac{1}{\Delta\eta}\left(\epsilon_{z,i,k+\frac{1}{2}}F_{i,k+\frac{1}{2}}\frac{u_{i,k+1}-u_{i,k}}{\Delta\eta}\right.\\
&\left.-\epsilon_{z,i,k-\frac{1}{2}}F_{i,k-\frac{1}{2}}\frac{u_{i,k}-u_{i,k-1}}{\Delta\eta}\right)^{n+1}\\
&+(1-W)\,F_{i,k}\frac{1}{\Delta\eta}\left(\epsilon_{z,i,k+\frac{1}{2}}F_{i,k+\frac{1}{2}}\frac{u_{i,k+1}-u_{i,k}}{\Delta\eta}\right.\\
&\left.-\epsilon_{z,i,k-\frac{1}{2}}F_{i,k-\frac{1}{2}}\frac{u_{i,k}-u_{i,k-1}}{\Delta\eta}\right)^{n}
\end{aligned}
\qquad (K.3)
$$

where W is a weighting factor which controls the relative importance of the variable values at the old and new time steps ($0.5 \le W \le 1.0$), subscripts i, k are the grid numbers in the x, η directions, respectively; The nonlinear advection terms are discretized by a time forward scheme as:

$$
u\frac{\partial u}{\partial x}=u_{i,k}^{n}\frac{u_{i+1,k}^{n}-u_{i-1,k}{}^{n}}{2\Delta x} \qquad (K.4)
$$

$$
wF\frac{\partial u}{\partial\eta}=\tilde{w}_{i,k}^{n}F_{i,k}\frac{u_{i,k+1}^{n}-u_{i,k-1}^{n}}{2\Delta\eta} \qquad (K.5a)
$$

where $\tilde{w}$ is the vertical velocity defined as:

$$
\tilde{w}_{i,k}=\frac{1}{4}\left(w_{i,k}+w_{i+1,k}+w_{i,k+1}+w_{i+1,k+1}\right) \qquad (K.5b)
$$

The terms in the y-directional momentum equation are discretized in a similar way.

Firstly, the x directional momentum equation (7.15) is thus transformed into the form:

$$\frac{u_{i,k}^{n+1}-u_{i,k}^{n}}{\Delta t}=\frac{\partial \tilde{U}_{i,k}}{\partial t}+P_{c,x}$$
$$-\left(u_{i,k}^{n}\frac{u_{i+1,k}-u_{i-1,k}}{2\Delta x}+\tilde{w}_{i,k}F_k\frac{u_{i,k+1}-u_{i,k-1}}{2\Delta\eta}\right)^{n}$$
$$+WF_k\frac{1}{\Delta\eta}\left(\epsilon_{z,i,k+\frac{1}{2}}F_{k+\frac{1}{2}}\frac{u_{i,k+1}-u_{i,k}}{\Delta\eta}\right.$$
$$\left.-\epsilon_{i,k-\frac{1}{2}}F_{k-\frac{1}{2}}\frac{u_{i,k}-u_{i,k-1}}{\Delta\eta}\right)^{n+1} \qquad \text{(K.6)}$$
$$(1-W)F_k\frac{1}{\Delta\eta}\left(\epsilon_{z,i,k-\frac{1}{2}}F_{k+\frac{1}{2}}\frac{u_{i,k+1}-u_{i,k}}{\Delta\eta}\right.$$
$$\left.-\epsilon_{i,k-\frac{1}{2}}F_{k-\frac{1}{2}}\frac{u_{i,k}-u_{i,k-1}}{\Delta\eta}\right)^{n}$$

$$\epsilon_{z,i,k+\frac{1}{2}}=l_{k+\frac{1}{2}}^{2}F\Big|_k\left|\frac{u_{i,k+1}-u_{i,k}}{\Delta\eta}\right| \qquad \text{(K.7)}$$

$$l_{k+\frac{1}{2}}=\kappa d\eta_{k+\frac{1}{2}}\sqrt[-\frac{1}{A}]{1-\eta_{k+\frac{1}{2}}^{-\frac{1}{A}}} \qquad \text{(K.8)}$$

$$F_k=-\frac{A}{d}\eta_{i,k}^{\frac{1}{A}+1} \qquad \text{(K.9)}$$

Equation (K.6) is then briefly expressed as:

$$L_{i,k}u_{i,k-1}^{n+1}+D_{i,k}u_{i,k}^{n+1}+U_{i,k}u_{i,k+1}^{n+1}=B_{i,k} \qquad \text{(K.10)}$$

where $(L,D,U,B)_{i,k}$ are defined as:

$$L_{i,k}=-F_k\frac{1}{\Delta\eta^2}\epsilon_{z,i,k-\frac{1}{2}}F_{k-\frac{1}{2}} \qquad \text{(K.11)}$$

$$D_{i,k}=\frac{1}{\Delta t}-F_k\frac{1}{\Delta\eta^2}\left(\epsilon_{z,i,k+\frac{1}{2}}F_{k+\frac{1}{2}}+\epsilon_{z,i,k-\frac{1}{2}}F_{k-\frac{1}{2}}\right) \qquad \text{(K.12)}$$

$$U_{i,j}=-WF_k\frac{1}{\Delta\eta^2}\epsilon_{z,i,k+\frac{1}{2}}F_{k+\frac{1}{2}} \tag{K.13}$$

$$\begin{aligned}B_{i,k}&=u^n_{i,k}+\frac{\partial\tilde{U}}{\partial t}+P_{c,x}\\&-\left(u_{i,k}\frac{u_{i+1,k}-u_{i-1,k}}{2\Delta x}-\tilde{w}_{i,k}F_k\frac{v_{i,k+1}+v_{i,k-1}}{2\Delta\eta}\right)^n\\&+(1-W)\left(F_k\frac{1}{\Delta\eta}\left(\epsilon_{z,i,k+\frac{1}{2}}F_{k+\frac{1}{2}}\frac{u_{i,k+1}-u_{i,k-1}}{\Delta\eta}\right.\right.\\&\left.\left.-\epsilon_{z,i,k-\frac{1}{2}}F_{k-\frac{1}{2}}\frac{u_{i,k}-u_{i,k-1}}{\Delta\eta}\right)^n\end{aligned} \tag{K.14}$$

At the upper and lower boundaries of the solution domain, it is necessary to include the model boundary conditions.

At the upper boundary, a zero gradient of horizontal velocities is used. Thus:

$$\frac{u_{i,1}-u_{i,2}}{\Delta\eta}=0 \tag{K.15}$$

In other words:

$$D_{i,1}=\frac{1}{\Delta\eta}\ ;\ U_{i,1}=-\frac{1}{\Delta\eta}\ ;\ B_{i,1}=0 \tag{K.16}$$

At the bed boundary, a non-slip boundary condition is applied for the horizontal velocities as:

$$u_{i,nk}=0 \tag{K.17}$$

Therefore, the diagonal values at the bed grid (nk) are not needed. The finite difference equations for all vertical grid (k) for the calculation column (i) over a time step construct a (nk-

1) by (nk-1) tridiagonal matrix.

$D_{i,1}$	$U_{i,1}$						x $u_{i,1}$ =	$B_{i,1}$
$L_{i,2}$	$D_{i,2}$	$U_{i,2}$						$B_{i,2}$
	$L_{i,3}$	$D_{i,3}$	$U_{i,3}$					$B_{i,3}$
		.	.	.				.
			.	.	.			.
				.	.	.		.
					$L_{i,nk-1}$	$D_{i,nk-1}$		$B_{i,nk-1}$

Tridiagonal matrix is solved by the Thomas algorithm, see Lapidus and Pinder(1982). The calculation of the horizontal velocities repeats for all columns ($2 \leq i \leq ni+1$).

Secondly, the y directional velocities (v) are calculated in a similar way for all columns ($2 \leq i \leq ni+1$), solving the following finite difference equation:

$$
\begin{aligned}
&\frac{v_{i,k}^{n+1}-v_{i,k}^{n}}{\Delta t}=P_{c,y}\\
&-\left(u_{i,k}\frac{v_{i,k+1}-v_{i,k-1}}{2\Delta x}-\tilde{w}_{i,k}F_k\frac{v_{i,k+1}-v_{i,k-1}}{2\Delta\eta}\right)^n\\
&+WF_k\frac{1}{\Delta\eta}\left(E_{i,k+\frac{1}{2}}F_{k+\frac{1}{2}}\frac{v_{i,k+1}-v_{i,k}}{\Delta\eta}\right.\\
&\left.-E_{i,k-\frac{1}{2}}F_{k-\frac{1}{2}}\frac{v_{i,k}-v_{i,k-1}}{\Delta\eta}\right)^{n+1}\\
&+(1-W)F_k\frac{1}{\Delta\eta}\left(E_{i,k+\frac{1}{2}}F_{k+\frac{1}{2}}\frac{v_{i,k+1}-v_{i,k}}{\Delta\eta}\right.\\
&\left.-E_{i,k-\frac{1}{2}}F_{k-\frac{1}{2}}\frac{v_{i,k}-v_{i,k-1}}{\Delta\eta}\right)^{n}
\end{aligned}
\qquad (K.18)
$$

with the top boundary condition as:

$$
\frac{v_{i,1}-v_{i,2}}{\Delta\eta}=0 \qquad (K.19)
$$

and the bed boundary condition as:

$$
v_{i,nk}=0 \qquad (K.20)
$$

Once the horizontal velocities are solved, the side boundary condition is applied, see Fig. K.1, that is:

$$
\begin{aligned}
u_{1,k}&=u_{ni+1,k}\ ;\ u_{ni+2,k}=u_{2,k}\\
v_{1,k}&=v_{ni+1,k}\ ;\ v_{ni+2,k}=v_{2,k}
\end{aligned}
\qquad (K.21)
$$

This enables the calculation of vertical velocities at all columns.

Thirdly, vertical velocities are calculated from the continuity equation (7.20), that is:

$$\frac{\partial u}{\partial x}+F\frac{\partial w}{\partial \eta}=0 \qquad (7.20)$$

The vertical velocity (w) can be obtained from a numerical integration starting from the seabed level where w=0, that is:

$$w_{i,k}=w_{i,k+1}-\Delta\eta F_k\frac{u_{i,k}-u_{i-1,k}}{\Delta x} \qquad (K.22)$$

APPENDIX L. EXAMPLE CALCULATION OF BED SHEAR STRESS, EDDY VISCOSITY, AND HORIZONTAL VELOCITIES

Variable	Value	Remarks
d (m)	5.0	Δ_r=10 cm
z_0 (cm)	1.0	
H (m)	2.0	
T (s)	7.0	
$\lvert\vec{U}\rvert$ (m/s)	1.0	
θ_c (°)	45	

d=depth; z_0=Nikuradse roughness/30; H=wave height; T=wave period; $\lvert\vec{U}\rvert$ =depth-mean current velocity; θ_c=WPA current direction; Δ_r=ripple height; θ_w=wave direction (=0).

Basic values are calculated from the given information.

$f_c = (0.4/\ln(d/z_0)-1)^2 = 0.005884$

$\lvert\vec{\tau}\rvert / \rho = f_c \lvert\vec{U}\rvert^2 = 0.005884$

From the dispersion relation,

$L = 45.6552$

$k = 0.1376$

$U_\infty = 1.2069$

$A = 1.3446$

Wave friction factor is obtained from equation (3.37):

$f_w = 0.000684 \exp(7.80\ (A/z_0)^{-0.106}) = 0.07078$

$\tau_{b,w}/\rho = f_w/2\ U_\infty^2 = 0.05155$

The non-dimensional groups (A/z_0) and $(\ |\vec{\tau}_{b,c}|\ /\tau_{b,w})$ are:

$A/z_0 = 134.46$

$|\vec{\tau}_{b,c}|\ /\tau_{b,w} = 0.1141$

1. Calculation of the bed shear stress

C_4 values for a $|\vec{\tau}_{b,c}|\ /\tau_{b,w}$ of 0.1141 are obtained from the values for $|\vec{\tau}_{b,c}|\ /\tau_{b,w}$ of 0.0625

and 0.125, for $(A/z_0=100,500)$, for $(\theta_c=0,90,180)$, see Figs. 7.33, 7.34.

$C_4 = 2.1285$ for $A/z_0=100$, $\theta_c=0$

$C_4 = 1.5723$ for $A/z_0=100$, $\theta_c=90$

$C_4 = 1.7635$ for $A/z_0=100$, $\theta_c=180$

$C_4 = 2.9264$ for $A/z_0=500$, $\theta_c=0$

$C_4 = 1.7741$ for $A/z_0=500$, $\theta_c=90$

$C_4 = 1.9156$ for $A/z_0=500$, $\theta_c=180$

C_4 values for A/z_0 of 134.46 are obtained by interpolation:

$C_4 = 2.1972$ for $\theta_c=0$

C_4 = 1.5897 for θ_c=90

C_4 = 1.7766 for θ_c=180

C_4 for θ_c of 45 ° is calculated from equation (7.35):

C_4 = 1/2 ((2.1972+1.7766)/2+1.5897)-(1.7766-2.1972)/2 · cos 45°

+ 1/2 ((2.1972+1.7766)/2-1.5897)cos 90°

= 1.937

Bed shear stress is calculated as:

$$\frac{|\vec{\tau}_{b,cm}|}{\rho} = C_4 \frac{|\vec{\tau}_{b,c}|}{\rho} = 0.01140\ (m^2/s^2)$$

$$\tau_{b,c,x} = |\vec{\tau}_{b,c}| \cos\theta_{wc}$$
$$\tau_{b,c,y} = |\vec{\tau}_{b,c}| \sin\theta_{wc}$$

2. Calculation of the vertical viscosity profile

Coefficient C_5, C_5, and C_6 for an (A/z_0) of 134.46 are obtained by an interpolation as:

C_5 = 0.2555

C_6 = 0.009000

C_7 = -1.4517

Firstly, eddy viscosity in the lower layer is calculated. C_8 is calculated from Figs. 7.33, 7.34 in a similar way to C_4.

C_8 = 1.507

The eddy viscosity profile in the lower layer is then obtained by the following equation as:

$$\epsilon_{z,low} = Az_0/T\ C_8C_5\ z/z_0\ \exp(C_6(z/z_0\ )^{C_7}\ )$$

$$= (1.3446 \cdot 0.01/7.0)\ 1.507 \cdot 0.2555\ (z/0.01)$$

$$\cdot \exp(-0.009(z/0.01)^{1.4517})$$

Secondly, the eddy viscosity in the upper layer is calculated from the interpolated coefficient C_9 in a similar way to C_4.

$C_9 = 1.830$

$$dP_c = C_9\ \frac{|\vec{\tau}_{b,c}|}{\rho} = 1.830 \cdot 0.005884 = 0.01077$$

The eddy viscosity in the upper layer is given by:

$$\epsilon_{z,up} = \kappa\ (dP_c)^{0.5}\ z(1-z/d)$$

$$= 0.4 \cdot 0.01077^{0.5}\ z(1-z/5.0)$$

At every vertical grid point, the final eddy viscosity is obtained by:

$$\epsilon_z = \max(\epsilon_{z,low},\ \epsilon_{z,up})$$

3. Calculation of the vertical velocity profile

For the lower layer, C_{10} is obtained by an interpolation as:

$C_{10} = 0.4556$

The velocity profile in the lower layer is then:

$$|\vec{u}_{low}| = \frac{1}{\kappa}\left(C_{10}\frac{|\vec{\tau}_{b,c}|}{\rho}\right)^{0.5}\ln\left(\frac{z}{z_0}\right)$$
$$= \frac{1}{0.4}\left(0.4556 \cdot 0.005884\right)^{0.5}\ln\left(\frac{z}{0.01}\right)$$

For the upper layer, C_{11} is obtained by an interpolation as:

$C_{11} = 2.451$

The velocity profile in the upper layer is then:

$$|\vec{u}_{up}| = |\vec{U}|\frac{\ln(z/ez_a)}{\ln(d/ez_a)}$$
$$= 1.0\frac{\ln(z/e \cdot 0.02451)}{\ln(d/e \cdot 0.02451)}$$

At every vertical grid point, the final horizontal velocity is obtained by:

$$|\vec{u}| = \max\left(|\vec{u}_{low}|, |\vec{u}_{up}|\right)$$

Veering of the velocity vector over the depth is ignored. Therefore, the two components of the horizontal velocity are:

$$u = |\vec{u}|\cos\theta_c \; ; \; v = |\vec{u}|\sin\theta_c$$

LIST OF REFERENCES

Abbott, M.B. 1975. Computational hydraulics: Elements of the theory of free surface flows. Fearon-Pitman, Belmont, California, USA.

Abbott, M.B. et al. 1978. On the numerical modelling of short waves in shallow water. J. Hydr. Res. Vol. 16, pp. 173-204.

Abramovitz, M. and Stegun, I.A. 1965. Handbook of mathematical functions. Dover Publications.

Ackers, P. and White, W.R. 1973. Sediment transport: New approach on analysis. J. of the Hydraulics Division, ASCE, No. HY11.

Amos, C.L., Powen, A.J., Huntley, D.A. and Lewis, C.F.M. 1988. Ripple generation under the combined influences of waves and currents of the Canadian Shelf. Continental Shelf Research, Vol. 8, No. 10, pp. 1129-1153.

Arcilla, A.S. and Lemos, C.M. 1990. Surf zone hydrodynamics. Edita Centro Internacional de Metodos Numericos en Ingenieria, Barcelona.

Armanini, A. and Ruol, P. 1988. Non-uniform suspended sediments under waves. ICCE, ASCE, pp. 1129-1139.

Asaeda, T., Nakai, M., Manandhar, S.K. and Tamai, N. 1989. Sediment entrainment in channel with rippled bed. J. Hyrdaulic Engineering, ASCE, Vol. 115, No. 3, pp. 327-339.

Bakker, W.T. 1974. Sand concentration in an oscillatory flow. ICCE, ASCE, pp. 1129-1148.

Bakker, W.T. and van Doorn, Th. 1978. Near-bottom velocities in waves with a current. ICCE, ASCE, pp. 1394-1413.

Bakker, W.T., van Kesteren, W.G.M. and Yu, Z.H. 1988. Grain-grain interaction in oscillatory sheetflow. ICCE, ASCE, pp. 718-731.

Barber, N.F. 1969. Water waves. Wykeham Publications (London) Ltd.

Barber, P.C. 1981. A further investigation into the causes of beach erosion at King's Parade on the North Wirral Coast. Ph. D. thesis, University of Liverpool, U.K.

Basco, D.R. 1982. Surf zone currents. Vol. I. State of knowledge. CERC Miscellaneous Report No. 82-7(I).

Basco, D.R. and Coleman, R.A. 1982. Surf zone currents. Vol. II. Annotated bibliography. CERC Miscellaneous Report No. 82-7(II).

Basco, D.R. 1983. Surfzone currents. Coastal Engineering, Vol. 7, pp. 331-355.

Battjes, J.A. and Janssen, J.P.F.M. 1978. Energy loss and set-up due to breaking of random waves. ICCE, ASCE,pp. 569-587.

Battjes, J.A. 1983. Surf zone turbulence. Proc. Seminar on Hydrodynamics of waves in coastal areas, IAHR, Moscow, pp. 139-140.

Battjes, J.A., Sobey, R.J. and Stive, M.J.F. 1990. 13. Nearshore circulation. The Sea: Ocean Engineering Science, Vol. 9.

Berkhoff, J.C.W. 1972. Computation of combined refraction-diffraction. ICCE, ASCE, pp. 471-490.

Berkhoff, J.C.W. 1976. Mathematical models for simple harmonic linear water waves: wave diffraction and refraction. DHL publication no. 163.

Berkhoff, J.C.W., Booy, N. and Radder, A.C. 1982. Verification of numerical wave propagation models for simple harmonic linear water waves. Coastal Engineering, Vol. 6, pp. 255-279.

Bettes, et al. 1978. Longshore currents due to surf zone barrier. ICCE, ASCE, pp. 776-790.

Bijker, E.W. 1967. Some considerations about scales for coastal models with movable bed. DHL Publication No. 50.

Bijker, E.W. 1971. Longshore transport computations. J. of the Waterway, Harbors, and Coastal Engineering Division, ASCE, Vol. 97, No. WW4.

Bijker, E.W. and Pieters, T. 1974. Mass transport in gravity waves on a sloping bottom. ICCE, ASCE, pp. 447-465.

Birkemeier, W.A. and Dalrymple, R.A. 1975. Nearshore water circulation induced by wind and waves. Proc. Modeling Tech.,ASCE, pp. 1062-1081.

Birkemeier, W.A. and Dalrymple, R.A. 1976. Numerical models for the prediction of wave set-up and nearshore circulation, Ocean Engineering Report No. 3, University of

Delaware, Newark, Delaware, USA.

Blondeaux, P. and Vittori, G. 1990. Oscillatory flow and sediment motion over a rippled bed. ICCE, ASCE, pp. 2186-2199.

Booij, N. 1981. Gravity waves on water with non-uniform depth and current. Rep. 81-1, Dept. Civil Engrg, Delft Univ. of Tech.

Bosman, J.J. 1982. Concentration measurements under oscillatory motion. DH Report M 1695, Part II.

Boussinesq, J. 1872. Theorie des ondes et de remous qui se propagent le long d'un canal rectangulaire horizontale, en communiquant au liquid contenue dans le canal des vitesses sensiblement pareilles de la surface au fond. J. Math. Pures Appliquees, Ser. 2.17, pp. 55-108.

Bowen, A.J. 1967. Rip currents. Ph.D. Thesis, University of California, Sandiego, California, USA.

Bowen, A.J. 1969. The generation of longshore currents on a plane beach. J. of Marine Research, Vol. 27, No. 2, pp. 206-215.

Broker, I. and Fredsoe, J. 1983. 3. Velocity measurements in oscillatory flow along a ripple-surface. Inst. Hydrodyn. and Hydraulic Engrg., Tech. Univ. Denmark. Prog. Rep. 59, pp. 23-32.

Brown, C.B. 1950. Sediment transportation. In "Engineering Hydraulics", Rouse, H.(Ed.),John Wiley and Sons, Inc., New York, USA.

Cacoutas, A. 1982. A microcomputer model for shoreline evolution. M. Sc. Thesis, University of Manchester.

Chapalain, G. and Boczar-Karakiewicz, B. 1992. Modeling of hydrodynamics and sedimentary processes related to unbroken progressive shallow water waves. Journal of Coastal Research, Vol. 8, No. 2, pp.419-441.

Chesher, T.J. and Miles, G.V. 1992. The concept of a single representitive wave for used in numerical models of long term sediment transport predictions. Proc. of the International Conference on Hydraulics and Environmental Modelling of Coastal, Estuarine, and River Waters, Vol. 1. Ashgate.

Chow, V.T. 1959. Open-channel hydraulics. McGraw-Hill.

Coffey and Nielsen, P. 1986. The influence of waves on current profile. ICCE, ASCE.

Copeland, G.J.M. 1985. A practical alternative to the "mild-slope" wave equation. Coastal Engineering, Vol. 9, pp. 125-149.

Craik, A.D.D. 1982. The drift velocity of water waves. JFM, Vol. 116, pp. 187-205.

Dalrymple, R.A. 1976. Wave-induced mass transport in water waves. J. of the Waterways, Harbours and Coastal Engineering Division, ASCE, Vol. 102, No. WW2, pp. 255-264.

Dalrymple, R.A., Eubanks, R.A. and Birkemeier, W.A. 1977. Wave-induced circulation in shallow basins. J. of the Waterway, Port, Coastal, and Ocean Engineering, ASCE, Vol. 103, No. WW1, pp. 117-135.

Dalrymple, R.A. and Kirby, J.T. 1988. Models for very wide-anlge water waves and wave diffraction. JFM, Vol. 192, pp. 33-50.

Davies, A.G., Soulsby, R.L., and King, H.L. 1988. A numerical model of the combined wave and current bottom boundary layer. JGR, Vol. 93, No. C1, pp. 491-508.

Davies, A.G. 1990. Modelling the vertical distribution of suspended sediment in combined wave-current flow. Proc. of the Fifth Int. Conf. on the Physics of Estuaries and Coastal Seas, Gregyrog, Univ. of Wales.

Davies, A.G. 1991. Transient effects in wave-current boundary layer flow. Ocean Engineering, Vol. 18, No. 1/2, pp. 75-100.

Davies, A.G. and Li, Z. 1991. Intercomparison of wave-current interaction models: effect of unsteadiness in the eddy viscosity prescription. Abstract-in-depth, Mid-term Workshop, MAST.

Davies, A.M. 1991. On the accuracy of finite difference and modal methods for computing tidal and wind wave current profiles. Int. J. for Numerical Methods in Fluids, Vol. 12, pp. 101-124.

Davies, A.M. and Jones, J.E. 1991. On the numerical solution of the turbulent energy equations for wave and tidal flows. Int. J. for Numerical Methods in Fluids, Vol. 12, pp. 17-41.

de Vriend, H.J. 1987. 2DH mathematical modelling of morphological evolution in shallow water. Coastal Engineering, Vol.11, pp. 1-27.

de Vriend, H.J. and Stive, M.J.F. 1987. Quasi-3D modelling of nearshore currents. Coastal Engineering, Vol. 11, pp. 5665-601.

Deigaard, R., Fredsoe, J. and Hedegaard, I.B. 1986a. Suspended sediment in the surf zone. J. of the Waterway, Port, Coastal, and Ocean Engineering, ASCE, Vol. 112, No.1, pp. 115-128.

Deigaard, R., Fredsoe, J. and Hedegaard, I.B. 1986b. Mathematical model for littoral drift. J. of the Waterway, Port, Coastal, and Ocean Engineering, ASCE, Vol. 112, No. 3, pp. 351-369.

Dobbins, W.E. 1944. Effect of turbulence on sedimentation. Transactions, ASCE, Vol. 109, pp. 629-656.

Door, B.D. 1977. On mass transport velocity due to progressive waves. Q. Jl. Mech. Appl. Math., Vol. XXX, Pt.2, pp. 157-173.

Door, B.D. 1982. On the second approximation to mass transport in the bottom boundary layer. Coastal Engineering, Vol. 6, pp. 93-120.

Du Toit, C.G. and Sleath, J.F.A. 1981. Velocity measurements close to rippled beds in oscillatory flow. JFM. Vol. 112, pp. 71-96.

Ebersole, B.A. and Dalrymple, R.A. 1979. A numerical model for nearshore circulation including convective accelerations and lateral mixing. Technical Report No. 4, Ocean Engineering Report No. 21, Department of Civil Engineering, University of Delaware, Newark, Delaware, USA.

Ebersole, B.A. and Dalrymple, R.A. 1980. Numerical modelling of nearshore circulation. ICCE, ASCE, pp. 2710-2725.

Ebersole, B.A., Cialone, M.A., and Prater, M.D. 1986. Regional coastal processes numerical modeling system. Report 1. RCPWAVE- A linear wave propagation model for engineering use. CERC, Department of the Army, US Army Corps of Engineers.

Einstein, H.A. 1950. The bed-load function for sediment transportation in open channel flows. United States Department of Agriculture, Technical Bulletin No. 1026.

Engelund, F. and Hansen, E. 1967. A monograph on sediment transport in alluvial streams. Nordic Hydrology, Vol. 7.

Fischer, H.B., List, E.J., Koh, R.C.Y., Imberger, J. and Brooks, N.H. 1979. Inland and Coastal Waters. Academic Press.

Flather, R.A. and Heaps, N.S. 1975. Tidal computations for Morecambe Bay. Geophys. J. R. Astro. Soc. 42.

Fredsoe, J. 1984. Turbulent boundary layer in wave-current motion. J. of Hydraulic Engineering, ASCE, Vol. 110, No. 8, pp. 1103-1120.

Fredsoe, J., Andersen, O.H. and Silberg, S. 1985. Distribution of suspended sediment in large waves. J. of the Waterway, Port, Coastal and Ocean Engineering, ASCE, Vol. 111, No.6, pp. 1041-1059.

Gilvert, G. and Abernethy, C.L. 1975. Refraction of wave spectra. Internal Report 117, Hydraulics Research Station, Wallingford, U.K.

Grant, W.D. and Madsen, O.S. 1976. Quantitative description of sediment transport by waves. ICCE, ASCE, pp. 1093-1112.

Grant, W.D. and Madsen, O.S. 1979. Combined wave and current interaction with a rough bottom. JGR, Vol. 84(C4), pp. 1797-1808.

Grant, W.D. and Madsen, O.S. 1982. Movable bed roughness in unsteady oscillatory flow. JGR, Vol. 87, No. C1, pp. 469-481.

Gravens, M.B. Kraus, N.C. and Hansen, H. 1991. GENESIS: Generalized model for simulating shoreline change. CERC Technical Report, CERC-89-19 Report 2.

Green, M.O. and Vincent, C.E. 1990. Wave entrainment of sand from a rippled bed. ICCE, ASCE, pp. 2200-2212.

Hansen, E.A., Fredsoe, J. and Deigaard, R. 1991. Distribution of suspended sediment over wave generated ripples. International Symposium on the Transport of Suspended Sediments and its Mathematical Modelling, Florence(Italy), pp. 111-128.

Hedegaard, I.B. 1985. Wave generated ripples and resulting sediment transport in waves. Institute of Hydrodynamics and Hydraulic Engineering, Tech. Univ. Denmark, Series Paper No. 36.

Hjelmfelt, A.T. and Lenau, C.W. 1970. Nonequilibrium transport of suspended sediment. J. of the Hydraulics Division, ASCE, Vol. 96, No. HY7, pp. 1567-1586.

Homma and Horikawa, K. 1962. Suspended sediment due to wave action. ICCE, ASCE.

Horikawa, K. 1978. Nearshore currents. In "Coastal engineering: An introduction to ocean engineering", John Wiley and Sons, Inc., New York, USA, pp. 185-230.

Horikawa, K. 1986. State of the art- prediction of beach evolution. Proc. 5th Congress, APD-IAHR, Seoul, pp. 15-77.

Horikawa, K. and Ikeda, S. 1990. Characteristics of oscillatory flow over ripple models. ICCE, ASCE, pp. 661-674.

Huynh-Thanh, S. and Temperville, A. 1990. A numerical model of the rough turbulent boundary layer in combined wave and current interaction. ICCE, ASCE, pp. 853-866.

Hwung, H.H. and Lin, C. 1990. The mass transport of waves propagating on a sloping bottom. ICCE, ASCE.

Ifuku, M. and Kakinuma, T. 1988. Suspended sediment concentration in the surf zone. ICCE, ASCE, pp. 1661-1675.

Irie, I. and Nadaoka, K. 1984. Laboratory reproduction of seabed scour in front of breakwaters. ICCE, ASCE, pp. 1715-1747.

Isaacson, M.De St Q. 1976. Mass transport in the bottom boundary layer of cnoidal waves. JFM, Vol. 74, part 3, pp. 401-413.

Isaacson, M.De St Q. 1978. Mass transport in shallow water waves. J. Waterway, Port, Coastal and Ocean Division, ASCE, Vol. 104, No. WW2, pp. 215-225.

Iskandarani, M. and Liu, P. 1991a. Mass transport in two-dimensional water waves. JFM, Vol. 231, pp. 395-415.

Iskandarani, M. and Liu, P. 1991b. Mass transport in three-dimensional water waves. JFM, Vol. 231, pp. 417-437.

Ito, Y. and Tanimoto, K. 1972. A method of numerical analysis of wave propagation: Application to wave diffraction and refraction. ICCE, ASCE, pp. 503-522.

Jacobs, S.J. 1984. Mass transport in a turbulent boundary layer under a progressive water wave. JFM, Vol. 146, pp. 303-312.

Jansen, R.H.J. 1981. Combined scattering and attenuation of ultrasonic sound. IAHR Workshop on Particle Motion and Sediment Transport, Rapperswil, Switzerland.

Jin, J.-Y., Kim, H., Lee, K.-S. and Yum, K.-D. 1992. A sediment transport model with bed schematization. Ocean Research, Vol. 14, No. 2.

Johns, B. 1970. On the mass transport induced by oscillatory flow in a turbulent boundary layer. JFM, Vol. 43, Part 1, pp. 177-185.

Johns, B. 1975. The form of the velocity profile in a turbulent shear wave boundary layer. JGR, Vol. 80, No. 36, pp. 5109-5112.

Johns, B. 1977. Residual flow and boundary shear stress in the turbulent bottom layer beneath waves. JPO, Vol. 7, pp. 733-738.

Jonsson, I.G., Skovgaard, O. and Jacobsen, T.S. 1974. Computation of longshore currents. ICCE, ASCE. pp. 699-714.

Jonsson, I.G. 1978. Energy flux and wave action in gravity waves propagating on a current. J. Hydraulic Research. Vol. 16, No. 3.

Justesen, P., Fredsoe, J. and Deigaard, R. 1986. The bottleneck problem for turbulence in relation to suspended sediment in the surf zone. ICCE, ASCE, pp. 1225-1239.

Justesen, P. 1991. A note on turbulence calculation in the wave boundary layer. J. of Hydraulic Research, Vol.29. No.5, pp 699-711.

Kajiura, K.A. 1968. A model for bottom boundary layer in water waves. Bulletin Earthquake Research Institute, No. 45, pp. 75-123.

Kalinske, A.A. and Pien, C.L. 1943. Experiments on eddy-diffusion and suspended material transportation in open channels. Transactions, Americal Geophysical Union, Part II, pp. 530-536.

Katopodi, I. and Ribbrink, J.S. 1992. Quasi-3D modelling of suspended sediment transport by currents and waves. Coastal Engineering, Vol. 18, pp. 83-110.

Katori, S. 1982. Measurement of sediment transport by streamer trap. Nearshore Environment Research Centre, Tokyo, Japan, Report No. 16, TR-81-2, Report of the 6th cooperative field investigation (in Japanese), pp. 138-141.

Kemp, P.H. and Simons, R.R. 1982. The interaction between waves and a turbulent current: waves propagating with the current. JFM, Vol. 116, pp. 227-250.

Kemp, P.H. and Simons, R.R. 1983. The interaction of waves and a turbulent current: waves propagating against the current. JFM, Vol. 130, pp. 73-89.

Kennedy, J.F. and Locher, F.A. 1972. Sediment suspension by water waves. Waves on beaches and resulting sediment transport. Academic Press, New York.

Kinderen, W.J.G.J.der. 1982. Silt siltation meters (in Dutch). Delft Hydraulics Laboratory, Report M1799I, Delft, Netherlands.

Kirby, J.T. 1983. Propagation of weakly-nonlinear surface gravity waves in regions of varying depth and current. Research Report No. CE-83-37. Department of Civil Engineering, University of Delaware, Newark, Delaware, USA.

Kirby, J.T. 1984. A note on linear surface wave-current interaction over slowly varying topography. JGR. Vol. 89, pp. 745-747.

Kirby, J.T. 1986. Higher-order approximation in the parabolic method for water waves. JGR, Vol. 91, No. C1, pp. 933-952.

Kirby, J.T. and Dalrymple, R.A. 1986. An approximate model for nonlinear dispersion in monochromatic wave propagation models. Coastal Engineering, Vol. 9, pp. 545-561.

KORDI, 1987. A study on the numerical models of coastal hydrodynamics and sediment transport for engineering applications: NUCS. Report BSPG 00043-157-2.

KORDI, 1988. A study on the numerical models of coastal hydrodynamics and sediment transport for engineerin applications: NUCS(II). Report BSPG 00064-195-2.

KORDI, 1989. A study on the numerical models of coastal hydrodynamics and sediment transport for engineering applications: NUCS(III). Report BSPG 00088-243-2.

Kraus, N.C. and Sasaki, T.O. 1979. Influence of wave angle on the longshore currents. Marine Science Communications, Vol. 5, No. 2, pp. 91-126.

Kraus, N.C., Isobe, M., Igarashi, H., Sasaki, T., and Horikawa, K. 1982. Field experiments on longshore sand transport in the surf zone. ICCE, ASCE, pp. 969-988.

Kraus, N.C., Gingerich, K.J. and Rosati, J.D. 1989. DUCK85 surf zone sand transport experiment. CERC, Department of Army, US Army Corps of Engineers, Technical Report CERC-89-5.

Kyriacou, A. 1988. Wave height attenuation in the presence of a current. Ph.D. Thesis. The University of London.

Kosyan, R.D. 1985. Vertical distribution of suspended sediment concentrations seaward of the breaking zone. Coastal Engineering, Vol. 9, pp. 171-187.

Lapidus, L., and Pinder, G.F. 1982. Numerical solution of partial differential equations in science and engineering. John Willey & Sons.

Larsen, J. and Darcy, H. 1983. Open boundaries in short wave simulations - a new approach. Coastal Engineering, Vol. 7, pp. 285-297.

Lee-Young, J.S. and Sleath, J.F.A. 1988. Initial Motion in combined wave and current. ICCE, ASCE, pp.1140-1150.

Lee-Young, J.S. and Sleath, J.F.A. 1990. Ripple formation in combined transdirectional steady and oscillatory flow. Sedimentology, Vol. 37, pp. 509-516.

Liang, S.-C. 1983. Prediction of wave induced surf zone current adjacent to breakwaters. Ph.D. Thesis, University College of Swansea, U.K.

Liu, P.L.-F. and Mei, C.C. 1975. Effects of breakwater on nearshore currents due to breaking waves. U.S. Army, CERC, TM-57.

Liu, P.L.-F. 1983. Wave-current interactions on a slowly varying topagraphy. JGR, Vol. 88, No. C7, pp. 4421-4426.

Liu, P.L.-F. and Boissevain, P.L. 1988. Wave propagation between two breakwaters. J. of Waterway, Port, Coastal and Ocean Engineering, ASCE, Vol. 114(2), pp.237-247.

Longuet-Higgins, M.S. 1953. Mass transport in water waves. Royal Soc. Phil. Trans., Vol. 245, A.903, pp. 535-581.

Longuet-Higgins, M.S. and Stewart, R.W. 1960. Changes in the form of short gravity waves on long waves and tidal currents. JFM, Vol. 8, pp. 565-583.

Longuet-Higgins, M.S. and Stewart, R.W. 1961. The changes in amplitude of short gravity waves on steady non-uniform currents. JFM, Vol. 10, pp. 529-549.

Longuet-Higgins, M.S. and Stewart, R.W. 1962. Radiational stress and mass transport in gravity waves, with application to 'surf beats'. JFM, Vol. 13, pp. 481-504.

Longuet-Higgins, M.S. and Stewart, R.W. 1964. Radiation stress in water waves; a physical discussion, with applications. Deep-Sea Research, Vol. 11, pp. 529-562.

Longuet-Higgins, M.S. 1970a. Longshore currents generated by obliquely incident sea waves, 1. JGR, Vol. 75, No. 33, pp. 6778-6789.

Longuet-Higgins, M.S. 1970b. Longshore currents generated by obliquely incident sea waves, 2. JGR, Vol. 75, No. 33, pp. 6790-6801.

Longuet-Higgins, M.S. 1981. Oscillating flow over steep sand ripples. JFM, Vol. 107, pp. 1-35.

Lungren, H. 1972. Turbulent currents in the presence of waves. ICCE, ASCE, pp. 623-634.

Macpherson, B. 1984. Flow and sediment transport over steep sand ripples. Ph.D. Thesis, The University of Cambridge.

Madsen, O.S., Mathisen, P.P. and Rosengaus, M.M. 1990. Movable bed friction factors for spectral waves. ICCE, ASCE.

Madsen, P.A. and Warren, I.R. 1984. Performance of a numerical short wave model. Coastal Engineering, Vol. 8, pp. 73-93.

Madsen, P.A. and Larsen, J. 1987. An efficient finite-difference approach to the mild-slope equation. Coastal Engineering, Vol. 11, pp. 329-351.

Madsen, P.A. and Sorensen, O.R. 1992. A new form of the Boussinesq equations with improved linear dispersion characteristics. Part 2. A slowly-varying bathymetry. Coastal Engineering, Vol. 18, pp. 183-204.

Massel, S.R. 1989. Hydrodynamics of coastal zone, Elsevier, pp.118-155.

McCowan, J. 1894. On the highest wave of permanent type. Phil. Mag. Ser. 5, 38, pp. 351-357.

McDowell, D.M. and O'Connor, B.A. 1977. Hydraulic behaviour of estuaries. The MacMillan Press Ltd.

Mei, C.C. 1969. Nonuniform diffusion of suspended sediment. J. of Hydraulics Division, ASCE, Vol. 95, No. HY1, pp. 581-584.

Myrhaug, D. 1989. A rational approach to wave friction coefficients for rough, smooth, and transitional turbulent flow. Coastal Engineering, Vol. 13, pp. 11-21.

Myrhaug, D. and Slaattelid, O.H. 1990. A rational approach to wave-current friction coefficients for rough, smooth, and transitional turbulent flow. Coastal Engineering, Vol. 14, pp. 265-293.

Nadaoka, K. Kondoh, T. and Tanaka, N. 1982. The structure of velocity field within the surf zone revealed by means of laser-Doppler anemometry. Report of Port and Harbour Res. Inst. Vol. 21, pp. 49-106.

Nairn, R.B. 1988. Prediction of wave height and mean return flow in cross-shore sediment transport modelling. Proc. IAHR. Symposium on Mathematical Modelling of Sediment Transport in the Coastal Zone, Copenhagen, pp. 193-202.

Nap, E. and van Kampen, A. 1988. Sediment transport in irregular non-breaking waves. Coastal Eng. Dep., Delft University of Technology.

Nicholson, J.M.C. 1978. A three-dimensional finite difference model of suspended sediment transport. Master Thesis at the University of Manchester.

Nicholson, J.M.C. 1983. Three-dimensional models of particulate and cohesive suspended sediment transport. Ph.D. Thesis at the University of Manchester.

Nicholson, J. and O'Connor, B.A. 1986. Cohesive sediment transport model. J. Hydraulic Engineering, ASCE, Vol. 112, No. 7, pp. 621-640.

Nielsen, P. 1977. Turbulent mixing and shear stresses in the surf zone. Progress Report No. 42, Institute of Hydrodynamic and Hydraulic Engineering, Technical University of Denmark, Lyngby, Denmark.

Nielsen, P. 1981. Dynamics and Geometry of wave-generated ripples. JGR, Vol. 86, No. C7, pp. 6467-6472.

Nielsen, P. 1984. On the motion of suspended sand particles. JGR, Vol. 89(C1).

Nielsen, P. 1986. Suspended sediment concentrations under waves. Coastal Engineering, Vol. 10, pp. 23-31.

Nielsen, P. 1988. Towards modelling coastal sediment transport. ICCE, ASCE, pp. 1952-1958.

Nieuwjaar, M. and van der Kaaij, Th. 1987. Sediment concentrations and transport in irregular non-breaking waves. Coastal Eng. Dep., Delft University of Technology.

Nishimura, H., Maruyama, K. and Sakurai, T. 1985. On the numerical computation of nearshore currents. Coastal Engineering in Japan, Vol. 28, pp. 137-145.

Nizam. 1992. Numerical modelling of three-dimensional wave induced nearshore current. Ph.D. Thesis at the University of London.

Noda, E.K. 1972. Rip currents. ICCE, ASCE, pp. 653-668.

Noda, E.K. 1974. Wave-induced nearshore circulation. JGR, Vol. 79, No. 27, pp. 4097-4106.

O'Connor, B.A. 1971. Mathematical model of sediment distribution. Proc. Fourteenth IAHR Congress, Paris.

O'Connor, B.A. 1979. Models of fine sediment behaviour. Proc. First Int. Symp. on Cohesive Sediments, Cambridge.

O'Connor, B.A. and Tuxford, C. 1980. Modelling siltation in dock entrances. Proc. Third Int. Symp. on Dredging Tech., Bordeaux.

O'Connor, B.A. and Nicholson, J. 1988a. A three-dimensional model os suspended particulate sediment transport. Coastal Engineering, Vol. 12, pp. 157-174.

O'Connor, B.A. and Nicholson, J. 1988b. Mud transport modelling. In "Physical processes in estuaries", Dronkers, J. and van Leussen, W. (Eds.), Springer-Verlag, Berlin.

O'Connor, B.A. and Nicholson, J. 1989. Modelling changes in coastal morphology. Proc. Int. Symp. Sediment Transport Modelling, ASCE, New Orleans, USA.

O'Connor, B.A. and Yoo, D. 1988. Mean bed friction of combined wave-current flow. Coastal Engineering, Vol. 12, pp. 1-21.

O'Connor, B.A. 1991. Suspended sediment transport in the coastal zone. Int. Symp. on the Transport of Suspended Sediment and Its Mathematical Modelling, Florence, Italy.

O'Connor, B.A. 1992. Prediction of seabed sand waves. Proc. International Conference on the Computer Modelling for Seas and Coastal Regions, Southampton.

O'Connor, B.A., Harris, J., Kim, H., Wong, Y.K., Oebius, H.U., and Williams, J.J. 1992a. Bed boundary layers. ICCE, ASCE.

O'Connor, B.A., Kim, H. and Yum, K.-D. 1992b. Modelling siltation at Chukpyon Harbour, Korea. Proc. International Conference on the Computer Modelling for Seas and Coastal Regions, Southampton.

O'Connor, B.A., Harris, J. and Savell, I. 1993. Manchester boundary layer experiments. Internal Report, Civil Engineering Department, University of Liverpool (in preparation).

O'Connor, B.A., Nicholson, J., MacDonald, N. and O'Shea, K. 1992c. Application of the Watanabe cross-shore transport model to prototype-scale data. Second Int. Conf. on Hydraulic and Environmental Modelling of Coastal, Estuarine, and River Waters. Bradforf, U.K.

Ozasa, H. and Brampton, H. 1980. Mathematical modelling of beaches backed by seawalls. Coastal Engineering, Vol. 4, No. 1, pp. 47-64.

Penney, W.T. and Price, A.T. 1952. The diffraction theory of sea waves and the shelter afforded by breakwater. Phil. Trans., Roy. Soc. (London), ser. A, 244. pp.236-253.

Peregrine, D.H. 1967. Long waves on a beach. JFM, Vol. 27, pp. 715-827.

Perlin, M. and Dean, R.G. 1983. A numerical model to simulate sediment transport in the vicinity of coastal structures. US Army, CERC Misc. Report, No. 83-10.

Phillips, O.M. 1977. Dynamics of the upper ocean. Second Edition. Cambridge University Press.

Proctor, R., Flather, R.A. and Elliot, A.J. 1993. Modelling tides and surface drift in the arabian gulf - application to the gulf oil spill. Cont. Shelf Research (to appear).

Radder, A.C. 1979. On the parabolic equation method for water-wave propagation. JFM, Vol. 95, pp. 159-176.

Raudkivi, A.J. 1988. The roughness height under waves. J. Hydraulic Research, Vol. 26, No. 5, pp. 569-584.

Raudkivi, A.J. and Dette, H.H. 1991. A simplified model for calculation of suspended load outside the surf zone. Sonderdruck aus Heft 111 (1991) der Mitteilungen des Leichtweiß-Instituts für Wasserbau der Technischen Universität Braunschweig.

Ribberink, J.S. and Al-Salem, A. 1990. Bedforms, sediment concentrations and sediment transport in simulated wave conditions. ICCE, ASCE.

Richtmyer, T.D. and Morton, K.W. 1967. Difference methods for initial-value problems. Second Edition, John Wiley and Sons, New York, USA.

Roache, P.J. 1982. Computational fluid dynamics. Hermosa Publishers.

Roberts, K.V. and Weiss, N.O. 1966. Convective difference schemes. Math. Comput. Vol. 20, pp. 272-299.

Rosati, J.D., Gingerich, K.J. and Kraus, N.C. 1990. SUPERDUCK surf zone sand transport experiment. CERC, Department of the Army, US Army Corps of Engineers, Technical Report CERC-90-10.

Salkield, A.P.Le, Good, G.P., and Soulsby, R.L. 1981. Impact sensor for measuring suspended sand concentration. Conf. Electronics for Ocean Technology, Birmingham, U.K.

Sasaki, T. 1975. Simulation on shoreline and nearshore current. Proc. of the Specialty Conference on Civil Engineering in the Ocean, III, ASCE, pp. 174-196.

Sato, S. 1987. Oscillatory boundary layer flow and sand movement over ripples. Ph.D. Thesis. The University of Tokyo.

Sato, S. 1988. Sand ripple geometry and sand transport mechanism due to irregular oscillatory flows. ICCE, ASCE, pp. 1748-1762.

Southgate, H.N. 1989. Computational modelling of waves in harbours using ray methods. Ph. D. thesis, The City University, U.K.

Savell, I.A. 1986. An experimental study of near-bed hydrodymanics of waves and steady current and the effect of this on sediment transport. Ph.D. Thesis. The University of Manchester.

Sheng, Y.P., Segur, H. and Lewellen, W.S. 1978. Application of a spatial smoothing scheme to control short-wave numerical oscillations. Technical Memorandum No. 78-8, Aeronautical Research Associates of Princeton, Princeton, USA.

Sheng, Y.P. 1983. Mathematical modeling of 3-dimensional coastal currents and sediment dispersion: Model development and application. CERC, Technical Report, CERC-83-2.

Simons, R. R. and Kyriacou. 1990. Developing wave-current boundary layers. ICCE, ASCE.

Sleath, J.F.A. 1972. A second approximation to mass transport by water waves. J. of Marine Research, Vol. 30, No. 3, pp. 295-304.

Sleath, J.F.A. 1973. A numerical study of the influence of bottom roughness on mass transport. Proc. Int. Conf. Num. Methods Fluid Dyn., Southampton, pp. 482-493.

Sleath, J.F.A. 1974a. Velocities above rough bed in oscillatory flow. J. of the Waterway, Harbor, and Coastal Engineering Division, ASCE, Vol. 100., No. WW4, pp. 287-304.

Sleath, J.F.A. 1974b. Mass transport over a rough bed. Journal of Marine Research, Vol. 32, No. 1, pp. 13-24.

Sleath, J.F.A. 1982. Friction coefficients of rippled beds in oscillatory flow. Continental Shelf Research, Vol. 1, No. 1, pp. 33-47.

Sleath, J.F.A. 1984. Measurements of mass transport over a rough bed. ICCE, ASCE, pp. 1149-1160.

Sleath, J.F.A. 1984. Sea bed mechanics. John Wiley & Sons.

Sleath, J.F.A. 1987. Turbulent oscillatory flow over rough beds. JFM, Vol. 182, pp. 369-409.

Sleath, J.F.A. 1990. Bed friction and velocity distributions in combined steady and oscillatory flow. ICCE, ASCE.

Sleath, J.F.A. 1991. Velocities and shear stresses in wave-current flows. JGR, Vol. 96, No. C8, pp. 15237-15244.

Smith, G.D. 1965. Numerical solution of partial differential equations. Oxford University Press.

Smith, R. and Sprinks, T. 1975. Scattering of surface waves by a conical island. JFM, Vol. 72, part 2, pp. 373-384.

Sommerfeld, A. 1896. Mathematische theorie der diffraction. Math. Ann. 47, pp. 317-374.

Sonu, C.J. 1975. Computer prediction of nearshore and surf zone statistics: Final Report. Report TC-394, Tetra Tech, Inc. Pasadena, California, USA.

Soulsby, R.L., Davies, A.G., Fredsoe, J., Huntley, D.A., Jonsson, I.G., Myrhaug, D., Simons, R.R., Temperville, A., and Zitman, T. 1993. Intercomparison of wave-current interaction models and data (in preparation).

Southgate, H.N. 1989. Computational modelling of waves in harbours using ray methods. Ph.D. Thesis, The City University, London, U.K.

Svendsen, I.A. and Lorentz, R.S. 1989. Velocities in combined undertow and longshore currents. Coastal Engineering, Vol. 13, pp. 55-79.

Swart, D.H. 1976. Coastal sediment transport: Computation of longshore transport. DL Report, R 968-I.

Takhar, H.S. and Thomas, T.G. 1991. Turbulent mass transport and attenuation in Stokes waves. Internal Report, Department of Civil Engineering, University of Manchester, U.K.

Tanaka, H. and Shuto, N. 1981. Friction coefficient for a wave-current coexisting system. Coastal Engineering in Japan, Vol. 24, pp. 105-128.

Tanaka, H., Chang, S.C. and Shuto, N. 1983. Experiments on an oscillatory flow accompanied with a unidirectional flow. Coastal Engineering in Japan, Vol. 26, pp. 19-37.

Tanaka, H. and Shuto, N. 1984. Friction laws and flow regimes under wave and current motion. J. Hydraulic Research, Vol. 22, No. 4, pp. 245-261.

Tanaka, H. 1989. Bottom boundary layer under nonlinear wave motion. J. Waterway, Port, Coastal, and Ocean Engineering, ASCE, Vol. 115, No. 1, pp. 40-56.

Taplin, M.G. 1989. Hydrodynamics of wave/current flows. M. Sc. thesis, University of Manchester.

Thomas, G.P. 1981. Wave-current interactions: an experimental and numerical study. Part 1. Linear waves. JFM, Vol. 110, pp. 457-474.

Thomas, G.P. 1990. Wave-current interactions: an experimental and numerical study. Part 2. Nonlinear waves. JFM, Vol. 216, pp. 505-536.

Thornton, E.B. 1970. Variation of longshore current across the surf zone. ICCE, ASCE, pp. 291-308.

Trowbridge, J. and Madsen, O.S. 1984a. Turbulent wave boundary layers. 1. Model formulation and first-order solution. JGR, Vol. 89, No. C5, pp. 7989-7997.

Trowbridge, J. and Madsen, O.S. 1984b. Turbulent wave boundary layers. 2. Second-order theory and mass transport. JGR, Vol. 89, No. C5, pp. 7999-8007.

Trowbridge, J.H., Kanetkar, C.N. and Wu, N.T. 1986. Numerical simulation of turbulent wave boundary layers. ICCE, ASCE, pp. 1623-1637.

U.S. Army, CERC. 1975. Shore Protection Manual.

van der Stel, J.A. and Visser, P.J. 1985. Model investigation of the effect of perpendicular waves on the longshore current (in Dutch). Coastal Eng. Dep., Civil Eng., Technical University of Delft.

van der Valden, E. 1986. Sand suspension in an oscillating flow near the bed. Delft University of Technology, Coastal Engineering Department, Delft, The Netherlands.

van Doorn, Th. and Godefroy, H.W.H.E. 1978. Experimental investigation of the bottom boundary layer under periodic progressive water waves. DHL Report M 1362.

van Doorn, Th. 1981. Experimental investigation of near-bottom velocities in water waves without and with a current. DHL Report M 1423.

van Kesteren, W.C.M. and Bakker, W.T. 1984. Near bottom velocities in waves with a current; analytical and numerical computations. ICCE, ASCE, pp. 1161-1177.

van Rijn, L.C. 1982. Equivalent roughness of alluvial bed. J. of the Hydraulics Division, ASCE, Vol. 108, No. HY10, pp. 1215-1218.

van Rijn, L.C. 1984. Sediment transport, Part I: Bed load transport. J. of Hydraulic Engineering, ASCE, Vol. 110, No. 10.

van Rijn, L.C. 1985. Two-dimensional vertical mathematical model for suspended sediment transport by currents and waves. DHL Report S 488, Part IV.

van Rijn, L.C. 1987. Data Base: Sand concentration profiles for currents and/or waves. Report M1695-04-1, Delft Hydraulics, Delft, The Netherlands.

van Rijn, L.C., and Meijer, K. 1988. Three-dimensional mathematical modelling of suspended sediment transport in currents and waves. Proc. IAHR Symp. on Math. Mod. of Sed. Transp. in the Coastal Zone, Copenhagen, pp. 89-99.

van Rijn, L.C. 1989. Handbook sediment transport by currents and waves. DH, Rep. H461.

van Rijn, L.C. 1990. The state of the art in sediment transport modelling. Int. Conf. on Sediment Transport Modelling. pp. 13-32.

van Rijn, L.C. and Meijer, K. 1991. Three-dimensional modeling of sand and mud transport in currents and waves. Int. Sym. on the Transport of suspended sediments and its mathematical modelling, Florence(Italy), pp. 683-708.

van Rijn, L.C. and Kroon, A. 1992. Sediment transport by currents and waves. ICCE, ASCE.

Vemulakonda, S.R., Scheffner, N.W., Earickson, J.A. and Chou, L.W. 1988. Kings Bay coastal processes numerical model. US Army, CERC, Technical Report, CERC-88-3.

Verboom, G.K. 1975. The advection-dispersion equation for an an-isotropic medium solved by fractional-step method. Proc. Int. Conf. on Math. Models for Environmental Problems, Southampton, U.K. (ed. Brebbia, C.A.).

Vongvisessomjai, S. 1984. Oscillatory ripple geometry. J. of Hydraulic Engineering, ASCE, Vol. 110, No. 3, pp.247-266.

Vreugdenhil, C.B. 1980. A method of computation for unsteady wave-driven coastal currents. Report No. 1174, Part I, Delft Hydraulics Laboratory, Delft, The Netherlands.

Watanabe, A., Riho, Y. and Horikawa, K. 1980. Beach profiles and on-offshore sediment transport. ICCE, ASCE, pp. 1106-1121.

Watanabe, A. and Maruyama, K. 1986. Numerical modeling of nearshore wave field under combined refraction and diffraction and breaking. Coastal Engineering in Japan, Vol. 29, pp. 19-39.

Watanabe, A., Maruyama, K., Shimizu, T. and Sakakiyama, T. 1986. Numerical prediction model of three-dimensional beach deformation around a structure. Coastal Engineering in Japan, Vol. 29, pp. 179-194.

Wiegel, R.L. 1964. Oceanographic Engineering. Prentice-Hall.

Wind, H.G. and Vreugdenhil, C.B. 1986. Rip-current generation near structures. JFM, Vol. 171, pp. 459-477.

Wong, Y.K. 1985. A numerical model for the interaction of combined wave and current boundary layers. M.Sc. Thesis, University of Manchester.

Yoo, D. 1986. Mathematical modelling of wave-current interacted flow. Ph.D. Thesis at the University of Manchester.

Yoo, D. and O'Connor, B.A. 1986a. Mathematical modelling of wave-induced nearshore circulation. ICCE, ASCE, pp. 1667-1682.

Yoo, D. and O'Connor, B.A. 1986b. Ray model for caustic gravity waves. Proc. Fifth Congress of Asian and Pacific Regional Division of IAHR, Seoul, Korea, pp. 1-13.

Yoo, D., O'Connor, B.A. and Hedges, T.S. 1988. Numerical modelling of waves in an estuary. Proc. Sixth Congress of Asian and Pacific Regional Division of IAHR, Kyoto, Japan, pp. 65-72.

Yoo, D., O'Connor, B.A. and McDowell, D.M. 1989. Mathematical models of wave climate for port design. Proc. Inst. of Civil Engineers, Part I, Vol. 86, pp. 513-530.

Yoon, S.B. and Lui, P.L.-F. 1986. Wave-and current interactions in shallow water. ICCE, ASCE, pp. 1682-1697.

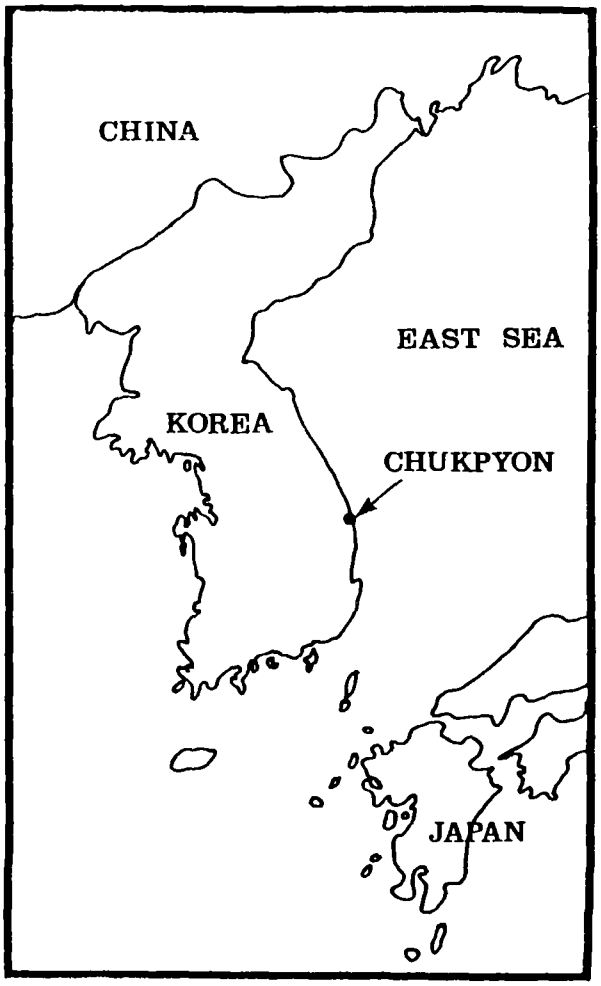

Fig. 1.1 Location of Chukpyon Harbour and Coast.

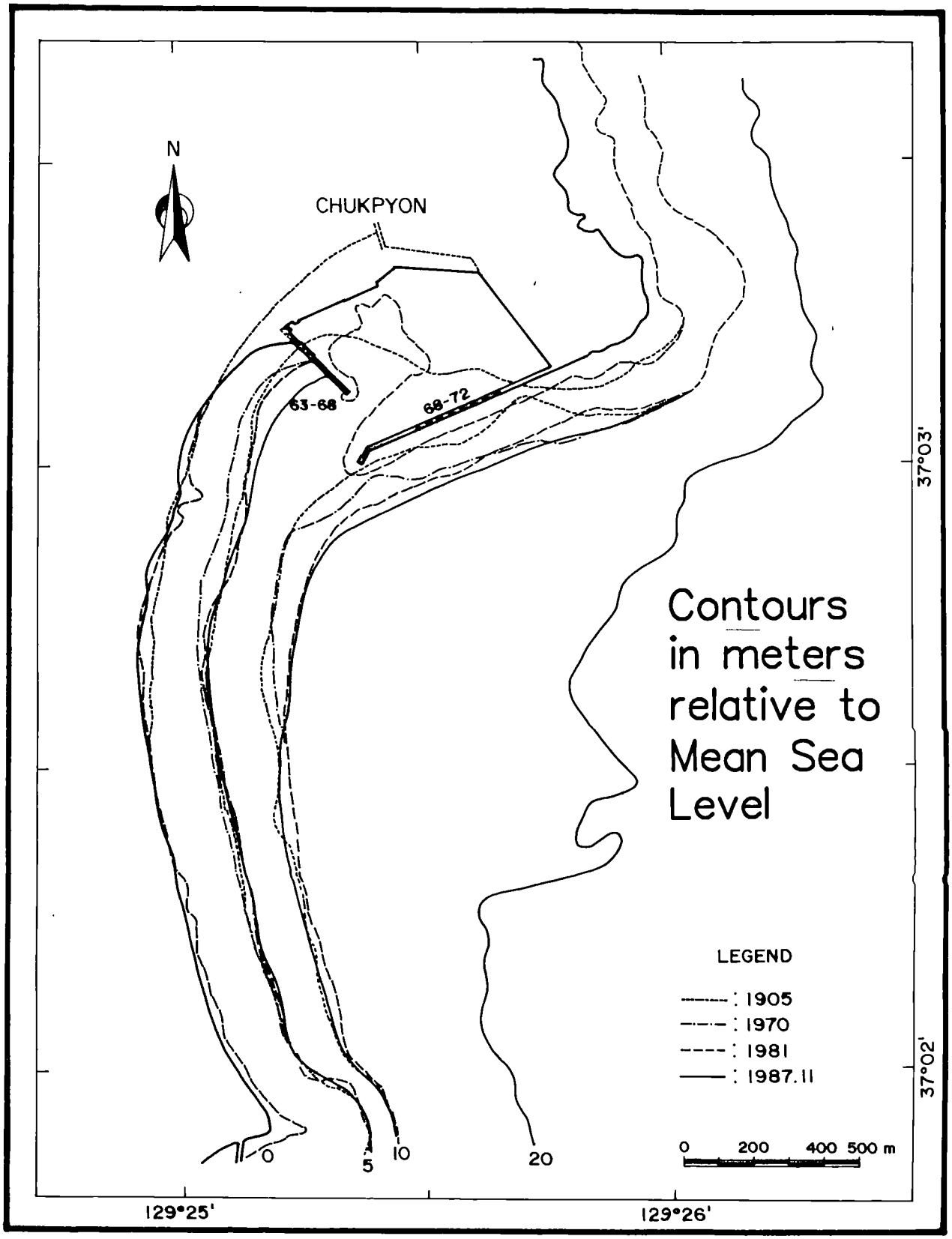

Fig. 1.2 History of depth change around Chukpyon Harbour.

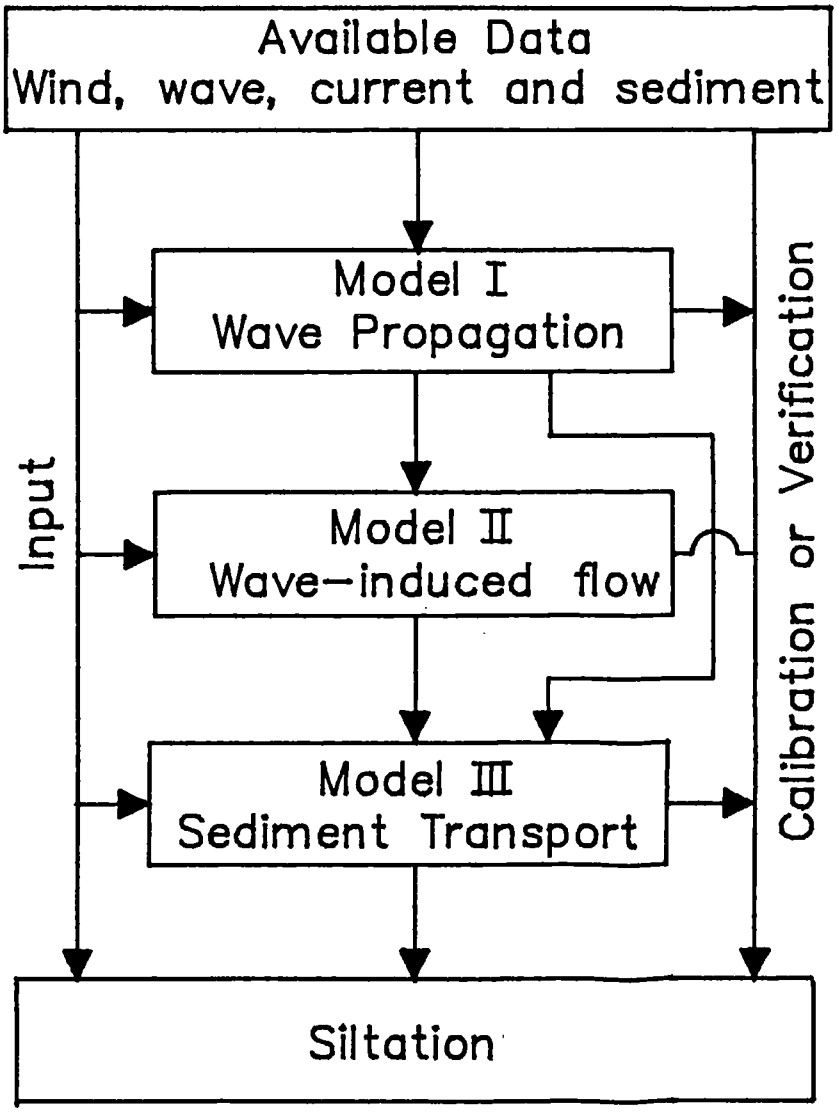

Fig. 1.3 Schematic diagram of the numerical model system.

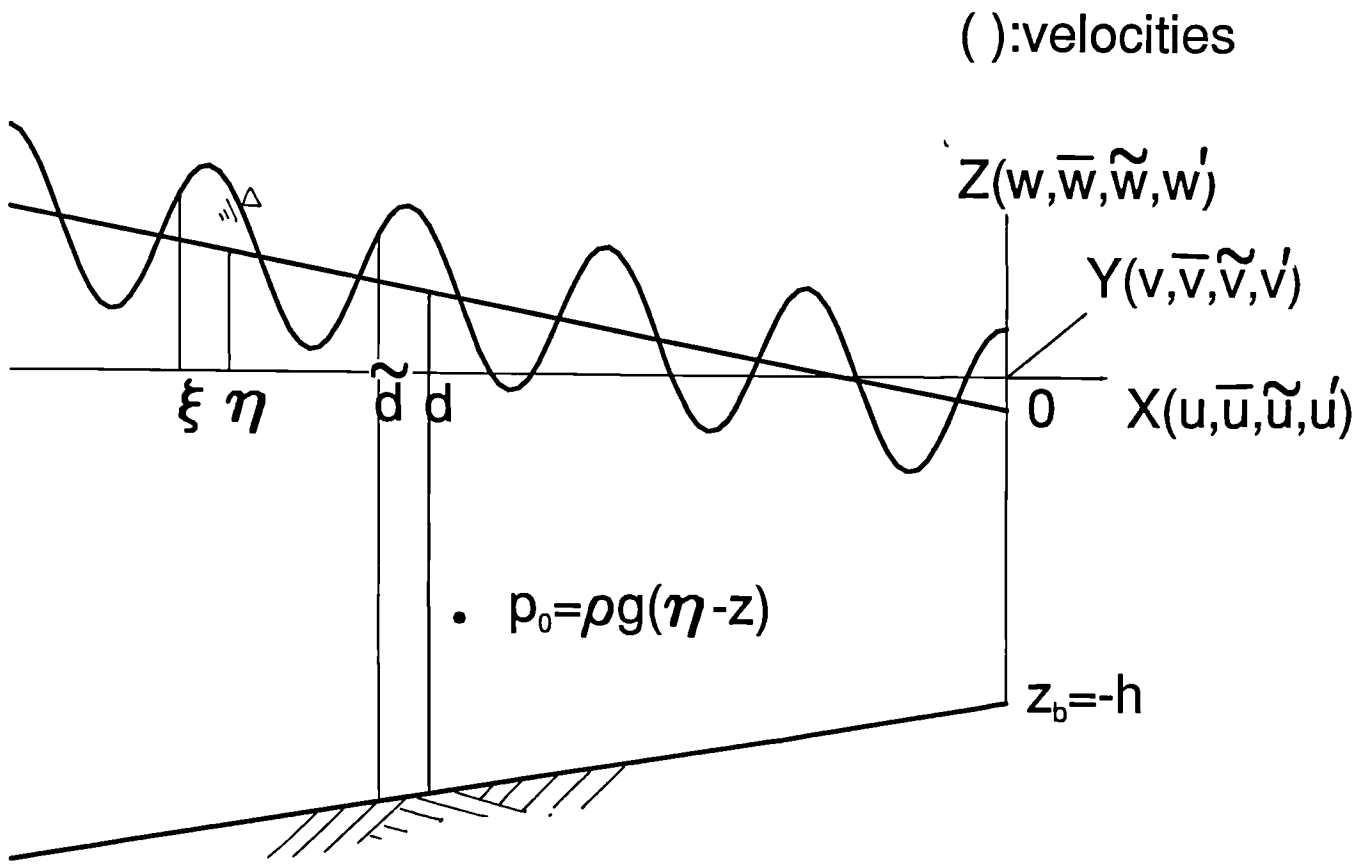

Fig. 2.1 Definition of the water depth and the water elevations.

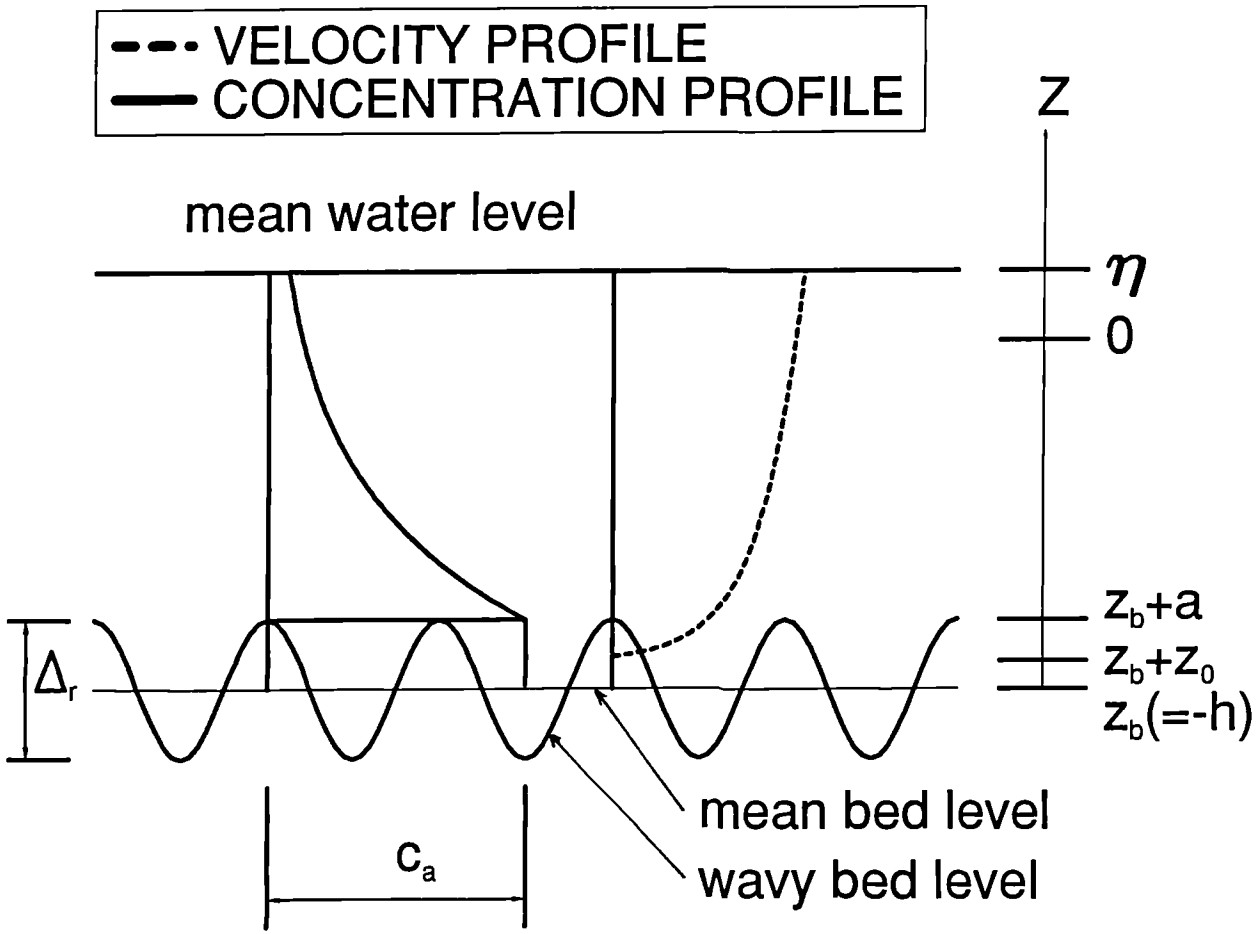

Fig. 3.1 Definition of the reference level.

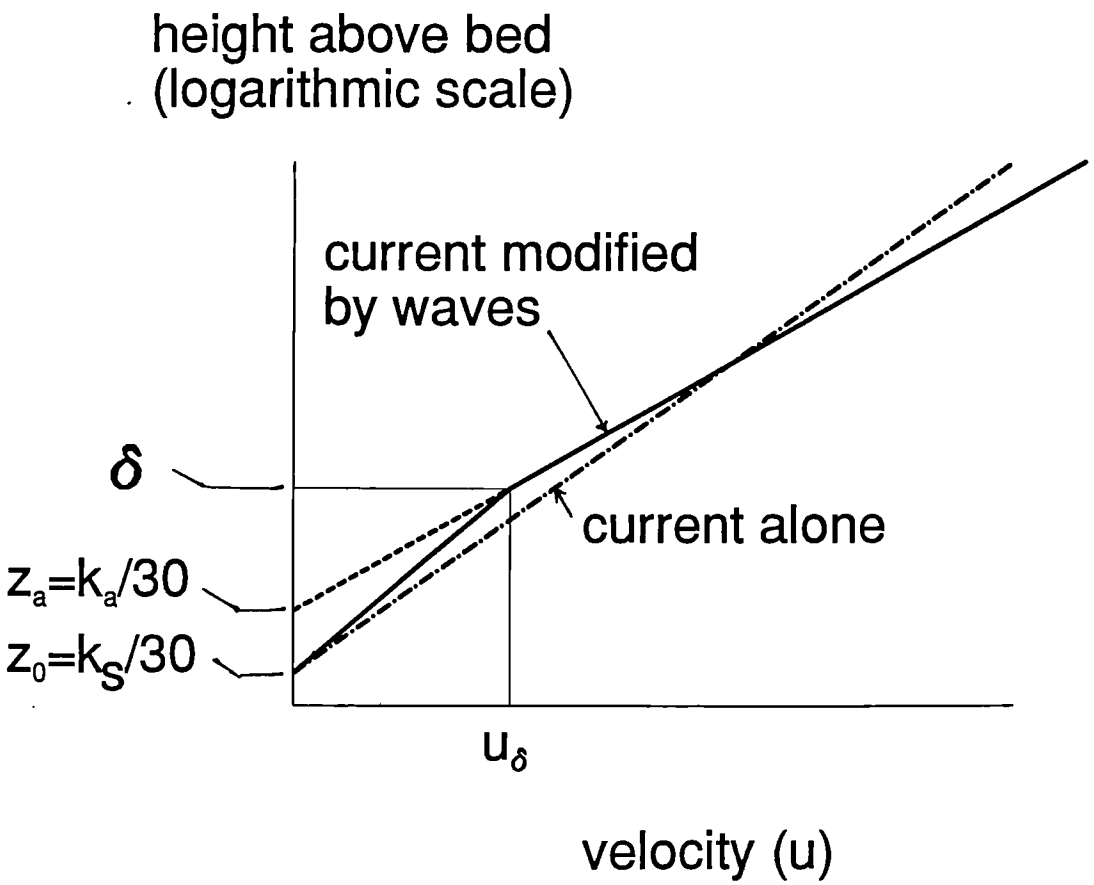

Fig. 3.2 Definition of the bed roughnesses.

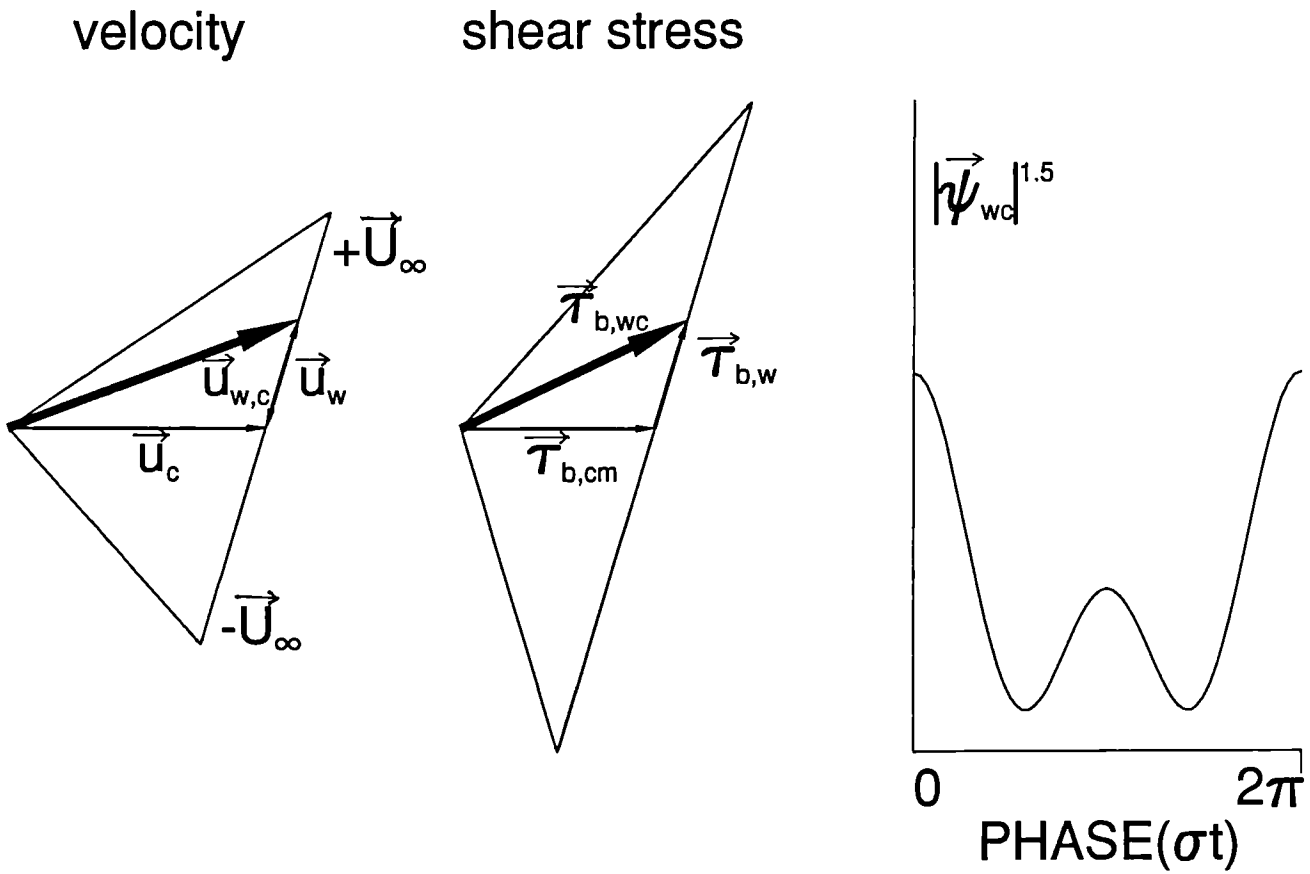

Fig. 3.3 Inter-wave-period variation of near bed velocity, bed shear stress, and the Shields parameter.

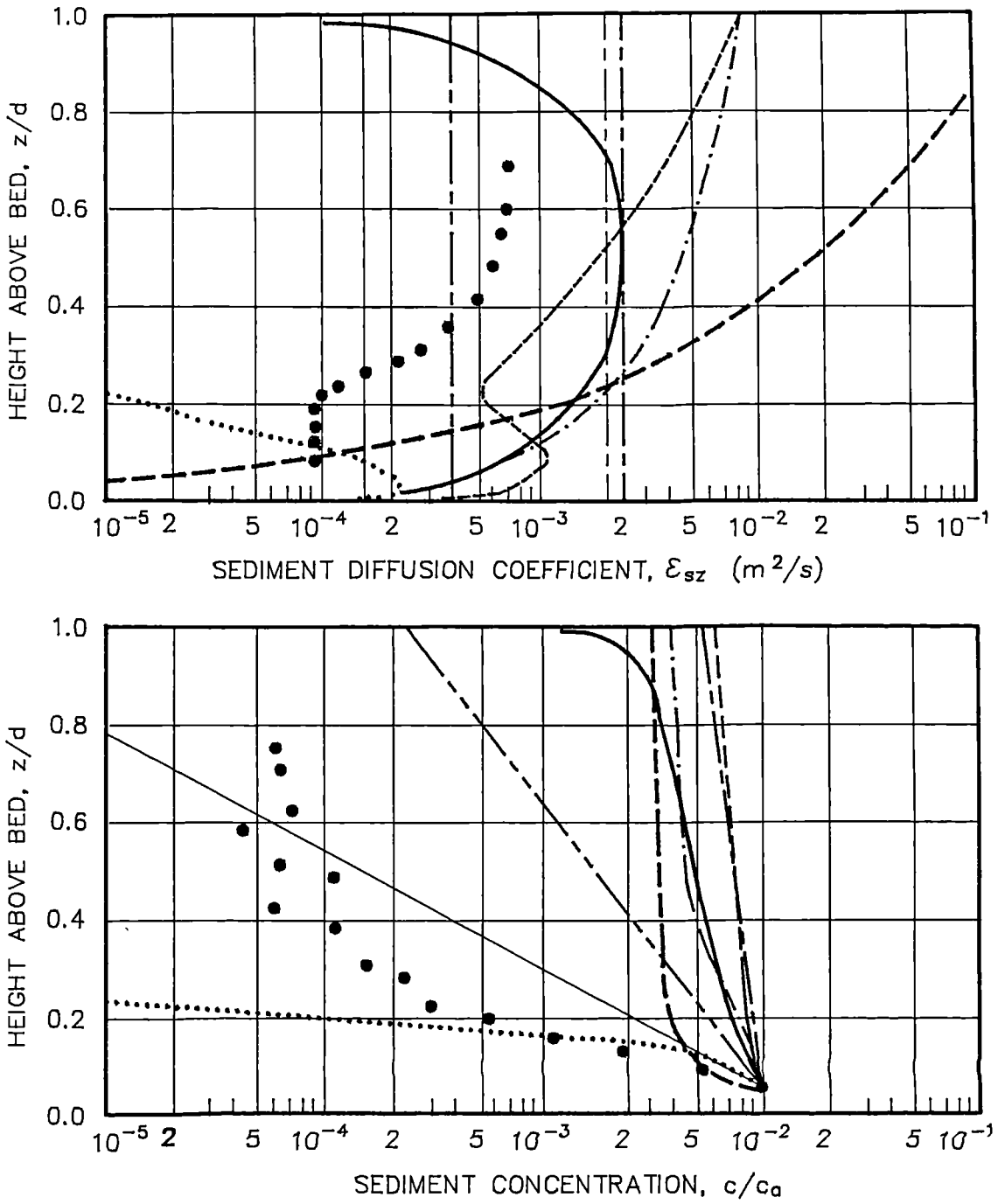

●	measured
– – – – –	Homma and Horikawa, 1962
———	Bijker, 1967
·····	Lundgren, 1972
– – – – –	Swart, 1976
———	Nielsen, 1979
– – ———	Dally, 1980
——– – –	Skafel and Krishnappan, 1984
–·—·—·—	Kos'yan, 1985

d	= 0.3	m
H	= 0.12	m
T	= 1.9	s
d_{50}	= 105	μm
w_p	= 0.005	m/s
$\rho_s c_a$	= 9500	mg/l

Fig. 3.4 Vertical diffusion coefficient profiles (after van Rijn, 1989).

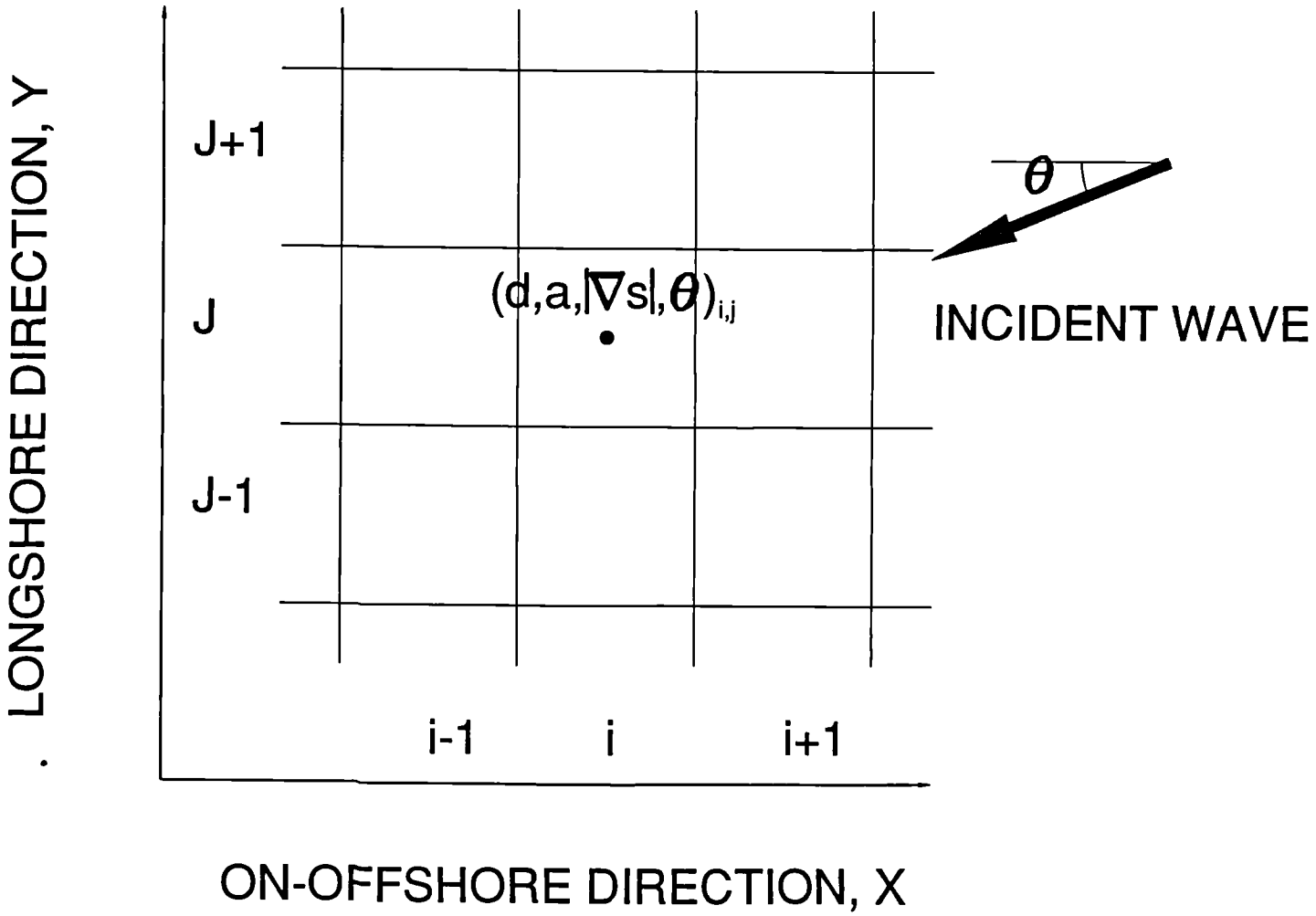

Fig. 4.1 Wave propagation model grid.

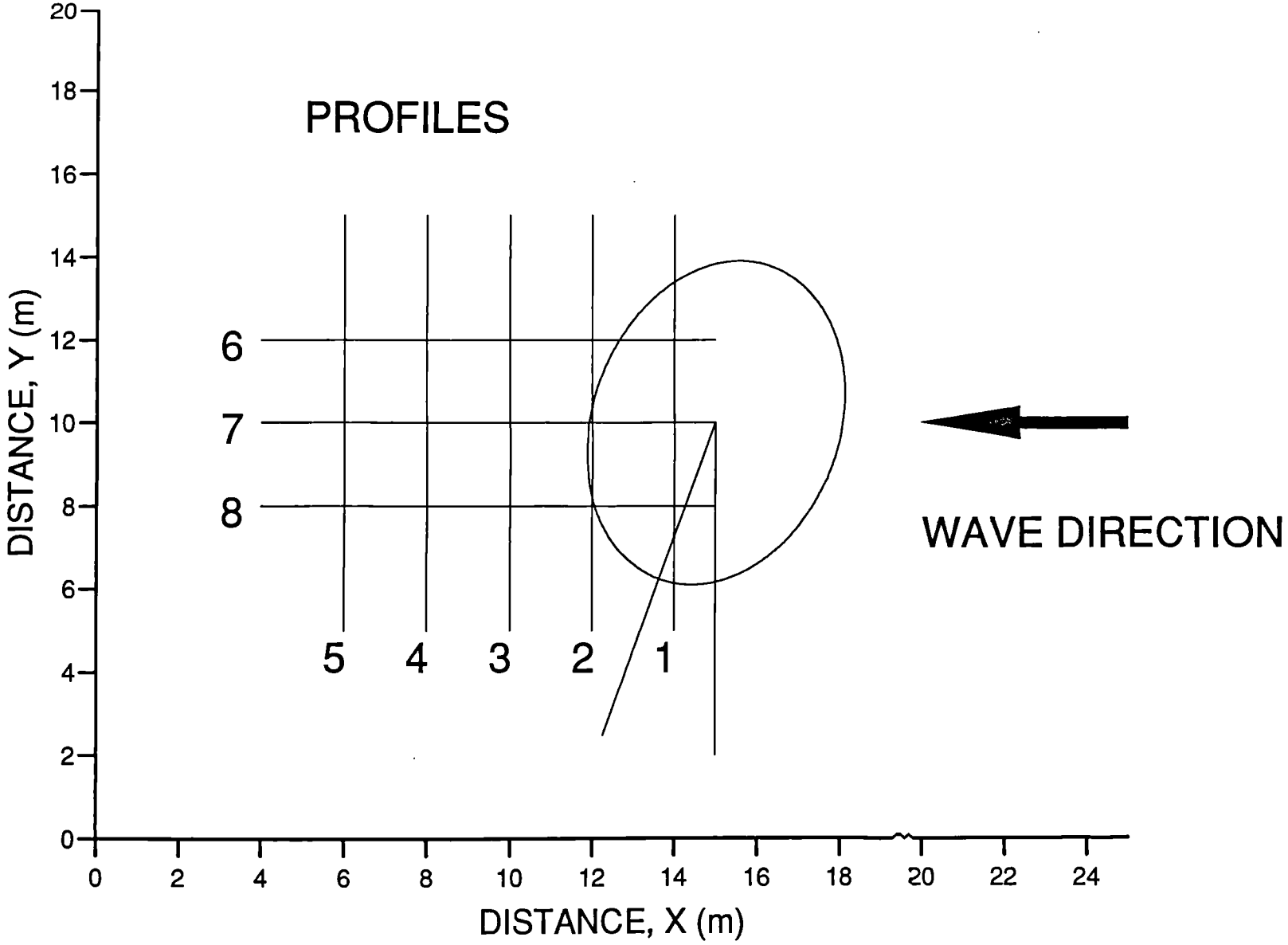

Fig. 4.2 Plan of the elliptic shoal test.

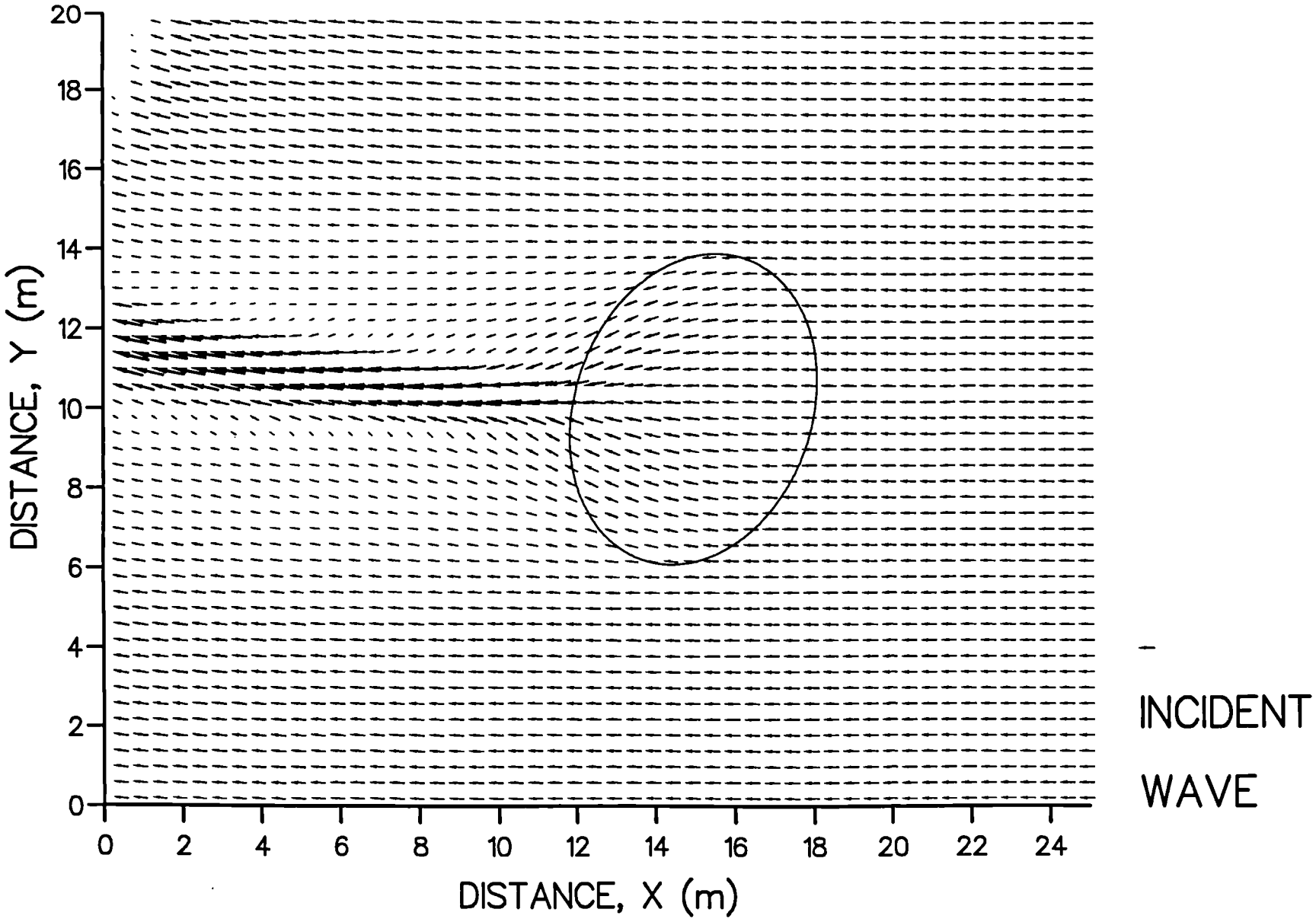

Fig. 4.3 Calculated wave height and direction vectors of the elliptic shoal test.

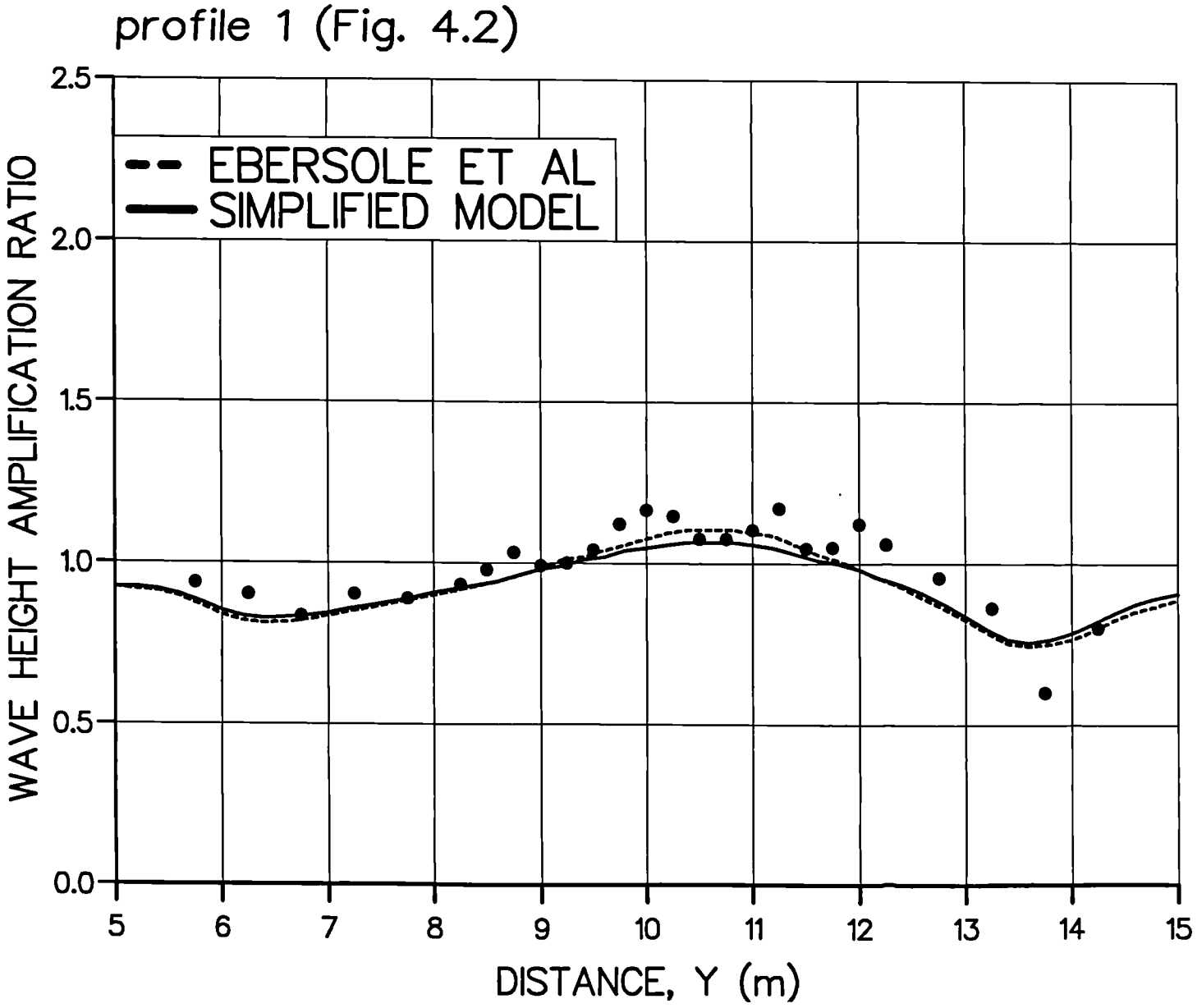

Fig. 4.4a Calculated and measured wave height profiles for elliptic shoal test: profiles 1.

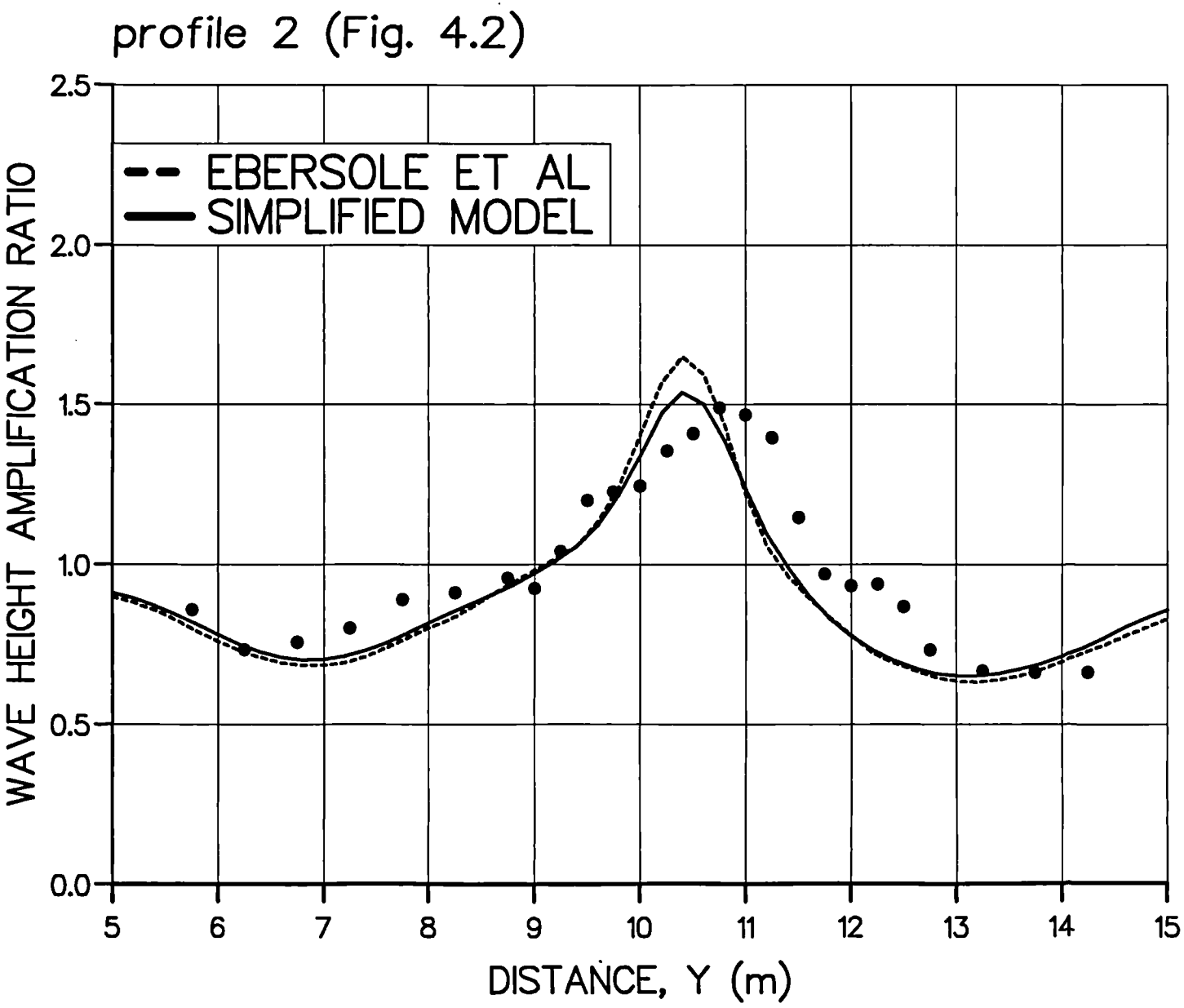

Fig. 4.4b Calculated and measured wave height profiles for elliptic shoal test: profiles 2.

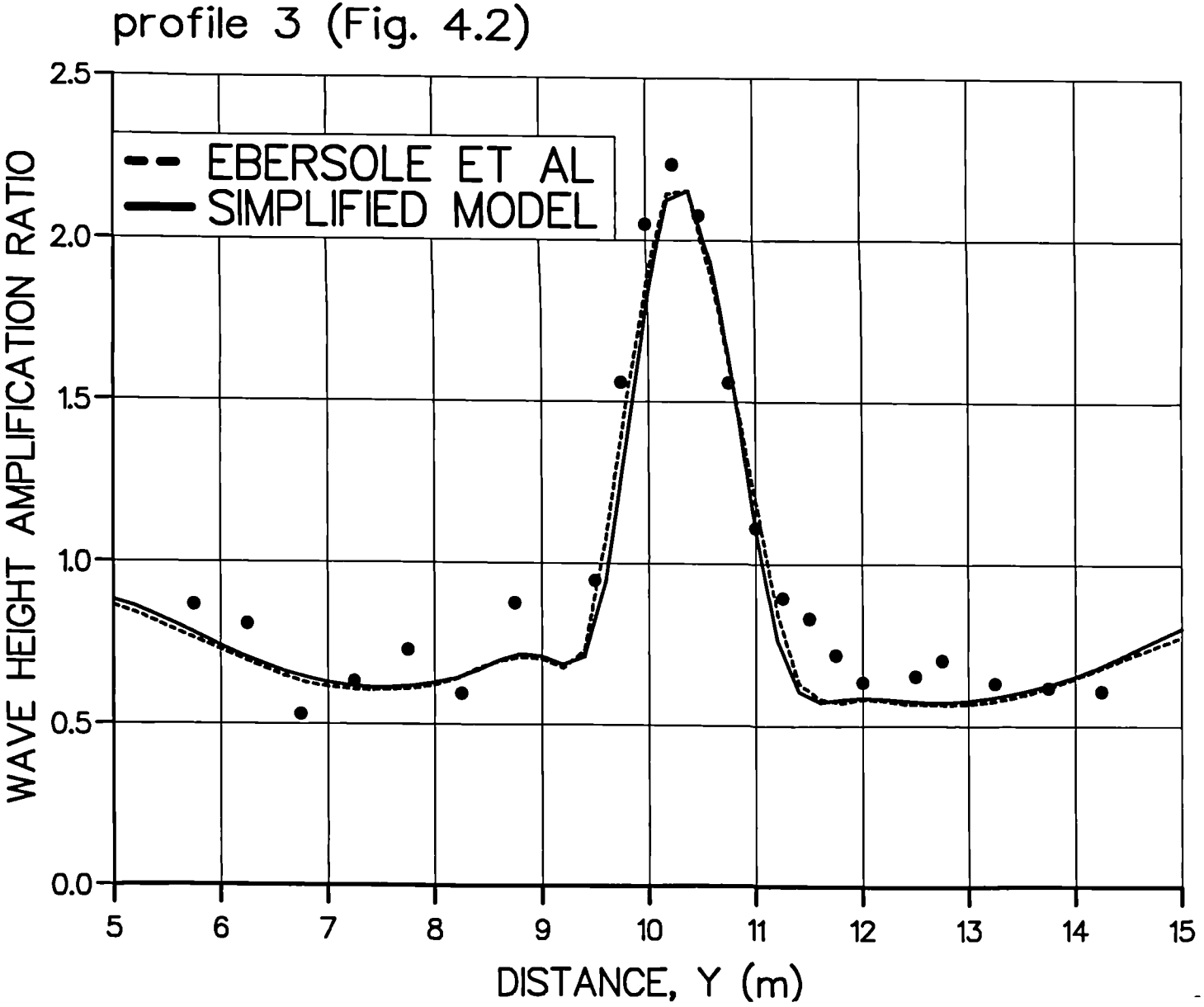

Fig. 4.4c Calculated and measured wave height profiles for elliptic shoal test: profiles 3.

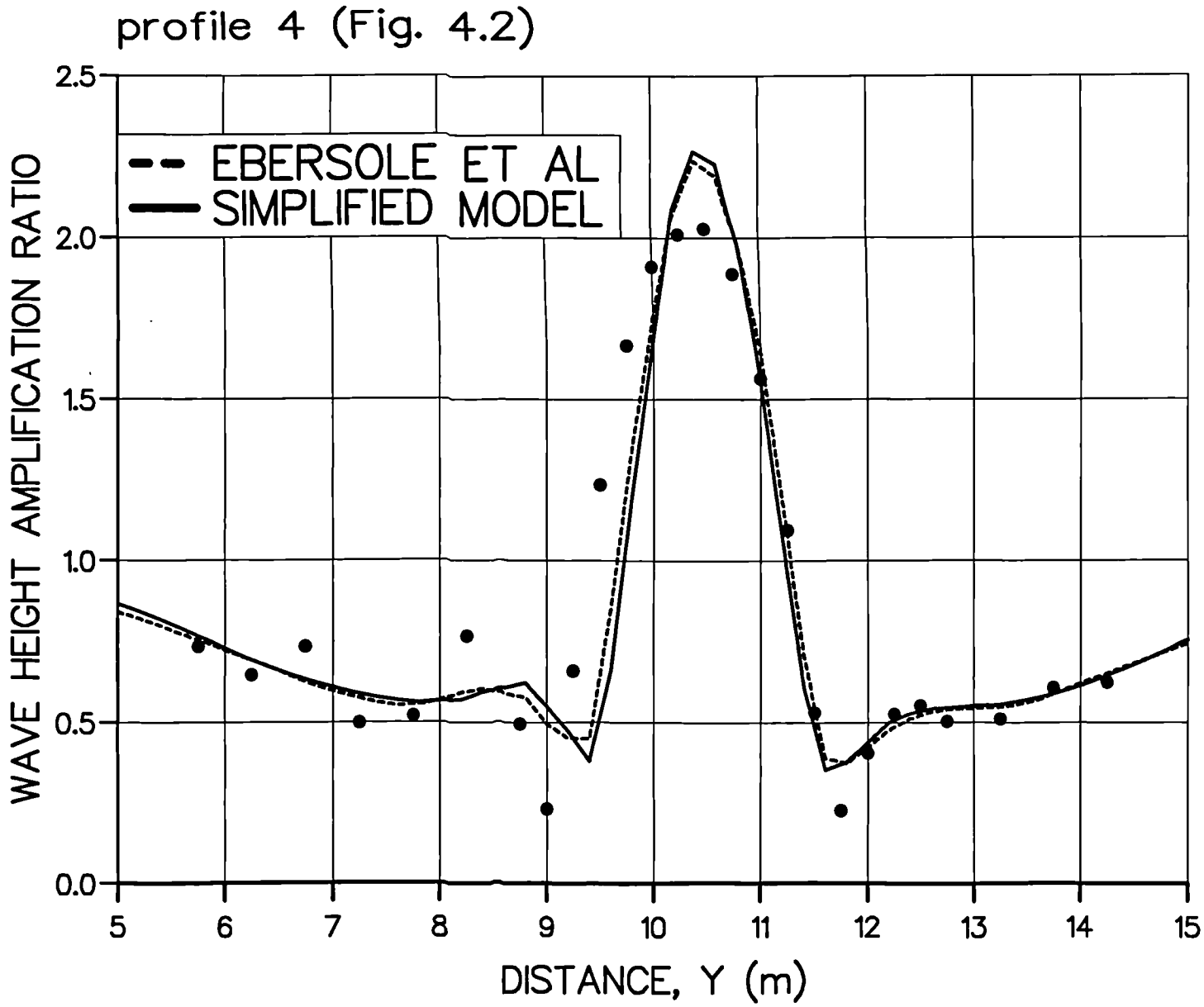

Fig. 4.4d Calculated and measured wave height profiles for elliptic shoal test: profiles 4.

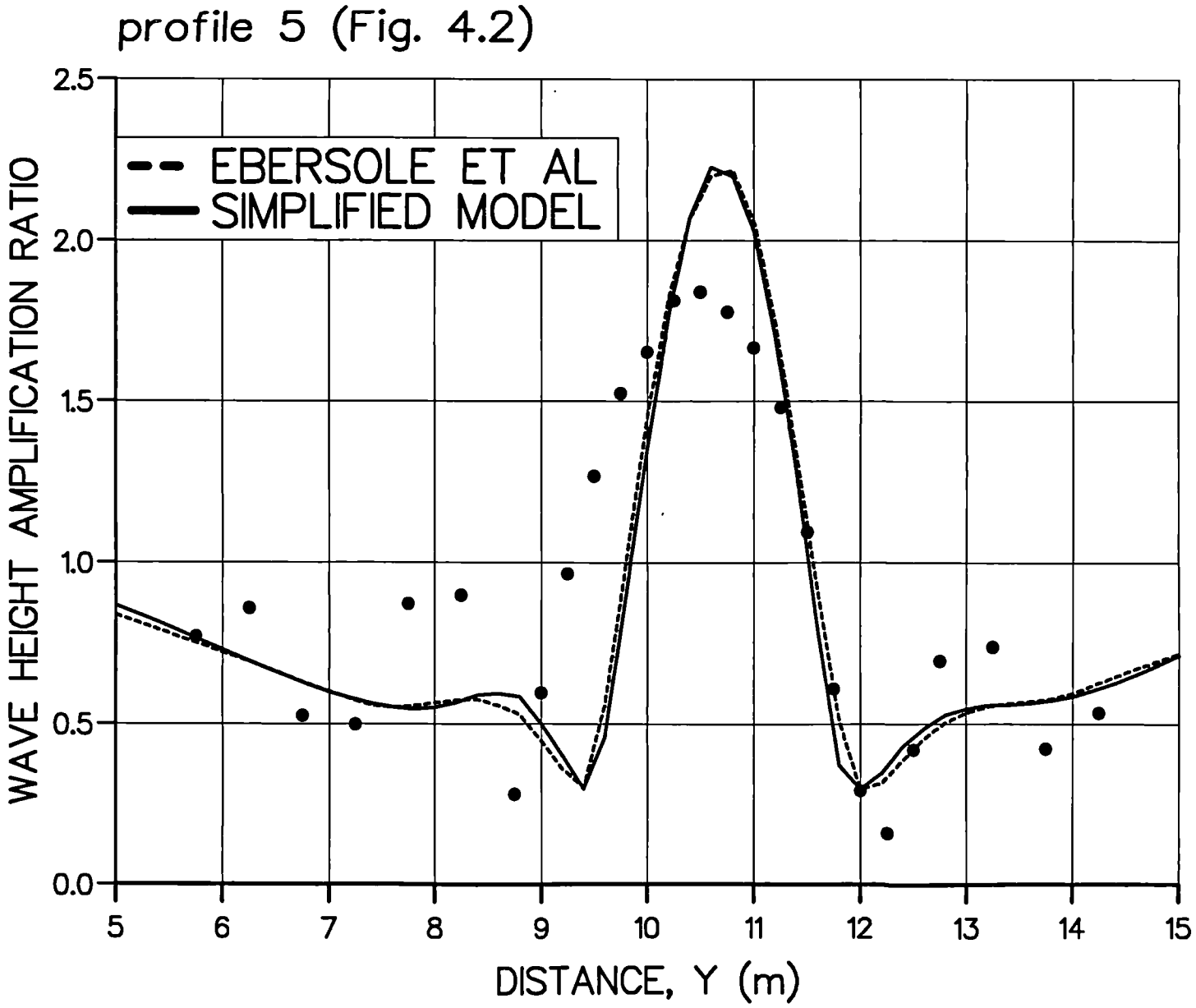

Fig. 4.4e Calculated and measured wave height profiles for elliptic shoal test: profiles 5.

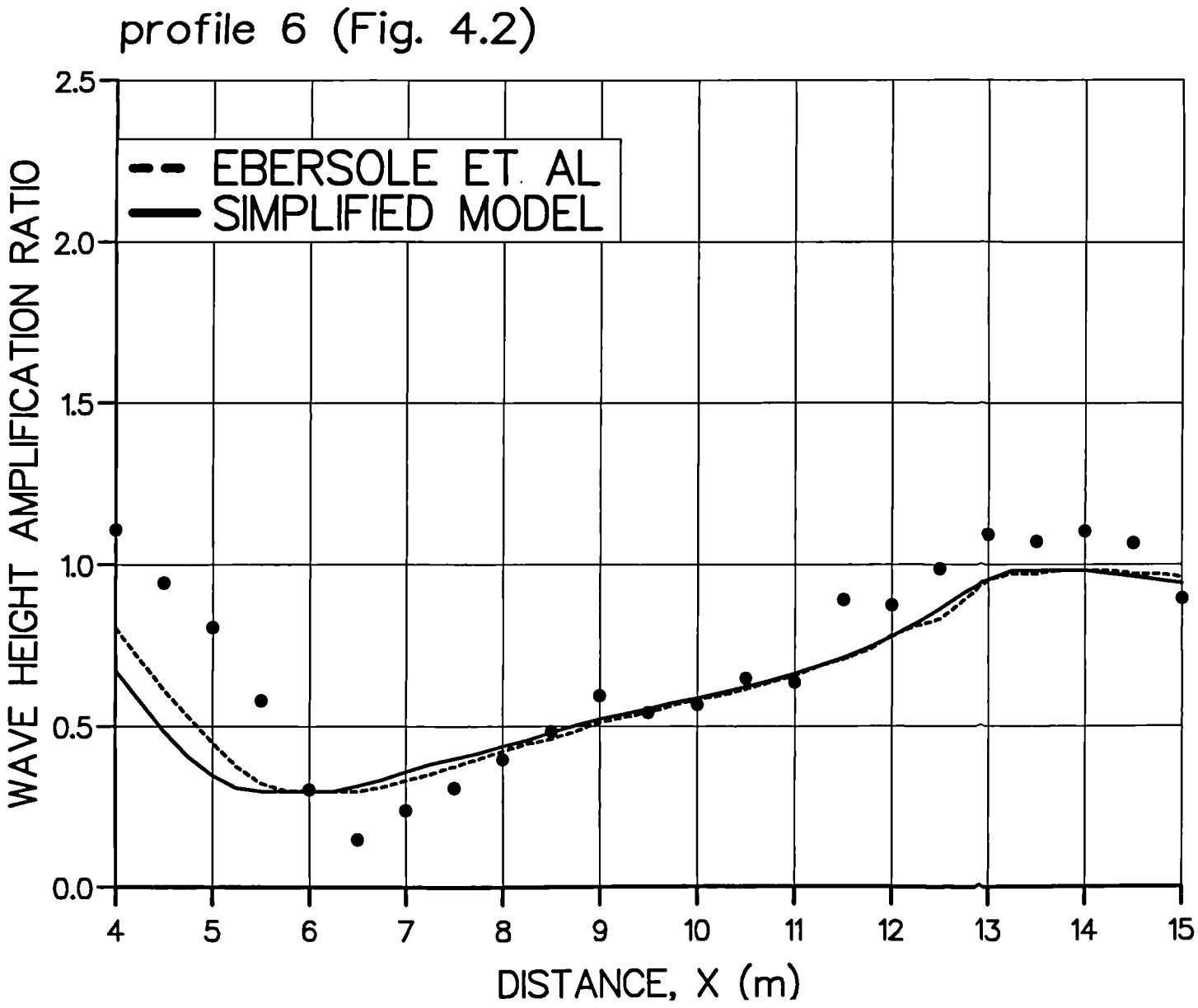

Fig. 4.4f Calculated and measured wave height profiles for elliptic shoal test: profiles 6.

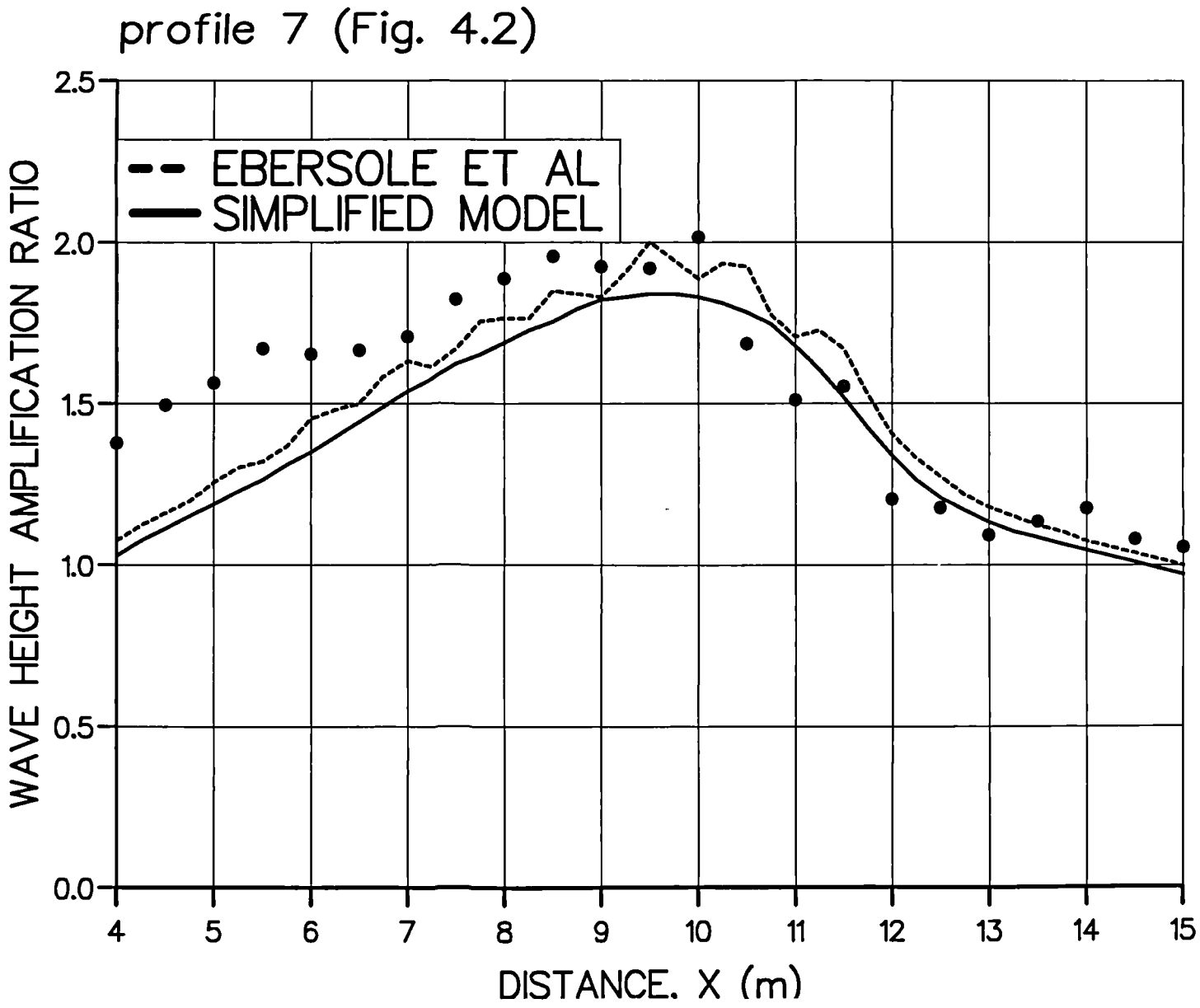

Fig. 4.4g Calculated and measured wave height profiles for elliptic shoal test: profiles 7.

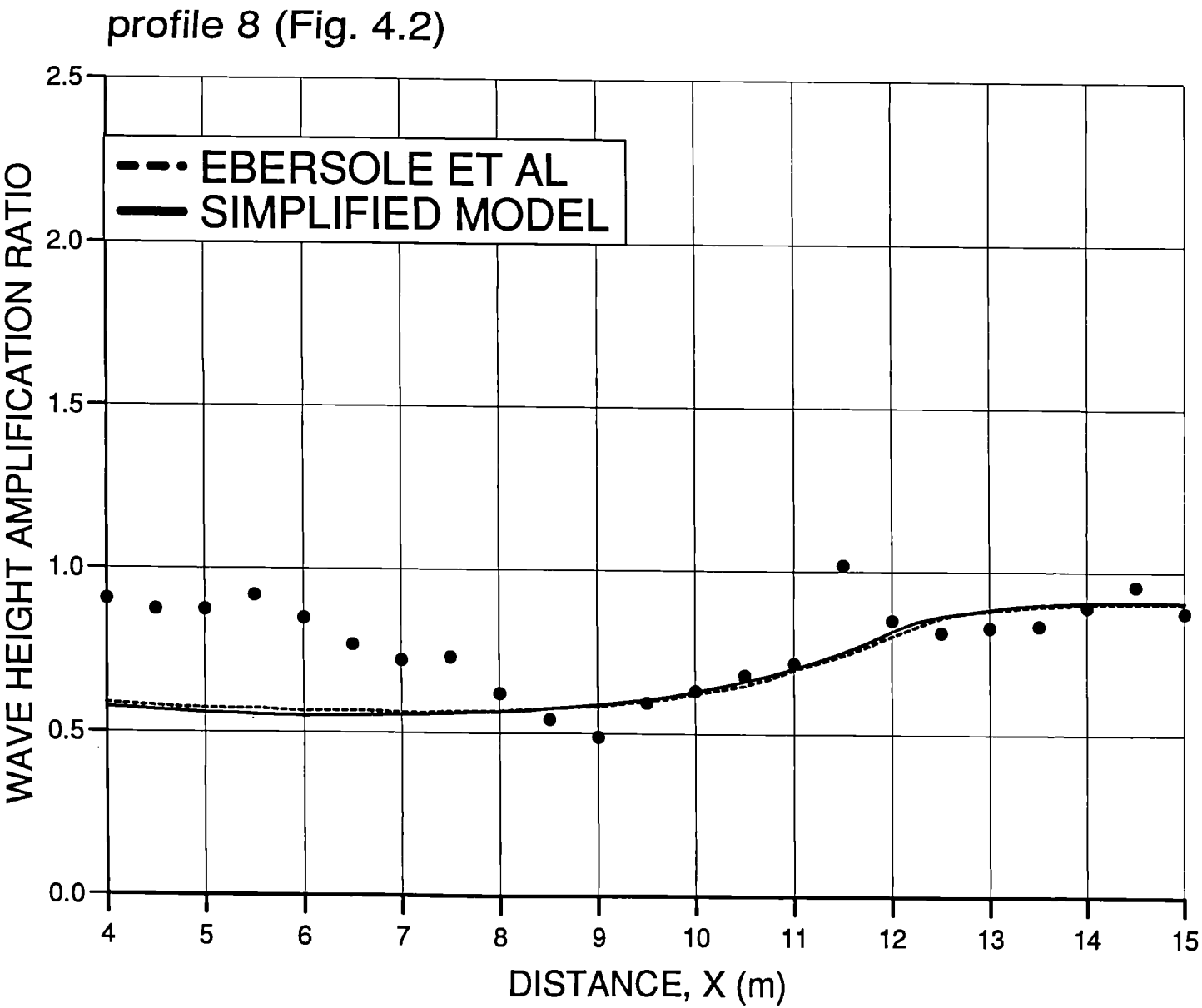

Fig. 4.4h Calculated and measured wave height profiles for elliptic shoal test: profiles 8.

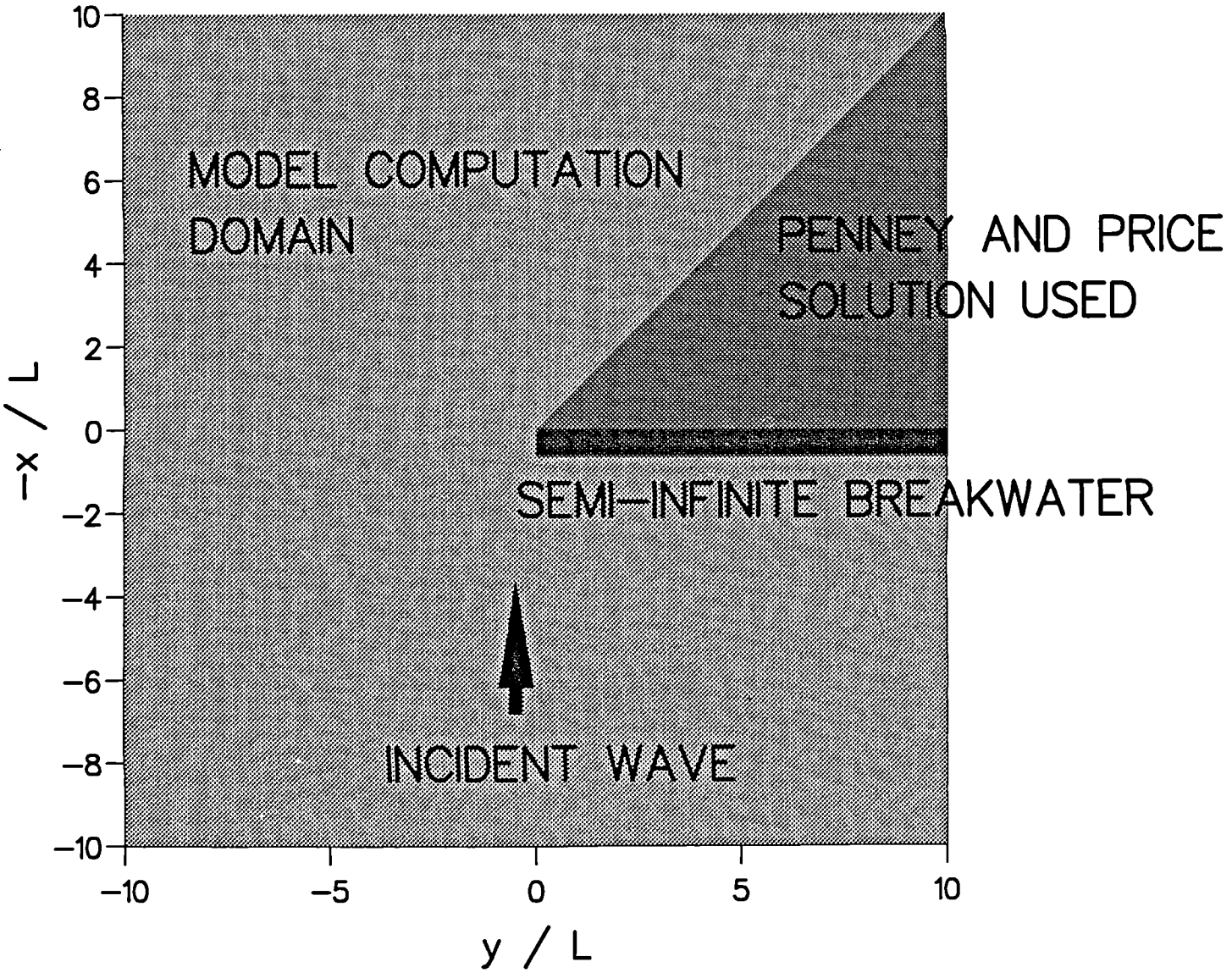

Fig. 4.5 Computational domains for the numerical model and the Penney and Price(1952) analytical method.

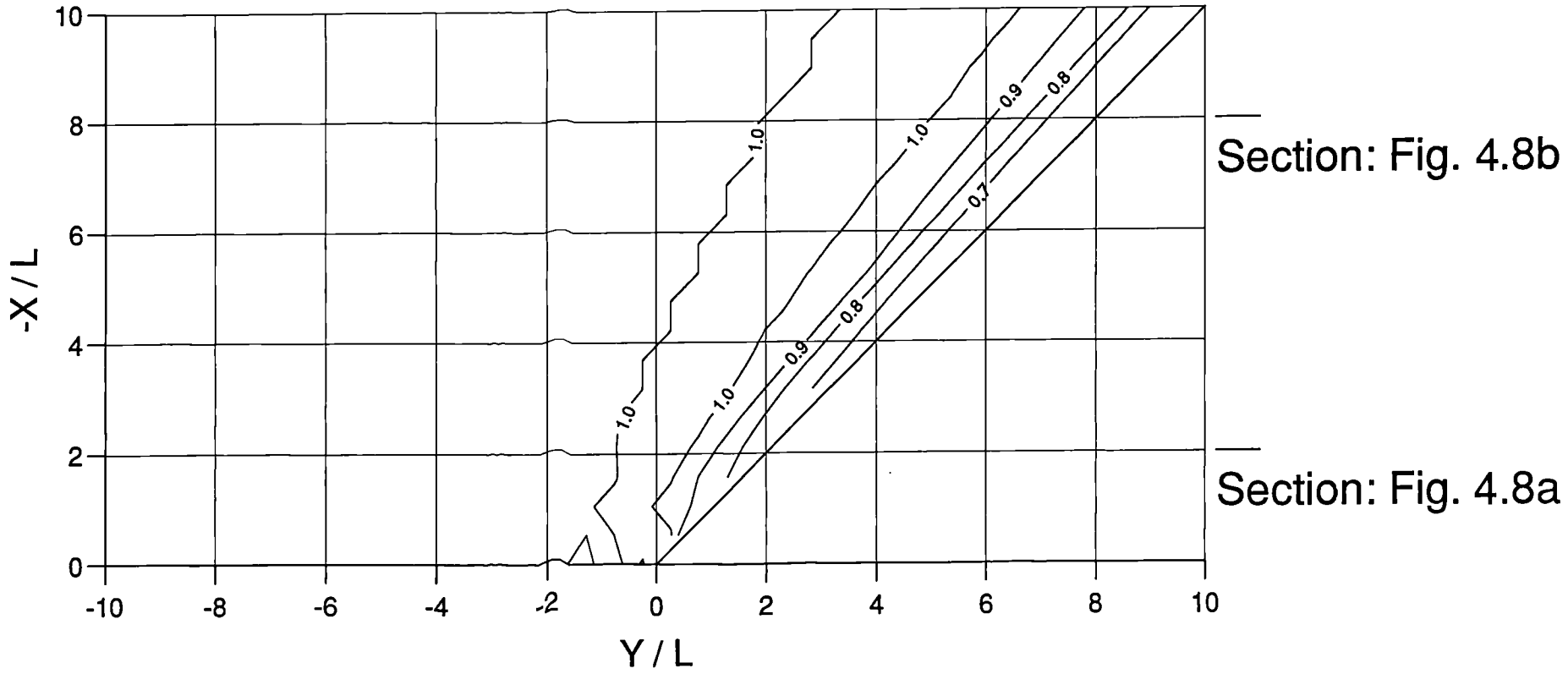

Fig. 4.6a The present model results on a semi-infinite breakwater: $\theta = -45°$.

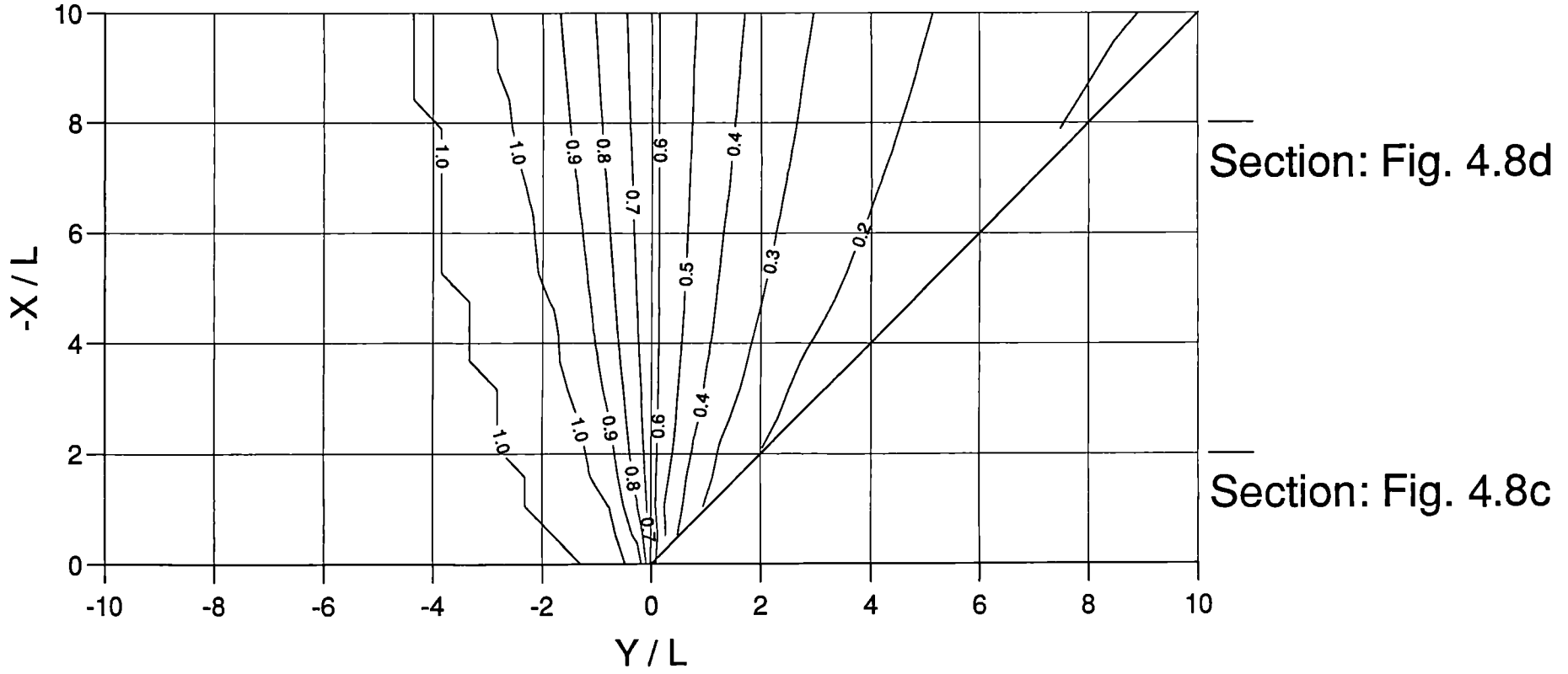

Fig. 4.6b The present model results on a semi-infinite breakwater: θ = 0.

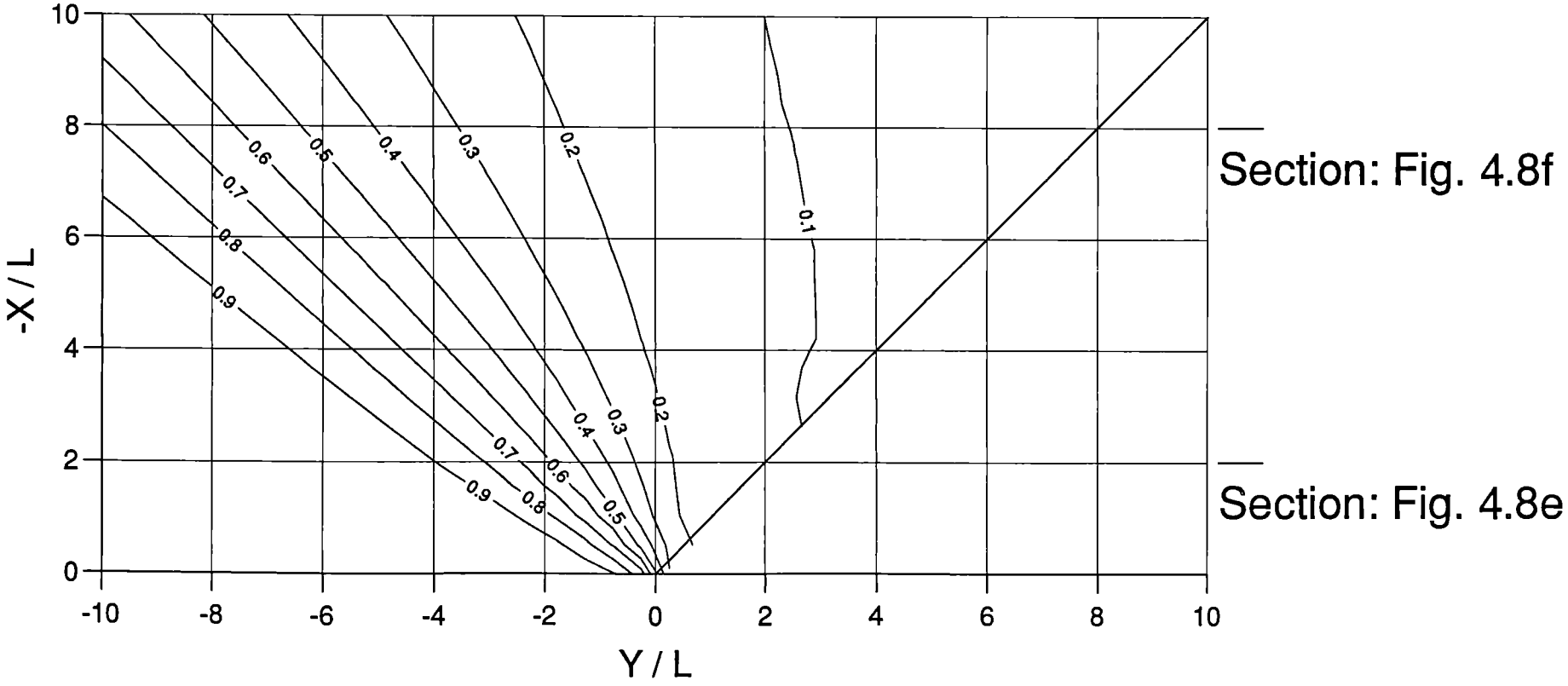

Fig. 4.6c The present model results on a semi-infinite breakwater: θ = 45°.

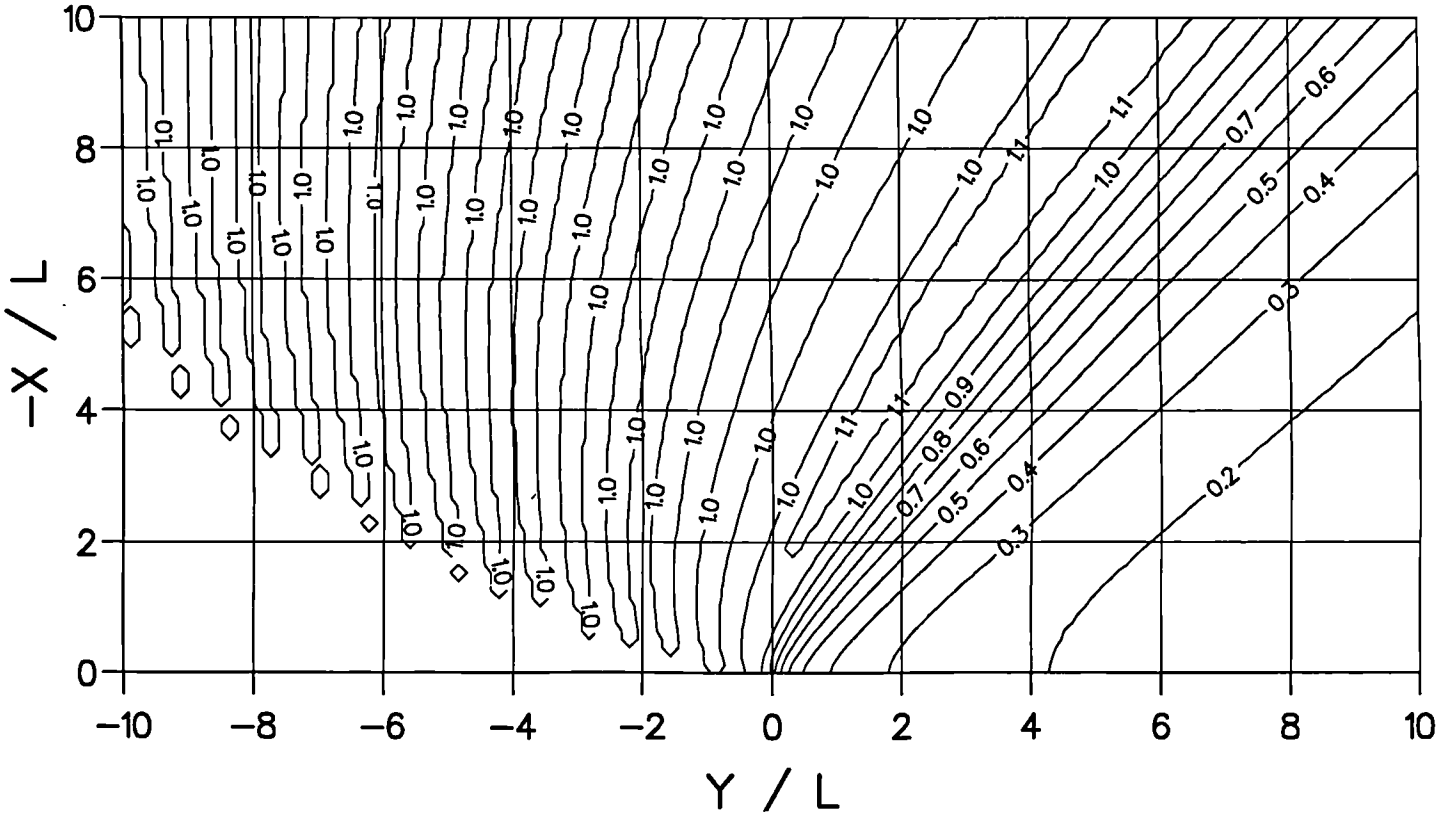

Fig. 4.7a Penney and Price's solution for diffraction:

θ = -45°.

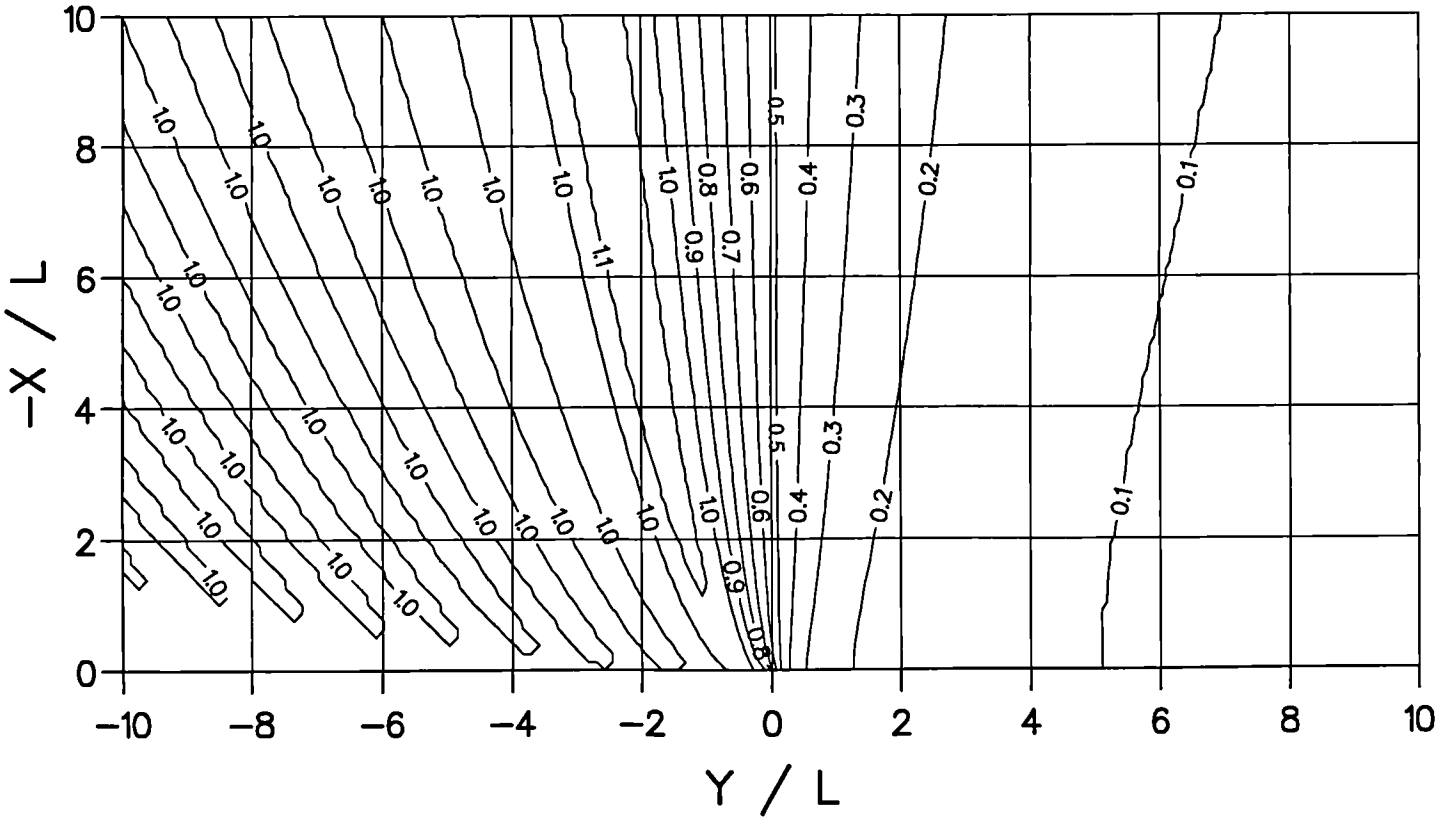

Fig. 4.7b Penney and Price's solution for diffraction:

$\theta = 0$.

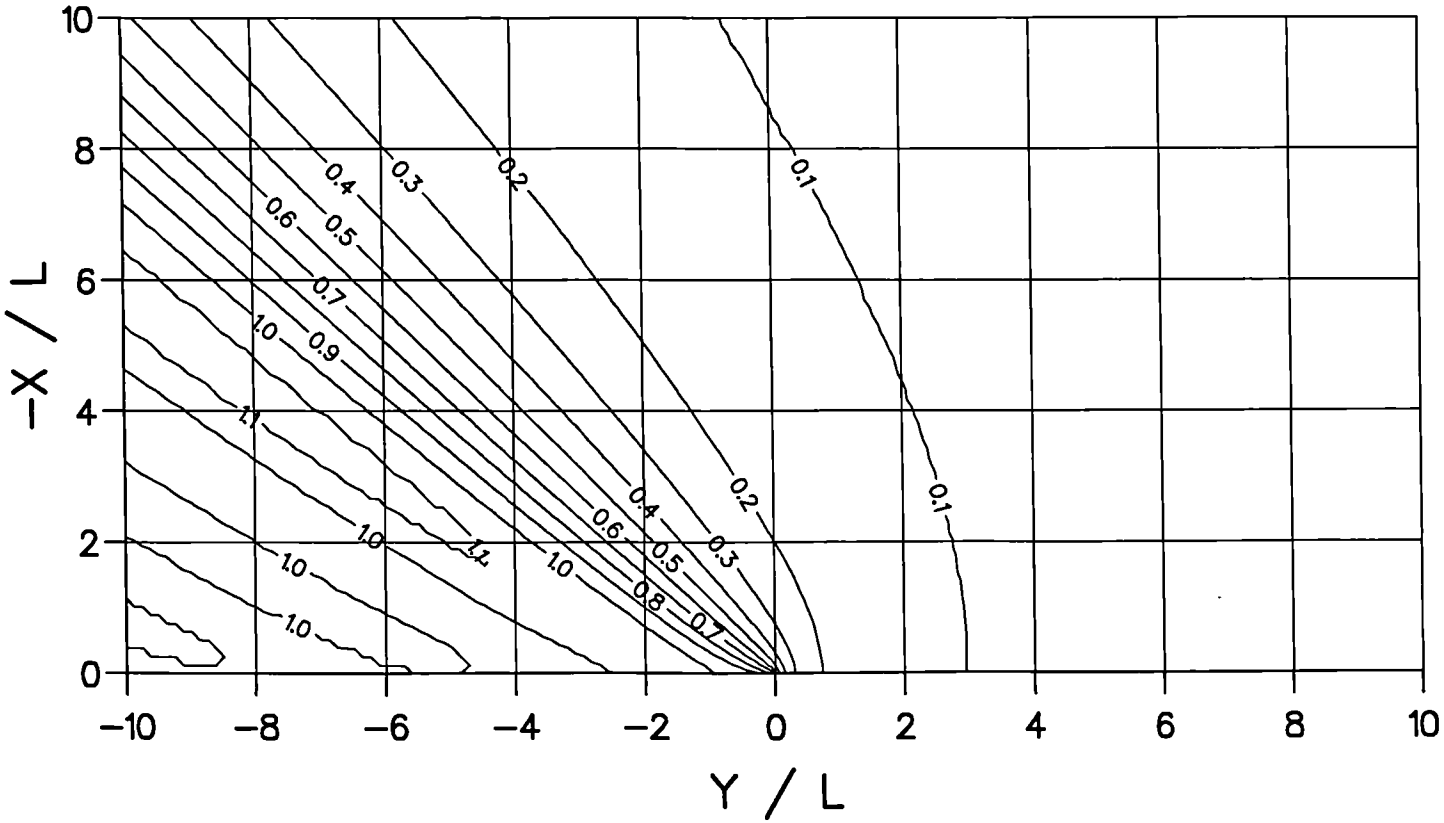

Fig. 4.7c Penney and Price's solution for diffraction:

θ = 45°.

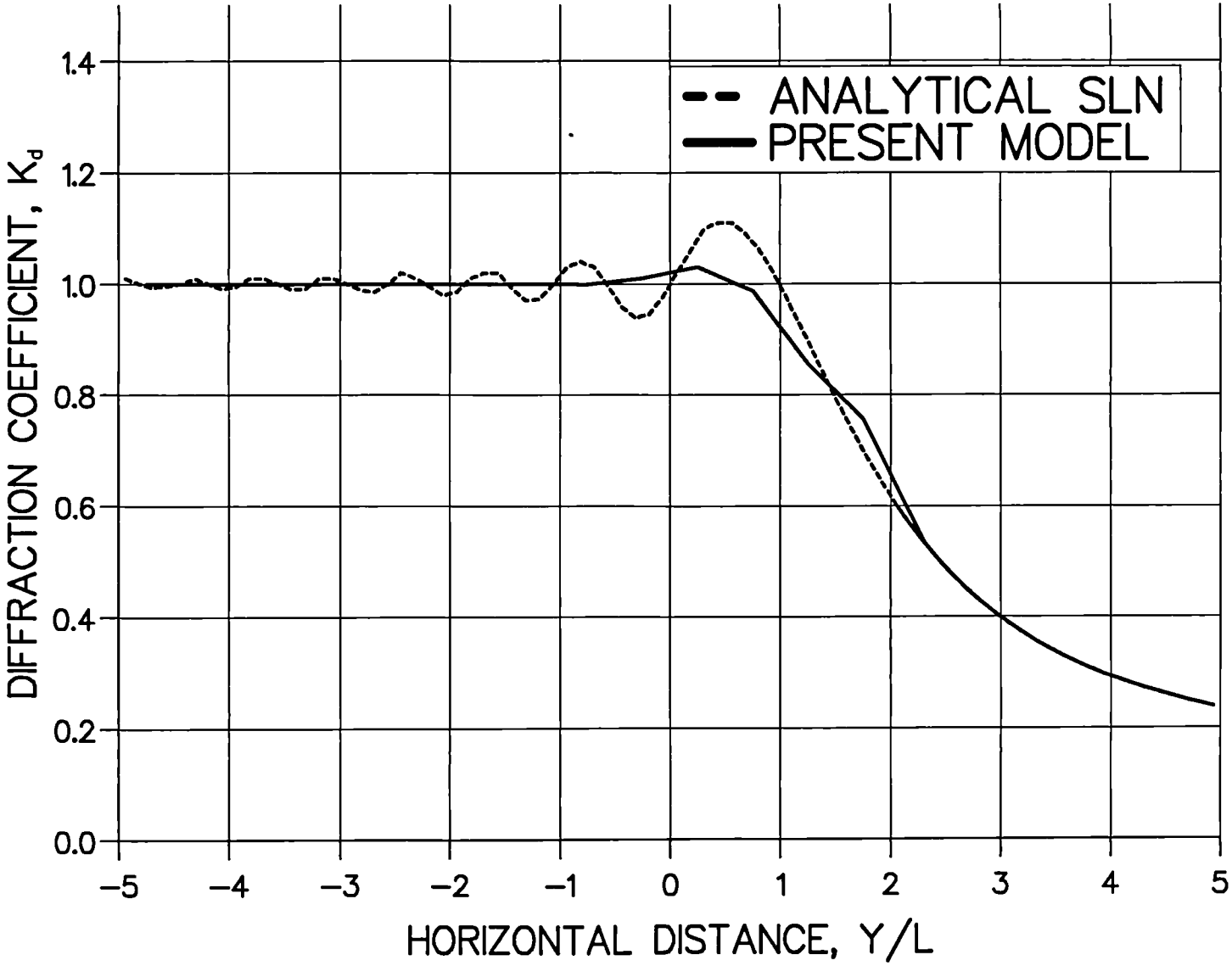

Fig. 4.8a Comparison of model results and analytic solutions: θ = -45°;-X/L=2.

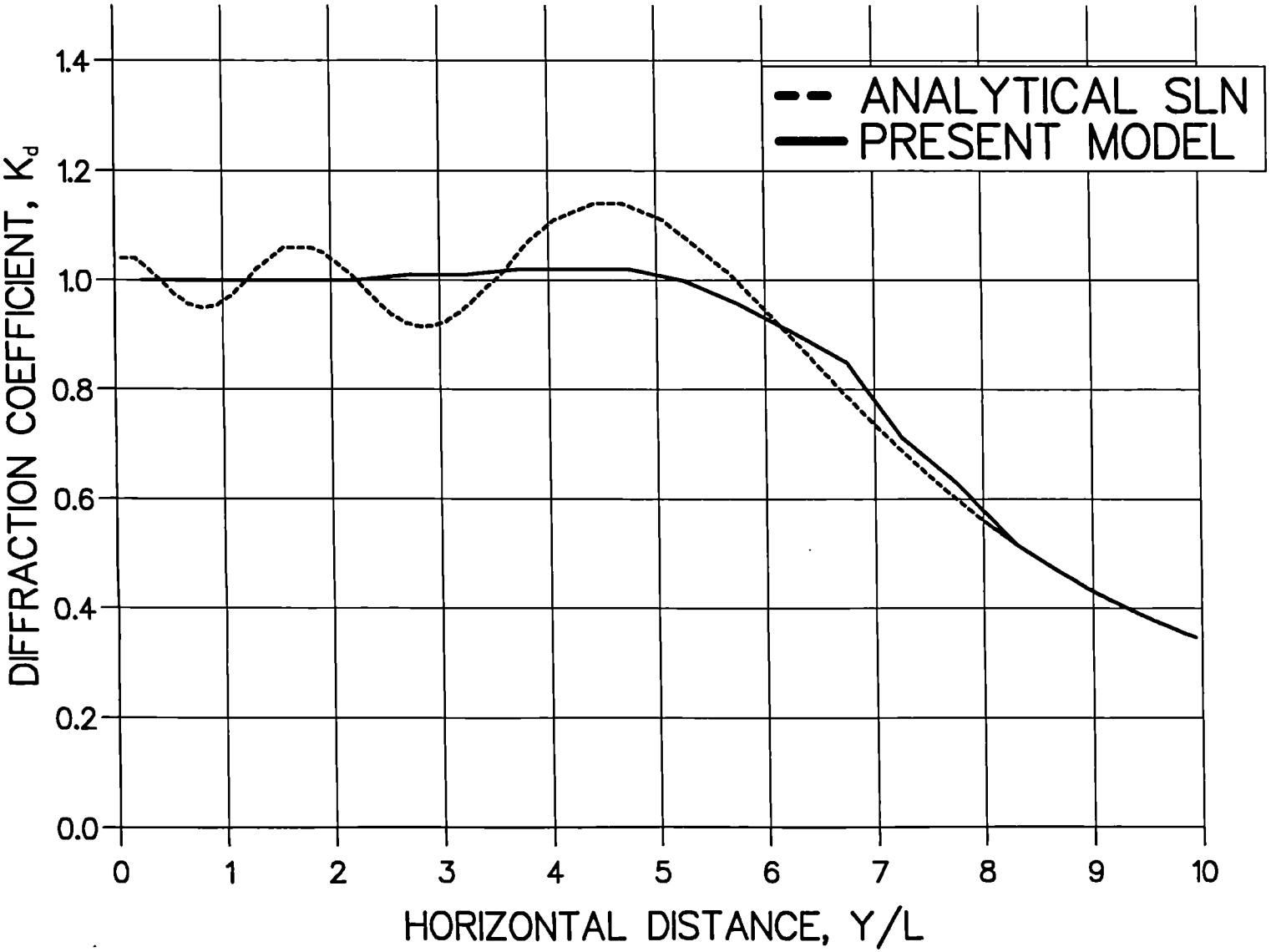

Fig. 4.8b Comparison of model results and analytic solutions:

θ = -45°;-X/L=8.

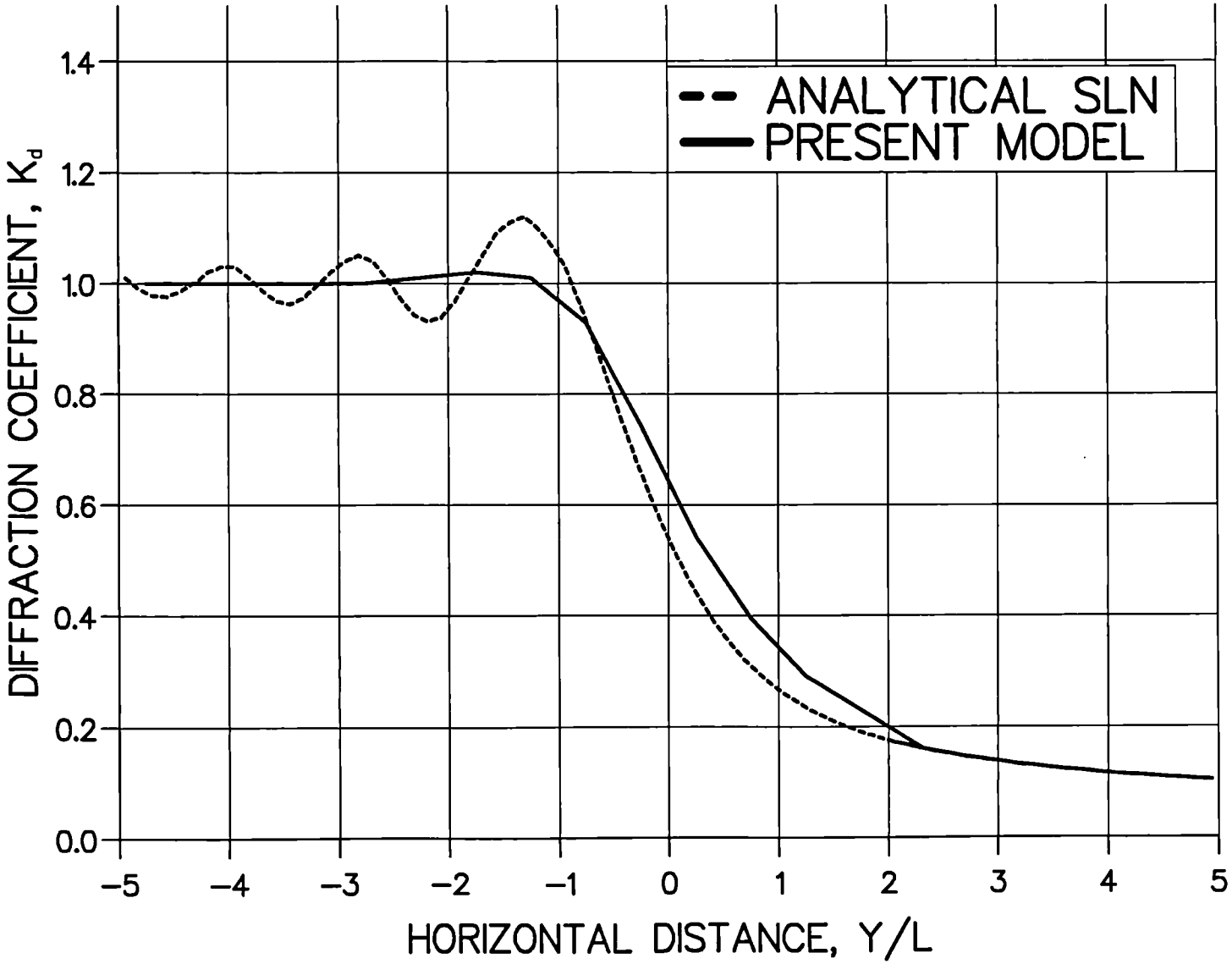

Fig. 4.8c Comparison of model results and analytic solutions: θ = 0°;-X/L=2.

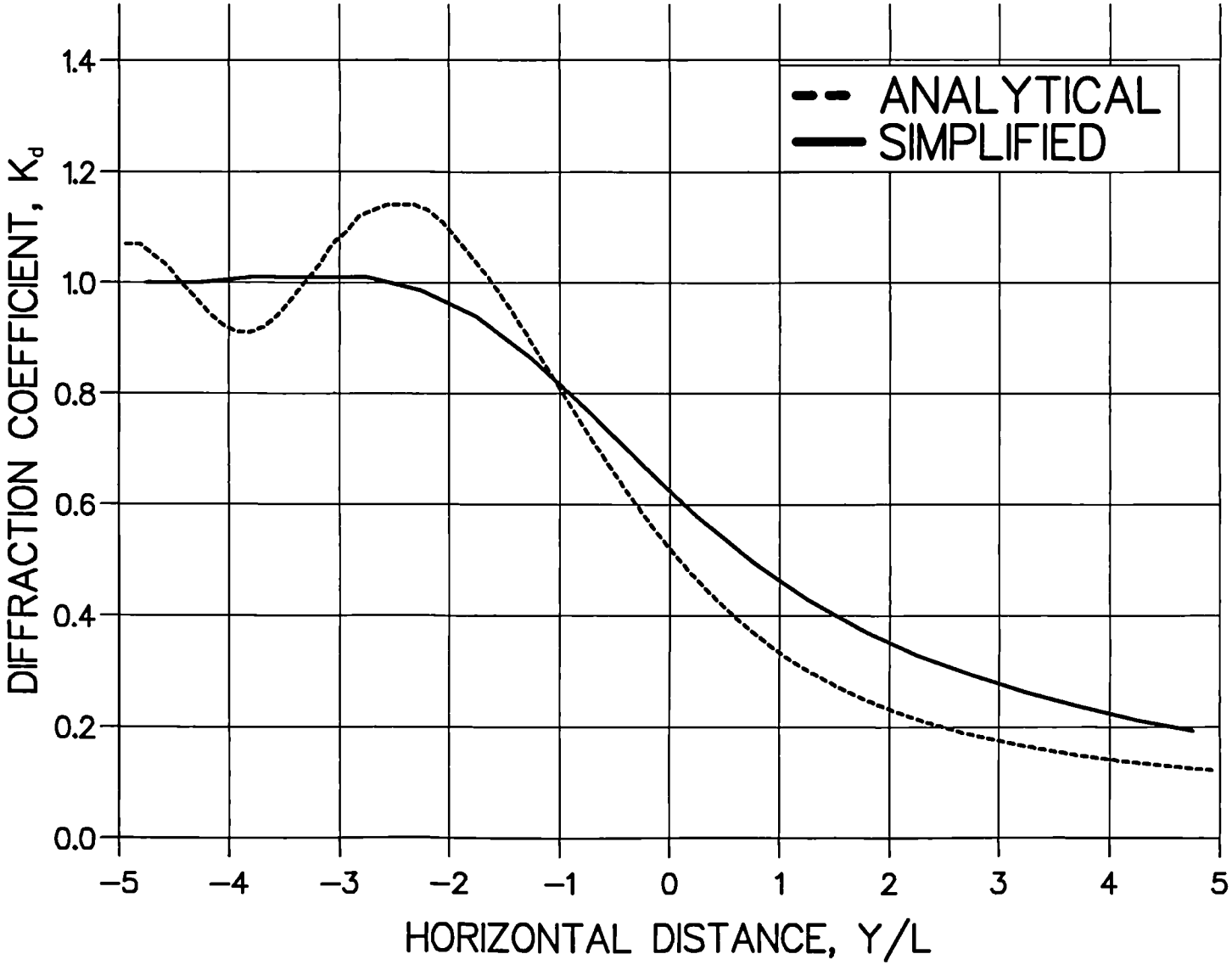

Fig. 4.8d Comparison of model results and analytic solutions: θ = 0°;-X/L=8.

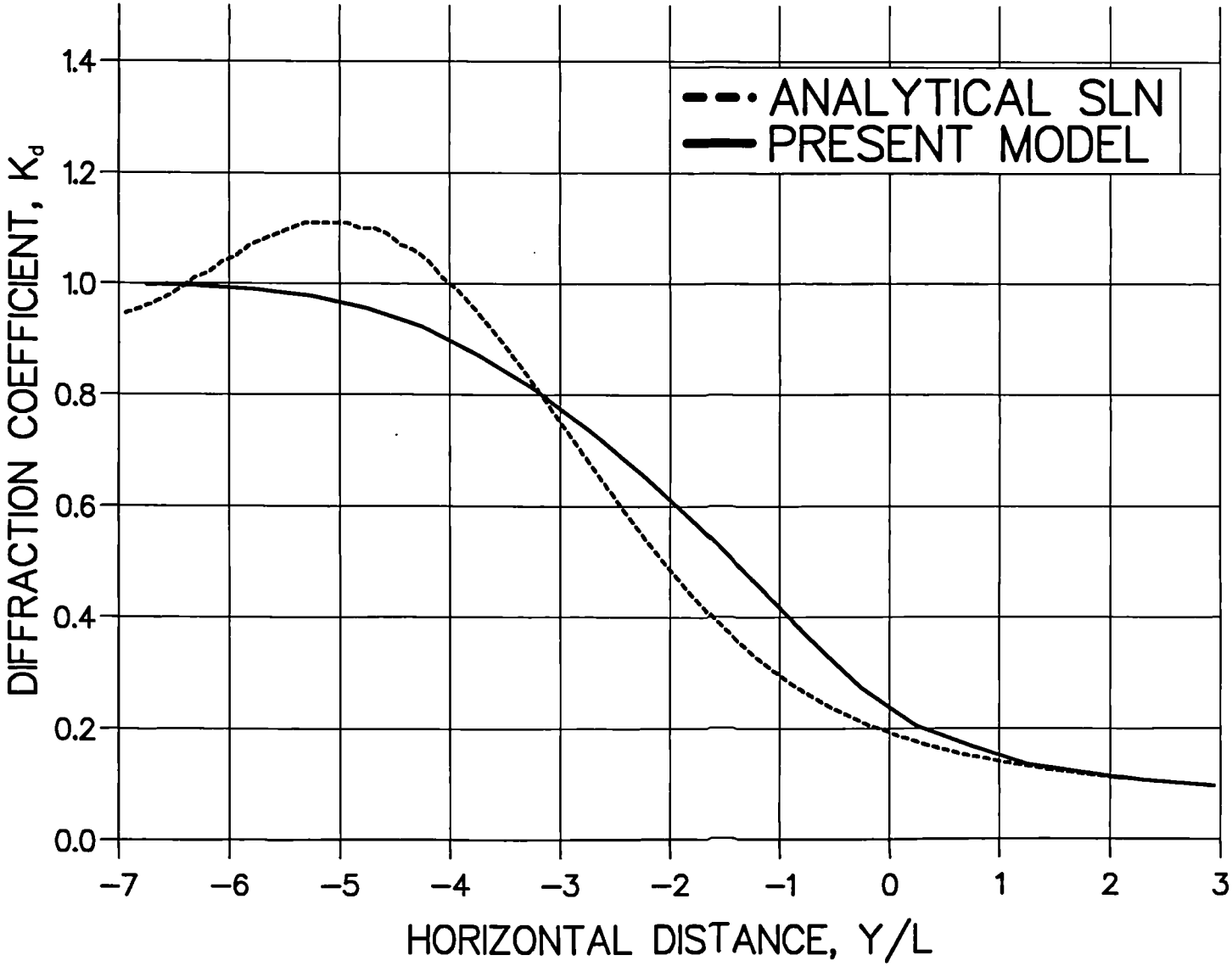

Fig. 4.8e Comparison of model results and analytic solutions: θ = 45°;-X/L=2.

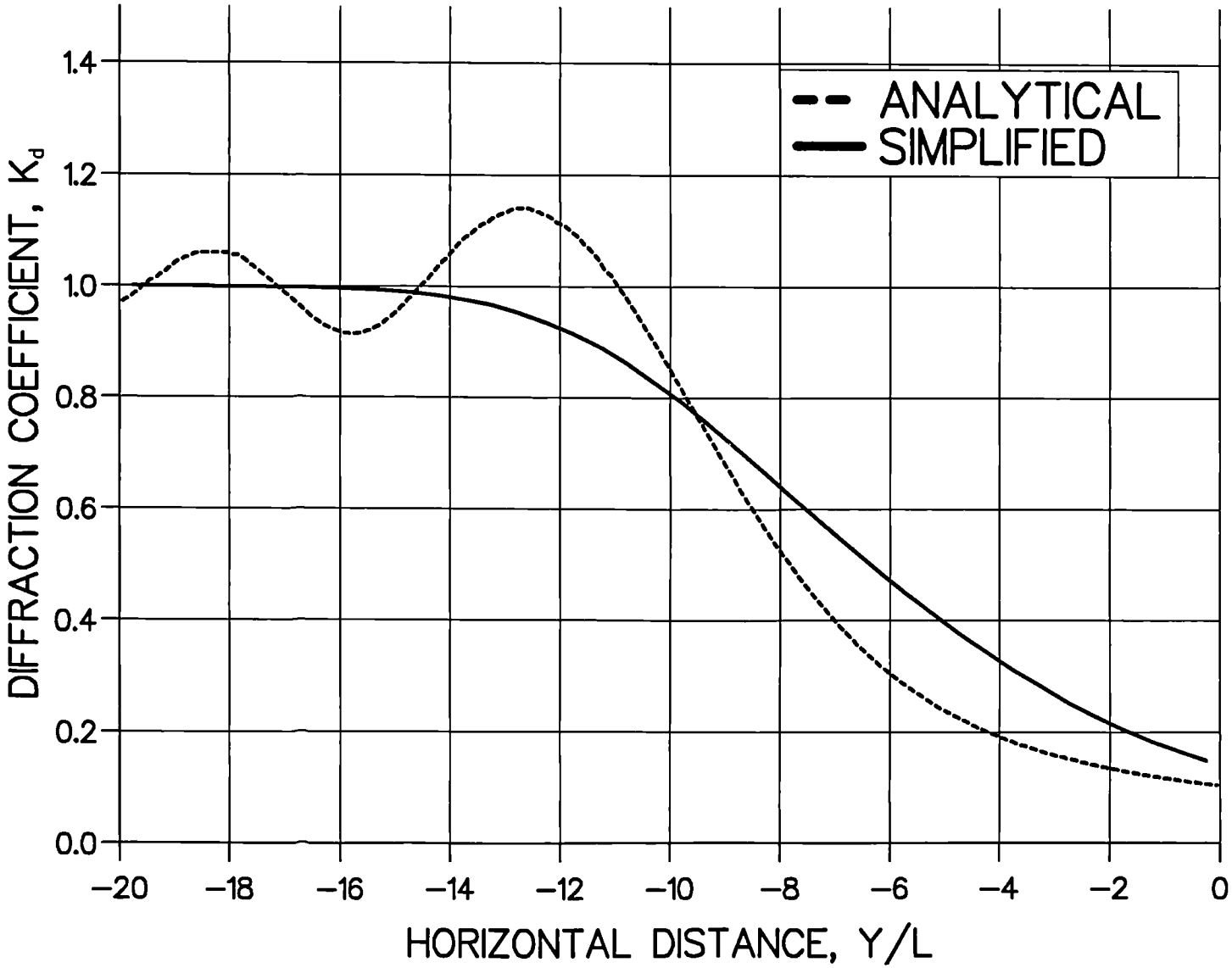

Fig. 4.8f Comparison of model results and analytic solutions: θ = 45°;-X/L=8.

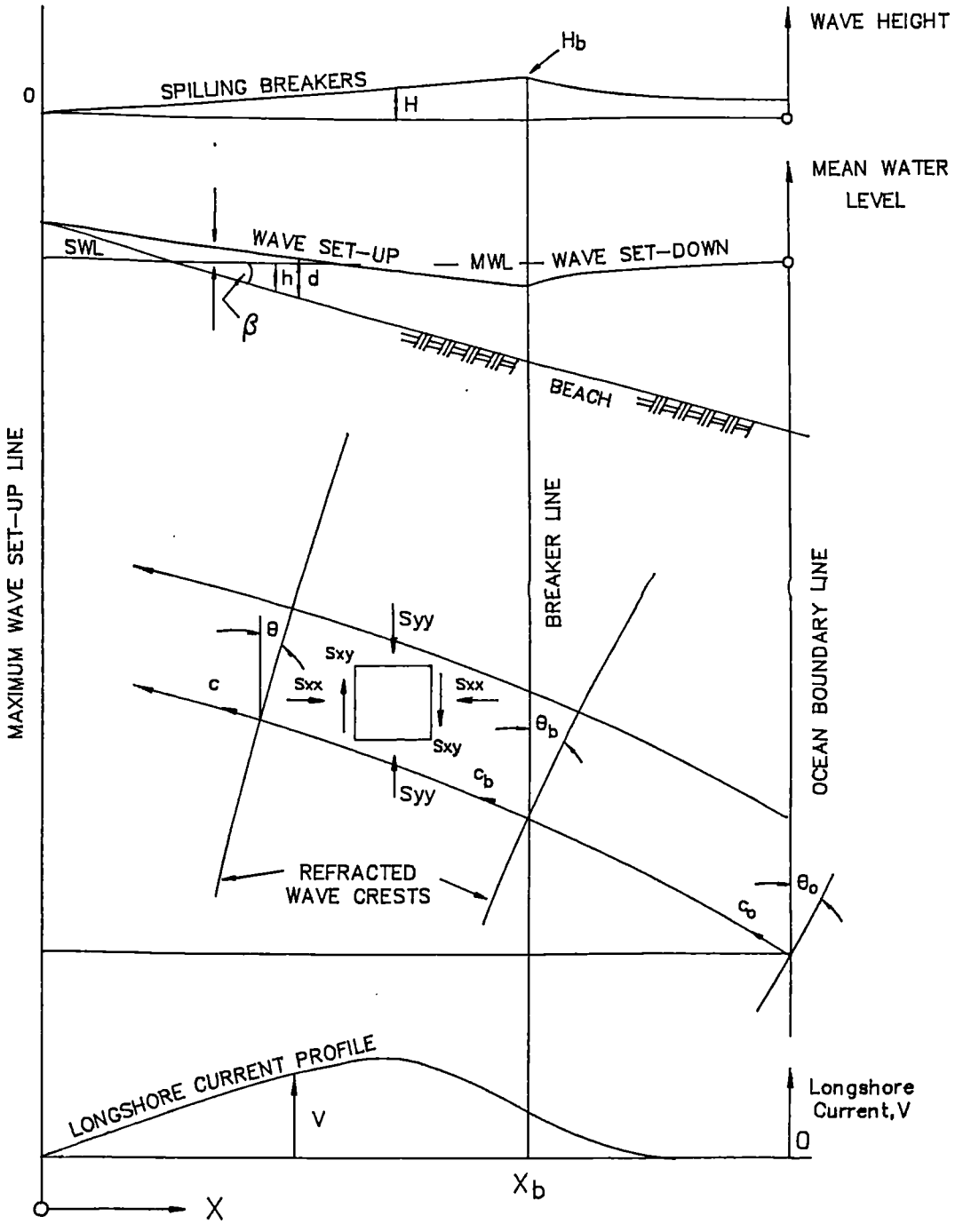

Fig. 5.1 Schematics of the longshore current on a plane beach (after Basco, 1982).

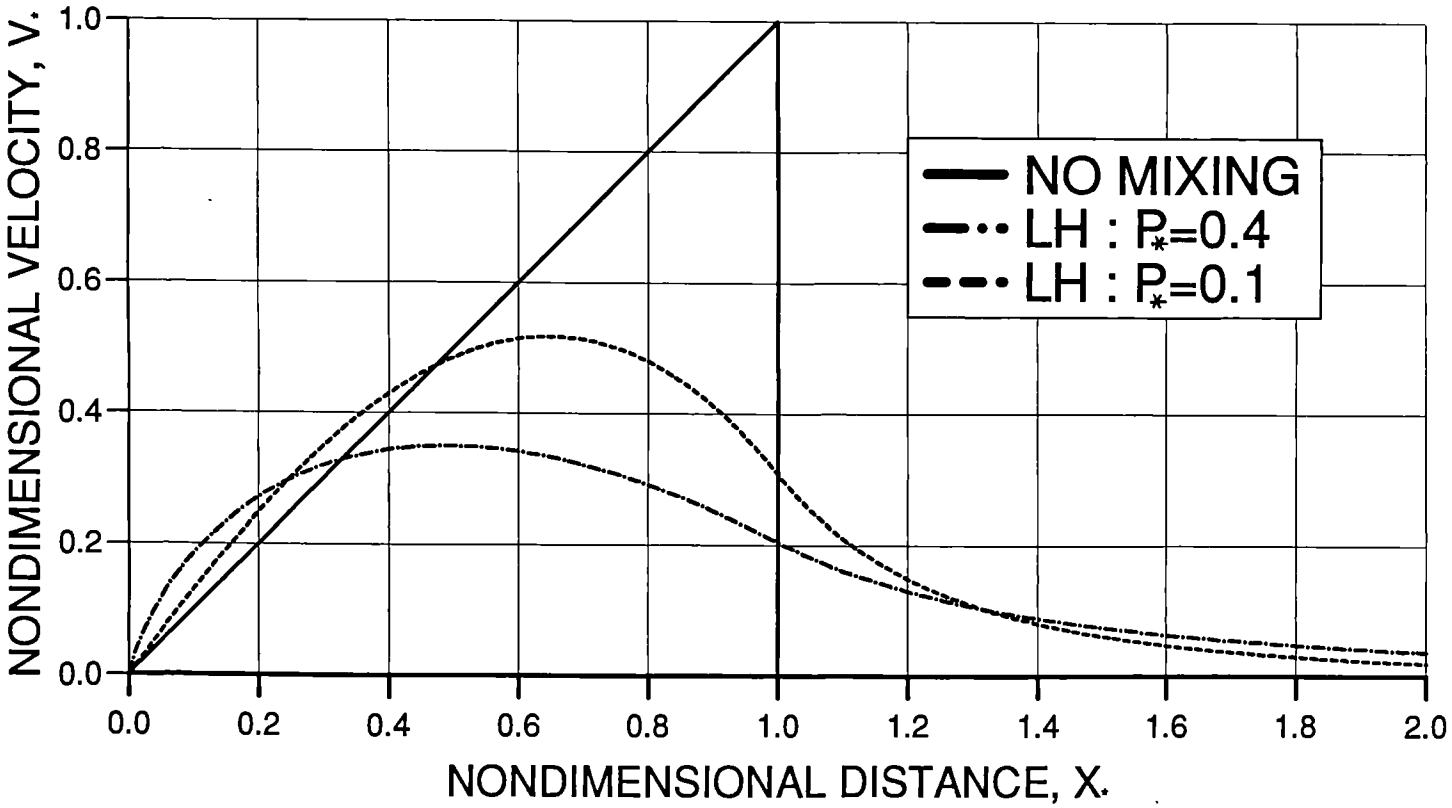

Fig. 5.2 Velocity profiles with and without lateral mixing term (after Longuet-Higgins, 1972).

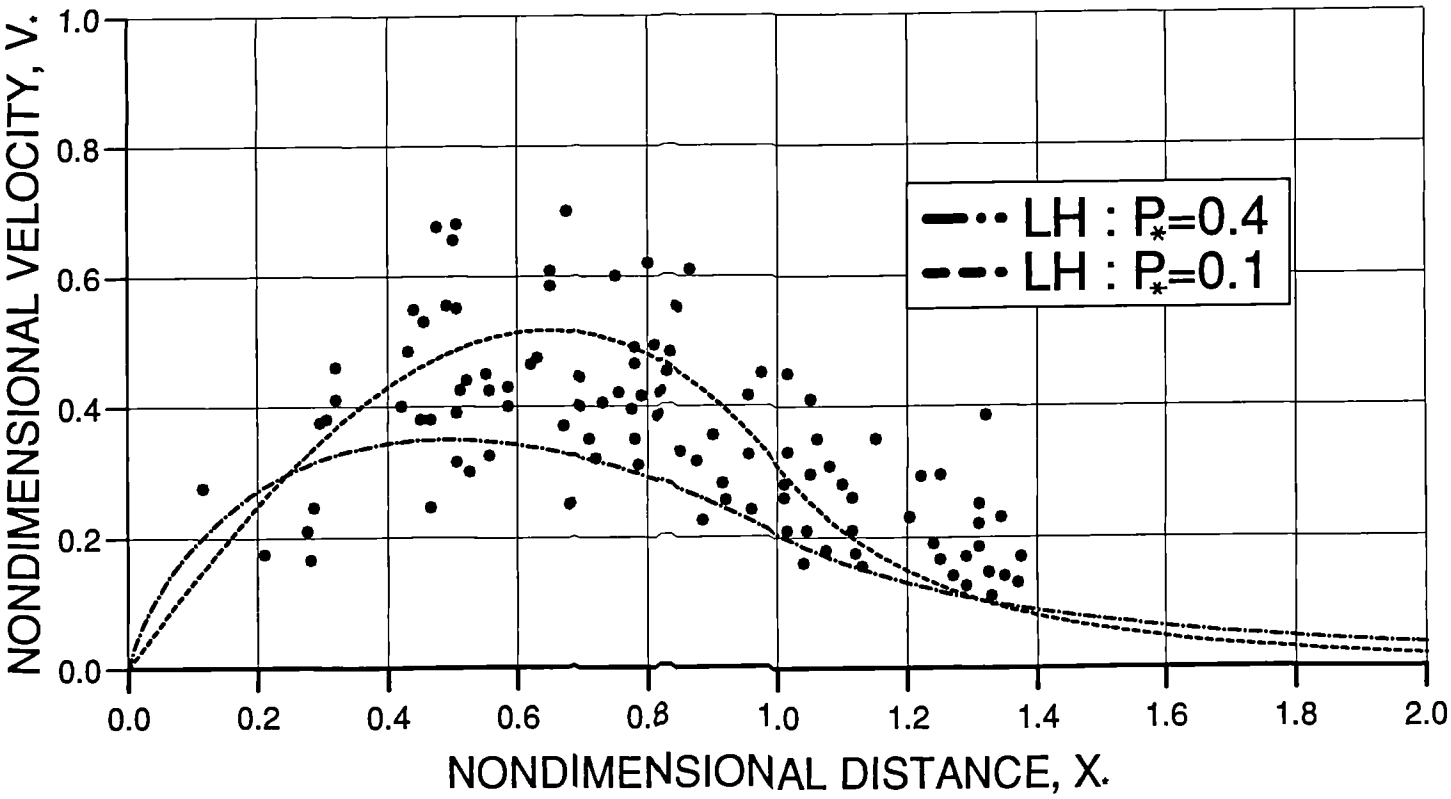

Fig. 5.3 Comparison of the Longuet-Higgins velocity profiles and measurements (after Sonu,1975).

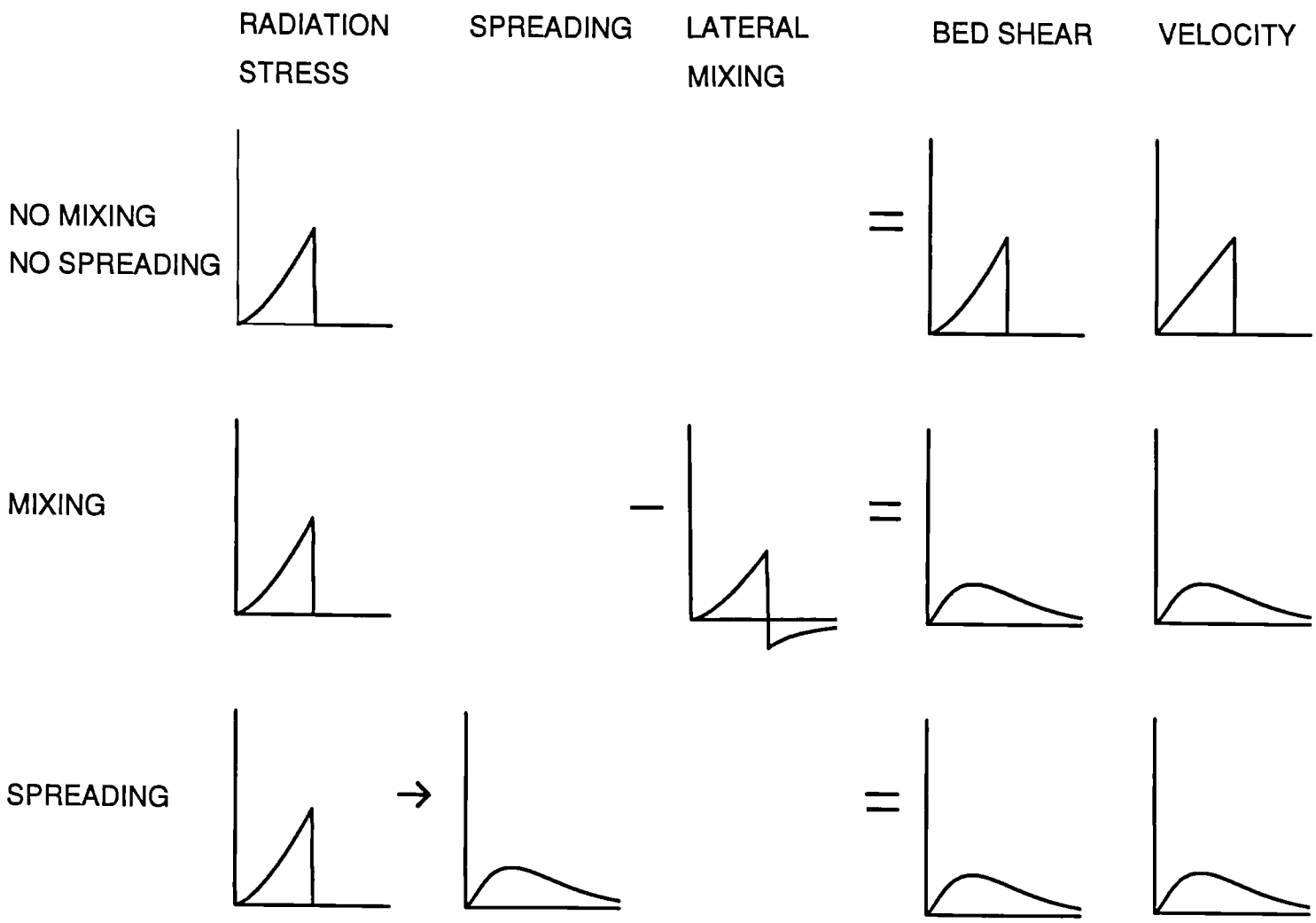

Fig. 5.4 The effect of the spreading operator and the lateral mixing term.

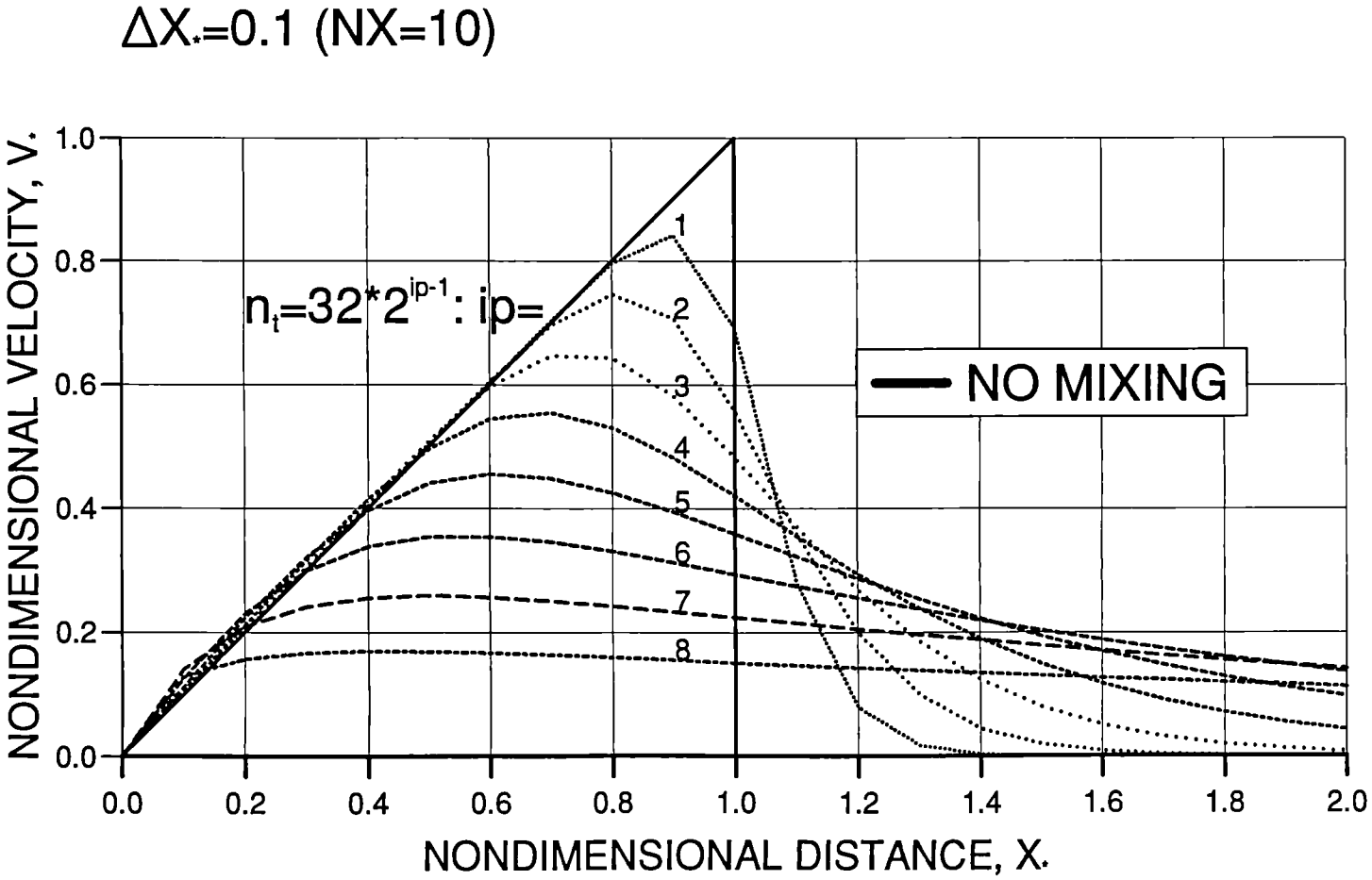

Fig. 5.5 Velocity profiles obtained at various times.

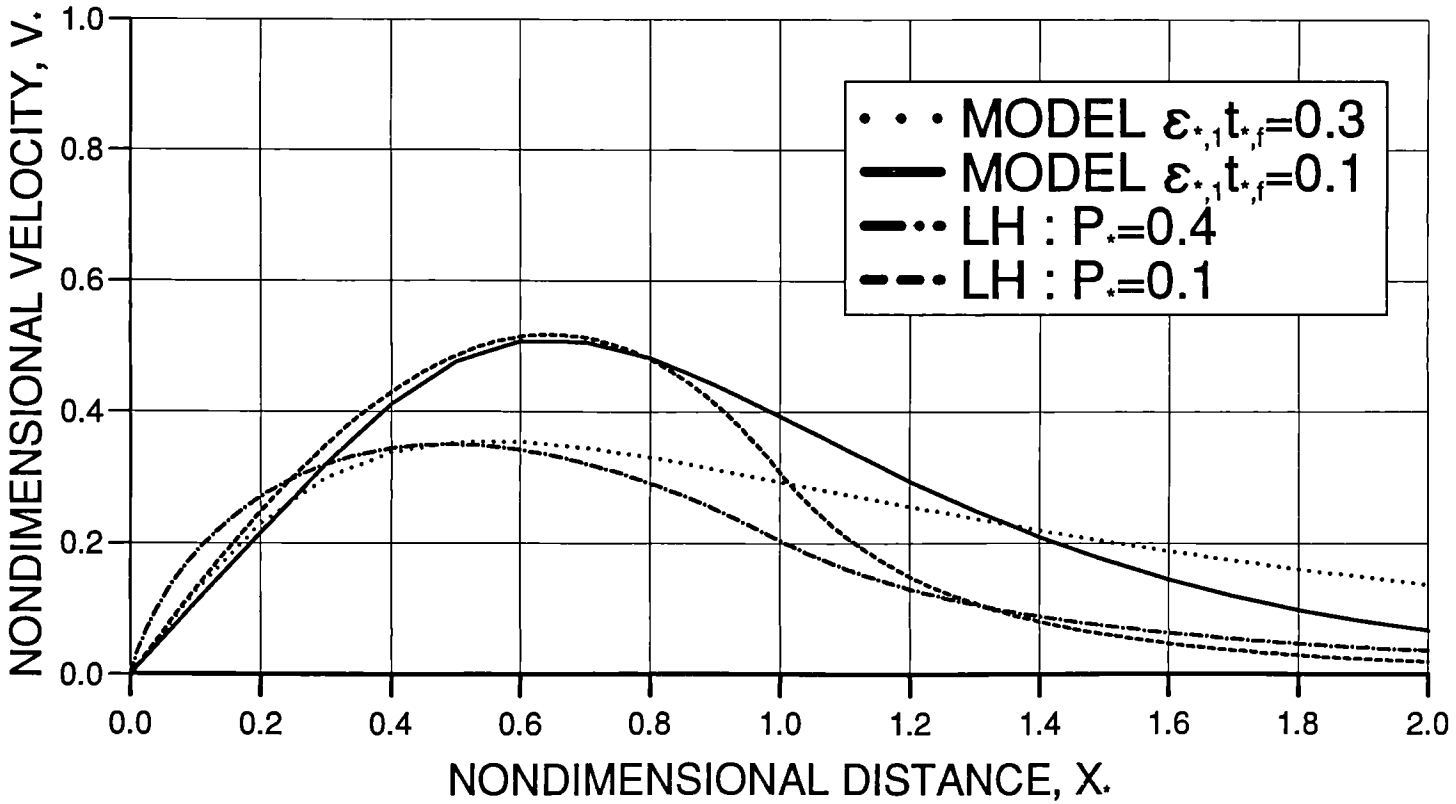

Fig. 5.6 Comparison of velocity profiles given by the present model and Longuet-Higgins' solution.

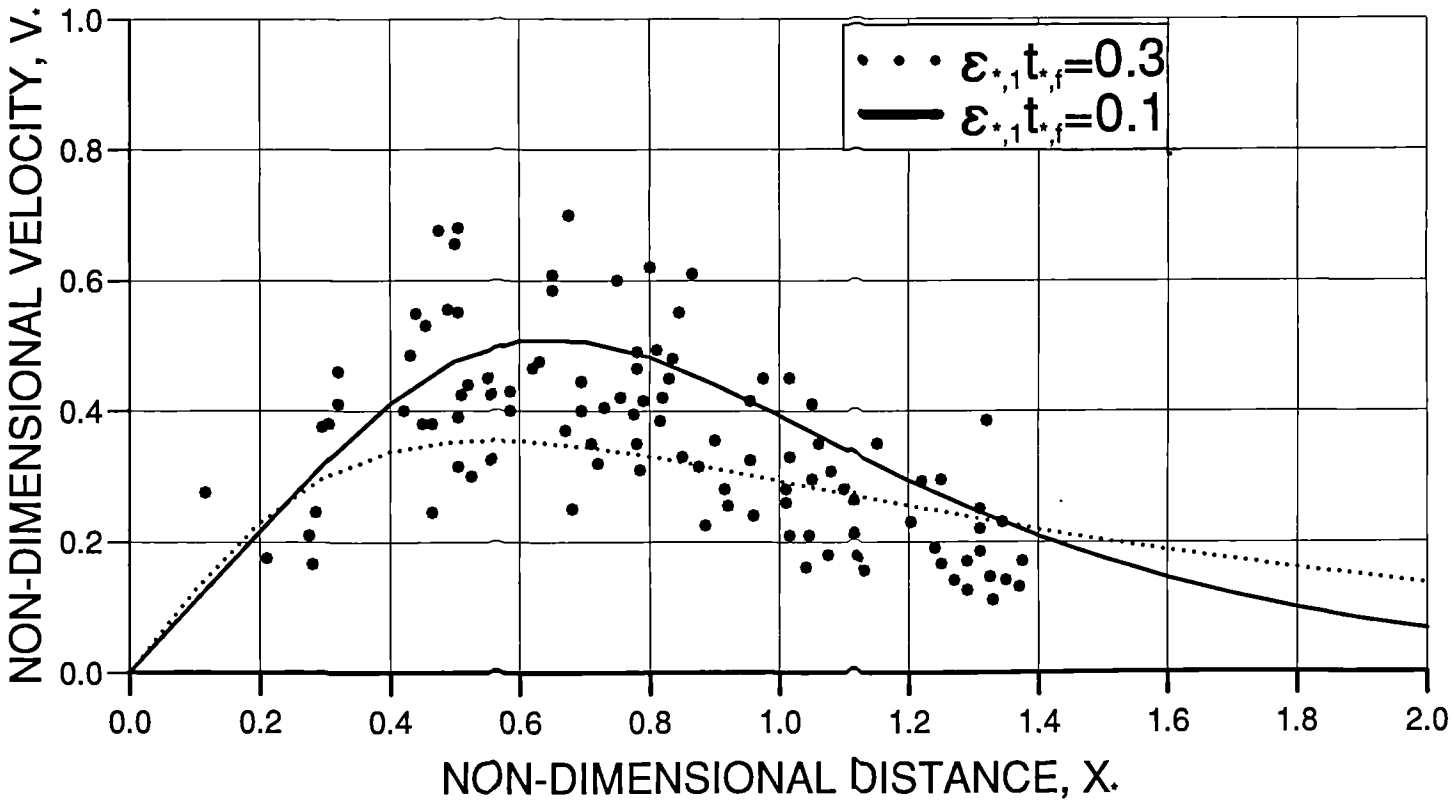

Fig. 5.7 Comparison of the present model results and measurements.

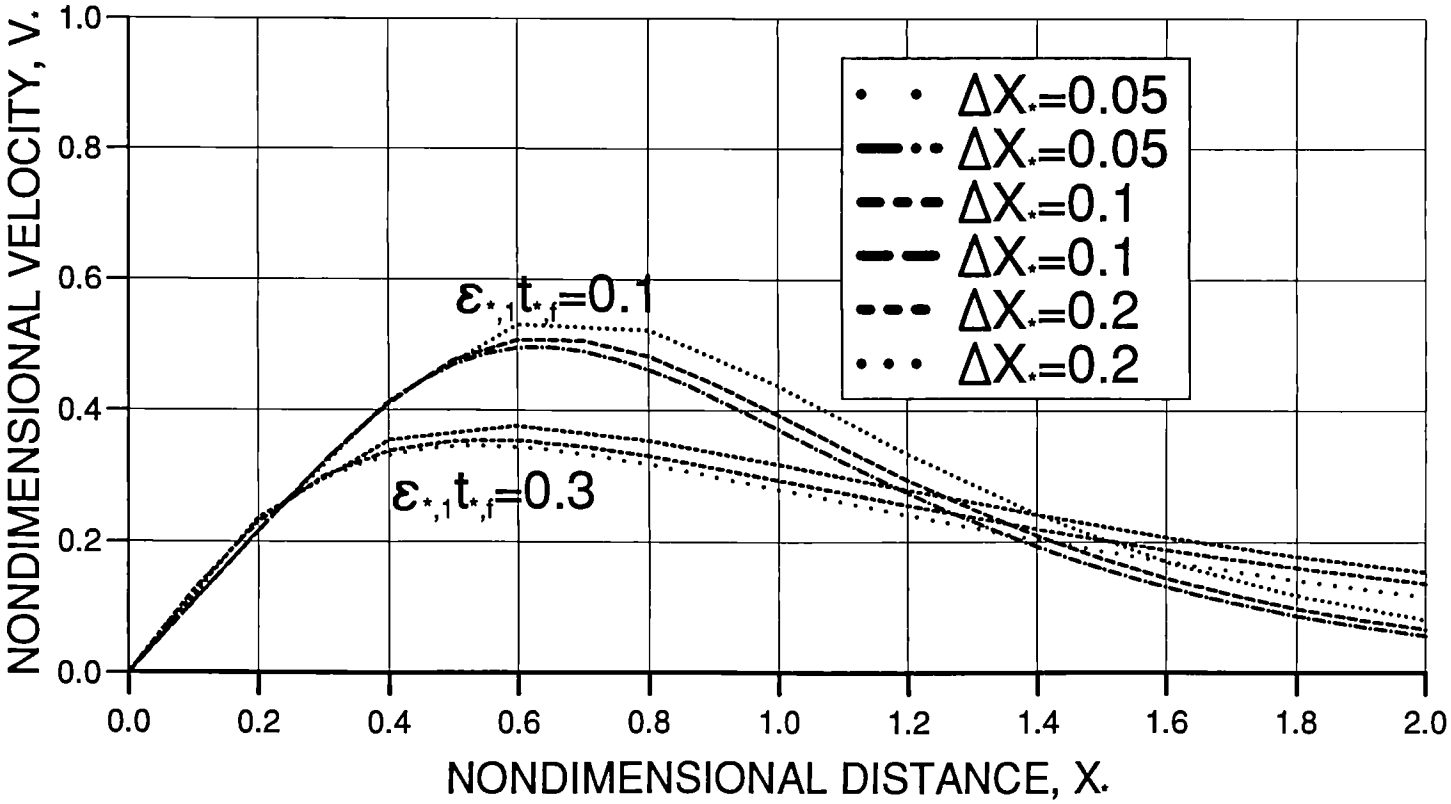

Fig. 5.8 The effect of horizontal grid size on the velocity profile.

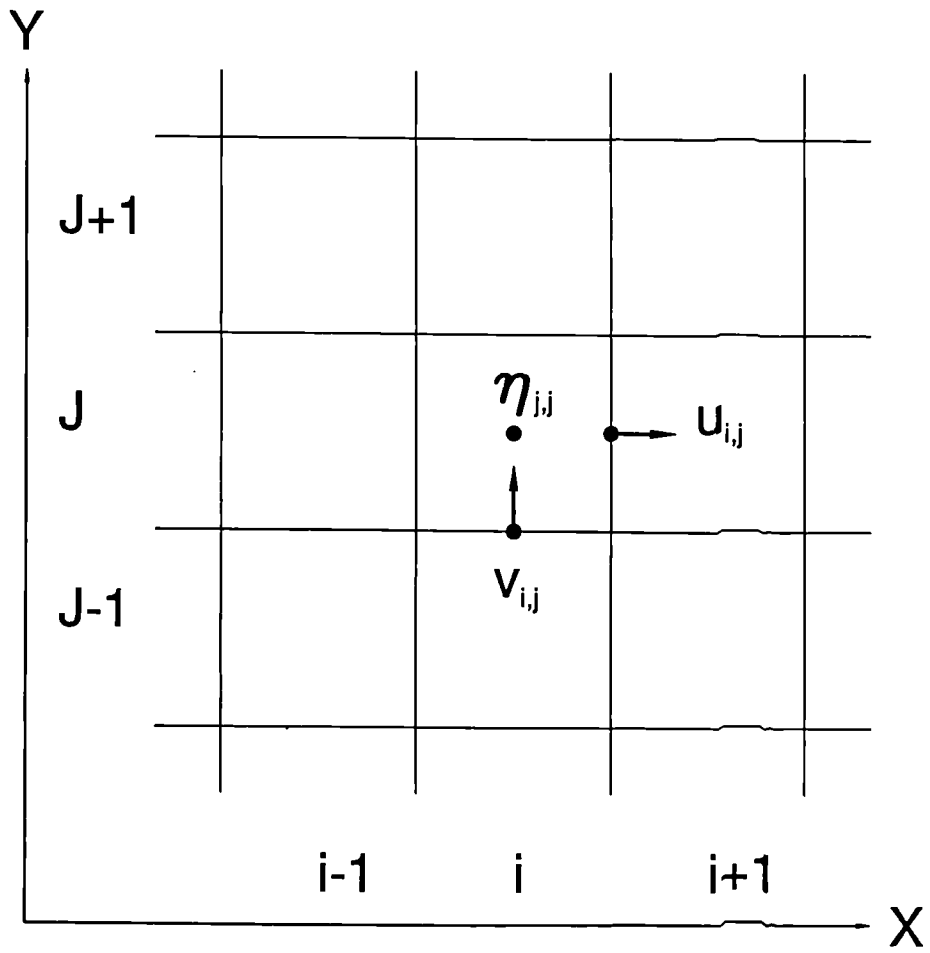

Fig. 5.9 Wave-induced flow model grid.

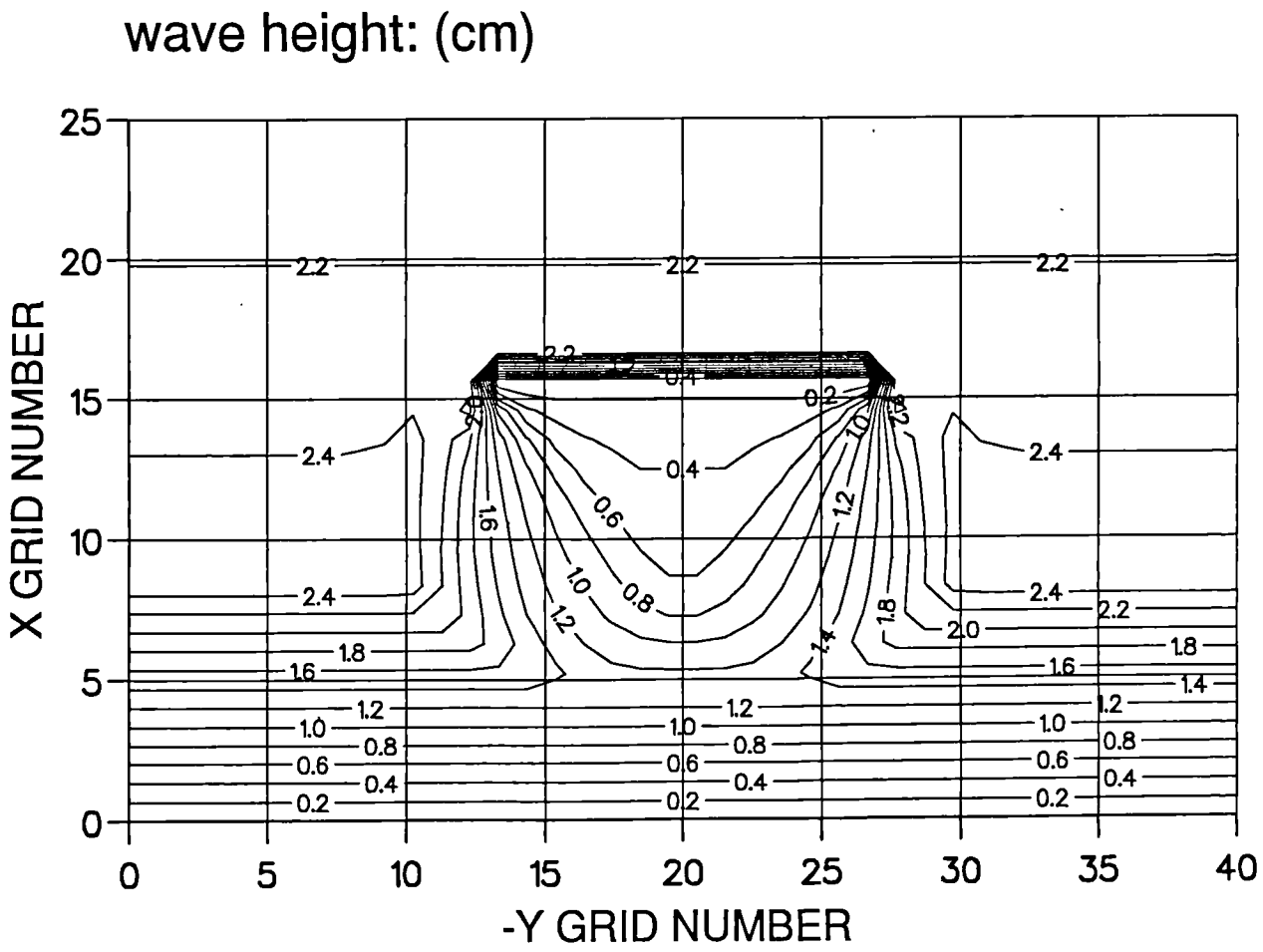

Fig. 5.10 Calculated wave height distribution around a detached breakwater.

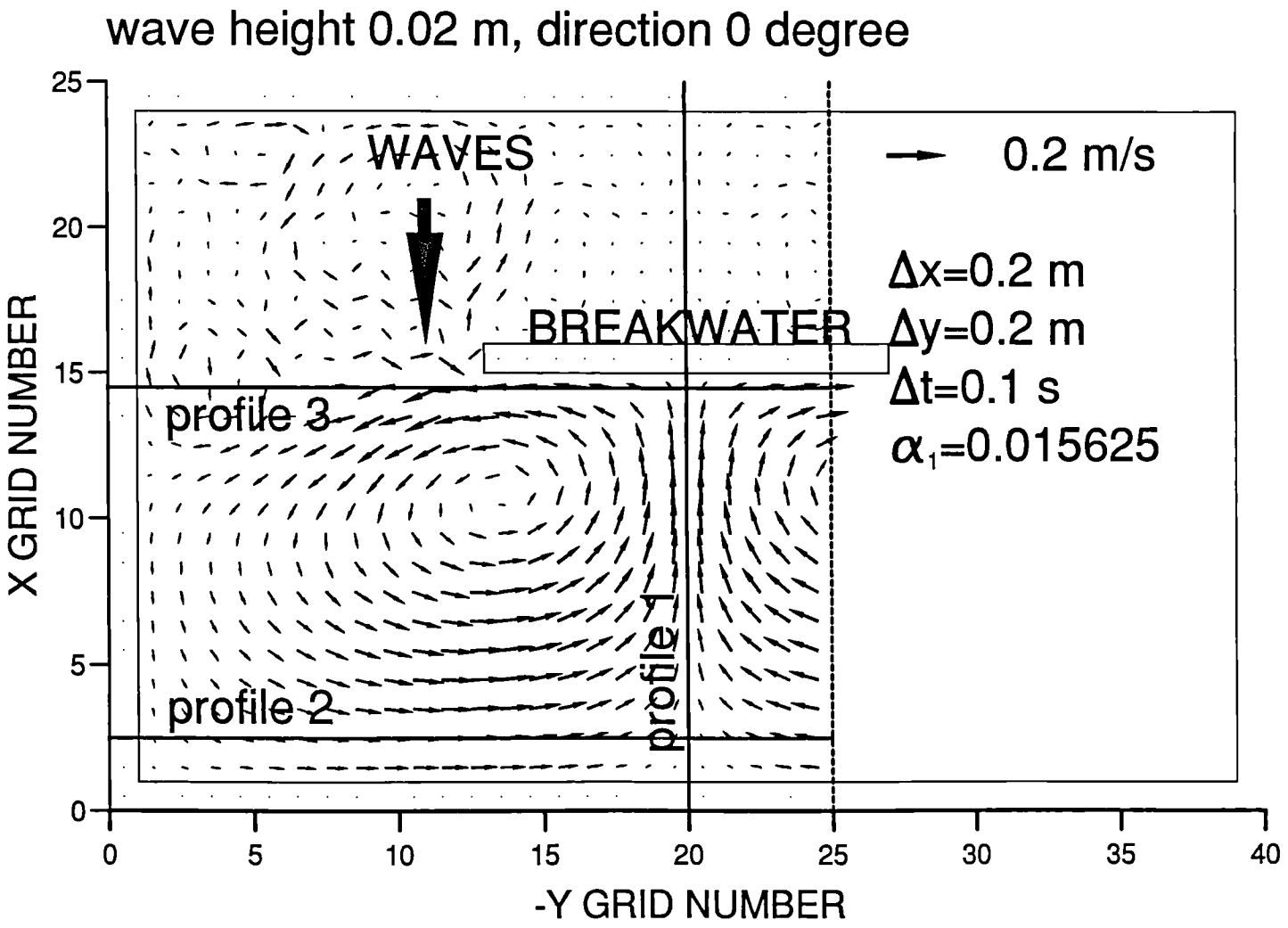

Fig. 5.11 Calculated wave-induced flow vectors around a detached breakwater.

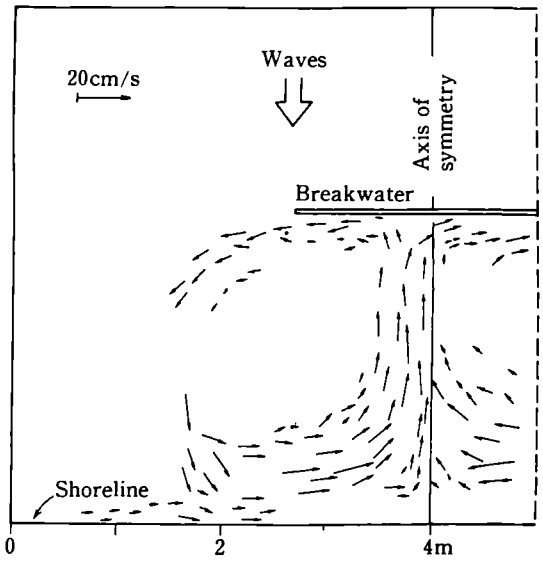

ig. 5.12 Measured flow field around a detached breakwater (Nishimura et al., 1985).

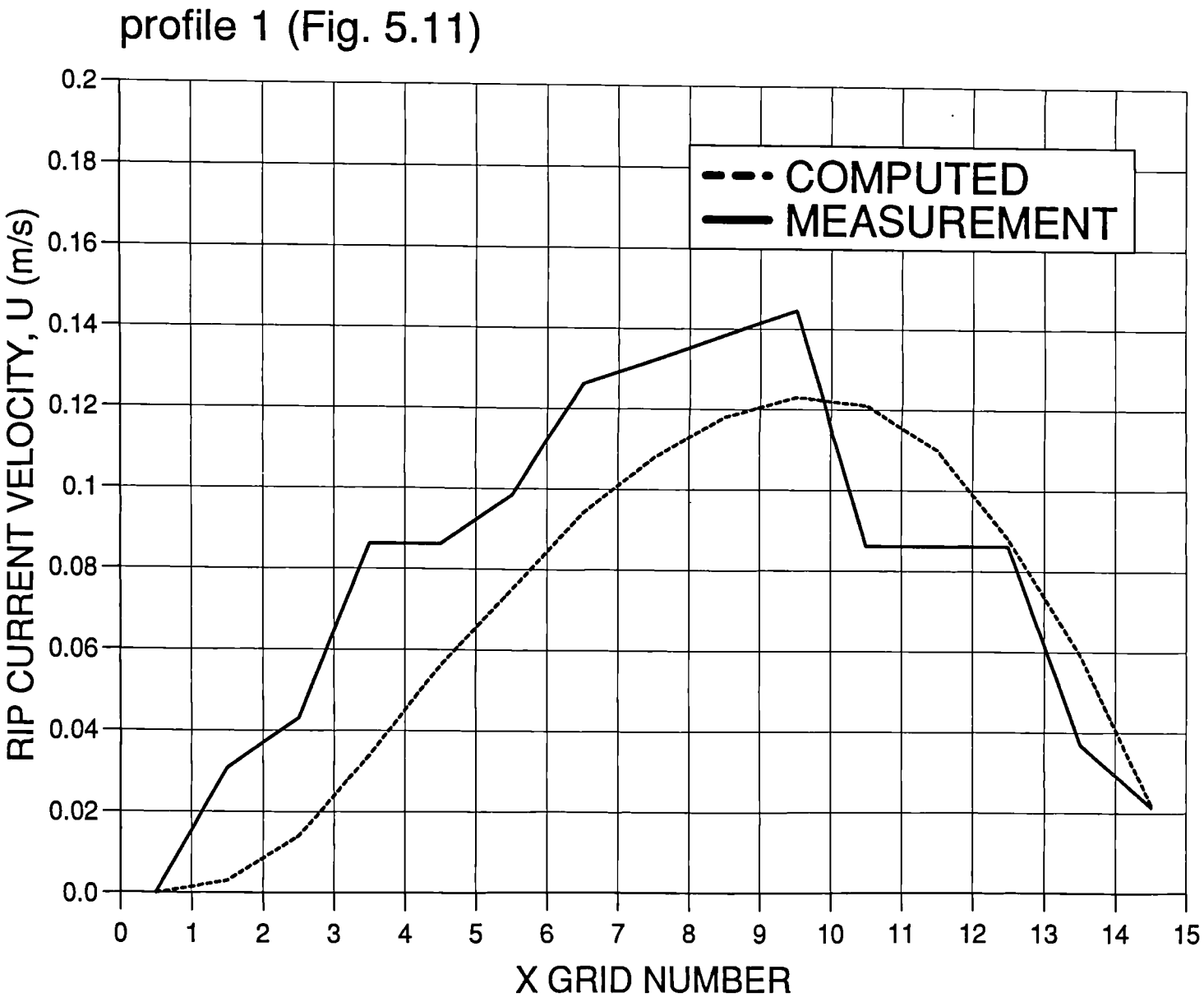

Fig. 5.13a Comparison of calculated and measured rip current profiles behind a breakwater: profiles 1.

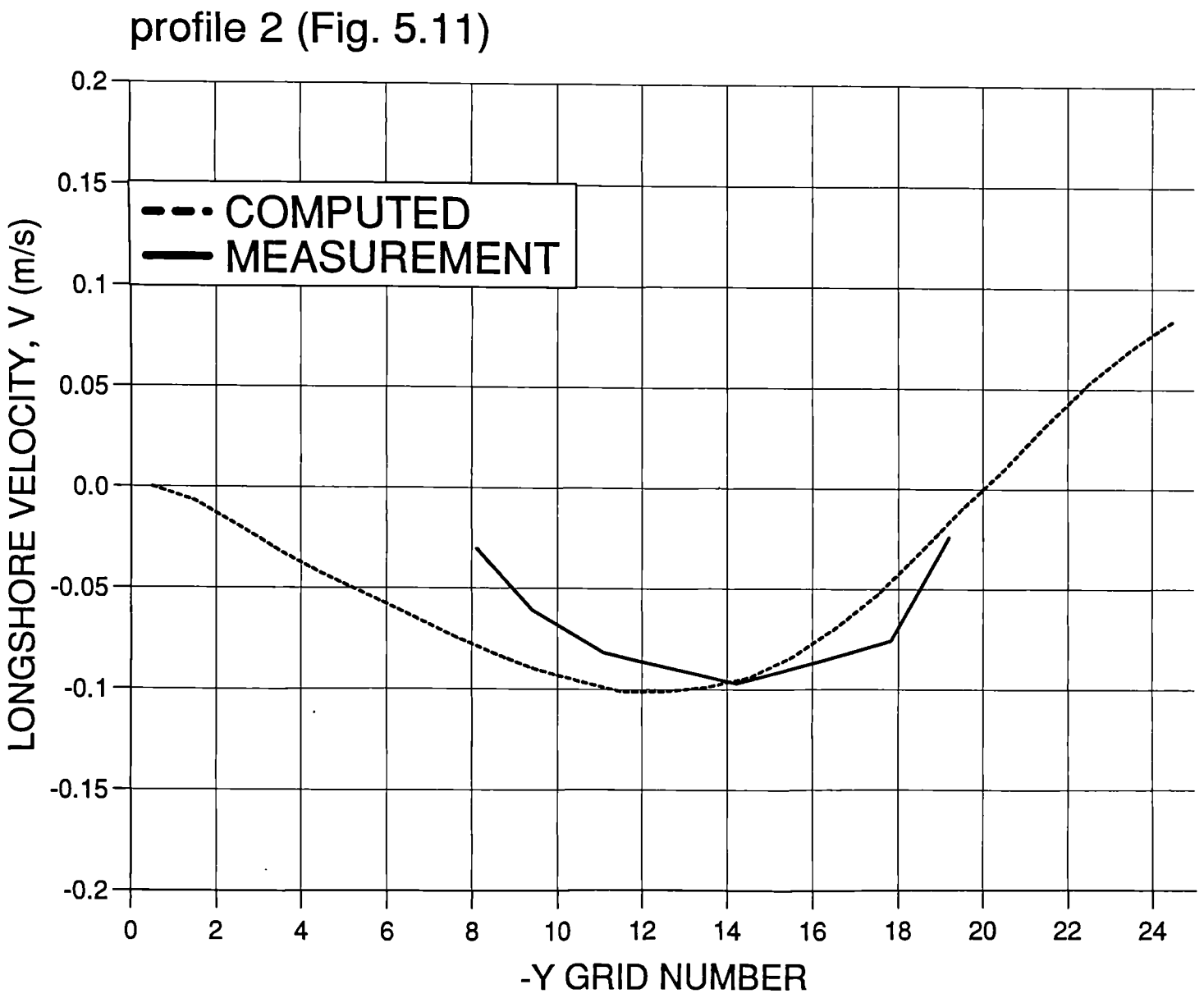

Fig. 5.13b Comparison of calculated and measured rip current profiles behind a breakwater: profiles 2.

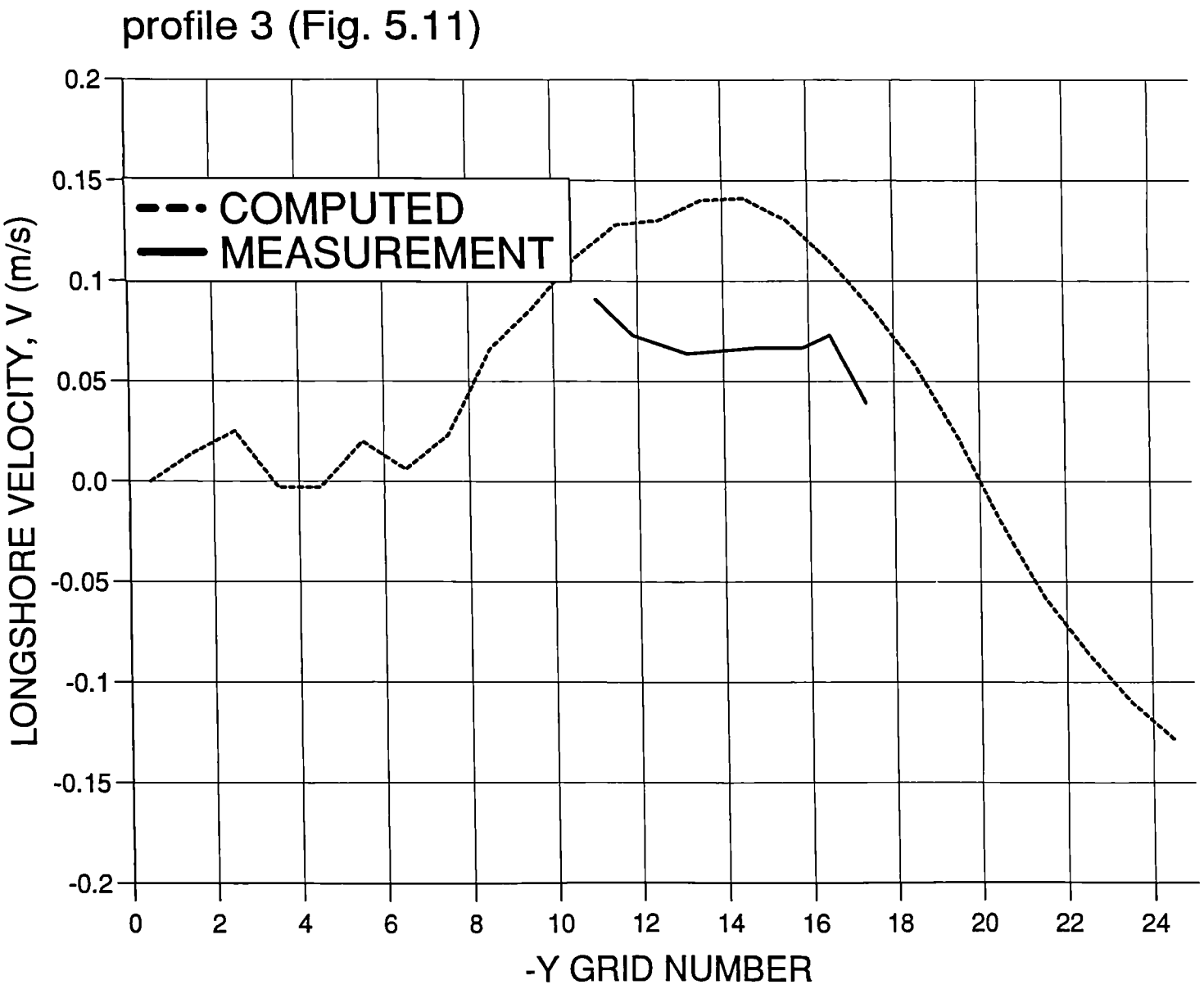

Fig. 5.13c Comparison of calculated and measured rip current profiles behind a breakwater: profiles 3.

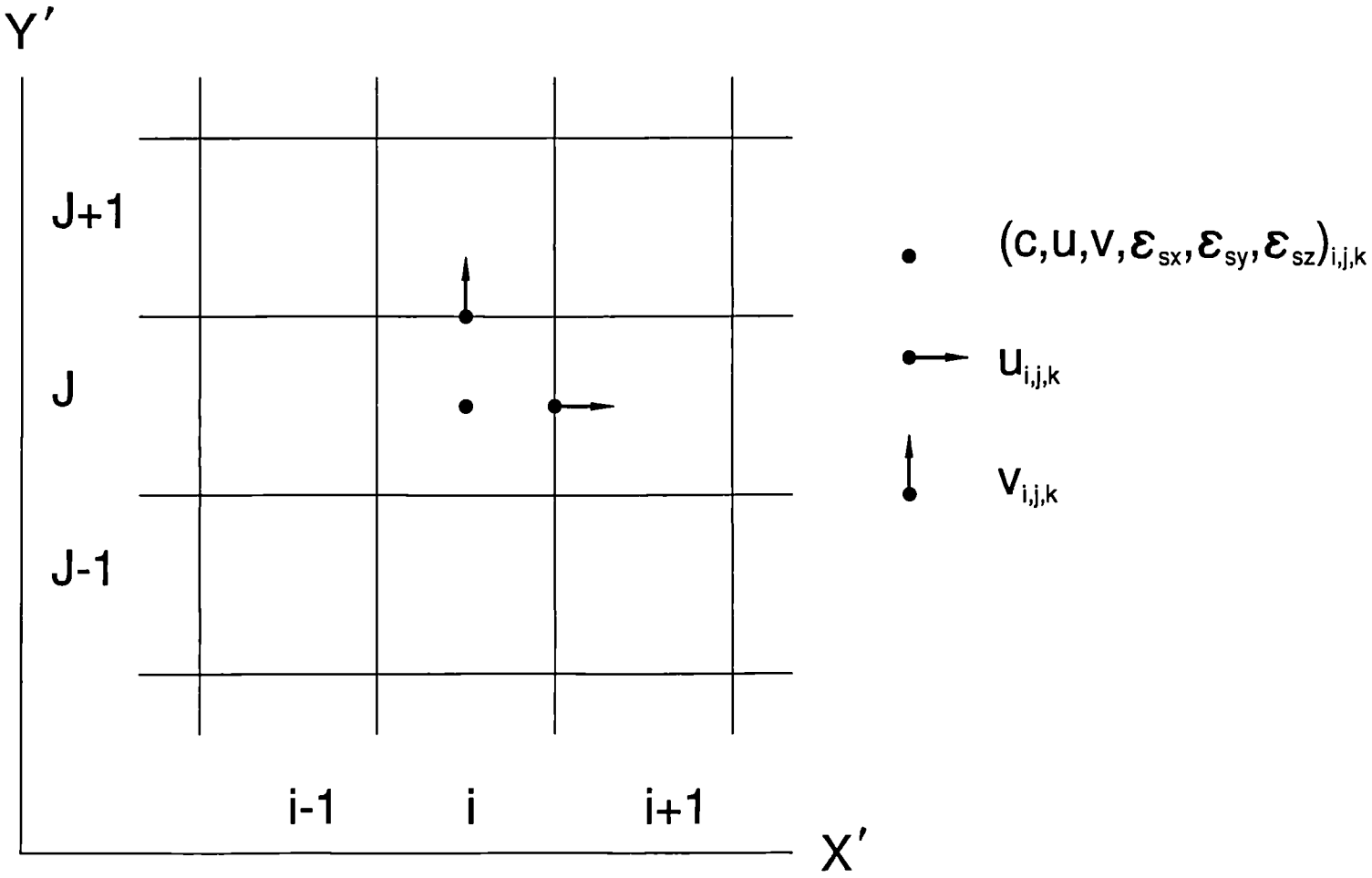

Fig. 6.1a Three-dimensional suspended sediment model grid: plan.

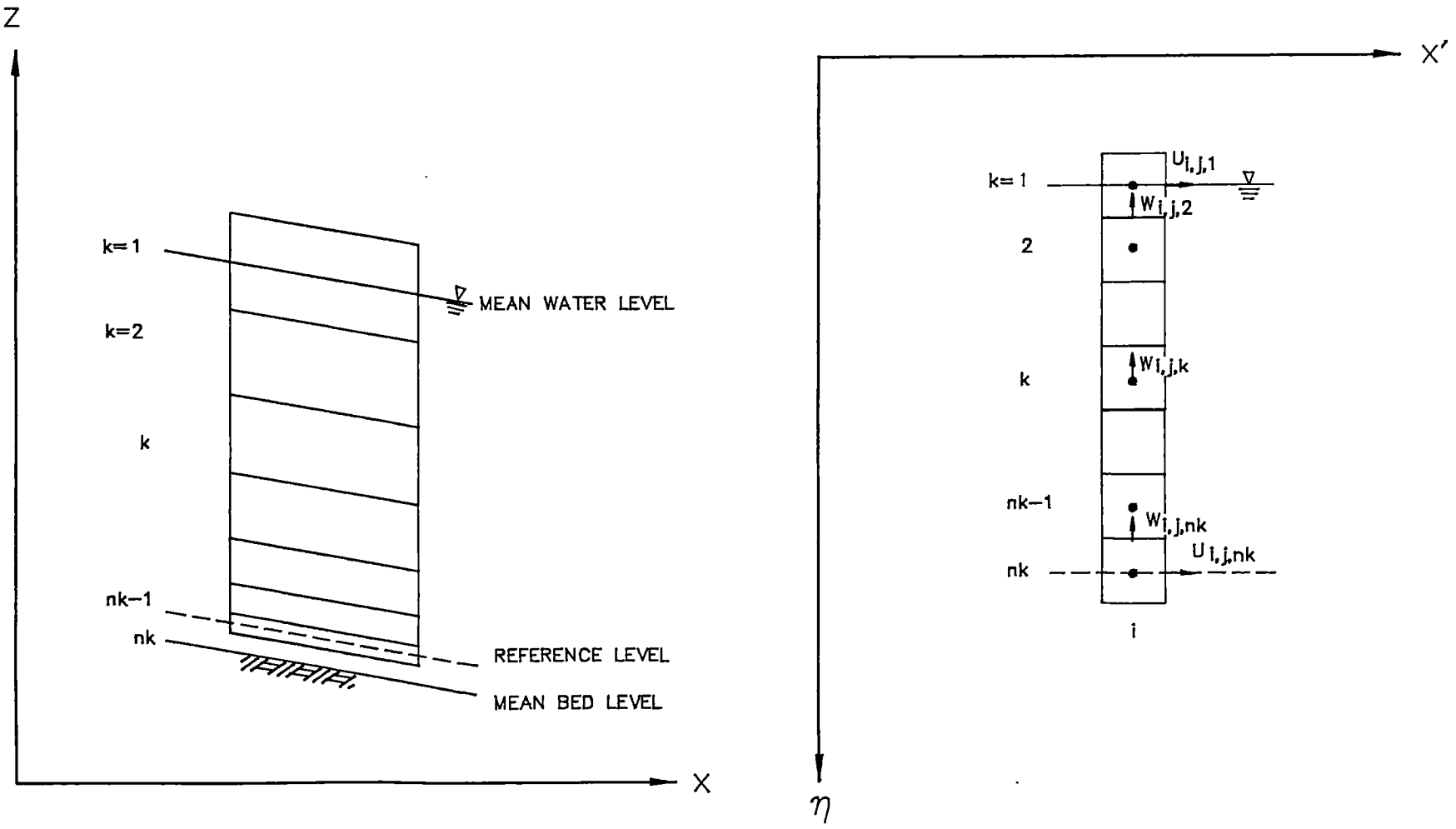

Fig. 6.1b Three-dimensional suspended sediment model grid: vertical.

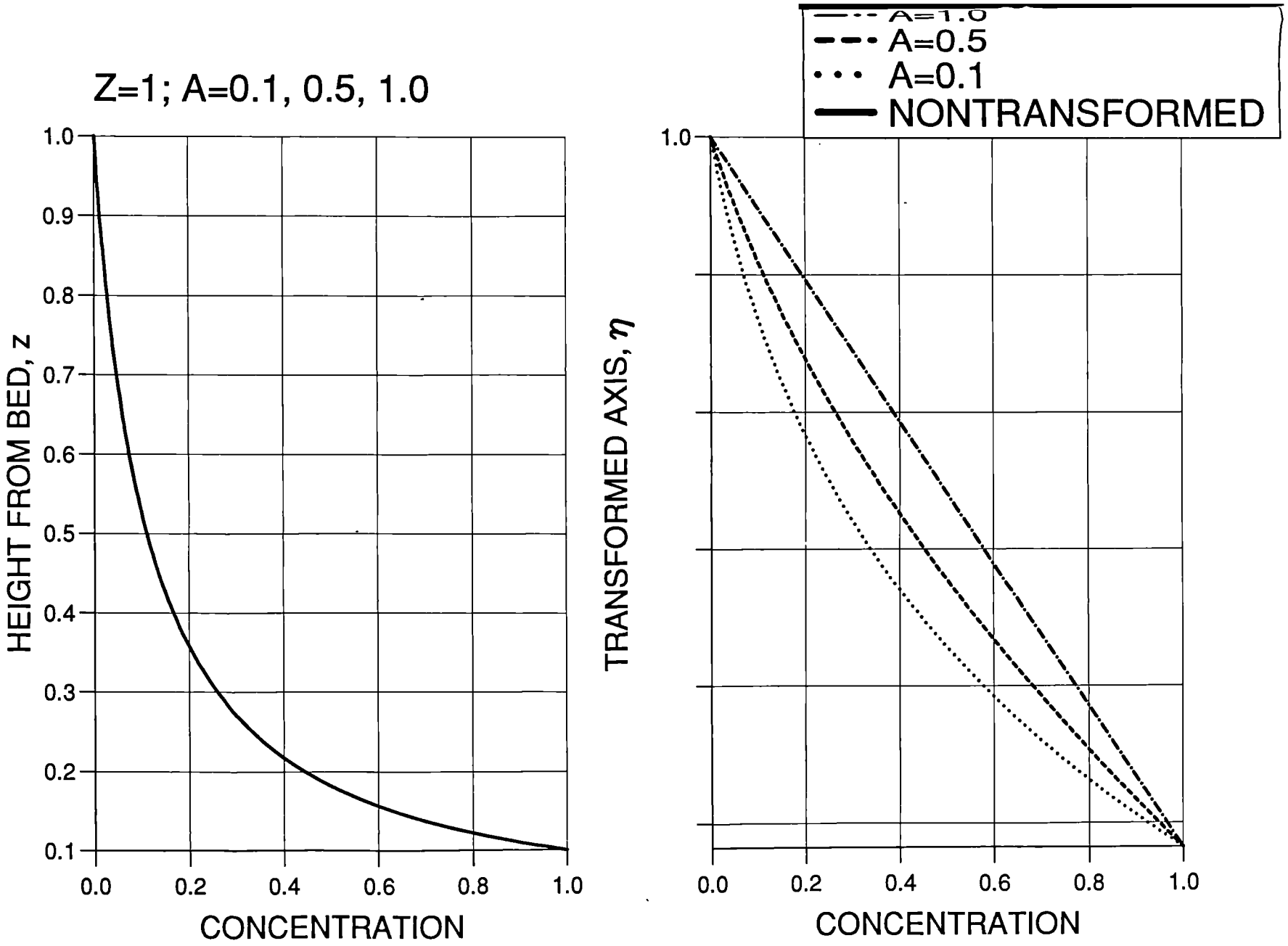

Fig. 6.2 The effect of coordinate transformation on the suspended sediment concentration profile.

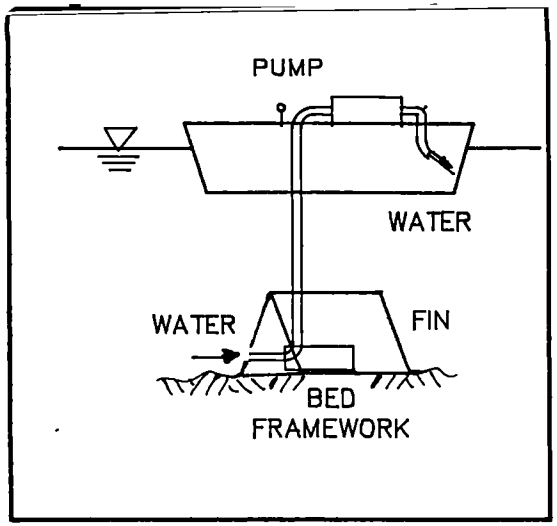

a) PUMP SAMPLER

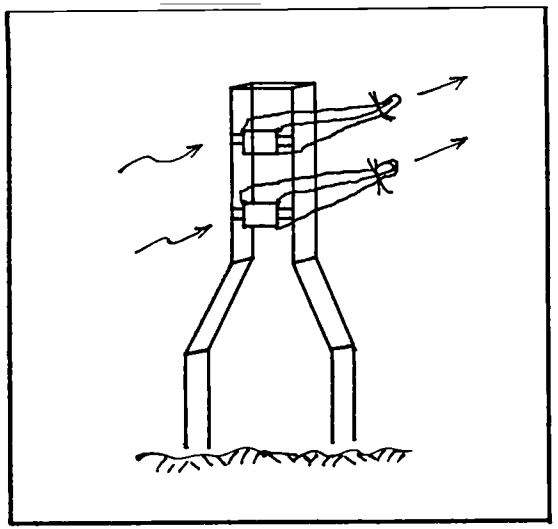

b) STREAMER TRAP

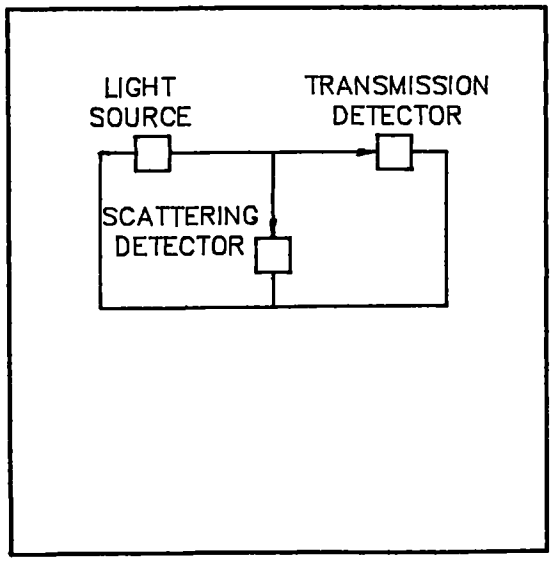

c) OPTICAL PROBE

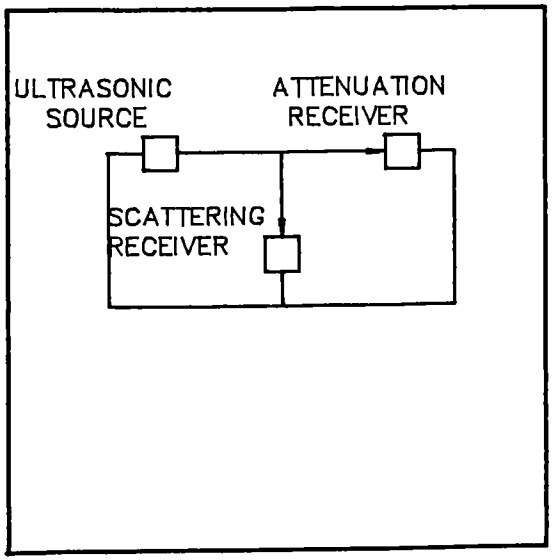

d) ACOUSTICAL PROBE

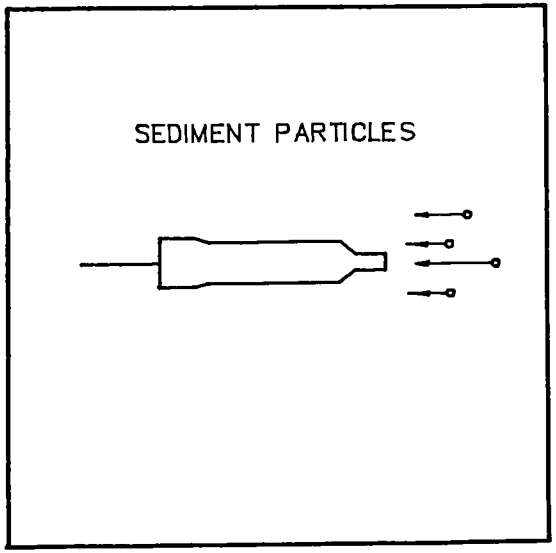

e) IMPACT PROBE

Fig. 6.3 Existing devices for measuring the near bed suspended sediment concentration.

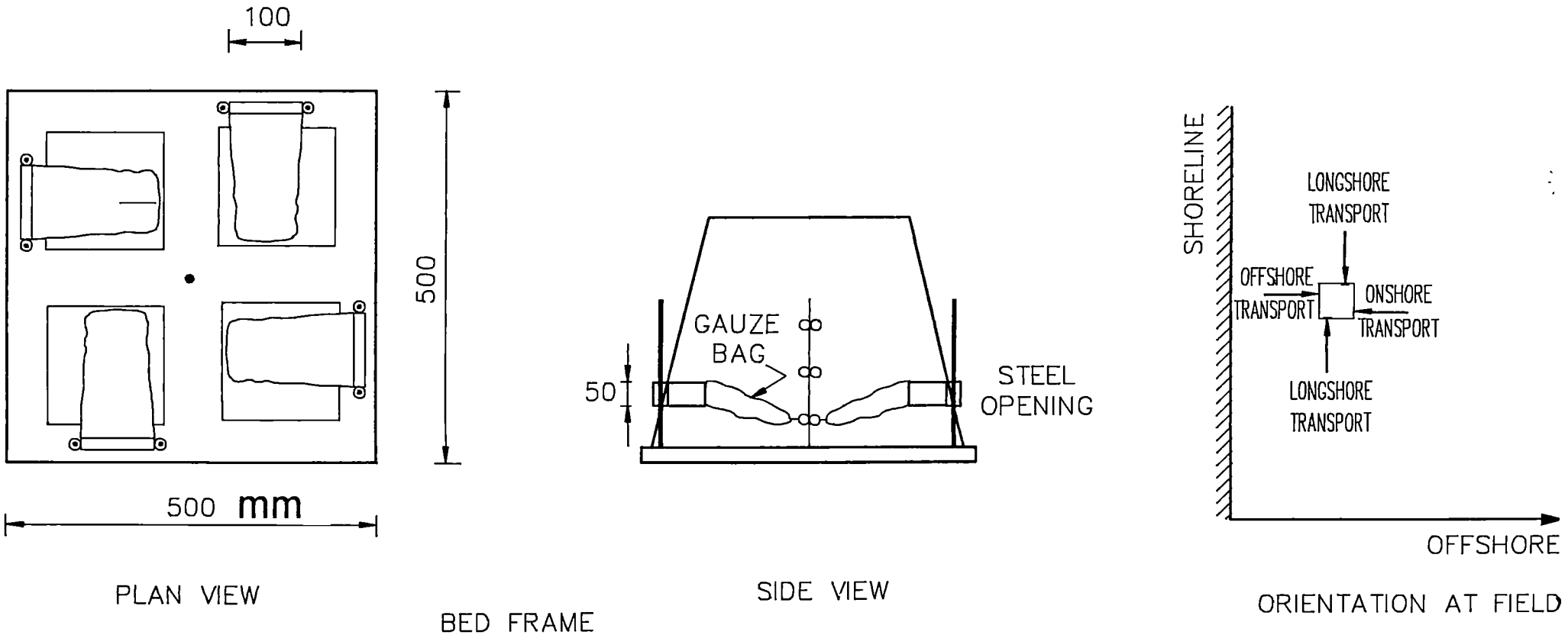

Fig. 6.4 The four-trap device for measuring the near bed suspended sediment concentration.

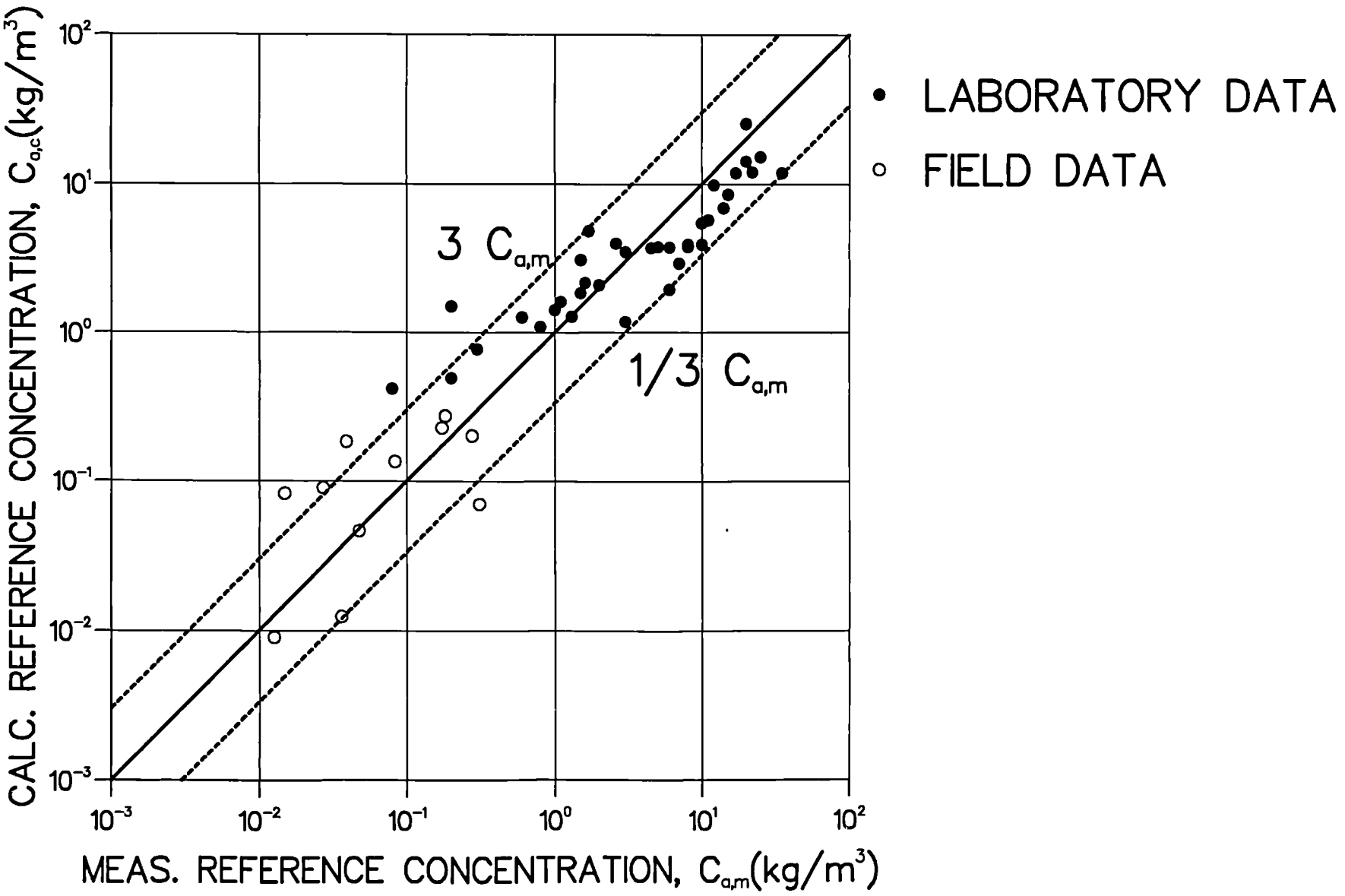

Fig. 6.5 Comparison of the present formula and measurements: suspended sediment concentration.

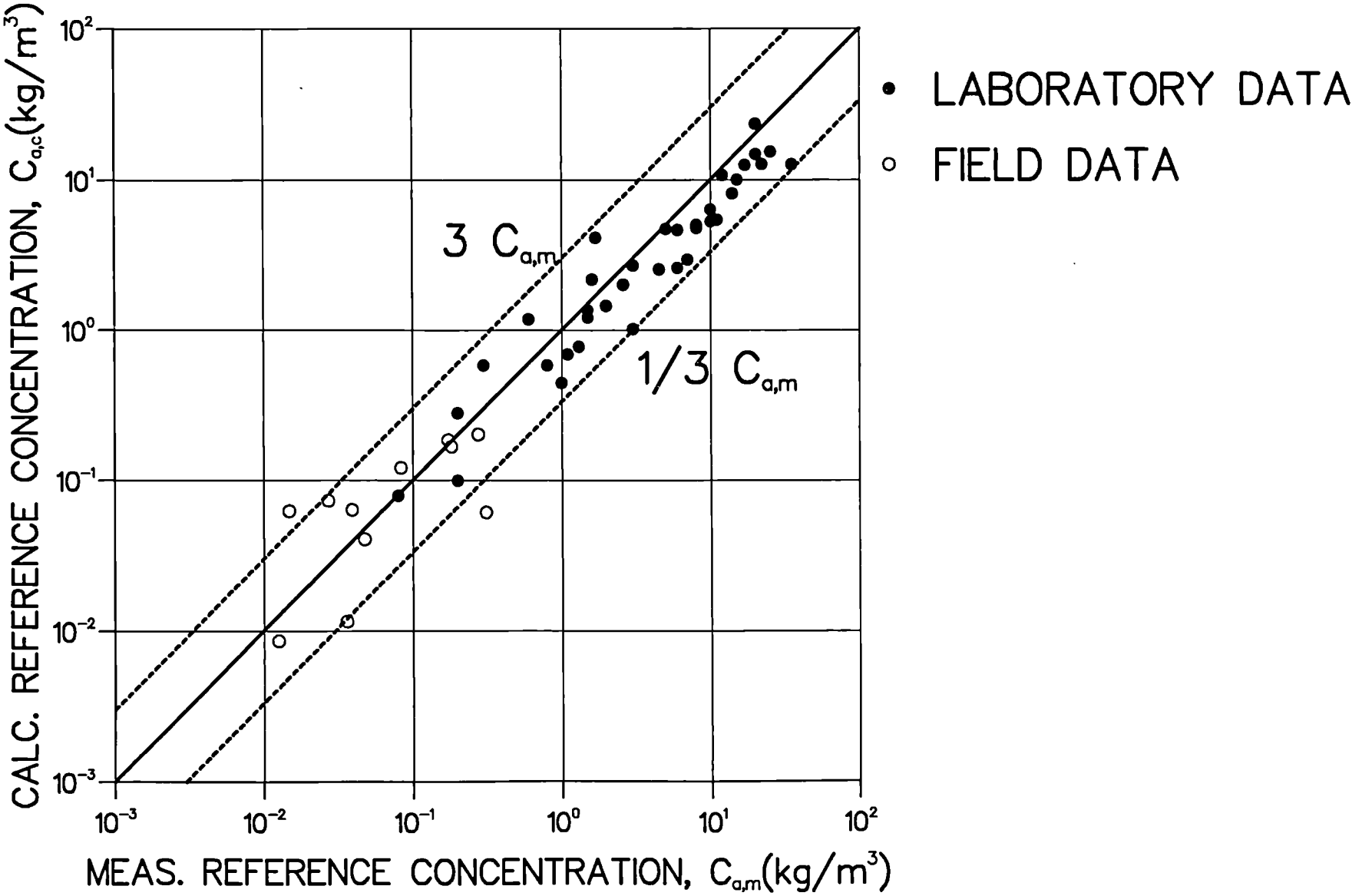

Fig. 6.6 Comparison of the van Rijn formula and measurements: suspended sediment concentration.

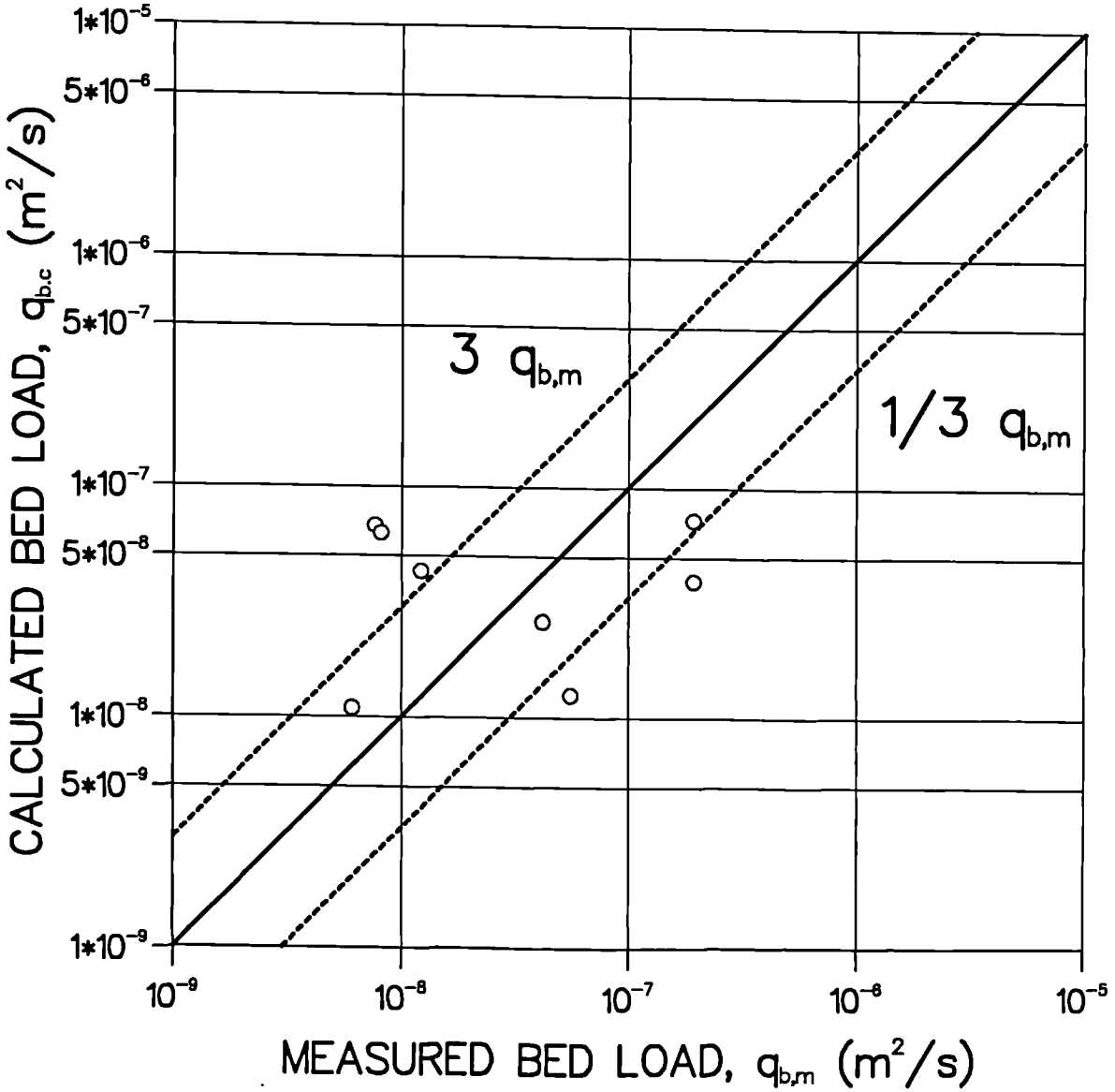

Fig. 6.7 Comparison of the present formula and measurements: bed load.

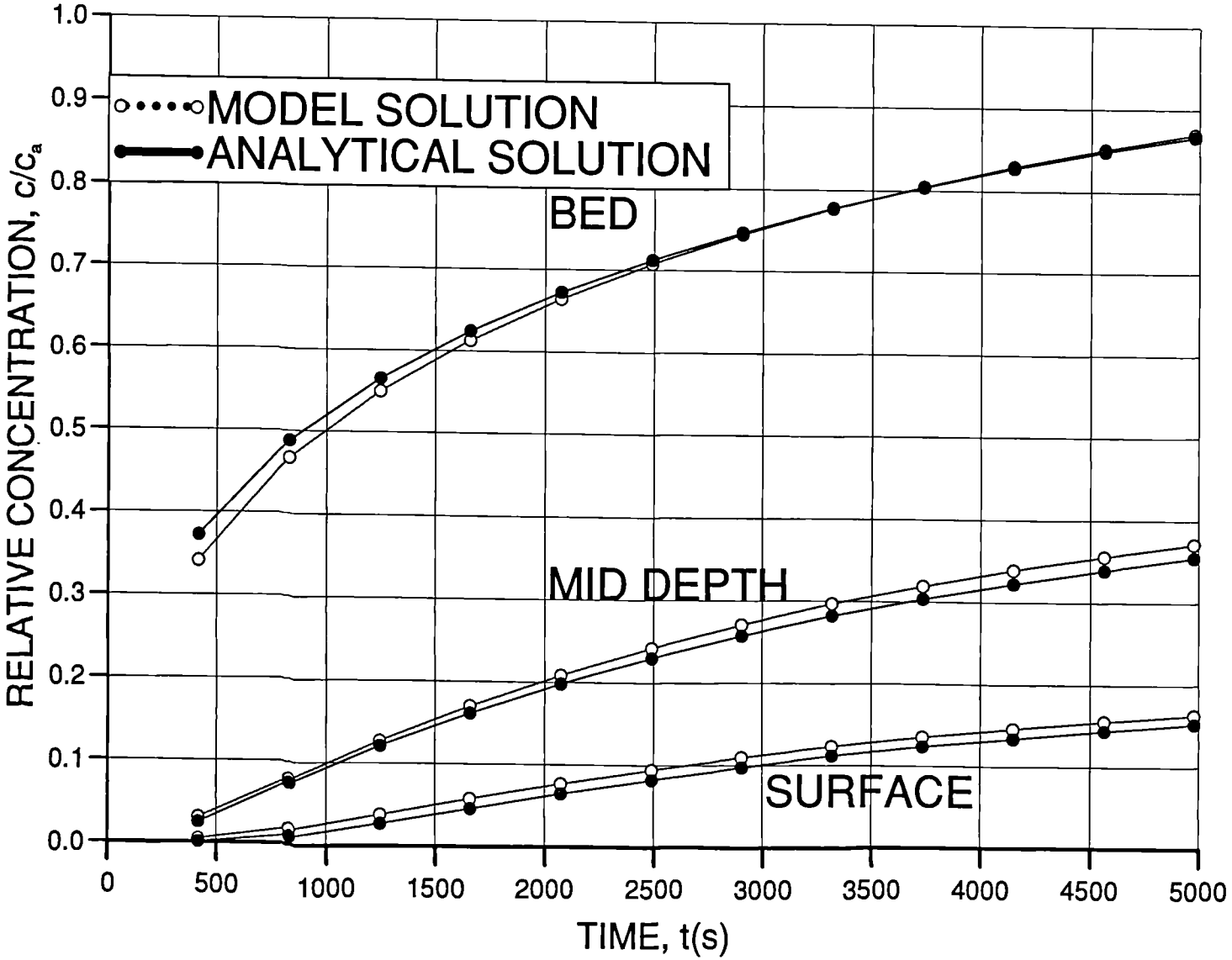

Fig. 6.8 Comparison of the present model results with the Dobbins(1944) analytical solution.

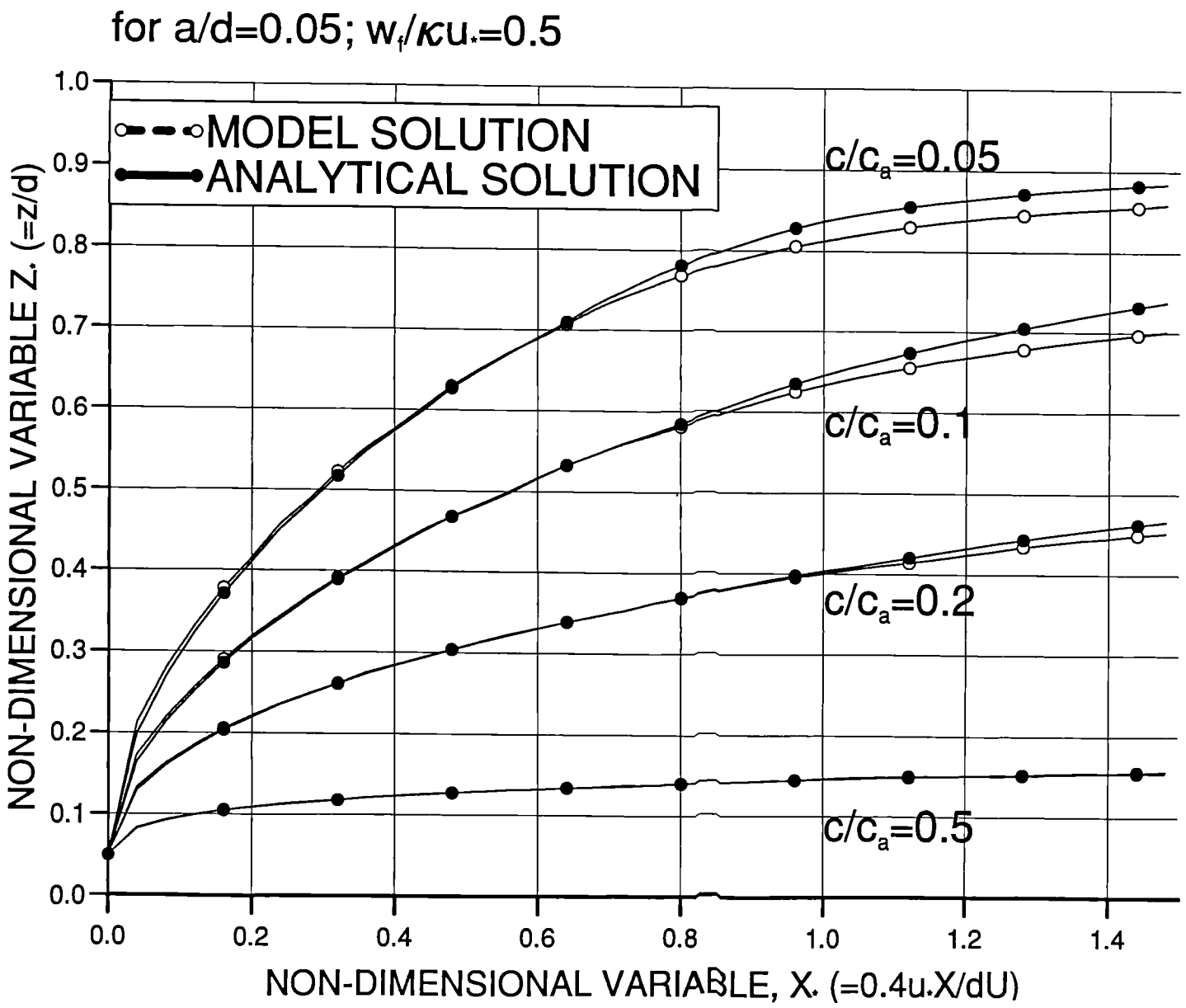

Fig. 6.9 Comparison of the present model results with the Hjelmfelt and Lenau(1970) solution.

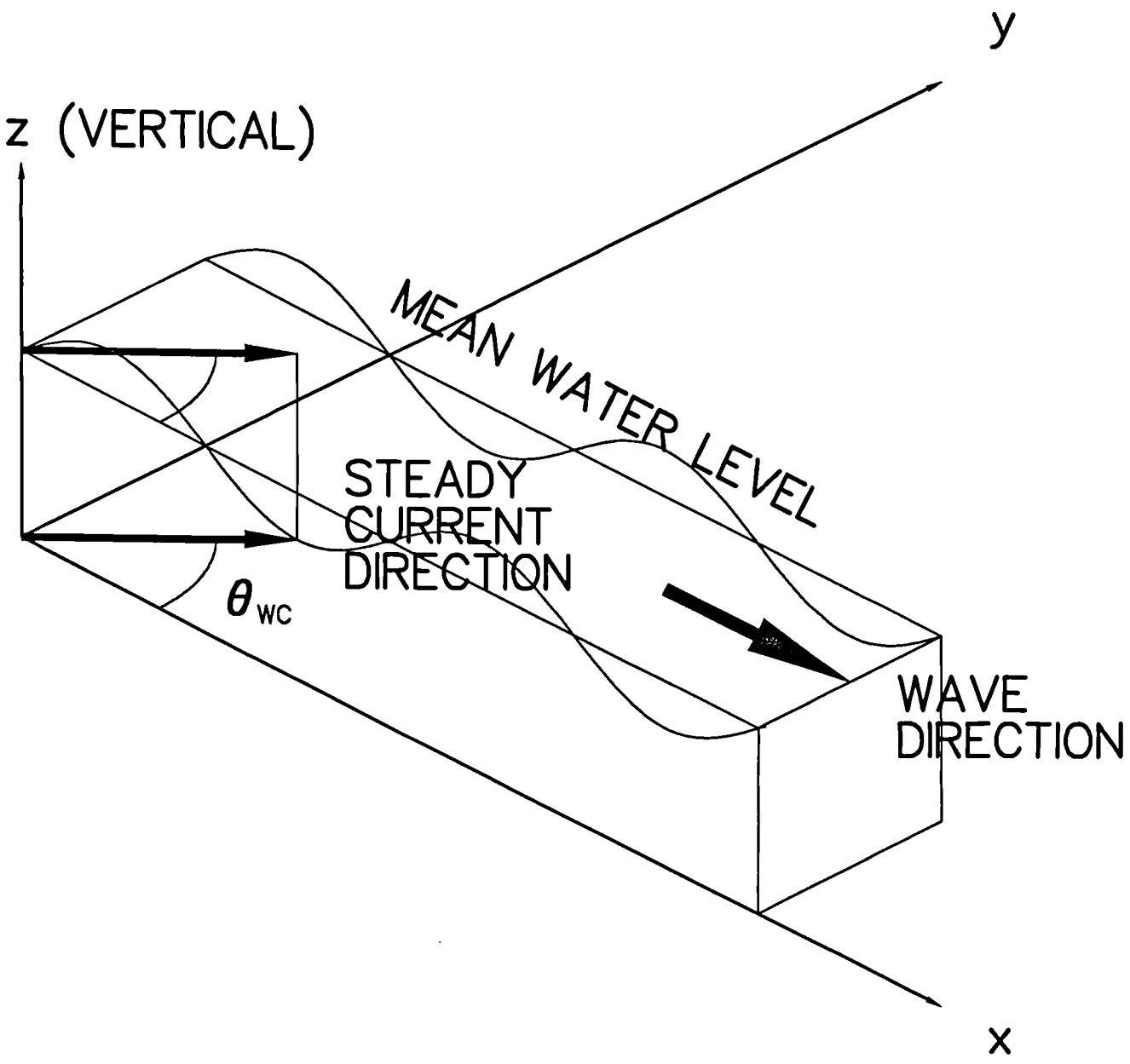

Fig. 7.1 Schematic diagram of two-dimensional vertical boundary layer model.

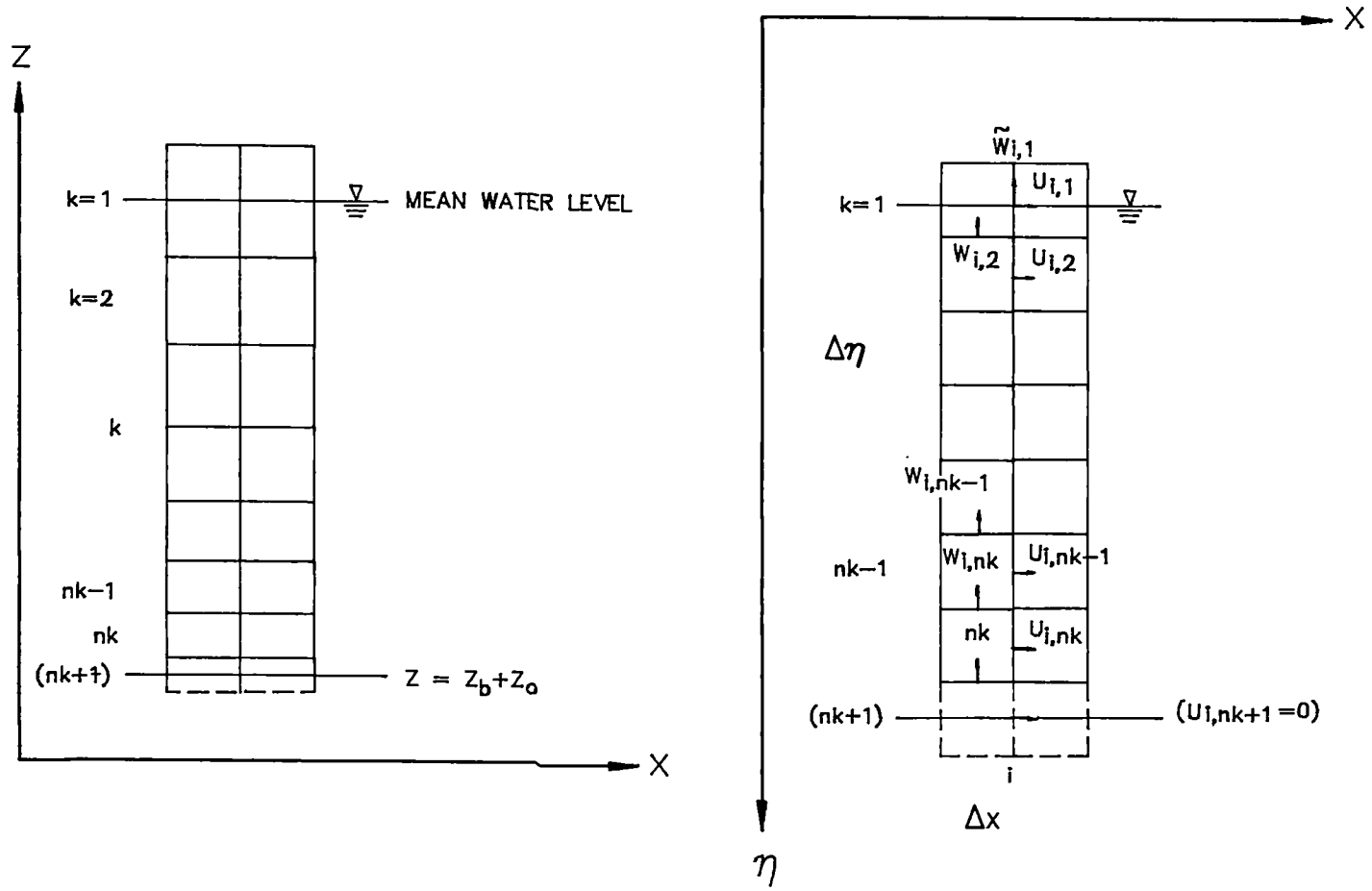

Fig. 7.2 Two-dimensional vertical boundary layer model grid.

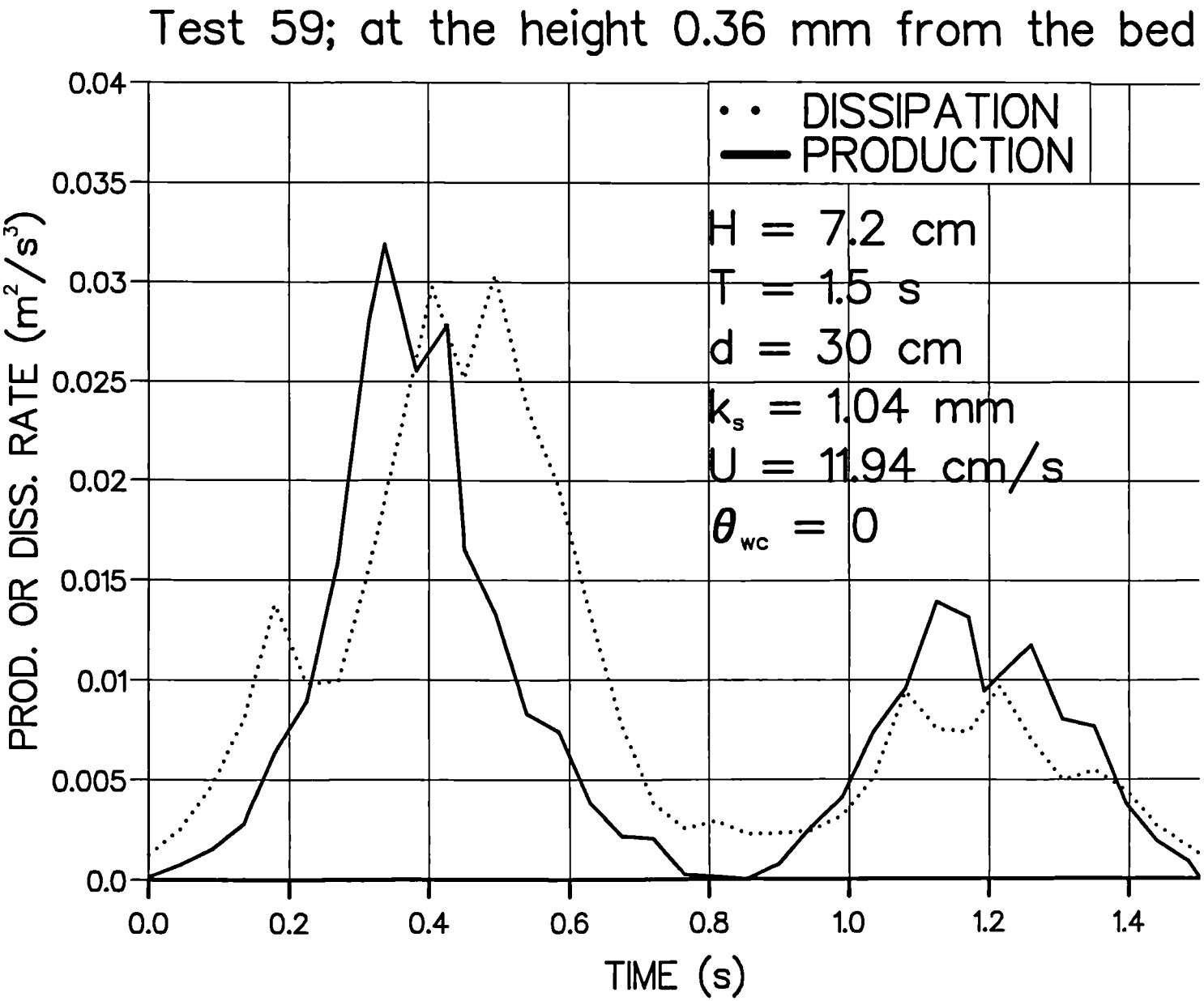

Fig. 7.3 Turbulence energy production and dissipation rate (after Taplin, 1989).

in the Whole Boundary Layer over a Ripple (Case 7)

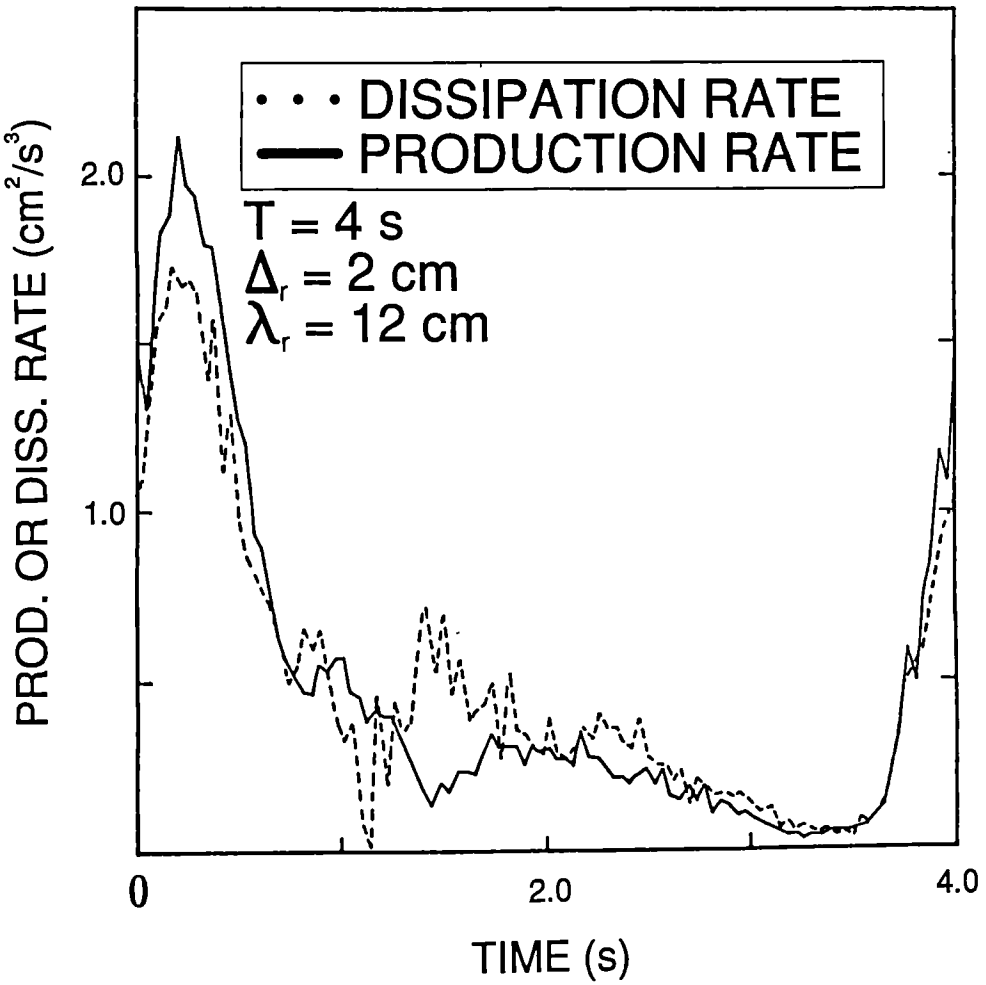

Fig. 7.4 Turbulence energy production and dissipation rate (after Sato, 1987).

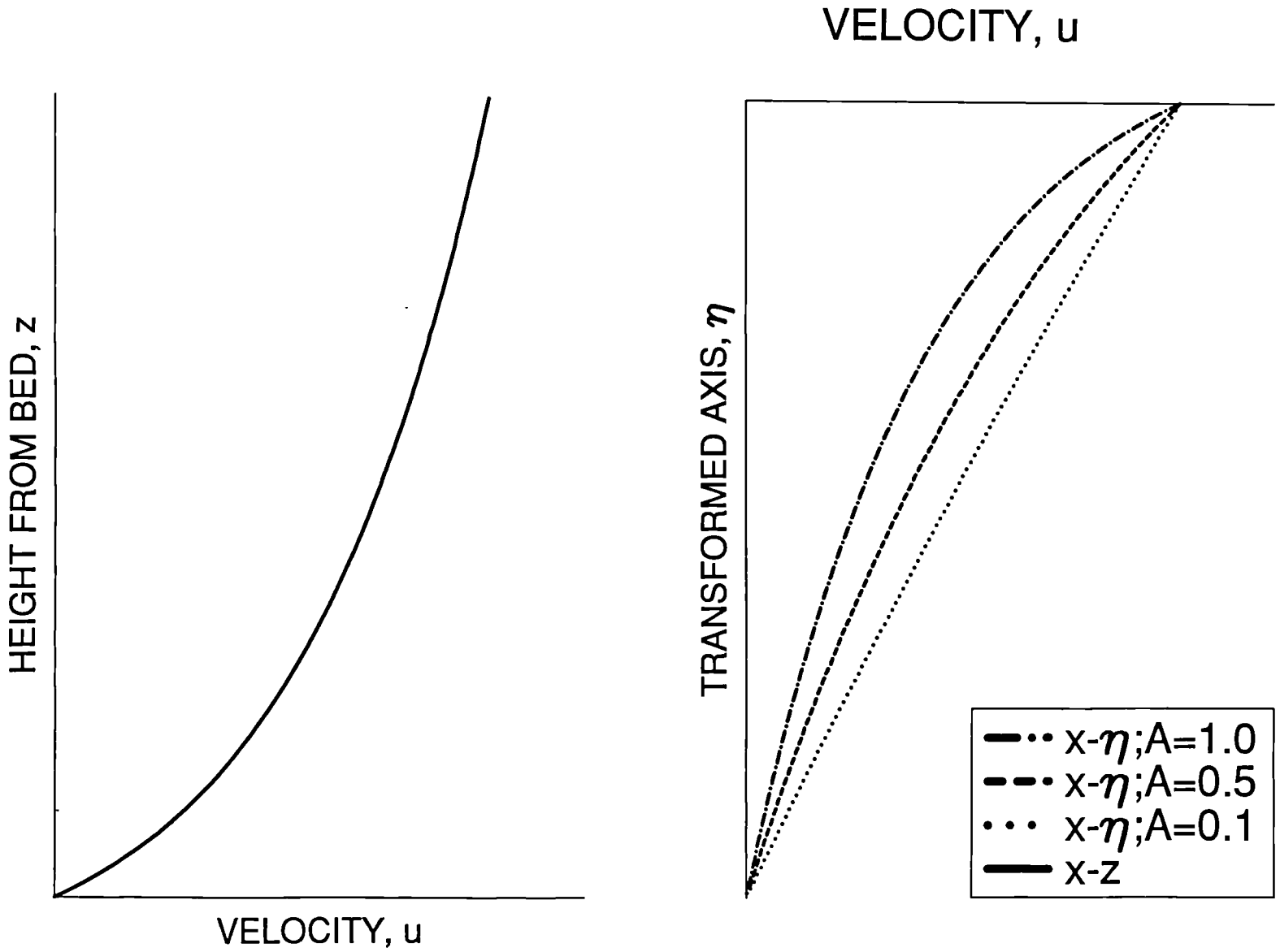

Fig. 7.5 The effect of the grid transformation on a logarithmic velocity profile.

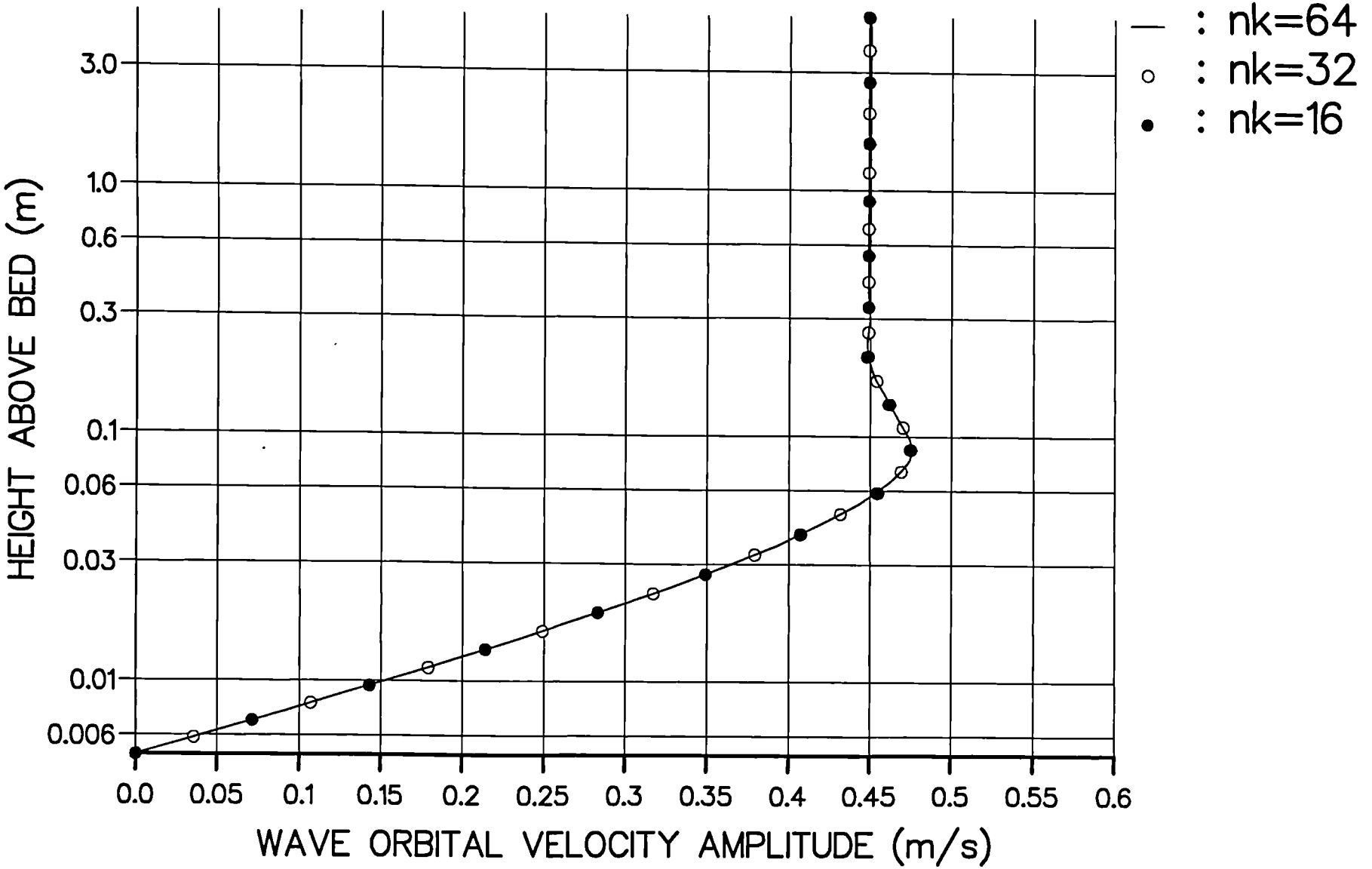

Fig. 7.6 The effect of the number of vertical grid points on orbital velocity amplitude profile.

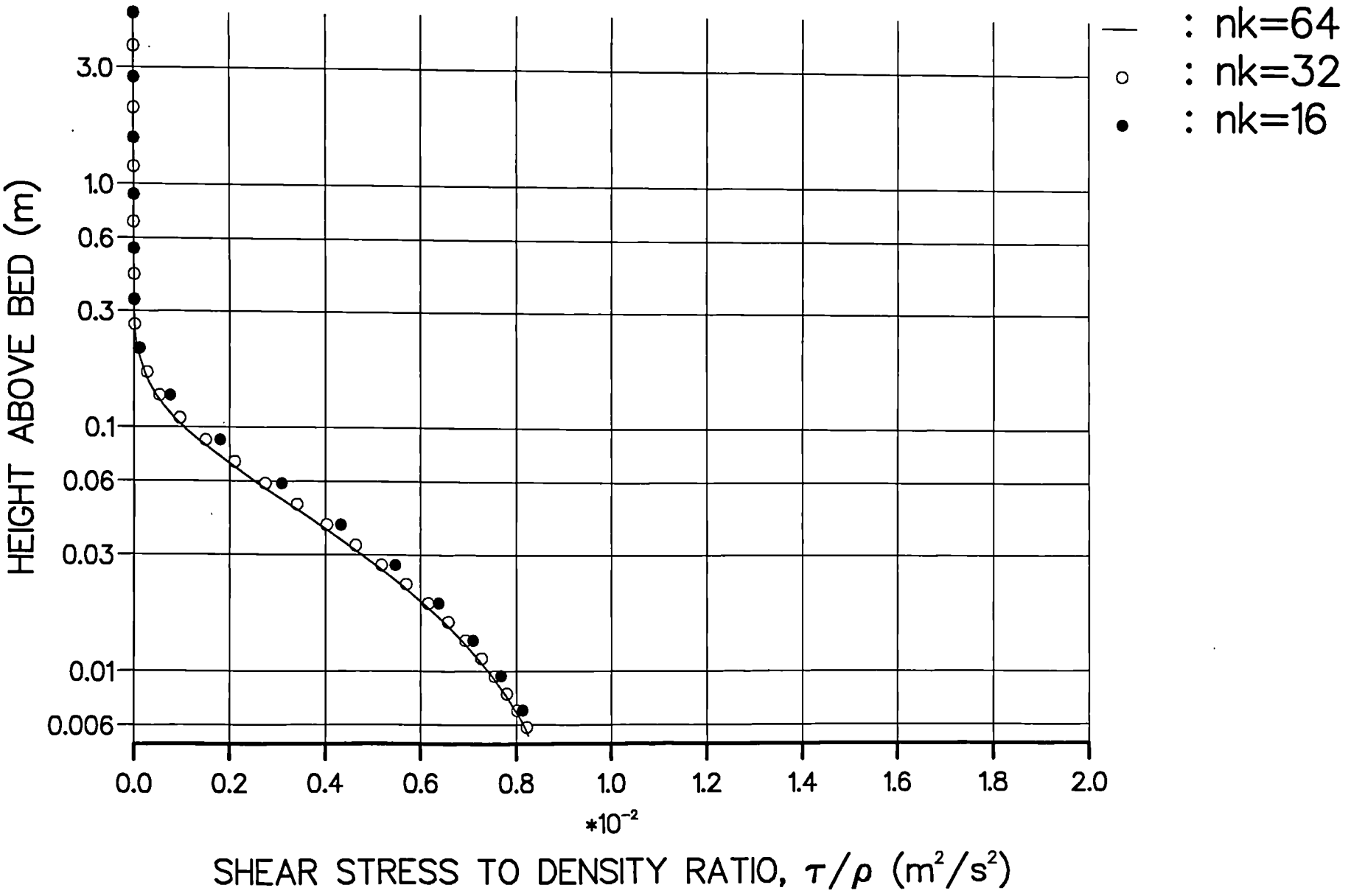

Fig. 7.7 The effect of the number of vertical grid points on shear stress amplitude profile.

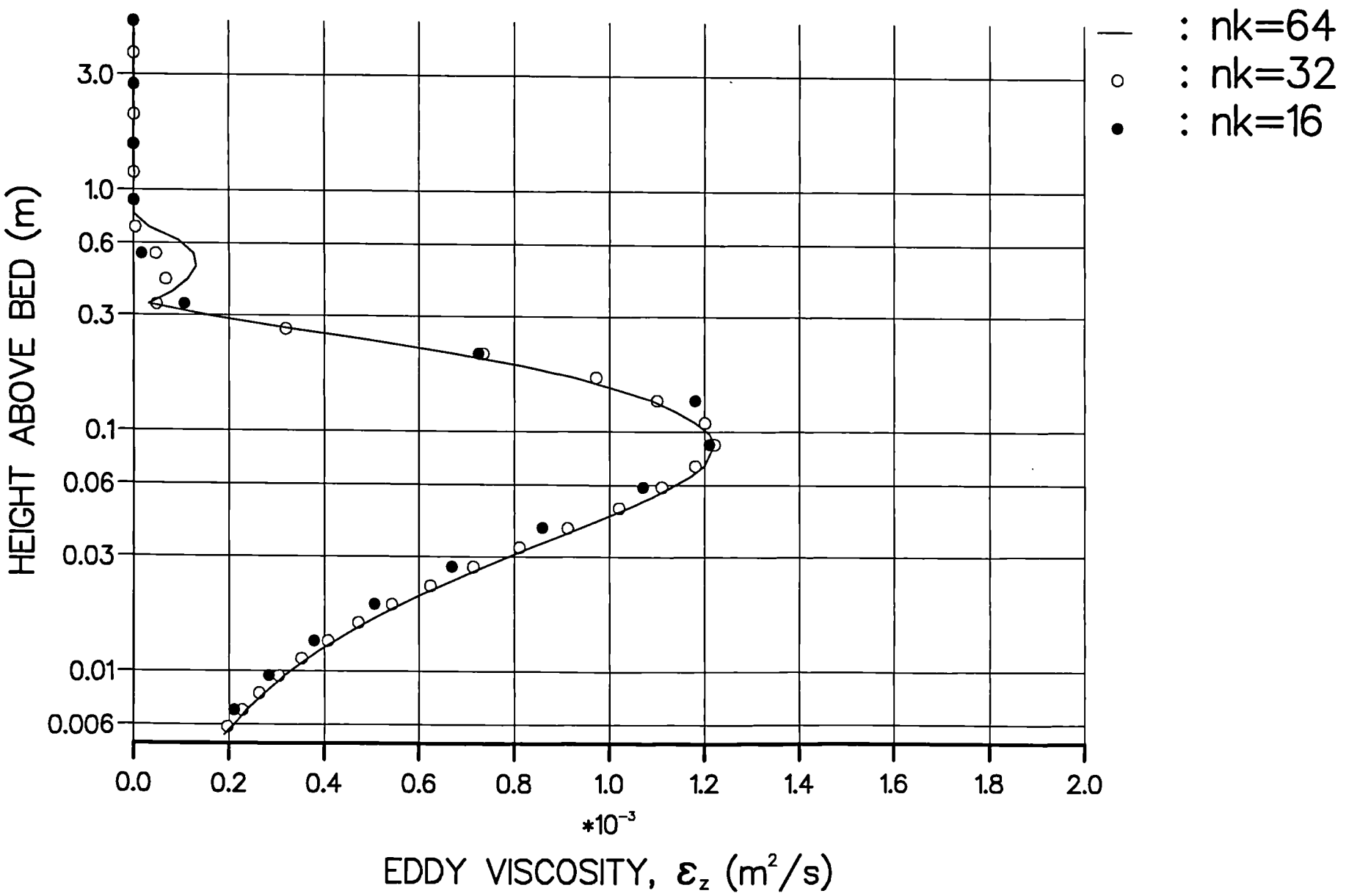

Fig. 7.8 The effect of the number of vertical grid points on the maximum eddy viscosity profile.

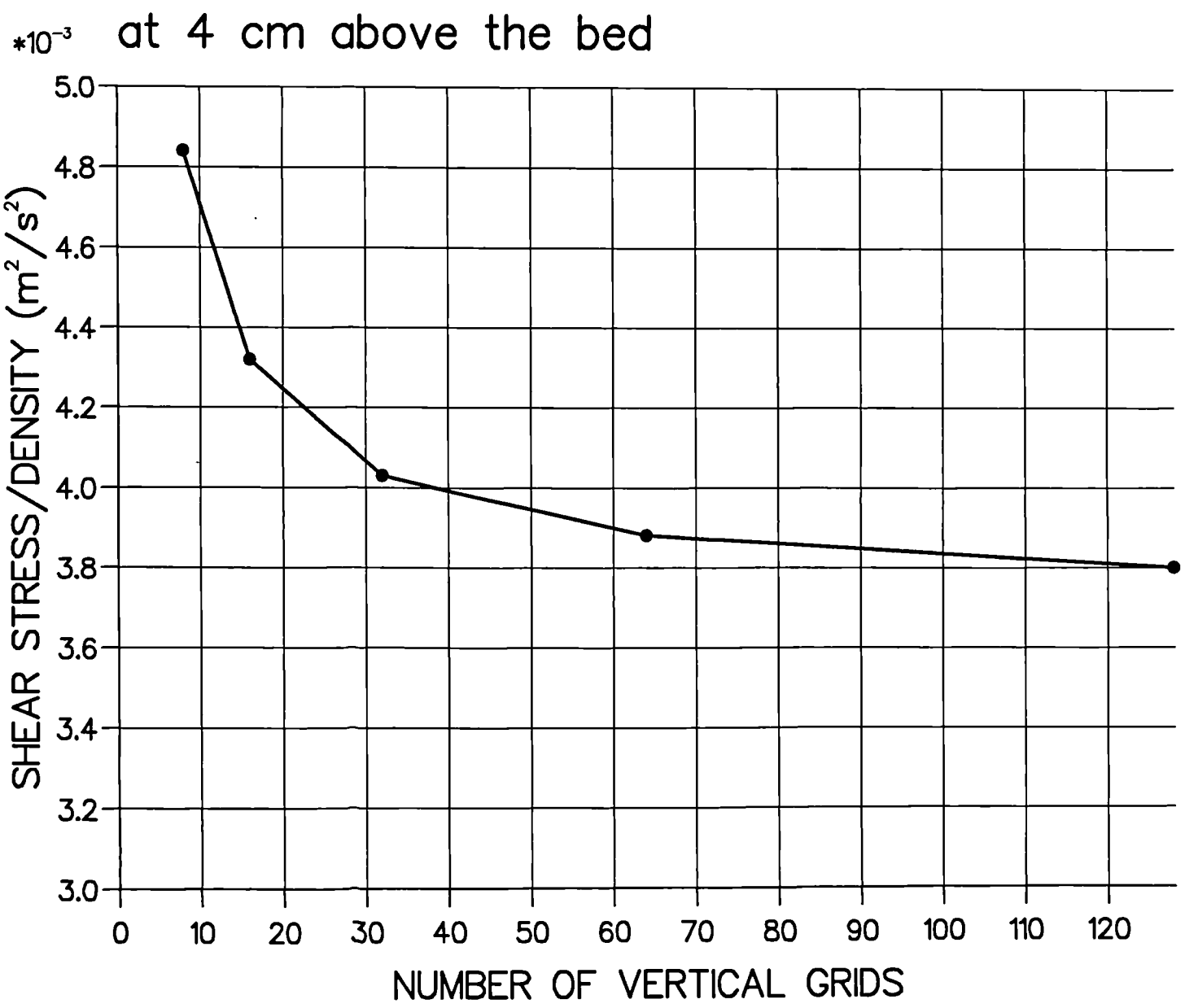

Fig. 7.9 The effect of the number of vertical grid points on the shear stress amplitude at a level.

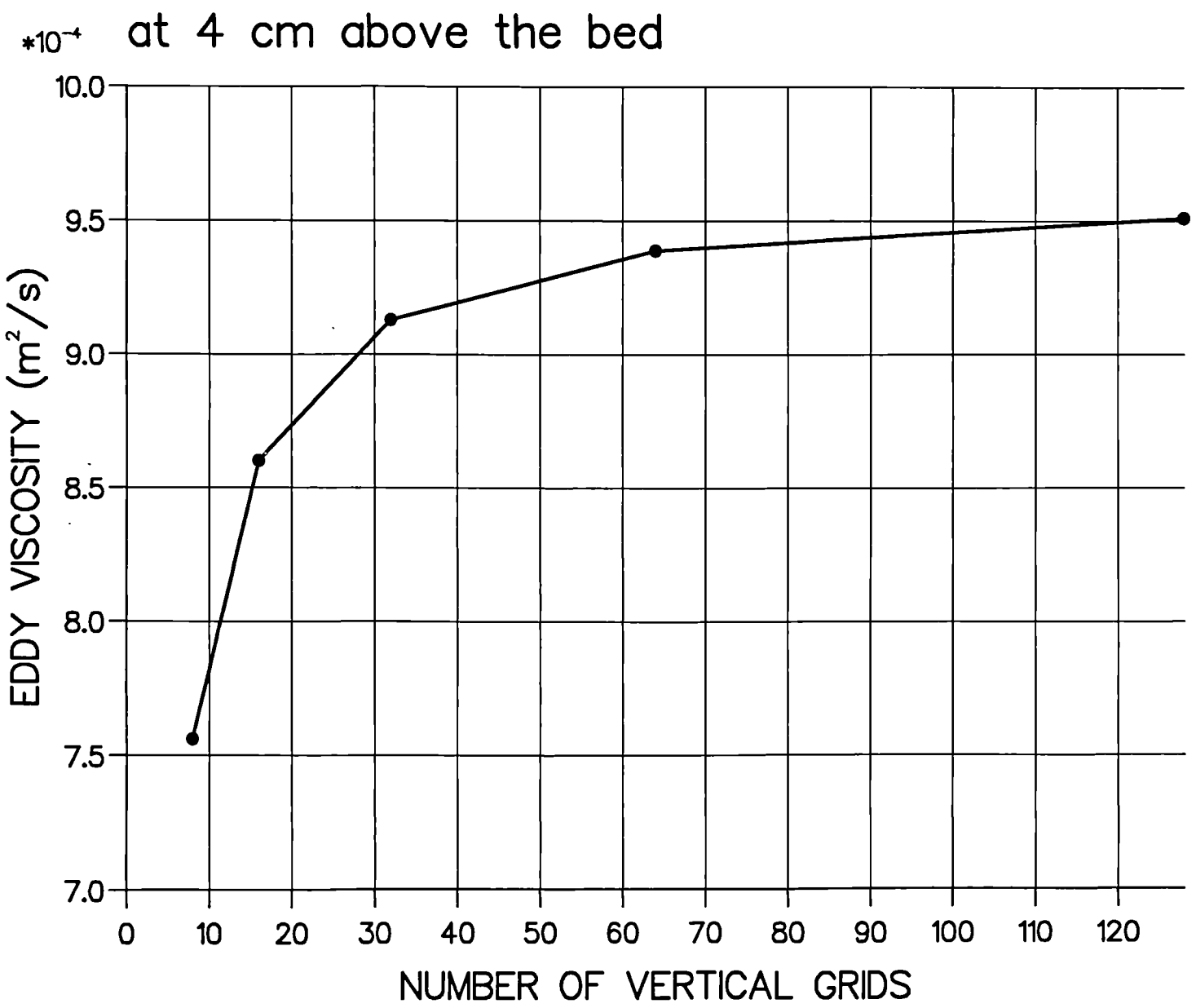

Fig. 7.10 The effect of the number of vertical grid points on the maximum eddy viscosity at a level.

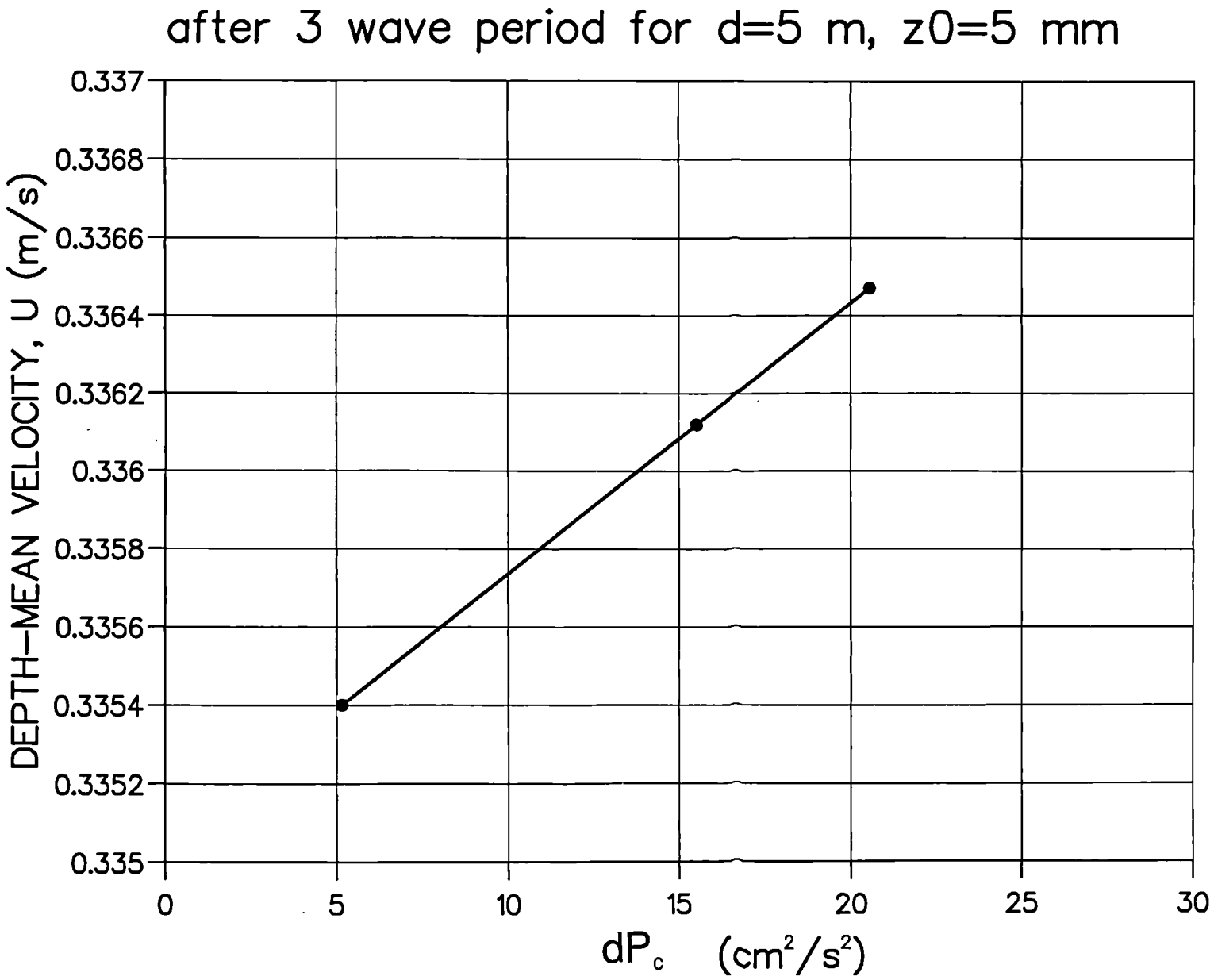

Fig. 7.11 The effect of the pressure gradient on the depth-mean velocity.

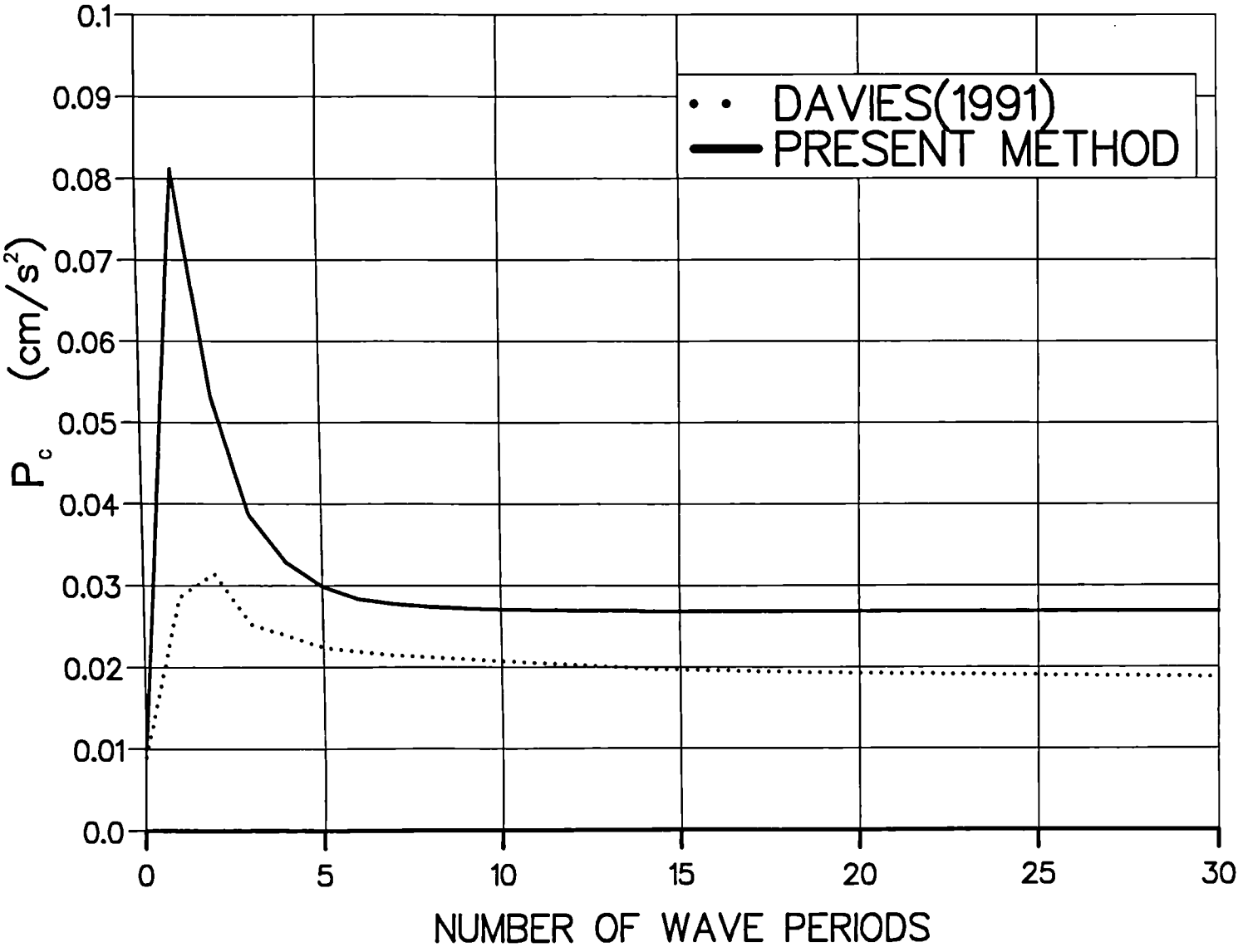

Fig. 7.12 Pressure gradient variation with time: present method and Davies(1991).

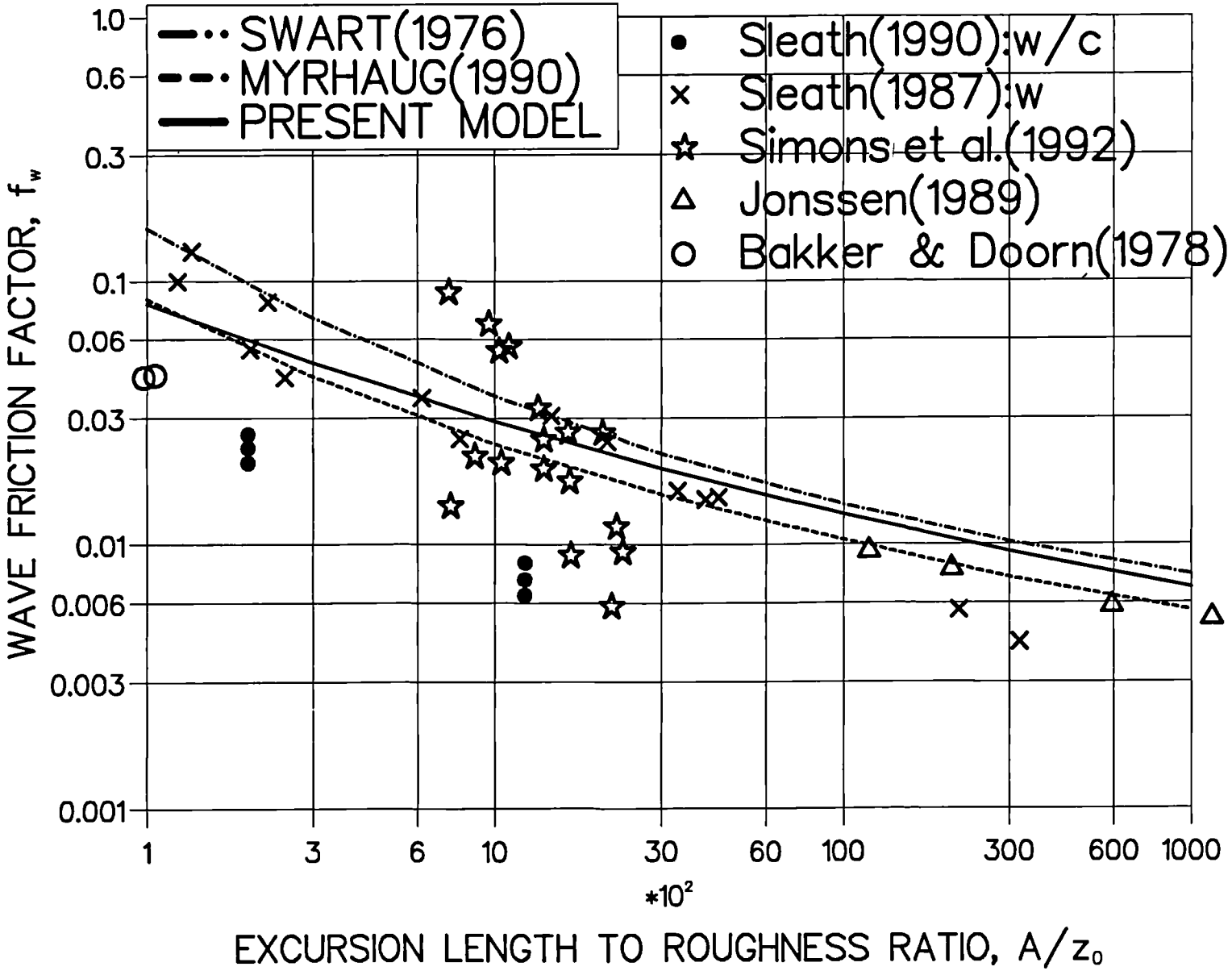

Fig. 7.13 Comparison of wave friction factors.

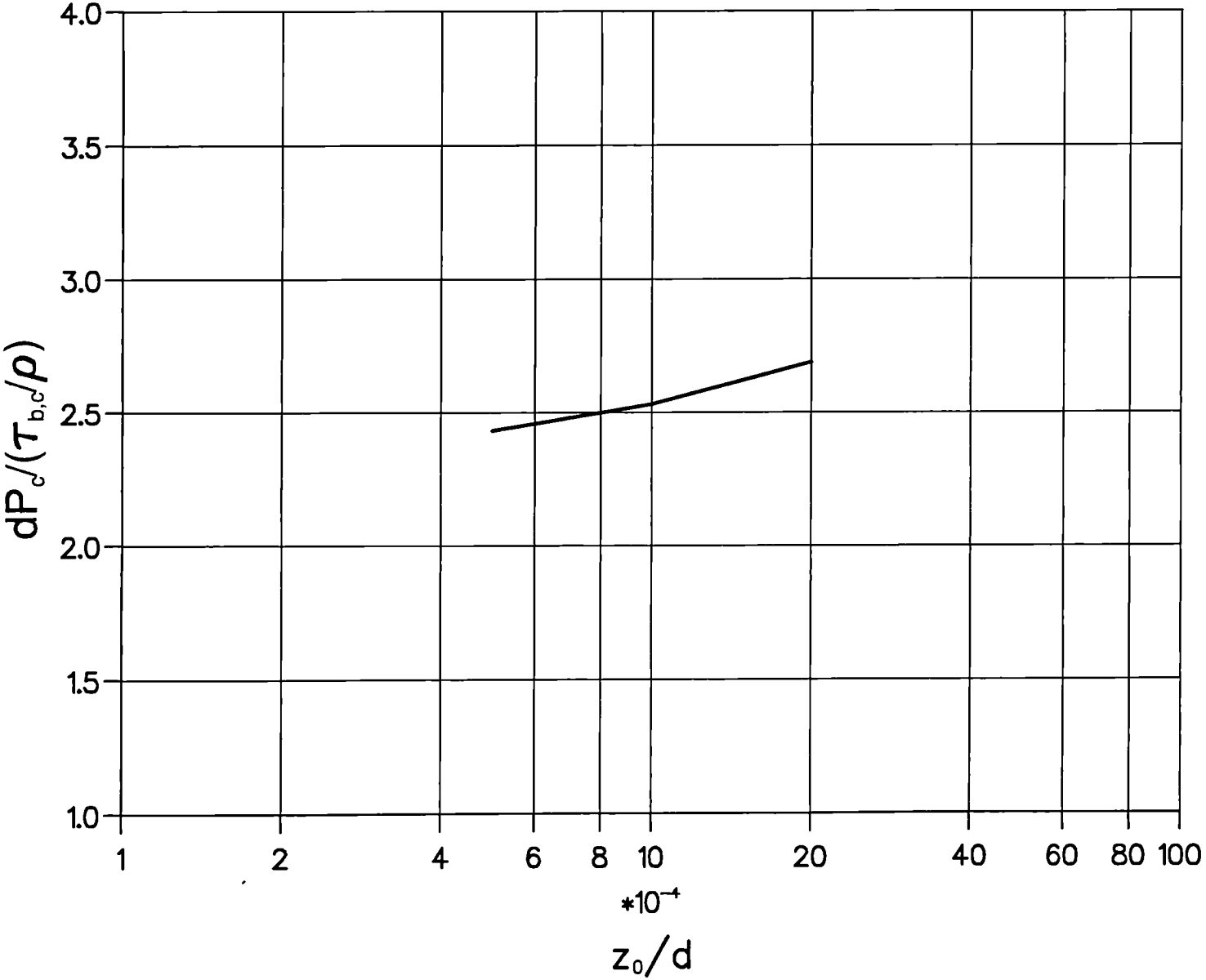

Fig. 7.14 The effect of z_0/d on the pressure gradient.

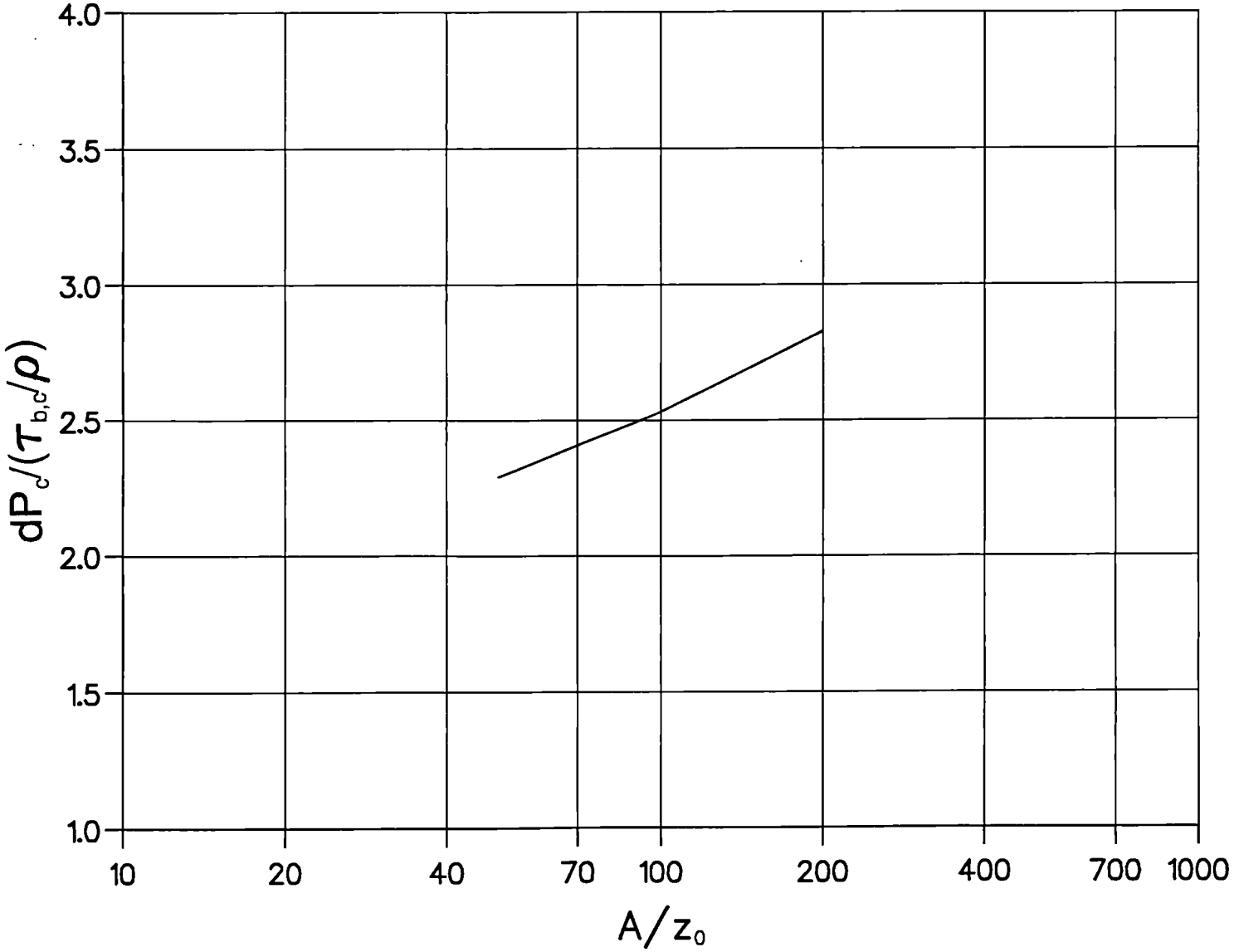

Fig. 7.15 The effect of A/z_0 on the pressure gradient.

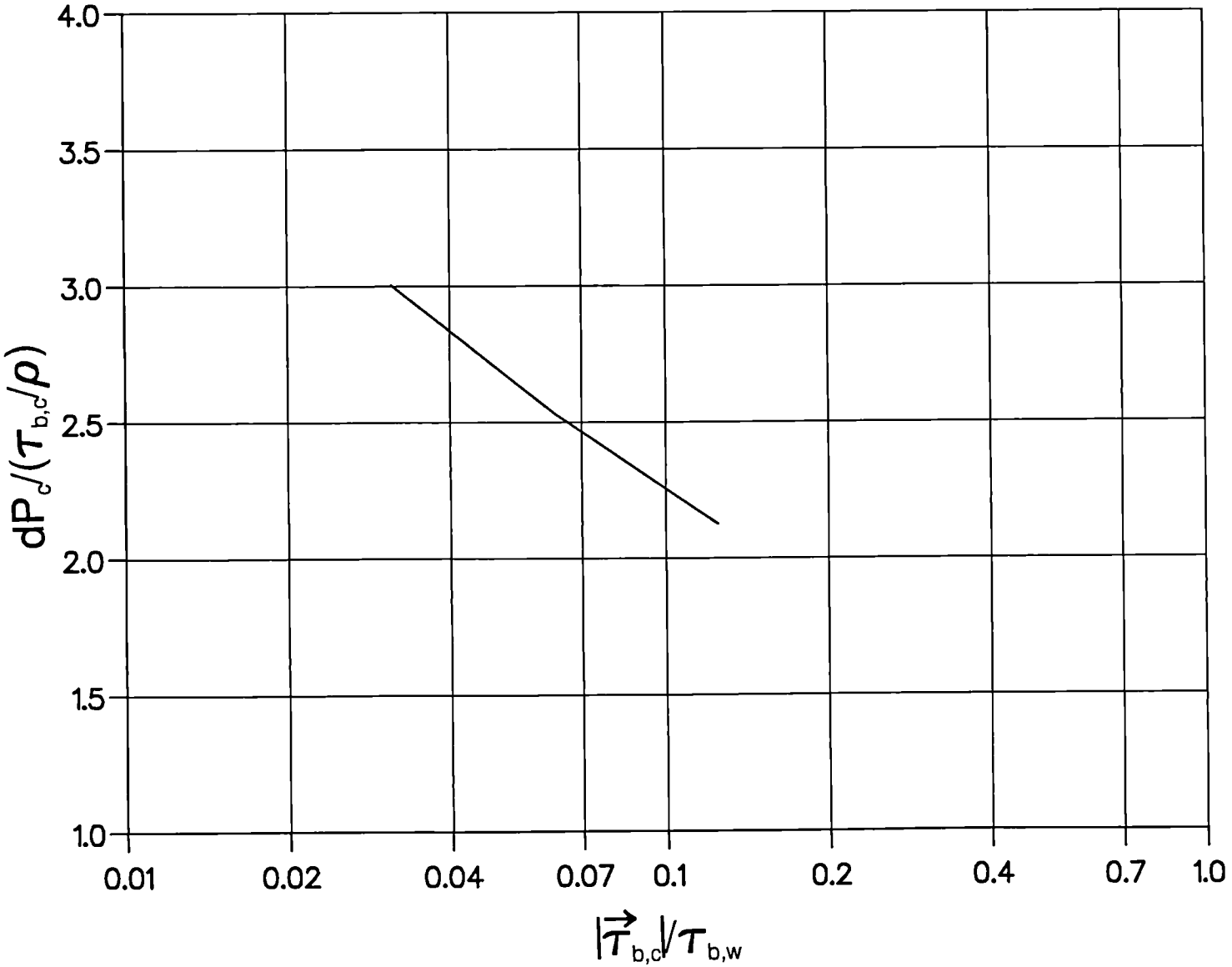

Fig. 7.16 The effect of $|\vec{\tau}_{b,c}|/\tau_{b,w}$ on the pressure gradient.

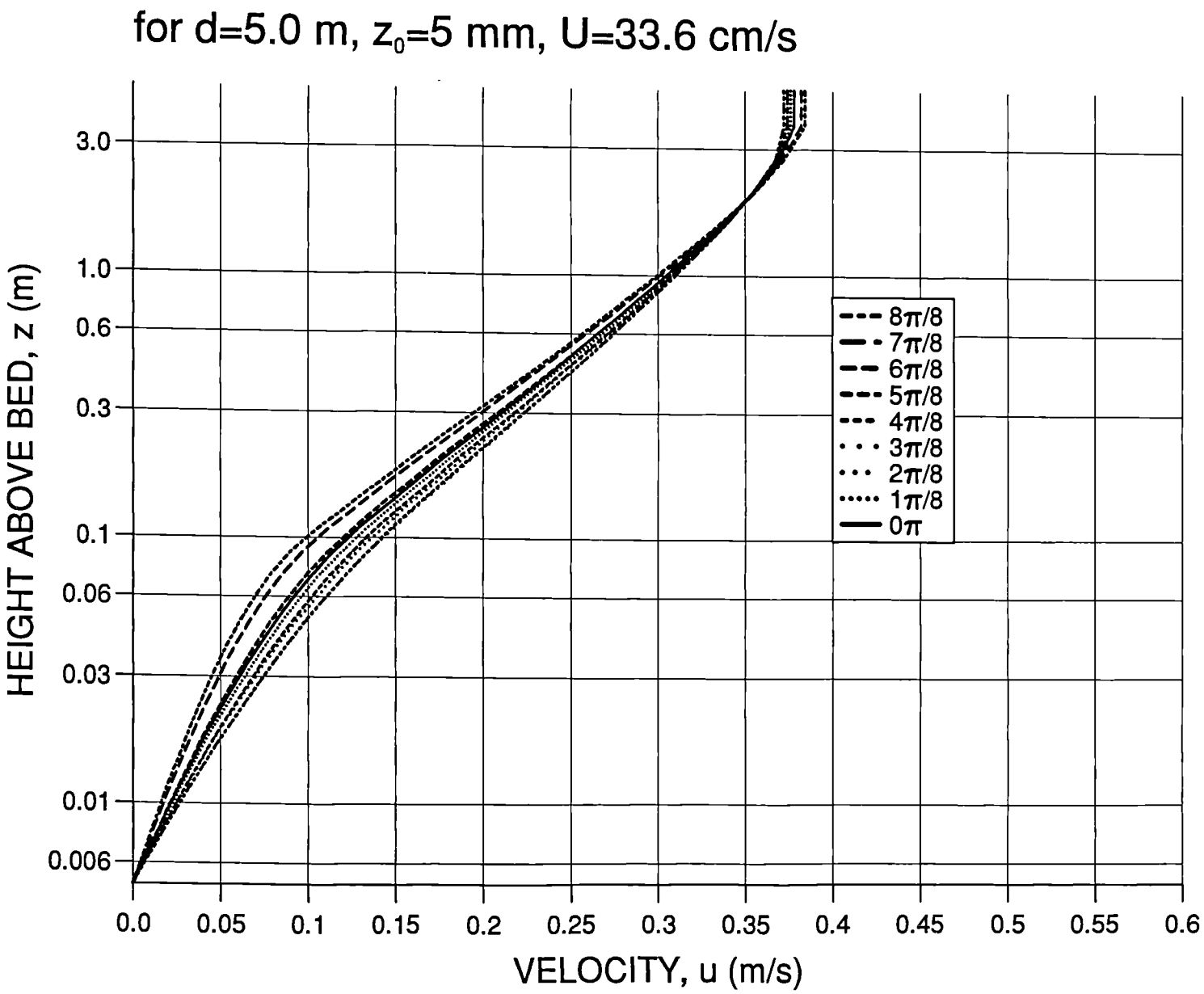

Fig. 7.17 The effect of θ_{wc} on the velocity profiles.

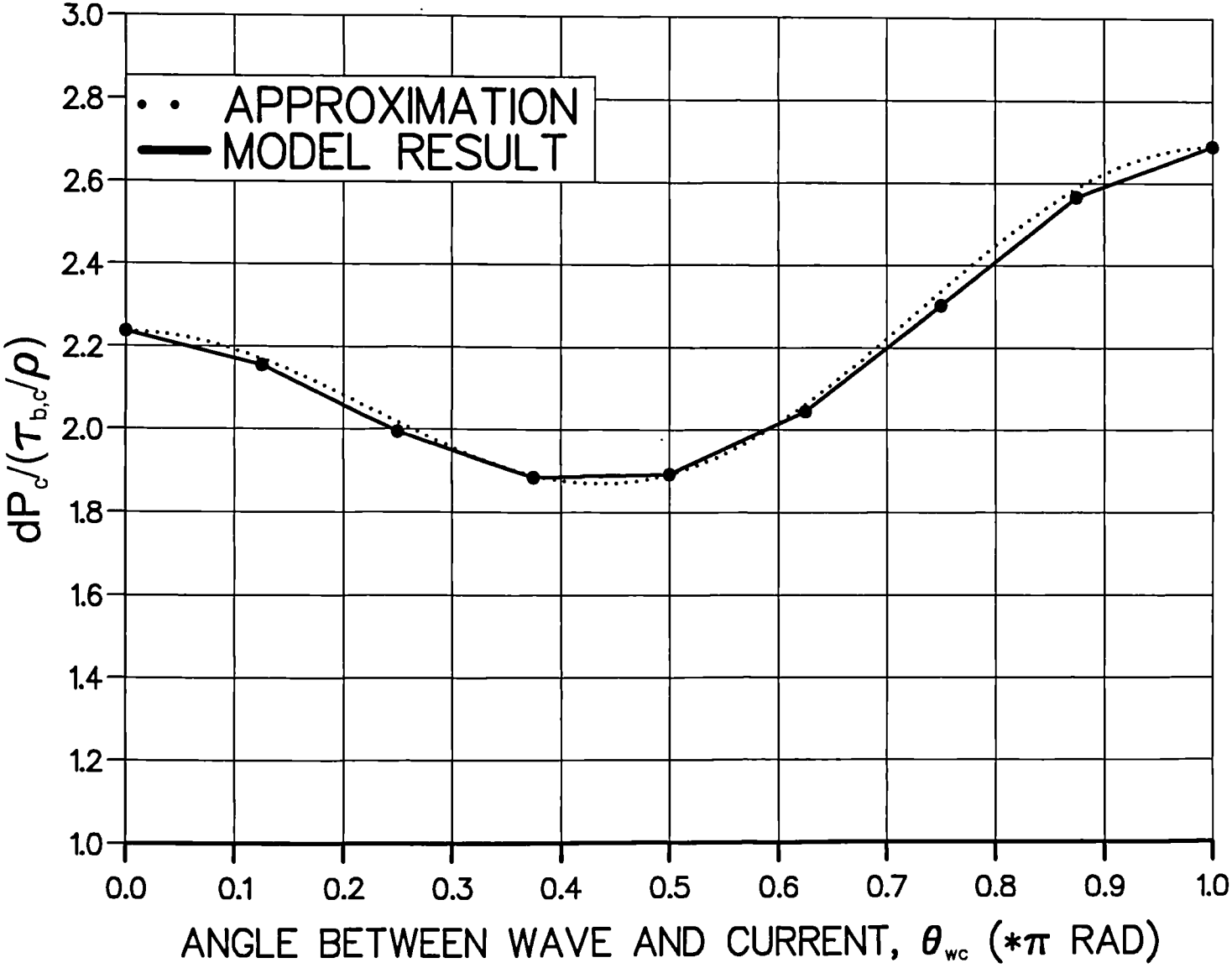

Fig. 7.18 The effect of θ_{wc} on the pressure gradient.

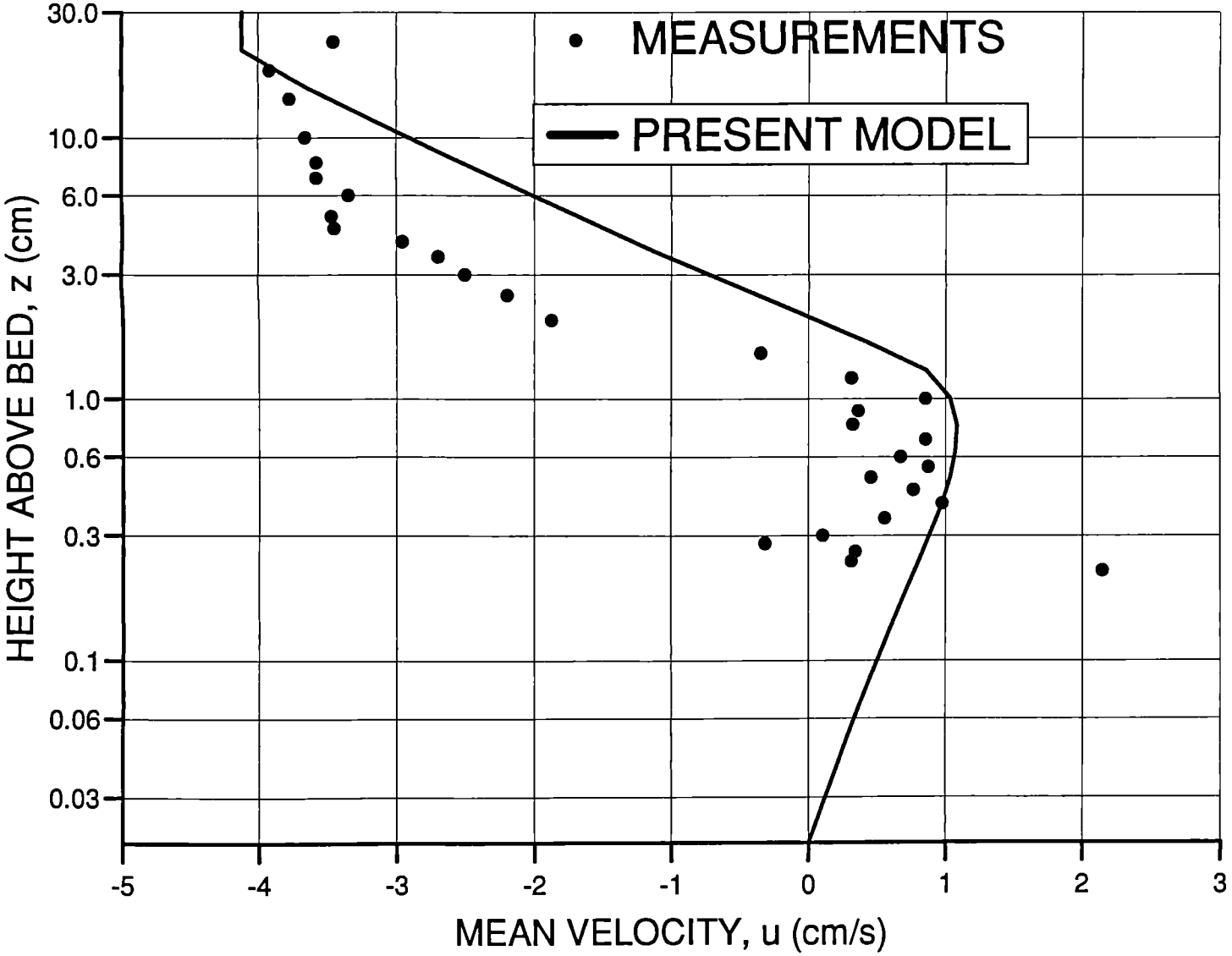

Fig. 7.19 Comparison of the present model results with van Doorn's(1979) measurements: mean velocity profile.

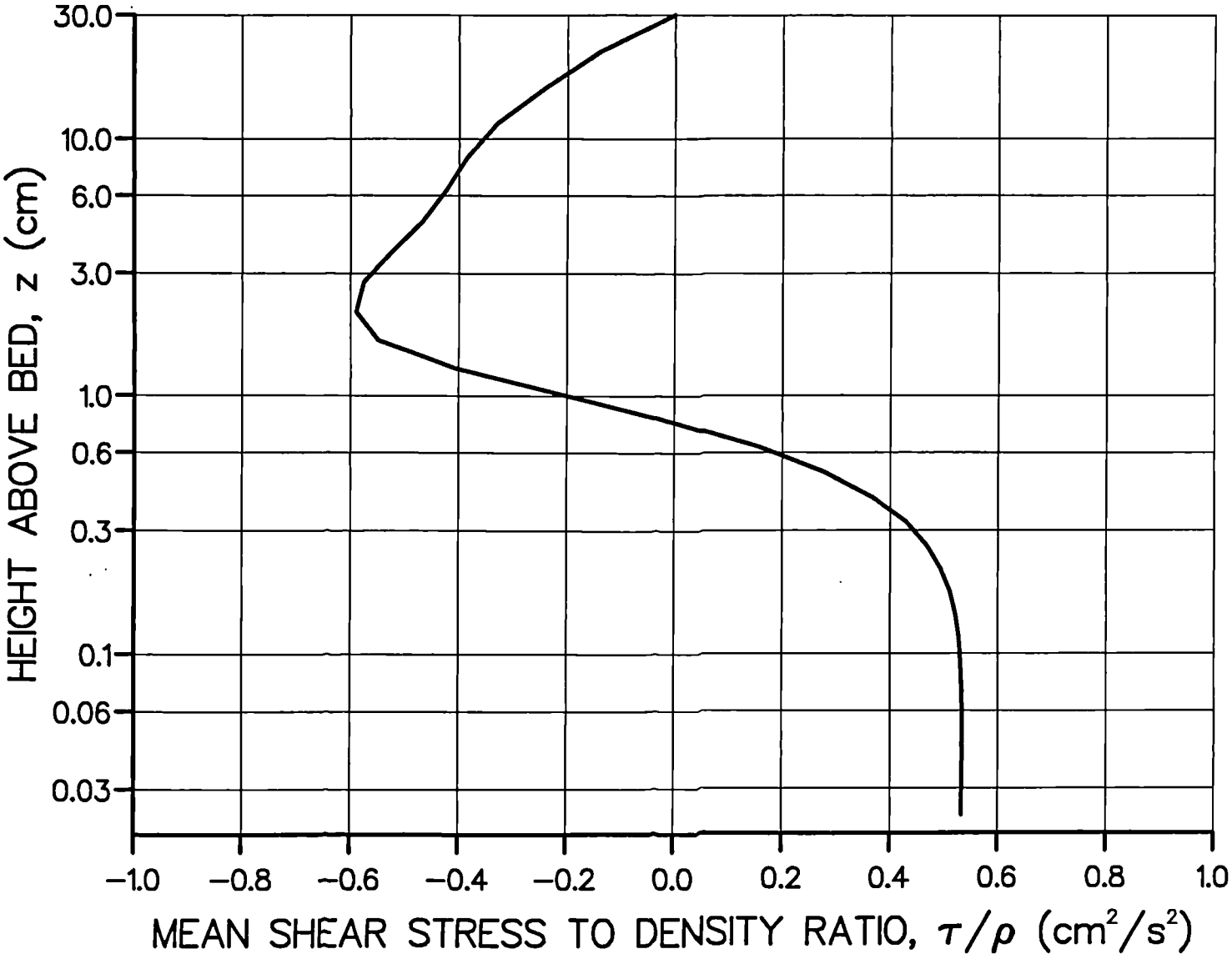

Fig. 7.20 Calculated mean shear stress to density for van Doorn's(1979) experimental condition.

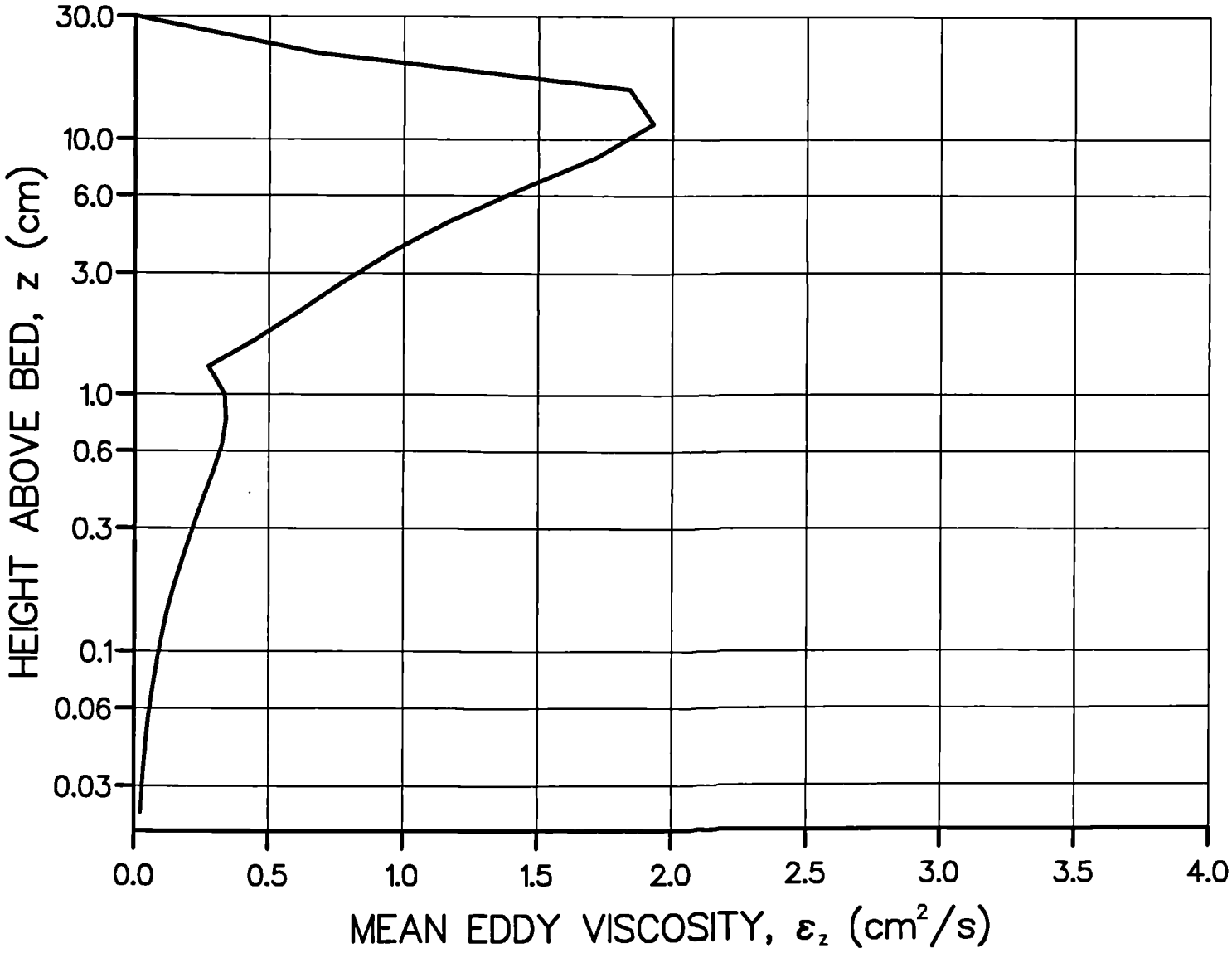

Fig. 7.21 Calculated mean eddy viscosity for van Doorn's experimental condition.

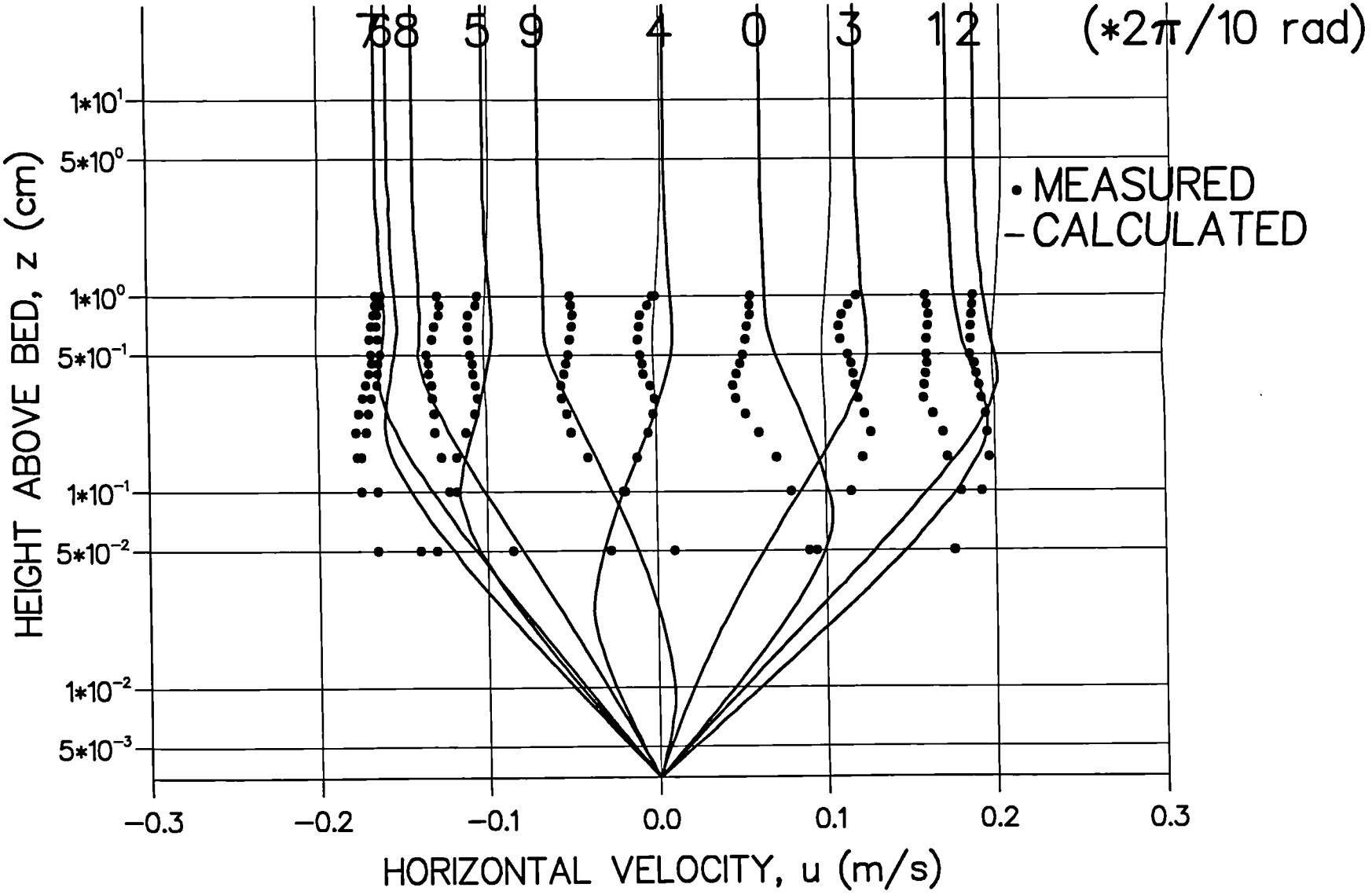

Fig. 7.22 Comparison of the present model results with Manchester experimental data: velocity profiles.

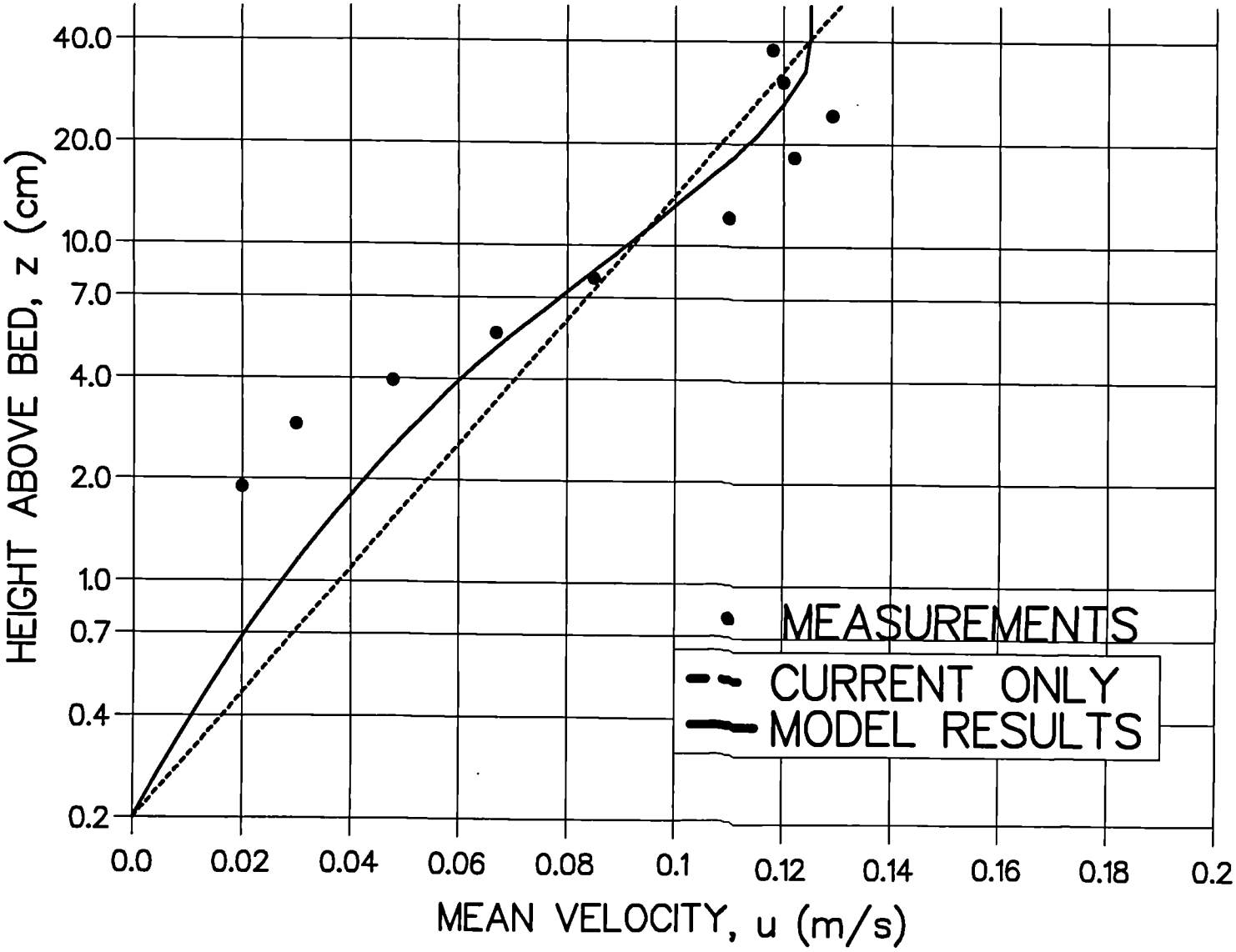

Fig. 7.23 Comparison of the present model results with Nieuwjaar and van der Kaaij's(1988) measurements for the following current: mean velocity profile.

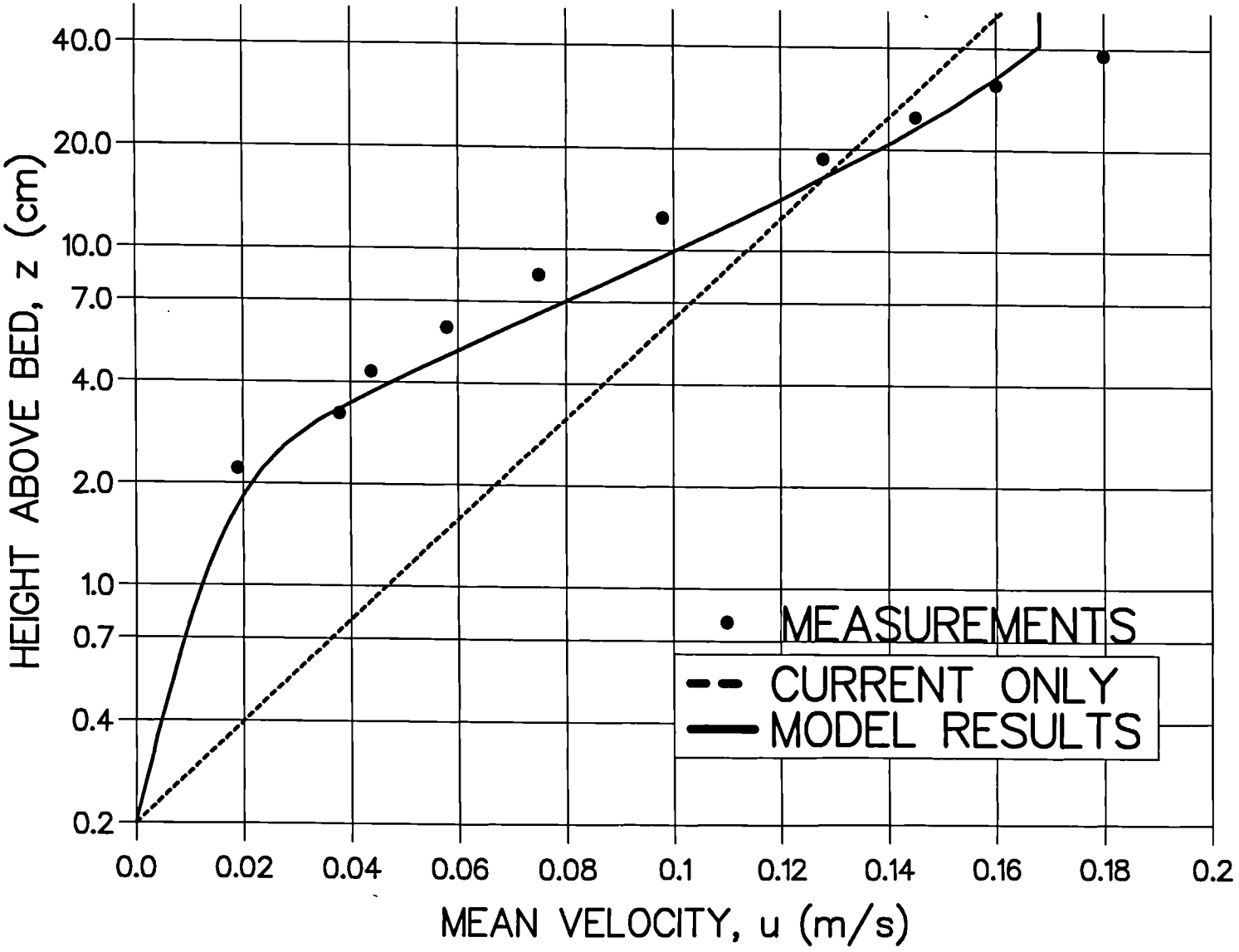

Fig. 7.24 Comparison of the present model results with Nieuwjaar and van der Kaaij's(1988) measurements for the opposing current: mean velocity profile.

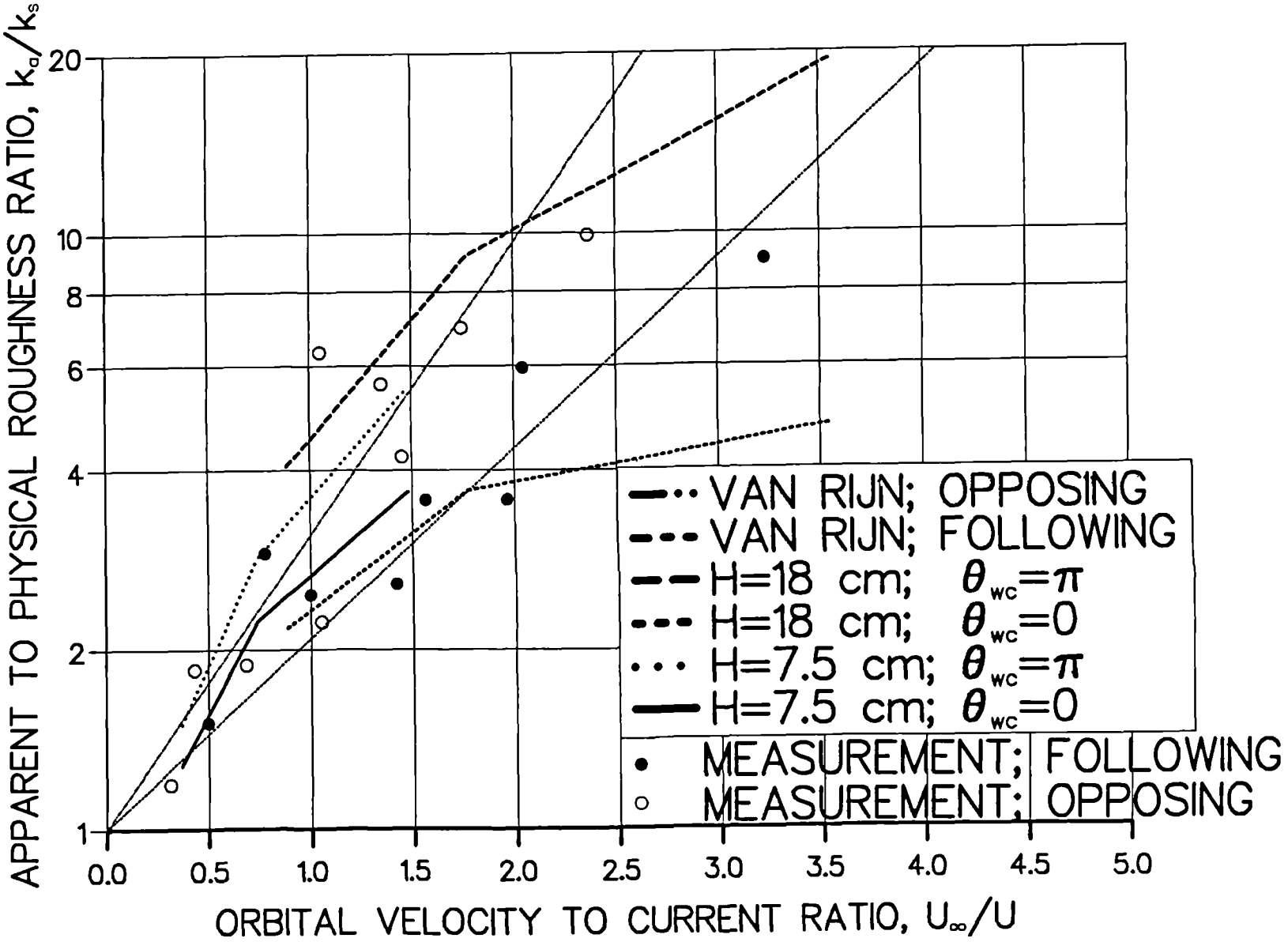

Fig. 7.25 Comparison of the present model results with Nap and van Kampen's(1988) measurements.

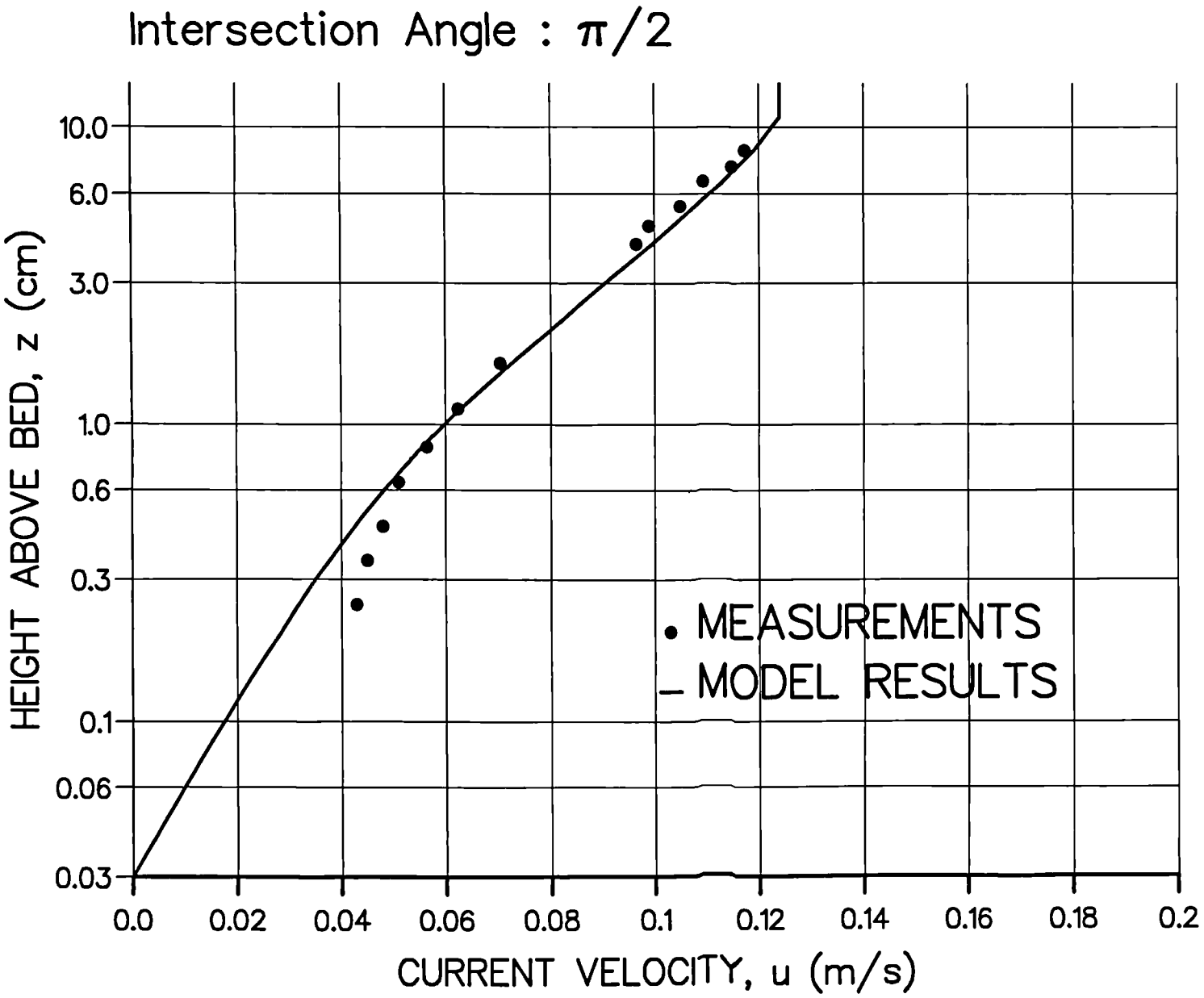

Fig. 7.26 Comparison of the present model results with van der Stel and Visser(1985)'s measurements.

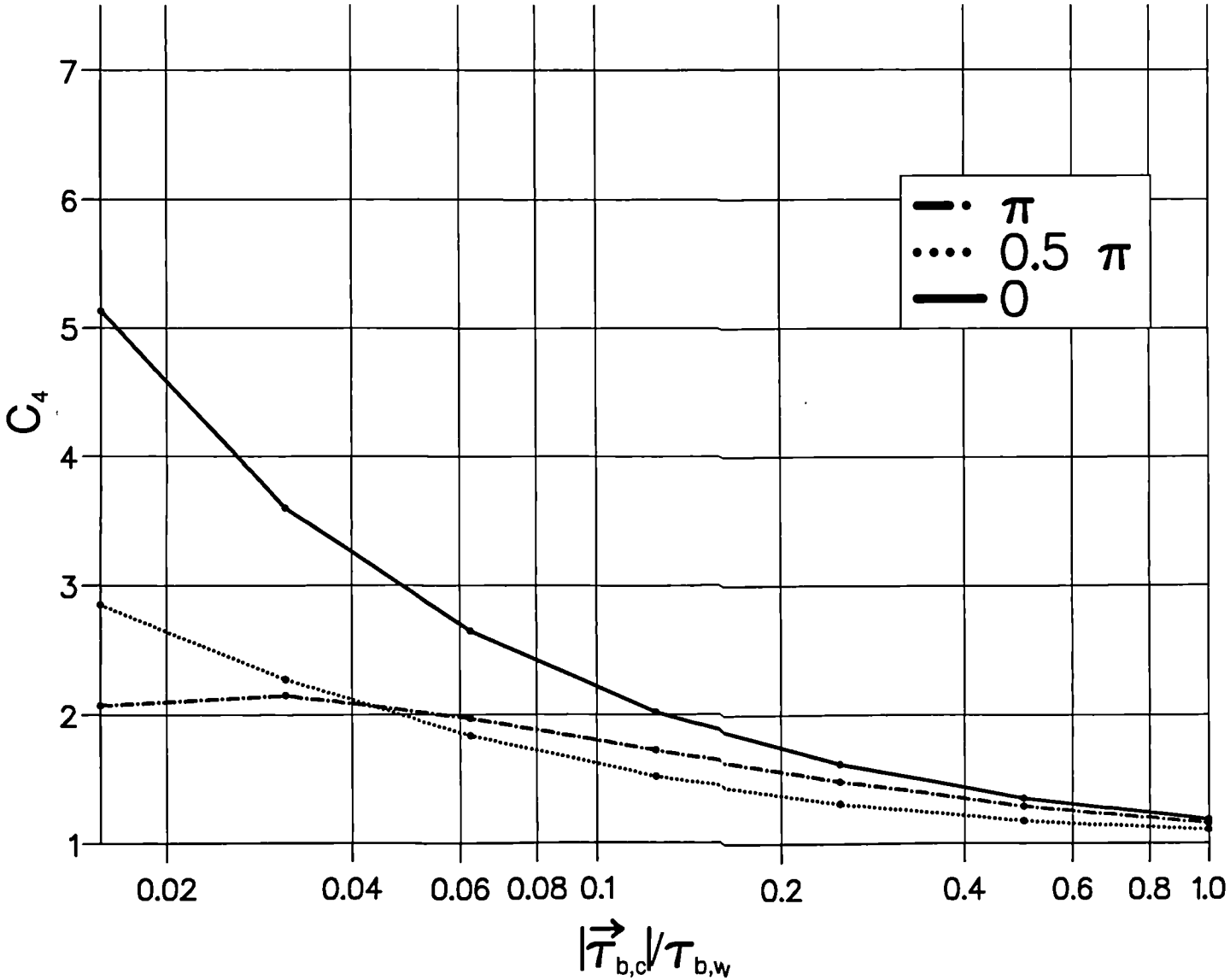

Fig. 7.27 The effect of $|\vec{\tau}_{b,c}|/\tau_{b,w}$ on the bed shear stress amplification factor (C_4): $A/z_0=100$.

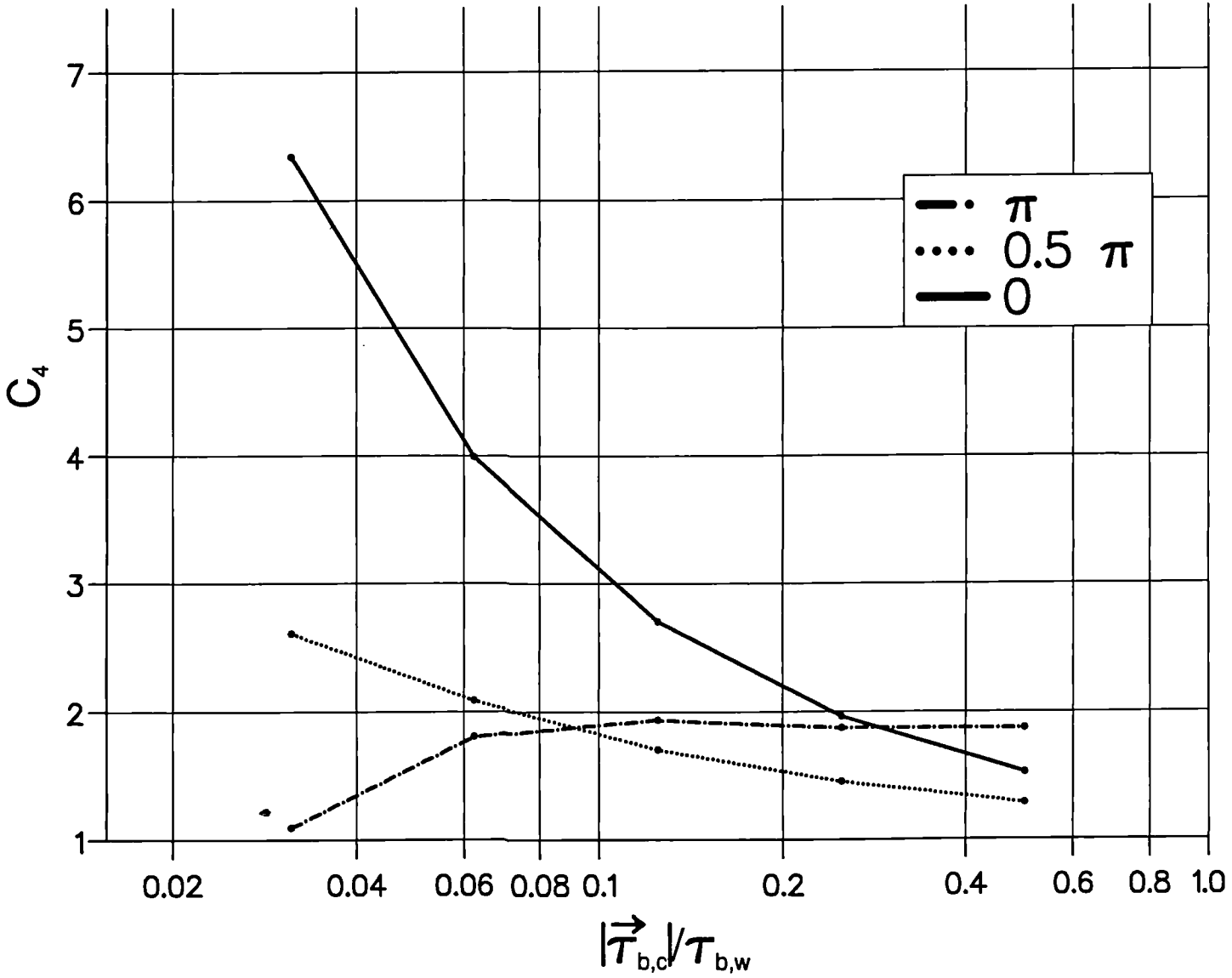

Fig. 7.28 The effect of $|\vec{\tau}_{b,c}|/\tau_{b,w}$ on the bed shear stress amplification factor (C_4): A/z_0=500.

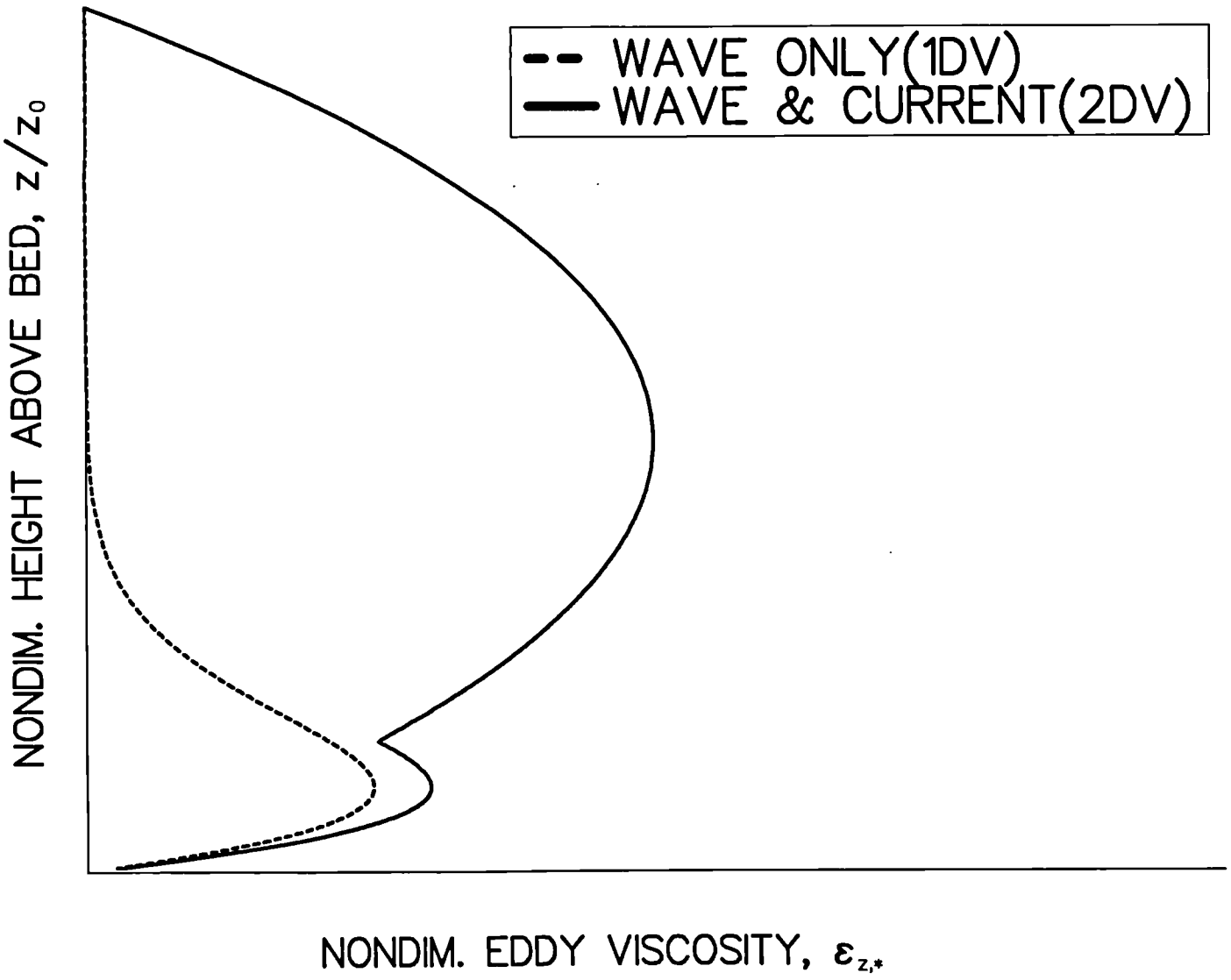

Fig. 7.29 The 1DV eddy viscosity profile for wave flows, and the 2DV eddy viscosity profile for wave and current flows.

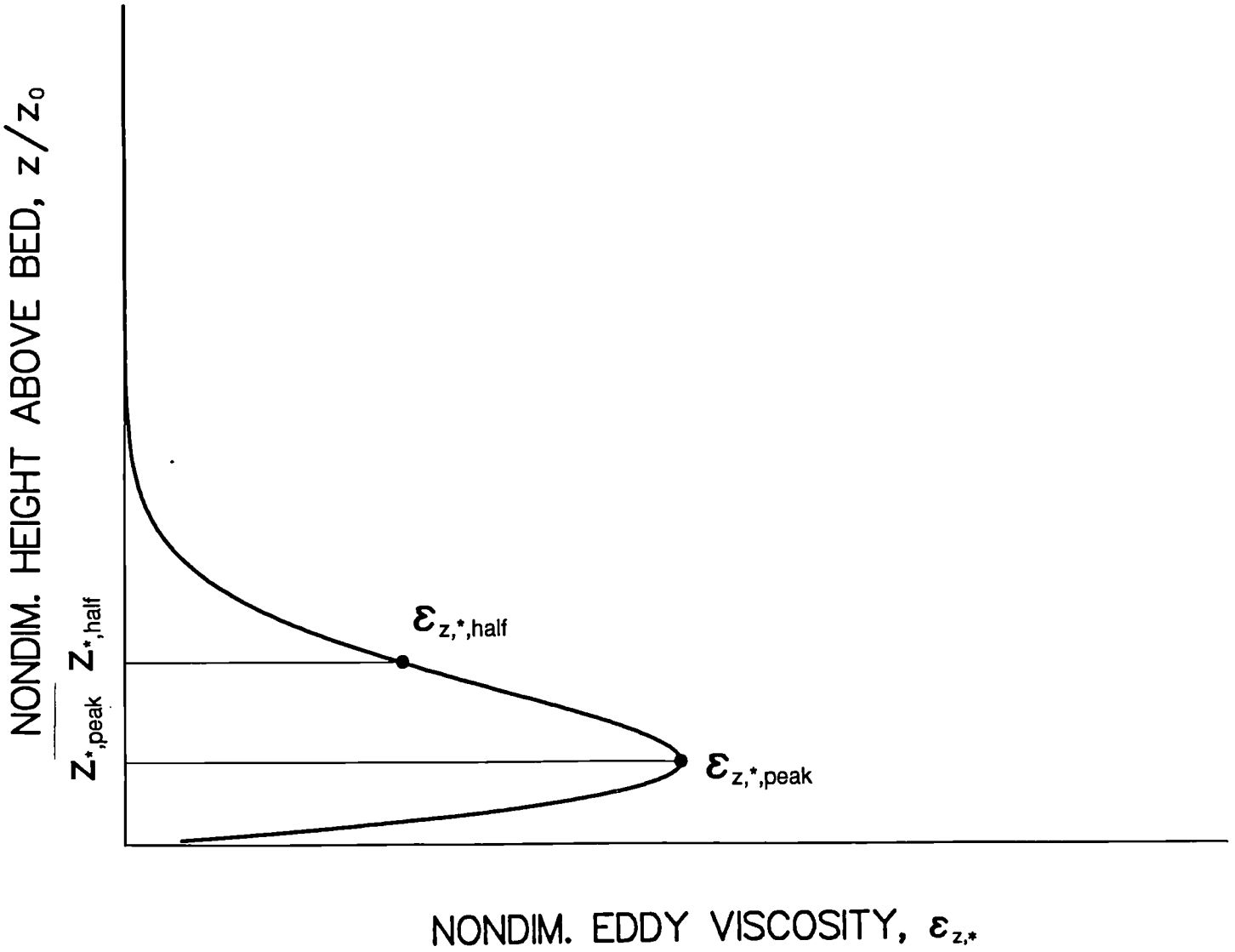

Fig. 7.30 Variables used in the approximation to the eddy viscosity profile.

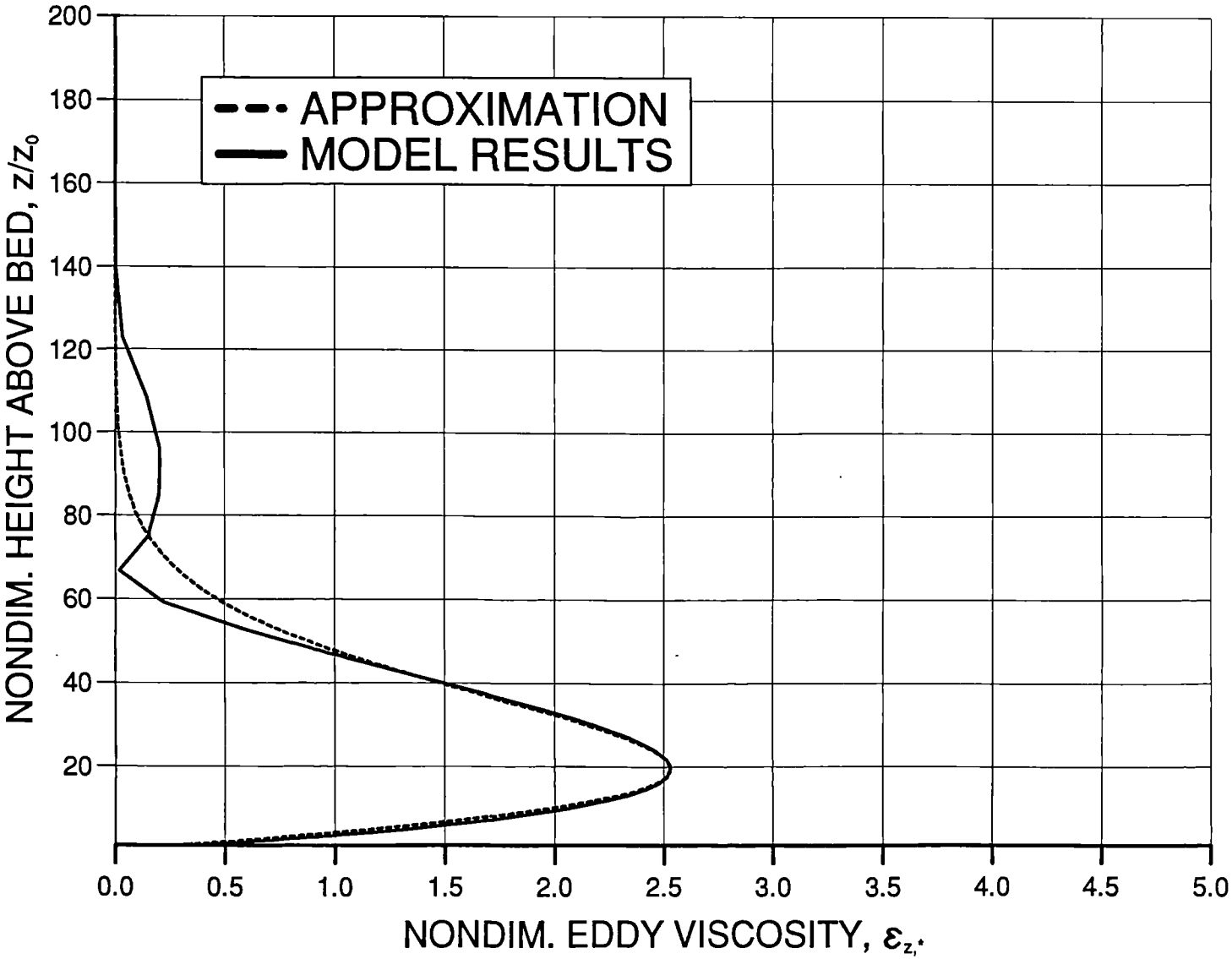

Fig. 7.31a Eddy viscosity profile given by the present model: $A/z_0=100$.

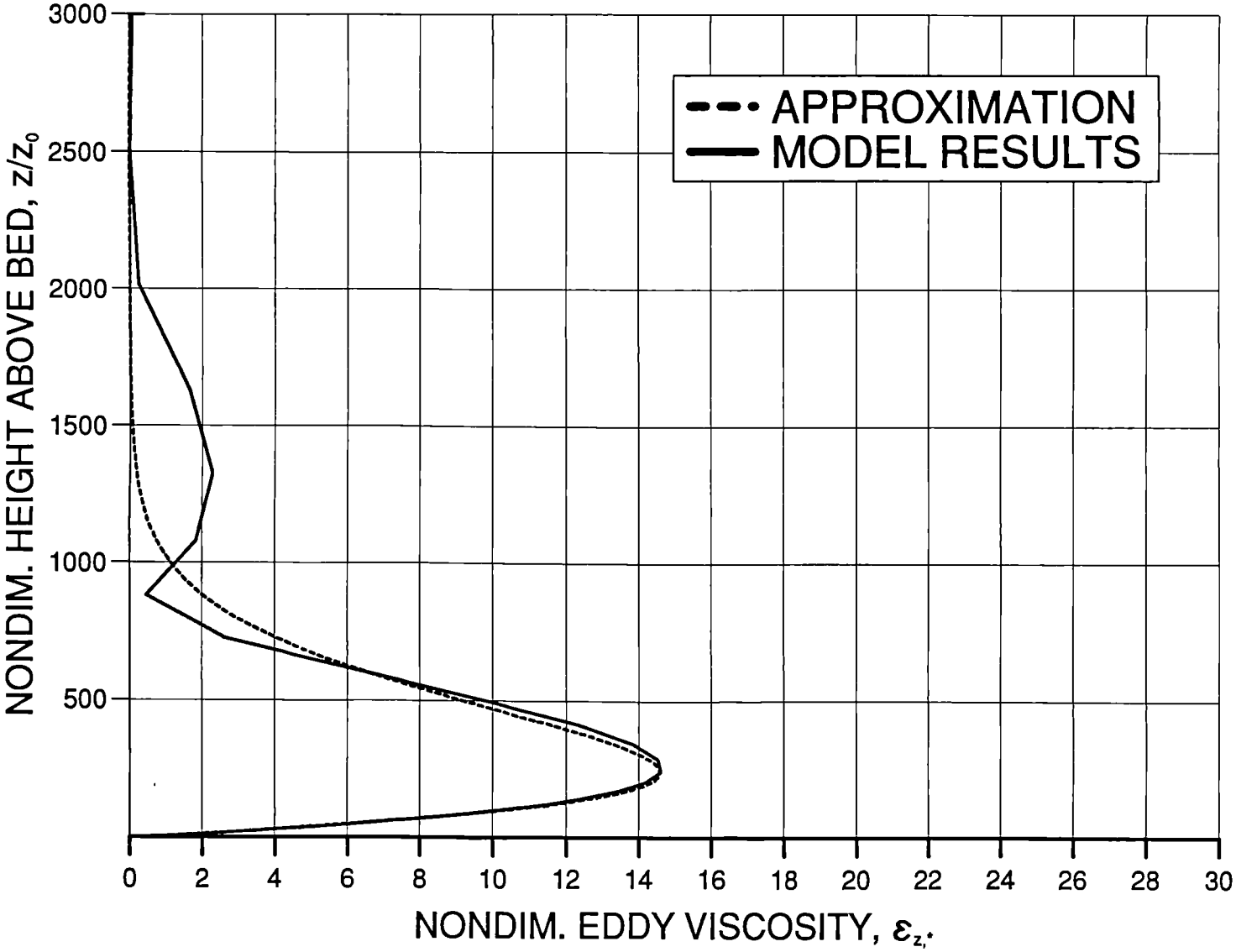

Fig. 7.31b Eddy viscosity profile given by the present model: $A/z_0=3000$.

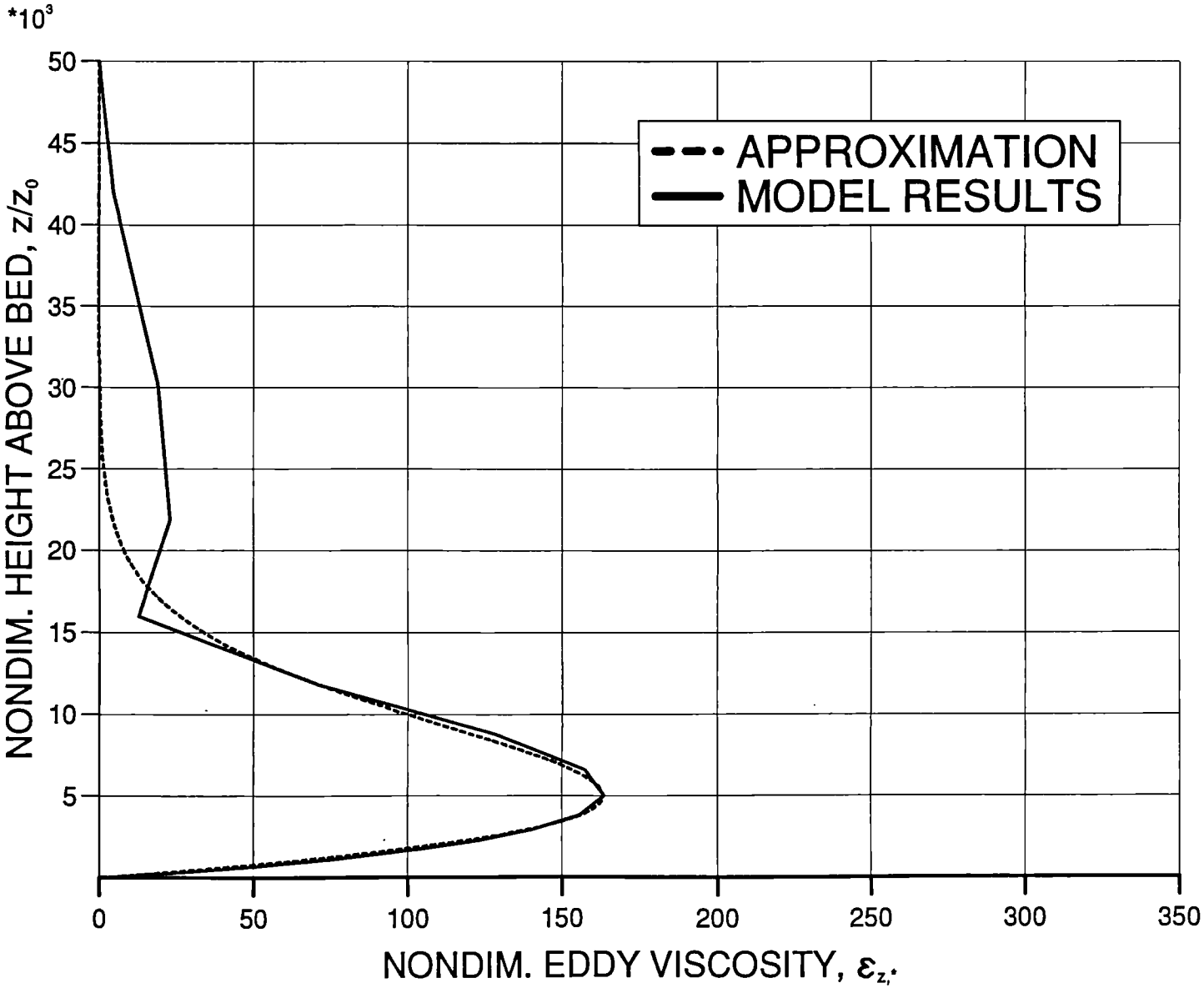

Fig. 7.31c Eddy viscosity profile given by the present model: $A/z_0=100000$.

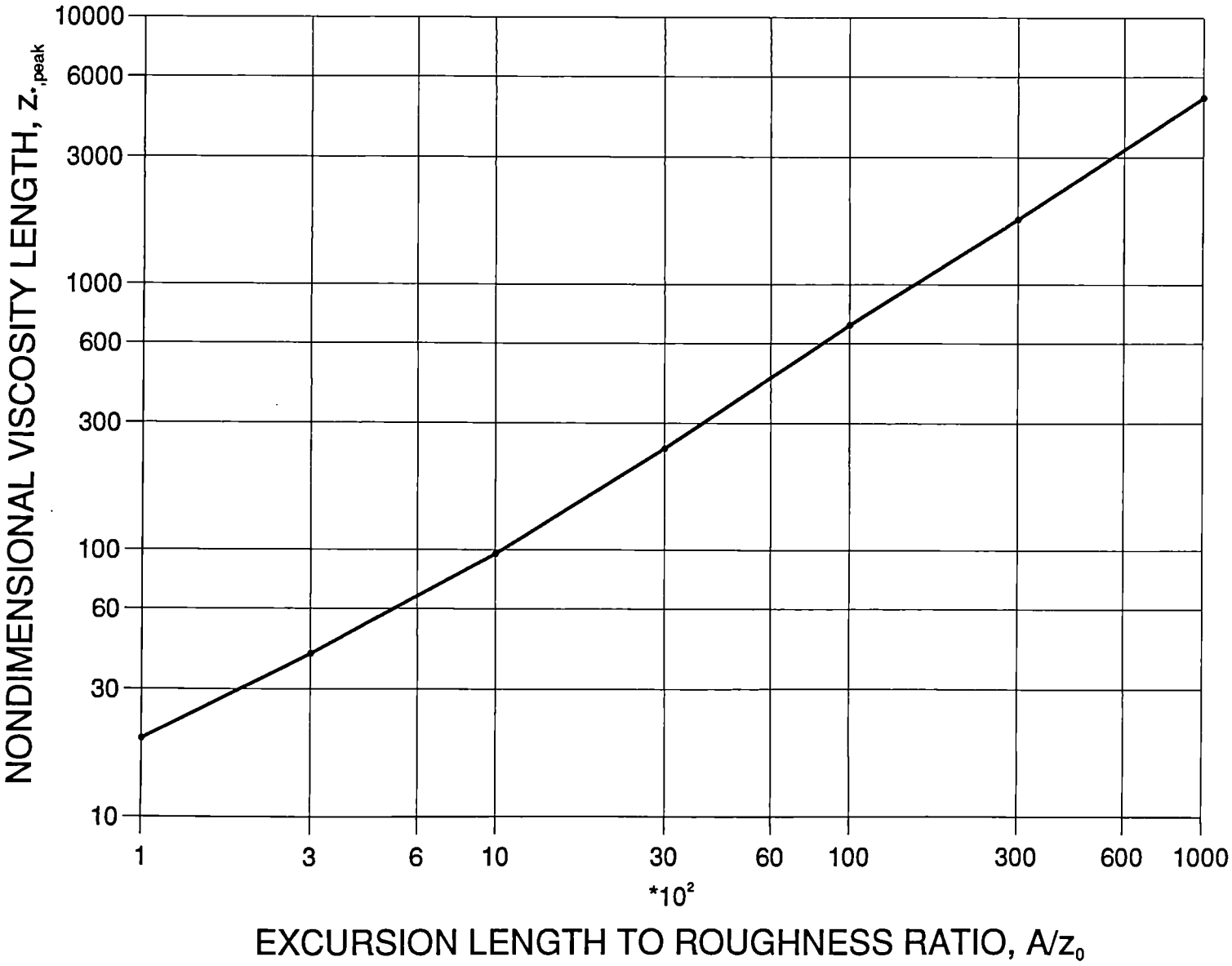

Fig. 7.32 The effect of A/z_0 on $z_{*,peak}$.

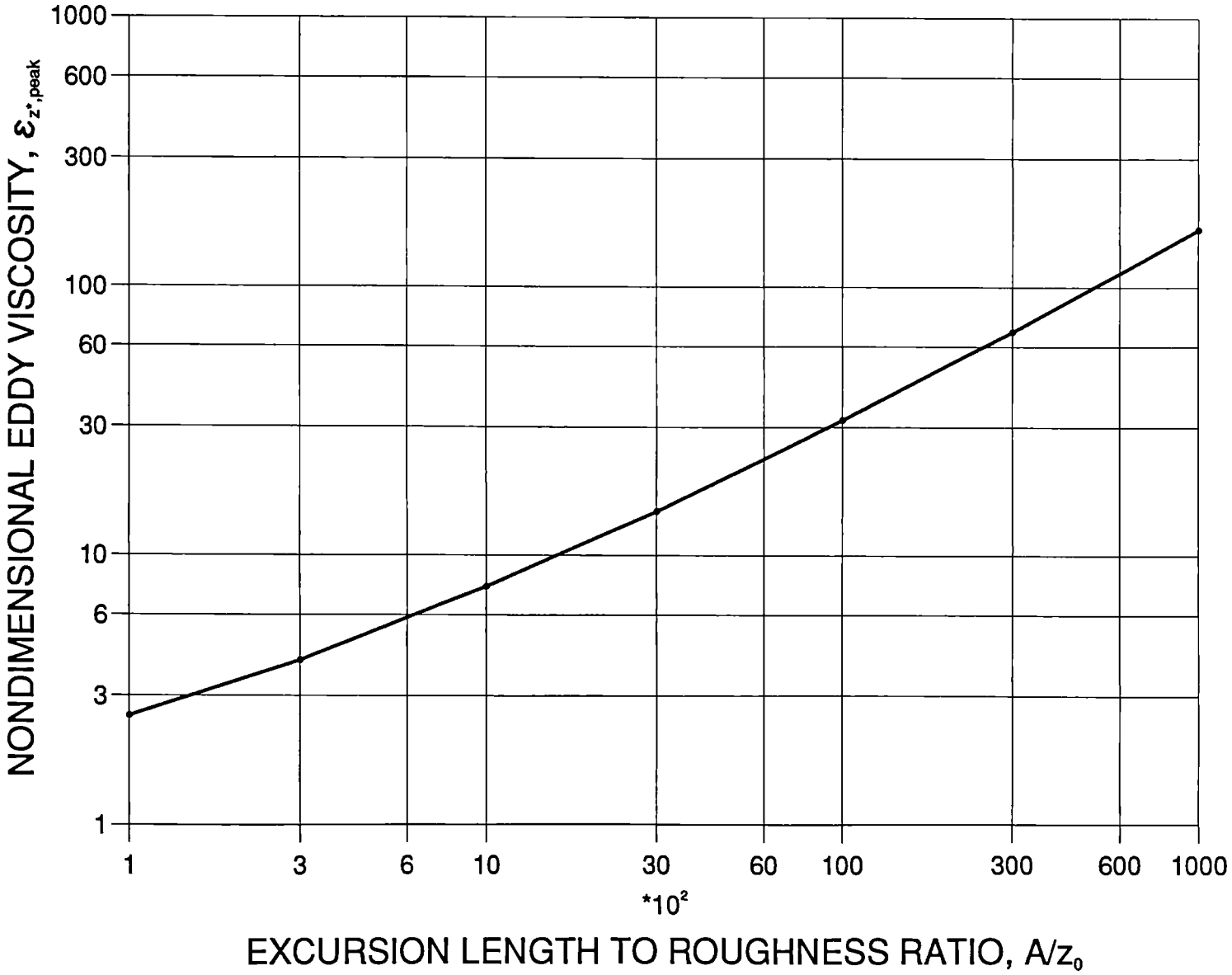

Fig. 7.33 The effect of A/z_0 on $\epsilon_{*,peak}$.

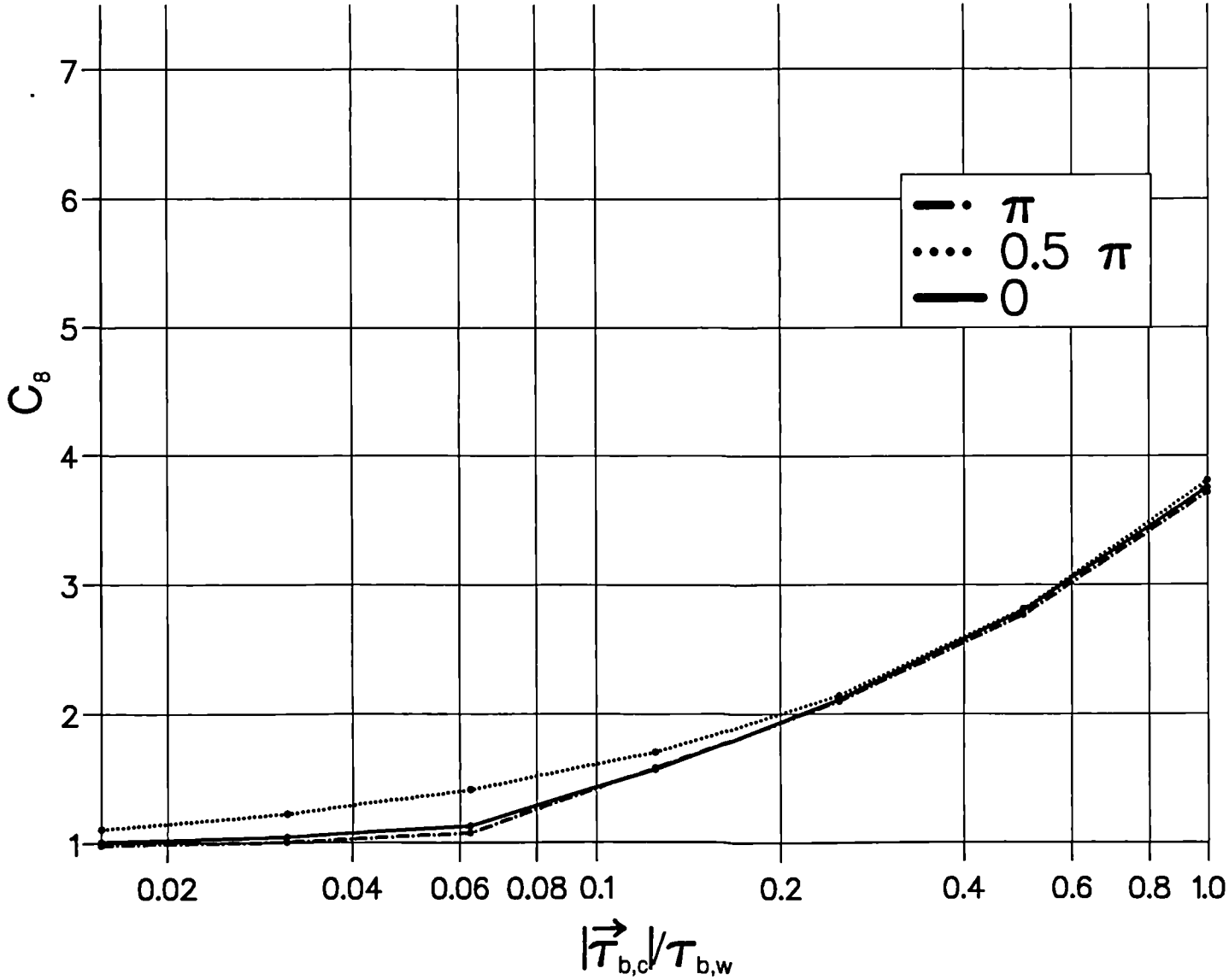

Fig. 7.34 The effect of $|\vec{\tau}_{b,c}|/\tau_{b,w}$ on the eddy viscosity amplification factor (C_8): A/z_0=100.

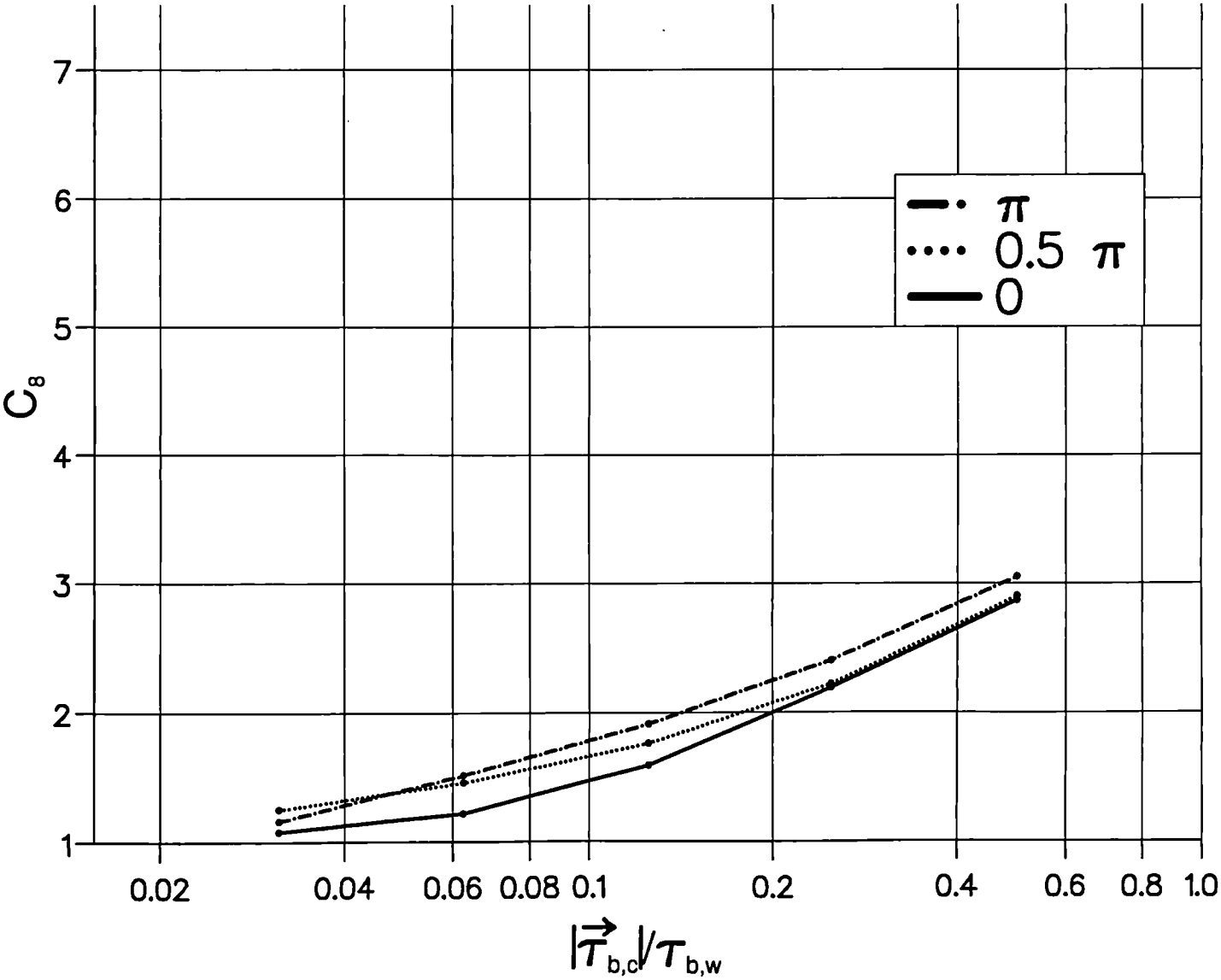

Fig. 7.35 The effect of $|\vec{\tau}_{b,c}|/\tau_{b,w}$ on the eddy viscosity amplification factor (C_8): A/z_0=500.

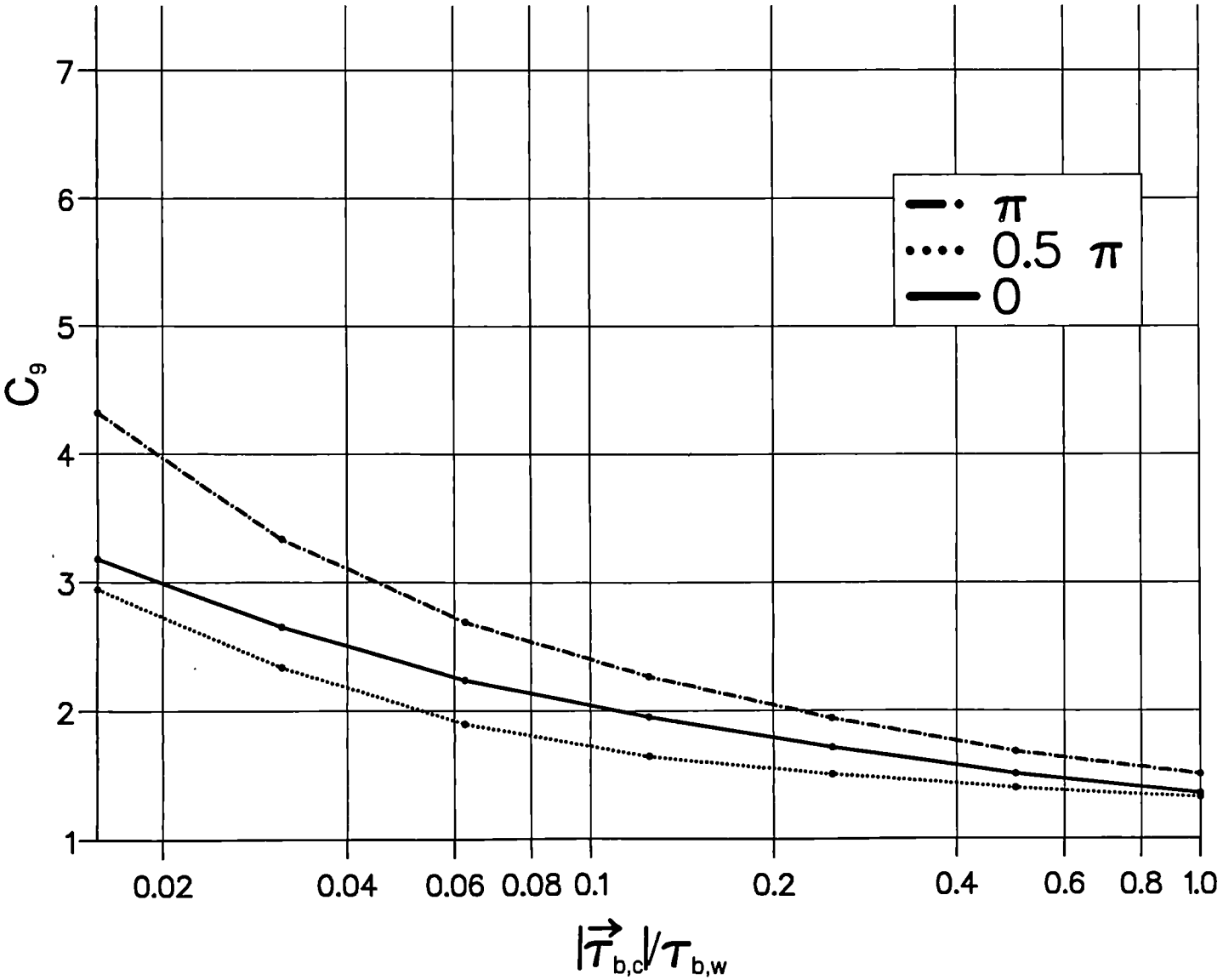

Fig. 7.36 The effect of $|\vec{\tau}_{b,c}|/\tau_{b,w}$ on the pressure gradient amplification factor (C_9): A/z_0=100.

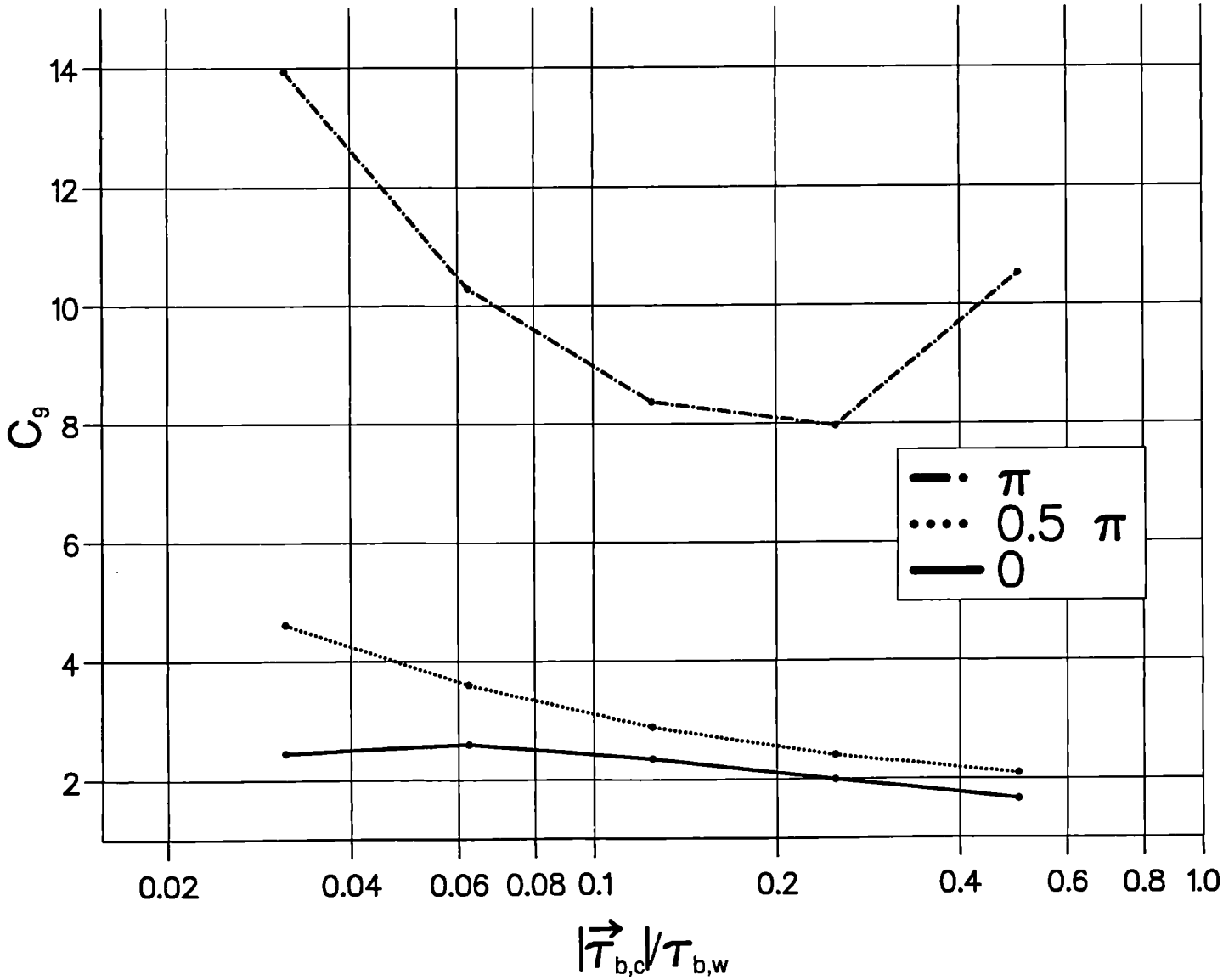

Fig. 7.37 The effect of $|\vec{\tau}_{b,c}|/\tau_{b,w}$ on the pressure gradient amplification factor (C_9): A/z_0=500.

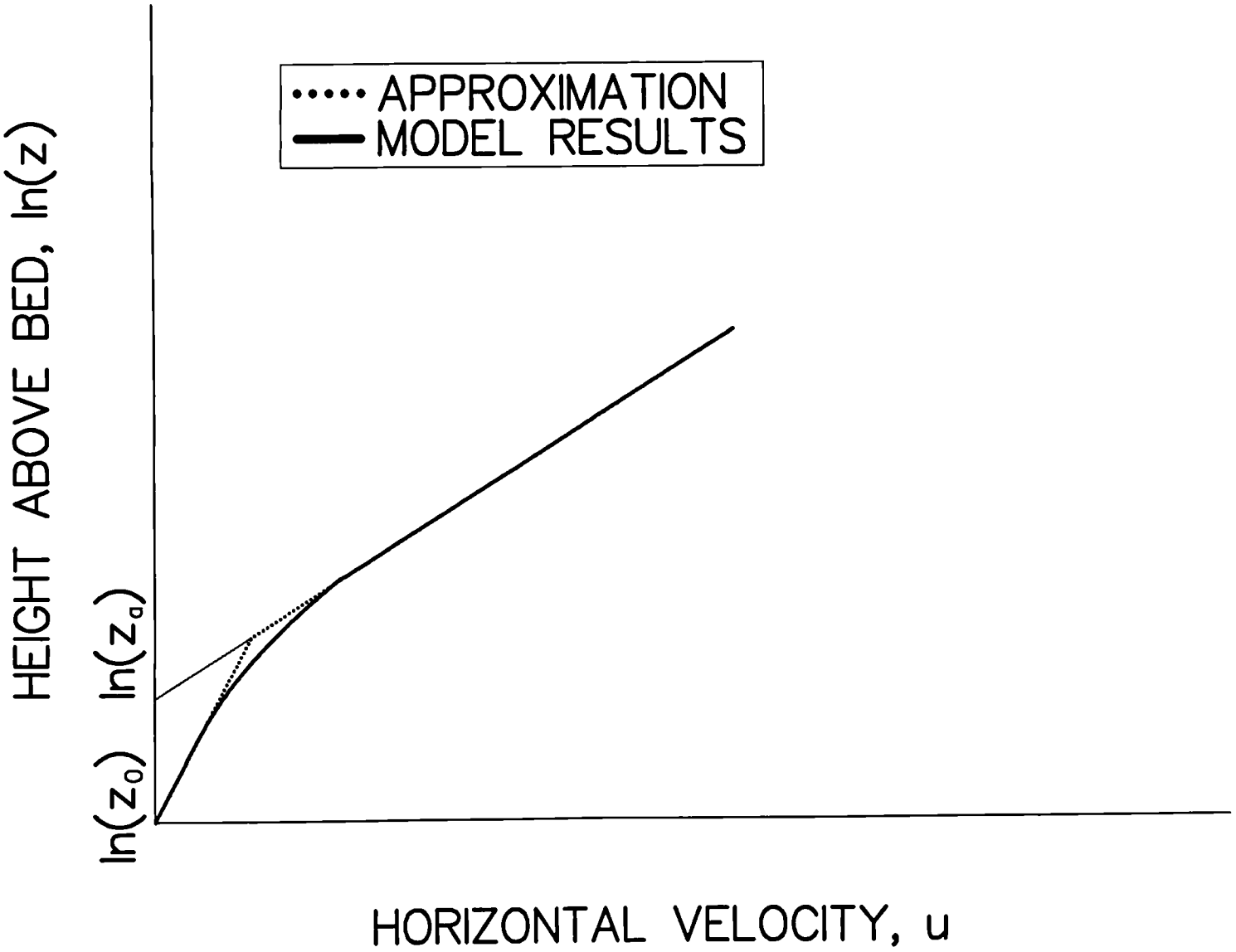

Fig. 7.38 Variables used in the approximation to the velocity profile.

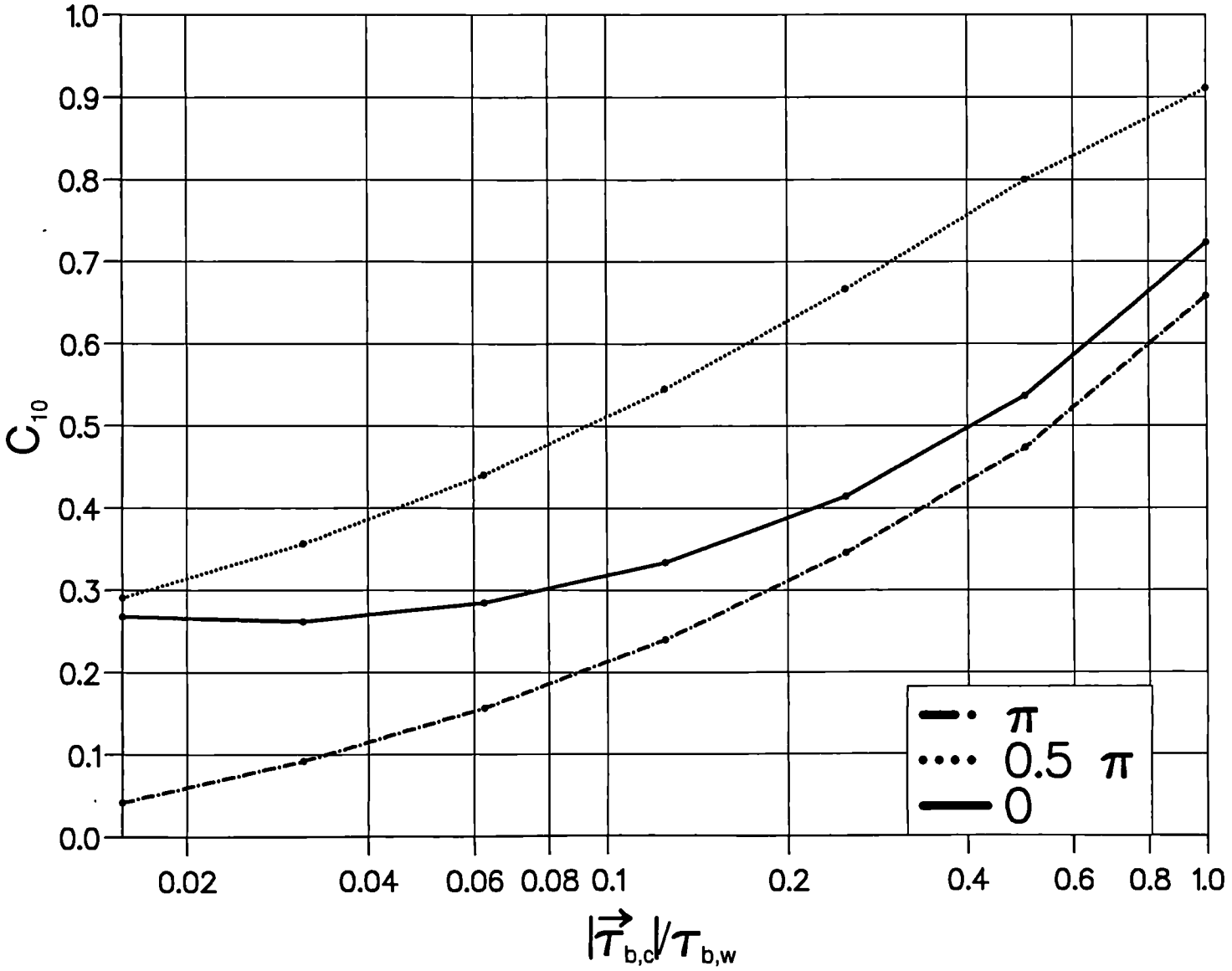

Fig. 7.39 The effect of $|\vec{\tau}_{b,c}|/\tau_{b,w}$ on the near bed velocity gradient (C_{10}): A/z_0=100.

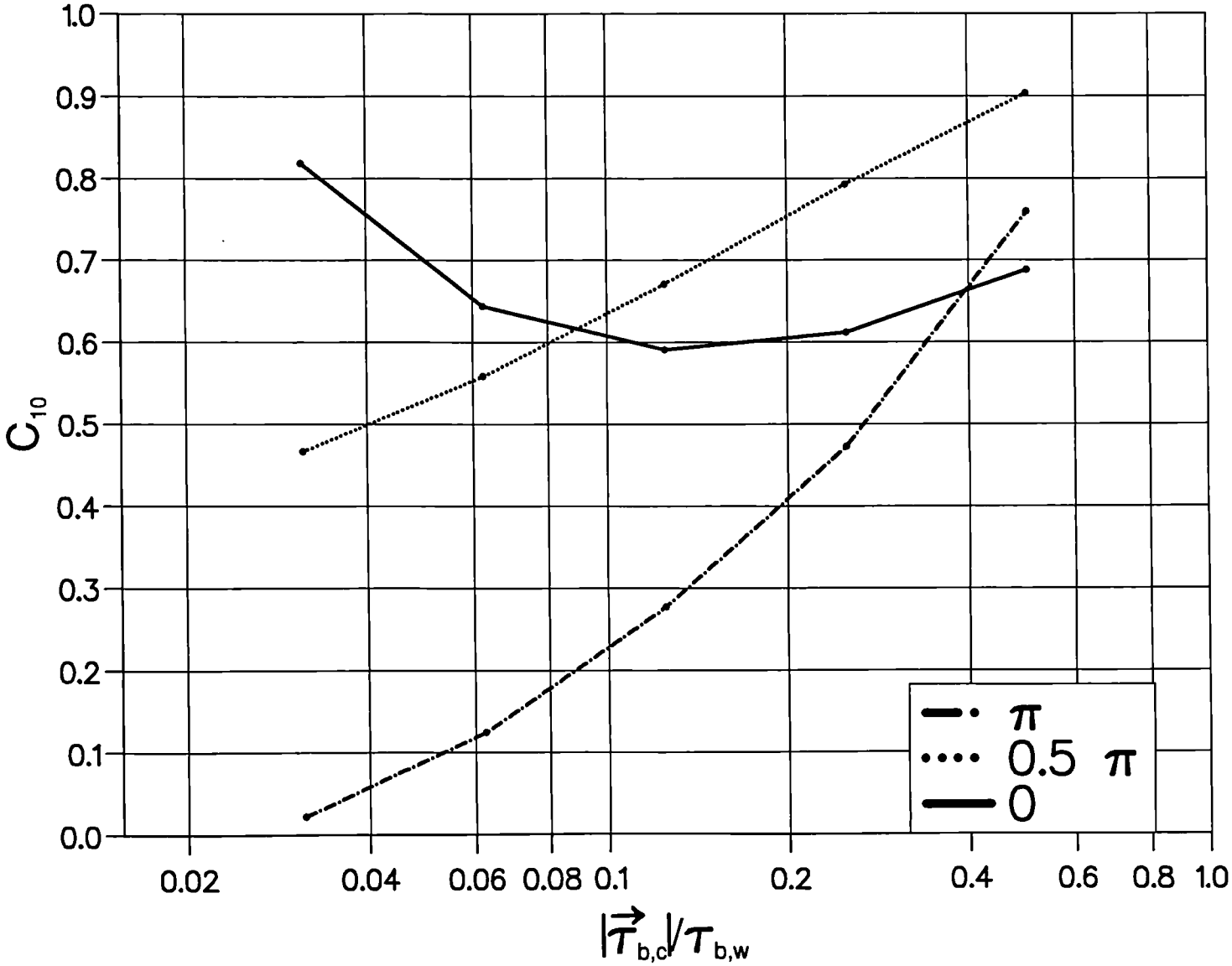

Fig. 7.40 The effect of $|\vec{\tau}_{b,c}|/\tau_{b,w}$ on the near bed velocity gradient (C_{10}): A/z_0=500.

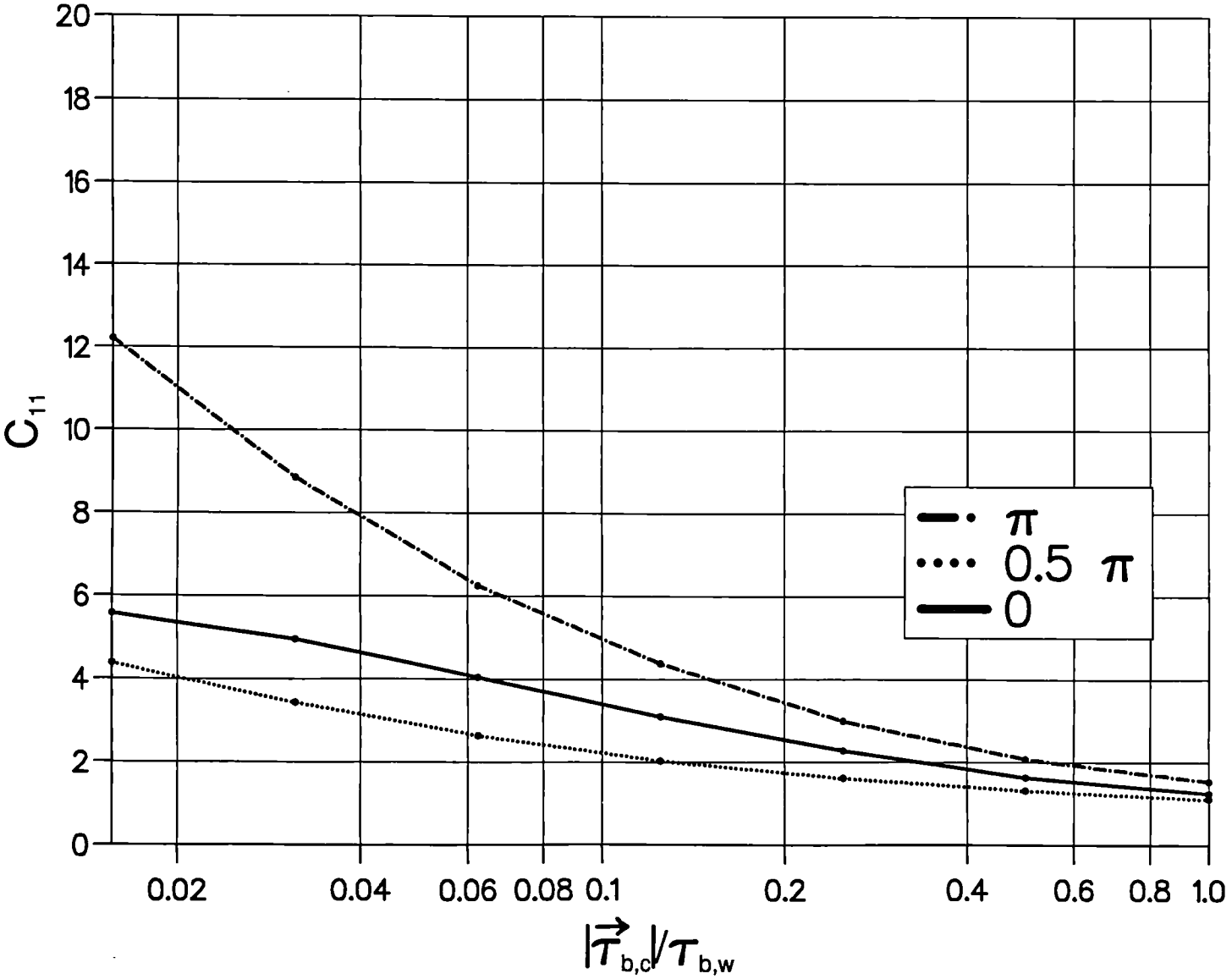

Fig. 7.41 The effect of $|\vec{\tau}_{b,c}|/\tau_{b,w}$ on the bed roughness amplification factor (C_{11}): $A/z_0=100$.

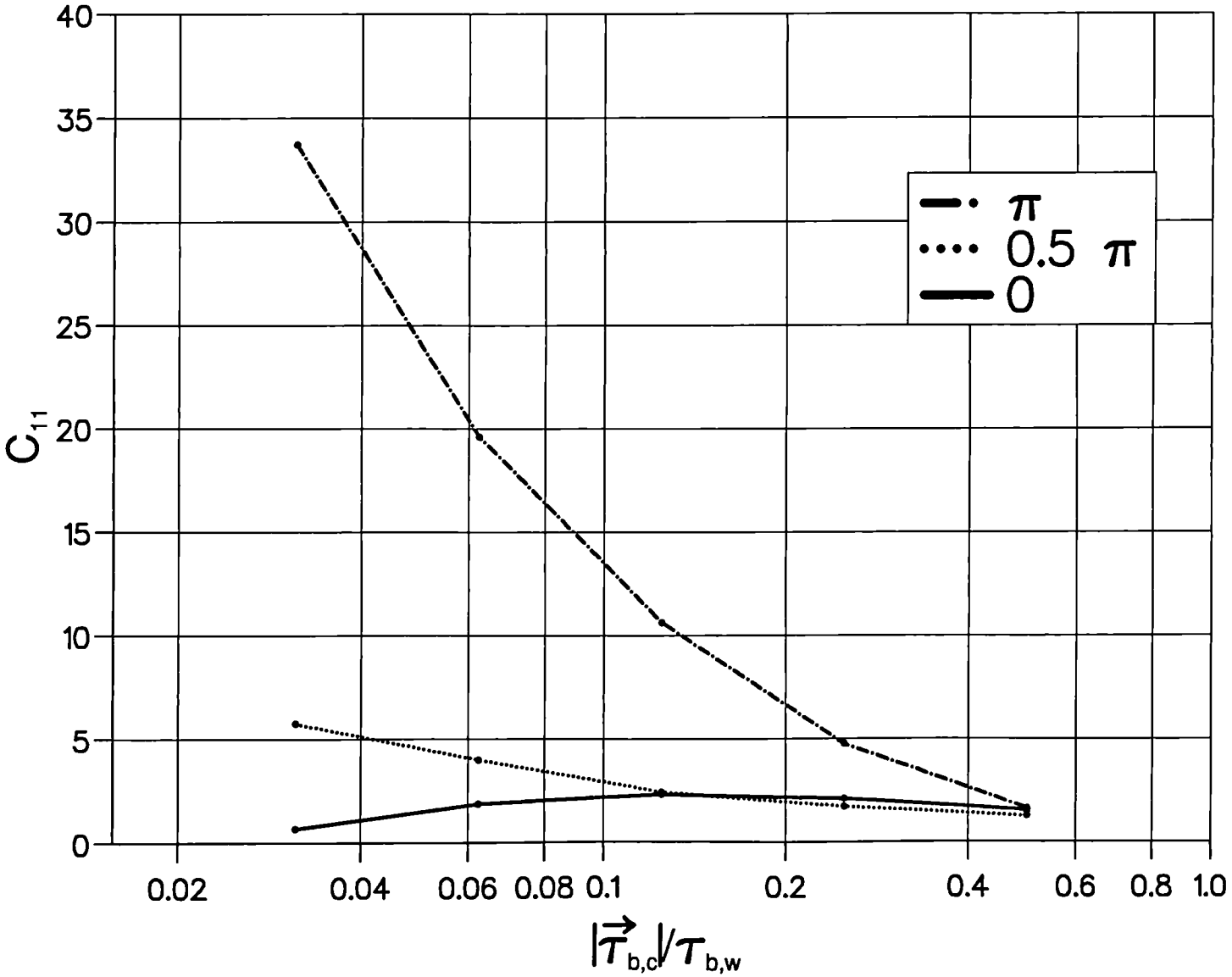

Fig. 7.42 The effect of $|\vec{\tau}_{b,c}|/\tau_{b,w}$ on the bed roughness amplification factor (C_{11}): A/z_0=500.

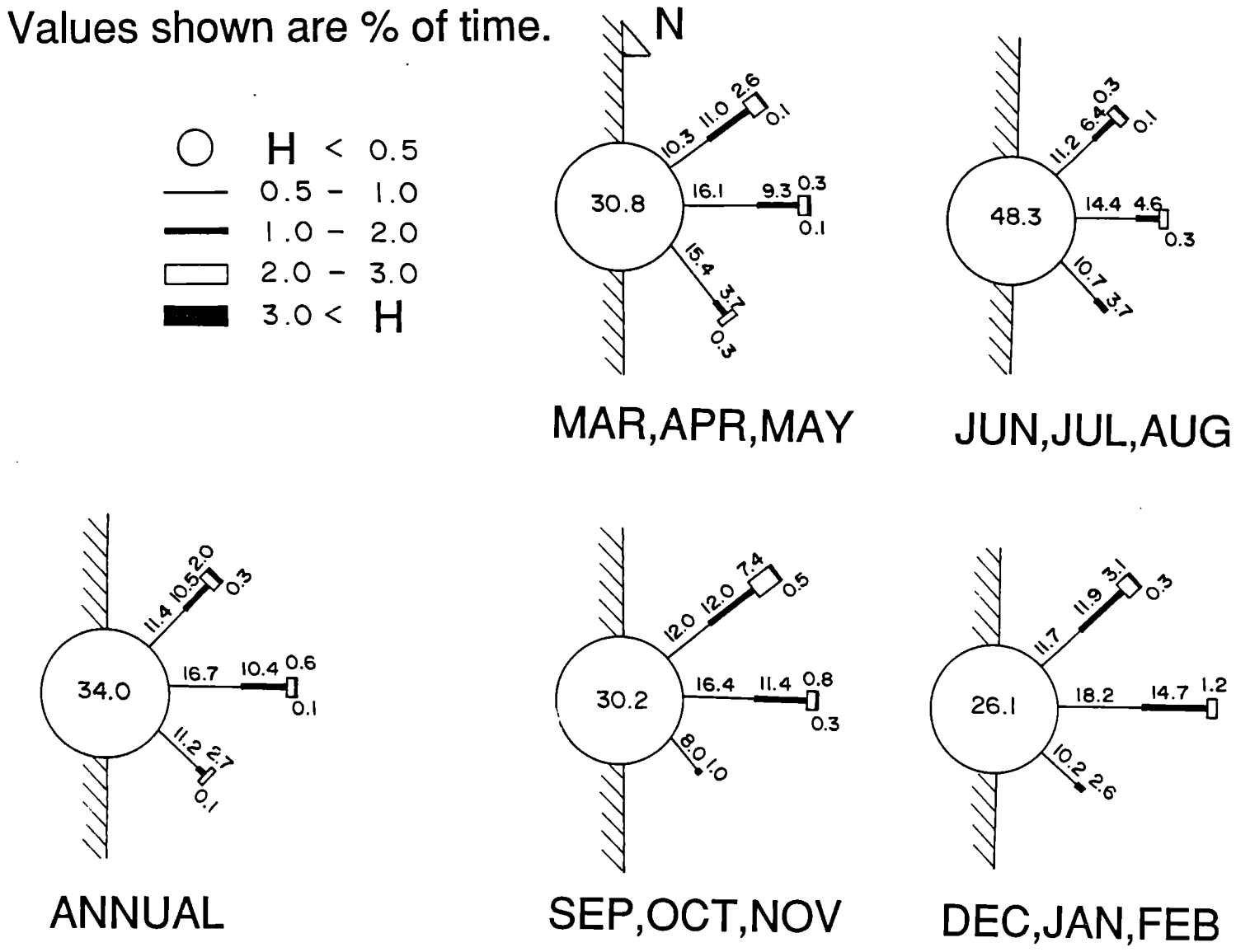

Fig. 8.1 Annual wave climate at Chukpyon.

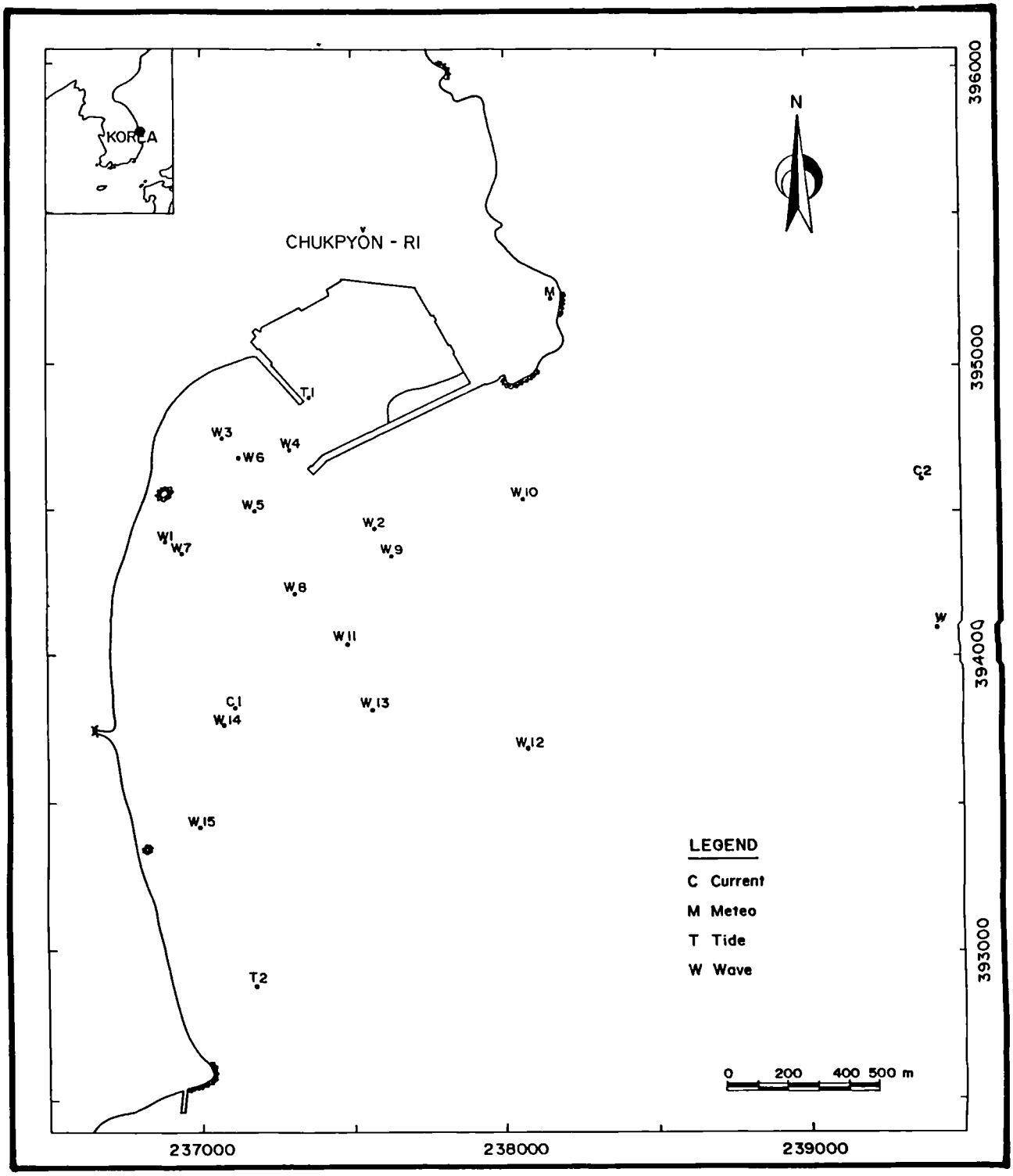

Fig. 8.2 Measurement stations for wave height.

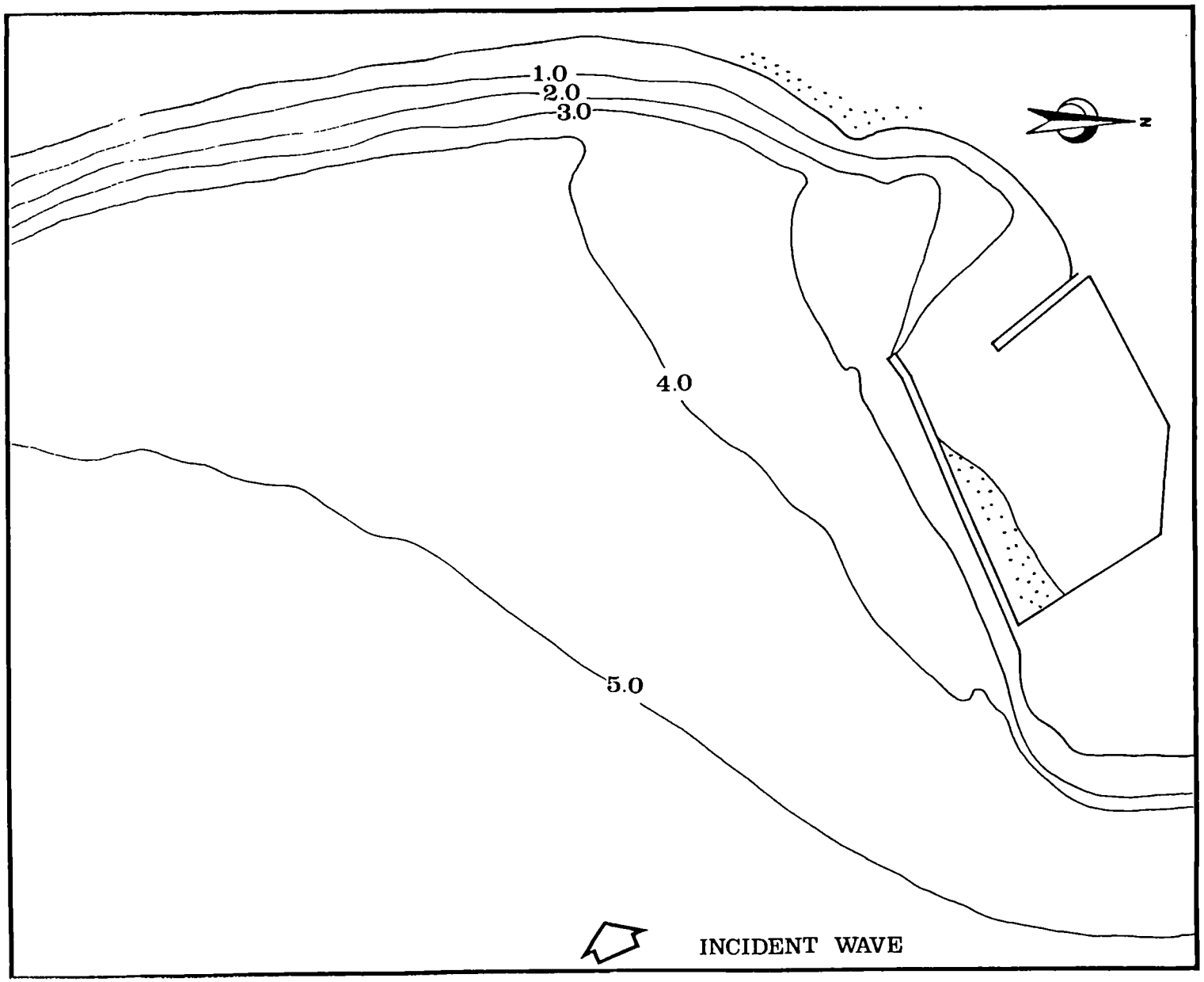

Fig. 8.3a Wave height distribution at Chukpyon given by the present model: wave directions of ENE.

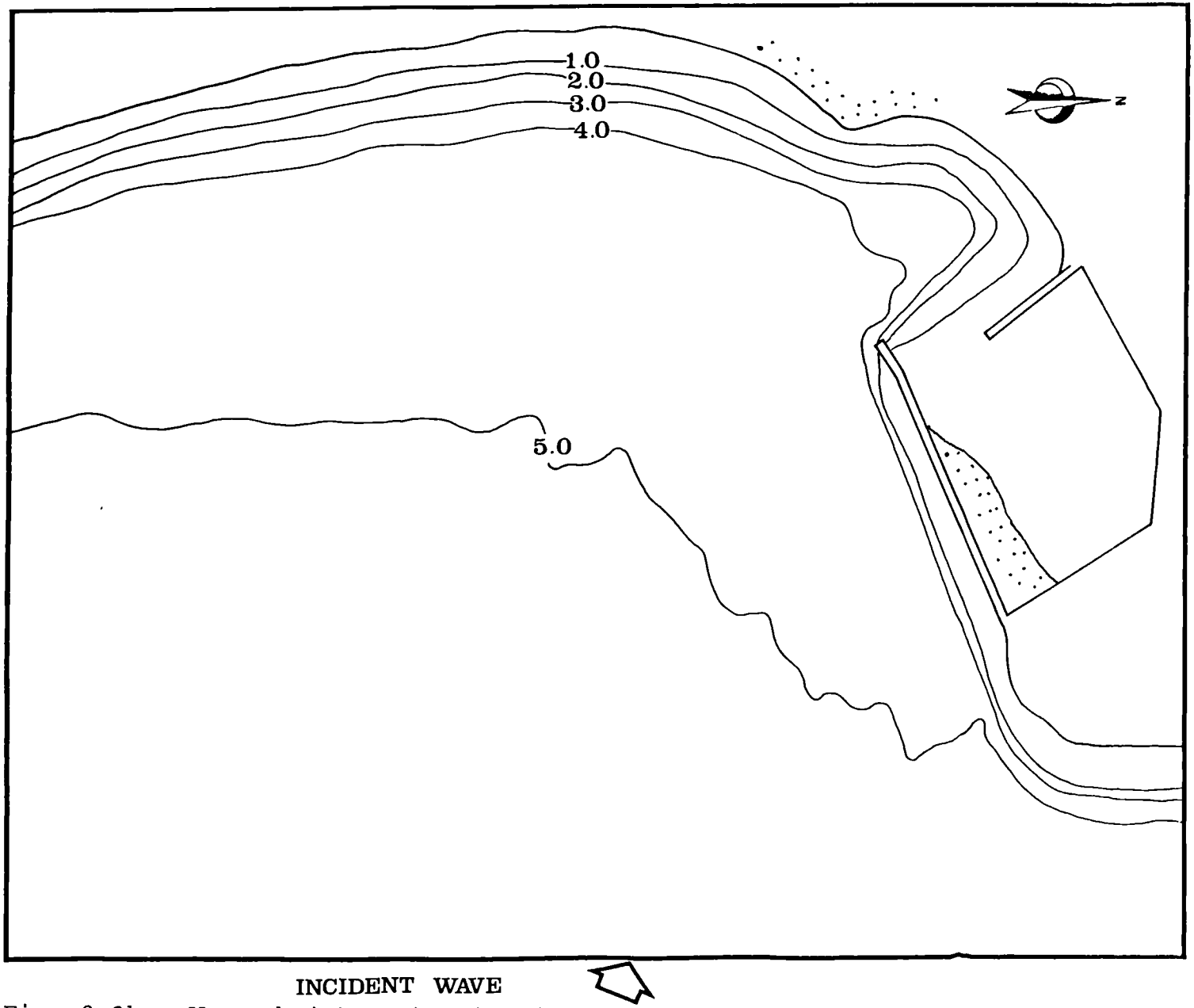

Fig. 8.3b Wave height distribution at Chukpyon given by the present model: wave directions of ESE.

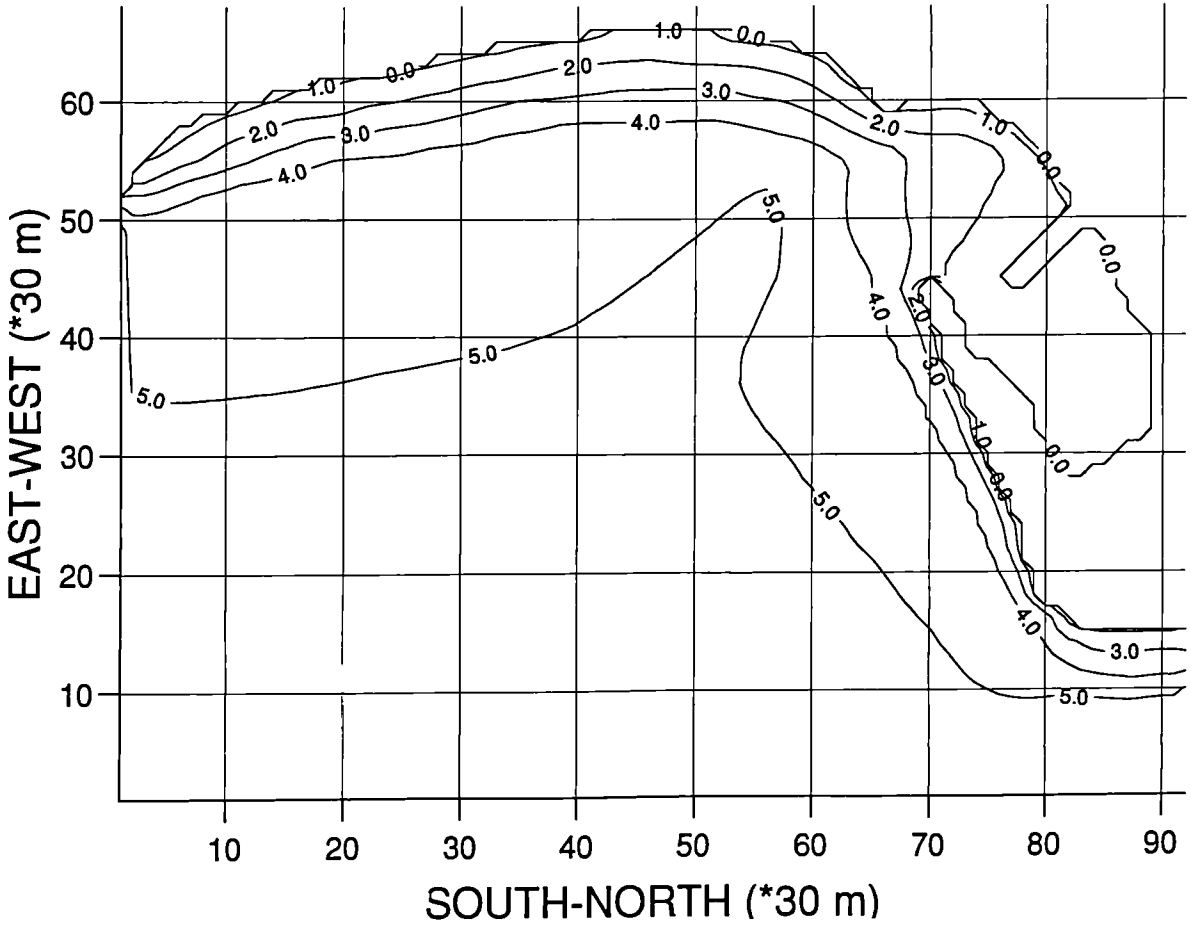

Fig. 8.3c Wave heitht distribution given by the Yoo and O'Connor model: wave direction of ESE.

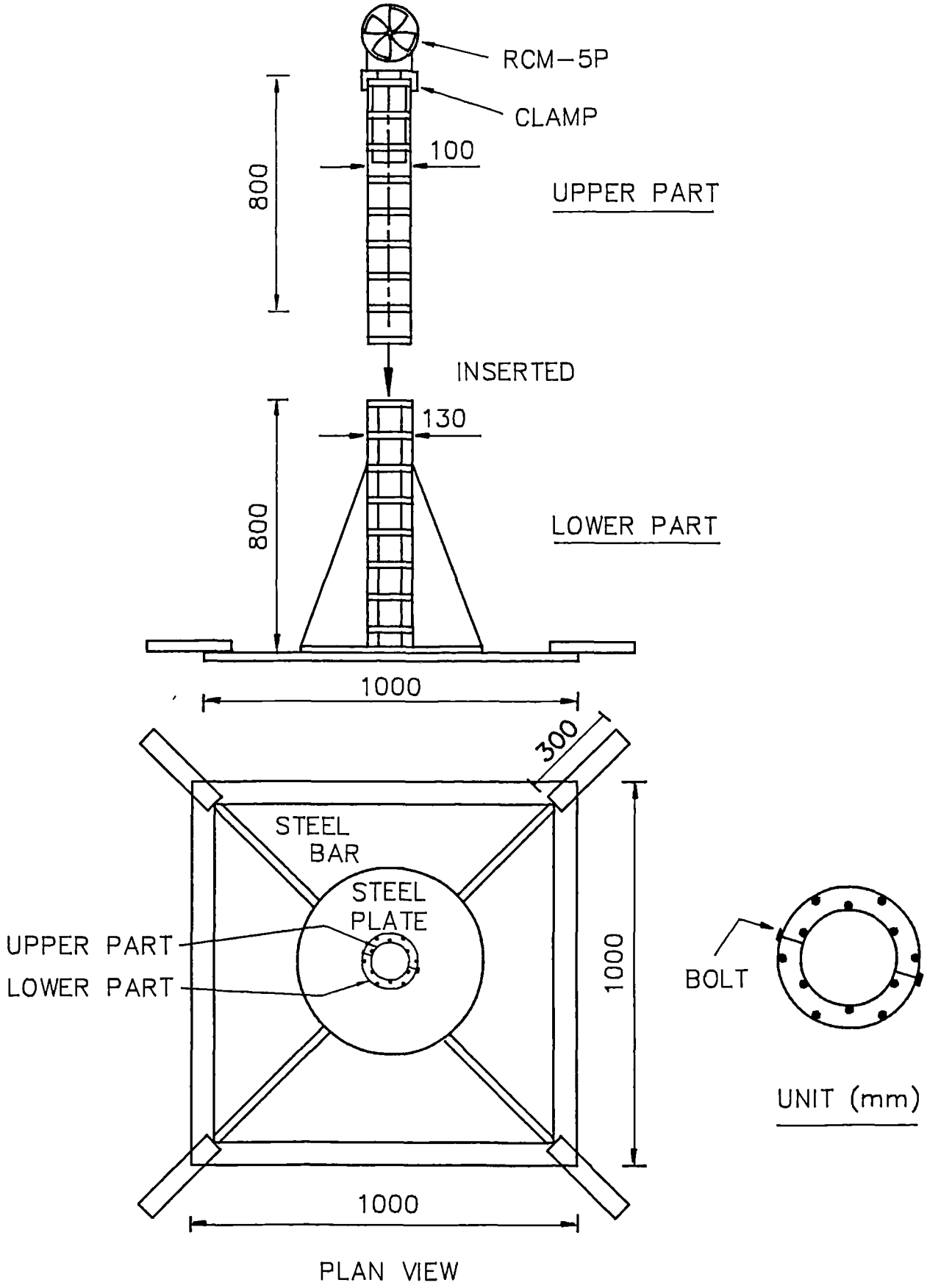

Fig. 8.4 Bed frame for the wave-induced current divice RCM-5P.

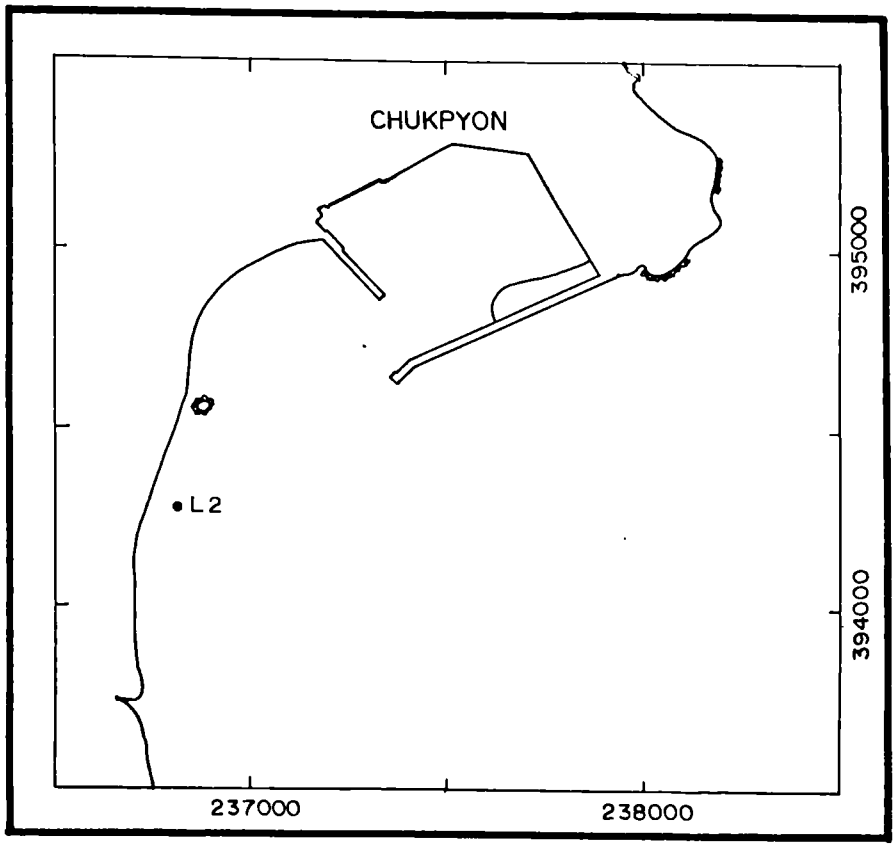

Fig. 8.5 Measurement station for wave-induced current.

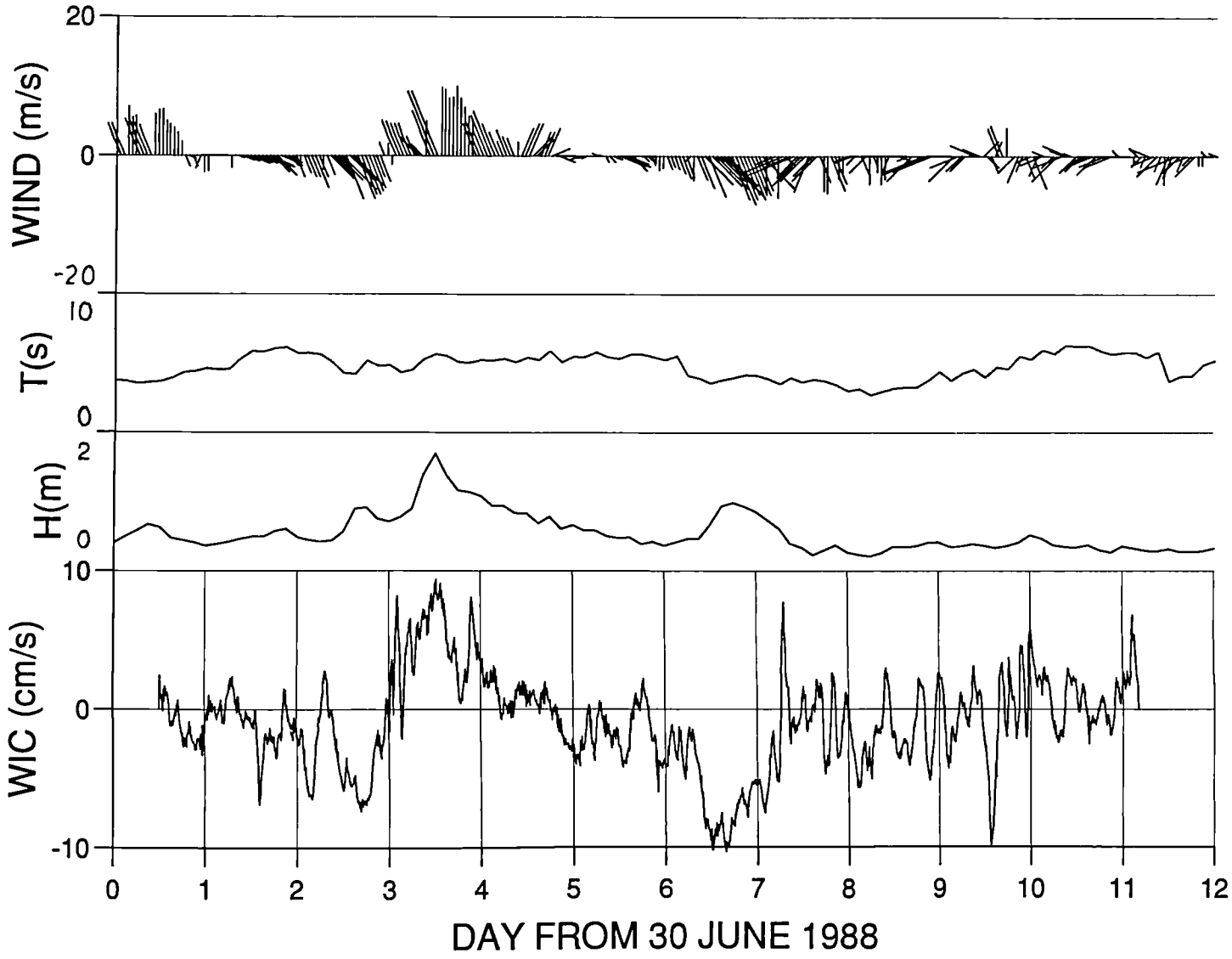

Fig. 8.6 A time-series of measured wave-induced current.

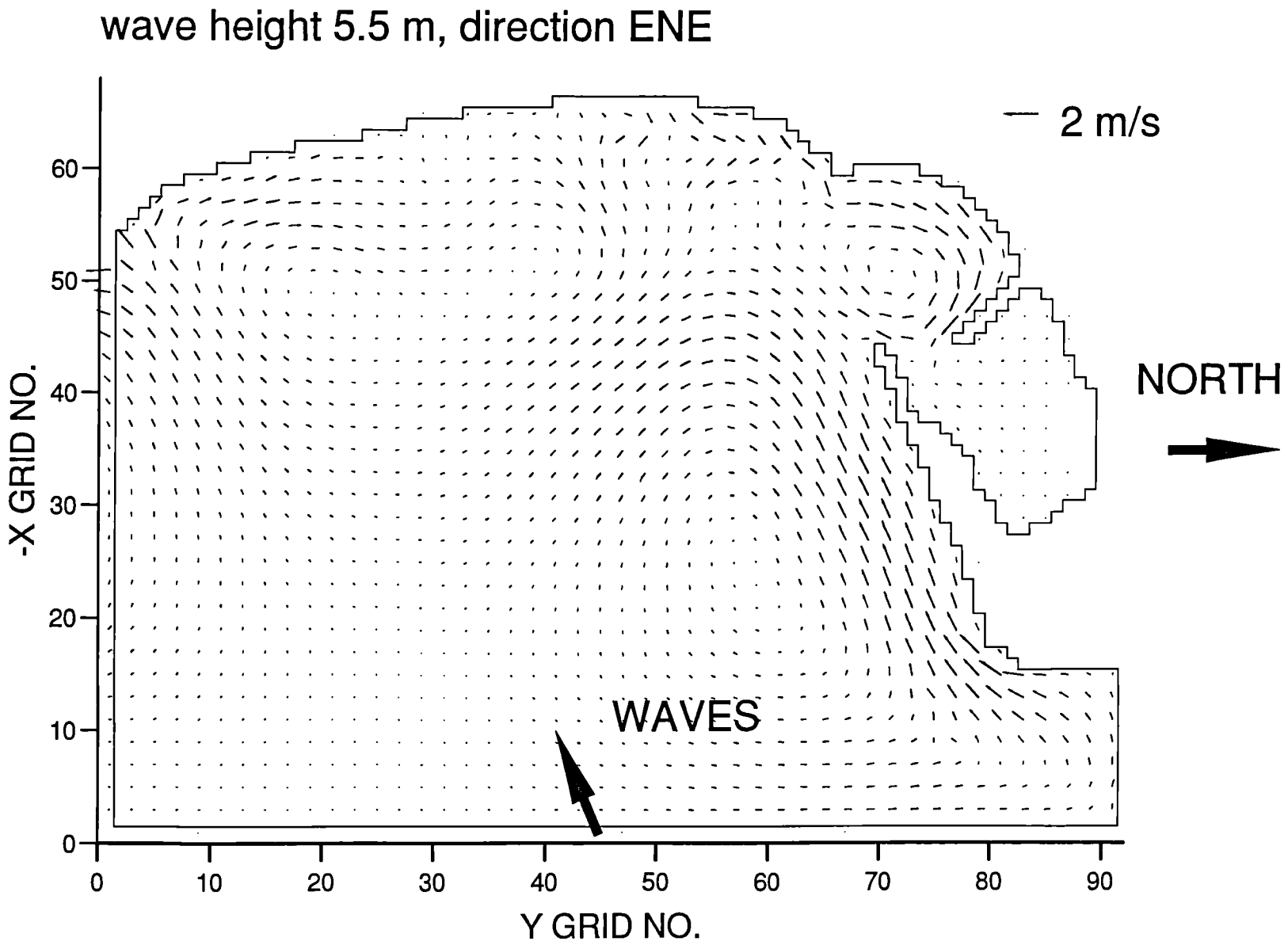

Fig. 8.7a Wave-induced current vectors given by the present model: wave directions of ENE.

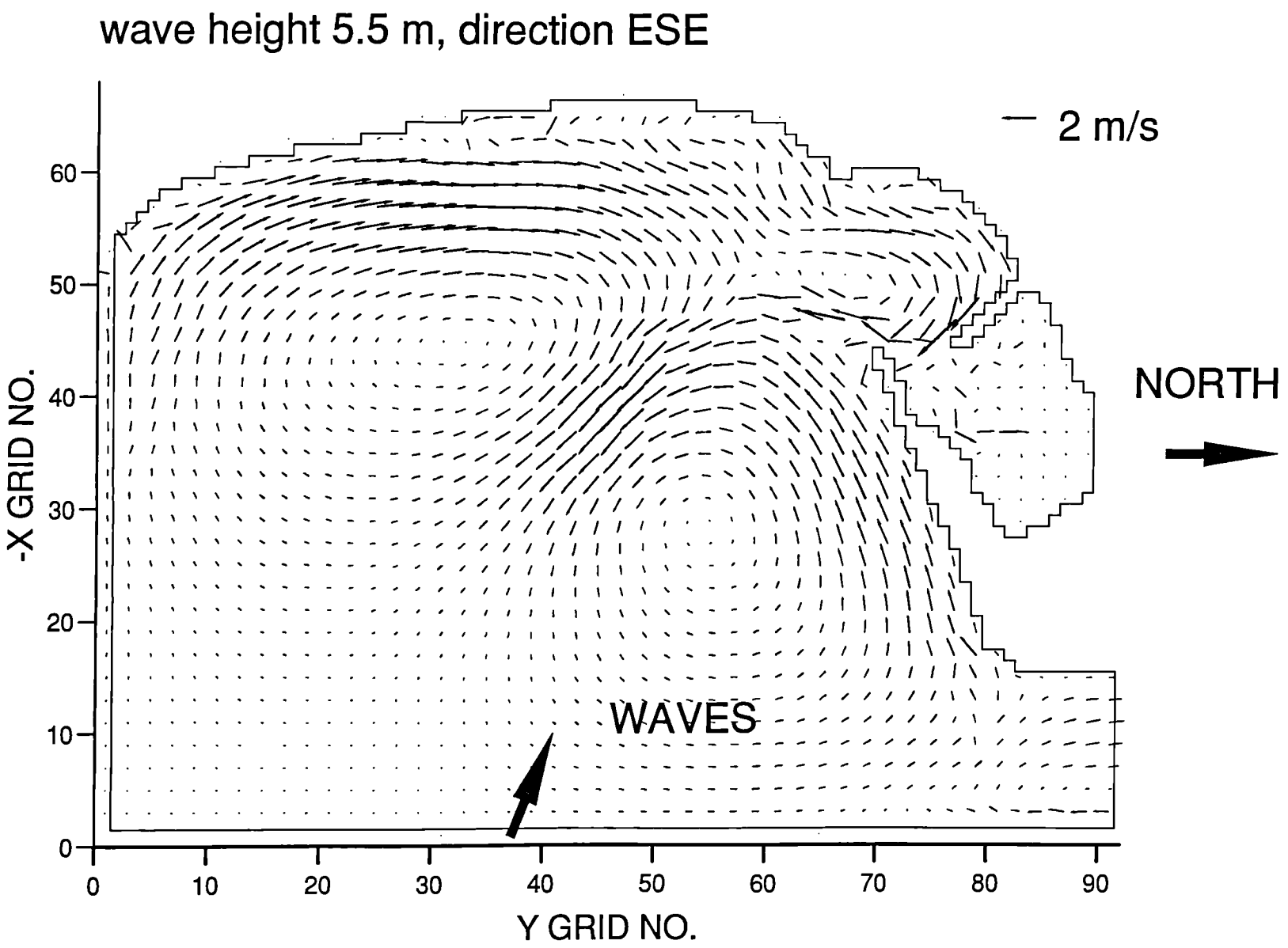

Fig. 8.7b Wave-induced current vectors given by the present model: wave directions of ESE.

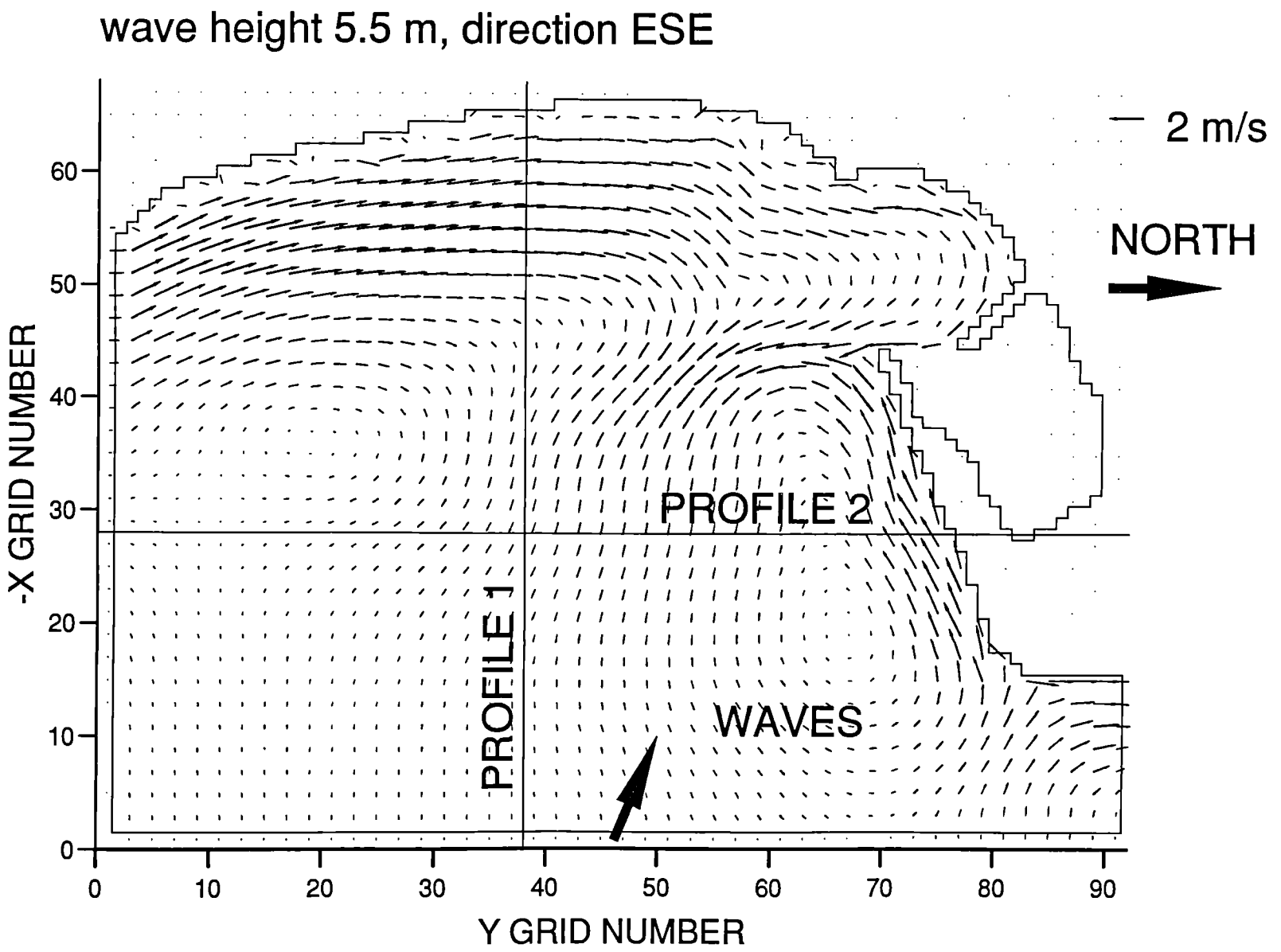

Fig. 8.8 Wave-induced current vectors given by the Yoo and O'Connor model: wave direction of ESE.

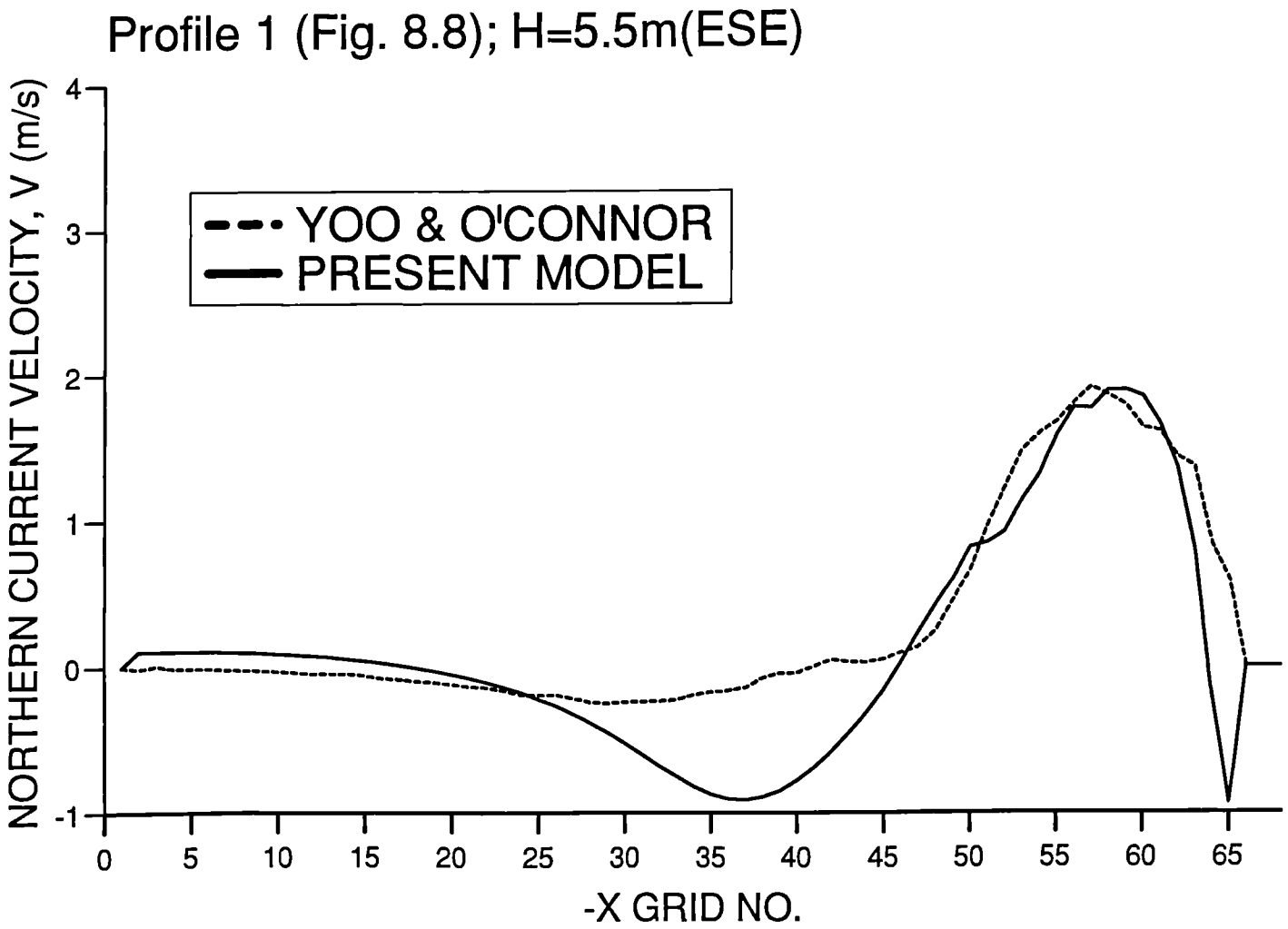

Fig. 8.9a Comparison of longshore current profiles given by two computer models: profiles 1.

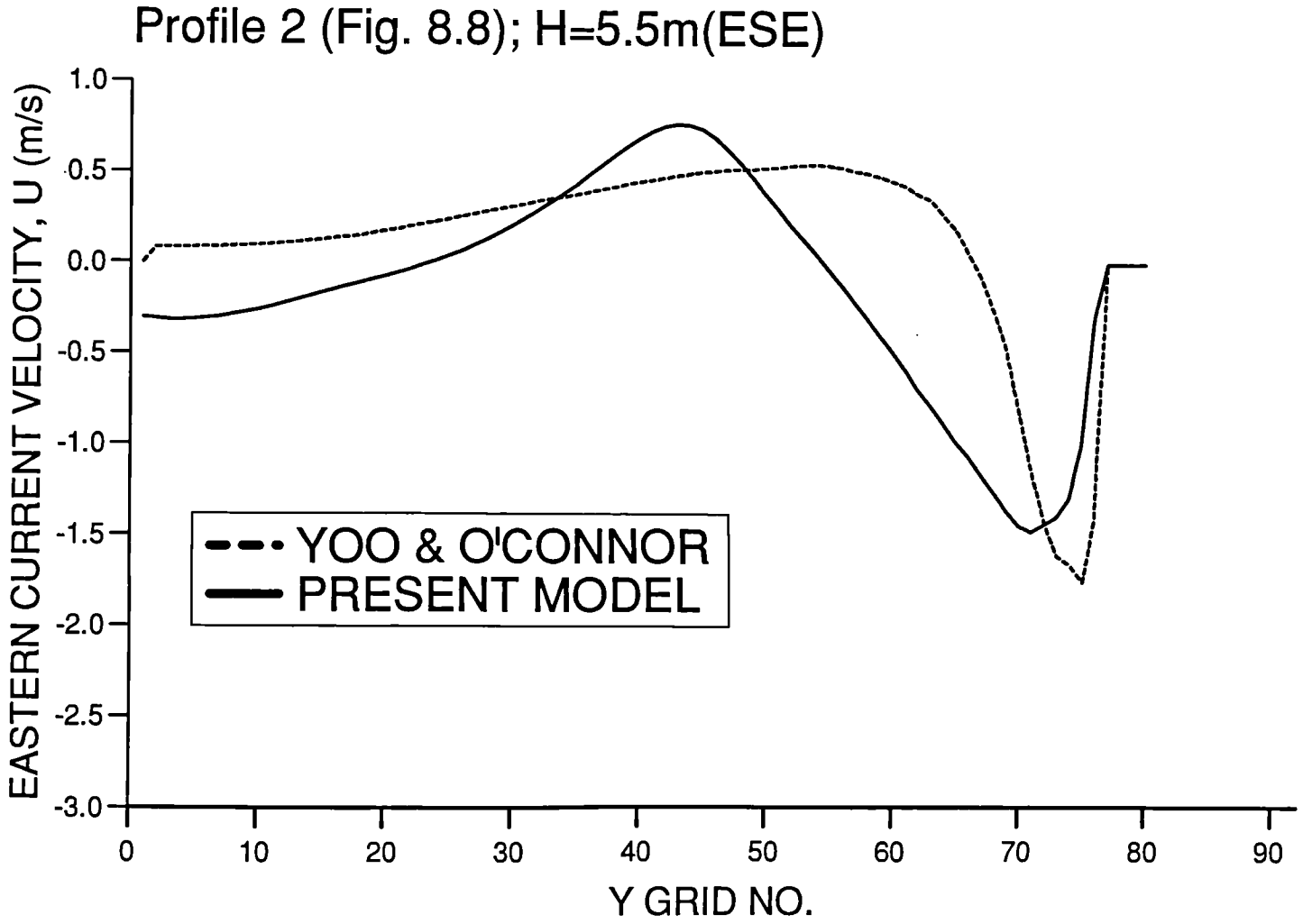

Fig. 8.9b Comparison of longshore current profiles given by two computer models: profiles 2.

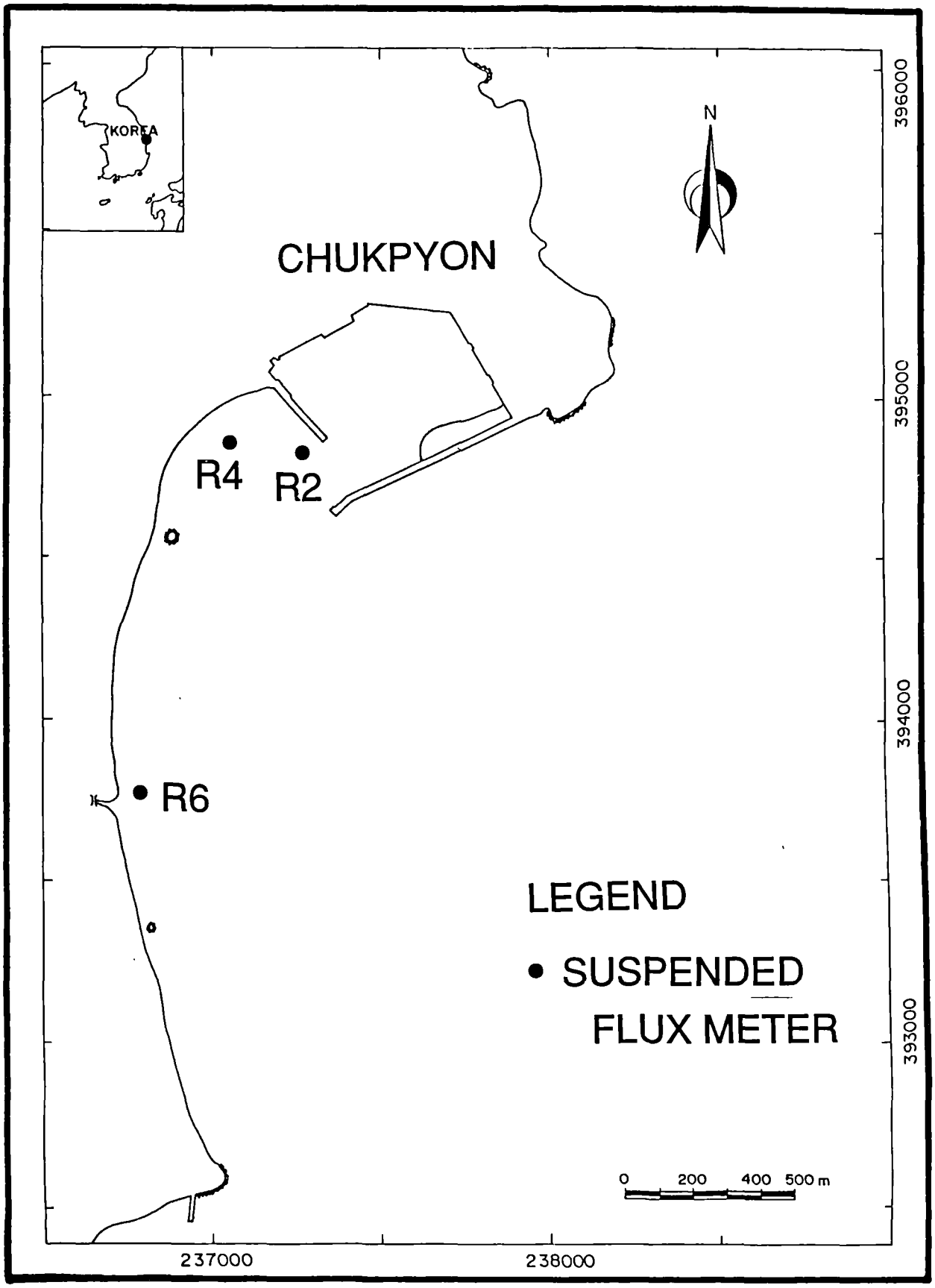

Fig. 8.10 Measurement stations for suspended sediment concentration.

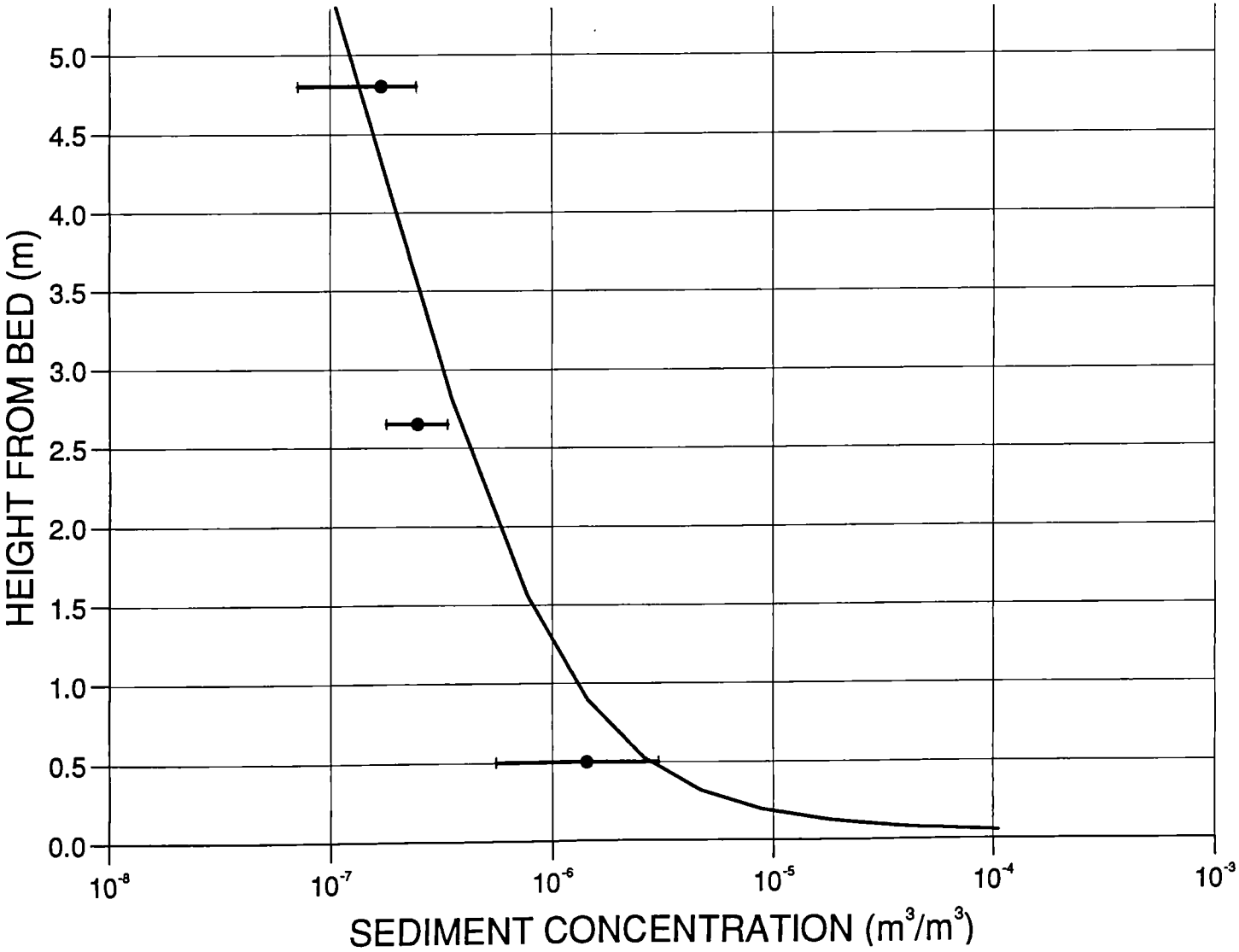

Fig. 8.11a Comparison of calculated and measured suspended sediment concentrations: Station R2.

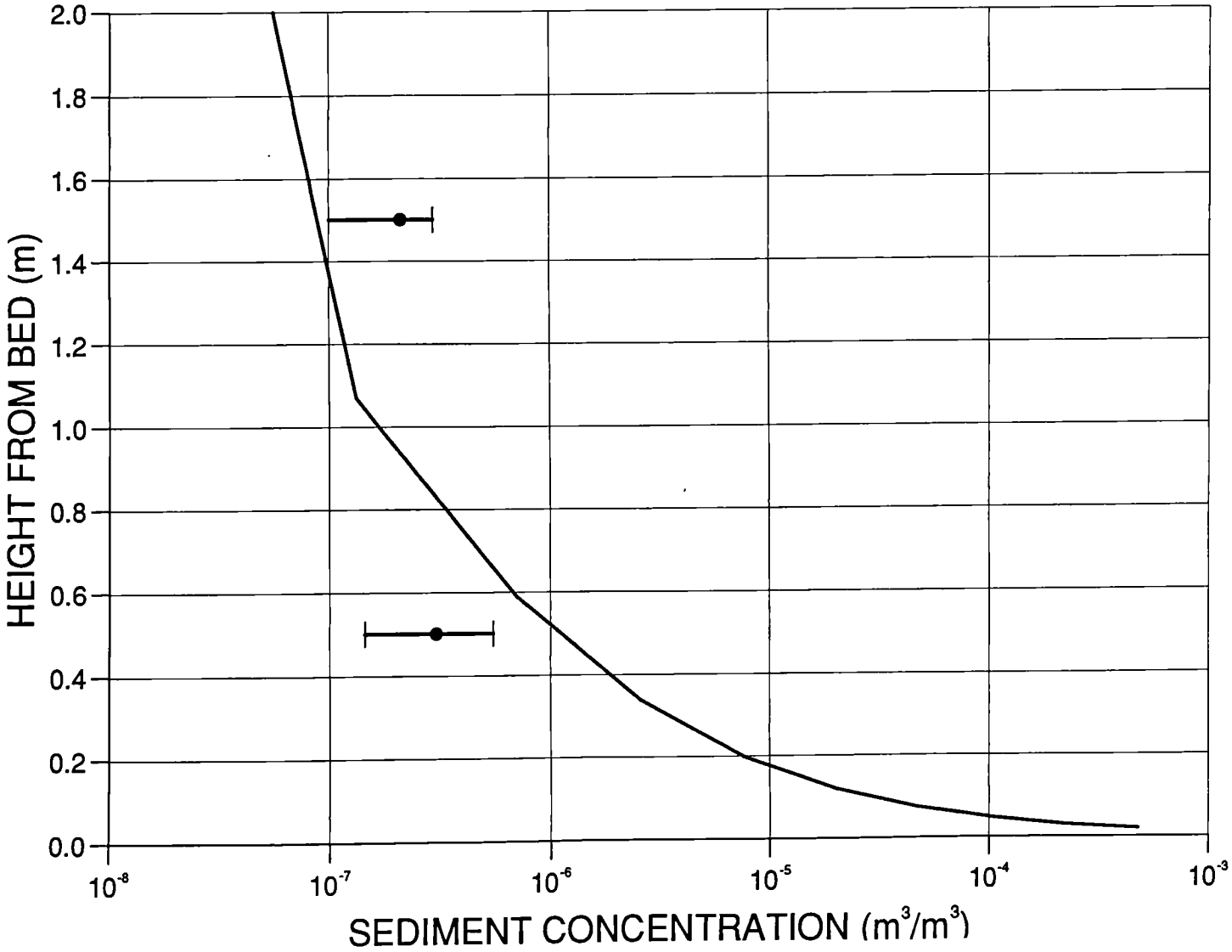

Fig. 8.11b Comparison of calculated and measured suspended sediment concentrations: Station R4.

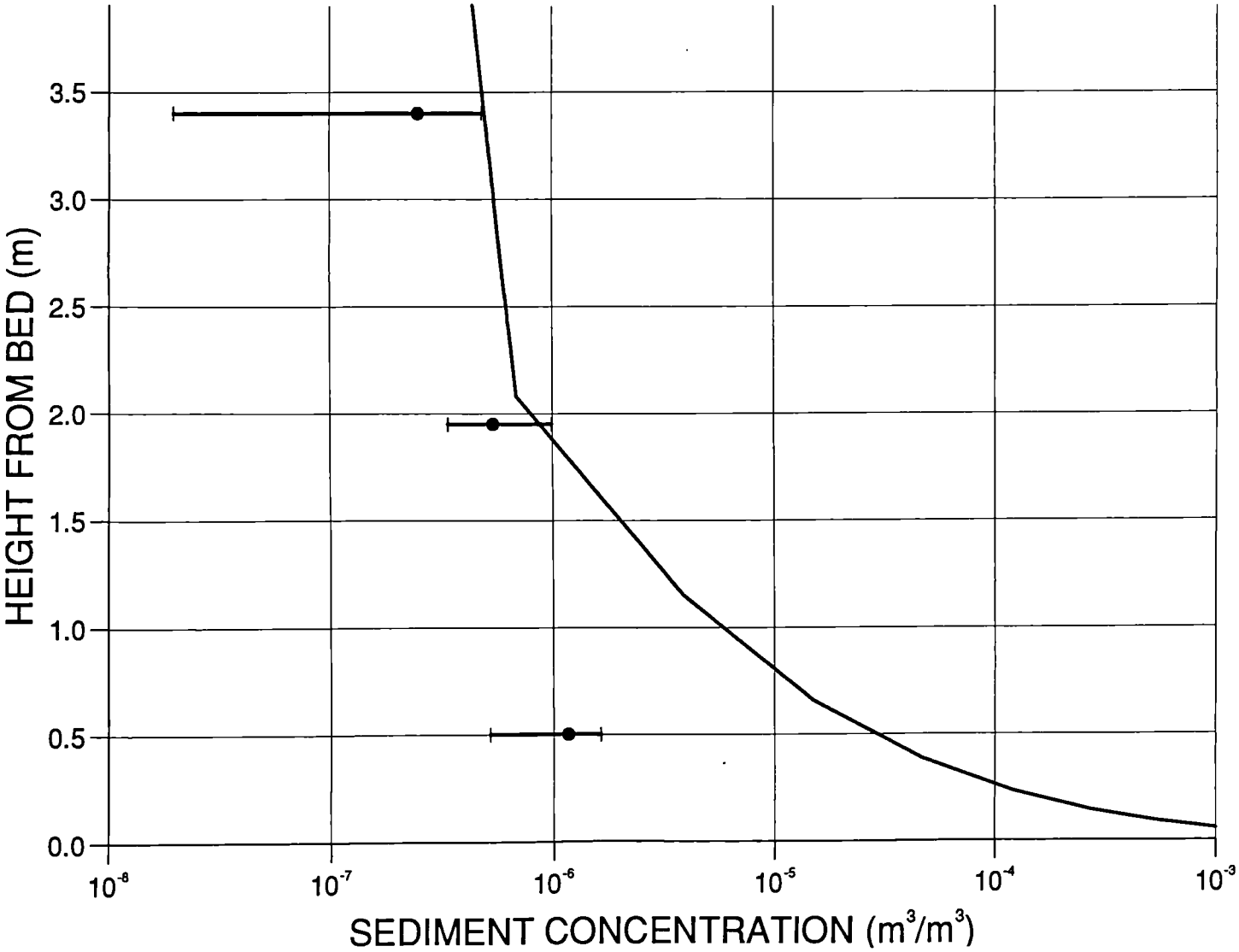

Fig. 8.11c Comparison of calculated and measured suspended sediment concentrations: Station R6.

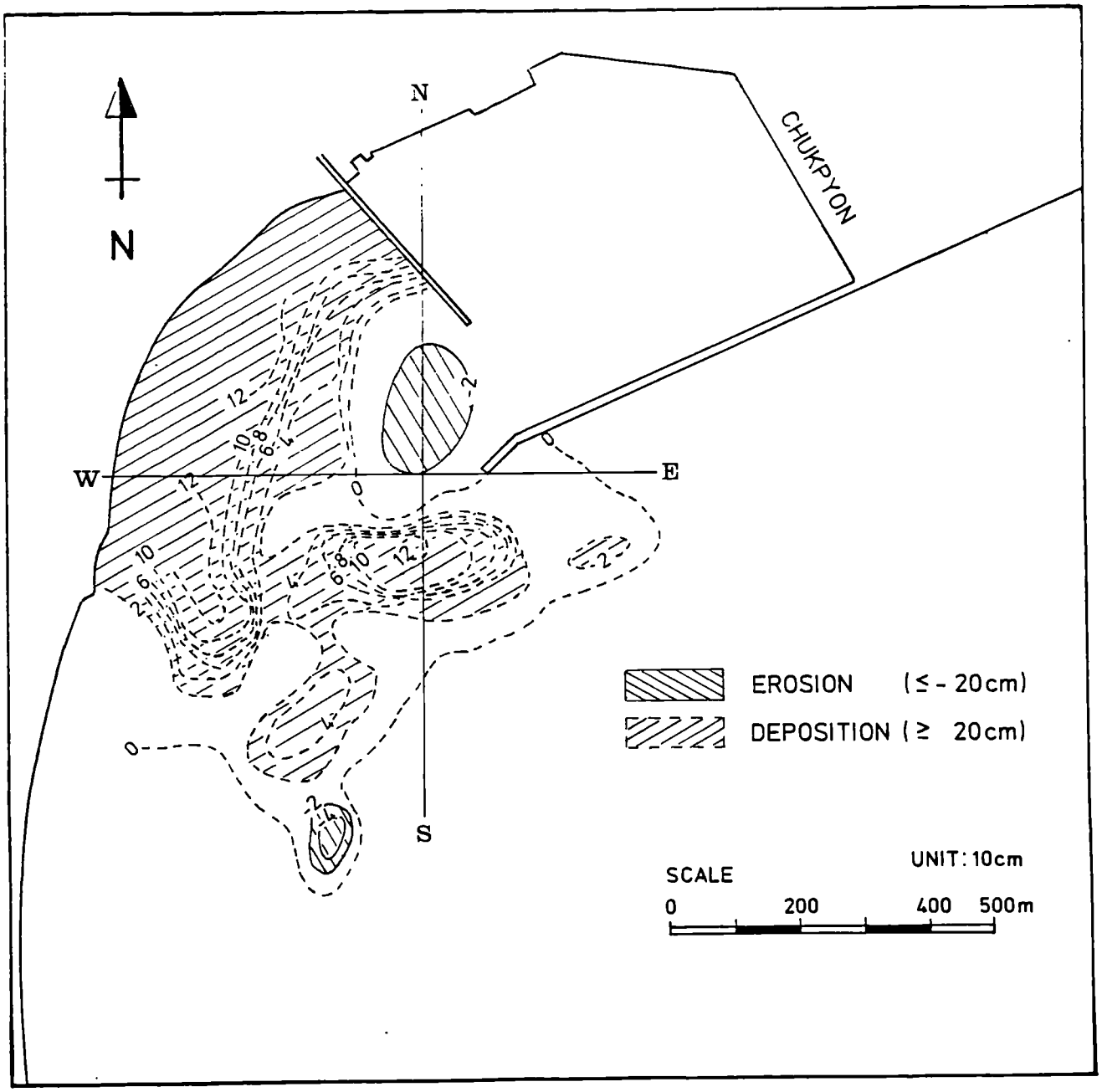

Fig. 8.12 Measured depth change between 10 June 1987 and 3 Nov. 1987.

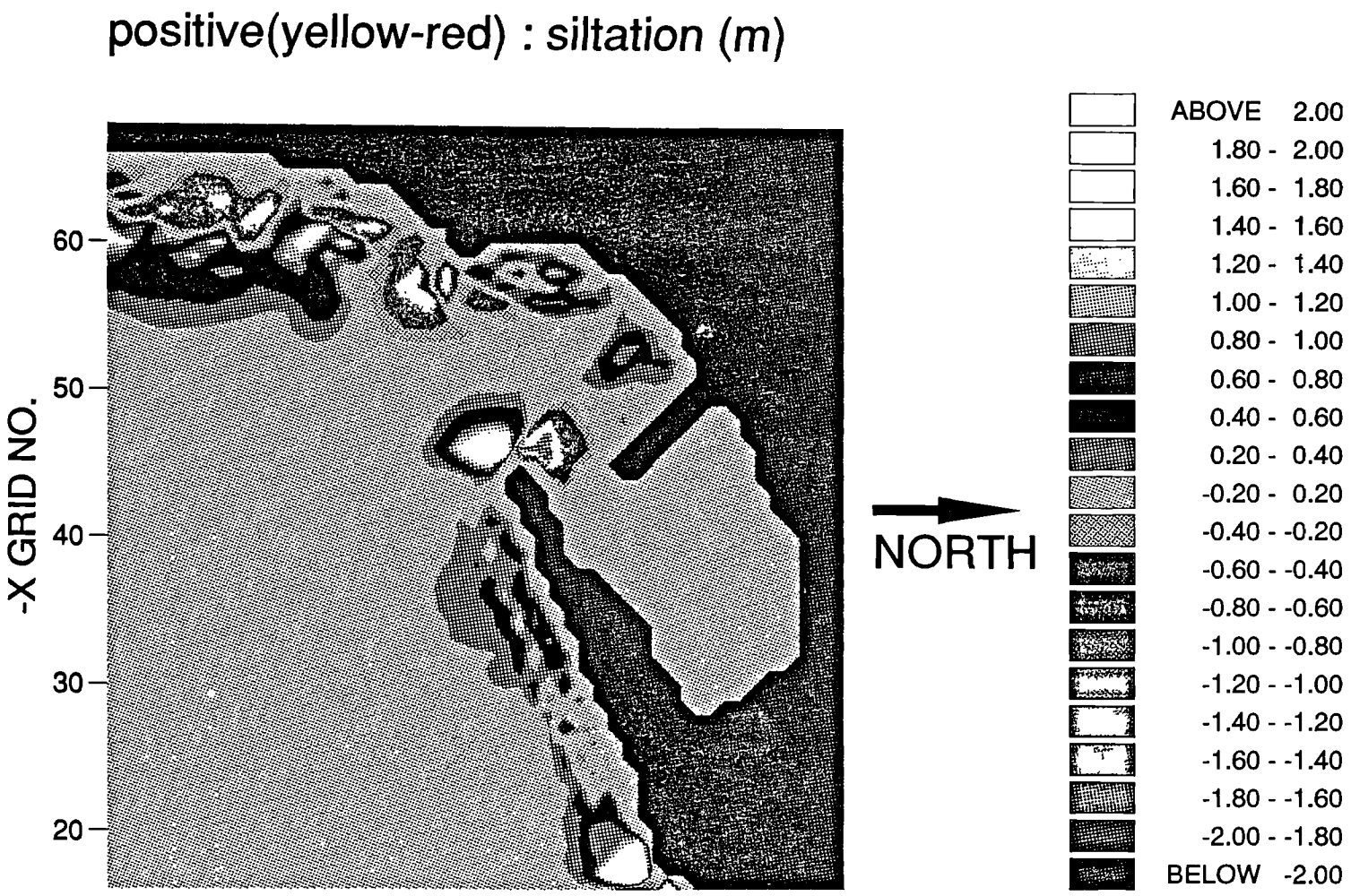

Fig. 8.13 Calculated depth change between 10 June 1987 and 3 Nov. 1987.

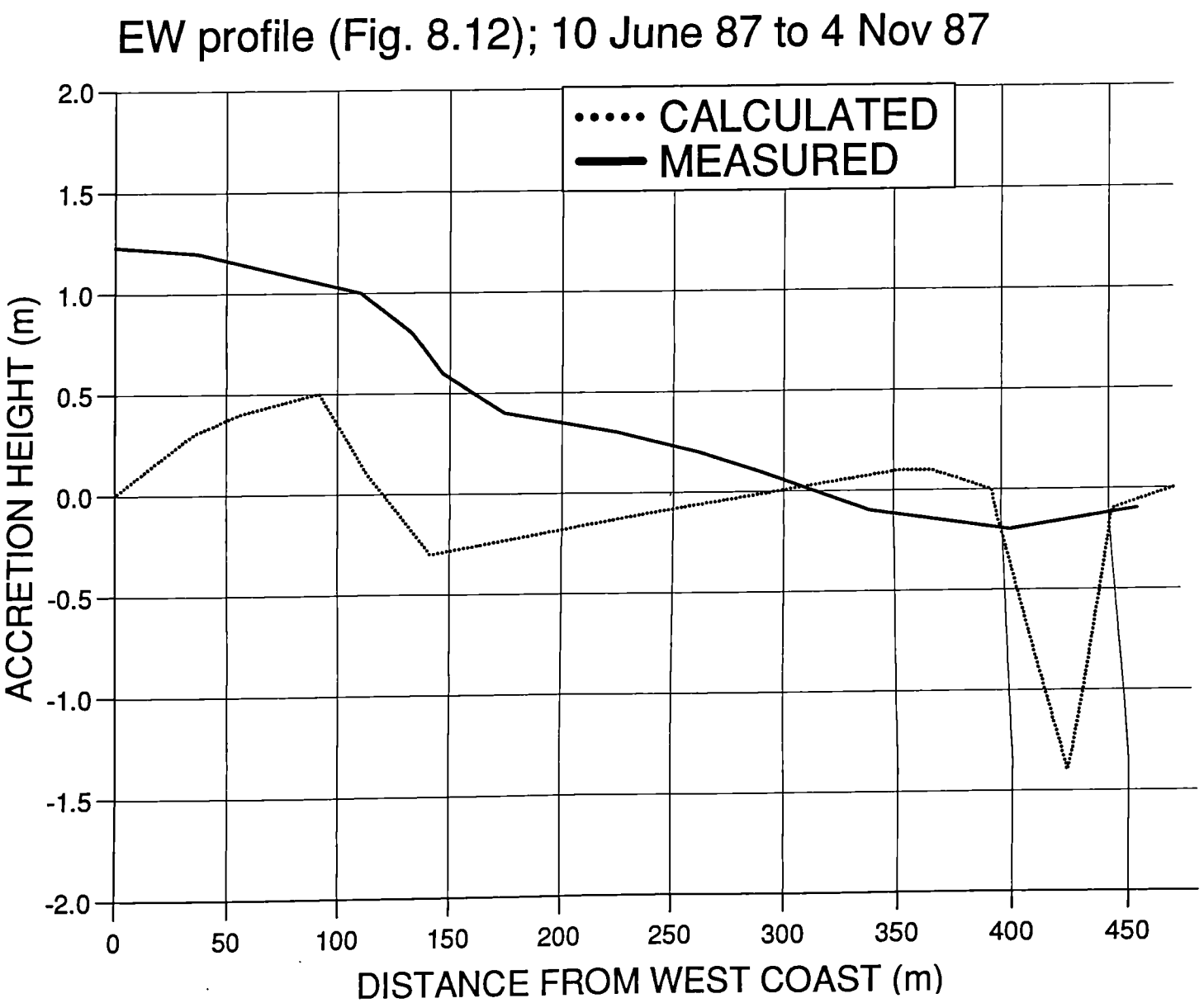

Fig. 8.14a Comparison of calculated and measured depth change profiles: profile EW.

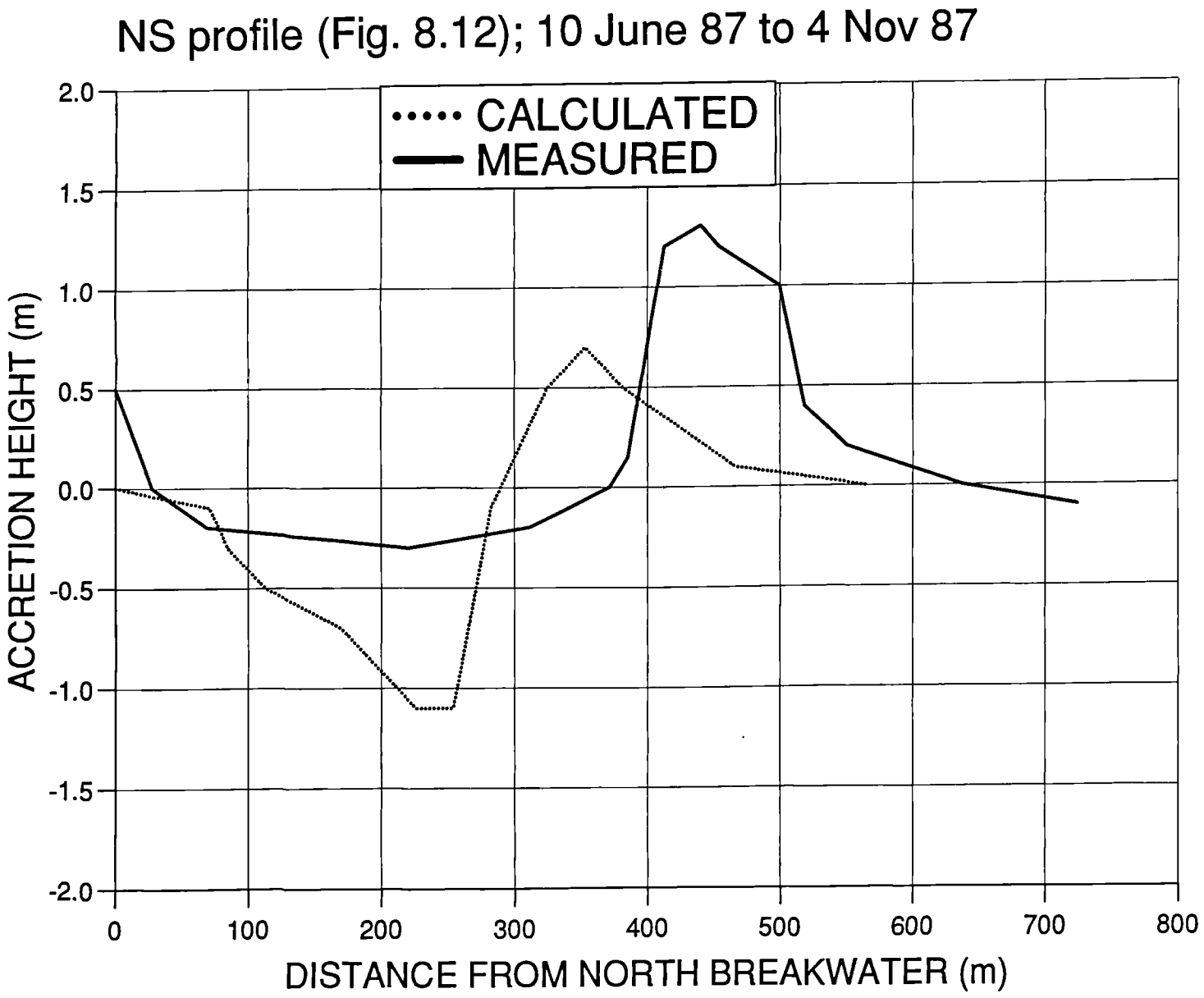

Fig. 8.14b Comparison of calculated and measured depth change profiles: profile NS.

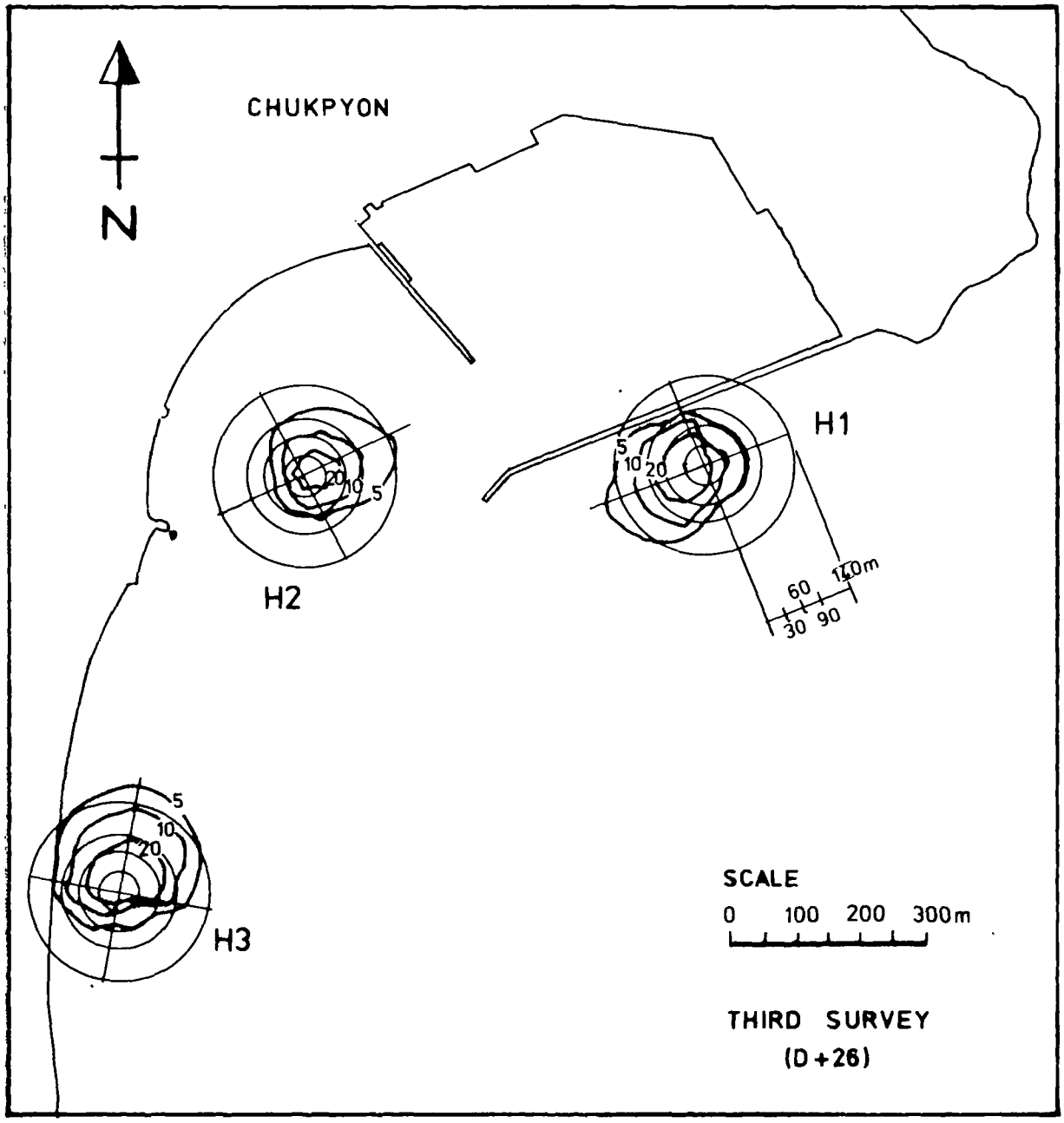

Fig. 8.15 Results of the fluorescent tracer tests at Chukpyon.

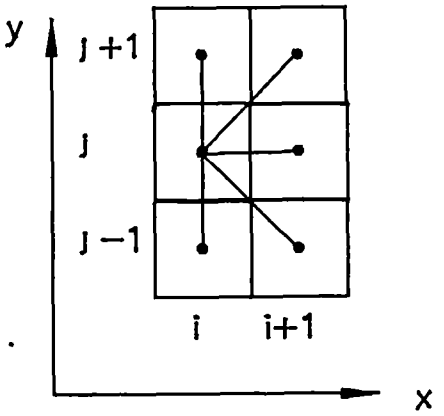

Fig. A.1

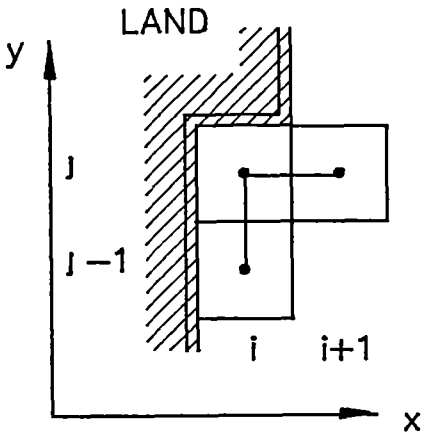

Fig. A.2

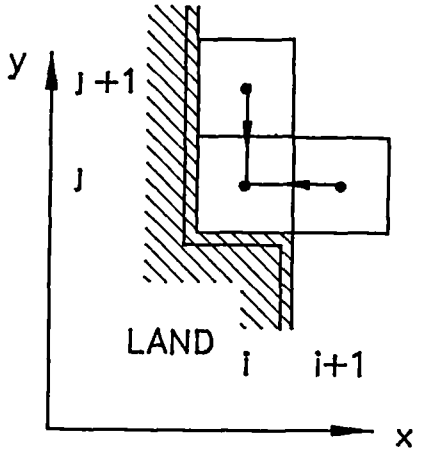

Fig. A.3

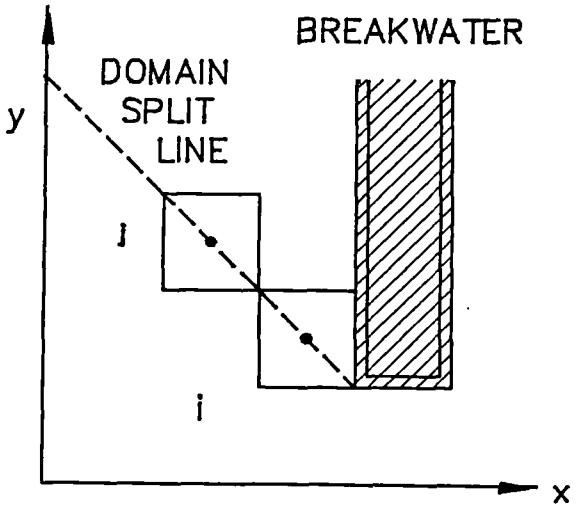

Fig. A.4

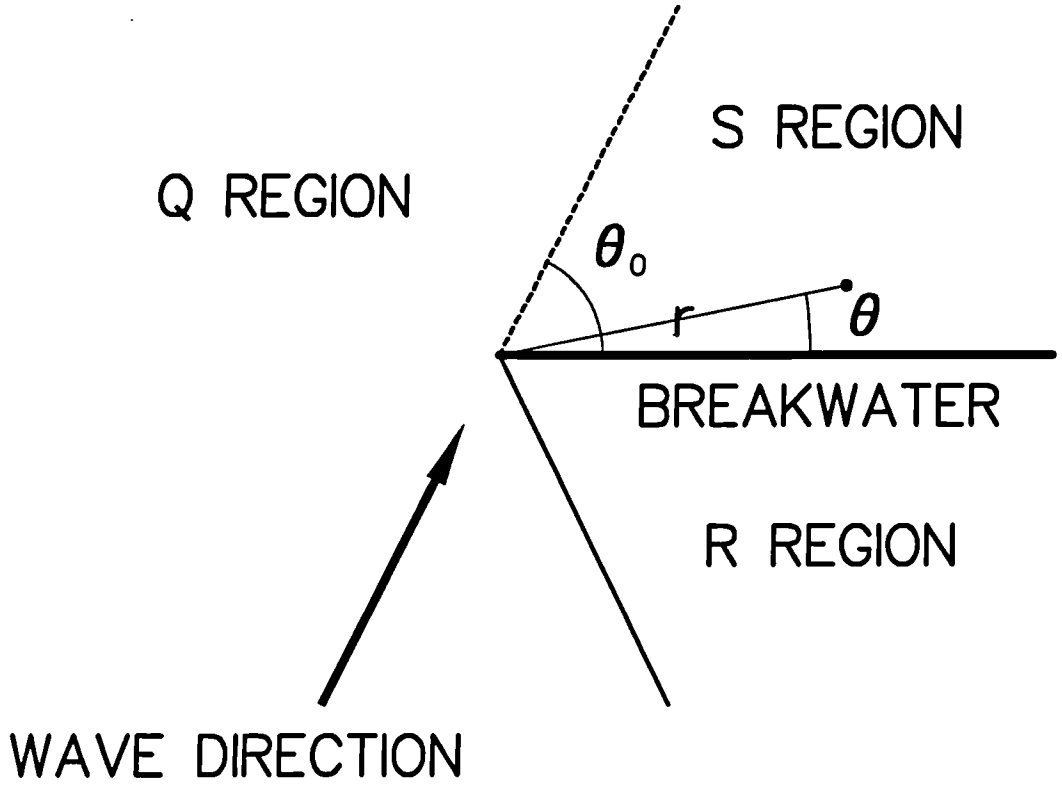
S REGION
Q REGION
θ_0
r
θ
BREAKWATER
R REGION
WAVE DIRECTION

Fig. B.1

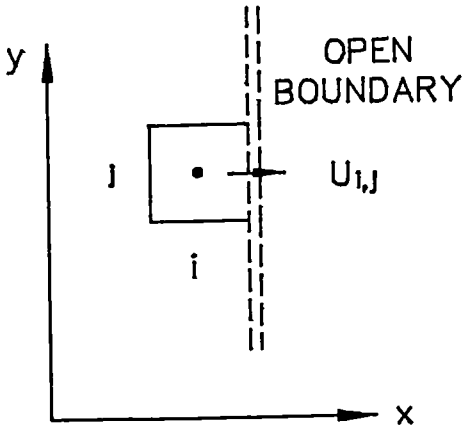

Fig. C.1

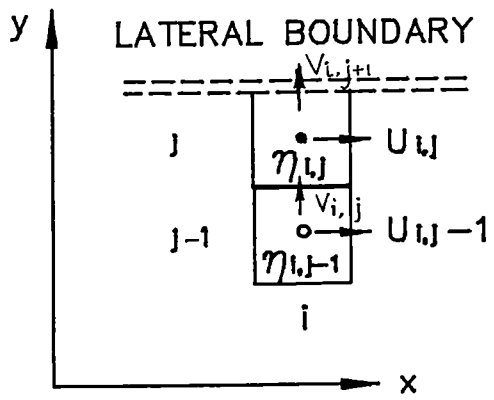

Fig. C.2

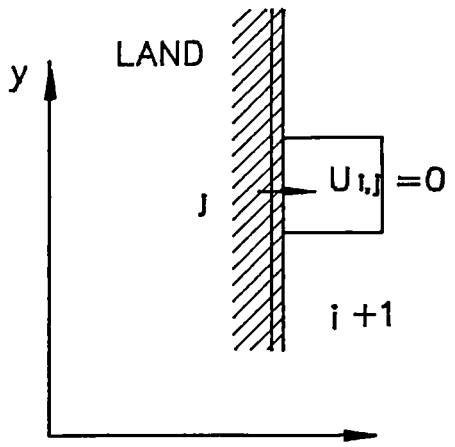

Fig. C.3

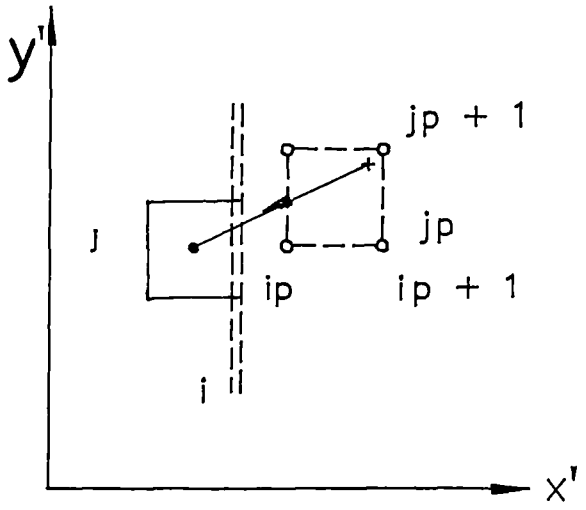

Fig. G.1

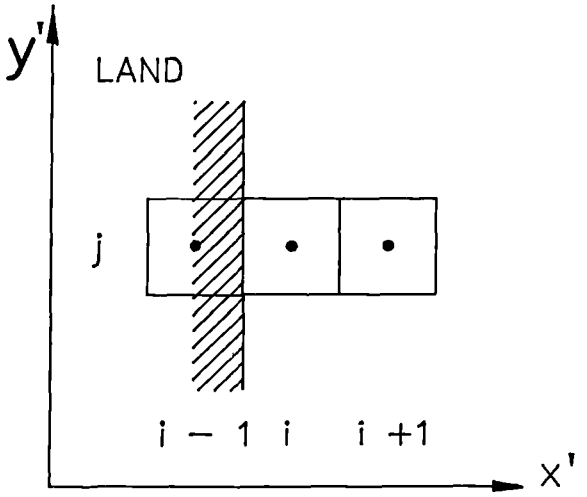

Fig. G.2

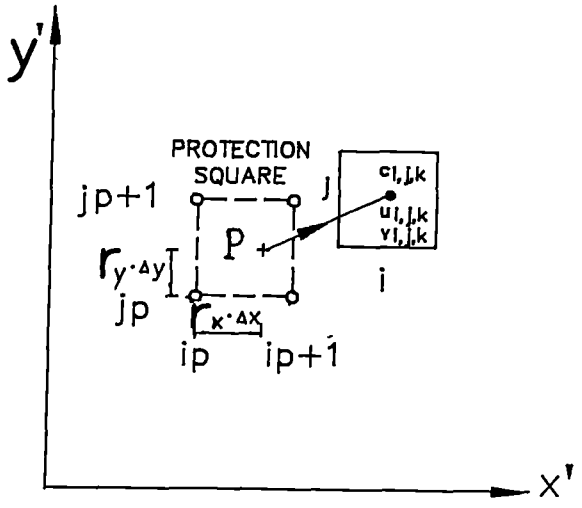

Fig. G.3

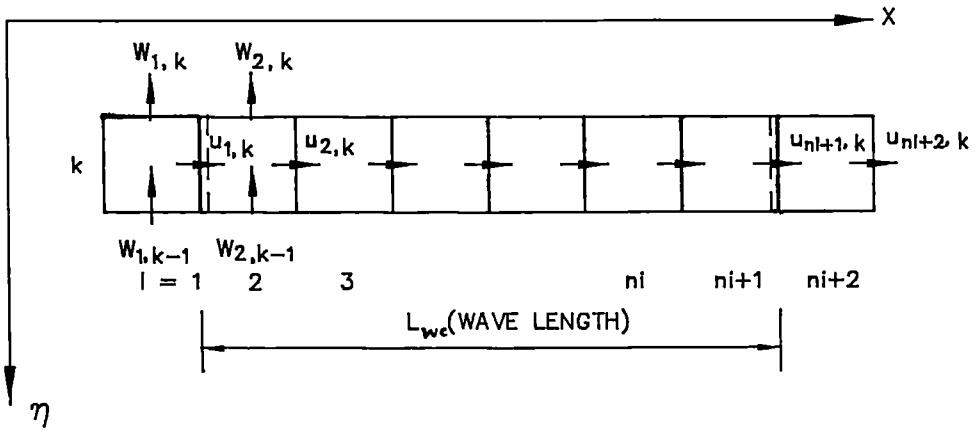
X
W1, k
W2, k
u1, k
u2, k
unl+1, k
unl+2, k
k
W1, k−1
W2, k−1
l = 1
2
3
ni
ni+1
ni+2
Lwc(WAVE LENGTH)
η

Fig. K.1

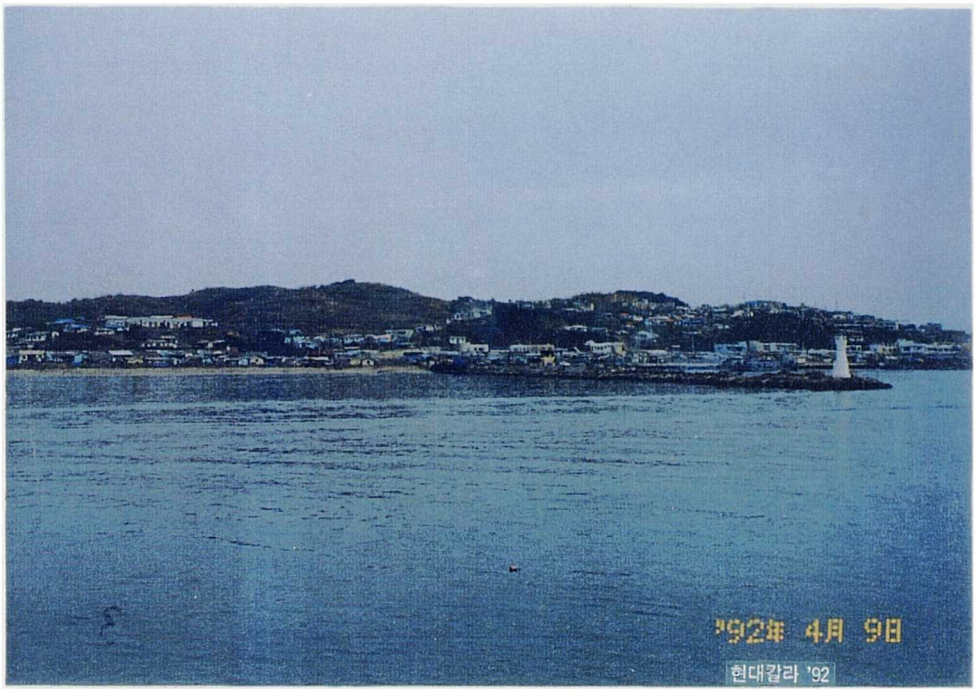

Plate 1.1 **Chukpyon Western Breakwater.**

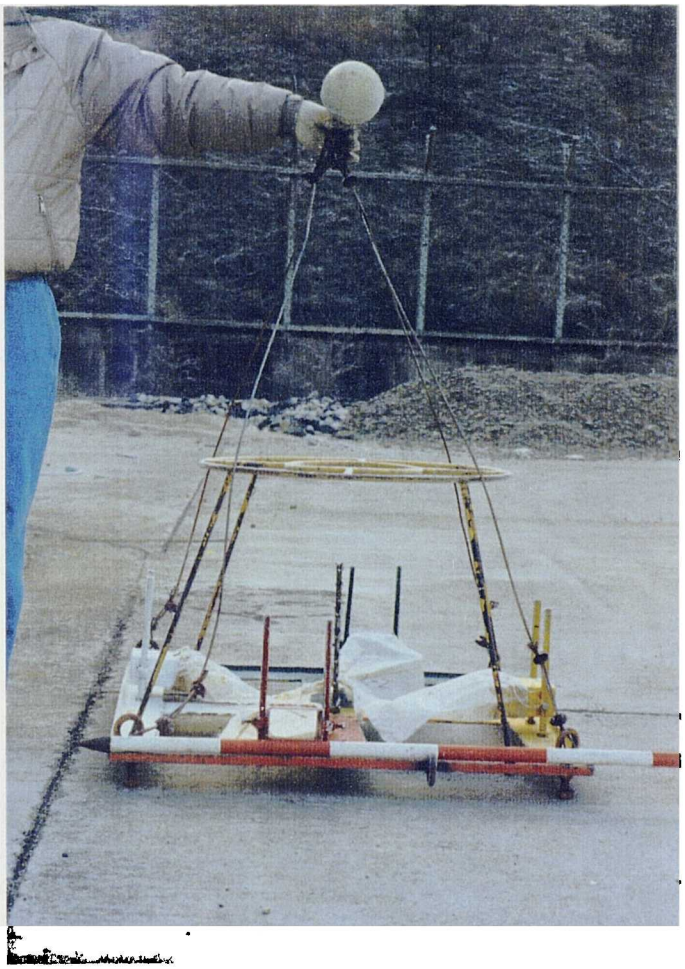

Plate 6.1 **Four-trap device used for measuring reference level suspended sediment concentration.**

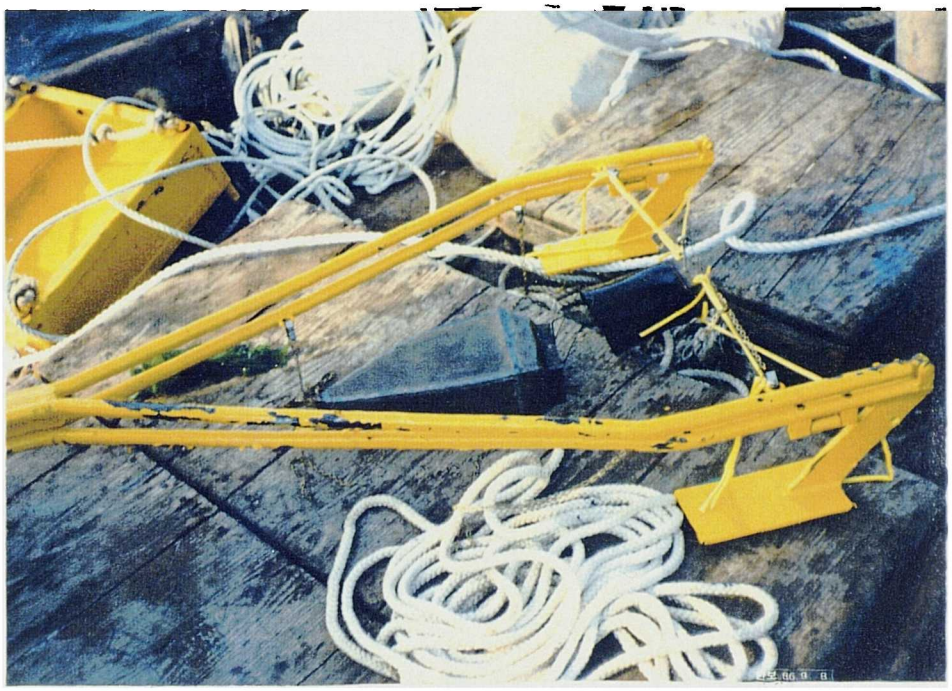

Plate 6.2 ARNHEM bed load sampler.

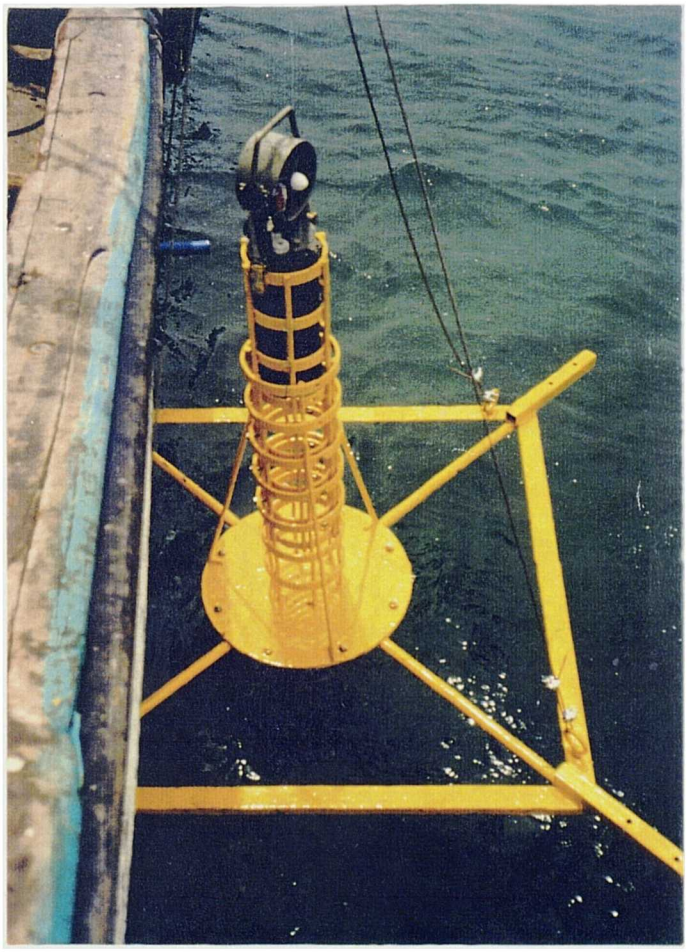

Plate 8.1 RCM-5P and the frame used for measuring wave-induced currents.

Plate 8.2a **HR suspended sediment pump sampler used for measuring suspended sediment concentration: intake pipe.**

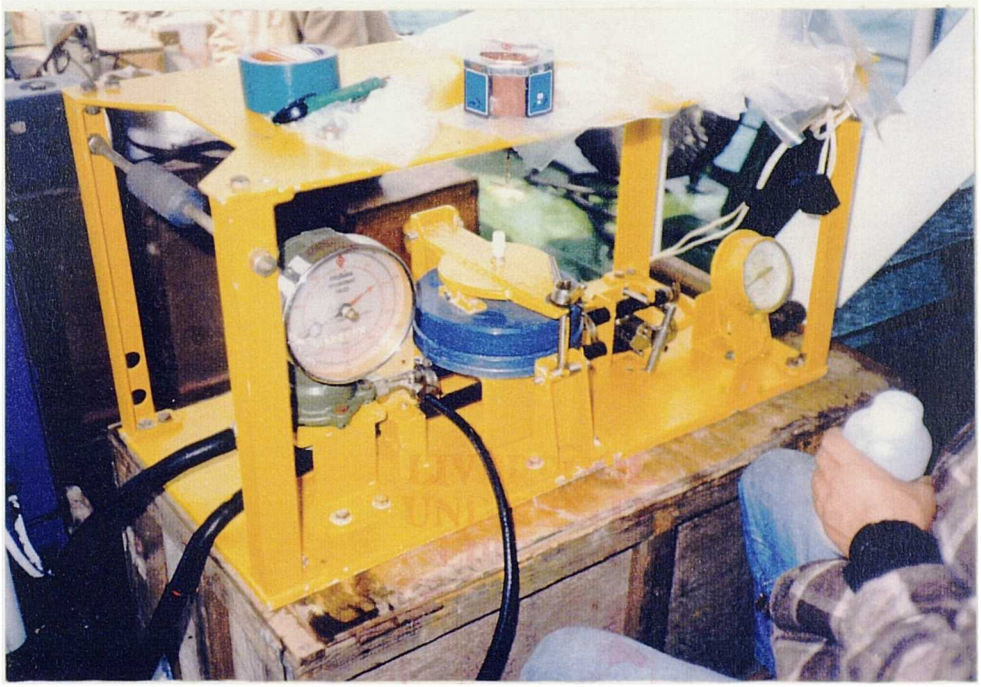

Plate 8.2b **HR suspended sediment pump sampler used for measuring suspended sediment concentration: on-board equipment (filter, discharge gauge).**